Transactions of the ASME®

Transactions of the ASME, Journal of Engineering for Gas Turbines and Power (ISSN 0742-4795) is published quarterly (Jan., April, July, Oct.) by The American Society of Mechanical Engineers, Three Park Avenue, New York, NY 10016. Periodicals postage paid at New York, NY and additional mailing offices. POSTMASTER: Send address changes to Transactions of the ASME, Journal of Engineering for Gas Turbines and Power, c/o THE AMERICAN SOCIETY OF MECHANICAL ENGINEERS, 22 Law Drive, Box 2300, Fairfield, NJ 07007-2300.
CHANGES OF ADDRESS must be received at Society headquarters seven weeks before they are to be effective. Please send old label and new address.
STATEMENT from By-Laws. The Society shall not be responsible for statements or opinions advanced in papers or ... printed in its publications (B7.1, par. 3).

INDEXED by Applied Mechanics Reviews and Engineering Information, Inc. Canadian Goods & Services Tax Registration #126148048

Journal of Engineering for Gas Turbines and Power

Published Quarterly by The American Society of Mechanical Engineers

VOLUME 123 • NUMBER 3 • JULY 2001

TECHNICAL PAPERS

(**Contents continued on inside back cover**)

This journal is printed on acid-free paper, which exceeds the ANSI Z39.48-1992 specification for permanence of paper and library materials. ♾™
♻ 85% recycled content, including 10% post-consumer fibers.

(**Contents continued**)

Journal of Engineering for Gas Turbines and Power **JULY 2001**

Volume 123, Number 3

(**Contents continued on facing page**)

Journal of Engineering for Gas Turbines and Power JULY 2001

Volume 123, Number 3

Power

ANNOUNCEMENTS AND SPECIAL NOTES

Mirror Gas Turbines: A Newly Proposed Method of Exhaust Heat Recovery

S. Fujii
K. Kaneko
K. Otani
Y. Tsujikawa

Department of Aerospace Engineering,
Osaka Prefecture University,
1-1 Gakuen,
Sakai, Osaka 599-8321, Japan

A new conceptual combination of Brayton and inverted Brayton cycles with a heat sink by intercooling, which is dubbed the mirror gas turbine, has been evaluated and proposed in this paper. Prior to such evaluations, a preliminary test on the inverted cycle without intercooling was made experimentally to confirm the actual operation. The conventional method of recuperation in gas turbines can be replaced by the mirror gas turbine with a low working temperature of about 450°C at heat exchanger. The combined cycle of Brayton/Rankine for electricity generation plant may be improved by our concept into a system with steam turbines completely removed and with still high thermal efficiency. Ultra-micro turbines will be possible, producing the output power less than 10 kW as well as thermal efficiency of 20 percent. [DOI: 10.1115/1.1366324]

1 Introduction

Gas turbines operate on the Brayton cycle which begins with compression, heat addition and terminates in expansion. In the inverted Brayton, the processes are reversed in which expansion first occurs and then heat of the working gas is extracted by a heat exchanger and sucked by a fan or compressor. The working principle of this cycle has been explained fully by Wilson [1]. However, nobody has paid attention because the thermal efficiency of cycle is very low. No hardware of test rig has been constructed. On the contrary, many efforts have been concentrated only on the Brayton cycle, mainly in improving the performance of turbomachinery and combustors for the past decades in the real world.

Users of gas turbines have spread in many sectors other than aircraft, which include land industries, marine, vehicles, and electric power generation. Heat energy of exhaust gas would be extremely large and therefore retrieved by cogeneration system in modern industrial gas turbines. The cogeneration is made by hot water and/or steam as a result of using hot gas as a heat source at turbine exit. Gas energy must be once changed and stored in the state of hot water and vapor for use in the cogeneration in a system of Brayton. On the other hand, there may be a possibility for reutilization of exhaust gas directly as a shaft horsepower working with a gas substance if the inverted Brayton cycle can be adequately used.

We conducted the basic experiment on the inverted Brayton cycle, and proceed to evaluate conceptually its applications and potentialities of a new combination of the Brayton/intercooled inverted Brayton cycle on a basis of thermal efficiency.

2 Reconsiderations of Inverted Brayton Cycle

2.1 Basic Experiment. The basic concept is shown in Figs. 1 and 2. Incoming hot gas expands in a process 1 to 2 through a turbine, and cools down from 2 to 3 by a heat exchanger. The compression is made by a compressor or draft fan from 3 to 4. A test rig by use of a radial turbine and compressor of 30-mm diameter was set up as illustrated in Fig. 3. A combustor employing swirl vanes and town gas/air premixture provided hot gas. It was very difficult to fabricate the shaft of connecting compressor and turbine in order to newly add a mechanical starter because it was slender and tiny. Therefore, another compressor driven by an electric motor was placed to start air flow. An increase of rotational speeds by the suction of an assisted compressor and fuel energy additions gave the turbine enough power to keep the rotational speed constant. At this point we gradually opened a valve to realize atmospheric pressure condition at the compressor exit. Finally, the motored compressor was shut down and the set of turbine and compressor was running at an idling speed in the operation mode of the inverted Brayton cycle. Figure 4 indicates various idling speeds experimentally obtained as the turbine inlet temperature was changed. This method of using an assisted compressor may be considered as a kind of aerodynamic starter for going up into idling speeds instead of a mechanically driven starting system for a general use in gas turbines.

Pipelines of the idling test rig were modified for the next test to confirm power generation as is shown in Fig. 5. For this time, the inverted Brayton cycle comprised the turbine and assisted motored compressor, although they were not connected to each other by a single shaft. Typical data showing a power difference between turbine and compressor is explained in the temperature/entropy diagram of Fig. 6. The measured adiabatic efficiency of turbine and compressor was plotted in Fig. 7. The turbine efficiency was pretty low because of operations far from the design point, since a flow rate of hot gas was up to 0.02 kg/s due to the capacity of combustion system. The set of compressor and turbine used in the tests was originally designed for the turbocharger of a small car engine with a gas flow rate of 0.06kg/s. All experimental data were based on total tubes and wall taps, and the thermocouple survey at each section is denoted by x in Fig. 3. The distribution of pressure and temperature at all sectional areas was almost flat. The uncertainty of measured pressure and temperature might be 10 Pa and 1 deg, respectively. Rotational speeds were

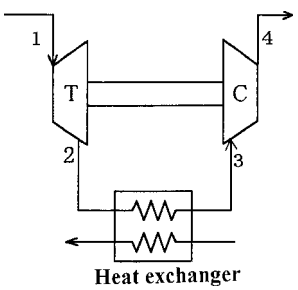

Fig. 1 Conceptual overview of inverted Brayton cycle

Contributed by the Advanced Energy Systems Division of THE AMERICAN SOCIETY OF MECHANICAL ENGINEERS for publication in the ASME JOURNAL OF ENGINEERING FOR GAS TURBINES AND POWER. Manuscript received by the AES Division, Sept. 2000; final revision received by the ASME Headquarters Oct. 2000. Editor: H. D. Nelson.

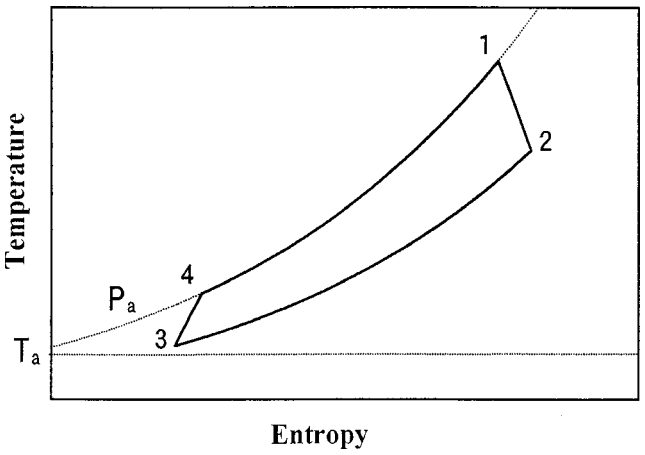

Fig. 2 Temperature and entropy diagram of inverted Brayton cycle

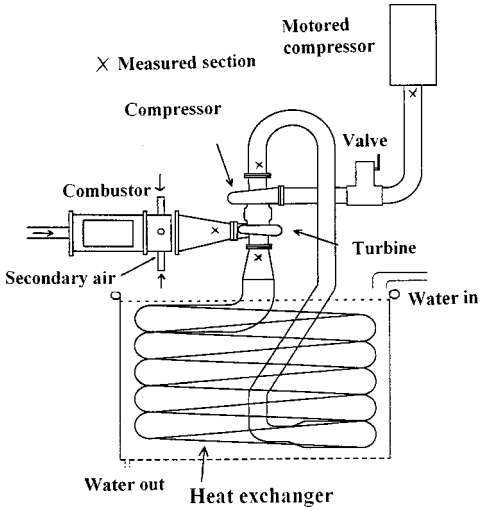

Fig. 3 Test rig of inverted Brayton cycle for idling operation

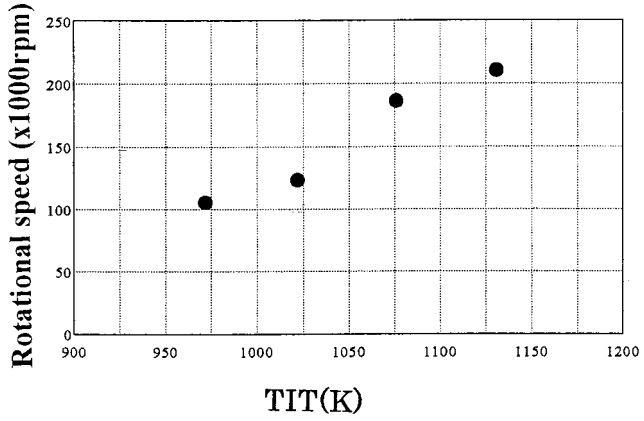

Fig. 4 Idling speeds at various temperature of turbine inlet

determined by the frequency change of the rotating magnetic force generated from a small magnet immersed in the shaft. The possible measurement error would be 4000 rpm.

The thermal efficiency thus obtained was compared with calculations in Fig. 8. Apparently there is a possibility that we have an efficiency of 20 percent with high values of turbomachinery efficiency of 0.9 at the turbine inlet temperature of 1100 K. The measured compression and expansion ratio are shown in Fig. 9.

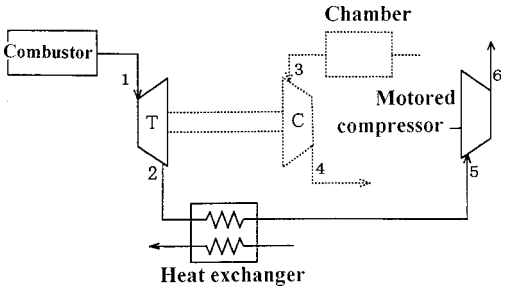

Fig. 5 Test rig for power generation

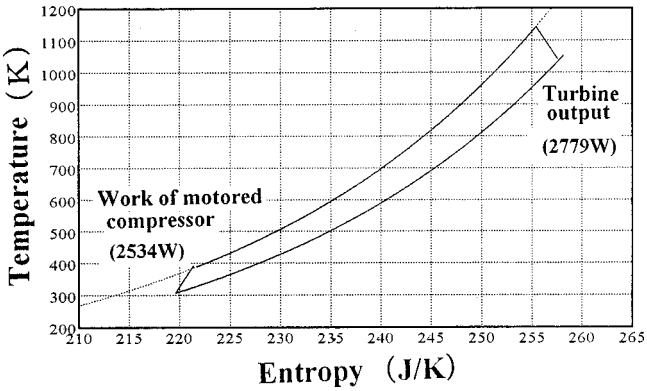

Fig. 6 Temperature and entropy diagram based on measured data

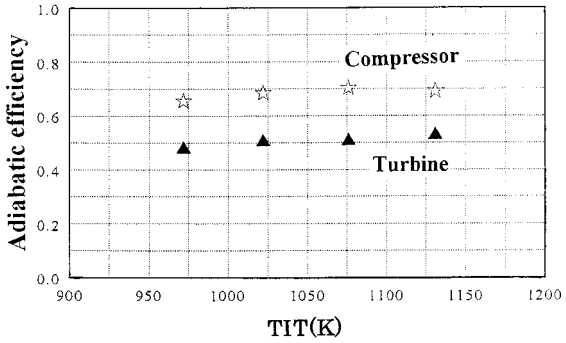

Fig. 7 Measured component efficiency

We assume that there is no loss in a cooling process. The specific power exerted is, with $R=\pi^{\gamma}$,

$$w=C_p(R-1)[RT_1(\eta_r-1)(1-\eta_T)-\eta_T T_1(\eta_C+\eta_r-1)-R\eta_r T_a]/\eta_C R \quad (1)$$

where $\gamma=0.286$ for air. The temperature efficiency of the heat exchanger in this paper is defined as $\eta_r=(T_2-T_3)/(T_2-Tw)$. For example, the heat exchange of working gas with an initial temperature of 616 K and final temperature of 309 K, which is cooled down by use of water with a room temperature of 293 K, may yield a temperature efficiency of $\eta_r=0.95$. Making a partial differentiation of Eq. (1) with R into zero to maximize the power gives an optimum pressure ratio as

$$\pi=[\{\eta_T T_1(\eta_C+\eta_r-1)\}/\{T_1(1-\eta_r)(1-\eta_T)+\eta_r T_a\}]^{1/2\gamma}. \quad (2)$$

If we have $\eta_r=1$, Eq. (2) reduces to

$$\pi=(\eta_T\eta_C T_1/T_a)^{1/2\gamma} \quad (3)$$

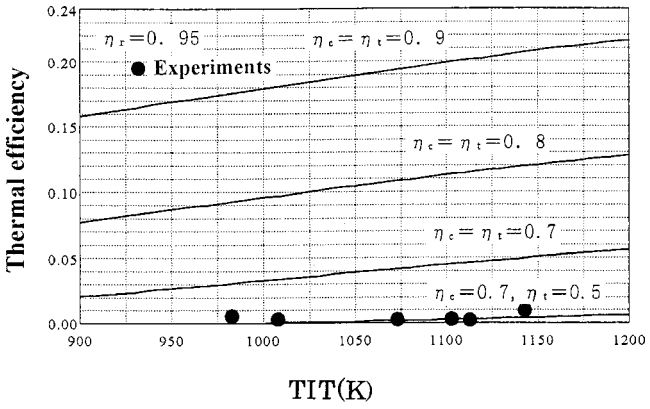

Fig. 8 Thermal efficiency of inverted Brayton cycle

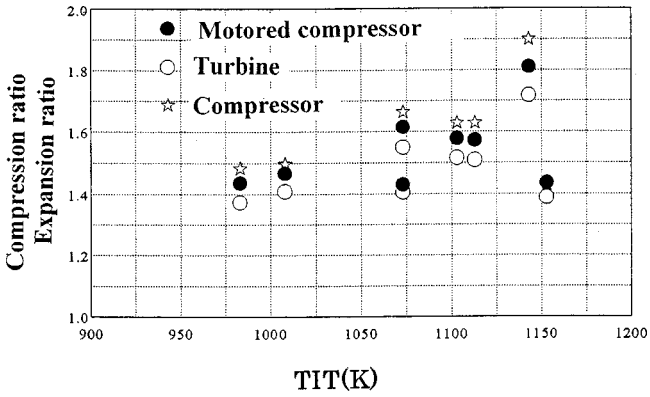

Fig. 9 Measured compression and expansion ratio

which is exactly equal to the expression of giving optimum pressure ratio in Brayton cycle.

2.2 Inter Cooling of Compression Process. The technique of cooling at intermediate processes of compression has sometimes been employed to raise the overall thermal efficiency of gas turbines. However, lowering of air temperature in entering a combustor requires a much larger fuel flow rate than that before cooling, particularly in case of a high turbine inlet temperature and high values of adiabatic efficiency of turbomachinery with large pressure ratio. Therefore, the intercooling sometimes gives no benefit. On the contrary, there is no burning in the inverted Brayton so that the thermal efficiency becomes always higher as the strength of a heat sink by the intercooling is much more increased. It can be fairly said that the intercooling is surely an effective way to improve the thermal efficiency only in the inverted Brayton machine.

Figure 10 is a calculation of indicating the effect of a number of cooling steps on thermal efficiency for three values of adiabatic efficiency of turbomachines at the turbine inlet temperature of 1200 K. It is revealed that three steps of intercooling may be most efficient from a viewpoint of engineering. The thermal efficiency of 30 percent would be possible at an inlet temperature of 1200 K with component efficiency of 0.9. which is an eight percent improvement in thermal efficiency from the uncooled cycle mentioned previously.

In the above discussions we assume no flow loss in all the cooling-down processes for simplicity, as was made in deriving Eq. (1). It can be then considered that such losses would be included in compressor and/or turbine adiabatic efficiency.

3 Proposals of Mirror Gas Turbines

3.1 Recuperation. The recuperation of an exhaust gas in front of a burning process has been made for many years to decrease the flow rate of fuel for an given output power and hence raise the overall thermal efficiency. However, complete heat exchange between hot gas and cold gas may be considered as one of the most difficult techniques. Particularly the materials of an exchanger must be changed into a super alloy or ceramics from a conventional aluminum alloy if the working gas temperature becomes high. Thermal properties of such high-cost materials are not necessarily of good quality for efficient heat transfer and not easy for fabrication. At the present time, to the authors' knowledge, a heat exchanger of a super alloy has not yet been successful in the commercial market of gas turbines.

We propose another method to raise thermal efficiency by use of an intercooled inverted Brayton cycle. A conceptual configuration of our proposed application and the corresponding temperature/entropy diagram are shown in Figs. 11 and 12. It can be said that the conventional gas turbine works as a topping cycle together with a bottoming cycle of an inverted Brayton. Compression, burning, and expansion, and then reversedly expansion,

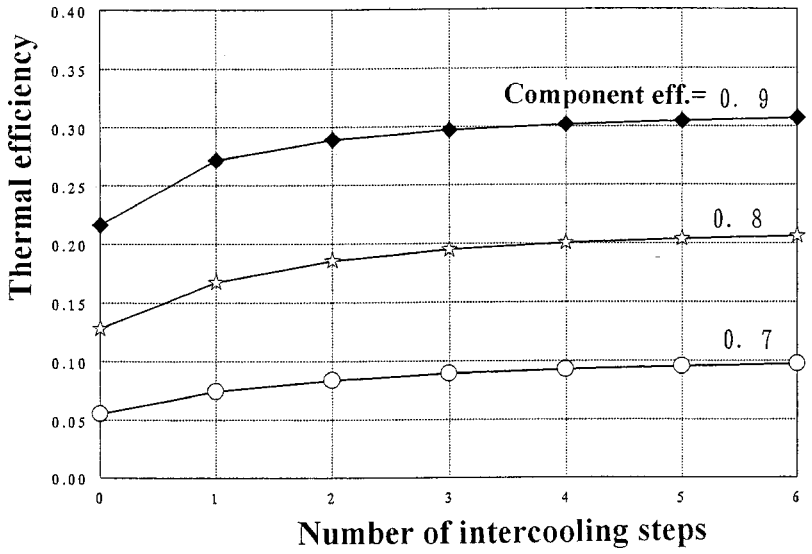

Fig. 10 Number of intercooling steps and efficiency

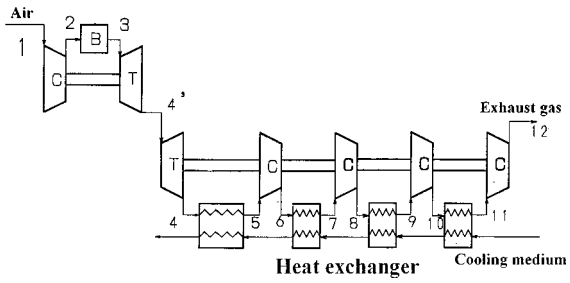

Fig. 11 Mirror gas turbine

cooling down, and compression would continuously proceed. It can be imagined that this might be realized as a result of reflection by a mirror virtually placed between both cycles. We dub herein the whole cycle as a ''mirror gas turbine.'' The main feature of a mirror cycle is that thermal efficiency may be raised up by an additional power generation from the bottoming cycle while the fuel flow rate is kept the same as that of a single gas turbine. Another feature is seen in the temperature/entropy diagram that the regime below atmospheric pressure but still above the surrounding temperature, which has never been taken into account in conventional gas turbines, will play an important role in energy utilization.

Calculated results of thermal efficiency of a mirror gas turbine are plotted and compared with those of a recuperated gas turbine in Figs. 13, 14, and 15 for three values of adiabatic efficiency of turbomachines. It is assumed that the temperature efficiency of 0.95 may be possible in the gas-to-liquid heat exchange of mirror gas turbines with a working temperature less than 725 K (=452°C). The thermal efficiency discussed herein is an overall efficiency of top and bottom cycles as a result of computer optimizations. However, the pressure ratio for a bottoming cycle is not necessarily taken as an optimum value for preventing large diameters of turbomachines in the inverted Brayton, which will be discussed later. In each figure the digits on solid lines indicate the number of intercooling steps while three values of 0.75, 0.5, and 0.25 are the temperature efficiency of heat exchange in recuperation. The temperature efficiency of 0.75 may be considered as a maximum value attainable in a gas-to-gas heat exchanger with the working temperature larger than 800 K. As the Fig. 13 shows, in case of adiabatic efficiency of 0.80, the thermal efficiency of a

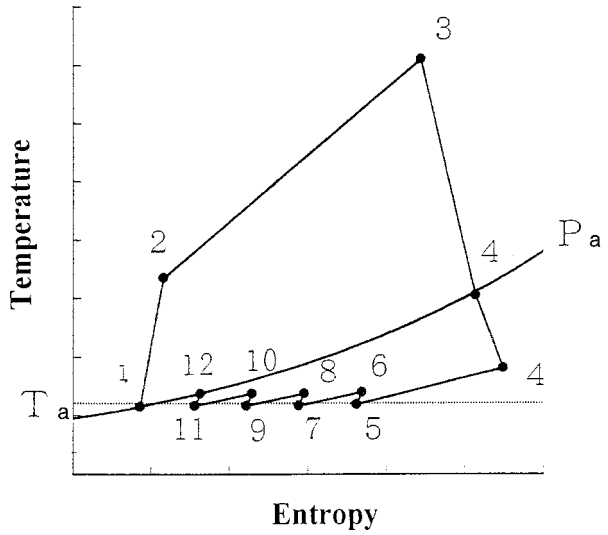

Fig. 12 Temperature and entropy diagram of mirror gas turbine

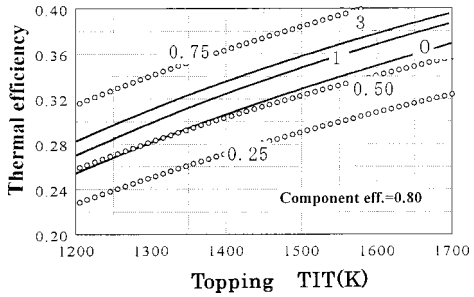

Fig. 13 Comparisons of mirror and recuperated gas turbine: solid lines indicate mirror gas turbines: white small circle lines indicate recuperated gas turbines at working temperature of 800–1000 K of a heat exchanger

recuperated gas turbine has a larger value than that of a mirror cycle only if we make a success of obtaining an extremely high temperature efficiency of 0.75 in gas-to-gas heat exchange at a working temperature of around 1000 K. If the temperature efficiency of the recuperator drops into some value between 0.75 and 0.50, the thermal efficiency of both cycles becomes competitive with each other. As the adiabatic efficiency of components goes up to 0.85, there will arise a case that the mirror cycle may be superior to the recuperated cycle, which strongly depends on how much the recuperation efficiency can attain with durability and dependability under conditions of a high working temperature of around 1000K. At the component efficiency of 0.90, which would be possible only in large diameter machines, the mirror gas turbine always has a larger value of thermal efficiency even with an uncooled bottoming cycle and a much lower working temperature than those of a recuperated gas turbine. It may be recommended that aluminum alloys be used in the heat exchanger of mirror gas turbines, additionally providing hot water as a side product by

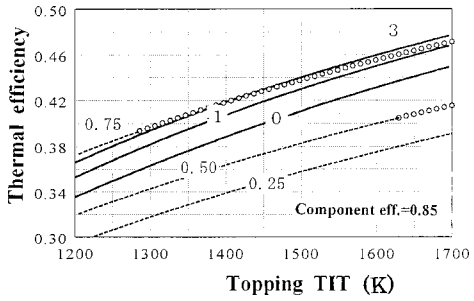

Fig. 14 Comparisons of mirror and recuperated gas turbines: dashed lines show recuperated gas turbines at working temperature of 750–800 K; white small circle lines indicate gas turbines with recuperator of 800–1000 K

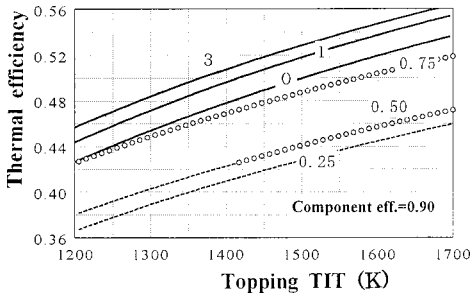

Fig. 15 Comparisons of mirror and regenerative gas turbines; solid lines indicate mirror gas turbines: small circle and dashed lines are for recuperated gas turbines

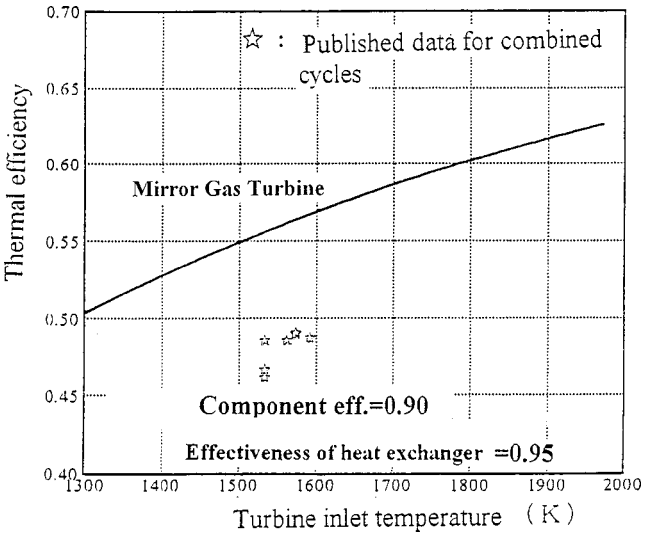

Fig. 16 Comparisons of mirror and combined cycle gas turbines

gas-to-water heat exchange if we suffer from a low value of efficiency of around 0.5 in a gas-to-gas heat exchanger working at a significantly high temperature of 1000 K.

3.2 Comparison With Combined Cycle. Figure 15 reveals that the conventional method of recuperation has disadvantages in the regime of high component efficiency of 0.90. Therefore, large gas turbines with a very high pressure ratio, in which it is no longer possible to employ the recuperation due to enough high temperature at the compressor exit, have been usually operated as a combined cycle of Brayton and Rankine cycles. The exhaust heat energy in the Brayton cycle has been recovered by steam turbines at a high pressure of 180–200 times the atmospheric pressure in the Rankine cycle. We tried to make a comparison of mirror and combined cycles in Fig. 16. Points denoted by stars in the figure indicate the thermal efficiency of combined gas turbines, published in the open literature, which is the experimental data in field tests during the yeas 1995–1998 by the Japanese turbine industries. The combined cycles cited herein have the compressor pressure ratio of 14–19 with a single or double shaft. Most of the output power is around 160 MW. All calculations were made by a computer optimization to obtain the maximum value of overall thermal efficiency in the mirror cycle. In comparing heat balance data for the actual combined cycle of the pressure ratio of 16 with the turbine inlet temperature of 1800 K, the corresponding proposed cycle gives an optimum pressure ratio of 25 with the lower exhaust temperature of around 100 degrees than that of the conventional gas turbine. The output power ratio of a topping and bottoming cycle is around 2.5.

The measured efficiency of turbomachines was reported as 0.90 and more for those gas turbines. A calculation of a mirror cycle with component efficiency of 0.90 is compared with the star points. An improvement of thermal efficiency by the employment of a mirror cycle can be recognized. However, this is a simple comparison between the measured and the calculated data. It is hoped that the hardware of the mirror cycle will be made for true comparisons in the future. This comparison implies that steam turbines may be replaced by the inverted Brayton. In other words, the mirror gas turbine, that is a set of positive and negative gas turbines, may be competitive with the combined gas and steam turbine. It is tentatively concluded that technical difficulties of using a high pressure and temperature steam turbine with a boiler, condenser, and pump will be removed by successful use of the mirror gas turbine in the future.

3.3 Selection of Pressure Ratio. The simple gas turbines with and without recuperation have the maximum output power at an optimum pressure ratio, which depends on turbomachinery efficiency and turbine inlet temperature. The power and efficiency are not maximized at the same pressure ratio. The pressure ratio of giving maximum thermal efficiency is usually higher than that of maximum power without recuperation. By recuperation the maximum efficiency point approaches the optimum pressure ratio and then goes down in cases with high efficient regeneration. This comes from the fact that input fuel energy depends on pressure ratio, output power, and recuperation. On the other hand, the mirror gas turbines have a set of two pressure ratios which would give the maximum overall efficiency. The mirror gas turbine efficiency is written as

$$\eta = (Wg + Wt)/Q, \tag{4}$$

that is, the efficiency is increased by additional power of the inverted Brayton, Wt, with input fuel energy, Q, kept as constant. The topping cycle efficiency is given by Wg/Q. As is well known, the single gas turbine efficiency is improved by the decrease of Q by recuperation with Wg constant. In a mirror gas turbine, however, the maximization of gas turbine efficiency at the topping cycle does not necessarily give the maximum overall efficiency. The values of Wg, Wt are a function of two pressure ratios of topping and bottoming cycles that interact with each other. We must find the maximum by computer optimization in changing pressure ratios. The optimum pressure ratio of an inverted Brayton, given in Eq. (2), has one constraint in actual application. As the pressure ratio is increased, that diameters of proceeding turbomachines must be made large to prevent a rapid acceleration of axial velocity in flows. Therefore, the pressure ratio of bottoming cycle is limited to 4 in all the calculations made above. The limit of 4 means that the diameter becomes 1.7 times greater than that of the topping cycle for no acceleration of axial flows through the turbine, taking into account the change in both gas density and temperature. If the further enlargement of the diameter of the compressor and the turbine is not tolerable for large gas turbines, it is suggested that two bottoming cycle machines should be placed in parallel. For small mirror gas turbines, an increase of diameter and hence of the Reynolds number will be beneficial to the component adiabatic efficiency. In our estimation the drop of overall efficiency is approximately two to three percent by a deviation of the pressure ratio from the optimum for the large gas turbine with adiabatic efficiency of 0.9.

The compressor of the bottoming cycle works under negative 0.25 times atmospheric pressure. An aeroengine compressor of high subsonic aircrafts cruising at an alutitude of 10,000 meters high will receive a total pressure of 0.30 times atmospheric in front. It must be kept in mind that the compressor design is made to minimize the performance deterioration due to low Reynolds numbers.

The characteristics of the heat exchanger under negative pressure can be discussed by use of two parameters. One is the dynamic pressure given by $\rho U^2/2 = mU/2$, which is directly proportional to the flow loss. In order to avoid the loss increase we must enlarge the size of the exchanger at the early stages but can gradually decrease the volume due to the increase of density through the compressor towards the latter stages. Drops of temperature by intercooling with pressure increase attendant make the flow Mach number lower in the downstream than at the inlet. The other is the Reynolds number defined as mL/μ, leading to the rate of heat transfer. Provided that a mass flow rate is not changed, a heat exchange rate is not promoted nor decreased under negative pressure.

3.4 A Possibility of an Ultra-Micro Turbine. Recently the name microturbine has appeared, which would be understood as the small gas turbine without turbine cooling in the output power of 30–300 kW. The tiny gas turbine less than 10 kW in output power can be called the ultramicro turbine in this sense. However,

at the present state of the art, ultramicro turbomachines will show very low efficiency due to the low Reynolds number for a small diameter with extremely high revolutions, which require a new alternator of very high frequency, and the recuperation does not work nicely at a small heat exchanger with rather high temperature of around 1000 K (=727°C).

We consider the application of a mirror gas turbine to the ultramicro field. The topping cycle machine has a small diameter working with an idling speed and the bottoming one possesses rather large diameters in turbomachines with intercooling. The overall thermal efficiency will rely only on the bottoming cycle. The topping cycle will play a role simply as a heat source. Equation (4) is rewritten by use of each efficiency,

$$\eta = \eta_g + (W_t/Q_t)(Q_t/Q) = \eta_g + \eta_t(1-\eta_g). \tag{5}$$

The effect of bottoming cycle efficiency on the overall efficiency is maximized when the topping cycle is operating at an idling speed. The basic scheme is that without diminishing the size of the bottoming cycle turbomachines we may have a tiny gas turbine with ultrasmall output in high thermal efficiency. Hot water will be again provided as a side product. From the calculations made it is revealed that there will be a possibility to produce an ultramicro turbine with the thermal efficiency of 20 percent. We can enjoy a small gas turbine with a large turndown ratio in the range of 30–6 kW. If there is no need to switch the micro to the ultramicro operation, we can employ an original combination of burner in front, turbine, and intercooled compressor. It may be said that the Brayton cycle cannot be diminished into ultramicro turbine, but that the inverted Brayton cycle would be operated as the ultramicro, mainly due to a small specific output power. A maximum of power and efficiency occurs at the same pressure ratio in the single operation of the inverted Brayton cycle because that input of exhaust energy is independent and not changed.

4 Conclusions

The first hardware test on inverted Brayton cycle was successfully made by use of tiny turbomachines to confirm the operation of inverted processes of expansion, cooling, and draft. It is calculated that drawbacks encountered in the inverted cycle may be improved by intercooling, showing a possibility of additionally raising up another eight percent in thermal efficiency.

A concept of mirror gas turbines has been proposed by a combination of Brayton and inverted Brayton cycles with intercooling employed. Exhaust heat energy from the topping gas turbine can be retrieved by the bottoming inverted Brayton. The mirror gas turbine may be applied to many fields in the recuperation, combined Brayton/Rankine cycle with great promise. The possibility of an ultramicro gas turbine is finally suggested. Hardware tests for the mirror gas turbine will be the next step in this research program to show potentialities of concept and configurations proposed in the present paper in the near future.

Another application of the mirror cycle can be considered for the gasification of LNG (liquid natural gas). Although it is only at the stage of a conceptual study, we have much better results of overall thermal efficiency in comparison with the conventional gasification terminals in Japan which use sea water. See the reference of Tsujikawa [2] for details. A study of energy recovery with a high temperature of 1200 K from a fuel cell (SOFC) is being conducted at the authors' institute by use of the inverted cycle turbomachines.

Nomenclature

B = burner
C = compressor
C_p = specific heat at constant pressure
L = length
P = pressure
P_a = atmospheric pressure
T = turbine or temperature
T_1 = turbine inlet temperature for inverted Brayton cycle
T_a = atmospheric or surrounding temperature
T_w = initial temperature of cooling medium
U = flow velocity
m = mass flow rate
Q = input heat energy
Q_t = exhaust heat energy
Wg = power of Brayton cycle
Wt = power exerted by inverted Brayton cycle
w = specific power
R = π^{γ}
π = compression or expansion pressure ratio
π_C = compression ratio
π_t = expansion ratio
η = thermal efficiency of mirror gas turbine
η_C = adiabatic efficiency of compressor
η_T = adiabatic efficiency of turbine
η_r = temperature efficiency of heat exchange
η_g = thermal efficiency of topping cycle
η_t = thermal efficiency of bottoming cycle
γ = $(\kappa-1)/\kappa$; 0.286 for air
κ = specific heat ratio
μ = friction coefficient for laminar flow
ρ = density

References

[1] Wilson, D. G., 1985, *The Design of High Efficiency Turbomachinery and Gas Turbine* M.I.T. Press, Cambridge, MA.

[2] Tsujikawa. Y., Kaneko, K, and Fujii, S., 2000, ''Utilization of Cryogenic Energy of LNG by Mirror Gas Turbine'' Paper No. 00-GT-0317, ASME Turbo Expo. Munich, Germany.

Limitations on Gas Turbine Performance Imposed by Large Turbine Cooling Flows

J. H. Horlock
Whittle Laboratory,
Engineering Department,
Cambridge University,
Madinglet Road,
Cambridge CB3 0DY UK

D. T. Watson
Rolls Royce plc,
Derby, UK

T. V. Jones
Osney Laboratory,
Engineering Science Department,
Oxford University,
Oxford, UK

Calculations of the performance of modern gas turbines usually include allowance for cooling air flow rate; assumptions are made for the amount of the cooling air bled from the compressor, as a fraction of the mainstream flow, but this fractional figure is often set in relatively arbitrary fashion. There are two essential effects of turbine blade cooling: (i) the reduction of the gas stagnation temperature at exit from the combustion chamber (entry to the first nozzle row) to a lower stagnation temperature at entry to the first rotor and (ii) a pressure loss resulting from mixing the cooling air with the mainstream. Similar effects occur in the following cooled blade rows. The paper reviews established methods for determining the amount of cooling air required and semi-empirical relations, for film cooled blading with thermal barrier coatings, are derived. Similarly, the pressure losses related to elements of cooling air leaving at various points round the blade surface are integrated over the whole blade. This gives another semi-empirical expression, this time for the complete mixing pressure loss in the blade row, as a function of the total cooling air used. These two relationships are then used in comprehensive calculations of the performance of a simple open-cycle gas turbine. for varying combustion temperature and pressure ratio. These calculations suggest that for maximum plant efficiency there may be a limiting combustion temperature (below that which would be set by stoichiometric combustion). For a given combustion temperature, the optimum pressure ratio is reduced by the effect of cooling air. [DOI: 10.1115/1.1373398]

1 Introduction

It is well established that the thermal efficiency of a gas turbine increases with its maximum nominal temperature, which will be denoted here as T_3. Within limits this statement is true for all gas turbine based cycles and can be sustained, although not indefinitely, as long as the optimum pressure ratio is selected for any value of T_3; further the specific power increases with T_3. But higher T_3 requires improved combustion technology, particularly if an increase in harmful emissions such as NO_x is to be avoided.

The temperature T_3 is therefore an important indicator of overall cycle performance, which is demonstrated by the fact that there is a near term desire to achieve maximum temperatures in excess of 2000 K. This paper examines and identifies the potential constraints or barriers faced in exploiting higher values of T_3.

For modern gas turbine based systems, which are cooled, a precise definition of T_3 is difficult; Mukherjee [1] has suggested three possible definitions, $(T_3)'$, $(T_3)''$, and $(T_3)'''$. The first is the combustor outlet temperature (T_{cot}) which is based on the averaged temperature at exit from the combustion chamber, so that $(T_3)'$ equals T_{cot}. However, in a practical system, this does not take into account the effect of cooling flows that are introduced in subsequent turbine components (nozzle guide vane and rotor rows). So a second definition, the rotor inlet temperature (T_{rit}) has tended to be used more widely within the gas turbine industry (Walsh and Fletcher [2]). T_{rit} is based on the averaged temperature taken at entry to the first rotor section (i.e., the exit of nozzle guide vanes 1, NGV1). T_{rit} can be calculated assuming that NGV1 cooling air has completely mixed with the mainstream, giving $(T_3)''=T_{rit}$. A third definition, the so-called ISO firing temperature, T_{ISO}, can be calculated from the combustion equations and a known fuel-air ratio to give $(T_3)'''=T_{ISO}$, but this definition is less frequently used.

T_{cot} and T_{rit} are both important in the understanding of relative merits of candidate systems, as evidenced in recent studies of closed loop cooling systems (see, for example, Watson and Ritchey [3]). In this respect we shall be emphasizing the significant difference between T_{cot} and T_{rit}. Without improvements in materials and/or heat transfer, it is doubtful whether much higher T_{rit} values can be achieved in practice; as a result, a practical limit on plant efficiency may be near, before the stoichiometric limit is reached.

The work presented here is related to the power generation plants but it has relevance for the aircraft gas turbine (the specific fuel consumption of which is inversely proportional to the product of the thermal efficiency and the propulsive efficiency), and to marine propulsion systems.

2 Cycle Calculations

The impact on performance of using some compressor air to cool certain turbine components (e.g., where air is abstracted at the compressor delivery pressure and temperature (p_2, T_2) or other intermediate pressures within the compressor) has been studied extensively. Two main approaches can be identified.

In the first of these, Traupel [4], Hawthorne [5], El-Masri [6], and Bolland and Stadhaas [7] all considered the effect of continuous cooling on the turbine expansion line, together with the consequent changes in polytropic efficiency and reheat factor that this brings (i.e., an infinite number of small stages is implied). In the second approach, developed by El-Masri [8], Brown et al. [9], and others, consideration of the effect of cooling on individual (i.e., discrete) blade rows is considered.

The latter approach, being closer to the situation in a real gas turbine implementation, is adopted here. It requires the develop-

Contributed by the Advanced Energy Systems Division of THE AMERICAN SOCIETY OF MECHANICAL ENGINEERS for publication in the ASME JOURNAL OF ENGINEERING FOR GAS TURBINES AND POWER. Manuscript received by the AES Division, Sept. 2000; final revision, Feb. 2001. Editor: H. D. Nelson.

ment of a cooling system model, and broadly involves the following steps: (i) an estimate of the open loop/film cooling air flow required in each cooled blade row (e.g., NGV1 of the high pressure (HP) turbine); (ii) the drop in stagnation temperature and the loss in total pressure associated with each stage of cooling (i.e., the effect on heat exchange between the mainstream and cooling flows and their subsequent mixing); and (iii) integration of (i) and (ii) into a cycle calculation.

The estimate of the required cooling airflow depends on a number of critical parameters including the allowable component (blade) material temperature (T_{bl}), the coolant supply temperature (T_{ci}), and the details of the internal and external heat transfer process involved in cooling turbine components. In this respect we both use and develop some of the published work for calculating the required coolant mass flow (w_c) which is normally expressed as a fraction (ξ) of the mainstream hot gas mass flow (w_g).

2.1 Previous Work. There are many papers in the literature which address the thermal efficiency of various cycles with practical (cooled) turbine configurations, using complex computer codes (e.g., El-Masri [10] and Brown et al. [9]). These have usually involved the consideration of the effects of real gas properties (as opposed to the assumption of a perfect gas as in air standard analyses) and representative types of cycle. However, few have investigated in detail the extrapolation of their work into regions with extremely high values of T_3 (where the assumptions underpinning the cooling model become critically important).

The work of Chiesa et al. [11] was an exception in this respect; it showed some evidence of a peak in thermal efficiency being attained as combustion temperature ($T_{\rm cot}$) was increased. El-Masri [6,8] also gave details of some calculations in which coolant flows achieve very large values, plant efficiency dropping at high $T_{\rm cot}$ and specific power reaching a maximum. It is believed that one element in this effect may have been the artificially high total pressure losses occurring in the later stages in the turbine (El-Masri [12]). These arose because compressor delivery air, at the stagnation pressure p_2, was assumed to be used in the cooling of these stages, which operate at a significantly lower working pressure. In practice it would be more likely for cooling air to be tapped at a lower pressure and temperature requiring less cooling air. (Although there is a mechanism to allow for this in El-Masri's GASCAN code ([10]) this does not seem to have been used in these particular calculations.) We consider this issue again later.

More recent work by MacArthur [13] has involved the study of how coolant flows in industrial gas turbines might be reduced through use of modern aircraft engine practice, leading to increased plant efficiency.

2.2 Computer Codes Used. Two separate codes have been used in this work to obtain overall cycle performance predictions, these are:

(i) a code developed by Young [14], and
(ii) a commercially available code known as PROVISION (distributed by Simulation Sciences).

3 Derivation of Required Cooling Flows

Several approaches to the determination of cooling air flow are given in the literature, see for example Ainley [15], also described by Horlock [16], Holland and Thake [17], El-Masri [8], Bolland and Stadaas [7], and de Ruyck et al. [18]. The general subject of cooling techniques has been summarized by Lakshminarayana [19].

An extension of the Holland and Thake analysis (which allows for external film cooling (flow through the blade surface) as well as internal convective cooling (flow through the internal passages)) is given below. It is based on the assumption that the external Stanton number ($\rm St_g$), which is generally a weak function of the Reynolds number, remains constant as engine design parameters ($T_{\rm cot}$ and r) are changed. But a variation of this approach, based on a constant external heat transfer coefficient (h_g), is also described in detail here.

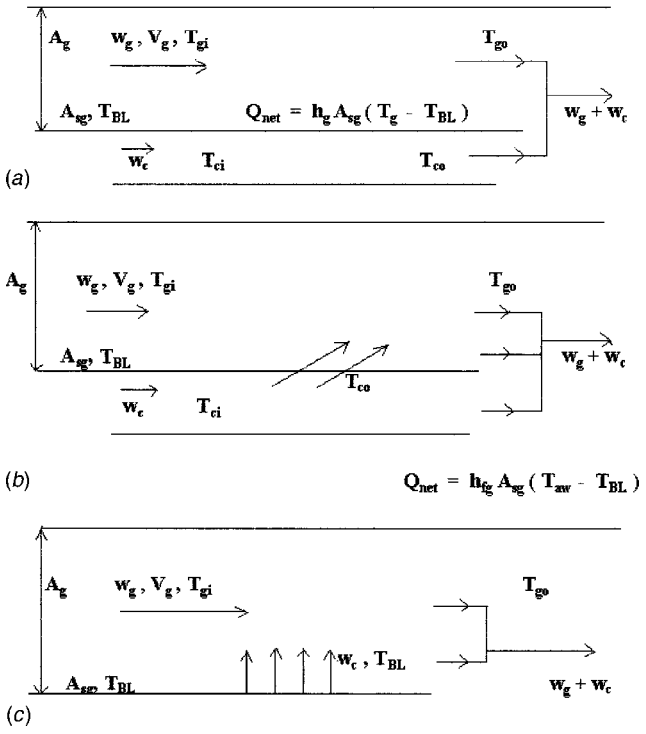

Fig. 1 (*a*) Simple model for convective cooling, (*b*) simple model for film cooling, (*c*) simple model for transpiration cooling

3.1 Convective Cooling Only. A simple heat balance for a typical convectively cooled blade (as illustrated in Fig. 1(*a*), which shows the notation) is

$$Q_{\rm net}=w_c c_{pc}(T_{co}-T_{ci})=w_g c_{pg}(T_{gi}-T_{go})=h_g A_{sg}(T_{gi}-T_{bl}). \tag{1}$$

It is assumed that the temperature of the coolant does not fully reach the temperature of the metal before it leaves the blade, i.e., $T_{co}<T_{bl}$. The concept of a cooling efficiency is introduced

$$\eta=(T_{\rm co}-T_{ci})/(T_{bl}-T_{\rm ci})$$

so that

$$Q_{\rm net}=w_c c_{pc}\,\eta(T_{bl}-T_{co})=w_g c_{pg}(T_{gi}-T_{go})=h_g A_{sg}(T_{gi}-T_{bl}). \tag{2}$$

The exposed area for heat transfer (A_{sg}) is then replaced on the premise that, for a set of similar gas turbines there is a reasonably constant ratio between A_{sg} and the cross-sectional area of the main hot gas flow A_g. Thus writing $A_{sg}=\lambda A_g=\lambda w_g/\rho_g V_g$ in Eq. (2) gives

$$w_c c_{pc}\,\eta(T_{bl}-T_{co})=\lambda[h_g/\rho_g V_g]w_g c_{pg}(T_{gi}-T_{bl})$$

so that

$$[w_c/w_g]=\lambda[c_{pg}/c_{pc}][h_g/c_{pg}\rho_g V_g](T_{gi}-T_{bl})/\eta(T_{bl}-T_{ci})$$
$$=\lambda[c_{pg}/c_{pc}]\rm St_g(T_{gi}-T_{bl})/\eta(T_{bl}-T_{ci}) \tag{3}$$

where $\rm St_g=h_g/(c_{pg}\rho_g V_g)$ is the external Stanton number.

For a row in which the blade length is H, the blade chord is c, the spacing is s and the flow discharge angle is α, the ratio λ is given approximately by $\lambda=A_{sg}/A_g=2\rm Hc/Hs\sin\alpha=2c/s\sin\alpha$.

With $s/c=0.8$ and $\alpha=75$ deg, a value of λ is then about 10. But in fact the total cooled surface area is greater than the surface area of the blade profiles alone, because of the presence of cooled endwall surfaces (adding another 30–40 percent of surface area), complex trailing edges and other cooled components. It would appear from examination of practical engines that $\lambda[c_{pg}/c_{pc}]$ could reasonably be given a value of about 20. Equation (3) then provides the basic form on which several cooling models can be based.

The first, more conventional, model is to take the external Stanton number as constant. Further, writing $(c_{pg}/c_{pc})(A_{sg}/A_g)\mathrm{St}_g$ as a constant C, indicative of a ''level of technology,'' Eq. (1) then becomes

$$\xi=w_c/w_g=Cw^+=C\varepsilon_0/\eta(1-\varepsilon_0), \tag{4}$$

where ε_0 is the overall cooling effectiveness, defined as

$$\varepsilon_0=(T_{gi}-T_{bl})/(T_{gi}-T_{ci}). \tag{5}$$

T_{gi} and T_{ci} are usually determined from and/or specified for the cycle calculation so that the cooling effectiveness, ε_0, implicitly becomes a requirement (subject to T_{bl} which again can be assumed for a ''level of technology'').

If η and C are amalgamated into a single constant K, then

$$\xi=K\varepsilon_0/(1-\varepsilon_0). \tag{6}$$

With $\eta=0.7$ and $C=0.035$ say, $K=0.05$ and Eq. (6) then correlates well with values used by El-Masri [8,10].

A second less conventional model is to assume that h_g is constant and that the specific mass flow is in a choking condition so that, taking the inlet gas conditions as representative,

$$\rho_g V_g=[2/(\gamma_g+1)]^{(\gamma_g+1)/2(\gamma_g-1)}p_g(\gamma_g/R_gT_g)^{1/2}.$$

It then follows that

$$\xi=w_c/w_g=[(\gamma_g+1)/2]^{(\gamma_g+1)/2(\gamma_g-1)}[\lambda/c_{pc}]\times\{R_gT_g/\gamma_g)^{1/2}/p_g\}\{h_g[T_g-T_{bl}]/\eta[T_{bl}-T_{ci}]\} \tag{7}$$

$$w_c/w_g=C'[T_g^{1/2}/p_g]\varepsilon_0/\eta[1-\varepsilon_0] \tag{7a}$$

where C' is another constant. Representative values for C and C' are derived below.

3.2 Film Cooling. The model used when film cooling is present is indicated in Fig. 1(*b*). Cooling air at temperature T_{co} is discharged into the mainstream through the holes in the blade surface to form a cooling film. The heat transferred is now

$$Q_{\mathrm{net}}=A_{sg}h_{fg}[T_{aw}-T_{bl}]=w_cc_{pc}[T_{co}-T_{ci}] \tag{8}$$

where T_{aw} is the adiabatic wall temperature and h_{fg} is the heat transfer coefficient under film cooling conditions. The film cooling effectiveness is defined as

$$\varepsilon_F=(T_{gi}-T_{aw})/T_{gi}-T_{co}). \tag{9}$$

The temperature ratio $W^+=[T_{aw}-T_{bl}]/[T_{co}-T_{ci}]$ may then be written

$$W^+=[\varepsilon_0-(1-\eta)\varepsilon_F-\varepsilon_0\varepsilon_F\eta]/\eta(1-\varepsilon_0), \tag{10}$$

Jones [20] uses superposition of temperature fields to argue that ε_F should be independent of temperature boundary conditions and in the subsequent calculations it is taken as 0.4, based on experimental data. (Note also a limiting case in which T_{bl} approaches T_{aw}, the heat transfer becomes zero, $T_{co}=T_{ci}$, $\eta=0$ and $\varepsilon_F=\varepsilon_0$).

It follows from (8) and (10) that

$$\xi=(w_c/w_g)=(c_{pg}/c_{pc})(A_{sg}\mathrm{St}_g/A_g)\mu W \tag{11}$$

where

$$\mu=h_{fg}/[h_g(1+B)]$$

in which h_{fg} is now the heat transfer coefficient under film cooling conditions and $B=h_{fg}t/k$ is the Biot number, which takes account of a thermal barrier coating (TBC) of thickness t and conductivity k. In practice h_{fg} increases above h_g, and $(1+B)$ is increased as TBC is added. We therefore take μ as unity and

$$\xi=CW^+ \tag{12}$$

where C is the same constant as that used for convective cooling only.

The corresponding expression for the alternative analysis assuming h_g constant is

$$\xi=C'T_g^{1/2}W^+/p_g \tag{13}$$

where C' also takes the values suggested for convective cooling only.

3.3 The Cooling Efficiency. Rather than assuming a specific value for η, the cooling efficiency can be determined from the internal heat transfer. If T_{bl} is taken to be more or less constant, then it may be shown that

$$\eta=1-\exp(-\psi) \tag{14}$$

where $\psi=(h_cA_{sc}/w_cc_{pc})=(\mathrm{St}_cA_{sc}/A_c)$, St_c is now the *internal* Stanton number, and A_{sc} and A_c refer to surface and cross-sectional areas of the coolant flow. Experience gives values of ψ for various geometries, but St_c is also a weak function of Reynolds number so in practice there is relatively little variation in cooling efficiency $[0.6<\eta<0.8]$. In the subsequent calculations we have taken η as 0.7; it is found that a given form of cooling geometry gives sensibly a constant value of η over the range of mass flows considered.

3.4 Transpiration Cooling—An Ultimate Cooling System. In transpiration cooling, coolant passes through many very small channels in the blade wall, i.e., the wall is a porous material (see Fig. 1(c)). The heat transfer coefficients within the wall channels are so high that the coolant achieves the wall temperature before emerging from the wall. It is assumed that this velocity is uniformly distributed and normal to the wall. A new, thick, transpired boundary layer is formed and serves to provide thermal protection for the vane.

As far as the external flow is concerned there are only two temperatures, that of the wall (T_{bl}) and that of the freestream (T_g). Thus the heat transfer can be described by a heat transfer coefficient, h_a, dependent on the coolant flow rate. Kays and Crawford [21], Eq. (13.41) provide a constant property solution for uniform coolant flow and constant wall temperature resulting in the following ratio of heat transfer coefficient to that without coolant flow:

$$h_a/h_g=\mathrm{St}_a/\mathrm{St}_g=b/(\exp(b)-1) \tag{15}$$

where $b=(w_c/A_{sg})/(\rho_gV_g\mathrm{St}_g)$, and (w_c/A_{sg}) is the coolant mass flow per unit area.

It is readily shown that $b=w^+$, as constant properties are assumed, i.e., $c_{pc}=c_{pg}$. The expression for vane effectiveness may then be found from the expression for convective cooling alone using the modified external heat transfer coefficient given above. Thus the modified value of nondimensional mass flow becomes $w^+(h_g/h_a)$ which equals $[\exp(w^+)-1]$ from Eq. (15). Substituting this value into Eq. (3) and taking cooling efficiency equal to unity as already assumed gives

$$\varepsilon_0=1-\exp(w^+),$$

so that

$$w^+=\ln[1/(1-\varepsilon_0)] \tag{16}$$

Substituting this value of w^+ into Eq. (4) gives the required estimate for cooling flow fraction.

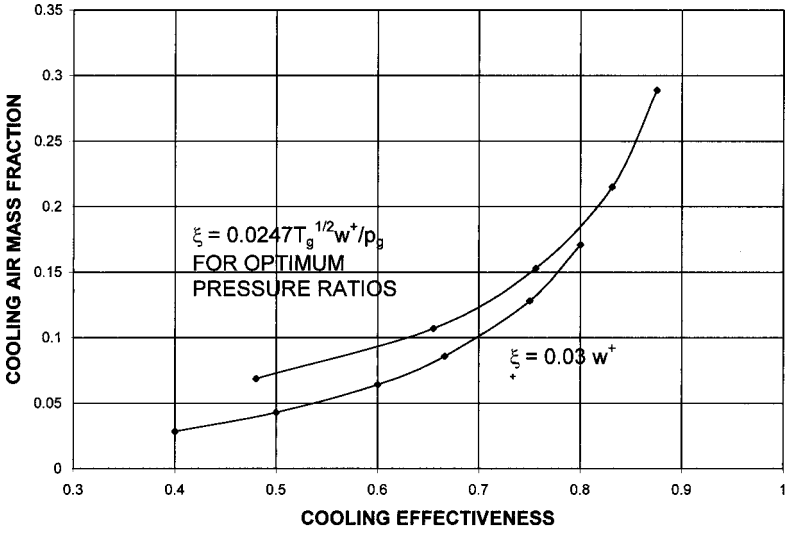

Fig. 2 Approximate expressions for cooling mass flow fraction ξ as a function of cooling effectiveness, for first nozzle guide vane row

3.5 Discussion. We summarize the options for determining the amount of cooling air.

For Convective (Internal) Cooling Only.

$$\text{(i)} \qquad \xi = Cw^+ \tag{17}$$

Taking $(c_{pg}/c_{pc})(A_{sg}/A_g = 20$ as representative of modern engine practice, and $\mathrm{St}_g = 1.5\times10^{-3}$ gives a value of $C = 0.03$. (The ratio (c_{pg}/c_{pc}) should increase with T_g (but only by about eight percent over the range 1500 K to 2200 K). We have neglected this variation in the subsequent cycle calculations described in Section 6.)

Alternatively

$$\text{(ii)} \qquad \xi = C' T_g^{1/2} w^+/p_g \tag{18}$$

Taking $(c_{pg}/c_{pc})(A_{sg}/A_g) = 20$ again, with $h_g/c_{pg} = 4.8$ kg/m^{2}s (a high value), $R_g = 300$ J/kg K and $\gamma = 1.3$, it follows that $C' \approx 0.0247$ bar/K$^{1/2}$.

For a cooled nozzle guide vane row, with internal cooling efficiency $\eta = 0.7$, Figure 2 shows plots of ξ against cooling effectiveness ε_0, based on equations (17) and (18) and the values of C and C' given above. Equation (18) also requires engine parameters, T_g and $p_g = r$ (bar) to be specified and it was assumed that they were related by an approximate equation for maximum efficiency conditions. The pressure ratio r gives the cooling temperature T_2 and the assumption of a blade temperature of 1073 K gave the cooling effectiveness. The two expressions thus give quite similar forms for the cooling air fractions, but they will differ as conditions move away from the optimum conditions for maximum efficiency. We discuss later how well they compare with practical designs.

For Film Cooling.

$$\text{(i)} \qquad \xi = CW^+ \tag{19}$$

with $C \approx 0.03$ or

$$\text{(ii)} \qquad \xi = C' T_g^{1/2} W^+/p_g \tag{20}$$

with $C' \approx 0.0247$.

For Transpiration Cooling.

$$\xi = C\ln[1/(1-\varepsilon_0)] \tag{21}$$

with $c = 0.03$.

Since film cooling is now used in most gas turbines, we have adopted the form of Eqs. (19) and (20) for most of our subsequent calculations. However, it was found that the cooling flows calculated from these equations are less than those used in recent and current practice in which film cooling is employed. This is for two main reasons (i) Designers are conservative, and choose to increase the cooling flows (a) to cope with entry temperature profiles the maximum temperature being well above the mean and local hot spots on the blade and (b) locally where cooling can be achieved with relatively small penalty on mixing loss (and hence on polytropic efficiency—see below). Thus regions remote from these injection points are cooled with this low loss air. (ii) In practice some surfaces in a turbine blade row will be convective cooled with no film cooling. The use of equation (19) or (20) for the whole blade row assembly will therefore lead to the total cooling flow being underestimated. (Film cooling leads to more efficient cooling, which is reflected in W^+ being much less than w^+; for the NGVs of a modern gas turbine W^+ may take a value of about 2 but w^+ may be about 4).

To allow for such practical issues, we have increased the values of the constants C and C' by a ''safety factor'' of 1.5, to 0.045, and 0.037, respectively, in the calculations described below.

4 Determination of Total Pressure Losses in Mixing of Coolant and Mainstream

It is well known that pressure losses have a major effect on cycle efficiency, so it is important to determine the mixing loss involved in discharging the cooling flow into the mainstream. Expressions given by Hartsel [22] for the total pressure loss in mixing go back to the simple one-dimensional momentum analysis given by Shapiro [23] for the flow model illustrated in Fig. 3.

Hartsel developed Shapiro's table of influence coefficients to allow for a difference between the total temperature of the injected flow (T_c) and the mainstream (T_g):

$$\Delta p_t/p_t = -\xi\gamma M_g^2/2\{1+(T_c/T_g)-2y\cos\phi\}. \tag{22}$$

Here y is the ratio of the velocity of the injected coolant and that of the free stream $(y = V_c/V_g)$, M_g is the Mach number of that free stream and ϕ is the angle at which the cooling air enters the mainstream.

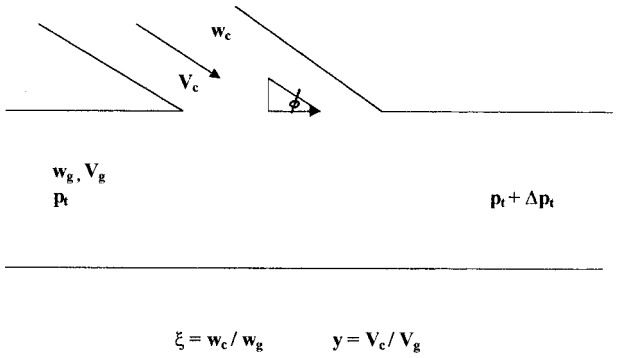

Fig. 3 The Shapiro/Hartsel model for simple mixing

Clearly the value of y is critical; an approximation suggested by Hartsel is to take $(p_t)_c=(p_t)_g$, so that $V_c/V_g \approx (T_c/T_g)^{1/2}$. A more sophisticated approach would not assume the total pressures of coolant and mainstream to be the same, but would derive them by accounting for losses as follows: in the *mainstream*, Δp_{tCC} in the combustion process, and Δp_{tN} in the nozzle row itself; for *coolant* air tapped at pressures other than the compressor discharge pressure, losses Δp_{tD} (in the ducting and disks before coolant enters the blade itself), and Δp_{tBL} (in the blading heat transfer process). Discharge at any local static pressure would then give different Mach numbers M_c and M_g and different velocities V_c and V_g.

El-Masri, Shrivastava, and Maccallum [24,25] and Day and Oldfield [26] have used cascade data with and without coolant discharge to obtain experimental relationships between ξ and the *extra* loss arising from injection of the cooling air (but note that injection near the trailing edge causes little total pressure loss—it may even reduce the basic loss in the wake). The *basic* uncooled loss is included in the value assumed for polytropic efficiency in the subsequent cycle calculations; there is no double counting involved in adding an extra penalty associated with the mixing loss arising from cooling air injection into the mainstream.

In practice the cooling flow leaves the blade surface at various points round the blade profile (say an elementary amount $d\xi$ at a particular location) and ϕ will vary with $d\xi$. To obtain an overall figure for the total coolant injection in a typical blade row, the cooling flow round the blade profile was ''integrated,'' using Eq. (22) for local exchange factors between $d\xi$ and the total pressure loss, $d(\Delta p_t/p_t)$. An overall exchange factor for the profile was thus obtained, which compared favorably with experimental data.

Thus in the subsequent cycle calculations an approximate practical expression relating the *extra* blade row stagnation pressure loss was used [or an efficiency penalty $\Delta\eta_{\text{stage}}$], of the form

$$\Delta p_t/p_t = -K\xi \tag{23}$$

or

$$\Delta\eta_{\text{stage}}/\eta_{\text{stage}} = -K'\xi \tag{24}$$

where

$$K'/K=[\Delta\eta_{\text{stage}}/\eta_{\text{stage}}]/[\Sigma\Delta p_t/p_t]\approx\{[\gamma-1]/\gamma\}[x_{\text{stage}}-1] \tag{25}$$

in which $x_{\text{stage}}=r_{\text{stage}}^{\{[\gamma-1]/\gamma\}}$ (see Hawthorne and Davis [27]).

For a nozzle guide vane row the experimental data suggested that $K'=0.125$,

$$\Delta\eta_{\text{stage}}/\eta_{\text{stage}} = -0.125\xi \tag{26}$$

in which account has been taken of the cooling air injected from other parts in addition to the blade profile (e.g., the blade platform). Then with $x=1.135$ for the row, and $\gamma=1.3$, so that $K'/K=1.8$, it followed that $K=K'/1.8=0.07$, so that an ''integrated'' empirical form of Eq. (16) for the complete cooled blade row is

$$[\Delta p_t/p_t] = -K\xi = -0.07\xi. \tag{27}$$

5 Methods of Calculating Cycle Efficiency

In determining cycle efficiency by use of Young's code, film cooling was assumed in the first three rows of the turbine (A, B, C). A simple approach was adopted, as follows.

As for an uncooled cycle calculation, the combustion temperature T_{cot}, the pressure ratio r, compressor and turbine (uncooled) polytropic efficiencies (0.9) and a combustion total pressure loss ($\Delta p_{tCC}=0.03$) were all specified. To obtain the cooling mass flow fraction required in the first NGV row (ξ_A) with $T_{gA}=T_{\text{cot}}$, a blade temperature T_{bl} (1073 K), a cooling air temperature T_{ci} (the compressor outlet temperature T_2 for the given pressure ratio, p_2/p_1), the cooling efficiency η (0.7) and the film cooling effectiveness ε_F (0.4) were all assumed. The cooling effectiveness ε_0 then followed from Eq. (5) and the quantity W_A^+ from Eq. (10). The cooling fractions were then obtained from Eq. (19) or Eq. (20), with C or C' specified.

For the determination of the cooling air fractions in the second and third blade rows, it was assumed that the pressure ratio of the HP turbine remained constant ($r_{HP}=3$) for varying r and T_{cot}, this figure reflecting aircraft gas turbine practice rather than industrial. In an iterative calculation the temperature at exit from the HP turbine (T_E) was obtained and this was taken as the gas temperature T_{gC} for the third row (the second NGV); the value of W_C^+ and the cooling fraction for that row followed immediately from Eq. (19). The gas temperature T_{gB} for determining W_B^+ in the first stage rotor row (the *relative* stagnation temperature), and hence the cooling fraction ξ_B, was assumed to be the arithmetic mean of the entry combustion temperature T_{cot} and the exit absolute temperature T_E (for an uncooled turbine stage of 50 percent reaction this relationship may be shown to be exact). An alternative would have been to take absolute stagnation temperature T_{rit} from the iterative calculation and then determine the relative stagnation temperature from representative velocity triangles, but sample calculations showed that taking T_{gB} as $[T_{\text{cot}}+T_E]/2$ was a good approximation even for the cooled turbine stage.

With the cooling fractions for all three rows thus obtained, the corresponding mixing losses were obtained from the approximate integrated equation ([27]). It was argued that the mixing in the second and third rows together constituted a pressure loss at exit from the HP turbine. Equation (25) shows that both the entry and exit losses can be converted into an efficiency reduction for the HP turbine. Numerical experiments showed that virtually identical plant thermal efficiencies were obtained by (i) converting the pressure losses to a turbine efficiency through equation (25); (ii) adding the first row pressure loss to the assumed basic combustion loss and inserting the combined second and third row loss at exit from the HP turbine; and (iii) adding all three losses to the assumed combustion loss.

The third method, the simplest, was therefore adopted for the parametric cycle calculations.

Data on both ξ and Δp_t estimated and used in the way described above were fed into the computer code, which yielded the specific work and the thermal efficiency (together with local exergy losses in components if required). Calculations have been undertaken with the various assumptions for the constants C and C', as described in Section 3.

A similar approach was followed in using the Provision code, which was used initially to check the numerical results and subsequently to investigate the effect of using cooling air tapped from along the compressor rather than solely from the compressor exit. Essentially the approaches described above appear to be similar to that adopted by El-Masri in his GASCAN code ([10]), but the methods used here for determining the amount of the cooling

flows are perhaps more sophisticated. It may also be noted that the approach is virtually the inverse of that followed by Brown et al. [9] in their calculations. They assumed a value of ξ initially, together with a compressor exit temperature and a blade temperature in order to work back to the maximum temperature; they then varied ξ to determine the maximum efficiency for a given T_2 and T_{bl}.

6 Results of the Computer Calculations

6.1 Cycle Efficiency for Varying Combustion Temperature and Pressure Ratio. The calculations, made with the Young code, used Equation (19) with C taken as 0045 (i.e., allowing a safety factor of 1.5). Plots of the thermal efficiency against pressure ratio for varying combustion temperature T_{cot} (1473 K to 2273 K) are shown in Fig. 4.

It is seen that for each value of T_{cot}, the thermal efficiency peaks at a pressure ratio of about 35. The maximum value of efficiency increases with T_{cot} up to 1900 K–2000 K but then decreases slightly. Some corresponding values of specific work (SW, kJ per unit of exhaust gas flow) are shown in Fig. 5. SW increases with T_{cot} for all pressure ratios.

6.2 The Effect of Changing Assumptions for Cooling Flow. The effect of changing the assumptions for determining coolant flows is illustrated in Fig. 6 for $r=30$, which also shows the uncooled efficiency for that pressure ratio. Use of the film cooling equations (19) with $C=0.045$ and (20) with $C'=0.037$ (but with p_g taken as p_2 for all three cooled blade rows) leads to similar values of thermal efficiency at low T_{cot}; but the second assumption, implying h_g constant, gives lower values of efficiency at higher T_{cot}. The assumption of ''ultimate'' transpiration cooling (Eq. (21)) gives thermal efficiencies close to the uncooled values, and represents an objective for designers, but one that is strictly limited.

6.3 The Effect of Changing the Number of Cooled Rows. Figure 7 shows the cycle efficiency with no cooling compared with (i) with one row cooled and (ii) with three rows cooled (both with film cooling and $C=0.045$). The efficiency drop with one cooled row is very small (indeed at the very highest combustion temperature there appears to be no decrease, probably because of a ''real gas'' effect balancing any possible decrease due to cooling). With three cooled rows there is a substantial drop in cycle efficiency.

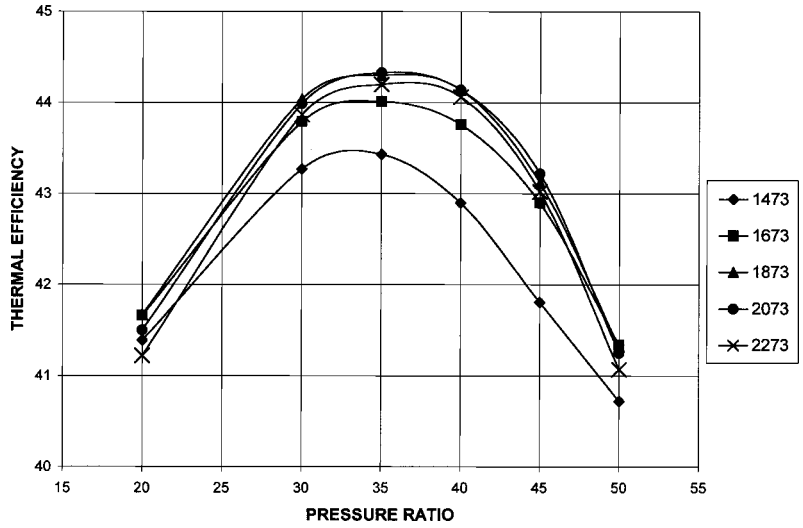

Fig. 4 Thermal efficiency as a function of combustion temperature T_{cot} and pressure ratio r (for film cooling, mass flow ratio $\xi=0.045W^+$)

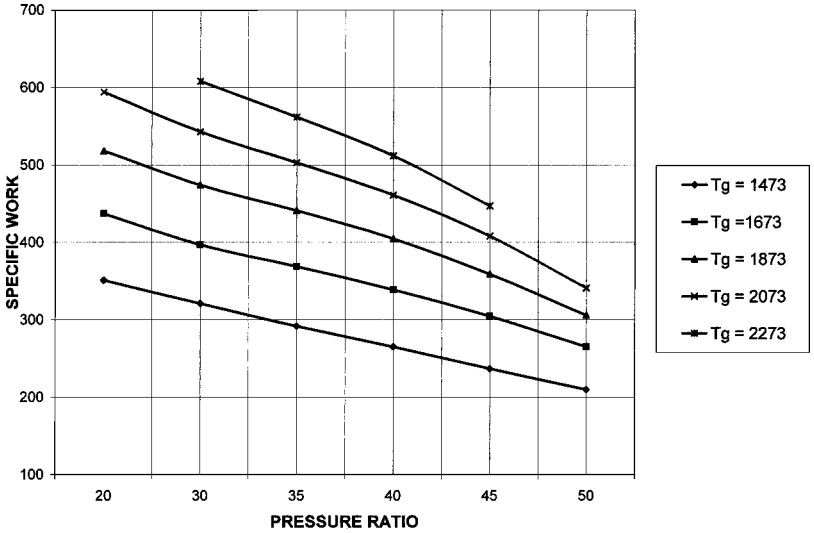

Fig. 5 Specific work as a function of combustion temperature T_{cot} and pressure ratio r (for cooling mass flow ratio $\xi=0.045W^+$)

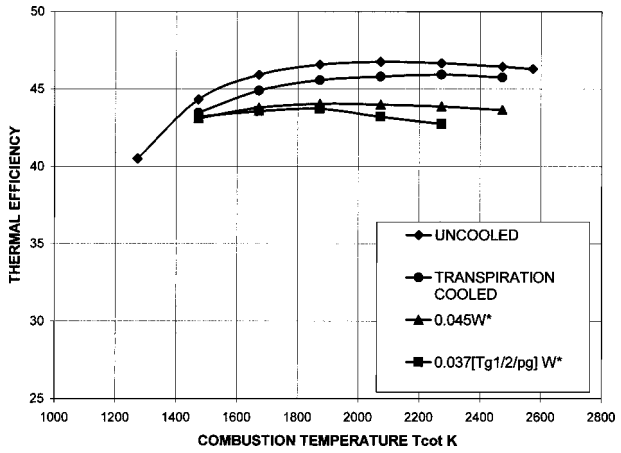

Fig. 6 Thermal efficiency as a function of combustion temperature T_{cot} for $r=30$ and for coolant mass flow ratios; (i) $\xi=0$ (uncooled); (ii) $\xi=0.045W^{+}$ (film cooling); (iii) $\xi=0.037T_g^{1/2}W^{+}/p_g$ (film cooling); (iv) transpiration cooling

6.4 Calculations Using the Provision Code. All the calculations reported above were made with the Young code with cooling air taken from compressor delivery. The Provision code was used to check those calculations and showed similar basic effects. It was also used to determine the thermal efficiency with lower pressure air used to cool the later (third) blade row, with the other assumptions essentially unchanged. Because the exergy loss in throttling the cooling air was eliminated, and a smaller quantity is used because it was taken at a lower temperature, the thermal efficiency was generally slightly higher, but the main point remained—there would appear to be a limit on T_{cot} beyond which the thermal efficiency begins to fall because of the penalty of excessive cooling air.

7 Limits on Thermal Efficiency

With the indications following from these various cycle calculations, it is appropriate to ask what improvements are necessary in order to take advantage of raising maximum temperatures much further beyond current values (with corresponding pressure ratios).

One obvious limit follows immediately from Eq. (3), that as the compressor discharge temperature approaches the allowable blade temperature the cooling requirement becomes very large, the rotor inlet temperature drops and the turbine work is reduced as a result. But another is less obvious; unless the pressure loss associated with mixing can be reduced, the increase of ξ with combustion temperature may lead to substantially increased stagnation pressure loss (with a corresponding drop in pressure ratio across the turbine) and any advantage of a higher T_{cot} is lost.

In the future it will certainly be necessary to improve internal cooling efficiency and film cooling effectiveness in order to capitalize on increases in T_{cot}; otherwise they could be counter productive. Emphasis must also remain on raising the allowable blade metal temperature. The feasibility of external cooling of the turbine cooling flow also merits attention.

The cooling of the blade rows downstream of the first (HP) stage appears to be quite critical. There is a penalty on efficiency in taking this cooling air from compressor discharge and the location of the optimum T_{cot} for maximum thermal efficiency is affected by how this cooling of the later stages is done.

8 Conclusions

The effects on the thermal efficiency of abstracting the large quantities of cooling air required for very high combustion temperatures T_{cot} have been assessed. It is shown that the gains in thermal efficiency with increasing T_{cot} can become marginal if not negligible. Indeed, a maximum in thermal efficiency is likely to be reached below stoichiometric conditions.

Doubt is therefore shed on whether major effort should be made to raise T_{cot} (and the corresponding pressure ratio) much further, unless material advances (allowing higher blade temperatures) and improved heat transfer mechanisms can restrict the increase in the cooling air quantities required.

There will still be advantage in increased specific work (and specific thrust for aircraft engines) resulting from increased T_{cot} although pressure losses in mixing will reduce the benefit.

Acknowledgment

The authors are grateful to Prof. J. B. Young of the Whittle Laboratory for use of his code and for assistance in its operation.

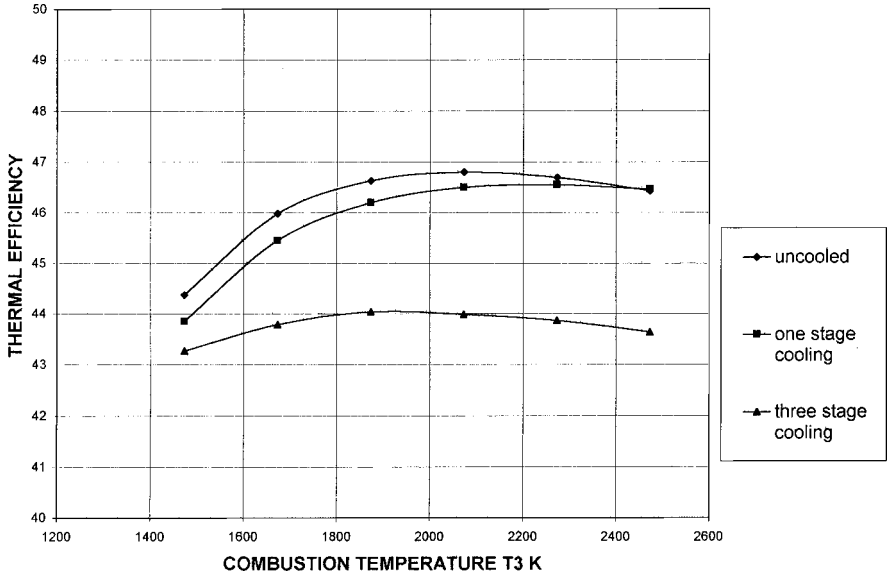

Fig. 7 The effect of number of cooled stages

Nomenclature

A = area
B = Biot number (ht/k)
c_p = specific heat at constant pressure
C, C' = constants
h = heat transfer coefficient
K = constant
M = Mach number
p = Pressure
Q_{net} = net heat transferred
R = gas constant
r = pressure ratio
t = thickness (of thermal barrier coating)
St = Stanton number, $h/(\rho V c_p)$
T = temperature
V = velocity
w = mass flow
w^+ = nondimensional quantity defined in Eq. (4)
W^+ = nondimensional quantity defined in Eq. (10)
x = $r^{(\gamma-1)/\gamma}$
y = ratio of velocities
ε_0 = overall cooling effectiveness
ε_F = film cooling effectiveness
η = cooling efficiency
η_c = compressor isentropic efficiency
η_t = turbine isentropc efficiency
η_{th} = thermal efficiency
ξ = coolant fraction (of mainstream gas flow)
ϕ = angle of discharge of coolant
ψ = quantity defined in Eq. (14)
μ = quantity defined in Eq. (11)
ρ = density

Subscripts

a = with transpiration cooling
bl = blade metal temperature
c = coolant
cot = combustion outlet (temperature)
E = exit from first turbine stage
f = with film cooling
g = gas (mainstream)
i = coolant inlet (temperature)
o = coolant outlet (temperature)
rit = rotor inlet (temperature)
sg = surface (for gas heat transfer)
stage = referring to stage
t = total (pressure)
1,2,3,4 = states in cycle (entry, compressor discharge, maximum temperature, turbine exit)

References

[1] Mukherjee, D. K., 1976, ''Design of Turbines, Using Distributed or Average Losses; Effect of Blading,'' *AGARD 195*, pp. 8–1–8–13.
[2] Walsh, P. P., and Fletcher, P., 1998, *Gas Turbine Performance*, Blackwell Science, Oxford, UK.
[3] Watson, D. W., and Ritchey, I., 1997, ''Thermodynamic Analysis of Closed Loop Cycles,'' ASME paper no. 97-GT-288.
[4] Traupel, W., 1966, *Thermische Turbomaschinen*, Springer-Verlag, Berlin.
[5] Hawthorne, W. R., 1956, ''The Thermodynamics of Cooled Turbines,'' Parts I and II, *Proceedings of the ASME*, Vol. 78, pp. 1765, 1781.
[6] El-Masri, M. A., 1986, ''On Thermodynamics of Gas Turbine Cycles—Part II: Model for Expansion in Cooled Turbines,'' ASME J. Eng. Gas Turbines Power, **108**, pp. 151–159.
[7] Bolland, O., and Stadhaas, J. F., 1995, ''Comparative Evaluation of Combined Cycle and Gas Turbine Systems With Water Injection, Steam Injection and Recuperation,'' ASME J. Eng. Gas Turbines Power, **117**, pp. 138–147.
[8] El-Masri, M. A., 1987, ''Exergy Analysis of Combined Cycles—Part I: Air-Cooled Brayton-Cycle Gas Turbines,'' ASME J. Eng. Gas Turbines Power, **109**, pp. 228–235.
[9] Brown, A., Jubran, B. A., and Martin, B. W., 1993, ''Coolant Optimization of a Gas Turbine Engine,'' Proc. Inst. Mech. Eng. Part A: Jrnl. of Power and Energy, **207**, pp. 31–47.
[10] El-Masri, M. A., 1988, ''GASCAN—An Interactive Code for Thermal Analysis of Gas Turbine Systems,'' ASME J. Eng. Gas Turbines Power, **110**, pp. 201–209.
[11] Chiesa, P., Consonni, S., Lozza, G., and Macchi, E., 1993, ''Predicting the Ultimate Performance of Advanced Power Cycles Based on Very High Temperatures,'' ASME paper no. 93-GT-223.
[12] El-Masri, M. A., 1997, private communication.
[13] MacArthur, C. D., 1999, Advanced Aero-engine Turbine Technologies and Their Application to Industrial Gas Turbines,'' 14th International Symposium on Air-Breathing Engines, Florence, Italy, ISABE Paper No. 99-7151.
[14] Young, J. B., 1998, ''Computer-Based Project on Combined-Cycle Power Generation,'' Cambridge University Internal Report.
[15] Ainley, D. G., 1957, ''Internal Cooling for Turbine Blades,'' Aeronautical Research Council R and M 3013.
[16] Horlock, J. H., 1966, *Axial Flow Turbines*, Butterworth, London.
[17] Holland, M. J., and Thake, T. F., 1980, ''Rotor Blade Cooling in High Pressure Turbines,'' AIAA J. of Aircraft, **17**, No. 6, pp. 412–418.
[18] De Ruyck, J., Bram, S., and Allard, G., 1996, ''Revap Cycle: a New Evaporative Cycle Without Saturation Tower,'' ASME paper no. 96-GT-361.
[19] Lakshminarayana, B. L., 1996, *Fluid Dynamics and Heat Transfer in Turbomachinery*, John Wiley and Sons, New York, Chapter 7.
[20] Jones, T. V., 1991, ''Definitions of Heat Transfer Coefficients in the Turbine Situation,'' *Turbomachinery—Latest Developments in a Changing Scene*, ASME paper no. C 423/046.
[21] Kays, W. M., and Crawford, M. E., 1993, *Convective Heat and Mass Transfer*, 3rd Ed., McGraw-Hill, New York.
[22] Hartsel, J. E., 1972, ''Prediction of Effects of Mass-Transfer Cooling on the Blade-Row Efficiency of Turbine Airfoils,'' AIAA Paper 72-11.
[23] Shapiro, A. H., 1953, *The Dynamics and Thermodynamics of Compressible Fluid Flow*, Ronald Press, New York.
[24] Shrivastava, K. D., and Maccallum, N. R. L., 1987, ''The Effect of a Transversely Injected Stream on the Flow Through Turbine Cascades—Part 1: Flow Effects,'' ASME paper no. 77-GT-87.
[25] Shrivastava, K. D., and Maccallum, N. R. L., 1987, ''The Effect of a Transversely Injected Stream on the Flow Through Turbine Cascades—Part II: Performance Changes,'' ASME paper no. 87-GT-88.
[26] Day, C. R. B., Oldfield, M. L. G., and Lock, G. D., 1999, ''Aerodynamic Performance of an Annular Cascade of Film Cooled Nozzle Guide Vanes Under Engine Representative Conditions,'' *Experiments in Fluids*, in press.
[27] Hawthorne, W. R., and Davis, G. de V., 1956, ''Calculating Gas Turbine Performance,'' Engng., **181**, p. 361.

The Methodology of Stochastic Optimization of Parameters and Control Laws for the Aircraft Gas-Turbine Engines Flow Passage Components

I. N. Egorov
G. V. Kretinin
S. S. Kostiuk
I. A. Leshchenko
Air-Force Engineering Academy,
Moscow, Russia

U. I. Babi
Techno-Pulsar,
Moscow, Russia

This paper presents the main theses of stochastic approach to the multimeasure parameters and control laws optimization for the aircraft gas-turbine engines. The methodology allows us to optimize the engines taking into account the technological deflections which inevitably take place in the process of manufacturing of the engine's components as well as engine's control deflections. The stochastic optimization is able to find highly robust solutions, stable to inaccuracies in technological processes. The effectiveness of the methodology is shown by example of optimization problem solution to find the control laws for the flow passage controllable elements of the fourth generation aircraft mixed-flow turbofan engine. The use of information about the existing and advanced production technology levels during the optimization process, including some components manufacturing accuracy, allows us to considerably increase the probability of optimum solution implementation in practice. In real engine there are some components manufacturing deflections as well as control accuracy deflections. This results in a certain engine's performance deviation. An engine optimization classic deterministic approach cannot take into account this circumstance, so the probability of an optimum design implementation is too low. [DOI: 10.1115/1.1285841]

Introduction

Till now a wide class of aircraft GTE optimization problems has been solved with the help of deterministic approach and it has been quite enough. GTE was considered as ideal system. Strictly speaking, such consideration of any engineering object is incorrect because under the real-life conditions an object is a stochastic system, which has certain indefinites. Therefore the probabilistic estimation of optimization problem results is required.

Let us consider from this point of view the GTE control laws optimization problem. As a control law we consider the dependence of position of a certain GTE controllable element upon a certain GTE mode operation parameter. As an example, for the case of GTE throttle performance optimization one can consider the position dependence upon an engine rotor rotation speed or upon an engine thrust. The optimum laws of control and therefore the optimization criterion extremum value obtained with the deterministic approach, are nothing but the maximum achievable effect, one ought to seek to. The question is being opened concerning the possibility of the maximum effect achievement. First, there is the problem of assurance of the stability of obtained solution under possible deflections of optimized parameters, which inevitably take place in practice while realizing any engineering project, even if the most perfect technology levels are used. Secondly, it is hard to predict if one can influence either the property or the extent of solution stability, optimizing the control laws of an object being researched.

Contributed by the International Gas Turbine Institute (IGTI) of THE AMERICAN SOCIETY OF MECHANICAL ENGINEERS for publication in the ASME JOURNAL OF ENGINEERING FOR GAS TURBINES AND POWER. Paper presented at the International Gas Turbine and Aeroengine Congress and Exhibition, Indianapolis, IN, June 7–10, 1999; ASME Paper 99-GT-227. Manuscript received by IGTI March 9, 1999; final revision received by the ASME Headquarters January 3, 2000. Associate Editor: D. Wisler.

The main theses of the stochastic approach to aircraft GTE and its components control laws optimization can be found in [1,2]. The implementation of any technical solution is known to be directly connected with an object production technology level. In real-life conditions the dispersion of design parameters is inevitable. This is shown in Fig. 1, which demonstrates the dependence of the deterministic solution implementation probability upon the production technology level [1,3]. Meanwhile it is important not only to obtain an object high performance, but to assure its fulfillment according to the high probability level as well. Concerning development of aircraft GTE, it makes necessary the search of the optimum control laws taking into account the dispersion of components parameters due to technological deflections.

The main idea is the following. The effectiveness indicator can be presented as a certain functional, depending upon the vector of the optimized parameters $\bar{a}$, which defines the control laws, and upon the vector of accidental parameters $\bar{\xi}$, which influences the value of the functional. The latter vector defines the errors in object control. Note that when the components of accidental vector $\bar{\xi}$ are fixed, the problem is nothing but the deterministic problem of control laws optimization.

In real-life conditions there is the lack of specific information about vector $\bar{\xi}$ components. However there is just enough practical experience of GTE production, which allows us to estimate the law of distribution of $\bar{\xi}$ components with acceptable accuracy. Moreover, in most engineering cases the components of vector $\bar{\xi}$ have normal or close to normal distribution laws [3]. Hence, for immutable conditions of engines components manufacturing, in the frameworks of our approach we use the hypothesis that the distribution law of $\bar{\xi}$ is known.

It should be noted that as well as the components of vector $\bar{\xi}$, the effectiveness indicator $Y(\bar{a},\bar{\xi})$ has an accident character. Here

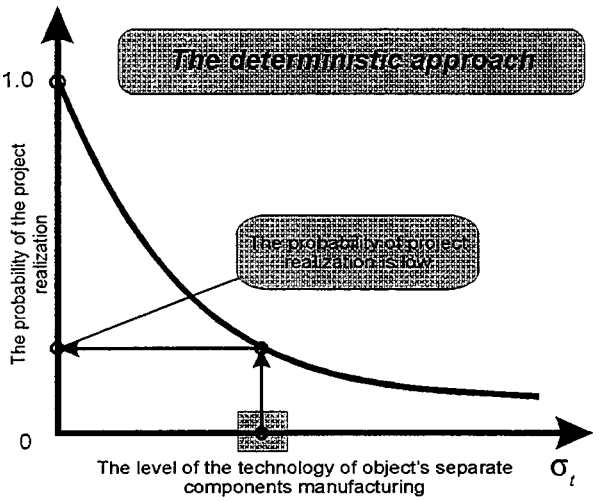

Fig. 1 The influence of production technology level upon the probability of the project implementation

the deterministic optimization can not be used. However, the stochastic optimization of some statistical indicators can be carried out.

Thus, when GTE control laws are optimized while using the stochastic approach, one ought to find the extremum of statistical criterion $Y(\overline{a},\overline{\xi})$, depending upon both deterministic component $\overline{a}$ and stochastic one $\overline{\xi}$. As the effectiveness indicators one can consider the same sense criteria, as for the deterministic case (the SFC, the thrust, the efficiency of elements, etc.), but these criteria must be presented in probabilistic form. For example, one can maximize the probability of such event as $c_R < c_{R\,\mathrm{Def}}$, where $c_{R\,\mathrm{Def}}$ is some pre-defined admissible value of c_R:

$$P_{\mathrm{Cond}}|Y(\overline{a}^*,\overline{\xi})| = \max P\{Y(\overline{a},\overline{\xi}) < Y_{\mathrm{Def}}(\overline{a})\}.$$

To calculate the probabilistic criterion we used the following algorithm. In the process of extremum search for each current vector of optimized parameters $\overline{a}$, the value of the stochastic criterion is obtained using the generation of the set of vectors $\overline{\xi}$ according to given distribution law (for example, the normal law), using the computer's generator of random numbers. Because of different control parameters dispersion inequality in a common case, we use the vector of middle-square deflection $\overline{\sigma}_{\mathrm{Def}}$. Thus, for each combination of deterministic vector and stochastic ones $(\overline{a},\overline{\xi_j}), j=\overline{1,m}$ the values of effectiveness indicators $Y(\overline{a},\overline{\xi_j}), j=\overline{1,m}$ are being determined. Here, m is the number of experiments. On the base of the results for current vector $\overline{a}$, we define the sequence $e_1, e_2, \ldots, e_m$, where

$$e_j = \begin{cases} 0, & \text{when } Y(\overline{a},\overline{\xi}) > Y_{\mathrm{Def}}(\overline{a}); \\ 1, & \text{when } Y(\overline{a},\overline{\xi}) \leqslant Y_{\mathrm{Def}}(\overline{a}) \end{cases}.$$

This expression corresponds to the case of minimization of an effectiveness criterion. Then the estimation of probability is carried out:

$$\hat{P}_{\mathrm{Cond}}(Y(\overline{a},\overline{\xi})) = \frac{1}{m}\sum_{j=1}^{m} e_j.$$

This probability converges to $P(Y(\overline{a},\overline{\xi}))$ if $m \to \infty$.

Besides the above mentioned probabilistic criterion, for stochastic optimization of control laws other statistical indicators of accidental value $Y(\overline{a},\overline{\xi})$ can be used too. For example, its mathematical expectation can be used as

$$M_x = M|Y(\overline{a},\overline{\xi})| = \frac{1}{m}\sum_{j=1}^{m} Y(\overline{a},\overline{\xi_j}). \qquad (A)$$

and the complex criterion as

$$\mu_x = \sigma_x M_x, \qquad (B)$$

where σ_x is middle square deflection.

$$\sigma_x = \sqrt{\sum_{j=1}^{m} \frac{(M_x - Y(\overline{a},\overline{\xi_j}))^2}{m-1}}.$$

Moreover, the dispersion can be used as criterion

$$D_x = \sigma_x^2. \qquad (C)$$

Some other probabilistic indicators can be also considered as criteria.

The obtained estimation $\hat{P}_{\mathrm{Cond}}(Y(\overline{a},\overline{\xi}))$ (M_x, μ_x, D_x) is used just in the algorithm of optimization to determine the direction of further extremum search. The peculiarity of such an approach is that it is not necessary to calculate highly accurate estimations of $\hat{P}_{\mathrm{Cond}}(Y(\overline{a},\overline{\xi}))$ (M_x, μ_x, D_x). It is explained by noiseproof features of the method of indirect optimization on the base of self-organization (IOSO) [4]. So, we can use low values of m (approximately 20) while solving stochastic optimization problem, in order to reduce time-consuming.

As we use the approximate estimations of probabilistic criteria during the optimization, after the solution has been obtained one can carry out special statistical research using the greater m values to improve the estimations.

As the drawbacks of criteria (A), (B), and (C) one can treat the fact that these criteria are connected directly with the probability of GTE control law implementation. The probabilistic characteristics are present here indirectly, through the statistical effectiveness indices. In this case, the solution obtained with these criteria is rough from the point of view of assurance of given probability level. However, when the distribution is normal or similar to it, such solutions can assure highly robust features [5].

Thus, in the frameworks of given approach we optimize GTE control laws in stochastic statement and search the extremum solution taking into account its implementation in accordance with existing level of production technology of concrete engines-manufacturing firm.

The Estimation of Mixed Flow Turbofan Engine Controllable Elements Optimum Control Concerning the Probabilistic Criteria

The first stage of research was to determine how control inaccuracies influence engine's performance when implementing the obtained optimum control laws.

As an example, Fig. 2 and Fig. 3 present the probabilistic performance of engine, obtained considering the noise only by the low pressure compressor IGV control law implementation. In this case the variable parameter (IGV position) is a random parameter, distributed (in accordance with the assumed conditions of statistical testing) according to normal law, with the mathematical expectation equal to the given IGV position defined by control law, with dispersion σ defined by admissible dispersions of modern engines LPC IGV angles setting.

Fig. 2 shows the excerpt, consisting of 50 possible realizations of IGV control laws, and corresponding to it the dependence of c_R upon the thrust. One can see that with the given level of IGV control disturbances the dispersion of c_R can exceed 2 percent. In this case the estimation of IGV control accuracy influence upon engine's performance is reasonable to be carried out using such probabilistic indicators as confidence probability of assurance of the given values of integral engine parameters (for example, the parameters has been obtained in deterministic statement), $P_{\mathrm{Conf}} = P(c_R \leqslant c_{R\,\mathrm{Def}})$, $P_{\mathrm{Conf}} = P(R \geqslant R_{\mathrm{Def}})$, as well as the confidence

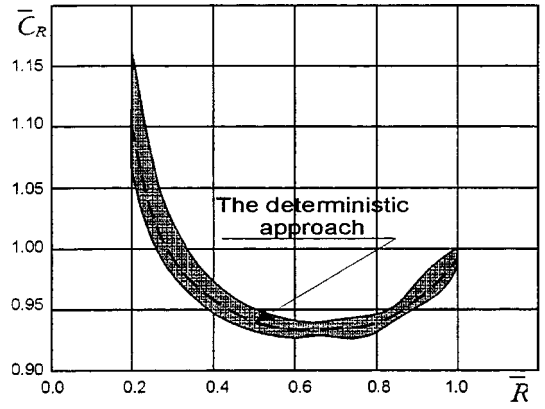

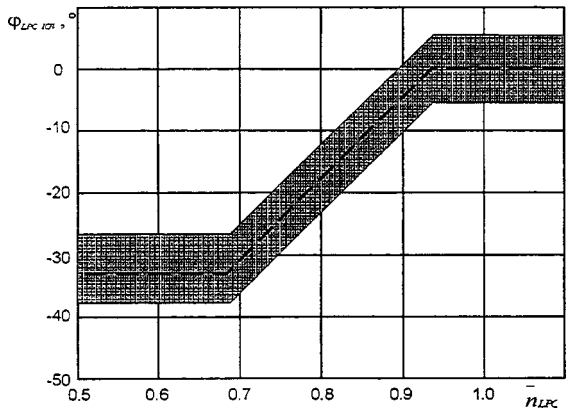

Fig. 2 The influence of IGV control dispersion upon engine's integral performance

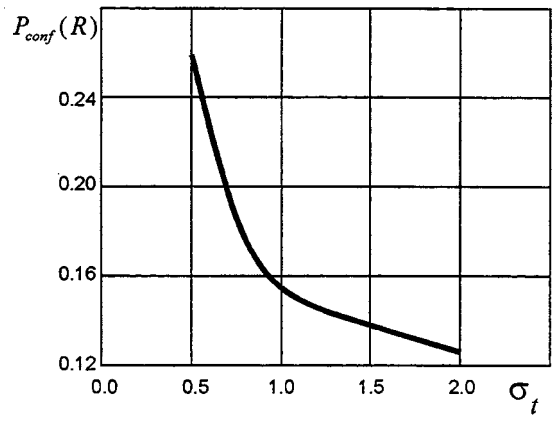

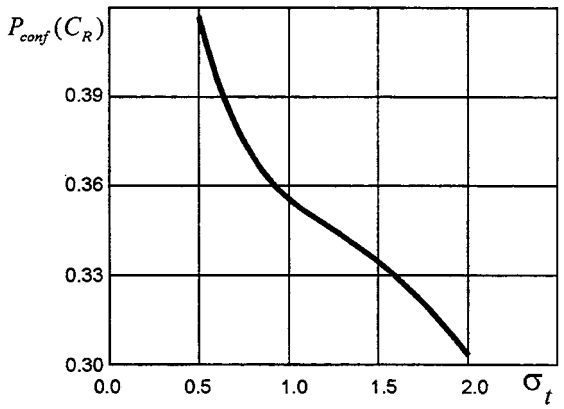

Fig. 3 The influence of IGV control dispersion upon engine's probabilistic characteristics

interval, within the frameworks of which one, the integral parameters will be insured with the given probability, as $P(c_R \leqslant c_{R\ \mathrm{Def}}) = 90$ percent, $P(R \geqslant R_{\mathrm{Conf}}) = 90$ percent.

The reason of dispersion of integral engine performance is obvious to be the dispersion of internal engine parameters due to changes of LPC characteristic.

The results of estimation of influence of disturbance level upon the engine performance is presented in Fig. 3, where the dependence of confident probability of insurance of the given integral engine parameters upon the level of disturbance σ_t is shown. These results show that increasing of disturbances level leads to worsening of probabilistic characteristics of engine.

Thus, the problems of optimum control laws search under the conditions of random character of control implementation are of great interest.

The Statement of the Optimization Problem

This paper presents some results dealing with the search of optimum control laws of mixed flow turbofan engine for throttle operating modes. The researches have been carried out using the mathematical model of the engine with two-dimensional axial symmetrical simulation of LPC [6]. The dispersions in the operation of actuators have been taken into account, i.e., we have treated the probabilistic character of obtained control laws.

For the simpler analysis let us consider the problem of search of optimum control laws of LPC IGV, HPC GV, and LPC rotation rate. The problem is to determine such optimum control laws, which would ensure the best engine economy within the wide range of operating modes under the required level of their implementation probability. In other words, it is the problem of search of stable (robust) control laws of controllable elements from the point of view of ensuring of high levels of fuel economy indices as well as observing of defined constraints.

Using the stochastic approach, we defined the accuracy $Z(\overline{\sigma}_{\mathrm{Def}})$, which could be ensured while implementing the control laws of one or another controllable element. For example, when $Z=3$, for fan IGV and HPC GV setting angles $\sigma=1$*, and for the rotation rate of LPC $\sigma=0.25$ percent. While varying the value of current disturbance $Z(\overline{\sigma}_{\mathrm{Def}})$ the value σ of each controllable element is being changed proportionally. The given levels of control accuracy correspond to the levels, inherent to the engine under consideration.

As the components of the vector of control we consider the control laws of regular controllable elements of the engine:

$$\overline{u}(n_{\mathrm{HPC}}) = (n_{\mathrm{LPC}}(n_{\mathrm{HPC}}), \varphi_{\mathrm{IGV}}(n_{\mathrm{HPC}}), \varphi_{\mathrm{GV}}(n_{\mathrm{HPC}})).$$

These control laws have been defined using different basic functions, such as piece-wise linear and piece-wise parabolic.

To the engine and control vector parameters the constraints have been applied to keep the main engine restrictions, such as maximal values of temperature before the turbine and rotors rotation rates, minimal surge margins etc.

Solving the optimization problem in stochastic statement. we've used the mathematical expectation M_x (A) and the complex criterion μ_x (B) as the probabilistic criteria of effectiveness indicator Y, which displays engine fuel economy in integral form

$$Y(\overline{a}^*) = \int_{R_{\mathrm{MIN}}}^{R_{\mathrm{MAX}}} c_R(R)\,dR.$$

The estimation of probabilistic criteria was carried out by the analysis of random excerpt, consisting of 20 experiments.

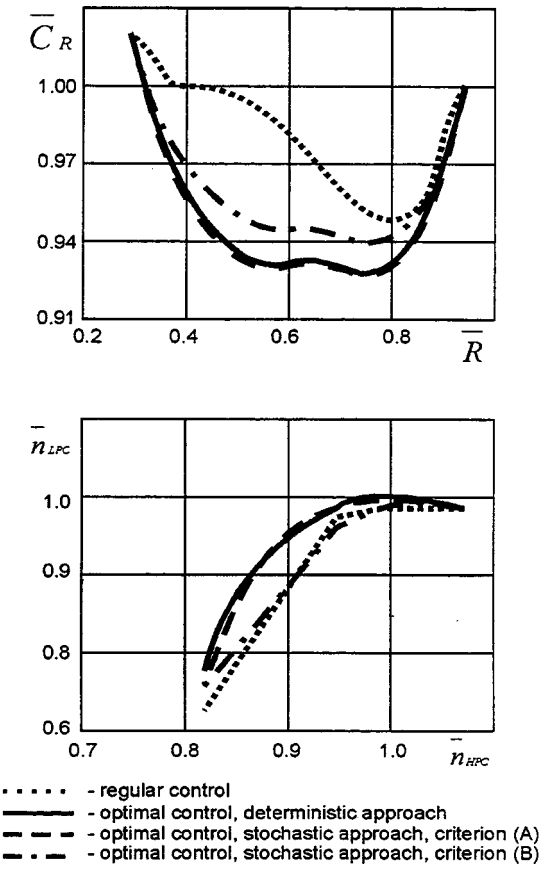

Fig. 4 Comparison of different optimization approaches effectiveness

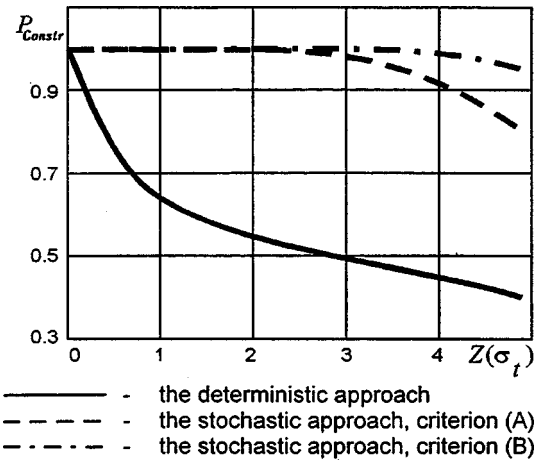

Fig. 5 The probability of constraints observing for different optimization approaches

As the result of solving of the series of optimization problems, we determined the optimum control laws in deterministic and stochastic statements. For comparison Fig. 4 shows the dependence $c_R(R)$ for different control laws, which were obtained for different effectiveness indices.

The data for Fig. 4 have been obtained without the disturbances upon the parameters of control laws, i.e. with $Z(\overline{\sigma}_{\text{Def}})=0$. The results are shown for four cases: regular control laws; optimum control, obtained with use of deterministic statement $Z(\overline{\sigma}_{\text{Def}})=0$; two cases of stochastic statement of the optimization problems with $Z(\overline{\sigma}_{\text{Def}})=3$.

One can conclude from the analysis of Fig. 4, that the best values of c_R are provided when solving the problems of optimum control in deterministic statement and in stochastic statement using the mathematical expectation as the effectiveness criterion (criterion A). It should be noted that the optimum solutions have the differences due to the parameters of control laws, i.e., the control laws themselves are different. The best advantage is ensured within the range of the thrust of about 40–80 percent of R_{Max} as well as for the deterministic case. A little bit worse result (about 2 percent) was reached when the effectiveness index was the complex criterion (*B*). Basing upon these results, one can make the important conclusion that the stochastic statement of the problem of optimum control of mixed-flow turbofan engine provides the fuel economy indicators extremely close to the best ones, having been obtained using the deterministic approach. Moreover, both deterministic and stochastic results are considerably better than the regular control performance. In other words, the solution has been obtained using the stochastic statement is quite acceptable for its use under deterministic conditions.

Of course, the question is stated concerning the truth of the following opposite assertion: At what degree is the deterministic solution effective under stochastic conditions? To answer this question one is to conduct the research in two directions. The first one is to determine how the constraints of optimization problem are stable under the dispersion of control parameters. The second direction is aimed at the estimation of the stability of optimum solution by means of the effectiveness criterion.

The analysis of the results presented in Fig. 5, shows the deterministic solution ($Z(\overline{\sigma}_{\text{Def}})=0$) under the conditions of noise of parameters. It is considerably worse than the optimum solution obtained using the stochastic statement. In this example as the robustness indicator we've used P_{Constr}—the probability of engine constraints observing while using the optimum control. Particularly, Fig. 5 shows the probability of defined engine constraints observing depending upon the value $Z(\overline{\sigma}_l)$ of normally distributed noise with zero mathematical expectation.

To determine the value of the probability P_{Constr} the noise has been simulated by the generation of the noise vector $\overline{\xi}$ random values. Then there has been done an excerpt of 100 effectiveness indicators. One can see that for the optimum control laws obtained using the deterministic approach even the low level of the noise $Z(\overline{\sigma}_l)=1$ reduces the probability of constraints observing down to $P_{\text{Constr}}=0.65$, while the increase of $Z(\overline{\sigma}_l)$ up to four reduces P_{Constr} down to 0.45. Thus, only a half of implementations of the deterministic optimum control ensures the required conditions of engine operation under the given level of parameters noise. In other words, the benefits of the deterministic optimum solution by fuel economy indicators, which can be about 2 percent (see Fig. 4), are practically realizable with the probability about 0.5. Hence it follows that the optimum solution obtained with deterministic approach is, first, the top achievable effect which could be possibly implemented, and secondly its practical implementation is possible only by low probability level.

As distinct from the deterministic solution, the stochastic optimum solution has the probability of ensuring of defined engine operating conditions about 1.0. It should be noted that the stochastic solutions with $Z(\overline{\sigma}_{\text{Def}})=3$ allow us to have the probability of constraints observing about 0.91 for criterion (*A*) by the current level of parameters noise $Z(\overline{\sigma}_l)=4$, and for criterion (*B*) under the same conditions the probability can reach ≈ 0.98. This fact characterizes the stability of the optimization problem solution, where as the measure of the stability we use the probability of insurance of defined engine operating conditions. Thus, we can conclude that in this case the use of the deterministic optimum result under the conditions of parameters noise is too problematical from the point of view of observing of the defined constraints.

The analysis of Fig. 6 allows us to understand the physical nature of improved stability (robustness) of the stochastic solution

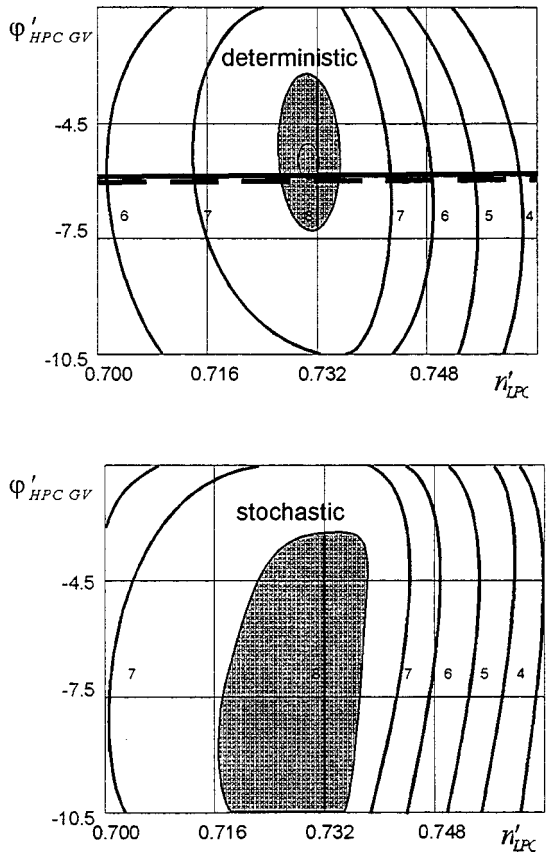

Fig. 6 The topology of object functions for different optimization approaches

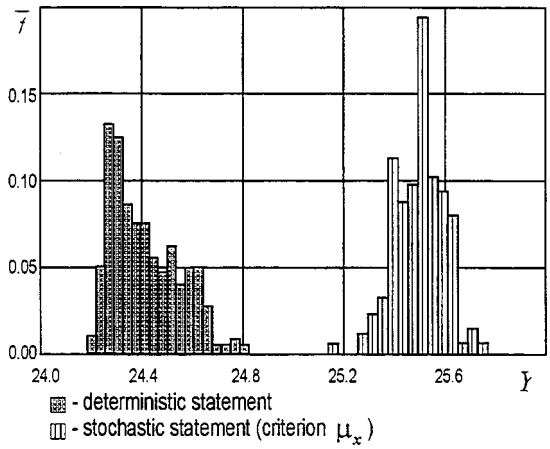

Fig. 7 The frequency diagram of effectiveness criteria

in comparison with the deterministic one. This figure shows the changes in effectiveness criterion contour lines for deterministic and stochastic solutions, depending upon two components of variable parameters vector, which are nothing but the coordinates of node points of control laws basic functions. Note, that as the effectiveness criterion both upper and lower maps use the value of the integral

$$Y(\overline{a}) = \int_{R_{\mathrm{MIN}}}^{R_{\mathrm{MAX}}} c_R(R)\,dR,$$

calculated for the region nearby the extremum under the deterministic conditions, i.e., with $Z(\overline{\sigma_t}) = 0$. As the results of the deterministic optimization problem and the stochastic one are different, the components of optimum vectors are different as well. So, despite of the proximity of two variable parameters, shown in Fig. 6, other components of variable parameters vector of deterministic and stochastic optimum solutions are reciprocally different.

One can see that the deterministic solution has the sharp extremum and is situated near the boundary of admissible region of control (the dotted line shows the active constraint of HPC surge margin). This leads to the fact that a slight deflection of control law parameters from optimum ones inevitably worsens the effectiveness of the engine. It is just the reason of low robustness of the deterministic solution.

For the probabilistic optimization criterion (*A*) the contour of objective function has more gently sloping character, and the optimum solution if far sufficiently from the boundary of the admissible region. This reduces the influence of changes in the components of optimized parameters vector upon the effectiveness criterion, so for the stochastic solution there is the less dependence of effectiveness indicator upon the dispersion of control laws parameters while their implementation. The result is not unexpected, because just this goal was pursued using the stochastic statement of the problem of mixed-flow turbofan engine control laws optimization.

No less important indicator of solution stability is the estimation of engine's performance (the effectiveness criterion), which has the probabilistic character under stochastic statement of the problem. For such analysis it should be necessary to know the distribution functions of researched random parameters. The components of the control vector are random parameters, distributed (according to the conditions of statistical testing) according to normal law. However, this doesn't mean that the other random parameters, such as effectiveness criterion or internal engine parameters, must be distributed by the same law. This law depend upon the topology of object function. The estimation of these distribution laws can be carried out only by means of the experimental methods.

As the example, Fig. 7 presents the histograms of distribution laws of effectiveness criteria, corresponding to the statistical tests, carried out for engine optimum control when $Z(\overline{\sigma_t}) = 3$. The dimension of statistical tests excerpt was 100 experiments. One can see that the distribution laws of effectiveness criteria random values are not normal. The reason of this is connected with the nonlinearity of engine mathematical model. Figure 8 shows that the stochastic solution obtained using the criterion (*B*) allows us to ensure the significantly less dispersion of specific fuel consumption values under parameters noise.

It should be noted that as the alternative indicator of the optimum control stability one can consider the total probability of

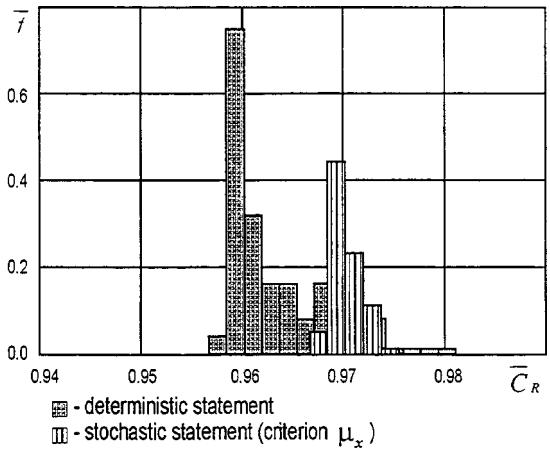

Fig. 8 The frequency diagram of SFC value for $R = 0.75R_{\mathrm{Max}}$

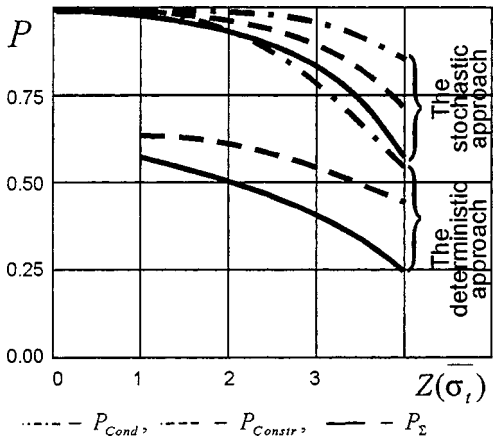

Fig. 9 The probabilistic characteristics for the different approaches solutions

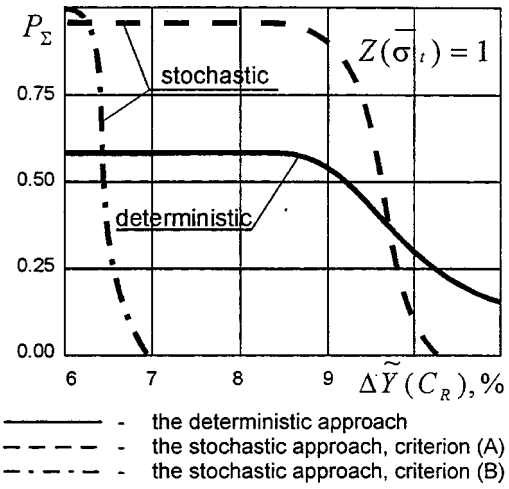

Fig. 11 The probabilities of ensuring of effectiveness criteria for different optimization approaches

ensuring of defined effectiveness criterion—P_Σ. Let us determine the probability of ensuring of some pre-defined value of effectiveness indicator for the range of varying of parameter $Z(\overline{\sigma}_t)$, which can be presented by

$$P_\Sigma = P_{\text{Constr}} * P_{\text{Cond}},$$

where P_{Constr} is the probability of ensuring of defined operating conditions (observing of the constraints), $P_{\text{Cond}} = P(Y \leqslant Y_{\text{Def}})$ is the probability of ensuring of the effectiveness criterion which is not worse than some defined value under the condition of the constraints observing. Note that in the optimization problems which were considered in this paper there was necessary to minimize the object function.

Figures 9–11 show the resuming results, which demonstrate the advantages of the stochastic approach as compared with the deterministic one. Figure 9 demonstrates the changes in the value of conditional probability of ensuring of defined effectiveness criterion value (which corresponds to 101 percent of minimal possible effectiveness criterion), for both deterministic and stochastic approaches. One can see that for $0 < Z(\overline{\sigma}_t) < 1$ the probabilities of ensuring of pre-defined value of effectiveness criteria are nearly the same, while for the cases of $Z(\overline{\sigma}_t) > 1$ the deterministic solution is worse than the stochastic one from this point of view. Moreover, there is an interesting fact that the values of the probabilities of defined constraints observing P_{Constr} for the deterministic solution are significantly lower than that of the stochastic solution within the whole range of $Z(\overline{\sigma}_t)$, and when $Z(\overline{\sigma}_t) = 1$, these values are correspondingly 0.63 against 0.99. As the result, the total probability of ensuring of pre-defined effectiveness indicator P_Σ for the case of implementation of the stochastic solution is considerably higher than that of the deterministic solution, for all values of $Z(\overline{\sigma}_t) > 0$.

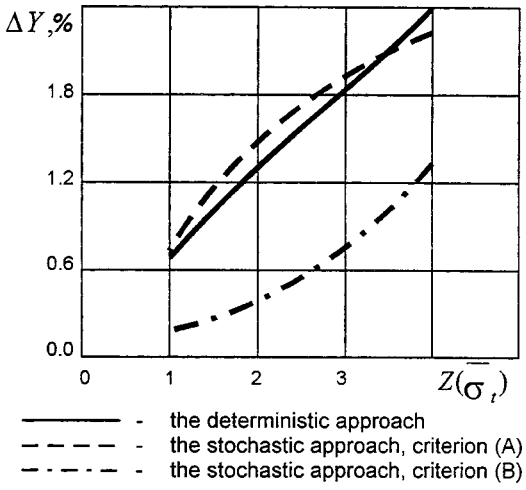

Fig. 10 The dispersion of effectiveness criteria depending upon manufacturing technology level

Figure 10 shows the dispersion of effectiveness criteria values depending upon $Z(\overline{\sigma}_t)$ for different solutions of the optimization problems, where the probability of ensuring of effectiveness criteria values is defined by

$$P\left(Y - \frac{\Delta Y}{2} \leqslant Y \leqslant Y + \frac{\Delta Y}{2}\right) = 90 \text{ percent}.$$

One can see that the stochastic solution using the criterion (*B*) provides twice as less dispersion of the effectiveness criterion as compared with the deterministic solution and the stochastic solution using criterion (*A*).

Figure 11 shows that the optimum solutions obtained using both the deterministic approach and the stochastic one by the criterion (*A*) can ensure the maximal improving of the effectiveness criteria $\Delta Y(c_R)$ equal to ≈ 9 percent under $Z(\overline{\sigma}_t) = 1$, but the probabilities P_Σ of these improving are 0.63 and 0.92 correspondingly. The 6 percent improving of the effectiveness criterion can be assured with $P_\Sigma = 1$ when using the complex probabilistic criterion (*B*). This result seems to us to be very important, because even for the high enough level of manufacturing technology ($Z(\overline{\sigma}_l) = 1$) it is very difficult to ensure the value of the effectiveness criterion equal to the value obtained using the deterministic approach.

Based upon this result, we can make the important conclusion, which seemed to be common for many branches of engineering. If one has the task to create some non-serial object with best performance and the expenditures to do it are not of paramount importance, it is reasonable to determine optimum parameters of the object using the deterministic approach. In such case the choice of one or several best specimens among the large enough series of the specimens, manufactured using such optimum solution, can ensure the record values of the object effectiveness indicator. But if one has the task to determine optimum parameters of some object designed for serial production, the stochastic approach will allow us to create the highly robust object, with well enough performances and low sensitivity to technological deflections of manufacturing.

Conclusions

The most important result of this research seems to be in substantiation of the reasonability to search the optimum control laws of aircraft GTE using the stochastic approach. The realization of optimum solution obtained using the deterministic optimization can be problematical due to the dispersion of object parameters. The use of the stochastic approach allows us to ensure the stability of the engine performance under the conditions of technological deflections and inaccuracies. This improvement of the solution stability is reached through the slight worsening of average value of effectiveness criterion as compared with the value of the deterministic solution criterion. The regions of optimum control laws parameters can be significantly different for the deterministic approach and for the stochastic one, because the stochastic solution is placed far enough from the active constraints and from the regions of sharp worsening of the effectiveness indicator.

Acknowledgments

This work was supported by the Russian Fund for Fundamental Research.

Nomenclature

GTE = gas turbine engine
LPC = low pressure compressor
HPC = high pressure compressor
IGV = inlet guide vanes
GV = guide vanes
SFC = specific fuel consumption
c_R = specific fuel consumption
R = thrust
σ = the middle square deflection
$Z(\overline{\sigma})$ = the scale factor for middle square deflections vector
P = probability

Subscripts

Conf = confidence
Cond = conditional
Constr = observing of constraints
Def = defined value
t = technological

References

[1] Egorov, I. N., 1992, ''Optimization of a Multistage Axial Compressor, Stochastic Approach,'' ASME Paper 92-GT-163.
[2] Egorov, I. N., 1993, ''Deterministic and Stochastic Optimization of Variable Axial Compressor,'' ASME Paper 93-GT-397.
[3] Draper, N. R., and Smith, H., 1981, *Applied Regression Analysis*, John Wiley & Sons, New York.
[4] Egorov, I. N., et al., 1989, ''Procedures of Indirect Statistical Optimization on the Basis of Self-Organization and Their Use in Aircraft GTE. Optimization Problems,'' VINITI (2622-B89).
[5] Egorov, I. N., and Kretinin, G. V., 1993, ''Optimization of Gas Turbine Engine Elements by Probability Criteria,'' ASME Paper 93-GT-191.
[6] Egorov, I. N., 1992, ''Optimization of a Multistage Axial Compressor in a Gas-Turbine Engine System,'' ASME Paper 92-GT-424.

Demonstration of Fluidic Throat Skewing for Thrust Vectoring in Structurally Fixed Nozzles

P. J. Yagle

D. N. Miller

K. B. Ginn

J. W. Hamstra

Lockheed Martin Aeronautics Company,
P.O. Box 748, MZ 9333,
Fort Worth, TX 76101

The experimental demonstration of a fluidic, multiaxis thrust vectoring (MATV) scheme is presented for a structurally fixed, afterburning nozzle referred to as the conformal fluidic nozzle (CFN). This concept for jet flow control features symmetric injection around the nozzle throat to provide throttling for jet area control, and asymmetric injection to subsonically skew the sonic plane for jet vectoring. The conceptual development of the CFN was presented in a companion paper (Miller et al. [1]). In that study, critical design variables were shown to be the flap length and expansion area ratio of the nozzle, and the location, angle, and distribution of injected flow. Measures of merit were vectoring capability, gross thrust coefficient, and discharge coefficient. A demonstration of MATV was conducted on a 20 percent scale CFN test article across a range of nozzle pressure ratios (NPR), injector flow rates, and flow distributions. Both yaw and pitch vector angles of greater than 8 deg were obtained at NPR of 5.5. Yaw vector angles greater than 10 deg were achieved at lower NPR. Values of thrust coefficient for the CFN generally exceeded published measurements of shock-based vectoring methods. In terms of vectoring effectiveness (ratio of vector angle to percent injected flow), fluidic throat skewing was found to be comparable to shock-based vectoring methods. [DOI: 10.1115/1.1361109]

Technical Need

As the requirements for tactical aircraft design evolve, the features needed in the exhaust systems expand to include such features as afterburning, thrust vectoring, and advanced shaping. Traditionally, afterburning and vector control methods have called for a nozzle whose geometry was variable. Typical turbofan engines require an increase in nozzle throat area while afterburning. Thrust vectoring has required either deflection of the nozzle divergent flaps or articulation of the nozzle itself. Advanced shaping of the nozzle aperture has led to the design of nozzles that are more two dimensional, and not axisymmetric. These additional capabilities required increased mechanical complexity, as illustrated by the F-15 Short Take-Off and Landing Maneuver nozzle and the F-22 nozzle, which are roughly 50 percent heavier than current fighter aircraft nozzles which lack these advanced capabilities.

So, there is a technical need for the ability to control the throat area and thrust-vector angle of a jet with the constraint that the nozzle be mechanically simple and have as much fixed structure as possible. This simple nozzle would reduce part-count, weight, and cost. The goal for this concept would be to obtain F-22-class nozzle performance from a fully fixed nozzle by aerodynamically controlling the flow of the jet.

Previous Work

In order to develop a fully fixed nozzle concept, existing techniques for fluidic jet throat area and vector control were examined. Fluidic jet area control is achieved via symmetric injection at the nozzle throat. This injection obstructs the nozzle primary flow at the throat, thus reducing the effective area of the jet. The results of Lockheed Martin's fully fixed nozzle concept were published by Miller and Catt [2] and Miller et al. [3].

Contributed by the International Gas Turbine Institute (IGTI) of THE AMERICAN SOCIETY OF MECHANICAL ENGINEERS for publication in the ASME JOURNAL OF ENGINEERING FOR GAS TURBINES AND POWER. Paper presented at the International Gas Turbine and Aeroengine Congress and Exhibition, Munich, Germany, May 8–11, 2000; Paper 00-GT-013. Manuscript received by IGTI Feb. 2000; final revision received by ASME Headquarters Jan. 2001. Associate Editor: M. Magnolet.

A summary of fluidic thrust vectoring concepts is found in a paper by Gridley and Walker [4]. The concepts presented there include: coanda surface blowing, counterflow, and shock-based thrust vector control.

The coanda surface blowing technique for thrust vector control was investigated by Chiarelli et al. [5]. This method achieves thrust vectoring if the wall-bounded jet adheres to a solid surface (the Coanda surface). For this concept, vectoring is achieved by moving Coanda flaps in the desired direction of jet turning. Secondary flow was introduced tangentially to the outward turned flap to prevent jet separation from the flap surface. This method achieved relatively low thrust-vector angles and required variable geometry (the Coanda flaps) for operation.

The ''counterflow'' thrust-vectoring method was investigated by Strykowski and Krothapalli [6]. This concept used a suction source to induce a secondary flow along one of the nozzle divergent flaps of a highly overexpanded nozzle. This ''counterflow'' vectored the primary jet by causing the jet to attach and, therefore, turn the jet toward the flap with secondary suction activated. Thrust vector angles of 16 deg were reported at relatively low suction mass-flow rates (Gridley and Walker [4]). Unfortunately, this concept must also contend with the thrust loss, weight penalty, and possible instability associated with a highly overexpanded nozzle, as well as finding a suitable suction source.

Historically, shock-based methods have been the most commonly investigated technique for fluidic thrust vector control (Gridley and Walker [4]; Gunter and Farenholz [7]; Walker [8]; Wing [9]). Shock vector control methods use the formation of a strong oblique shock in the divergent section of the nozzle to turn the primary jet. The oblique shock is generated by introducing an injected flow into the *supersonic* primary nozzle flow, as shown in Fig. 1. This approach achieves thrust vectoring with no variation in primary nozzle throat area. Though it may be effective in vectoring the nozzle stream, this method is also characterized by large nozzle expansion area ratios, large thrust losses, and moderate variation in vector angle with nozzle pressure ratio (Wing [9]).

The fluidic throat skewing concept (Miller et al. [1]) incorporates previously developed methods for optimum jet area control (Catt and Miller [10]; Miller et al. [3]) with additional features for efficient thrust vectoring. The fluidic throat skewing technique

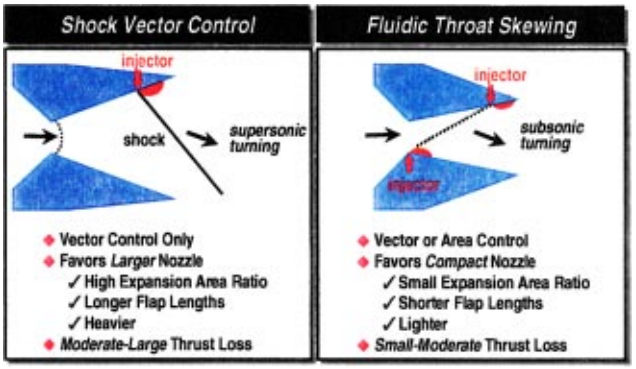

Fig. 1 Characteristics of shock vector control and fluidic throat skewing for jet flow control

features symmetric injection near the throat for jet area control and asymmetric injection to *subsonically* skew the sonic plane for thrust vector control (Fig. 1). Secondary injection slots are located at the throat and nozzle flap on both interior sides of the nozzle. Asymmetric injection at the throat actually skews the sonic plane, which turns the flow subsonically, as opposed to turning the flow by the introduction of an oblique shock. The injection ports on the nozzle flap are used to further skew the sonic plane, which increases vectoring performance. By controlling the distribution of the injected flow between the throat and flap, area control is maintained while vectoring the jet. While simultaneous vectoring and jet area control are possible, completely decoupling them may be challenging.

Since fluidic throat skewing turns the jet without the formation of a shock in the nozzle, it may have a smaller impact on thrust efficiency (C_{fg}) than shock vector control (Fig. 1).

Configuration Development

The fluidic thrust vectoring concept presented here was developed by Miller et al. [1]. Additional development has since been performed to assess the time response of a fluidic thrust vectoring system.

Previous Development Efforts. The fluidic thrust vectoring concept presented here was developed by Miller et al. [1] using CFD methods and a Design of Experiments (DOE) approach to investigate effects of nozzle contour, injector geometry, and flow properties. The main figures of merit were thrust vector angle (δ) and gross thrust coefficient (C_{fg}). Still, throttling performance was also monitored to ensure that jet area control (measured by RTAC) was not compromised. The design process was first applied to a single-axis thrust-vectoring concept using 2D CFD methods and later reapplied to a multiaxis concept using 3D CFD methods. Optimum performance was achieved with a relatively short nozzle divergent flap and low nozzle expansion area ratio (Miller et al. [1]). The test data presented in this paper was obtained in a test of this optimum configuration.

Time-Accurate CFD Analyses. With thrust vectoring methods, the time response of the thrust vectoring system is of great interest. With mechanically vectored nozzles, such as the F-22, the vectoring rates are more easily determined from the kinematics of the actuators and control surfaces. With fluidic vectoring methods, it is not necessarily clear what the time response of the system will be.

In order to identify the first-order transient response of a fluidic thrust-vectoring nozzle, time-accurate two-dimensional CFD analyses were performed. The code used for the computational flow field solutions was LM Aero's Falcon, a Reynolds-averaged Navier-Stokes code, which uses an approximate Lower-Upper (LU) implicit solver (Yokota et al. [11]). The primary and secondary inflow boundary conditions (BC's) are modeled as characteristic theory-based total pressure/total temperature boundaries. Walls are modeled as nonslip and adiabatic. The external far field boundaries are modeled using inflow/outflow BC's based on characteristic theory. A two-equation k-kl turbulence model is used for accurate macroscopic turbulence calculations (Smith [12]). Flow was modeled as turbulent, compressible, adiabatic, and calorically perfect.

The time response was computed for a case whose initial condition is asymmetric injection at the nozzle throat and whose final state is asymmetric injection at the nozzle throat and flap (Fig. 2). The total amount of secondary injection remained constant throughout the calculation; it was simply redistributed. Valve response was assumed to be instantaneous. The solution was allowed to iterate until any oscillations in the thrust-vector angle had damped out. The time response of the thrust-vector angle can be seen in Fig. 3. The thrust vector angle damped out very quickly, with major oscillation ceasing after 3 or 4 milliseconds. This translates to a vectoring response rate of greater than 1000 degrees per second. Clearly, the vector response rate will be governed by the time response of the valves used to control the amount of injected secondary flow.

Another concern with any time-varying system is sensitivity to initial conditions, or hysteresis. To determine if fluidic throat skewing is subject to hysteresis effects, two additional time-accurate CFD analyses were performed. Both of these analyses had injection settings for asymmetric throat injection (Fig. 2) as their final state. One solution had symmetric throat injection (no thrust vectoring) as the initial state. The other solution had asymmetric throat and flap injection as its initial state. Both solutions damped out to the same final state; no hysteresis was observed.

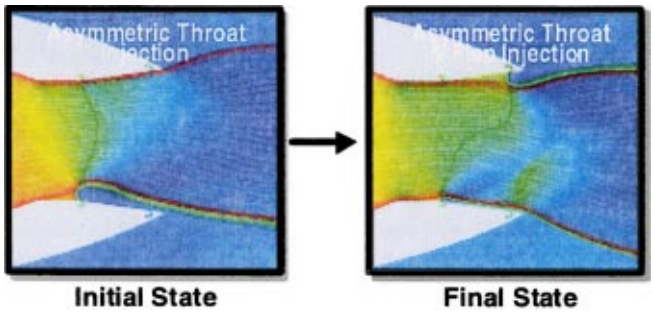

Fig. 2 Initial and final state for time-accurate CFD calculations

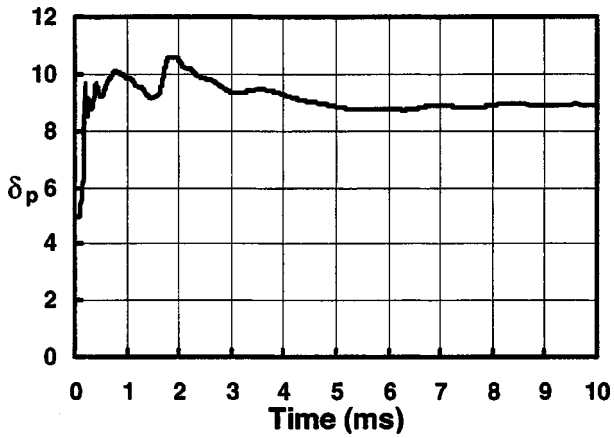

Fig. 3 Time response of thrust vector angle

Test Preparation and Execution

Testing was conducted in October 1998 at LM Aero's Thrust Measurement Facility (TMF) (Fig. 4) in Fort Worth, Texas. The objective of the test was to determine the on and off-design performance of the three-dimensional conformal fluidic nozzle concept.

Thrust Measurement Facility. LM Aero's TMF consists of a six component thrust stand housed in an altitude chamber. This setup allows testing over a wide range of nozzle pressure ratios (NPR) at relatively constant mass flow. As a result, the thrust stand operates within a narrow band of its calibrated mass flow and force measurement range, which improves accuracy and repeatability and minimizes Reynolds number variations. In addition, by varying back pressure and limiting flow rate, model loads can be reduced enough to use resin-based (plastic) model parts. Multiple independently controlled and metered flow supplies are available. The capabilities of the TMF are summarized in Table 1.

Model Design. The optimum CFN concept arrived at using the CFD/DOE process was the only one tested. This design represents a next generation fighter-aircraft nozzle; it has a nonaxisymmetric exit and is swept in planform (Fig. 5). The nozzle features an elliptic cross-section throat and a biconvex aperture shape.

Fluidic thrust vectoring was implemented using eight injector slots, shown in red in Fig. 5. Four slots are arrayed around the nozzle throat for area control and thrust vectoring. The remaining four slots are arrayed around the nozzle exit for enhanced thrust vectoring. The four slots at the nozzle throat and exit are arrayed in a top-bottom-left-right fashion. Top and bottom slots effect pitch vectoring, while left and right slots effect yaw vectoring. Each injector slot was designed to flow a corrected weight flow

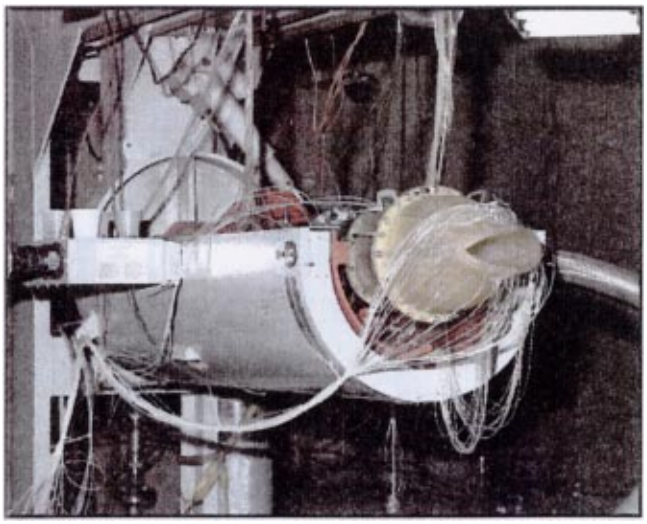

Fig. 4 LMTAS thrust measurement facility

Table 1 Thrust measurement facility capabilities

	MIN	MAX	NOTES
Chamber	1.2 psia	ambient	With 3.0 lbm/s inflow
Test Air	Jet-off	300 psia	5 lbm/s, multiple air sources if needed
Axial Force	-225 lbf	225 lbf	±0.25% repeatability
Side Force	-125 lbf	125 lbf	±0.25% repeatability
Normal Force	-125 lbf	125 lbf	±0.25% repeatability
Approach Duct Area	0 sq. in.	25.518 sq. in.	Stand geometric limit
ASME Nozzle	NPR 0.0	NPR 6	With 11.21 sq. in. throat

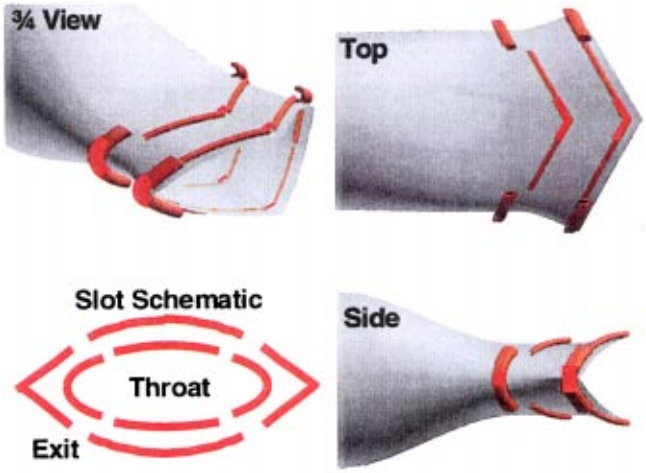

Fig. 5 Conformal fluidic nozzle internal flowpath geometry

($\omega\sqrt{\tau}$) of 7 percent at a secondary pressure ratio (SPR) of 6.0. Other model design guidelines are summarized below:

- 20 percent scale model.
- Primary expansion area ratio ($A9/A8$) of 1.3.
- Throat and exit aspect ratio of 2.5.
- Injector exits angled to be highly opposed to the primary flow.
- Nozzle geometric throat area ($A_{p,\mathrm{thr}}$) of 10.64 sq.in.

Model Fabrication. The CFN model was constructed entirely from resin using stereo-lithography (Fig. 6). Note that the secondary flow paths for the injection slots are integrated into the region between the inner and outer surfaces of the nozzle. This required that the wall of the nozzle be thick to accommodate the secondary flow paths. This causes the ''fat'' appearance of the nozzle. The outer surfaces of a full-scale CFN would not be as bulky. An adapter was also constructed from resin to adapt the nozzle plenum diameter to that of the primary flow source of the test facility. An aluminum flow distribution plate was sandwiched between the adapter and the nozzle. This plate had several small holes drilled into it which lie in the secondary flow path. These holes were selectively plugged to allow for variation in flow distribution to the injector slots.

Test Setup and Procedure. During the cold-flow test, a primary flow rate of 3 lbm/sec was maintained. NPR was controlled

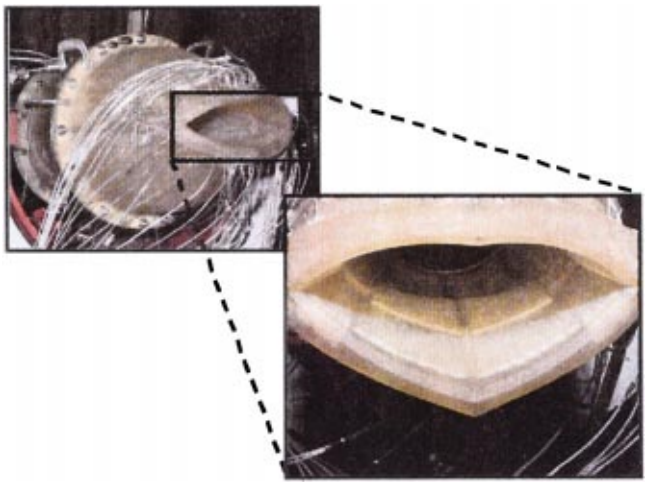

Fig. 6 Conformal fluidic nozzle model

by varying the chamber pressure. NPR was set as high as 5.5 by lowering the chamber pressure to as low as 2.25 psia. Chamber pressure was increased incrementally to achieve NPR's as low as 2. $\omega\sqrt{\tau}$ was varied by increasing injector weight flow from no flow to as high as 0.21 lbm/sec (7 percent of the primary flow).

Test Results

The test results showed, in general, that fluidic throat skewing is an effective and efficient means of achieving thrust vector control. The impact of thrust vectoring on C_{fg} was not excessive.

Yaw Vectoring Data Trends. Figure 7 shows the general data trends for yaw vector angle (δ_y) as a function of injected flow rate. The data shown were obtained with a single yaw slot flowing at the nozzle exit. The data show that vectoring performance increases as the amount of injected secondary mass flow increases. At the design NPR of 5.5, yaw vector angles up to 7.23 deg were achieved. At lower NPR, vector angles as high as 13.66 deg were obtained. This increased vectoring at low throttle setting (low NPR) provides greater control authority for take-off and landing flight conditions. Note that, in practical application, it is not required that secondary flow be injected into the nozzle at all times. If thrust vectoring is not required, no secondary mass flow is required. There is no bleed penalty on the engine in this case.

This particular injection configuration shows that thrust vectoring is possible without injecting at the nozzle throat. Since injecting at the nozzle flap produces little throttling, it is also possible to vector the primary nozzle flow with little undesired reduction in $C_{d,p}$.

Figure 8 shows the general data trends for gross thrust coefficient (C_{fg}) while yaw vectoring as a function of injected flow rate. As the amount of injected flow and, therefore, yaw-vector angle was increased, C_{fg} did decrease. However, at the design NPR (5.5), the loss was small; 2.6 percent of thrust efficiency. At off-design conditions, thrust loss was only as high as 3.1 percent. Yaw vectoring does not have a drastic impact on thrust efficiency. Note that C_{fg} is quite good when not vectoring.

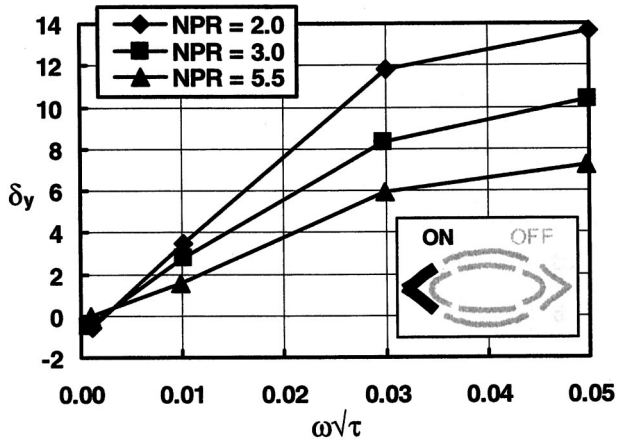

Fig. 7 Yaw performance—δ_y

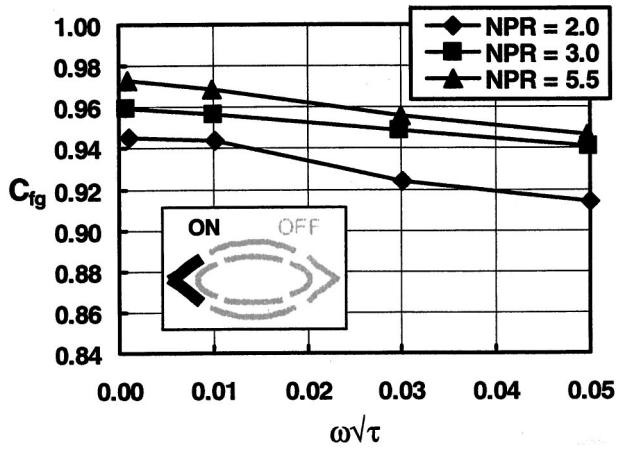

Fig. 8 Yaw performance—C_{fg}

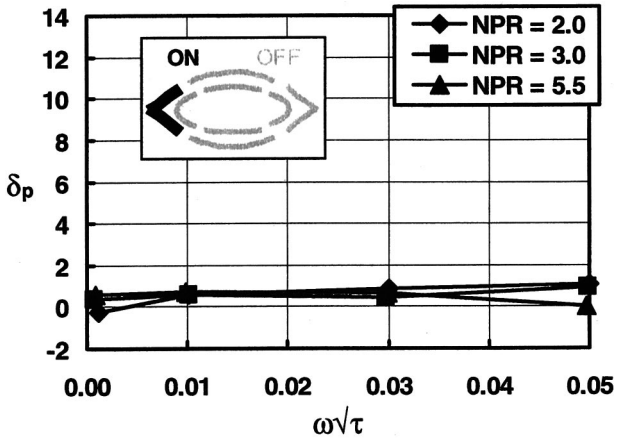

Fig. 9 Yaw performance—δ_p

One concern with a multiaxis thrust-vectoring concept is whether the two vectoring directions can be decoupled; that is, it is desirable to be able to vector in yaw without any accompanying vectoring in pitch. Figure 9 shows that no significant pitch-vectoring component was seen while vectoring in yaw.

Fluidic throat skewing appears to be an effective and efficient means of achieving yaw vectoring in a fixed geometry nozzle. At the design NPR, vectoring effectiveness, measured as degrees of thrust vectoring per percent injected mass flow (K_{vc}) was as high as 2. At off-design conditions, K_{vc} was as high as 3.9. The impact of fluidic thrust vectoring on C_{fg} was small.

Pitch Vectoring Data Trends. Figure 10 shows the general data trends for pitch vector angle (δ_p) as a function of injected flow rate. The data shown were obtained with a ''top'' pitch slot flowing at the nozzle throat and a ''bottom'' pitch slot flowing at the nozzle exit. As the amount of injected secondary was increased, δ_p increased. The design NPR of 5.5, pitch vector angles of up to 8.5 deg were achieved. At off-design conditions, δ_p as high as 12.3 degrees were observed. As with the yaw vectoring results, increased δ_p at low NPR will provide improved control authority for take-off and landing flight conditions.

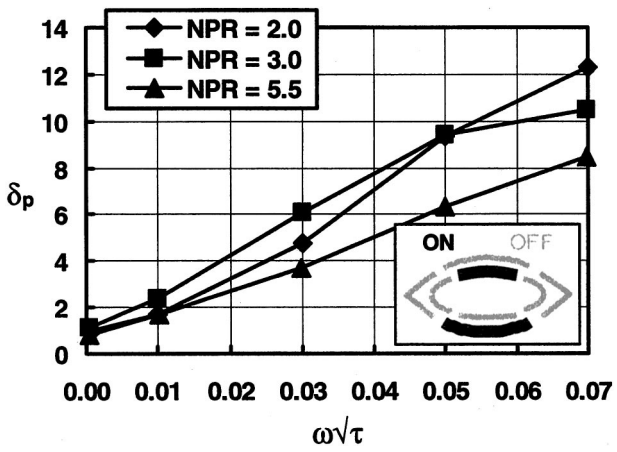

Fig. 10 Pitch performance—δ_p

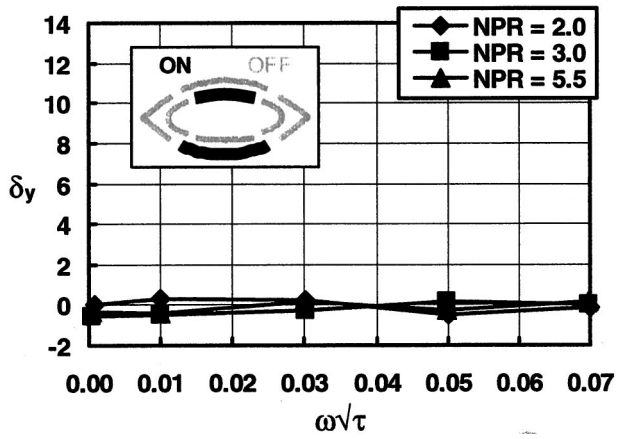

Fig. 11 Pitch performance—δ_y

Figure 11 shows the general data trends for δ_y as a function of injected mass flow rate while pitch vectoring. There was no significant yaw vector component observed while vectoring in pitch.

The data trends for $C_{d,p}$ and C_{fg} while pitch vectoring were similar to those observed while yaw vectoring. Fluidic throat skewing appears to be an effective and efficient means of achieving pitch vector control in a fixed geometry nozzle. At the design NPR, vectoring effectiveness, measured as degrees of thrust vectoring per percent injected mass flow (K_{vc}) was as high as 1.7. At off-design conditions, K_{vc} was as high as 2.4. The impact of fluidic thrust vectoring on C_{fg} was small.

Multi-Axis Thrust Vectoring Results. A nozzle designed to vector in both yaw and pitch will often be required to do both simultaneously. In order to assess the multiaxis thrust capability of this concept, data were obtained with both a yaw slot and a pitch slot flowing at the nozzle exit. Figure 12 shows the data obtained for this configuration. At the design NPR, δ_y up to 6.3 deg and δ_p up to 5.2 deg were observed. At lower throttle settings, δ_y up to 8.5 deg and δ_p up to 9 deg were observed.

The data trends for primary discharge coefficient and gross thrust coefficient were similar to those seen for yaw vectoring.

Comparison to Other Thrust Vectoring Methods. In order to assess the merits of fluidic throat skewing as a method of achieving thrust-vector control, comparisons to other methods were made at an NPR of 5.5. Figure 13 shows a comparison of fluidic throat skewing to the mechanical throat skewing results of Wing et al. [13] and the shock vector control (SVC) results of Wing [9]. The CFN has a higher C_{fg} for a given thrust vector angle than both the mechanical and SVC methods. Note the large increment in C_{fg} when not thrust vectoring ($\delta_y = 0$ deg); the CFN is more than 3.5 percent more efficient than the SVC concept with the largest vectoring capability ($A9/A8 = 1.944$).

Figure 14 shows a comparison of fluidic throat skewing and shock-vector control in terms of thrust vectoring versus injected mass flow. Fluidic thrust vectoring and shock-vector control show comparable performance in terms of vectoring effectiveness.

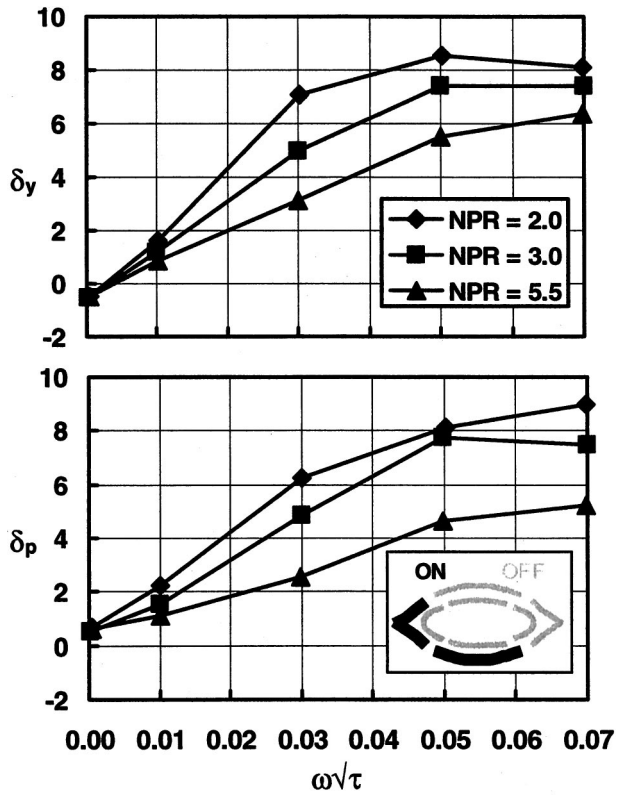

Fig. 12 Multiaxis vectoring performance

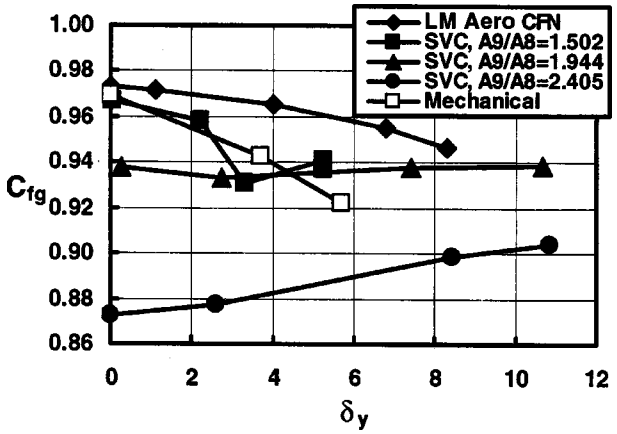

Fig. 13 Comparison of thrust vectoring methods

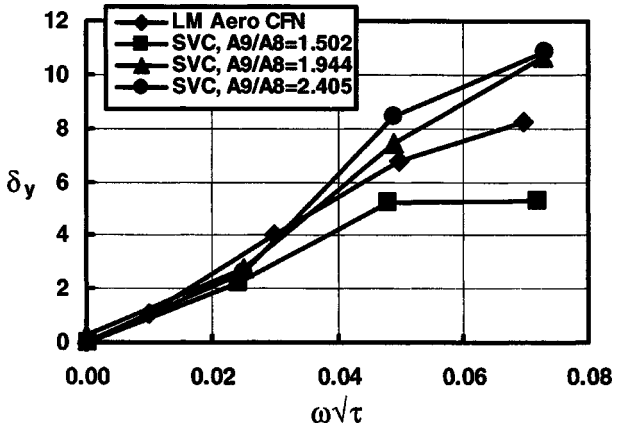

Fig. 14 Comparison of fluidic throat skewing and shock vector control

Conclusions

Based on the trends seen in the experimental data, fluidic throat skewing is an effective and efficient means of providing multiaxis thrust vectoring control in a fixed-geometry nozzle. At design conditions, fluidic throat skewing achieved a vectoring effectiveness (K_{vc}) of 2 deg in yaw for every 1 percent of injected mass flow and 1.7 deg in pitch. Still higher vectoring effectiveness was observed at lower NPR. Fluidic throat skewing proved as effective for multiaxis thrust vectoring as it was for yaw or pitch.

Fluidic throat skewing achieved multiaxis thrust vector control without large impacts on thrust efficiency. Fluidic throat skewing is as effective as other advanced means of thrust vectoring while maintaining superior gross thrust efficiency.

Acknowledgment

The authors would like to express our gratitude to Lockheed Martin's model fabrication and test teams, especially to Bruce Tilley, Eric Caldwell, and Ed Kocialski. We would also like to thank Erich Bender, Brian Smith, and Chris Reed for their expertise and assistance in the CFD analyses.

Nomenclature

- $A9/A8$ = Nozzle expansion area ratio
- $C_{d,p}$ = Nozzle discharge coefficient: $W_p / W_{p,\text{ideal}}$
- C_{fg} = Nozzle thrust (F) efficiency referenced to ideal thrust of all streams: $F/(F_{p,\text{ideal}}+F_{s,\text{ideal}})$
- CFD = Computational Fluid Dynamics
- DOE = Design of Experiments
- LM Aero = Lockheed Martin Aeronautics Company
- K_{vc} = Vectoring effectiveness: $=\delta/(100^*\omega_i)$
- p = Subscript: primary nozzle entrance flow stream
- s = Subscript: secondary injection flow stream
- RTAC = Range of throat-area control: $=100^*(A_{\text{max,eff}}-A_{\text{min,eff}})/A_{\text{min,eff}}$
- SPR = Secondary pressure ratio $=P_{t,s}/P_{t,p}$
- thr = Subscript: throat location or conditions
- W = Mass flow rate
- δ_p = Pitch Thrust Vector Angle (degrees)
- δ_y = Yaw Thrust Vector Angle (degrees)
- τ = Ratio of secondary to primary total temperature
- ω = Mass flow ratio: $\omega_i = W_s / W_p$
- $\omega\sqrt{\tau}$ = Corrected weight flow ratio

References

[1] Miller, D. N., Yagle, P. J., and Hamstra, J. W., 1999, ''Fluidic Throat Skewing for Thrust Vectoring in Fixed Geometry Nozzles,'' AIAA 99-0365.

[2] Miller, D. N., and Catt, J. A., 1995, ''Conceptual Development of Fixed-Geometry Nozzles Using Fluidic Injection for Throat-Area Control,'' AIAA 95-2603.

[3] Miller, D. N., Catt, J. A., and Walker, S. H., 1997, ''Extending Flow Control of Fixed Nozzles Through Systematic Design: Introducing Assisted Reinjection,'' ASME FEDSM97-3680.

[4] Gridley, M. C., and Walker, S. H., 1996, ''Inlet and Nozzle Tech. for 21st Century Aircraft,'' ASME 96-GT-244.

[5] Chiarelli, C., Johnsen, R. K., and Shieh, C. F., 1993, ''Fluidic Scale Model Multi-Plane Thrust Vector Control Test Results,'' AIAA 93-2433.

[6] Strykowski, P., and Krothapalli, A., 1994, ''Thrust Vector Control of Rectangular Jets Using Counter Flow,'' AFOSR Contractors Meeting Abstract.

[7] Gunter, F., and Fahrenholz, F., 1961, ''Final Report on a Study of Rocket Thrust Control by Gas Injection,'' MIT Naval Supersonic Lab, Technical Report 430.

[8] Walker, S., 1997, ''Lessons Learned in the Development of a National Program,'' AIAA 97-3348.

[9] Wing, D. J., 1994, ''Static Investigation of Two Fluidic Thrust-Vectoring Concepts on a Two-Dimensional C-D Nozzle,'' NASA TM 4574.

[10] Catt, J. A., Miller, D. N., and Giuliano, V. J., 1995, ''A Static Investigation of Fixed-Geometry Nozzles Using Fluidic Injection for Throat-Area Control,'' AIAA 95-2604.

[11] Yokota, J. W., et al., 1988, ''A Diagonally Inverted LU Implicit Multigrid Scheme,'' AIAA 88-3565-CP.

[12] Smith, B. R., 1990, ''The k-kl Turbulence Model and Wall Layer Model for Compressible Flows,'' AIAA 90-1483.

[13] Wing, D. J., Mills, C. T. L., and Mason, M. L., 1997, ''Static Investigation of a Multiaxis Thrust-Vectoring Nozzle With Variable Internal Contouring Ability,'' NASA TP 3628.

The Potential Impact of Utilizing Advanced Engine Technology for a Combat Capable Unmanned Air Vehicle (UAV)

G. B. Bruening
Turbine Engine Division,
Air Force Research Laboratory,
Wright-Patterson Air Force Base, OH

J. R. Snyder

R. E. Fredette

Universal Technologies Corporation,
Dayton, OH

This paper evaluates the potential impact of utilizing advanced engine technology for a limited life, combat capable, unmanned air vehicle (UAV) application. A study was conducted to define payoffs in terms of mission capability and system level life cycle costs (LCC) associated with implementing three different engine development approaches into a combat capable UAV design. The three different approaches considered were: a new, advanced technology engine; an existing (off-the-shelf) engine; and a derivative of an existing engine with limited technology insertion. A detailed vehicle configuration design was developed to conduct this assessment, including a low observable (LO), highly integrated engine/airframe layout for survivability and mission adaptable considerations. The vehicle is designed with multirole mission capability such as suppression of enemy air defense (SEAD), close air support (CAS), and battlefield air interdiction (BAI). A system level performance comparison is assessed with the three different engine approaches, specifically for the SEAD-type mission. For the cost analysis, the multirole mission capability is reflected in the overall assumptions such as in the number of aircraft needed to meet the mission requirements. A system level assessment such as in this study is essential in determining whether the additional costs associated with the development of a new, advanced engine is worth the investment. The results of this study suggest that advanced engine technology insertion can provide significant benefits in terms of mission range capability, vehicle weight/size, and overall life cycle costs versus an existing engine.
[DOI: 10.1115/1.1362666]

Introduction

Unmanned air vehicles are in military operation today, designed primarily for reconnaissance roles. The next generation of UAV's are being designed for air-to-ground attack roles, undertaking the more dangerous missions such as the suppression of air defenses (SEAD) and deep penetration strikes. The UAV concept entails a communications and control system with trained personnel to operate the vehicles remotely from their station. There are significant advantages with a pilotless aircraft, foremost of which is the elimination of risk to the aircrew in a high-threat environment. Combat UAV's will be significantly smaller and lighter than manned aircraft, which, along with utilizing stealth technologies, greatly reduces the threat of enemy detection. In terms of cost, the smaller aircraft will greatly reduce acquisition costs relative to manned aircraft carrying the same payload. Elimination of manned aircrew allows for radical aircraft design changes and reduces the development and maintenance costs. Much of the personnel training can be conducted in a virtual simulation environment, allowing more vehicles to remain in storage until required for operational deployment. While in storage containers, the air vehicle will require minimal, if any, maintenance.

There are specific propulsion needs in the areas of performance, affordability, and supportability for a combat capable UAV. Low cruise specific fuel consumption is the key to achieving acceptable mission range capability. The need to reduce the size of the aircraft requires a high specific thrust (thrust per airflow) engine characteristic to limit the engine size. For survivability, the aircraft is designed for LO capability which makes engine/airframe integration design important to minimize installation losses.

Tradeoffs associated with the engine development, production, and operational costs as well as engine performance must be considered. The need for lower cost systems is an important consideration in the development and production cost aspects of the propulsion system. In terms of operations and support (O&S) costs, the UAV propulsion system will require high reliability with minimum maintenance, as well as long term storage capability.

Engine Development Approaches

There are three different engine development approaches that might be considered for a new air vehicle. Figure 1 illustrates each of these three possible development program scenarios that would lead to initial engine production.

One approach is to utilize an existing engine currently in operation. This engine may have been initially developed for either a commercial or military application. The intent of this approach is to minimize the upfront costs associated with a full engine development program. A limited development program, however, would still be required to include some modifications to the existing engine. This would also require some level of engine testing, dependent on the degree of modifications. For example, the shaft bearings may need to be replaced with a different material to improve extended storage capability. The lubrication system may need to be redesigned to handle a more demanding type of mission, which may include inverted flight. The engine control system will need to be modified to interface with the new vehicle flight controls. Also, engine testing will be required to verify performance and operability when integrated with an LO inlet and exhaust system. Since an existing engine was probably designed for a different type of mission, vehicle performance may be sig-

Contributed by the International Gas Turbine Institute (IGTI) of THE AMERICAN SOCIETY OF MECHANICAL ENGINEERS for publication in the ASME JOURNAL OF ENGINEERING FOR GAS TURBINES AND POWER. Paper presented at the International Gas Turbine and Aeroengine Congress and Exhibition, Munich, Germany, May 8–11, 2000; Paper 00-GT-014. Manuscript received by IGTI Feb. 2000; final revision received by ASME Headquarters Jan. 2001. Associate Editor: M. Magnolet.

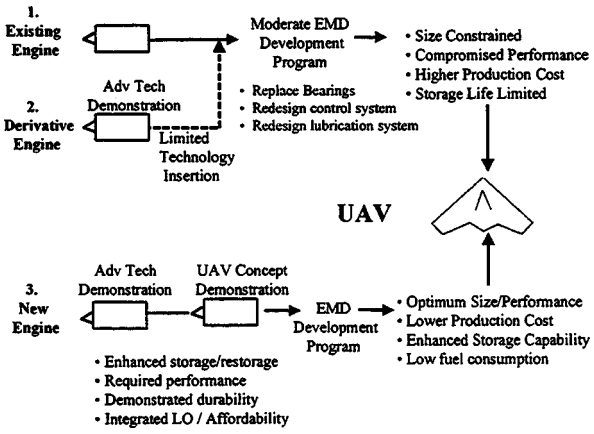

Fig. 1 Engine development approaches

nificantly compromised due to the engine cycle being less than optimal. The vehicle size and weight are also constrained by the engine thrust capability.

An alternative approach is to develop a derivative engine based on an existing engine. For example, a new low spool (fan and low pressure turbine) can be designed to better optimize the cycle (i.e., higher bypass ratio) or to reduce the number of fan stages. Another option is to ''throttle push'' the existing engine by increasing the turbine inlet temperature. This will increase thrust to meet vehicle requirements, but at the expense of engine life. A derivative engine approach can be used to obtain a more optimal engine cycle but the improvement in overall engine performance is constrained by the engine core (high-pressure compressor, combustor, and high-pressure turbine) of the existing engine.

A third approach is to develop a new engine with a full engine EM&D development program by implementing advanced technologies that have been successfully demonstrated in advanced research programs. The technologies assumed have a technology availability date (TAD) of 2003. This approach increases the overall engine development costs, but maximizes the vehicle capability in terms of improved performance, reduced vehicle size, lower fuel consumption, and better LO integration. A reduced number of parts in the engine, improved manufacturing processes, as well as a smaller engine size, will reduce the engine production costs as well. There are technologies that can enhance storage capability (i.e., oil-free bearings) that will reduce vehicle O&S costs.

Engine Cycle Characteristics

Figure 2 compares the uninstalled engine characteristics of a notional existing engine, a derivative engine, and a new engine

	Existing Engine	Derivative Engine (New Low Spool)	New Engine (Advanced)
Design Condition	SLS	SLS	0.8Mn/40K
BPR_{Design}	0.5	1.0	2.5
FPR_{Design}	3.0	2.6	3.8
OPR_{Design}	17.9	16.4	38
T_{41}, Max (°F)	2470	2340	3150
$T_{Exhaust\ @cruise}$ (°F)	946	603	702
Inlet Dia. (in)	23.3	24.2	23.0
Length (in)	77.0	80.6	58.0
Weight (lbm)	1313	1291	664
FN, 0.8Mn/40K (lbf)	1571	1255	1359
SFC, 0.8Mn/40K	0.982	0.856	0.784
Development Cost ($M)	20	74	160
Unit Production Cost ($M)	1.5	1.2	0.6

Fig. 2 Engine characteristics

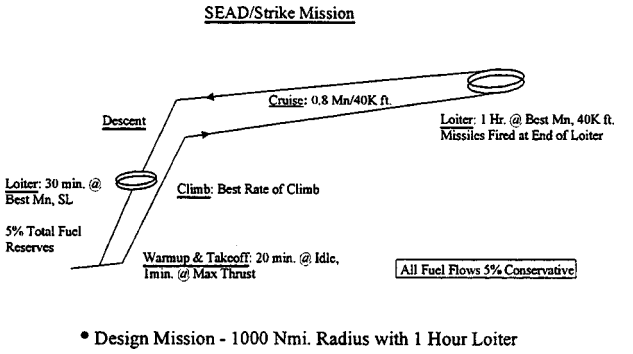

Fig. 3 Baseline UAV mission

that were created using in-house modeling programs. All three engines are a nonafterburning, mixed-flow turbofan with both a low spool (fan+LPT) and a high spool (HPC+combustor+HPT). The derivative engine assumes the same engine core as the existing engine, with a new low spool. The new engine utilizes advanced technologies to increase turbine inlet temperature ($T_{4.1}$) and overall pressure ratio (OPR). The result is a significantly smaller core and higher bypass ratio at approximately the same inlet diameter as the existing engine. The higher bypass ratio reduces the specific fuel consumption for improved mission range.

Another outcome of a higher bypass ratio cycle is the reduced exhaust temperatures (as shown in Fig. 2.). Both the derivative and new engine cycles have a significantly lower temperature than the existing engine with approximately the same exhaust area. This reduces the infrared (IR) signature for improved stealth capability. The new engine exhaust temperature, however, is 100 deg F higher than the derivative engine due to the significantly higher turbine rotor inlet temperature ($T_{4.1}$) to maximize the fuel efficiency.

Figure 2 also compares the estimated development cost and unit production cost for each engine approach. The development costs were determined from a cost-modeling program based on a 1000 hr engine life and the number of engine test hours required, dependent on how unique the engine is relative to an existing engine. The percent uniqueness assumed for the existing, derivative, and new engines are 100, 50, and 20 percent, respectively. The number of development test engines required for each development approach is based on the number of test hours required. The engine production costs are compared in terms of engine unit cost per pound of thrust at sea level.

Air Vehicle Configuration

The UAV's mission profile assumed in this study is shown in Fig. 3. The vehicle configuration is designed for a SEAD type mission with a 1000 nautical mile (nm) mission radius, with cruise segments at 0.8 Mach Number and 40,000 ft, and a 1 hour loiter time. It is assumed that two AGM-88 HARM missiles are fired from the aircraft at the end of its loiter before returning home.

The baseline UAV was configured to accomplish the design mission and to maximize the number of these UAV's that can fit into the cargo bay of the C-17 military transport to minimize deployment costs. Figure 4 shows the dimensioned three view drawing of the baseline UAV as well as some of its basic configuration characteristics. The baseline vehicle is designed assuming the new advanced engine and an airframe technology availability date (TAD) of 2003. The engine is designed to maximize the mission radius and to provide an adequate rate of climb. The selected main and nose gear lengths provide the UAV with a ground attitude of five degrees. This angle of attack allows the vehicle to fly off the ground, without rotation, in 5400 feet. At the

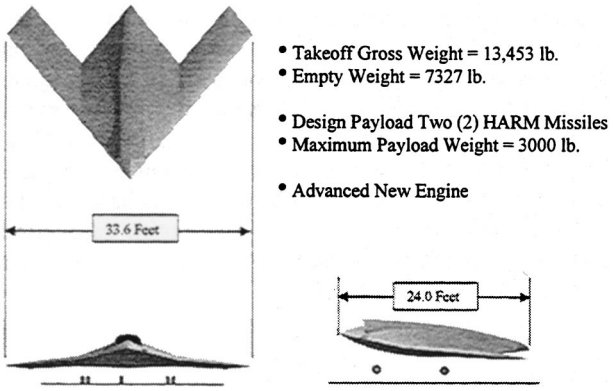

Fig. 4 Baseline UAV configuration

end of the outbound cruise leg (flown at 0.8 Mach Number and 40,000 ft.) the UAV's rate of climb is over 1400 feet per minute. Low observable (LO) treatments of the inlet and exhaust are assumed but not shown.

The arrangement of the internal components is particularly important to the mission efficiency of the LO vehicle. The HARM's length and its large nonfolding wings make a conventional internal component layout very inefficient. A conventional layout would place the engine, inlet, and exhaust systems on the vehicle centerline and the two HARM missiles in weapons bays on either side. For an LO UAV configuration, this internal arrangement produces a large, low density aircraft with two relatively small weapon bays of limited utility. The resulting vehicle size also limits the number of UAV's that can be carried by a C-17.

To improve the internal packaging of the UAV, the unsymmetrical configuration shown in Fig. 5 was developed. The internal arrangement of the propulsion system, avionics package, landing gear, and the two HARM missiles is highlighted. The HARM missiles are placed in a piggy-back arrangement and staggered fore and aft for wing and fin clearance. The engine is placed unsymmetricly to the left of the missiles. The exhaust system has a horizontal ''S'' turn for 100 percent line of sight (LOS) blockage and returning the gross thrust vector to the aircraft center line. The exhaust duct transitions from circular at the engine exit to near rectangular at the duct exit. The inlet system transitions from

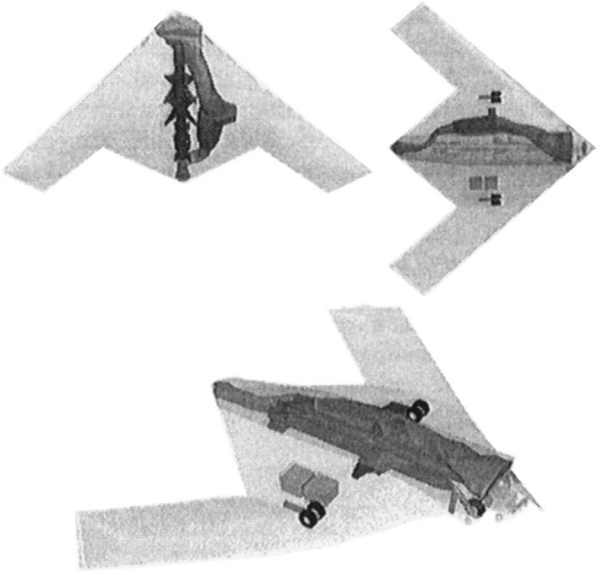

Fig. 5 Vehicle internal arrangement

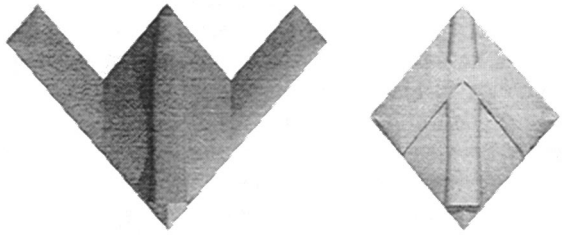

Fig. 6 UAV storage

circular at the engine face to a higher aspect ratio shape at the vehicle inlet face. The inlet system, in effect, does a ''barrel roll'' around the piggy-backed missiles. The offset hides the engine face and places the ram drag vector on the airplane centerline.

This packaging arrangement minimizes the thickness of the UAV and allows two containerized UAV's to be stacked vertically on the C-17's cargo bay floor; thereby, doubling the number that can be carried. Also, this packaging arrangement minimizes the length of the root chord and maximizes the number of containers that can be placed on the cargo floor. The single weapons bay is longer and larger than the dual HARM bays and can accommodate a significantly larger selection of air-to-ground and air-to-air missiles. The weapons bay is stressed to carry up to 3000 lbs. in anticipation of future use of this larger bay.

The fuel tanks are not shown, but are arranged symmetrically about the centerline. There are four tanks on each side of the UAV to help provide center of gravity management for both pitch and roll moments.

Figure 6 illustrates the baseline UAV in both the folded and unfolded condition. The UAV is designed to fit in the storage container also used for shipping the vehicle in a C-17. The outer wing panels are removed and stored above the aft part of the center body. This arrangement allows the vehicle to be stored in a container that is just a few inches bigger than the center body itself. Ten baseline UAV's can be containerized and transported in a C-17. An increase of only seven inches in length of the baseline vehicle's 24 foot root chord results in the C-17 being able to carry only 8 UAV's in the cargo bay.

The baseline UAV is capable of carrying different weapons loadouts due to the offset engine configuration. Figure 7 illustrates three sample missions and the possible weapons loadouts for those missions. The offset engine configuration results in a single large unsymmetrical weapons bay of much improved utility com-

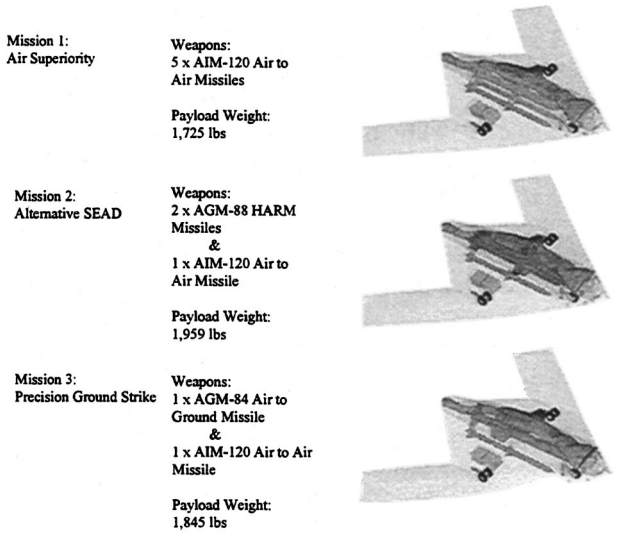

Fig. 7 Other missions and payloads

pared to that of two smaller single HARM bays. Mission #1 is an air superiority/combat air patrol (CAP) mission. This weapon loadout allows the UAV to carry five AIM-120's in the payload bay. In this configuration the UAV could provide CAP over a given area or hunt high value targets or other UAV's. An alternative SEAD mission weapons loadout is shown under mission #2. In addition to the two AGM-88 HARM missiles of the design mission, the UAV also carries one AIM-120 missile for self-protection. A precision strike mission is shown under mission #3. This weapons loadout provides a precision strike capability by carrying a AGM-84 SLAM as well as an AIM-120 for self-protection.

Other weapons loads can be carried in this large bay further increasing the number of potential missions for this UAV. It should also be mentioned that all missions could benefit from weapons with folding fins. This could further increase the number of weapons in the bay or reduce the size, weight, and cost of the airframe.

Air Vehicle System Impact

Each of the three engine cycles previously described were installed in our in-house vehicle simulation model and flown in the mission simulation to define the performance benefits of using a new advanced engine versus a derivative or existing engine. The installation losses associated with the inlet, exhaust, horsepower extraction, and LO device were accounted for in the installed engine performance of each engine cycle. The size of the UAV is fixed for the vehicle performance analysis, using the baseline UAV originally sized with the new advanced engine to accomplish the design mission of one hour of loiter time and 1000 nm radius. Two HARM missiles is assumed for the payload for each case. As shown in Fig. 8, the UAV performance with the new advanced engine is significantly better than either the derivative engine or the existing engine. At the design endurance of one hour the new advanced engine provides a radius improvement of 84 percent over that of the existing engine. At a fixed radius of 400 nautical miles, the endurance time improvement is 160 percent. In addition, the UAV's gross weight with the new advanced engine is about 6 percent less than the gross weight when the existing engine is used due to the lower engine and engine installation weights of the new advanced engine.

Figure 9 illustrates the impact that the three different engine technologies have on the size and weight of the UAV for each vehicle to accomplish the same mission of one hour of loiter and 1000 nm radius. The use of a derivative engine or an existing engine results in a significant increase in UAV size and weight when compared to the baseline UAV. For example, use of the existing engine increases the gross weight 34 percent and the empty weight by 26 percent when compared to the UAV using the new advanced engine. The linear dimensions are also increased by

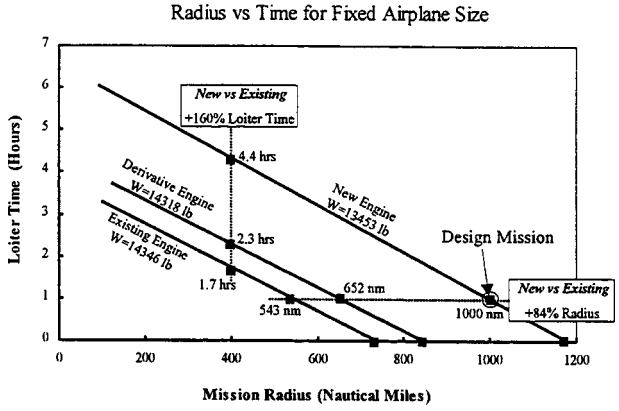

Fig. 8 System performance impact

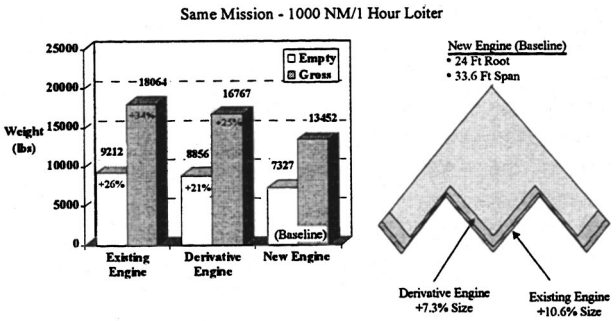

Fig. 9 System weight and size impact

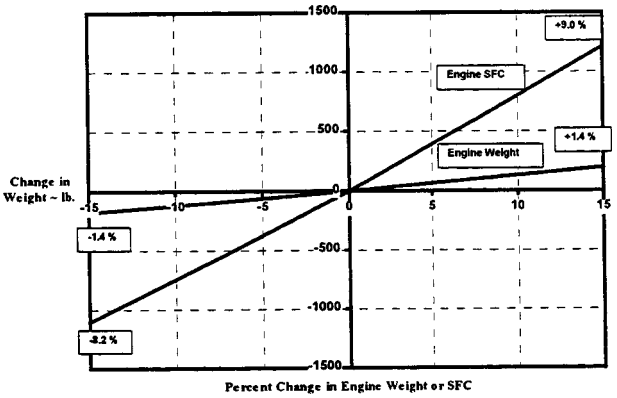

Fig. 10 Aircraft gross weight sensitivity to engine changes

10.6 percent. The vehicle size increase due to the use of the derivative engine or the existing engine would reduce the number of UAV's that can be carried in the cargo bay of a C-17 from 10 to 8. This would require 25 percent more C-17 flights to transport the same number of UAV's, impacting O&S costs.

As previously stated, a new advanced engine will improve both engine SFC and engine weight, which has a positive impact on aircraft gross weight. Figure 10 illustrates these sensitivities to aircraft gross weight for the baseline UAV, assuming a fixed design mission of 1000 nm and one hour loiter. As shown, gross weight change is much more sensitive to variations in the engine's SFC than it is to changes in engine's weight. A 15 percent increase in the new advanced engine's SFC results in a 9.0 percent increase in the UAV's gross weight to accomplish the same mission. A 15 percent increase in the new advanced engine's weight results in only a 1.4 percent increase in vehicle weight. The aircraft gross weight is more sensitive to SFC than to engine weight due to the vehicle's fuel weight fraction (.32) being significantly larger than its engine weight fraction (.05).

UAV Cost Assessment

The vehicle was flown in a SEAD mission to compare the system performance capability with each engine technology. However, the UAV design of this study possesses inherent capabilities in the various attack roles as well—especially with respect to close air support (CAS) and battlefield air interdiction (BAI). This study did not include an electronic warfare role, but with some revisions and additions to the avionics suite, this additional role might also be accommodated by this UAV. Accordingly, a basic assumption for this UAV cost assessment is that both SEAD *and* attack combat roles will be expected of the UAV designs. The major affect of this decision is that greater numbers of the aircraft will be needed than for a SEAD—only application.

Table 1 UAV life cycle costs

	Existing	Derivative	New
Acquisition	$ 10.481 B	$ 10.192 B	$ 9.325 B
RDT&E	$ 1.853 B	$ 1.889 B	$ 1.865 B
Production	$ 8.628 B	$ 8.302 B	$ 7.459 B
Sustained Engineering	$ .043 B	$ .041 B	$ .036 B
O & S	$ 3.942 B	$ 3.913 B	$ 3.838 B
Total Life Cycle Cost* (20 yrs)	$ 14.466 B	$ 14.146 B	$ 13.197 B

*All Costs in Year 1999 Dollars

For purposes of compiling systems life cycle cost (LCC) in this UAV study, an organizational structure for operations was developed that has the following characteristics:

- 14 UAV squadrons of 32 air vehicles (AV) each.
- 28 AV's per squadron are made available for combat operations when general or expeditionary force deployment is effected. In combat mission operations, 20–24 AV's are employed in flights of four each so that four to eight AV's are positioned for stand-by status and as attrition replacements.
- 4 AV's per squadron are permanently dedicated to peacetime live fire training operations and always remain at the continental U.S. (CONUS) home base.
- Total buy quantity is 470 AV's.

This study assumes a 20-year life cycle of the vehicles with both peacetime operations and wartime operations scenarios. Each operator will fly two three-hour practice missions and one six-hour mission per year to complement continuing on-simulator exercises. The wartime scenario assumes three conflict types within the 20-year period: two simultaneous conflicts of 12-month duration, two separate conflicts of nine-month duration, and ten separate (short term) conflicts of two months each.

The UAV system costs are compared for the three different engine technologies assumed. This was done at each costing level: RDT&E, production, sustained engineering, O&S, unit flyaway, and total life cycle cost (LCC). Detailed life cycle cost results are shown in Table 1. The acquisition costs (RDT&E+production) include both the air vehicle and nonflight equipment. This includes such items as the communications and control stations, training simulators, air vehicle containers, and maintenance equipment. Nonflight equipment O&S costs, however, are not included in the total LCC shown. The acquisition costs constitute some 71 percent of the total LCC while sustained engineering and O&S costs make up the remainder. However, it is important to note that the O&S costs due to C-17 hauling are not included in the UAV O&S costs. The UAV configuration using a new engine is smaller than one with an existing engine, allowing more UAV's to fit in a C-17 at one time, resulting in reduced C-17 operation costs.

It is significant that the corresponding increase in system development costs (+0.6 percent, +12.2M$ RDT&E) due to a new engine approach ultimately results in a 1.3B$ LCC reduction.

The unit flyaway costs (UFC) are shown in Table 2. For each UAV engine technology classification, the UFC is divided between engine, avionics, and airframe. Notice that engine related costs contribute the least to overall UFC while avionics costs clearly dominate. The UFC greatly improves as the progression from ''existing'' to ''new'' is traversed. The influence of engine technology is the combined effect of engine size and cost as embodied in the air vehicles sized to the common design mission.

Table 2 Unit flyaway costs

	Existing	Derivative	New
Unit Flyaway Cost*	$ 18.358 M	$ 17.665 M	$ 15.870 M
Engine	$ 2.305 M	$ 1.826 M	$ 0.952 M
Avionics	$ 9.639 M	$ 9.639 M	$ 9.639 M
Airframe	$ 6.414 M	$ 6.200 M	$ 5.279 M

*All Costs in Year 1999 Dollars

Concluding Remarks

The study results indicate that overall costs are relatively insensitive to engine acquisition costs. Therefore future UAV studies might consider engine life longer than the 1000 hours assumed in this study. The degree of intensity for future wartime usage is difficult to predict, especially for a new type of system such as a UAV. High intensity employment of these systems can be very demanding, requiring much higher engine life than originally assumed.

The number of aircraft needed to meet the system requirements became an important factor in the cost assessment. This is directly influenced by the multimission capability of the vehicle. If the role of this UAV was limited to just one specific mission, the quantities assumed would be significantly less, making it difficult to justify the development of a new engine based on cost alone. This was an important consideration in the vehicle design, resulting in a unique engine/airframe layout.

This study has shown that advanced engine technology can significantly improve combat UAV system performance, reduce overall costs, and provide the opportunity to satisfy UAV unique propulsion needs. These benefits are not apparent without conducting a system level analysis such as this to understand the full impact.

Nomenclature

UAV = unmanned air vehicle
LCC = life cycle cost
LO = low observable
SEAD = suppression of enemy air defense
CAS = close air support
BAI = battlefield air interdiction
EM&D = engineering, manufacturing, & development
TSFC = thrust specific fuel consumption (lbm/lbf-hr)
FN = net thrust (lbf)
BPR = engine bypass ratio
OPR = overall pressure ratio
FPR = fan pressure ratio
HPC = high pressure compressor
HPT = high pressure turbine
LPT = low pressure turbine
$T_{4.1}$ = high pressure turbine rotor inlet temperature (°F)
IR = infrared
Mn = mach number
SLS = sea level static inlet condition
Max A/B = maximum afterburner
FN/Wa = specific thrust (lbf/lbm/sec)
T/W = engine thrust-to-weight ratio
TAD = technology availability date
HARM = high speed antiradiation missile
O&S = operations & support
RDT&E = research, development, test, & evaluation
UFC = unit flyaway cost

Performance Benefit Assessment of Ceramic Components in an MS9001FA Gas Turbine

C. M. Grondahl
Power Generation Systems,
One River Road,
General Electric Company,
Schenectady, NY 12345

T. Tsuchiya
Energy Conversion Department,
Energy and Environment R&D Center,
The Tokyo Electric Power Company, Inc.

The introduction of a ceramic gas turbine component in commercial power generation service will require significant effort. A careful assessment of the power plant performance benefit achievable from the use of ceramic components is necessary to rationalize the priority of this development compared to other alternatives. This paper overviews a study in which the performance benefit from ceramic components was evaluated for an MS9001FA gas turbine in a combined cycle power plant configuration. The study was performed with guidelines of maintaining constant compressor inlet airflow and turbine exit NOx emissions, effectively setting the combustion reaction zone temperature. Cooling flow estimates were calculated to maintain standard design life expectancy of all components. Monolithic silicon nitride ceramic was considered for application to the transition piece, stage one and two buckets, nozzles and shrouds. Performance benefit was calculated both for ceramic properties at 1093°C (2200°F) and for the more optimistic 1315°C (2400°F) oxidation limit of the ceramic. Hybrid ceramic-metal components were evaluated in the less optimistic case. [DOI: 10.1115/1.1335476]

Introduction

Performance benefits from ceramic gas turbine hot section components are derived from operating them at higher temperatures with less cooling than the metal parts they replace. Development of ceramic materials for these components has been progressing steadily. Yet, there is still a significant effort required to implement a ceramic component in a utility-size turbine in commercial service for power generation. It was desirable from the point of view of both GE and TEPCO to determine whether that effort is prudent at this time in light of other advanced power plant options such as closed circuit steam cooling and reheat turbine technology that are being developed. To that end, a program was initiated to determine the power plant thermal efficiency benefits achievable by using state of the art monolithic ceramic components in a utility-size gas turbine.

Figure 1 identifies the ceramic components considered in this performance assessment. They include the combustion transition piece, stage one bucket, nozzle and shroud, and stage two bucket and nozzle.

Performance Analysis Guidelines. To assure that the study was firmly based on actual product considerations, a recent production MS9001FA gas turbine in a single shaft advanced combined cycle power plant configuration was specified as the baseline of comparison. The particular unit used for the baseline was the S109FA combined cycle power plant configured for Tokyo Electric Company (TEPCO) Yokohama ACC using one PG9311FA gas turbine, one reheat unfired heat recovery steam generator (HRSG), and one steam turbine and selective catalytic reaction (SCR) in the HRSG for NOx control. Combined cycle performance was calculated using the same design point procedures used for the Yokohama ACC power plant including exact temperatures, pressures, and turbine efficiencies. Performance benefit results utilizing ceramic components are reported relative to baseline performance.

The primary performance evaluation study was done at a constant NOx emission level of 25 PPM in the exhaust of the baseline MS9001FA turbine so that ceramic component contributions to output and efficiency could be evaluated on a consistent environmental basis. Since NOx emissions are directly related to the turbine combustion reaction zone temperature, the turbine inlet temperature (defined at the exit plane of the combustion system transition piece) was held constant in each analysis. Baseline compressor airflow was maintained constant throughout the study. However, combustion system pressure drop reduction and reduced compressor discharge extraction cooling flow with ceramic components tends to increase airflow through the combustor. This results in reduced fuel-to-air ratio, lower flame temperature, and less NOx. To sustain the study guideline of constant emissions, fuel flow and turbine firing temperature (defined at the exit plane of the first stage nozzle) were increased as necessary in each analysis to keep turbine inlet temperature, at transition piece exit, constant.

Cooling and sealing requirements of both the near adiabatic ceramic components and conventional components affected by the

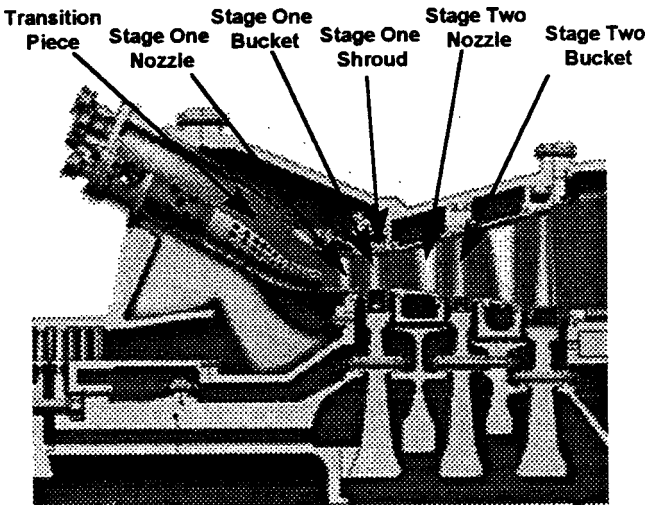

Fig. 1 MS9001FA turbine—note ceramic components in benefit assessment

Contributed by the International Gas Turbine Institute (IGTI) of THE AMERICAN SOCIETY OF MECHANICAL ENGINEERS for publication in the ASME JOURNAL OF ENGINEERING FOR GAS TURBINES AND POWER. Paper presented at the International Gas Turbine and Aeroengine Congress and Exhibition, Stockholm, Sweden, June 2–5, 1998; ASME Paper 98-GT-186. Manuscript received by IGTI March 3, 1997; final revision received by the ASME Headquarters November 1, 2000. Associate Technical Editor: R. Kielb.

Table 1 ''Optimistic'' and ''less optimistic'' conceptual design considerations

	Producibility & Acceptance	Temperature Limit, Ceramic Material	Cooling of Ceramic Components	Seal Leakage Assumptions
'Optimistic' Case	Neglected	1315°C (2400°F) oxidation limit at surface Tmax.	Used as necessary to meet oxidation limit.	Ceramic interface seal leakage same as metal parts.
'Less Optimistic' Case	Hybrid ceramic-metal components evaluated as more readily accepted, reliable parts.	1204°C (2200°F) oxidation limit and greater strength at design temp.	Used as needed to meet ceramic and metal parts design life.	More seal leakage with more ceramic parts.

introduction of ceramic parts were evaluated using current design practices and turbine models to assure a careful and realistic assessment of performance benefits. As firing temperature increased relative to the baseline (to meet the study guideline of constant emissions), additional cooling air was required to preserve conventional component lives. Cooling technology curves similar to those described in [1], and shown in Fig. 6, were used in estimating additional cooling flow requirements. Cooling flow reductions, resulting from the use of ceramic components, as well as cooling flow increases to maintain equivalent conventional part life, also required redistribution of spent cooling flows re-entering the turbine gas path. These effects were included in the performance analysis using existing turbine models to provide a consistent basis of comparison. An exception was made for the third stage bucket which is uncooled. Baseline third stage bucket material temperature limits are exceeded as exhaust temperature increased with higher firing temperatures. The impact of air cooling this bucket, or other means of relief, is not addressed in this paper.

Conceptual ceramic component design configurations were selected from those illustrated in recent technical papers. Detailed mechanical design review and analysis was not performed. However, sufficient thermal analysis relative to local MS900FA gas path conditions was done to establish that ceramic material properties met requisite oxidation limits and had sufficient strength to be considered a reasonable starting point for design studies of each application. Since this design analysis was of a limited nature, a range of potential performance benefit for each ceramic component was considered. Conceptual designs and assumptions that maximize performance benefit potential without regard for ceramic component producibility or acceptance concerns were considered in the ''Optimistic'' case. ''Less Optimistic'' conceptual designs at lower ceramic operating temperature were also considered. These included hybrid metal—ceramic configurations that use ceramic materials to their best advantage and improve the chance of developing successful manufacturing processes. The ''Optimistic'' and ''Less Optimistic'' case analyses provide a bracket of ceramic component performance benefit under a range of design assumptions.

Development of successful ceramic attachments and support methods was assumed to be feasible in both the ''Optimistic'' and ''Less Optimistic'' cases. Both cases also assumed that the surface roughness of ceramic components is similar to that of the conventional materials they are replacing and that there is no performance degradation due to aerodynamic shape changes that may be required to accommodate ceramic component design.

Table 1 summarizes ''Optimistic'' and ''Less Optimistic'' conceptual design considerations.

Ceramic Materials and Properties. Materials considered in this study were limited to monolithic ceramics. Monolithic silicon nitride, SN-88, ceramic was the primary candidate for each component considered. Monolithic silicon carbide was also considered, but thermal analysis did not identify any components that would have a performance benefit over that of silicon nitride. Physical properties of SN-88 used in the evaluation, shown in Table 2, were provided by NGK Insulators, Ltd.

A fracture map of SN-88 material strength capability used in this study is shown in Fig. 2. These data are considered preliminary SN-88 design data. They were obtained as part of the ''Ceramic for Gas Turbines'' program with the Electric Power Research Institute under contract no. EPRI WO8512-05 (formerly RP2608-03).

The highest temperature application of SN-88 ceramic is oxidation limited in the ''Optimistic'' case to 1315°C (2400°F). The ''Less Optimistic'' case oxidation temperature limit for SN-88 is estimated to be 1204°C (2200°F).

Table 2 Properties, SN-88 sintered silicon nitride

Property	Temperature (°C)				
	25	400	800	1200	1400
Density (g/cm^3)	3.52	-	-	-	-
Young's Modulus (GPa)	300	300	300	290	280
Shear Modulus (GPa)	120	120	120	116	112
Poisson's Ratio	0.27	0.27	0.27	0.27	0.27
Coeff. of Thermal Expansion [1]	-	2.7	3.3	3.5	3.5
Thermal Conductivity (W/m-K)	71.1	33.5	25.1	20.9	-
Specific Heat (J/kg-K)	669	1004	1213	1297	-

[1] ($\times 10^{-6}$/K) measured between 40 °C and the temperature indicated.

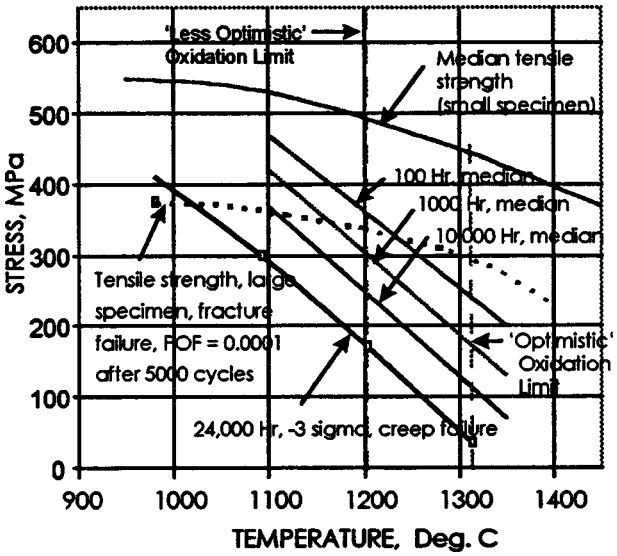

Fig. 2 Fracture mechanism map, SN88

Ceramic Component Thermal Analysis

Ceramic components included in this performance benefit analysis are shown in Fig. 1; the MS9001FA turbine hot gas path cross section. Thermal analyses of the conceptual transition piece,

stage one shroud, stage one and two buckets, and stage one and two nozzles are discussed below. The stage two shroud was also considered, but the baseline design is uncooled and no performance benefit is to be derived from ceramic substitution.

Transition Piece. The baseline MS9001FA combustion system utilizes an impingement cooled transition piece. Pressure drop for impingement cooling to acceptable transition piece material operating temperature contributes to the overall combustion system pressure drop. The ceramic transition piece concept formulated for this analysis is a ceramic liner within an outer shell. This concept is similar to the ceramic transition piece discussed in [2] and illustrated in Fig. 3 with the omission of insulation between the ceramic liner and outer shell.

The outer metal shell in this concept is intended to support the combustion system external to internal differential pressure and minimize ceramic liner tile leakage. An attachment method supporting the ceramic liner pieces within the outer shell was assumed to be feasible in a configuration that allows radiation exchange between the outer shell and ceramic.

Radiation from the ceramic liner to the surrounding casing is an effective heat transfer mechanism at the ''Optimistic'' case oxidation limit of 1315°C (2400°F). Convective backside cooling heat transfer of the outer shell is needed to maintain the approximately 760°C (1400°F) temperature required for the radiation heat transfer thermal load. For the ''Optimistic'' case, all impingement cooling pressure drop was subtracted for the performance benefit assessment.

Conventional transition piece exit seal leakage area was assumed to be the same for the ceramic design. However, at the reduced pressure ratio these leakage flows are reduced. Cooling flows to the exit frame and side seals were maintained on the assumption that a ceramic design will require similar cooling in those areas or other attachment interfaces. Power plant performance improves as a result of the increased firing temperature to maintain constant turbine inlet temperature and lower compressor pressure ratio that requires less compressor work.

The ceramic transition piece concept formulated for the ''Less Optimistic'' case analysis is the same as the ceramic lined ''Optimistic'' case shown in Fig. 3 with the addition of some impingement cooling. The reduced SN-88 oxidation limit of 1204°C (2200°F) requires cooling since radiation heat transfer is less effective at the lower ceramic temperature. Impingement cooling through holes in the outer shell is postulated. Approximately 25 percent of the conventional, baseline impingement pressure drop was estimated from experimental data to be sufficient to maintain the ceramic at 1204°C (2200°F). Therefore, the ''Less Optimistic'' transition piece concept retained about 75 percent of the ''Optimistic'' case transition piece performance benefit.

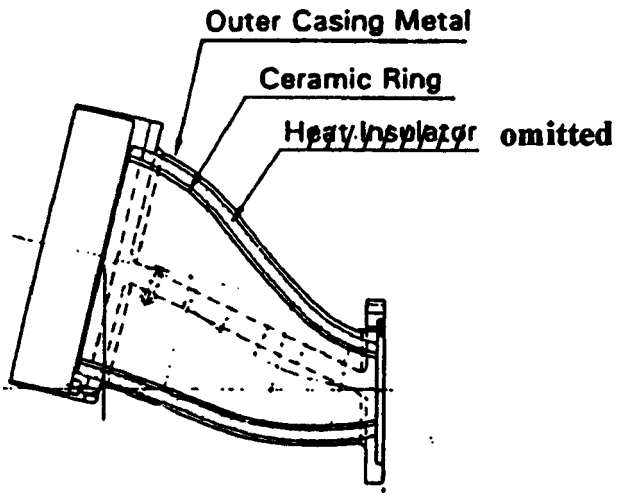

Fig. 3 Ceramic transition piece concept

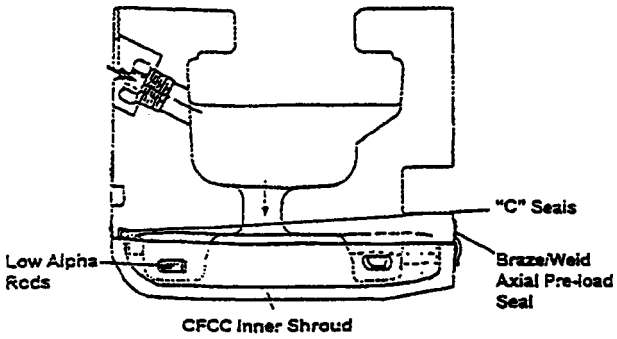

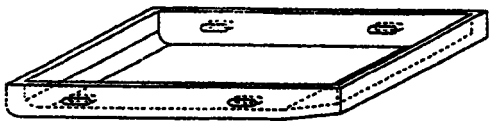

Fig. 4 Ceramic shroud concept

Stage 1 Shroud. The baseline MS9001FA Stage 1 shroud is cooled by compressor discharge air. The maximum shroud gas path temperature is below the ''Less Optimistic'' SN-88 ceramic material oxidation temperature limit of 1204°C (2200°F). Therefore, an uncooled ceramic inner shroud design is feasible from a thermal perspective. However, outer shroud sealing and leakage air flow would still be required to protect those pieces from ingestion of hot gas. Figure 4, taken from [3], illustrates a ceramic inner shroud design concept that formed the basis for this evaluation. The ''Optimistic Case'' Stage 1 ceramic shroud evaluated the performance benefit of a redesigned and modified outer shroud that minimizes leakage and sealing flows. Based on design projections, a 66 percent reduction in baseline Stage 1 shroud cooling and sealing flow was estimated for that design.

The ''Less Optimistic'' performance analysis limited benefits to those incremental to reductions in cooling that may be possible with TBC technology developments. Comparing the minimum flow established for the ''Optimistic Case'' with TBC shroud study results, a 25 percent reduction in shroud cooling and sealing air was predicted at baseline conditions. For the cases where a turbine with a ceramic Stage 1 nozzle was considered to be operating at constant NOx, and significantly higher firing temperature, a 33 percent reduction was estimated.

Stage 1 Nozzle. The baseline MS9001FA stage one nozzle utilizes film cooling from a large number of holes in the vane airfoil and sidewalls to efficiently reduce heat transfer to nozzle surfaces by reducing the surface film temperature. A ceramic stage one nozzle design to meet the SN-88 oxidation life at 1315°C (2400°F), would also require cooling. However, film cooling a ceramic part with many cooling holes penetrating the surface was not considered viable. Instead, an impingement cooled configuration (similar to the ceramic nozzle discussed in [4] and illustrated in Fig. 5) was taken as the ceramic nozzle concept. Thermal analysis was done using baseline turbine gas path aerodynamic geometry for number of vanes, axial length of sidewalls and surface area to be cooled. Ceramic airfoil vane and sidewall thicknesses of 5 mm (0.2 in.) and 6 mm (0.25 in.) respectively were assumed for the calculation of ceramic temperatures. Baseline turbine heat transfer coefficients and gas path temperatures with typical radial profile and pattern factors were used to define external heat transfer.

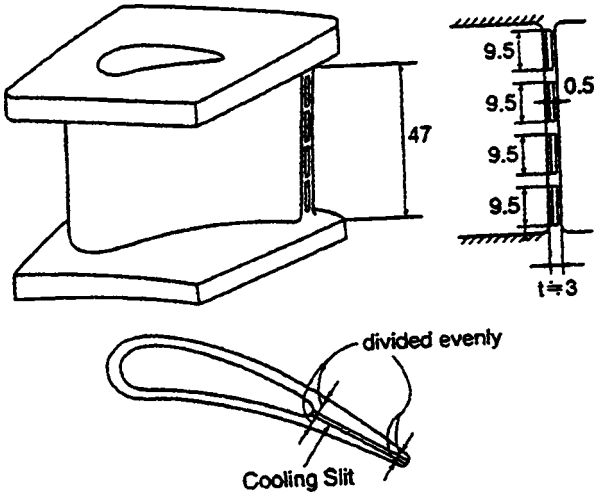

Fig. 5 Ceramic nozzle concept

Internal heat transfer utilized impingement cooling of the vane and sidewalls with compressor discharge air from an array of holes in a perforated plate within the airfoil and behind the sidewalls. Impingement heat transfer coefficients were calculated as described in [5] including crossflow effects. Spent impingement cooling air from the airfoil flowed through trailing edge slots. Convection cooling was shown to adequately cool the trailing edge to ceramic material oxidation limit.

Nozzle analysis also considered design pressure requirements to prevent hot gas ingestion. These pressure margin criteria preclude impingement cooling the vane and sidewalls sequentially in series flow. Sidewalls and nozzle vane are both cooled with air at compressor discharge temperature and pressure. Spent sidewall and vane cooling air discharges into the gas path.

Inner and outer sidewall split line leakage areas per seal for the ceramic nozzle were assumed to be the same as the baseline design in the ''Optimistic'' case nozzle performance benefit analysis. Retaining ring and flange hook leakage flow areas were also unchanged. However, sealing and leakage flows were recalculated for compressor discharge pressure and temperature of each analysis. Lower combustion system pressure drop, resulting from the ceramic transition piece, reduced sealing, and leakage flows.

Cooling required for the ''Optimistic'' case ceramic nozzle vanes and sidewalls was calculated to be only 20 percent of the baseline requirement. Comparison was made with appropriate cooling technology curves similar to that shown in Fig. 6 from [1]. The combined cooling and sealing flow to meet ''Optimistic'' case assumptions is 65 percent less than that of the baseline MS9001FA Stage 1 nozzle.

This reduction in Stage 1 nozzle cooling diverts more airflow through the combustion system, lowering turbine inlet temperature and NOx emissions. At constant firing temperature there would be no performance benefit, but with increased fuel flow and firing temperature to restore turbine inlet temperature and NOx level, there is significant performance improvement. The ''Optimistic'' case ceramic Stage 1 nozzle cooling and sealing flow reduction resulted in an increase in firing temperature of from 88 to 124°C (190 to 256°F) for various combinations of ceramic components. Performance benefits include the effects of additional cooling needed to preserve baseline turbine component life of other parts at elevated firing temperatures as noted before.

The ''Less Optimistic'' Stage one nozzle concept followed that of the ''Optimistic'' design discussed above with revised cooling flow estimates to meet the ''Less Optimistic'' SN-88 ceramic oxidation limit of 1204°C (2200°F) on the nozzle surface. A single vane per segment design was considered prudent for the ''Less Optimistic'' case to reduce operating thermal stress. This doubled inner and outer sidewall split line leakage flow.

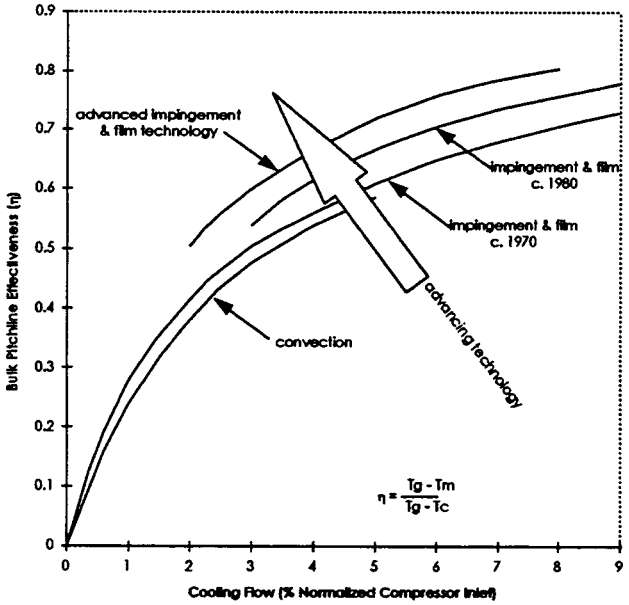

Fig. 6 Typical airfoil cooling technology curves

Thermal analysis using the ''Optimistic'' case analysis described above in conjunction with technology curve projections established the ''Less Optimistic'' vane and sidewall cooling requirement at approximately 39 percent of the baseline. The lower ceramic oxidation temperature limit requires nearly twice the amount of compressor discharge cooling air than the ''Optimistic'' case stage one nozzle. The combined cooling and sealing flow to meet the ''Less Optimistic'' case assumptions is 40 percent less than that of the baseline MS9001FA Stage 1 nozzle. This result reflects the increased seal leakage of a single vane per segment design assumption.

Stage 1 Bucket. The MS9001FA baseline Stage 1 bucket is convectively cooled by air extracted from the 17th stage of the compressor and fed within the turbine rotor to the buckets. An uncooled ceramic bucket at baseline bucket relative gas temperature is below the ''Less Optimistic'' SN-88 oxidation limit of 1204°C (2200°F) and has approximately 170 MPa (25 ksi) tensile strength. A bucket design with these engineering properties is conceptually feasible if the ceramic bucket attachment to turbine rotor problem was solved. Reference [6] reports development activity with several attachment concepts including one approach with metal pads, shown in Fig. 7, to distribute load. This effort illustrates that ceramic turbine component development requires more than material substitution in a conventional design. How-

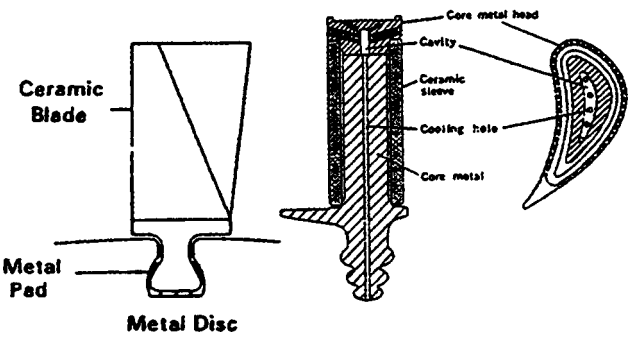

Fig. 7 Ceramic bucket concepts

ever, for the purpose of performance benefit assessment, a ceramic bucket with integral blade attachment was assumed to be feasible for the ''Optimistic'' case analysis.

The ''Optimistic'' case uncooled SN-88 ceramic Stage 1 bucket operating at relative gas path temperature would eliminate all 17th stage compressor cooling and leakage air flow required for conventional MS9001FA baseline Stage 1 buckets.

The ''Less Optimistic'' performance assessment evaluated a hybrid bucket concept. This approach with an air cooled metal spar and ceramic shell is reported in [7] and illustrated in Fig. 7. It is considered a more attractive design with the ceramic member carried in compression. The reduced mass of the ceramic shell may also pose a less catastrophic failure mode.

One-dimensional heat transfer modeling of the hybrid ceramic shell and metal spar bucket was done to estimate cooling air required for the spar. Spar stress analysis was not done but a bulk spar temperature below 845°C (1550°F) was considered necessary for adequate superalloy strength. This temperature established the cooling air requirement for the ''Less Optimistic'' bucket concept. External heat transfer to the spar is greatly reduced because it is not exposed to the high velocity gas path. A thermal barrier coating on the spar member was included in the analysis to further reduce heat transfer within the ceramic shell. These analyses predict a 66 percent reduction in baseline bucket cooling air flow for the hybrid ceramic shell and spar bucket concept. Supply passage leakage from the 17th compressor stage to the bucket of the baseline MS9001FA design was assumed to be the same for this design. The combined cooling and sealing flow to meet the ''Less Optimistic'' case assumptions is 60 percent less than that of the baseline MS9001FA Stage 1 bucket.

Stage 2 Nozzle. The MS9001FA baseline Stage 2 nozzle is convectively cooled by air extracted from the 13th stage of the compressor. Spent cooling air exits from holes in the nozzle trailing edge or discharged into the interstage structure for wheel space purge. Turbine gas path temperature that the Stage 2 nozzle is exposed to is lower than the ceramic oxidation limit for the ''Less Optimistic'' case. Mechanical properties of SN-88 at those temperatures are adequate for ceramic nozzle concept thermal evaluation. Therefore, an uncooled ceramic nozzle operating at turbine gas path temperature was evaluated but mechanical stress analysis was not done. Sealing air requirements of the baseline design were assumed to be unchanged.

The ''Optimistic'' design concept evaluated the benefit of a 50 percent reduction in wheel space purge airflow that is possible if the air is delivered to the interstage at a lower temperature making it more effective. In addition, the vane trailing edge exit hole flow is eliminated with an adiabatic ceramic design. The combined total of 13th stage compressor cooling, sealing and purge flow requirements to meet the ''Optimistic'' case assumptions is 65 percent less than that of the baseline MS9001FA Stage 2 nozzle.

The ''Less Optimistic'' case evaluated the performance benefit of a 32 percent reduction in 13th stage air, half that of the ''Optimistic'' case. This reduction is the amount of air discharged from the vane trailing edge cooling holes without any reduction in wheel space purge flow.

Stage 2 Bucket. The MS9001FA baseline Stage 2 bucket is convectively cooled by air extracted from the 17th stage of the compressor and fed within the rotor to the buckets. The maximum performance benefit for these buckets would be an uncooled SN-88 ceramic bucket operating at relative gas temperature. SN-88 ceramic tensile strength is over 350 MPa (50 ksi) at those conditions. As noted in the Stage 1 bucket discussion, monolithic ceramic dovetail attachment directly in a metal wheel is assumed to be feasible for the ''Optimistic'' case concept and performance assessment.

''Optimistic'' case ceramic Stage 2 buckets therefore eliminated 100 percent of 17th stage compressor cooling and leakage flows required for MS9001FA baseline buckets.

Table 3 Cooling and sealing air reduction summary

	Baseline	Optimistic Case	Less Optimistic Case
Transition Piece Delta P	1.0	0.0	0.25
Stage 1 Shroud	1.0	0.33	0.75
Stage 1 Nozzle	1.0	0.35	0.6
Stage 1 Bucket	1.0	0.0	0.4
Stage 2 Nozzle	1.0	0.35	0.68
Stage 2 Bucket	1.0	0.00	0.52

The ''Less Optimistic'' performance benefit assessment concept follows that of the Stage 1 bucket discussed above and illustrated in Fig. 7. A hybrid, cooled metal spar and ceramic shell concept for a large part such as the Stage 2 bucket with integral rotating shroud was considered more feasible than a monolithic concept but no mechanical design stress analysis was done. A 66 percent reduction in cooling flow was determined in the Stage 1 bucket analysis. This same percentage reduction was used for the ''Less Optimistic'' Stage 2 bucket performance assessment as an approximate value. Leakage flows of the baseline stage 2 cooling circuit were retained. The combined bucket cooling and leakage airflow reduction is approximately 48 percent of 17th stage compressor airflow supplied to baseline Stage 2 buckets.

Cooling and Sealing Air Reduction Summary. Table 3 summarizes ceramic component cooling and sealing air requirements that were used in the performance benefit assessment. Values are stated as a fraction of baseline values.

Combined Cycle Power Plant Performance Benefit Analysis Results

Power plant gross combined cycle efficiency and output improvements for the ''Optimistic'' and ''Less Optimistic'' cases are presented in Fig. 8 relative to the baseline. These results include the benefit of increased fuel flow and firing temperature that is needed to maintain turbine inlet temperature and NOx emis-

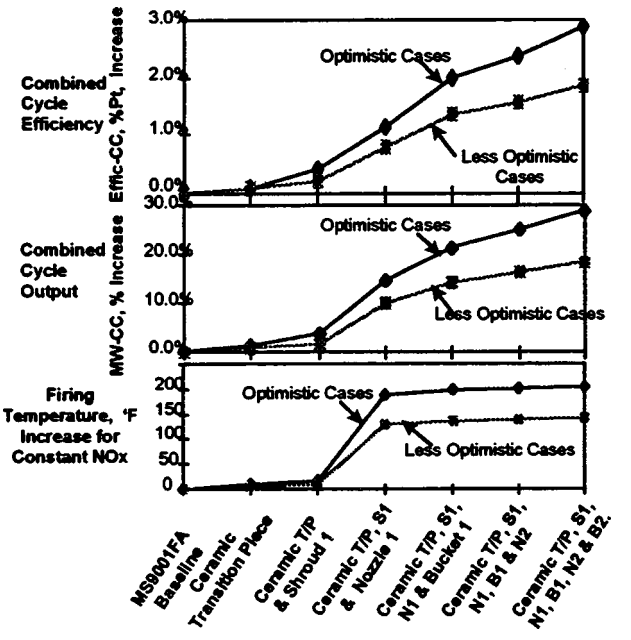

Fig. 8 Cumulative ceramic performance benefits, constant NOx

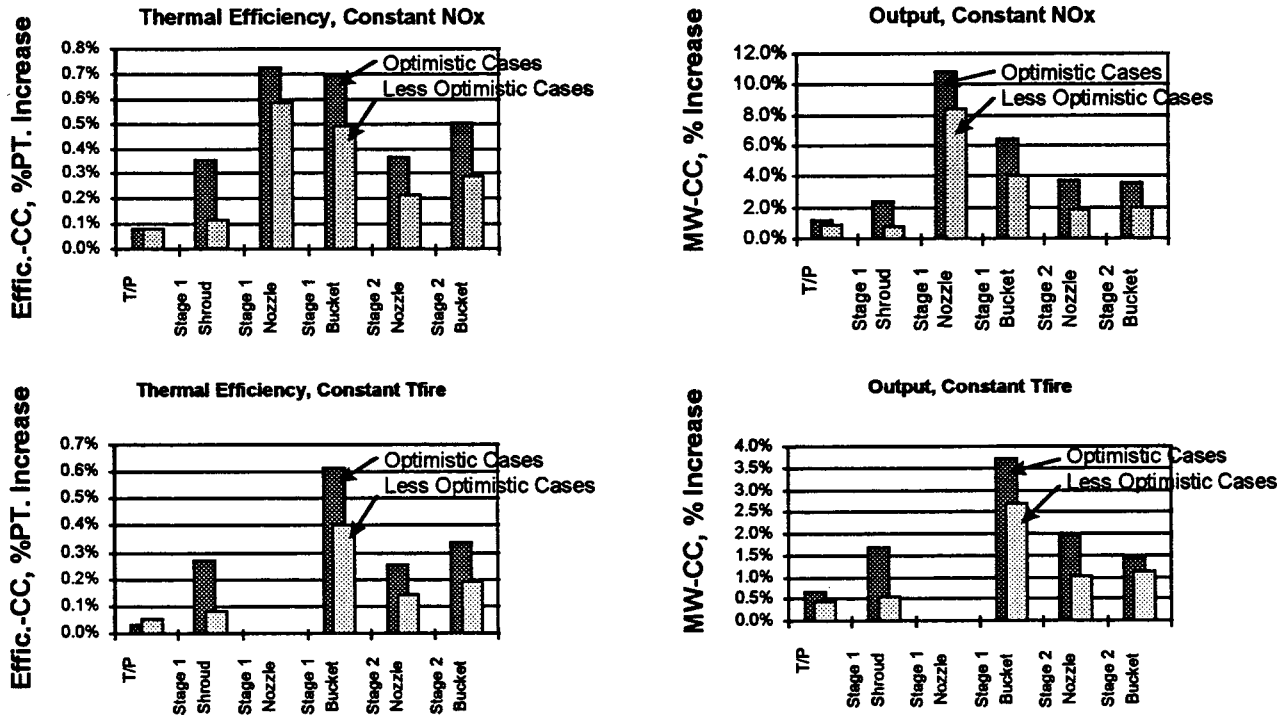

Fig. 9 Individual ceramic component performance benefits, constant NOx, and firing temperature

sions constant. The firing temperature increase associated with each incremental ceramic component is presented in the lower plot of Fig. 8.

The presentation of results in Fig. 8 focuses attention on the cumulative performance benefit with additional ceramic components and the relative magnitude of ''Optimistic'' and ''Less Optimistic'' case assumptions. The maximum combined cycle efficiency benefit with all six ceramic components for the ''Optimistic'' case is just under 3 percentage points increase in combined cycle efficiency. The ''Less Optimistic'' case performance benefit for all six components is less than 2 percentage points increase in combined cycle efficiency or about two-thirds of the ''Optimistic'' case.

The largest individual component benefits are those of the stage one nozzle and bucket. Reduced stage one nozzle cooling with a ceramic design provides significant additional airflow through the combustor. Analysis at equivalent fuel to air ratio for constant NOx, results in the large firing temperature increase noted in Fig. 8.

Figure 9 presents performance benefits of individual ceramic components at both constant NOx and constant firing temperature conditions. This figure illustrates that the stage one nozzle performance benefit is entirely associated with the increase in firing temperature. At constant firing temperature there would be a significant reduction in emissions but no change in output or efficiency. The Stage 1 bucket performance benefit of 0.4 to 0.6 percentage point increase in combined cycle efficiency at constant firing temperature is only 0.1 percentage point less than the constant NOx results. It is also noted that there is significant stage one bucket performance benefit to be derived with either the ''Optimistic'' monolithic design assumption or the ''Less Optimistic'' ''shell and spar'' configuration.

Conclusions

The performance benefit of six monolithic hot gas path ceramic components in a utility gas turbine and combined cycle operation has been carefully evaluated at two material temperature limits and conceptual design assumptions. Mechanical design issues were largely neglected, but thermal analysis was done with sufficient attention to heat transfer and secondary cooling and sealing flows of both ceramic components and conventional parts operating with them, to establish the magnitude of benefit that could be derived from their use.

Ceramic components operating at near adiabatic conditions offer the prospect of performance benefit but come with the development risks associated with an immature material and a limited application experience base. Current gas turbine technology development is advancing performance through increasingly complex cooling of advanced alloys such as the closed circuit steam cooling of the stage one nozzle and bucket in the General Electric ''H'' design. Figure 10, shows the progress of General Electric combined cycle efficiency improvement with advancing technology. ''F'' Class technology with all six 9FA ceramic components evaluated in this study would approach a combined cycle efficiency of 58 percent. These results show the development of ceramic gas turbine components to be a potential alternate route to improved combined cycle performance.

Finally, while this study has focused on monolithic ceramic

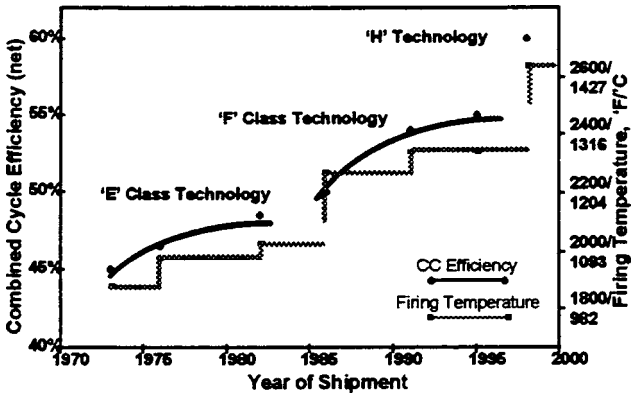

Fig. 10 History of combined cycle efficiency

material, the thermal analysis and benefit assessment with other ceramic materials is not expected to change the results significantly unless there is a large increase in their temperature capability. One additional observation is that progress in ceramic application technology from smaller engine development programs may open niche opportunities in larger turbines. For example, breakthrough on ceramic bucket attachment could open the way for ceramic component retrofit on ''E'' and ''F'' class turbines with significant uprate performance benefit.

Acknowledgments

This work was performed by GE under a contract with the Tokyo Electric Power Company (TEPCO). Ceramic material data sited was obtained from the ''Ceramics for Gas Turbines'' program sponsored by the Electric Power Research Institute under Contract No. EPRI WO8512-05 (formerly RP2608-03) and NGK Insulators, Ltd. The authors are grateful for the technical consultation and direction of G. Scheper, H. Miller, T. Farrell, R. Orenstein, T. Davidson, and Y. Furuse.

References

[1] Miller, 1996, ''Gas Turbines,'' *Mechanical Engineers' Handbook*, John Wiley and Sons, New York.

[2] Hara, Furuse, Y., Tsuchia, T., Maeda, F., Tsujji, I., and Wada, K., 1991, ''Development of a 20 MW Class Ceramic Gas Turbine for Power Generation,'' 91-YOKOHAMA-IGTC-99.

[3] Corman, Heinen, J., and Goetze, R., 1995, ''Ceramic Composites for Industrial Gas Turbine Engine Applications: DOE CFCC Phase 1 Evaluations,'' ASME Paper 95-GT-387.

[4] Tsuchiya, Furuse, Y., Yoshino, S., Chikami, R., Tsukagoshi, K., and Mori, M., 1995, ''Development of Air-Cooled Ceramic Nozzles for a Power Generating Gas Turbine,'' ASME Paper 95-GT-105.

[5] Kercher, and Tabakoff, W., 1970, ''Heat Transfer by a Square Array of Round Air Jets Impinging Perpendicular to a Flat Surface Including the Effect of Spent Air,'' ASME J. Eng. Power, **92**.

[6] Teramae, and Furuse, Y., Wada, K., and Machida, T., 1994, ''Development of Ceramic Rotor Blade for Power Generating Gas Turbine,'' ASME, Paper 94-GT-309.

[7] Okabe, Ikeda, T., Okamura, A., Koga, A., Izumi, A., and Hirata, H., 1991, ''An Experimental Study on Ceramic Moving Blades for Heavy Duty Gas Turbine,'' 91-YOKOHAMA-IGTC-102.

G. Wahl
IOPW
Braunschweig, Germany

W. Nemetz
IOPW
Braunschweig Germany

M. Giannozzi
Nuovo PIgnone
Florence, Italy

S. Rushworth
EPICHEM
Bromborough, Great Britain

D. Baxter
IAM JRC
Petten, Netherlands

N. Archer
ATL
Uycomb, Great Britain

F. Cernuschi
ENEL Ricerca
Milano, Italy

N. Boyle
SIFCO
Cork, Ireland

Chemical Vapor Deposition of TBC: An Alternative Process for Gas Turbine Components

This paper deals with the development of a new process for the deposition of thermal barrier coatings (TBC) based on chemical vapor deposition (CVD). The research program started in September 1998 under a BRITE/Euram III project. The CVD process involves the evaporation of zirconium and yttrium starting from metal-organic precursors and their reaction with oxygen in a hot wall reactor in order to deposit TBC layers. The influence of different deposition parameters such as evaporation temperature, pressure, and substrate temperature on structure, deposition rate, and process yield are described. The characterization of different precursors behavior is also described. Preliminary results, obtained with optimized conditions, have shown ZrO_2-Y_2O_3 *columnar layers with deposition rates of interest from an industrial point of view.* [DOI: 10.1115/1.1364495]

Introduction

The efficiency and the specific output of gas turbines are strongly influenced by their operating temperature. Substantial performance gains can be realised by increasing the operating temperature. To accomplish this there are two realistic options:

- a more temperature resistant turbine materials, e.g., single crystal (SX) nickel base superalloys.
- the use of thermal barrier coatings applied to cooled turbine parts, so that the base materials operate at lower temperatures.

The first option (SX) is used to some extent in the aerospace sector, but it is less practical for large land based gas turbines due to economic and technical drawbacks. Therefore the second option (TBC) is one that can possibly serve the industrial need.

Air plasma spraying (APS) and electron beam physical vapor deposition (EB-PVD) are well established processes for TBC deposition in both aircraft engines and industrial gas turbines [1].

EB-PVD TBC's made from yttria stabilized zirconia (YSZ) have a columnar structure that results in a long lifetime even under severe cycling conditions, when compared with porous APS TBC [2,3]. Both EB-PVD and APS are ''line-of-sight'' processes, which are limited to the coating of simple shaped components unless complex robotic motions are used. In addition, deposition on shadowed regions, for instance, on nozzles, is very difficult. Finally, the EB-PVD equipment involves heavy investment, which has hindered the spread of this technology in particular for industrial gas turbines.

These limitations make it very desirable to develop an alternative process that would have the quality of EB-PVD TBC's, but would not have the abovementioned limitations.

The CVD technique for the deposition of YSZ layers has been demonstrated for small-scale applications, starting from metal-organic compounds as sources for zirconium and yttrium [4]. The aim of this project is to develop the CVD process in order to coat large industrial gas turbine hot gas path components such as buckets and nozzles.

Lab-scale CVD Equipment

The lab-scale CVD equipment mainly consists of an evaporator, a deposition reactor and a vacuum system, which is shown schematically in Fig. 1.

A hot wall reactor with a three-zone resistance furnace is used. The reactor with a stagnation flow arrangement consists of a quartz tube in which the substrate holder is placed.

The deposition temperature is directly measured on the substrate with a NiCr/Ni thermocouple. The advantage of the stagnation flow reactor is that a homogeneous mass transport to the substrate, in the diffusion-controlled part of the process, can be obtained.

The vaporised precursor, with the carrier gas Ar, is fed trough a nozzle into the reactor. Inside the nozzle a thermocouple is installed to monitor the gas temperature outside the deposition zone. Preheated oxygen is added into the nozzle. A schematic diagram of the deposition chamber is shown in Fig. 2.

The precursors are evaporated separately in a crucible. The crucibles are heated in hollow steel blocks with heating cartridges to guarantee a short heating-up time and then uniform heating. The

Contributed by the International Gas Turbine Institute (IGTI) of THE AMERICAN SOCIETY OF MECHANICAL ENGINEERS for publication in the ASME JOURNAL OF ENGINEERING FOR GAS TURBINES AND POWER. Paper presented at the International Gas Turbine and Aeroengine Congress and Exhibition, Munich, Germany, May 8–11, 2000; Paper 00-GT-077. Manuscript received by IGTI Oct. 1999; final revision received by ASME Headquarters Oct. 2000. Associate Editor: Wisler.

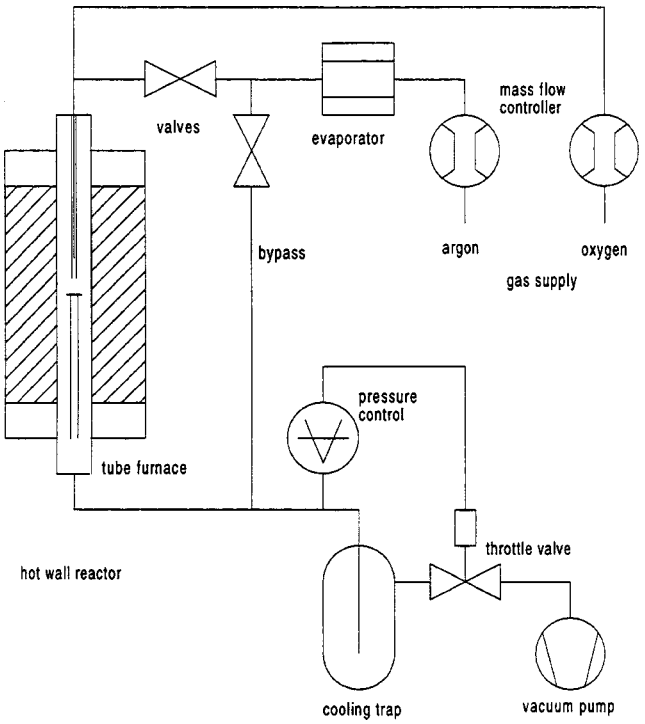

Fig. 1 CVD Equipment

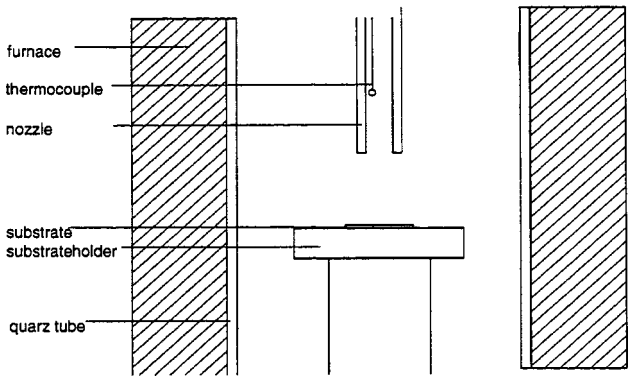

Fig. 2 Deposition chamber

evaporation temperature is measured in the crucibles under the precursor by NiCr/Ni thermocouples. The pipes between the evaporator and the reactor are heated to temperatures higher than the evaporation temperature, to avoid condensation of the compounds [4–6].

Precursors

The β-diketonates $Zr(tmhd)_4$ and $Y(tmhd)_3$ [EPICHEM Limited, Bromborough, England] were identified as the precursors of choice and used as source materials for the deposition of YSZ. Both are easy to handle and can be stored in a simple desiccator. Both compounds are well suited for the CVD process because of their high vapor pressure at temperatures below 250°C and its thermal stability in the gas phase at elevated temperatures [7]. Another precursor which has been tested is an alkoxide $Zr(OiPr)_3THD$. Despite its potential lower cost it is more sensitive to hydrolysis and is difficult to handle [8].

The standard experimental route employed to prepare both these source materials involves the conversion of the metal or metal halide into an intermediate alkoxide species followed by the formation of the desired THD product.

The final compound is isolated by filtration and subsequent trace solvent removal in vacuum. Further details of an approach to larger scale production of this type of precursor are given by Jones [9].

The purity of the batches produced is assessed by a number of techniques to establish acceptable levels of various contaminants. First, nuclear magnetic resonance (NMR) is performed to observe any organic contaminants (i.e., residual solvent, incomplete reaction products, etc.). Secondly, inductively coupled plasma (ICP) is employed to determine the levels of metallic impurities. Thirdly, Karl Fischer analysis is used to establish water contents. Finally thermal gravimetric analysis (TGA) data can be obtained to detail evaporation characteristics.

CVD Process Description

Chemical vapor deposition is a process whereby chemical precursors, in this case metal-organic compounds, are vaporized into a gas phase which subsequently reacts on the surface of the substrate to gradually building up an outer layer with characteristics much different to the substrate material.

The decomposition of the vaporized compounds takes place in the hot zone of the furnace. The deposition temperature is typically in the range of 850 to 1200 K. The CVD process takes place under a reduced pressure of 500 Pa or 1000 Pa [10].

The gaseous by-products flow out of the reaction zone trough the cooling trap after desorption from the surface of the substrate.

The CVD process can be described in the following partial processes [11].

- production of the vaporized reactants
- convective mass transport to the diffusion boundary layer of the substrate
- homogeneous reactions in the gas phase producing gaseous or solid by-products
- desorption of the gaseous reaction products
- diffusion of the gaseous reaction product through the boundary layer
- convective discharge of the by-products from the reactor zone

The advantage of the CVD process over EB-PVD and plasma spraying is in its superior throwing power, so it is possible to coat large and complex shaped parts in large batches with good uniformity [12].

Results of Deposition Trials

The evaporation behavior of the precursors was measured in a microbalance equipment which has been described in detail previously [7]. The results of the evaporation experiments for $Zr(thd)$ produced by Epichem Ltd. in comparison to other suppliers are shown in Fig. 3, where the evaporation rates are plotted in a logarithmic scale versus the reciprocal evaporation temperature.

The experiments were carried out at a total pressure of $p_{total}=1000$ Pa. Argon was used as the carrier gas.

The activation energy E_a of $Zr(tmhd)_4$ is about 100 kJ/mol while the activation energy of the $Zr(OiPr)_3THD$ is lower, even though the vapor pressure of $Zr(OiPr)_3THD$ is much higher.

The activation energy of $Y(tmhd)_3$ is about 117 kJ/mol which is similar to that of material from other suppliers. The evaporation behavior in the stagnation flow equipment was determined by measuring the weight of the precursor before and after the experiments. If the precursors are evaporated separately nearly the same evaporation behavior is found.

The initial deposition trials have been carried out using polycrystalline Al_2O_3 wafers (20×20 mm^2) to determine useful process parameters for the bond coated superalloy substrates. Initial experiments examined the deposition behavior for yttria and zirconia separately in order to optimize process conditions. Subsequent experiments examined the codeposition of zirconia-yttria.

The stagnation flow equipment is realized with two evaporators in a row, each for one compound, in order to control the Zr:Y stoichiometry. In the hot wall reactor the deposition of YSZ from $Zr(tmhd)_4$ and $Y(tmhd)_3$ was carried out in the range of 900 to 1300 K, the evaporation temperatures of $Zr(tmhd)_4$ and $Y(tmhd)_3$ were more than 423 K. Unfortunately with this configuration it has so far been found that it is very difficult to reach a controlled and continuous evaporation rate. Nevertheless, under optimized conditions, continuous coating layers have been obtained with the desired columnar structure.

The gas phase concentration is very important for the structure of the layer and the deposition rate. As gas phase concentration increases deposition rates increases too reaching 100 μm/h. However, while the grains are initially columnar, this preferred structure subsequently disappears. The latter layers exhibit poor adherence to the substrate. This behavior is schematically shown in Fig. 4 with the relevant pictures.

The deposition rate versus temperature is shown in Fig. 5. The precursors activation energy is in the same range as in the previous measurements [4].

At temperatures below 970 K the deposition is controlled by the kinetics of thermal decomposition of the precursors. At higher temperatures the deposition rate becomes almost independent of the temperature. This means that diffusion through the gas phase to the substrate surface becomes a rate determined process. In this range the maximum deposition rate was about 50 μm/n.

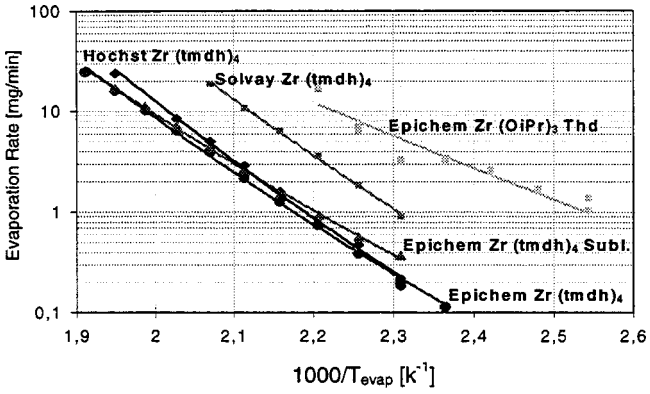

Fig. 3 Evaporation behavior of $Zr(thd)_4$

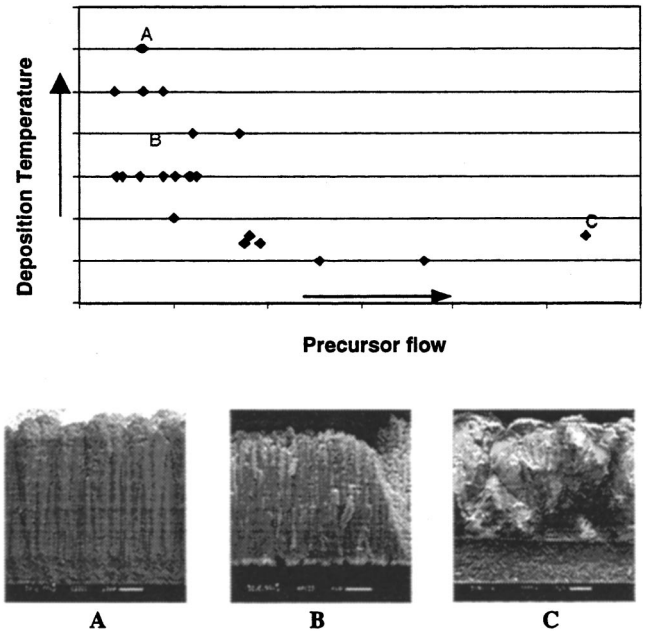

Fig. 4 Influence of gas phase concentration and deposition temperature on microstructure

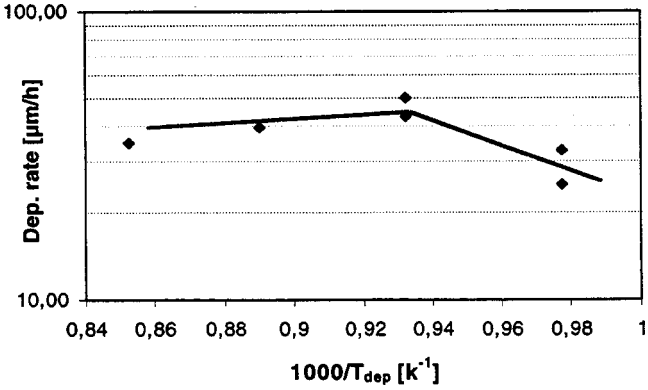

Fig. 5 Deposition rate versus temperature

The calculation of the layer growth rates has been determined from SEM micrographs. The yield of the process in the equipment used, due to reactor geometry and gas velocity, is typically in the range for CVD processes and equal to 10–15 percent.

As an alternative to the β-diketonate precursor $Zr(tmhd)_4$, the alkoxide $Zr(OiPr)_3$ THD was used to deposit ZrO_2 layers. To obtain a similar evaporation rate of $Zr(tmhd)_4$ the evaporation temperature of $Zr(OiPr)_3$ THD must be lowered. Nevertheless, deposition rates of about 10 μm/h (20 percent higher) have been obtained. The layer shows a columnar structure with good adherence. $Zr(OiPr)_3$ THD might be an alternative to the expensive β-diketonate precursor bearing in mind the careful handling requirements of the alkoxides.

Analysis of Initial Trials Coating

Coatings produced on alumina plates have been examined using a range of analytical techniques in order to establish coating composition and microstructure as a function of coating application parameters. Coating composition analysis by x-ray diffraction has shown the presence of monoclinic ZrO_2 on samples coated only with ZrO_2. This is the thermodynamically stable phase at room temperature and the one to be avoided if good mechanical performance is to be obtained. In principles, if ZrO_2 containing about 8 wt. percent (4.5 mol percent) Y_2O_3 is cooled quickly from the molten regions of the $ZrO_2-Y_2O_3$ phase diagram [13] as in the plasma or EBPVD coating processes, the nontransformable tetragonal (T') phase will be produced [14]. The T' phase should not transform to the monoclinic phase during thermal cycling in service, thereby avoiding mechanical failure of the TBC.

Columnar grains perpendicular to the substrate surface were formed under all conditions of coating. In the absence of Y_2O_3 the grains were narrow (typically 2 μm) and extended from substrate surface to the outer coating surface is 30 μm thick.

On samples produced by simultaneous deposition of ZrO_2 and Y_2O_3 the main phase detected by x-ray diffraction was cubic and could be closely matched with the standard, yttrium zirconium oxide (card No. 30-1468), a cubic oxide with a composition of ''common'' yttria stabilized zirconia. While a degree of tetragonality has been detected, the extent has not been determined quantitatively. One concern with the CVD process is that, when it is conducted at a relatively low temperature, the conditions may be inadequate to form the T' phase. Nevertheless, given a sufficiently high Y_2O_3 content formation of the T' phase should still be possible. The yttrium composition of the coatings as determined by wave length dispersion analysis in the EPMA ranged from 2 to 24 wt percent (equivalent to 2.5 to 30 wt percent Y_2O_3,

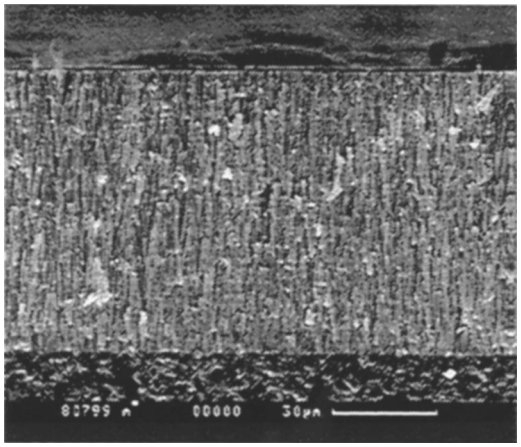

Fig. 6 TBC Structure (*T*1)

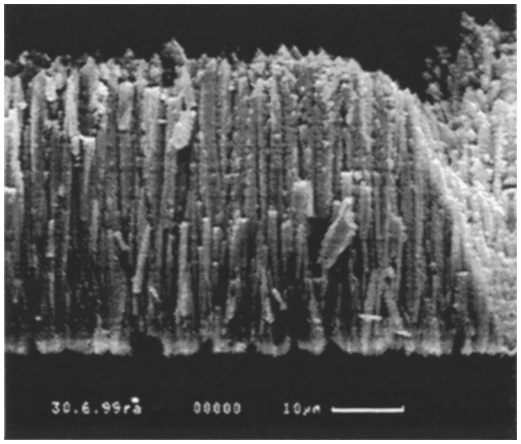

Fig. 7 TBC Structure (*T*2)

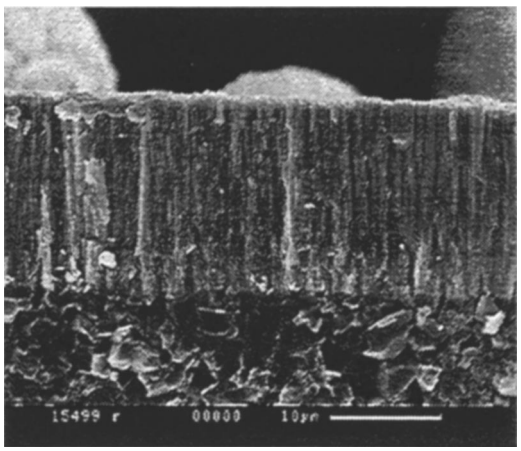

Fig. 8 TBC Structure (*T*3)

respectively). Upon exposure above 1200°C separation of the metastable T' into transformable T' phase and a high Y_2O_3-content cubic phase occurs.

At low temperature ($T1$), when both Y_2O_3 and ZrO_2, are codeposited, columnar grains were generally shorter, uniform in thickness with a smooth surface and pure white in color (Fig. 6).

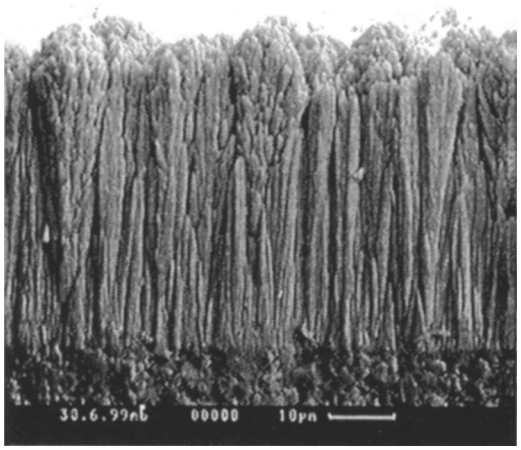

Fig. 9 TBC Structure (*T*4)

Microcracking in the TBC's parallel to the substrate surface was also observed.

With increasing deposition temperature ($T2$), the deposition rate increases and also the diameter of the columns increases. However, there were no discrete columns extending from the inner to the outer surfaces of the coatings (Fig. 7).

Continuing to increase the deposition temperature ($T3$ and $T4$) results in discrete columns, with a rough outer surface, growing on the substrate. Typical examples are shown in Figs. 8 and 9.

Experiments with a total pressure of 500 Pa were also performed. The layer becomes dense, without a columnar structure and with poor adhesion to the substrate.

Summary

The precursors synthesis routes have been reviewed and optimised making it possible for a significant reduction of initial precursors costs. Another Zr precursor was identified $Zr(OiPr)_3$ THD that might be a cheaper alternative, having regard to the sensitive handling of the alkoxides.

Under optimised precursor evaporation conditions, deposition rate increases with temperature, while the columnar structure tends to disappear. ZrO_2-Y_2O_3 layers, displaying the desired columnar structure and morphology, have been deposited. ZrO_2-Y_2O_3 layers have shown mainly cubic phase, therefore more work is needed in order to obtain layers with the aimed ZrO_2-Y_2O_3 ratio and crystallography.

Once the deposition parameters will be adjusted and YSZ layers deposited on bond coat materials (PtAl and NiCoCrAlY), the performances of CVD TBC's will be tested and compared with EB-PVD TBC's.

Acknowledgments

The authors would like to thank the valued input of numerous colleagues in the various participating organization and the European Commission both for funding this research program under Britelll/Euram (Contract No. BRPR-CT98-0733: PROTECT) and for permission to publish this paper.

References

[1] Miller, R. A., 1997, ''Thermal Barrier, Coatings for Aircraft Engines: History and Directions,'' J. Thermal Spray Technol., **6**, No. 1.
[2] Anderson, N. P., and Sheffler, K. D., 1983, ''Development of Strain Tolerant Thermal Barrier Coating System,'' Tasks I-III NASA CR-168251, National Aeronautics and Space Administration.
[3] Duvall, D. S., 1981, ''Processing Technology for Advanced Metallic and Ceramic Turbine Airfoil Coatings,'' *Proc. 2nd Conference Advanced Materials for Alternative Fuel Capable Heat Engines*, EPRI RD-2369-SR.
[4] Pulver, M., and Wahl, G., 1994, *Proceedings of the 8th CIMTEC-World Ceramics Congress*, P. Vincenzini, ed., Faenza, Italy, p. 167.

[5] Pulver, M., and Wahl, G., 1997, Electrochem. Soc. Proc., **97–25**, p. 960.
[6] Pulver, M., 1999, ''CVD of ZrO2, Y2O3, Al2O3,'' Ph.D. thesis, Braunschweig.
[7] Pulver, M., Wahl, G., Scheytt, H., and Sommer, M., 1993, J. Phys. IV, **3**, pp. C3–305.
[8] Funakubo, H., Hioki, T., Matsuyama, K., Shinozaki, K., and Mizutani, N., 1994, J. Chem. Vap. Deposition, **2**, p. 218.
[9] Jones, A. C., 1994, ''MOCVD of Electroceramic Oxides: A Precursor Manufacturer's Perspective,'' J. Chem. Vap. Deposition, **4**, No. 5, pp. 169–179.
[10] Hitchman, M. L., and Jensen, K. F., 1993, *Chemical Vapor Deposition*, Academic Press, London.
[11] Wahl, G., 1993, *Möglichkeiten der Hochgeschwindigkeitsbeschichtung durch CVD*, Jahrbuch Oberflächentechnik, Band 49, pp. 253-281.
[12] Stolle, R., 1997, *Kinetische Messung und Simulation der Abscheidung von Bornitrid*, CVD/CVI-Prozessen, Braunschweig.
[13] Miller, R. A., Smialek, J. L., and Garlick, R. G., 1981, ''Phase Stability in Plasma Sprayed, Partially Stabilised Zirconia-Yttria,'' *Advances in Ceramics, Vol. 3, Science and Technology of Zirconia*, A. H. Heuer and L. W. Hobbs, eds., American Ceramics Society, Wasterville, OH, pp. 241–252.
[14] Miller, R. A., Garlick, R. G., and Smialek, J. L., 1983, ''Phase Distributions in Plasma Sprayed Zirconia-Yttiia,'' Ceram. Bull., **62**, No. 12, pp. 1355–1358.

Update on the Progress of the Brazilian Wood BIG-GT Demonstration Project

L. Waldheim
TPS Termiska Processer AB,
Studsvik, 611 82 Nyköping, Sweden
e-mail: tps@tps.se

E. Carpentieri
Companhia Hidro Elétrica do São Francisco,
Rua Delmiro Gouveia,
333-Anexo 1-Bloco B-sala 3,
Bongi-50761-901-Recife, Pernambuco, Brazil
e-mail: carpent@elogica.com.br

Biomass integrated gasification-gas turbine (BIG-GT) technology offers the opportunity for efficient and environmentally sound power generation from biomass fuels. Since biomass is ''carbon-neutral'' it can be used in power generation equipment without contributing to the ''greenhouse effect'' if it is grown sustainably. The Brazilian BIG-GT initiative is one of a number of initiatives world-wide aimed at demonstrating, and thereby establishing, biomass as an energy resource for power production. The goal of the Brazilian BIG-GT project is to confirm the commercial viability of producing electricity from wood through the use of biomass-fueled integrated gasification combined-cycle (BIG-GT) technology. To fulfil this goal a 32 MWe eucalyptus-fueled demonstration power plant will be built in Brazil on the basis of a design made by TPS Termiska Processer AB (TPS). The first two phases of the project, which included experimental and engineering studies and the basic engineering of the plant, were completed in 1997. The next phase of the project, the construction and commissioning of the plant, is the recipient of a U.S. $35 million grant from the Global Environmental Facility (GEF) of the United Nations Development Program (UNDP), in addition to financing from the World Bank (WB). The plant will be built in Bahia, north-eastern Brazil. The customer of the plant is a consortium, SER—Sistemas de Energia Renovável, comprising of CHESF (Companhia Hidro Elétrica do São Francisco), a federally owned electricity generation and distribution company, Electrobras (Centrais Elétricas Brasileiras), a holding company comprising of the main Brazilian companies from the electric generation and distribution sector, and Shell Brasil. Start-up of the plant is scheduled for the year 2000. The plant will be based on a TPS designed atmospheric-pressure gasification/gas cleaning process. The product gas will be fired in a modified GE LM 2500 gas turbine. The gasification and gas cleaning process is based on the use of a circulating fluidized bed gasifier, secondary stage catalytic tar cracker and conventional cold filter and wet scrubbing technology. The feedstock to the plant will be mainly eucalyptus wood from a dedicated plantation which is harvested on a three-year cycle. This paper describes the background of the project leading up to the technology selection, the technology that will be employed in the plant and the outline of the economics of this ''first-of-a-kind'' plant. The progress made in establishing the organization and the formal framework (e.g., securing the electricity and fuel contracts) are also reported. Future projections of likely technological improvements and cost reductions, and their effect on the overall economics of an N^{th} plant, are presented.
[DOI: 10.1115/1.1335482]

Introduction

The Brazilian BIG-GT initiative is one of a number of initiatives world-wide aimed at demonstrating, and thereby establishing, biomass as an energy resource for power production.

The net production of biomass by plant photosynthesis has been estimated to be 120 billion dry tons per year, having an energy content equivalent to over 5 times the present world energy demand [1]. Although biomass contributes to more than 10 percent of the world's primary energy input (ranging from 3 percent in the industrialized countries to 38 percent in the developing world), much of which is unaccounted in commercial energy statistics, it remains a significant but largely ignored resource.

Typical biomass steam boiler plants, of which there is installed capacity of 9000 MW in the U.S. alone [2], are in the 10 to 40 MWe range and often operate in a cogeneration mode, producing process steam and/or heat. Efficiencies, in condensing mode, range between 20 to 35 percent lower heating value (LHV), depending on size and sophistication of the design. Costs for these types of steam power plants are in the 1500 to 3000 $/kW range [3].

Studies made by *academia*, e.g., the Universities of Princeton [4–6] and Utrecht [7] institutes such as VTT, The Royal Institute of International Affairs and Centro para a Conservacao de Energia [8–10] as well as by utilities like CHESF [4], ENEL [3] and Vattenfall [11] on the use of biomass as a primary fuel for electricity production using modern conversion technology, have shown that it has both technical and commercial potential. BIG-GT technology, in addition, offers the opportunity of efficient and environmentally sound power generation from biomass fuels. Since biomass is ''carbon-neutral'' it can, if it is grown on a sustainable basis, be used in power generation equipment without contributing to the ''greenhouse effect.''

These studies suggest that biomass power plants utilizing integrated gasification combined cycles (IGCC) in the 10–60 MWe range could achieve efficiencies of 40 to 45 percent (on a Lower Heating Value—LHV basis) and eventually reach above 50 percent in a mature plant by benefiting from future improvements in gas turbine technology [5]. Many studies also conclude that the

Contributed by the International Gas Turbine Institute (IGTI) of THE AMERICAN SOCIETY OF MECHANICAL ENGINEERS for publication in the ASME JOURNAL OF ENGINEERING FOR GAS TURBINES AND POWER. Paper presented at the International Gas Turbine and Aeroengine Congress and Exhibition, Stockholm, Sweden, June 2–5, 1998; ASME Paper 98-GT-472. Manuscript received by IGTI January 3, 2000; final revision received by the ASME Headquarters January 3, 2000. Associate Technical Editor: R. Kielb.

costs of such plants will be sufficiently low, 1000 to 1500 $/kW for commercial application in a wide range of circumstances [5,2,11,12].

A combination of such suitable circumstances for the exploitation of biomass to energy systems can be found in north-east Brazil. Since the early eighties, a group of interested parties (of mainly Brazilian origin) have studied scenarios for future power production in this region. As, however, no commercial system was available in the early 90s these parties undertook, with financial support from the United Nations Global Environment Facility, through the United Nations Development Program—UNDP and the International Bank for Reconstruction and Development—IRDB (commonly known as the World Bank), to promote the technology development. The mechanism was to provide ''seed'' money in a competitive structure to a small number of leading technology developers, selected on the basis of the their experience, concept and commercial potential. For these technology developers, the prize to win in this contest was to be singled out for the design contract for a full scale power plant in Brazil, the very first demonstration of its kind. As a result of this competition, a 32 MWe eucalyptus-fueled demonstration power plant will be built in Brazil on the basis of the development work and engineering made by TPS. The Brazilian BIG-GT project can then achieve its goal; to confirm the commercial viability of producing electricity from wood utilizing BIG-GT technology.

Background

The Brazilian Situation. Brazil's main power utilities are all federal or state-owned companies. More than 90 percent of their production capacity is based on hydropower. Brazil's economic situation during the last decade has created major difficulties for the power companies. Today, most of them are undergoing the painful process of change in order to overcome severe financial problems. As a result of the tariff system, new investments have lagged in the power while the demand for power has continued to increase over this period, resulting in an imminent risk of frequent and severe power shortages.

In Brazil, 35 to 30 percent of the energy use originates from biomass fuels (Fig. 1), notably from wood and bagasse (sugar cane residues) [1,4]. In the past, the use of wood biomass has been uncontrolled leading to deforestation, soil erosion and other well-known problems. On the other hand, large industrial sectors in Brazil have relied on wood fuel as both a feedstock and a fuel, e.g., paper and pulp industry, cement industry, and metallurgical industry. Today, there is an estimated 4 to 6 million hectares of plantations in Brazil, an area equivalent to the size of Denmark in Europe, and more than 200,000 jobs have been created. The result has also been a dramatic improvement in every aspect of plantation technology. In addition, the sugar industry in Brazil produced 13 million tons of oil equivalent as bagasse in 1991 in 426 installations, and has the potential to also produce a somewhat lower quantity of cane trash annually when ''green harvesting'' is adopted fully. The generation capacity could, if cane trash is also used with advanced technologies such as BIG-GT, provide a year-round production of 5000 MW in the state of São Paulo alone.

This situation, and the potential in both the sugar industry and from wood-fueled power plants have made the Brazilian government take a strategic interest in the development of power production from biomass [12]. In 1991, the Secretary of Science and Technology, today Ministry of Science and Technology, MCT, invited 18 companies and organizations to a meeting with the aim to create a project development group for a demonstration project to promote biomass technology. At the time, five organizations expressed their interest in continuing this development; Eletrobras, the governmental holding company for the local electrical companies (and thus the parent of CHESF, see below) supported the development; Companhia Vale do Rio Doce, the world's largest iron ore producer, being also a considerable forest owner with interest in the paper and pulp industry and having a responsibility

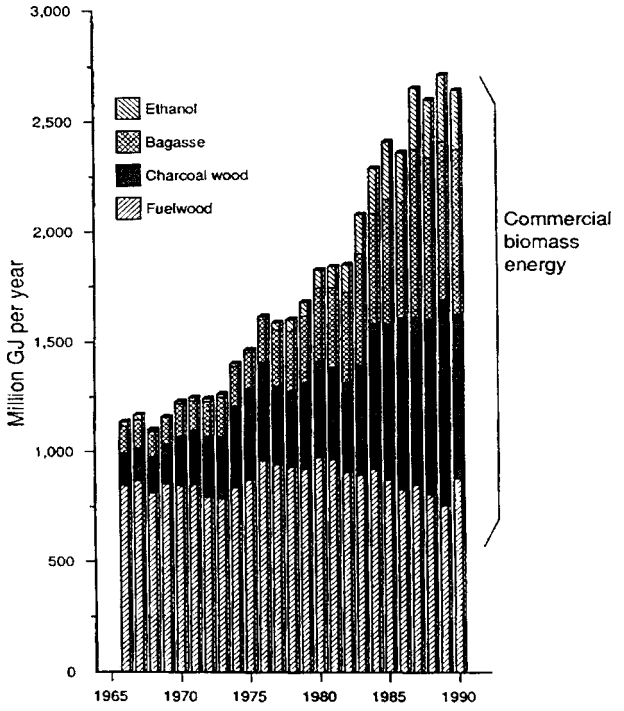

Fig. 1 Biomass energy usage in Brazil

for infrastructural and social development in it's area of operation could also see a role for itself as a fuel supplier; Shell Brasil, at the time owning a 34,000 ha plantation in Bahia; Companhia Hidro Elétrica do São Francisco, CHESF, a federally owned power company responsible for the production and transmission of electricity in the northeast region of Brazil, and for a long period engaged in studies of biomass power generation and its benefits to the Northeast region; and Fundação de Ciência e Tecnologia, CIENTEC, a state owned research institute with extensive experience in gasification.

From a northeast regional (the states of Alagoas, Bahia, Ceará, Maranhão, Paraíba, Pernambuco, Piauí, Rio Grande do Norte and Sergipe, at the time the service area of CHESF, see Fig. 2) standpoint, the requirements for biomass power generation exist [4]. This land-rich region has the lowest population density of the three coastal regions (the fraction of the population in urban areas being relatively lower than in other parts of Brazil) as well as the lowest per capita income of all regions. The per capita electricity consumption in this region is the lowest in the five regions of Brazil, about 700 kWh/y per capita in 1990 (the Brazilian average being around 1300 kWh/y) but with a projected growth rate similar to Brazil as a whole, about 5 percent. To put these figures into perspective, the average consumption in the developing countries is about 500 kWh/y per capita whereas in the industrialized world the average is about 7000 kWh/y.

In this northeast region, all electricity generation, about 10 GW installed, is from hydropower. The eastern regions will already have exploited the potential hydropower sources by the year 2005 to meet the increased demand, while exploiting less and less attractive sites. The installed cost of incremental power supply will rise sharply from a level of about $1000/kW in 1990 to $2500/kW twenty years later, as well as the cost of electricity generation, from $0.03 to 0.075/kWh. The total investment required to meet the growing demand in the region averages one billion U.S.$ per year between 1990 and 2015.

The prognosis indicated above was realized by CHESF in 1980. Options such as importing fossil fuel or importing power from the Amazon river basin hydrostations had little effect on the cost conditions, and would have provided less contribution to regional

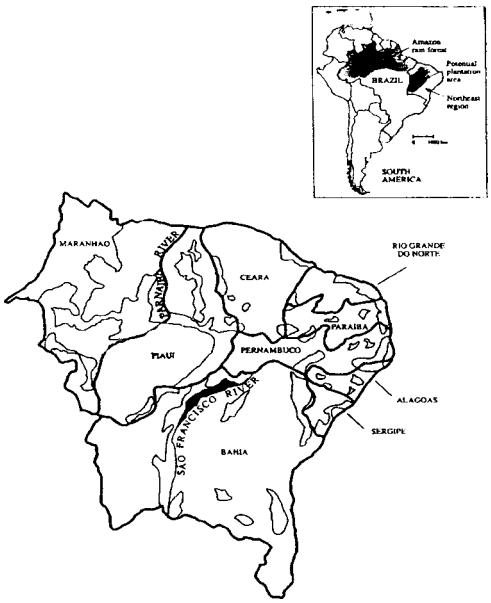

Fig. 2 The northeast region of Brazil

development. Studies made by CHESF in the northeast region have indicated that biomass could have an enormous potential in this area. Excluding land which could be used for agriculture, about 500,000 km^2 was found to be both available and suitable for energy plantations, i.e. 33 percent of the total land area in the region which is larger than the total area of Sweden.

A high annual production average, about 25 m^3 per ha, was concluded to be possible from a study based on data from existing plantations and on local bioclimatic conditions. This translated into an average cost of $1.4/GJ, but as much as 86 percent of the total quantity of 13,000 PJ was available at a cost of less than $1.35/GJ (Fig. 3).

A comparative study of biomass utilization scenarios, compared to a scenario based on new installations in the northeast region (6 GW, installed from 1994 to 2005), import of hydropower from the north (Amazonas) region (11 GW, exhausting the identified sites if an additional 40 percent of the installed capacity is used locally in the Amazonas) and taking into account the growth of demand to the year 2015, showed that biomass compared very favorably with the hydropower scenario. To install the required capacity from biomass, also taking into account biomass fuel already available from sugar cane cultivation in the region, only 1.5 percent of the land area would be put to use for wood plantations, i.e., less than 5 percent of the total available area. Capital investment and both electricity cost and marginal cost of new supply would be lower for the biomass scenario, whilst 150,000 new jobs would be created in the region.

State of the Art of Biomass Gasification. For a recent review of the state of the art in the biomass gasification area, please refer to a recent report published by the EU [13]. Figure 4 shows a generalized thermal capacity range diagram for various biomass gasifier designs. In general, the gasifier technology is selected on the basis of available fuel quality, capacity range considered, and gas quality conditions.

In Fig. 5, a summary is made of the biomass gasification development activities from the early 1980s to date, showing the organizations involved, evolution of the capacity and operating conditions in the various facilities and plants built or planned.

Downdraft Gasifiers. Downdraft gasifiers were developed mainly before and during World War II, to generate gas for use in motors, both stationary and automotive. The gas quality requirements for these applications, essentially low tar content, is

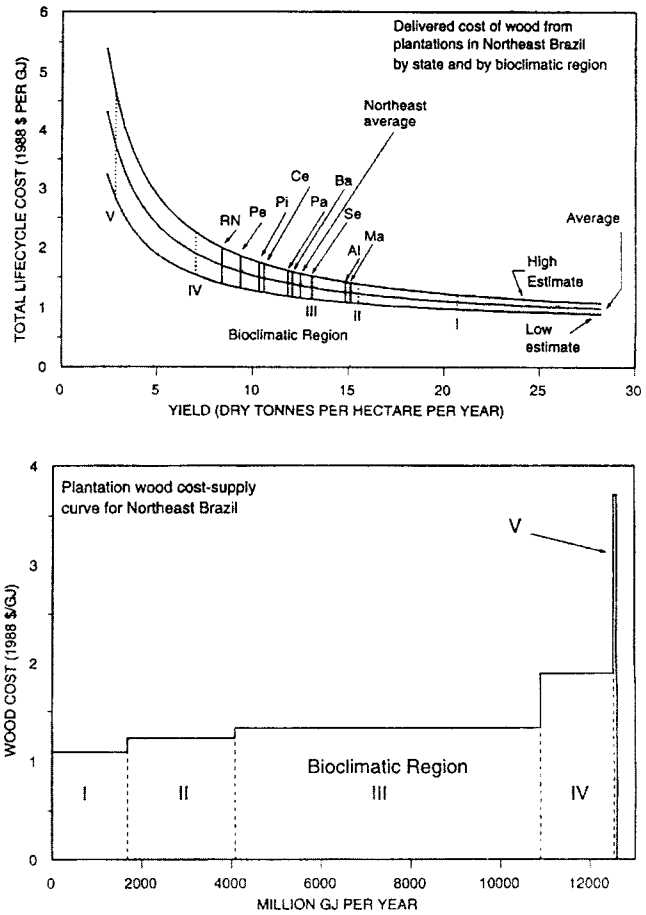

Fig. 3 Biomass cost and volume versus productivity in the northeast region of Brazil

achieved in a narrow throat section. A major obstacle to scale-up above 1 MW thermal is the geometry of the throat section. In spite of development efforts, no breakthrough has been achieved, whilst other environmental concerns and cost of manual labor have restricted the use of this technology in the developing world. From the perspective of a power company, this technology is therefore limited in both capacity and efficiency.

Updraft. Updraft gasifiers also have a long history starting with primitive blast furnaces. The main use of such gasifiers has been with direct use of the gas in a closely-coupled boiler or furnace, as the extremely high tar content of the gas, typical 100 to 200 g/Nm^3, limits its use in other applications unless expensive gas cleaning equipment is used. Again, the capacity is limited to below approximately 20 MW thermal, as otherwise the diameter of the gasifier becomes very large. The high tar content in the gas

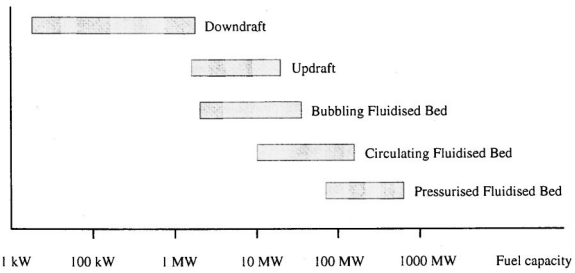

Fig. 4 Fuel capacity of different types of biomass gasifiers

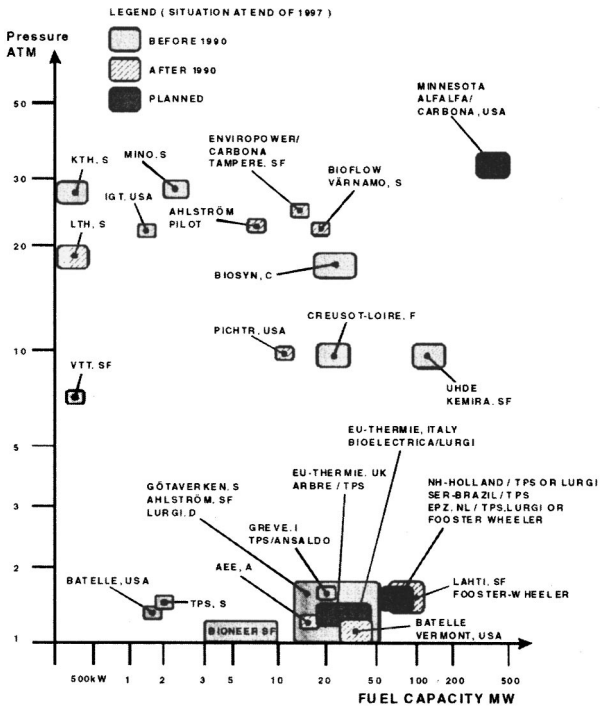

Fig. 5 Biomass gasification development units

has limited the use of updraft gasifiers from power generation in motors, and, in combination with capacity limitations, also in gas turbines.

For the more advanced applications, and in particular for larger capacities, fluidized beds, conventional and circulating beds, operating at atmospheric or elevated pressure have been the main focus of attention since the 1970s, when gasification regained interest during the oil crisis.

Synthesis Gas production for Automotive Fuels. Due to the oil crisis in 1974, an alternative motor fuels program was established in most western countries. The use of solid fuels, wood and peat in Scandinavia in particular, to generate synthesis gas for methanol production was investigated. This interest triggered development of oxygen/steam blown gasification in fluidized beds operating under pressure.

The choice of this gasification technology was made on the basis of the requirement of matching the pressure of the synthesis processes and to benefit from the economy of scale in large scale installations as used in the petrochemical industry. Until the mid 1980s, when the automotive fuel scarcity scenario was largely abandoned, all aspects of large scale gasification plants were investigated including pilot plant scale activities, and in these activities up to the bidding of full scale plants, the predecessor of TPS was heavily engaged. One such plant was installed in Finland and operated for some time. It is fair to say that this has been an important foundation for all the work in the 90s, and that both many organizations and individuals involved at that time are still engaged in gasification activities, although with a different aim.

The Introduction of CFB's. In the mid eighties, the paper and pulp mills in Scandinavia started to take an interest in bark gasification. The impetus for this work was the use of bark waste material (which was subjected to a dumping fee) as a fuel in lime kilns, substituting for fuel oil. Based on technical considerations, direct combustion of bark was not suitable alternative, as contamination of the lime by ash components could result in severe effects on the cooking liquor system availability. Commercial interest was high for a few years until oil prices dropped around 1987–88.

TPS, as well as the other companies involved in CFB boiler development and design, had anticipated this emerging market and were introducing similar systems with a varying degree of success. The systems offered were similar in appearance; a dryer to increase the heating value of the fuel and consequently, the heating value of the gas; a CFB gasifier; one or two stages of cyclones for dust removal; gas cooling to around 600°C by air preheat and sending the product gas to the burner. A number of such installations were built and operated in an industrial environment (i.e., continuous operation) by Ahlström (now Foster-Wheeler, 4 units), Lurgi (1 unit), Götaverken (now Kværner, 1 unit) and TPS (2 units for a slightly different application—see below) in sizes of 10 to 50 MW thermal. CFB technology is favorable for gasifiers with fuel capacities greater than 10 MWth for the following reasons:

- good fuel flexibility
- compact gasifier even at atmospheric pressure means cost-effective large scale construction
- good controllability and good low load operation characteristics
- uniform process temperature due to highly turbulent movement of solids
- optimum gas quality (high carbon conversion)

In the case of TPS, CFB gasification technology development for application to wood fuels, peat, RDF and other reactive solid fuels was started in 1984 [14,15]. ABB Flakt, as a licensee, tried unsuccessfully to introduce the technology in the market during the period to 1988. The gasification concept selected by TPS was an air-blown circulating fluidized bed (CFB) type that operated at 850 to 900°C and produced a hot tarry gas (typical tar content of 0.5 to 2 percent of dry gas) with a heating value of 4 to 7 MJ/Nm^3, i.e., performance typical to these type of gasifiers.

In addition to the general CFB gasifier qualities, the TPS CFBG design has the following specific features:

- no extensive fuel treatment required; fuels with a considerable fraction of coarse particles can be utilized as well as pelletized fuels; and
- increased carbon conversion is achieved by partially recycling the fines from a secondary solids separator.

Grève-in-Chianti Waste Gasification Plant. In 1989, TPS sold a license for its CFB gasification technology to Ansaldo Aerimpianti SpA for the construction of a waste-fueled gasification plant in Grève-in-Chianti, Italy [16–18,14,15]—see Fig. 6. As part of this project, TPS conducted test work in its pilot plant using refuse-derived fuel (RDF) pellets as feedstock.

The gasification plant has a total capacity of 200 tons of RDF per day. The RDF is delivered to the plant in pellet form, which is fed into the lower sections of two CFB gasifiers, each of 15 MWth fuel capacity. The TPS-designed gasifiers operate at close to atmospheric pressure at approximately 850°C, employing air as the gasification/fluidizing agent. Part of the air is injected into the gasifier vessel through the bottom section and the remainder part way up the vessel. This pattern of air distribution creates a high-density bed in the lower part of the vessel, which allows the gasifier to handle relatively large-sized fuel particles.

The raw gas from each gasifier passes through two stages of solids separation before being fed to a furnace/boiler. Alternatively, part of this raw gas stream can be led to a nearby cement factory to be used as fuel in the cement kilns. Ash and lime are fed to the cement factory as ballast material. The flue gas exiting the boiler is cleaned in a three-stage dry scrubber system (Teller technology from Research-Cottrell) before being exhausted through the stack. Steam produced in the boiler drives a 6.7 MWe steam turbine.

Integrated Gasification Motor and Gas Turbine Combined Cycles. By utilizing the energy-rich gas from a gasifier in an

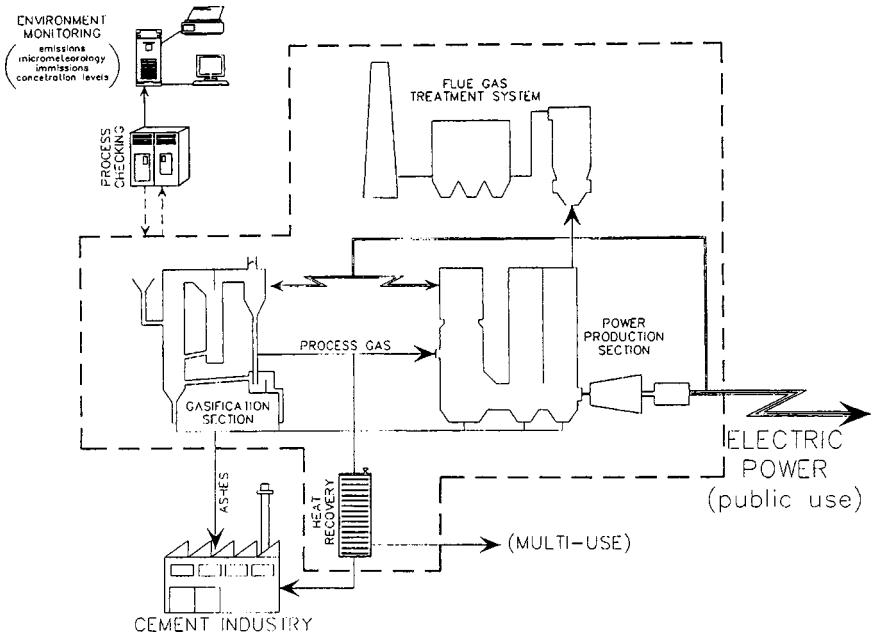

Fig. 6 Grève-in-Chianti plant process scheme

engine or a gas turbine, the net generating efficiency to electrical power can be increased substantially, compared to similar sized boiler-steam turbogenerators. However, to realize this potential, removing tars, particulates, acids, and nitrogen compounds from the gas is a prerequisite to meet process, operational and emission standards, as well as an overall system integration to fully utilize the available heat (Fig. 7).

When Fig. 3 is combined with the approximate optimum size range of the prime movers, it is quite apparent why the interest has focused on fluidized beds operating at atmospheric or elevated pressure for biomass power applications (Fig. 8).

Product Gas Cleaning [14,19,15]. When biomass is gasified, relatively large quantities of tar are produced, e.g., from 10 percent of the fuel in an updraft gasifier to 2 to 4 percent in a fluidized bed. The amount and composition of the tars are dependent on the fuel, the pyrolysis conditions and the secondary gas phase reactions. If the tar is allowed to condense when the gas is cooled (condensation temperature of tar from woody biomass is 200 to 500°C) considerable problems with equipment contamination (such as filter clogging) result. Fuel nitrogen is largely converted to ammonia, which on firing of the gas will form nitrogen oxides. Apart from tars, both motors and gas turbines require a minimum LHV of the gas and are sensitive to dust. In addition, alkali compounds are detrimental to modern gas turbines, causing corrosion and deposits at the high working temperatures of modern gas turbines. In the case of motors, these can be self-aspirating and therefore the gas can be at atmospheric pressure, which is not possible when utilizing gas turbines. The requirement for a higher gas pressure has led to the development of two distinct schemes for integrating the gasification system to the gas turbine; pressurized gasification-hot gas filtering and cleaning and; atmospheric gasification-cold gas filtering and cleaning (Fig. 9).

The rationale for these two different systems are that in the case of pressurized gasification the gas can be fed to the gas turbine after dust removal only. If dust removal can take place at a sufficiently low temperature to remove the alkali from the gas and at sufficiently high temperature to maintain the tars in the vapor phase, an efficient process with a simple, and hence less costly, equipment train will result. Development needs include the reliable feeding of the fuel at elevated pressure, the gas quality and reliability of the hot gas filter, as well as the heavily integrated control system required. This was the route taken by Bioflow (a joint venture between Sydkraft AB and Ahlström Oy) when they announced in 1990 the construction of a 6 MW electrical biomass gasification gas turbine cogeneration plant to be built in Värnamo, Sweden (Fig. 10, [12]).

In the case of atmospheric gasification, the gas needs to be compressed. This is most efficiently done at low temperature and after condensation of the water vapor contained in the gas. Because of the high volumetric flows encountered, the costs of high temperature filters are not justified. Thus, the filtering takes place at lower temperatures, typically 200°C, in conventional baghouse filters. This low temperature filtering puts more stringent demands

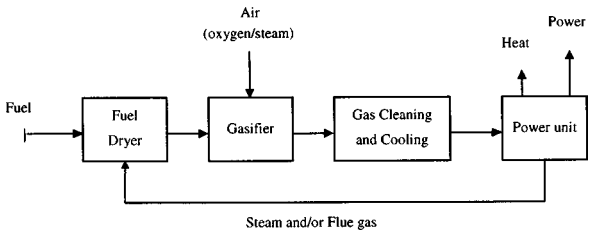

Fig. 7 General process scheme, gasification for power production

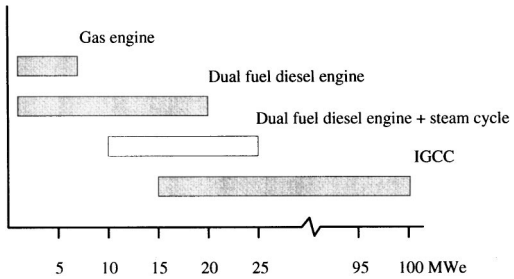

Fig. 8 Output capacity of different biomasss gasification system arrangements (multiple units to be used for engines)

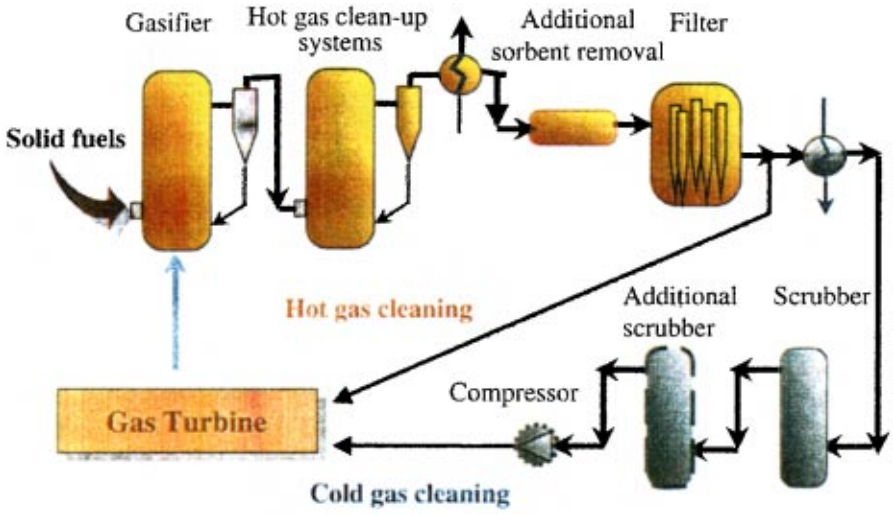

Fig. 9 Schematic of BIG-GT process system options

on tar cleaning prior to the cooling of the gas, as condensation will otherwise occur in the filter or the scrubber, whilst alkalis and dust limits are more easily met. On the other hand, cold gas cleaning gives an added flexibility for removal of ammonia and other contaminants, which in combination with atmospheric fuel feeding puts less demand on the fuel quality, thus opening up the possibility to use a broader spectrum of fuels, including various waste materials. It also adds redundancy for the gas filter unit, which improves plant reability.

In 1985, TPS started work on developing a hot gas cleaning process for application to the CFB gasifier. In this TPS-patented process, the tars are cracked catalytically to simpler compounds at about 900°C in a dolomite-containing vessel located immediately downstream of the gasifier. This tar conversion process does not result in any significant reduction in the gas's chemical heating value. In 1987, the laboratory-scale development of the catalytic tar cracking process had progressed to a level where pilot plant testing was deemed worthwhile. An engineering study showed that a secondary CFB cracker was preferred for implementation in the TPS pilot plant (see Fig. 11).

The cogeneration possibility and the high electric efficiency of a large dual-fuel diesel engine plant fired on product gas from biomass attracted such attention that in late 1987 the CFB gasifier pilot plant built in 1985 was extended by the installation of a dolomite-containing CFB tar cracker, a wet scrubber and a modified 500 kW shaft-power turbo-charged eight-cylinder dual-fuel diesel engine. Following modification of the pilot plant, long-term test work using wood chips as feedstock was performed. The plant was operated for 1300 h, of which 750 h also included operation of the motor. In 1990 and 1991, a gas filter was added and test work was conducted utilizing several waste materials as feedstock. In 1990, TPS evaluated the atmospheric-pressure gasification process for application to combined-cycle operation for small- to medium-scale plants. Following a positive outcome of

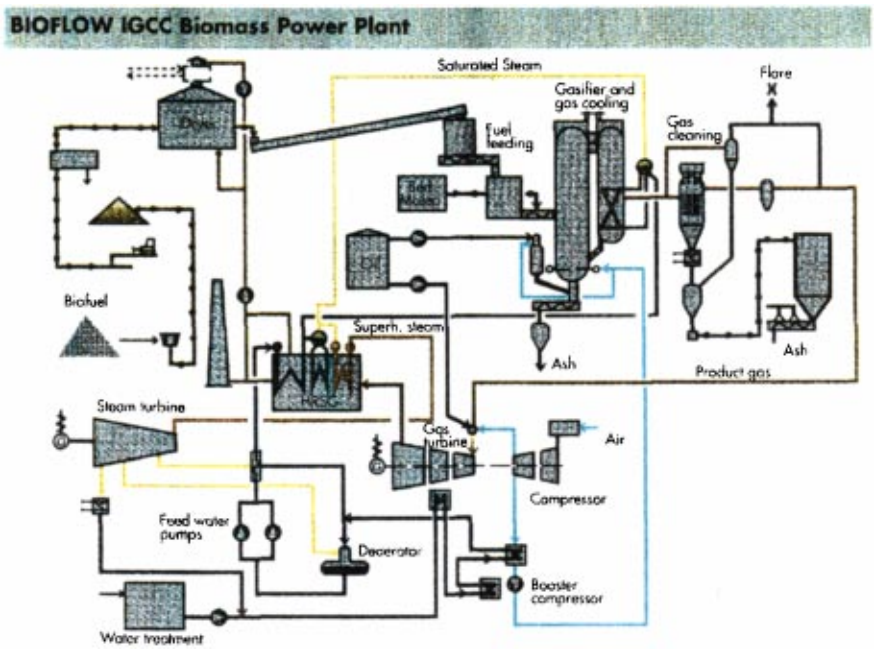

Fig. 10 Flowsheet of the bioflow plant at Värnamo

Fig. 11 TPS's CFB gasification and hot gas cleaning pilot plant

this evaluation, it was decided to develop and commercialize the biomass-fueled integrated gasification combined-cycle (BIG-CC) technology [14]. A schematic flow sheet of the TPS atmospheric gasification combined cycle technology is shown in Fig. 12.

Advantages of the atmospheric-pressure BIG-CC technology over pressurized technology include the following:

- less development required—reliable operation
- simpler fuel and ash handling systems
- more reliable gas purification—use of gas scrubber ensures that the product gas is of sufficient quality for gas turbine operation

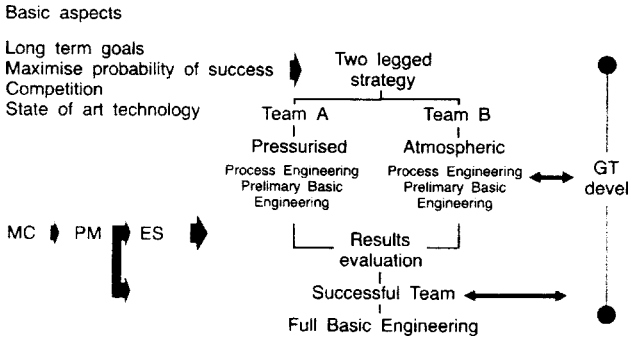

Fig. 12 Two legged strategy for phase II management philosophy

- higher heating value of the product gas
- supplementary firing of the heat recovery steam generator allows plant output to be boosted without throttling loss
- weak process coupling between gasifier and gas turbine
- greater possibilities to use difficult feedstock (e.g., waste)

The Brazilian BIG-GT Project Initiative

Phase I, 1991–1992 [1,12,20,21]. The Brazilian situation, as described above, made the Brazilian Government take a strategic interest in the development of power production from biomass. In 1991, the state secretary of Ministry of Science and Technology took the initiative to invite 18 companies and organizations to a meeting with the aim to create a project development group for a demonstration project to promote biomass technology. The five organizations named earlier, MCT, Eletrobras, Companhia Vale do Rio Doce, Shell Brasil and CHESF formed the core of a project group. CHESF took the role of coordinator and project manager for the project development group. The aim of the group was to develop the loose organization and the number of potential technical options into a project based on a feasible technical and economic plan.

Funding from the Rockefeller Foundation, Winrock International, U.S. Environmental Protection Agency (EPA) and U.S. Agency for International Development (AID), made it possible to start Phase I in mid 1991 and finish in early 1992. A number of issues were addressed.

An overview of technological options was prepared, followed by a survey of process developers and equipment manufacturers. When this survey was performed in 1992, the BIG-GT technology was, in general, unproven and no single plant was in, or close to being in, operation. However, on the gasification side promising developments could be found, mainly in Scandinavia, addressing the relevant process and gas cleaning problems when operating on woody biomass and when integrated with a gas turbine. Also, most importantly, these developments were sufficiently advanced to allow their demonstration in Brazil within three years. As there was no selected gasification route, substantial development work still being necessary, the decision taken was to maintain a high level of competitivity and success probability by contracting two qualified development teams for the next phase of the project, and to select only one of these for the demonstration plant on the basis of their project performance.

The gas turbine options were also explored, resulting in a recommendation to use an aeroderivate gas turbine due to their inherent higher efficiencies, appropriate capacity range and development pace and long term potential including advanced cycles (Steam Injected Gas Turbine—STIG, Intercooled Recuperative—ICR, Intercooled Steam Injected Gas Turbine—ISTIG, etc.). However, because of the target of demonstrating the complete BIG-GT technology within three years, a conventional combined gas turbine-steam turbine cycle was proposed. The size of the gas turbine considered, both from technical and economic aspects, was limited to 15 to 35 MW.

On the basis of the information collected, an analysis of the short term and long term (N^{th} plant) investment costs was made. The economic analysis of the first plant was translated to a tentative budget for the following phases of the project. The analysis showed that the first plant cost would be about \$2500 to 3000/kW (1992), which would then drop to about half for the N^{th} plant, and would have a targeted efficiency of 43 percent. On the basis of the Brazilian cost structure, and on an initial screening indicating three suitable plantation sites in the northeast region, it was found that if one-third equity capital was geared by soft financing, one-third grant and one-third loan, a power generation cost of \$50 to 60/MWh would result and also provide a reasonable, but low, rate of the return for the project owners. As has been discussed earlier, in the northeast region of Brazil this is a competitive cost compared with available alternative power sources, in spite of the high costs of a first-of-its-kind plant.

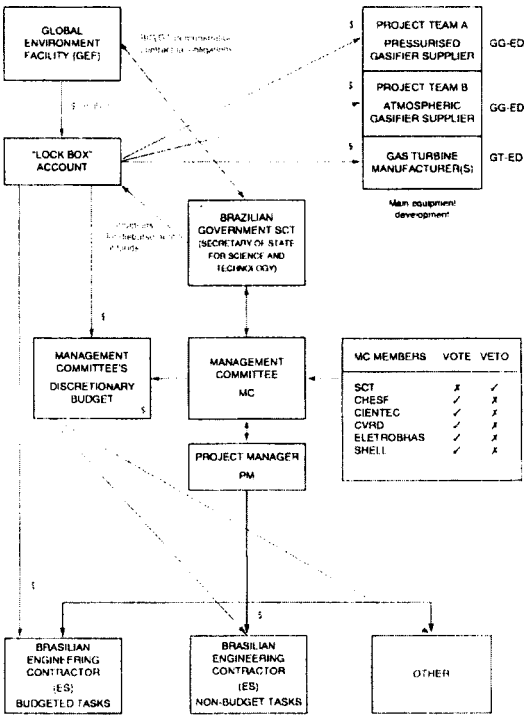

Fig. 13 Brazilian BIG/GT WBP project. Phase II organization and Management

Phase I also resulted in a Memorandum of Understanding, which formed a basis for the future cooperation between the various private and governmental entities that were to be involved in Phase II and also provided the impetus for the period after this phase.

A deliverable of Phase I was also a complete plan for the continuation of the project in terms of a work program and budgetary requirements for Phase II. The proposal was to contract two gasification systems developers (the so called ''two-legged strategy'' (see Fig. 12)). Bioflow for pressurized gasification and TPS for atmospheric gasification, to mitigate technological risks, mainly with the pressurized system proposed by Bioflow. GE was contracted to develop and integrate the LM 2500 gas turbine with both these systems. From a financial standpoint, Phase II was supported by the Global Environment Facility (GEF) and by the participating companies (see Fig. 13).

The GEF was formed in 1990, and is administered by the World Bank. Its task is to fund environmental conservation projects, mainly in the Third World in the following four areas:

- global warming from the use of fossil fuels, and deforestation
- reduction of biological diversity
- pollution of international waters by oil spills, and the accumulation of wastes in oceans and international river systems
- ozone depletion from CFC's

As a result of the potential available in BIG-GT technology on global warming issues, and the need for ''seed'' money to trigger the development of this technology itself and thereby put the technology onto the learning curve, GEF provided $8.1 million for Phase II, and is expected to commit another $35 million as a grant for Phases III and IV. This funding was, however, not sufficient to carry out the total development program and thus the development companies involved had to provide some additional funding, $4.2 million for Phase II and $25 million for Phase III, respectively. This company funding has been obtained internally, within the organizations, or from third party sources.

Phase II, April 92–June 95 (Actual June 1997)

Establishment of Phase II. Phase II was started according to plan. A project management group was formed and contracts, payment structures, and arrangements for safeguarding intellectual property were formalized. On the basis of proposals from the companies involved, each company was contracted to do the technical development work deemed necessary. The gasification systems developers were also responsible for co-ordination with GE, liaison with a Brazilian engineering company selected to look at site specific issues, permitting and utilities, and to produce a preliminary basic engineering package, detailing cost and performance figures.

After some delay, Jakko Pöyry Engenharia Ltda was contracted to provide the local engineering services as well as to provide assistance in technical matters.

On the basis of the technical work performed in the two first years, a choice would be made to carry on into Phase III with only one of the gasification system suppliers, Bioflow or TPS.

Technical Development. The goal of the technical development was to optimize the conceptual designs proposed to meet targets on cost, efficiency, availability and environmental performance, and, by references and test results, etc., to confirm to the extent possible, the data used and the underlying assumptions. Fuel testing at both laboratory and pilot/prototype scale at TPS (Studsvik) and Bioflow (Värnamo) was planned, as well as desktop studies.

GE performed an analysis of the combustion system, both from a combustor point of view for which tests on annular combustor and sector combustors were made and also developed the mechanical hardware and control system software for the gas turbine package. This work will not be dwelt on further here as it will be presented by GE and the Brazilian consortium (SER) in a separate paper.

Initial Technical Work at TPS. Test work in the CFBG pilot plant using eucalyptus wood as feedstock started towards the end of 1993 and was completed in 1994. In the same period, several other biomass-fueled tests were conducted in the pilot plant as part of biomass-fueled projects in Sweden. During these two years more than 1200 h of pilot plant operation were achieved. The pilot plant experience, in combination with the scale-up experience from the Grève-in Chianti plant, mentioned earlier, provided the basis of data and know-how. A number of desktop studies on, e.g., gas cleaning, gas turbine integration and plant optimization, also added to the concept that was fully developed and costed.

The total number of operational hours of the 2 MW pilot plant up to December 1997 was about 4000 h. Table 1 is a summary of the pilot plant tests performed at TPS between 1993 and 1997.

Another GEF-funded project in collaboration with Copersucar, Brazil, to test also bagasse on a pilot scale, as well as tests on various wastes are planned for 1998. In spite of the fact that each client will have their own test, the benefit of the total experience is available as background to TPS design work.

Bioflow Technical Work. A similar scope of studies and engineering was carried out by Bioflow in parallel with the work by

Table 1 Pilot plant testwork at TPS between 1993 and 1997

Project	Number of tests	Feedstock
BIG-GT Brazil	10	Eucalyptus wood
Fabel	2	Forestry residues
APAS	2	Wood residues/lignite
THERMIE	2	Short rotation coppice (SRC)
THERMIE	1*	SRC and forestry residue
Fabel	1	RDF
North-Holland project	1**	Waste wood, demolition wood, sewage sludge

* Long term test (600 hours).
** 11 days duration

TPS. This work was, however, interrupted by various commissioning and start-up problems in the 6 MWe prototype plant in Värnamo, which caused at least 6 months delay in Phase II of the BIG-GT project, and parts of the program needed to be replanned.

The Technology Selection Process. The complexity of the project itself, the number of organizations involved, the size of the grant from GEF, the international interest in the Brazilian development activities as well as the impact of the decision on the gasification system developers involved, put some demands on the selection procedure; it should be logical and as transparent as possible such that the final outcome could be accepted by all parties.

CHESF, as the project manager, proposed to use a procedure called the Analytical Hierarchy Process [22], which had already been used in Phase II, for the selection of JPE, the engineering services company, with great success. This is a method well suited to the break-down of a complex, unstructured problem into component parts, or decision criteria. These are then structured into an hierarchical order and each criterion is, on the basis of subjective judgement, assigned values reflecting its relative importance. Having established the hierarchy, and the weights associated with each criterion, the alternatives (in this particular case, TPS and Bioflow) were given a score on each criterion which, by the hierarchical structure and the weights assigned in advance, leads to a final score, with the highest scoring alternative winning.

This method is a tool for organizing relevant information and judgements, and by breaking down the decision criteria into smaller parcels, it acknowledges that subjective opinions, is an important part of decision making, as such factors become visible and are assigned mathematical values and weights. In this particular case, where the wish was to reach a unanimous decision among all the participants, the break-down into this structure focused the discipline of thinking of a group, and, allowing sufficient time for discussion, this resulted in that each criterion was scored by the group as a whole.

During 1994, the hierarchy and weights were developed by the participating companies and agreement on the procedure was reached by TPS, Bioflow, GE and JPE.

During the second week of August 1995, representatives of the project group and JPE met in Recife to perform the scoring of TPS and Bioflow. During a week of intense discussions, approximately 60 individual criterias were scored on the basis of all reports, data and other information made available by TPS, Bioflow, GE and JPE. After scoring, the rest was a mere exercise of matrix algebra. All the work performed and all aspirations and creativity generated by several scores of people in a number of countries for more than three years was flattened out and condensed into two bare decimal numbers, TPS: 0.57 and Bioflow: 0.43.

Following this outcome, firstly the companies, and then MCT and UNDP in late August 1995, ratified the decision that TPS was the selected technology developer for the demonstration in Phase III. It was, however, also stated by the Management Group that in spite of the materialization of some of the technical risks and development risks associated with the Bioflow pressurized system, identified already in Phase I, Bioflow had fulfilled the contractual requirements and that a successful commercialization of their technology was probable.

Basic Engineering. Following the selection of TPS as the technology supplier, TPS and JPE made a review of the basic engineering, going further into the details of the plant. This enabled the cost estimate to be improved further, on the basis of quotations, detailed estimates of quantities of bulk materials and a detailed Piping and Instrument Diagram (PID). In addition, JPE made the background documentation for the environmental permitting, grid regulator permits, etc. The tender documentation required for the procurement of the main equipment was also prepared. These activities concluded the technical work, starting with the concept development and ending in a complete plant design, cost, and performance estimate.

Financing. When the basic engineering for the plant was completed and a tentative budget made, the project participants applied to the World Bank and GEF for a loan and a grant, respectively. This application was made by the appropriate Brazilian government agency in September 1996.

Formation of the Consortium. From the beginning of the project, it had been clear that if the plant were going to be constructed, an equity participation would be required from the participating entities, and that the World Bank favored, as a policy, more than 50 percent private company equity position, also linking this to their loan/equity rating. On the other hand, Brazilian legal constraints make it very difficult for public sector companies to take stakes in limited liability companies. To solve this, rather than to go through time consuming formal and political problems associated with forming a company, a joint legal agreement was entered into to build and operate the power plant by a Consortium. The Consortium could be registered as such in the Brazilian trade register to allow it to enter legal obligations and contract with third parties. The Consortium is backed by parent company guarantees. In spite of this relative simplicity, the formation of the Consortium proved to be more time consuming than expected. In this case, some institutional factors made things more complicated. Of the original Phase II participants, CVRD was privatized during the period of Phase II, and Eletrobras and CHESF were put on the list of public sector companies to be privatized. To safeguard such companies from various forms of asset-stripping prior to the sell out, all major new engagements have to be approved by a specially instituted governmental body. Prior to signing the Consortium Agreement, Shell Brasil also had to perform a ''shareholders review'' involving experts from other parts of the Shell organization.

Finally, in December 1996, the Consortium SER (Sistemas de Energia Renovável) was formed by Shell Brasil, Eletrobras and CHESF. CVRD, which could not engage at that time for the reasons indicated above, had an option to join at a later time. Formation of the Consortium is an important milestone, as it means that legally binding contracts can be signed with third parties for goods and services provided for the construction and operation of the plant, as well as for the power produced.

The TPS Atmospheric Gasification Technology Selected

The atmospheric-pressure BIG-CC technology proposed by TPS for the Brazilian BIG-GT project and for other similar project involving power generation or cogeneration of heat and power (Fig. 14) is comprized of the following:

- fuel preparation and drying
- air-blown gasification in an atmospheric-pressure CFB reactor
- tar cracking using a dolomite catalyst in a secondary CFB reactor
- product gas cooling and cleaning in a conventional filter/scrubber unit (to remove particulates, chloride (as $CaCl_2$), remaining tars, alkali, ammonia, moisture and so on from the fuel gas, as required)
- fuel gas compression in a multiple-stage compressor
- fuel gas combustion and expansion in a gas turbine-generator
- gas turbine exhaust gas heat recovery by employing a steam turbine generator

The plant is designed to generate low heating value fuel gas, typically 6 to 7 MJ/Nm^3. By virtue of the tar-cracking process, fouling is avoided on gas coolers, and a filter combined with a wet scrubbing system can be used for final gas cleaning. As the gas is essentially free from tars, the scrubber water will contain only minor quantities of contaminants, and blinding of the filter does

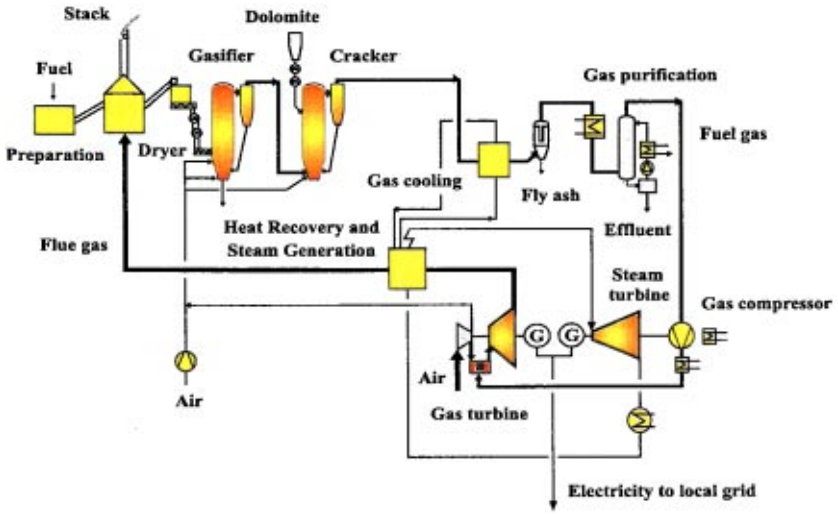

Fig. 14 Schematic flowsheet of TPS atmospheric BIG-GT process

Table 2 Typical emission data for a BIG-CC plant

Component	Emission value
CO	10 - 20 ppm (GT specific)
THC	2 - 5 ppm (GT specific)
NOx	10 - 30 ppm (no supplementary firing)
Dust	5 - 10 mg/Nm^3

not occur. Water scrubbing will, in addition to the filtration, be very effective against alkalis, and ammonia can also be dissolved (and upgraded to a sellable product) as a means to reduce NO_x formation from fuel nitrogen, this being more of a concern than thermal NO_x when firing gases of low heating value.

From the environmental standpoint, the technology has much to commend it. Sustainably grown biomass used for power generation is essentially ''carbon neutral'' to the atmosphere; energy plantations can be designed for biodiversity with multiple tree species; and extensive afforestation offers the opportunity to rehabilitate deforested or otherwise degraded lands.

Typical emission data for a BIG-CC plant is shown in Table 2.

For budgeting purpose of the BIG-GT project, an efficiency of 40 percent with an electrical net output of 32 MW is used, these values being on the conservative side. A major difference between the targeted efficiency of 43 percent and the present value is that the wood fuel is dryer on arrival at the plant than initially assumed (i.e., the LHV of fuel being higher while not generating more MW). The heat recovery from low temperature heat in the flue gas leading to an increase in the fuel LHV is an efficient energy recover, however, in this case, the power output of the steam cycle has been increased instead. A plant capacity factor of 85 percent has been estimated after the commissioning and running-in period of several years of duration, at which time the plant will operate as a base-load generator. The wood usage is 238,000 m^3 per year, which dictates a plantation area of approximately 5300 ha, and a total area of 7000 ha unplanted areas including roads and fire barriers etc.

Entering into Phase III, 1997–Present

Guaranteeing the Wood Supply. Three plantation sites, all in Bahia, had been shortlisted in Phase I. Following the sale of the Shell plantation, Floryl, and negative contacts with the plantation rated third in Phase I, CAF, negotiations were conducted for a lengthy period with COPENER, in Alagoinhas county. The plantation, 66,000 ha in total, was established during the oil crisis as a strategic energy source for the Copene petrochemical complex. Later, it had since been earmarked to provide raw material for a planned pulp mill to be built by Copener together with other companies. For this reason, only a limited quantity of fuel was available for other customers on long term contracts. In spite of a very positive attitude in the early days of the project, the overall outlook had changed when negotiations to arrive at a long term contract began. The pulp and paper industry had come out of a recession and was selling its product at high prices. Not only were the plans for the pulp mill revisited, the chase for marginal wood supplies was at its height resulting in exportation of the high-priced wood to Portugal and other countries. This made price expectations increase, and a deal could not be concluded.

At this point, December 1996, although an alternative had been developed since the middle of 1995, it was not available. The process of changing the mindsets of the companies in the Consortium, and making them agree on developing a new forest for the wood supply has proved extremely time consuming. The plant site was moved to southern Bahia and negotiations with plantation owners in this area heavily dominated by pulp mills proved difficult. Finally, a decision was taken to buy portions of land where new plantations would be established. To back this up further, a deal was made with the local pulp mills, Aracruz and Bahia do Sul, to utilize their undersize logs, at present being leftovers at the felling site. This waste material has been the raw material for small and sometimes, unauthorized, entrepreneurial charcoal manufacturing, causing both environmental problems and outbursts of fire. The electrical grid in the area is weak and susceptible to black-outs. The establishment of a biomass power plant in the vicinity of the pulp mills was, on these grounds, viewed as providing added value rather than competition for raw materials. However, integrating the ownership of a forest and its establishment into the project work program has been very time consuming and has caused delays of 12 to 18 months. All land contracts, etc., were in place by the end of 1997. In the real case, the fuel cost estimated is slightly higher than the cost projected earlier, as a conservative approach on the productivity and the cost for recovering waste wood has been adopted.

Electricity Contract. The outline energy contract suggested by the Consortium had innovative features without any precedent. Therefore, ANEEL (Agência Nacional de Energia Elétrica), the regulator, CHESF and the Consortium SER went through a lengthy process of formulating and negotiating the contract. In short, the contract provides the consortium the right to be a priority dispatched unit within the CHESF grid, selling all power produced to CHESF at a fixed indexed price above the current production cost of CHESF. CHESF, on the other hand, is allowed to

Table 3 Specific investment costs for demonstration and N^{th} plants

Cost Structure ($/kW)		
Investment	**Demo. plant**	**Commercial plant**
Wood preparation	200	100
Gasification	1,300	600
Power Plant	1,000	800
Total	**2,500**	**1,500**

Table 4 Power production cost and tariff for the demonstration plant and the N^{th} plant

	N^{th} plant.		
Tariff/Cost ($/MWh)	**without GEF Grant**	**with GEF Grant**	**Commercial Plant**
Fuel	15	15	13
O & M	12	12	7
Capital rel. cost	39	25	23
Production cost	**66**	**52**	**43**
Brazilian taxes & social costs	11	8	9
Tariff	**77**	**60**	**52**

Table 5 Demonstration plant budget and financing

Budget	**Million $ US**
Power plant	83
Land Purchase	7
Start-up, grid connection	4
Interest and taxes	19
Total capital requirement	**113**
Funding	
Equity	25
GEF grant	35
WB loan	53
Total funding	**113**

recover this higher cost by dispersing it over the entire CHESF annual power sales of approximately 6000 MW years, i.e., a 0.5 percent overall tariff increase.

The economics underlying the tariff calculations are presented in Tables 3 and 4. In Table 3, the specific investment of the demonstration plant is indicated, and also the corresponding estimate for a future commercial plant. The reduction in the specific investment cost is due to the learning curve effect, i.e., the combined effect of cost reduction achieved by improving the plant design, by cost reductions from equipment being more standardized, an efficiency increase following the improved design (such that more MW are generated), and the effect of economy of scale, as a more mature technology is used in larger capacity installations.

The specific cost and plant performance used in the Phase III budget gives a tariff requirement for Brazilian conditions as shown in Table 4. Note that the impact of the GEF grant is approximately 25 percent on the tariff, and thus, without such a grant or similar subsidy, the demonstration of this technology would not have been feasible for a profit-oriented company, in spite of the huge future potential of the technology, i.e., the use of ''seed'' money subsidies are justifiable on the grounds that otherwise nobody would have threaded the path of the learning curve. Note also that the Brazilian taxes and social costs are both based on pre-profit turnover and profit related factors.

Financing. In Table 5, the Phase III budget and financing are shown. This gives a power plant specific investment cost of 2600 $/kW.

Following the formation of the Consortium, the equity capital was made available by the companies. The GEF grant was formally approved by the World Bank in June 1997.

Following the application to the World Bank by the Brazilian Government, the World Bank will make a banking assessment of the project situation, the economics of the project and hence, the associated risks. Following this Project Preappraisal (PPA), a recommendation will be made by the officials to the WB board on what line of action to take, and under which conditions. The prerequisites to start this discussion were that the Consortium was formed (such that there was a legal party operating the project), the necessary permits had been approved, and a long term fuel supply at a feasible cost had been secured as well as a long term power contract.

As indicated above, these conditions were only fully met in October 1997. Because of the innovative technical content of the project, the WB felt that the normal procedures for making risk assessments (e.g., performance of reference plants, vendor guarantees, etc.) were not applicable in this case. Therefore, the WB contracted EPRI to carry out a risk mitigation study, to be further refined in a seminar to which all the parties involved in the Brazilian project, as well as selected international experts will attempt to arrive at a consensus on the risks involved and on how to minimize their economic impact. As this will form an important part of the PPA report, the WB financing will not be formally decided upon until about the middle of 1998.

Conclusions

When setting out on the exploratory part of this project, in spite of all due diligence in planning the itinerary, it was found that reality did not necessarily match the plan. This caused delays and rescheduling and priorities had to be changed. The number of parties involved and duration of the project resulted in a change of the individuals involved. Due to the novel technology, the process of seeing the symptoms of a problem, identifying the ''real'' problem, and achieving a consensus on how to solve it, is very time consuming. Institutional barriers, due to new demands without precedents and external organizations operating to different schedules and priorities, also caused delays.

In spite of these problems, and in spite of large geographical distances, different cultures and languages (three continents and at least six different nationalities), it has been possible to maintain the objective of the project in focus. This could only have succeeded where there was a basic credibility in the project, and the soundness of the technology and a trust amongst the parties, as well as a strong commitment on the part of the individual parties.

At present, only the World Bank approval of the loan is required to advance the project, so that the construction phase may start in 1998. At the turn of the century, and three years later than originally planned, a 32 MWe plant will be operated in Mucuri, Bahia, Brazil. An artist's impression of the plant is shown in Fig. 15.

As all other similar projects (Arbre, Bioeletrica, North-Holland, etc.) have also suffered delays, for much the same reasons as indicated here and therefore the Brazilian BIG-GT project will continue to maintain its pioneering status in spite of the delays suffered.

Fig. 15 An artist's impression of the Brazilian BIG-GT plant

References

[1] Shell Brazil, 1992, Phase I Final Report to the Global Environment Facility, Brazilian Biomass Power Generation Project BIG/GT, BRASCEP, CHESF, CIENTEC, CVRD, Electrobras, MCT do Brasil, Shell International Petroleum Ltd.

[2] Craig, K. R., Bain, R. L., and Overend, R. P., 1995, ''Biomass Power Systems—Where are we, Where are we going and How to get there? The role of Gasification,'' *EPRI Conference on New Power Generation Technology*, San Francisco, October 25–27, 1995, CA, USA.

[3] Trebbi, G., 1993, ''Power Production Options from Biomass: The Vision of a Southern European Utility,'' Bioresource Technology, **46**, Nos. 1&2, pp. 23–30.

[4] Carpentieri, A. E., Larson, E. D., and Woods, J., 1992, ''Prospects for Sustainable, Utility Scale, Biomass-Based Electricity Supply in Northeast Brazil,'' *Center for Energy and Environmental Studies*, PU/CEES Report No. 270, Princeton University, Princeton, NJ, USA.

[5] Consonni, S., and Larson, E. D., 1994, ''Biomass-Gasifier/Aeroderivative Gas Turbine Combined Cycles, Part A and B,'' *ASME Cogen Turbo Power'94*, Oct. 25–27, 1994, Portland, OR.

[6] Larson, E. D., 1993, ''Technology for Electricity and Fuels From Biomass,'' *Annual Review of Energy and the Environment*, **18**, pp. 567–630.

[7] Faaij, A. P. C., 1997, ''Energy from Biomass and Waste,'' thesis from Universiteit Utrecht, Facultiet Schiekunde, Utrecht, ISBN-90393-1592-2.

[8] Solantausta, Y., Bridgwater, T., and Beckman, D., 1996, ''Electricity Production by Advanced Biomass Systems,'' VTT research notes 1729, Technical Research Center of Finland, Espoo.

[9] Paterson, W., 1994, *Power From Plants*, The Royal Institute of International Affairs, Energy and Environmental Programme, Earthscan Publications Ltd. London.

[10] Ricardo J., Semedo, H., Johansson, T. B., and Larson, E. D., 1993, ''Gas Turbine Power Generation From Gasified Wood,'' *Centro para a Conservacao de Energia*. Lisboa, Portugal, June 30, 1993, study prepared for the EC Alternative Energy Programme, ALTERNER.

[11] Bodlund, B., and Bergman, J., 1993, *Bioenergy in Sweden: Potential. Technology and Application Bioresource Technology*, **46**, No. 1&2, pp. 31–36.

[12] Elliott, P., 1993, ''Biomass-Energy Overview in the Context of Brazilian Biomass-Power Demonstration,'' Bioresource Technology, **46**, No. 1&2, pp. 13–23.

[13] Kaltschmitt, M., et al., 1994, ''Analysis and Co-ordination of the Activities Concerning Gasification of Biomass,'' report from a Concerted Action within the EC Argoindustrial Research Program, Nov. 1977, contract AIR3-CT94-2284.

[14] Blackadder, W., Lundberg, H., Rensfelt, E., and Waldheim, L., 1992, ''Heat and Power Production via Gasification in the Range 5–50 MWe,'' *Advances in Thermochemical Biomass Conversion*, Interlaken, Switzerland, May 11–15, 1992.

[15] Rensfelt, E., 1977, ''Atmospheric CFB Gasification—The Grève Plant and Beyond,'' *International Conference on Gasification and Pyrolysis of Biomass*. April 9–11, 1977, Stuttgart, Germany.

[16] Barducci, G., Daddi, P., Polzinetti, G., Ulivieri, P., Baldacci, A., Traniello, A., and Zeppi, C., 1994, ''Use of Lean Gas From Sorghum Bagasse in the Cement Production,'' 8th European Conference on Biomass for Energy and Environment, *Agriculture and Industry*, October 3–5, 1994, Vienna, Austria.

[17] Barducci, G., Daddi, P., Polzinetti, G., and Ulivieri, P., 1995, ''Thermic and Electric Power Production and Use From Gasification of Biomass and RDF, Experience at CFBG Plant at Grève-in-Chianti,'' *2nd Biomass Conference of the Americas: Energy, Environment Agriculture and Industry*, August 21–24, 1995, Portland, Oregon, USA.

[18] Barducci, G. L., Ulivieri, P., Polzinetti, G. C., Donati, A., and Repetto, F., 1996, ''New Developments in Biomass Utilization for Electricity and Low Energy Gas Production on the Gasification Plant of Grève-in-Chianti, Florence,'' *Developments in Thermochemical Biomass Conversion*, Vol. 2, Bridgwater, A. V., and Boocock, D. G. B., eds.; and ''Bioenergy 96—The Seventh National Bioenergy Conference,'' Sept. 15–20, Nashville, TN.

[19] Pitcher, K., and Lundberg, H., 1995, ''Wood Energy: The Development of a Gasification Plant Utilising Short Rotation Coppice,'' Project ARBRE, Third International Wood Fuel Conference, October 9–15, 1995, Glasgow, Scotland.

[20] Elliott, P., and Booth, R., 1993, ''Brazilian Biomass Power Demonstration Project,'' special project brief, Shell International Petroleum Company, September.

[21] Elliott, P., and Booth, R., 1996, ''Biomass Energy for the Twenty-First Century. Commercial Demonstration of a Modern Power System Based on Gasification-Combined Cycle Technology,'' Energy and Environment, **7**, No. 2, pp. 191–208.

[22] Saaty, T. L., 1992, *Decision Making for Leaders*, ISBN 0-534-97959-9.

The Effect of Fuel/Air Mixing on Actuation Authority in an Active Combustion Instability Control System

J. M. Cohen

J. H. Stufflebeam

W. Proscia

United Technologies Research Center,
East Hartford, CT 06108

The authority of an active combustion instability control system was improved by increasing the degree of mixing between a modulated gaseous fuel source and the remainder of the premixed reactants in a low-emissions combustor. Nonreacting acetone PLIF measurements were used to assess the mixedness of various fuel injection configurations, in both time-averaged and phase-locked modes. These configurations were also evaluated in combustion tests in which the authority of the actuator and the ability of the control system to attenuate the instability were measured. The results indicated that both control authority and emissions performance are tied directly to the ability to achieve temporal control over the spatially averaged fuel/air ratio leaving the premixer at any point in time while simultaneously maintaining the high spatial uniformity of this mixture. The cold-flow diagnostic techniques were proven to be an effective and low-cost method for screening fuel injection concepts. [DOI: 10.1115/1.1373399]

Introduction

The lean, premixed combustor designs utilized in low-emissions industrial gas turbines are often prone to combustion instabilities. Significant efforts to suppress these instabilities using active control techniques have been reported. Researchers at the United Technologies Research Center ([1,2]) have demonstrated up to 15 dB suppression of combustion instabilities in a full-scale single-combustor and a 6.5 dB attenuation in a three-nozzle sector combustor. Engineers at Siemens kWU ([3,4]) have deployed an active instability control system on a full-scale engine, resulting in reductions in fluctuating pressure of as much as 17 dB. ABB investigators ([5]) have performed considerable work on a laboratory-scale combustor, yielding suppression levels of up to 12 dB. Other organizations have demonstrated similar levels of success in other premixed combustors, including the U.S. Department of Energy ([6]) and Westinghouse/Georgia Tech ([7]).

Based on these successes, it is clear that this technology holds promise as a means for attenuating combustion instabilities. Actuation technology is often identified as a critical-path item for the product deployment of active instability control systems in real engines. The majority of successful efforts in this area have used modulation of some sort of fuel flow as an actuation technique. These techniques have used existing fuel system components or have added ''secondary'' fuel injectors. The obvious actuation technology barrier is represented by the ability to modulate large fuel flows at the high frequencies at which combustion instabilities occur (normally hundreds of Hertz in gas turbines). A second, and less obvious, barrier that relates to actuation is the physics of the actuation process. For an actuator to be effective, it must have the ability to interfere with the coupling process between the acoustic pressure field and the combustion heat release rate. An actuator that modulates fuel flow may not have significant authority (effectiveness) if the fuel is not injected in a manner which allows it to interfere with the coupling process.

The study described in this paper investigated the effect of the injection configuration used to inject a modulated fuel flow as an actuation system for an active instability control system. In particular, it addressed the degree to which the mixing of that modulated fuel with the rest of the fuel and air passing through the premixer influenced the authority of the actuation system while minimizing emissions.

Background

The instability mode (~200 Hz) investigated here was a Helmholtz mode, in which the fluctuating pressure was uniform within the combustor. Pressure fluctuations were coupled with the heat release process through their effect on the flow rate of air delivered through the fuel nozzle. The time-varying air flow rate produced a time-varying equivalence ratio at the fuel nozzle exit and, therefore, time-varying heat release rate. This conceptual model of the instability was discussed in more detail by Peracchio and Proscia ([8]), and the phenomenon has been described by a number of other authors ([5,6,9]). Fuel concentration measurements performed by Lee and Anderson ([10]) in the combustor used in the current study confirmed this link between equivalence ratio fluctuations and pressure fluctuations. Figure 1 shows the spectrum of the fluctuating pressure for this instability, as observed in the single-nozzle combustor used in this study.

The premixing fuel injector used in this study has been described in detail by Stufflebeam et al. ([11]). The nozzle is shown schematically in Fig. 2. Air was delivered into the premixing chamber through two tangentially-oriented air slots that ran the entire axial length of the chamber. Natural gas fuel was injected through a row of orifices in the inlet section to each of these air slots. Fuel/air mixing was measured and optimized for low-emissions operation, as described by Stufflebeam et al. ([11]).

A similar liquid-fueled premixed system exhibited the same instability, which was effectively suppressed by 15 dB in a single-nozzle combustor using active control ([2]). In that demonstration, the fuel flowing to one of the six fuel injectors within the premixer was modulated using a high-speed solenoid valve. The gas-fuel actuation system discussed in this paper was initially designed based on the same actuation concept.

The fundamental problem of actuation system design for low-

Contributed by the International Gas Turbine Institute (IGTI) of THE AMERICAN SOCIETY OF MECHANICAL ENGINEERS for publication in the ASME JOURNAL OF ENGINEERING FOR GAS TURBINES AND POWER. Paper presented at the International Gas Turbine and Aeroengine Congress and Exhibition, Munich, Germany, May 8–11, 2000; Paper 00-GT-083. Manuscript received by IGTI Oct. 1999; final revision received by ASME headquarters Oct. 2000. Associate Editor: D. Wisler.

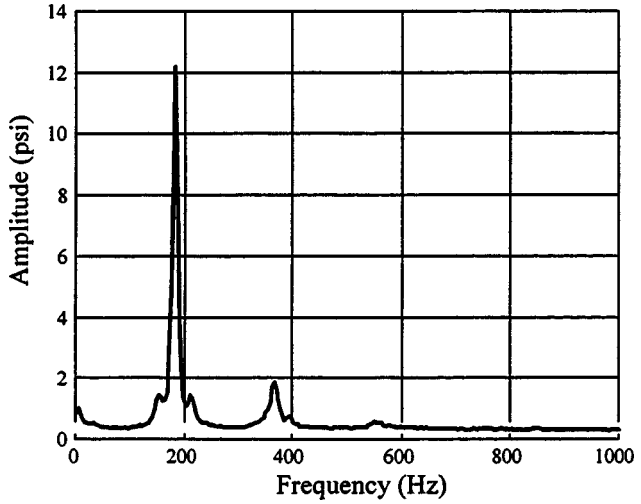

Fig. 1 Spectrum of uncontrolled combustion instability, showing high-amplitude pressure fluctuations at approximately 200 Hz.

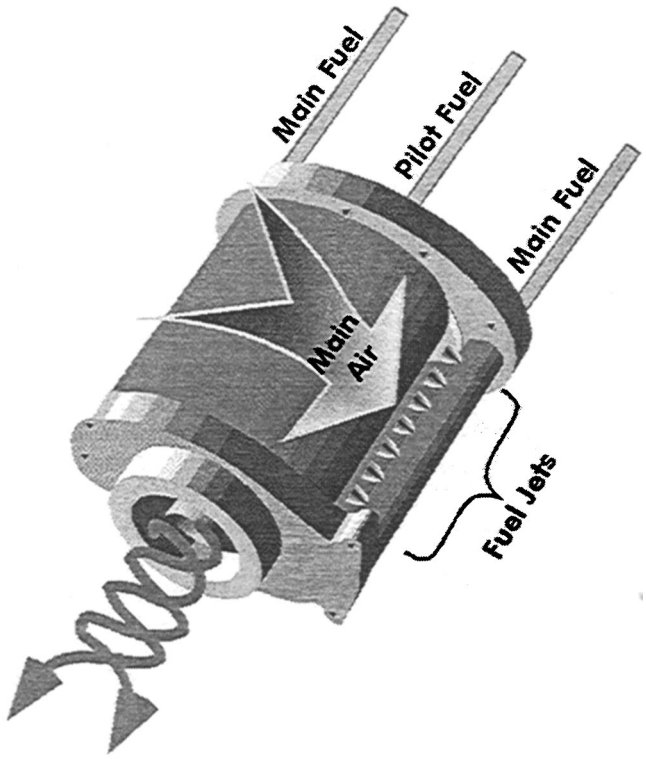

Fig. 2 Schematic of premixing fuel nozzle

emissions combustors is to maximize the system's authority over the relevant dynamic processes while minimizing the combustor's emissions.

Approach

A combination of nonreacting mixing experiments and actively controlled combustion experiments were used to evaluate a series of actuated fuel injection schemes. The functionality of the fuel modulation hardware (valving) was not changed appreciably over this series of tests. All the tests performed with unsteady fuel flow used on/off modulation of a portion (approximately 10 percent) of the gaseous fuel flow entering the premixer. Because on/off modulation of the flow was used for a fixed mean control flow, the amplitude of the imposed fuel flow variations was held constant. As a result, these tests investigated the sensitivity of actuation authority to the injection configuration and not the high-speed valve characteristics.

Mixing Experiments. An acetone PLIF (planar laser-induced fluorescence) technique was utilized to study the mixing effectiveness of the premixing nozzles used for experiments on instability control. The experiments were performed in a cold-flow facility at one atmosphere pressure to allow rapid configuration changes. Engine flow conditions were simulated through pressure/temperature scaling. The fuel/air momentum ratio at the injection site was set to match the momentum ratios experienced in the engine. The details of the specific equipment, procedure and data analysis are fully discussed in Stufflebeam, et al. ([11]). Acetone-seeded air was injected, as a gaseous fuel simulant, through the orifices along the inlet slot of the premixing nozzle, to mix with the main air. A laser sheet (10 cm wide $\times$ 0.25 cm thick) at a wavelength of 266 nm (the fourth harmonic of Nd:YAG) was projected across the fuel nozzle exit plane, exciting the acetone and generating fluorescence over a bandwidth from 350–550 nm in the visible region of the spectrum. A fluorescence image was acquired with a CCD camera and was quantified by comparison to a similar image taken with a uniform acetone/air mixture at known concentrations. 1800 images were acquired and combined to produce an averaged image. The procedure yielded two-dimensional maps of the fuel/air ratio with high spatial resolution (300 microns) and without perturbing the aerodynamic flowfield or mixing process. Statistics generated from the PLIF data allowed ranking of injection schemes according to their ability to achieve the most uniform mixing of fuel and air.

Two series of tests were conducted during these experiments. The first series screened designs of fuel injectors to determine the one that delivered the most uniform distribution of total fuel (main fuel plus modulated fuel). Uniform fuel distribution has been correlated with reduced emissions of NO_x and CO. 90 percent of the fuel was injected through the fuel orifices along the inlet air slot and 10 percent was injected through the modulating injector configuration. The fuel actuator valve was held open for these experiments to exclude possible temporal effects on the mixing results. Identification of the optimum fuel injection configuration led to further investigation of the temporal characteristics of the mixture during its fuel actuation cycle.

The tests used to measure the authority of the fuel modulation scheme were performed by synchronizing the PLIF data acquisition to the opening of the actuation valve. As in the previous tests, 90 percent of the fuel was flowed through orifices in the main air inlet slots and 10 percent modulated by the valve, was injected through the controlled system. The valve (General Valve model 9-967-900) was driven by a square wave (50 percent on, 50 percent off) at 200 Hz, a frequency similar to that observed for the pressure oscillations in combustion tests of these premixing nozzles. The laser timing was initiated from the valve opening and a variable delay was added to form the external laser trigger. The laser was allowed to accept only one trigger every 50 msec, which produced optimum lasing efficiency and pulse stability. It was able to be synchronously driven at selected time delays throughout the 5 millisecond period of the 200 Hz cycle.

Combustion Experiments. Combustion experiments were conducted in a 4-MW single-nozzle, flametube combustor (see Fig. 3). The combustor used premixing fuel nozzles designed for engine use. The 15.2-cm-diameter combustor test section was water-cooled with a thermal barrier coating on the inner wall. A sidewall diffusion pilot injector was located 2.5 cm downstream of the premixer on the combustor wall. The tests discussed in this paper were conducted at a combustor pressure of 1.5 MPa, an inlet air temperature of 710 K and a combustor fuel/air equivalence ratio of 0.53–0.56. These conditions are representative of engine operating conditions. The fuel and air flow rates required

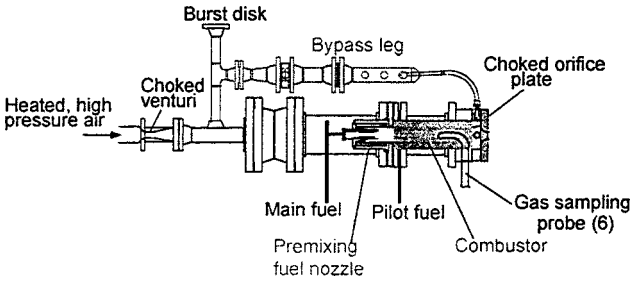

Fig. 3 Schematic of 4-MW single-nozzle combustor. Operating pressure=1.5 MPa. Inlet temperature=710 K.

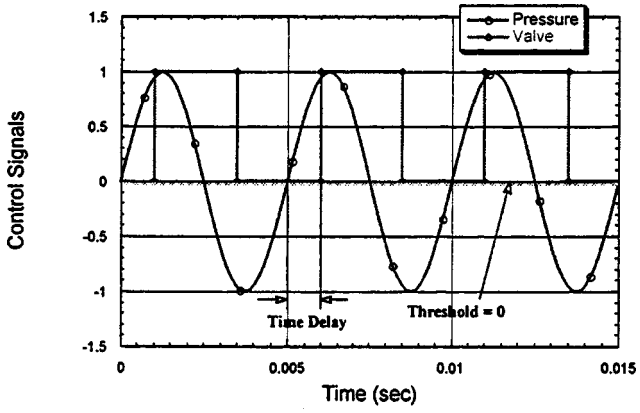

Fig. 4 Schematic of threshold control algorithm, showing method of time-delayed on/off actuation

in the single-nozzle combustor are equivalent to those required in a full engine on a nozzle-by-nozzle basis. The percentage of the fuel flow delivered to the control fuel system varied between 7 percent and 10 percent of the total fuel flow. Small changes to the test hardware, actuation system and premixer were made over the course of the combustion testing. All actively controlled results presented in this paper are referenced to uncontrolled results acquired with the same hardware in back-to-back tests in order to assure proper comparisons.

Upstream of the combustor, the air flow rate was metered using a choked venturi. After passing through the venturi, the air flow was split between the fuel nozzle and a bypass leg. The air that flowed through the bypass leg was injected at the downstream end of the combustor (upstream of the orifice plate), simulating the combustor dilution air. A water-cooled orifice plate provided a choke point to simulate the acoustic boundary of the engine's turbine inlet guide vanes.

The volumes and lengths of the combustor, diffuser region upstream of the fuel nozzle and bypass leg were set in order to reproduce the 200 Hz Helmholtz mode instability observed in a full-annular engine combustor.

Natural gas fuel was delivered to the main and pilot fuel systems using independent choked venturies. The flow delivered to the control fuel system was metered through an unchoked venturi, due to the time-varying back pressure that the control valve imposed. The control fuel flow was modulated in an on/off fashion at a location between 5 cm and 15 cm from the final injection point, depending on the injector. The volume of plumbing between the venturi and the modulating valve in the control fuel system was large, so that fluctuations in the fuel pressure induced by the valve would not significantly affect the measurement of the time-averaged fuel flow rate at the venturi.

An array of six gas-sampling probes, located upstream of the bypass air injection as used to measure NO_x and CO concentrations as well as combustor fuel/air ratio and combustion efficiency. Species concentrations were corrected to a 15 percent oxygen basis for a ganged probe arrangement. Fast-response data were collected at a rate of 5 kHz on a simultaneous sample-hold data acquisition system. The analog signals were low-pass filtered at 2 kHz to prevent aliasing. Fluctuating pressures were measured at two locations in the combustor using high-response pressure transducers.

The active control system consisted of three parts: a pressure sensor, a control algorithm, and an actuator. Because of the uniform spatial distribution of the fluctuating pressure within the combustor, only one combustor pressure measurement was required to describe the unsteady pressure field as input to the control system. A bandpass (100–300 Hz) filter was used to condition the pressure signal before input to the control algorithm. For diagnostic purposes, a simple threshold control algorithm was designed. The principle of its operation is shown in Fig. 4. Whenever the control sensor signal crossed an established threshold level, a command was sent to the on/off valve. On positive-direction crossings, the valve was opened and on negative-direction crossings, it was closed. A time delay between the moment of crossing and the valve command was also imposed. The same delay was used for both opening and closing commands. The threshold level and time delay were manipulated via a user interface to the control algorithm. This time delay represented an arbitrary control time delay, and is not indicative of the physical delay times in the mixing/combustion dynamic system. For a stationary (fixed frequency) instability, the control time delay translates simply into an effective control phase delay between the pressure signal and the actuator command.

Injection Configurations. An illustration of the actuation physics is shown in Fig. 5. The intent of the controlled fuel injection system was to reduce variations in the fuel/air ratio at the exit of the premixer by introducing a modulated fuel flow into it. The goal of the system was to keep the fuel/air ratio being delivered to the combustor uniform in both time and space. Temporal uniformity inhibits the development of combustion instabilities, and spatial uniformity inhibits the production of NO_x. Complete can-

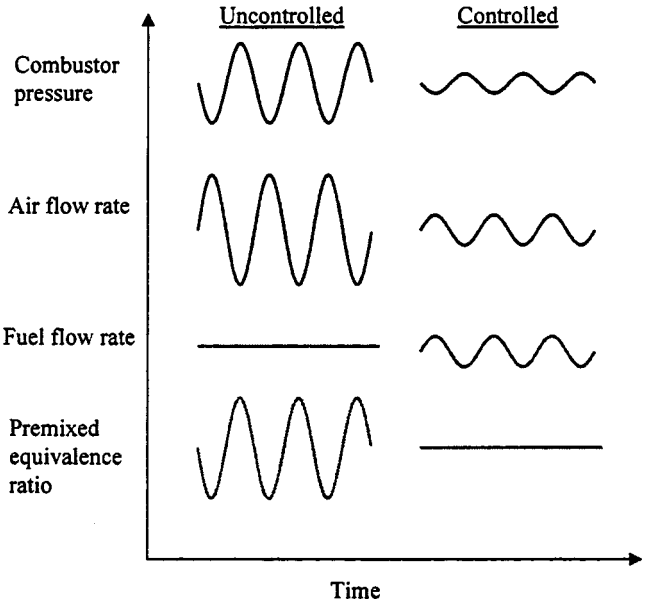

Fig. 5 Illustration of the intent of the actuation technique, utilizing the reduction of equivalence ratio fluctions by pulsed fuel injection

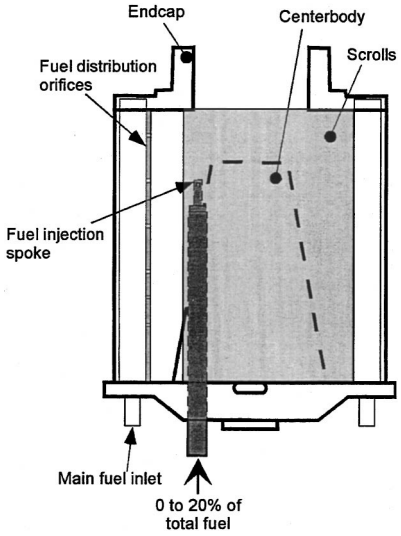

Fig. 6 Cross section schematic of premixing fuel nozzle with actuated fuel injection spoke for introduction of control fuel flow (configurations 1-3)

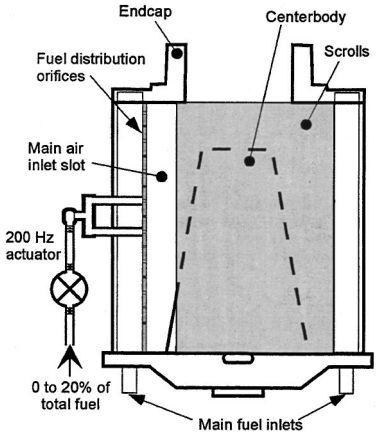

Fig. 8 Cross section schematic of premixing fuel nozzle with actuation of a portion of the main fuel injection array (configuration 4)

cellation of fuel/air variations would likely require on-line adaptation of the amplitude of the fuel flow modulation. Only fixed-amplitude actuation was used in this study.

Four different injection configurations, providing different degrees of fuel/air mixing, were investigated in both the mixing and combustion experiments. All of these designs were intended to introduce a minimal disturbance to the mechanical design of the premixing fuel nozzle.

Three of these injectors used a ''spoke'' design, which protruded from the premixer's centerbody (Fig. 6). Detailed views of the spoke tip injectors are shown in Fig. 7. The spoke arrangement allowed the control fuel system plumbing to be routed easily and quickly out of the nozzle and connected to the high-speed valve without significant alterations. Configuration 1 used a short extension tube with an open end, and directed fuel axially downstream. Configuration 2 used the same length tube, but with a capped end and two small slots milled in the side. The slots were 180 deg apart and directed fuel in a direction tangential to the centerbody surface. Configuration 3 used a longer (capped) tube, with a series of four holes along its length. The hole furthest upstream had a 50 percent larger flow area than the two center holes and the hole furthest downstream was 50 percent smaller. The larger and smaller holes were located 180 deg apart. The center holes were located at 90 deg between the others and directed fuel radially outward from the centerbody axis.

The fourth injection configuration (Fig. 8) made use of the main fuel injection array built into the air inlet slot of the premixing nozzle. This main fuel injection array had previously been optimized for spatial mixing uniformity with steady fuel flow ([11]). Two of the orifices near the center of this array were manifolded together and plumbed to the high-speed valve. The net volume of tubing was slightly longer than that used in the spoke configuration, due to the manifold plumbing.

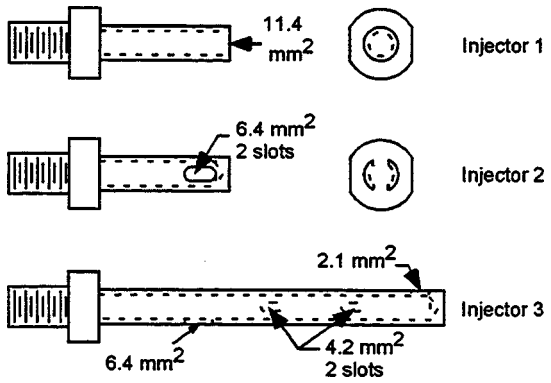

Fig. 7 Detailed view of three ''spoke'' injection configurations

Mixing Results

The acetone PLIF technique was used to assess the steady-state mixing features of each injection concept. The fuel flow was not modulated during these tests. In each of the tests, 10 percent of the total fuel simulant injected into the premixer was passed through the control fuel system. The results of these tests are shown in Fig. 9. The fuel concentration at the exit of the premixing nozzle is shown for each configuration. For the three ''spoke'' injectors, the nonuniformity created by the localized fuel injection can be observed in the concentration profiles as a locally richer spot. Figure 9 also shows the spatially averaged unmixedness, as represented by the ratio of the standard deviation of the concentration distribution (σ) to the mean concentration value (μ), for each configuration.

All three of the ''spoke'' mixing concepts demonstrated poorer steady-state mixing than the baseline premixer. It can be seen that, for the spoke configurations, mixing improved as the fuel was injected through a larger number of sites over a larger area. Injection through the main orifice array gave the best mixing, which is consistent with the fact that this array has been optimized for good mixing.

Phase-locked PLIF measurements were made for the best-mixing configuration, which used the main orifice array (configuration 4). The high-speed on/off valve in the control fuel system was driven at 200 Hz. The Nd:YAG laser pulses were triggered by an ''open'' command to the valve, and fired at 20 Hz. A time delay between the valve trigger and the laser firing was imposed with a timer circuit. By varying this time delay, it was possible to vary the phase of the PLIF imaging relative to that of the fuel injection. Five different time/phase delays were used over the full cycle of injection at 200 Hz. 1800 images were acquired at each delay setting and averaged together to generate a representative, ensemble-averaged image of the fuel concentration distribution at the exit of the premixer during a cycle of fuel modulation. Figure 10 shows these results. They demonstrate that the spatial distribution of fuel changed only slightly over the period of one cycle. Figure 11 shows how the spatially averaged fuel concentration (fuel/air ratio) changed over one cycle. The unmixedness (σ/μ =standard deviation/mean) changed over the range of 3.6 percent

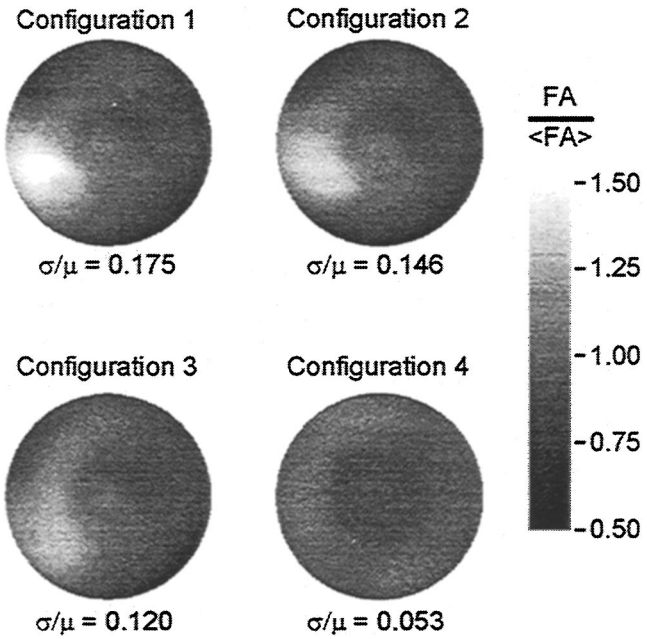

Fig. 9 Steady-state fuel/air concentration profiles at premixer exit for three spoke injection concepts and configuration 4 (two-port main fuel injector). Concentration values have been normalized by the mean value for each case.

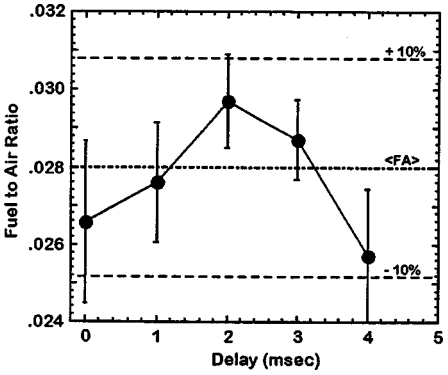

Fig. 11 Variation of spatially averaged fuel/air ratio at premixer exit over one period (5 msec) of 200 Hz fuel flow modulation. Bars indicate spatial variance about average value at each time.

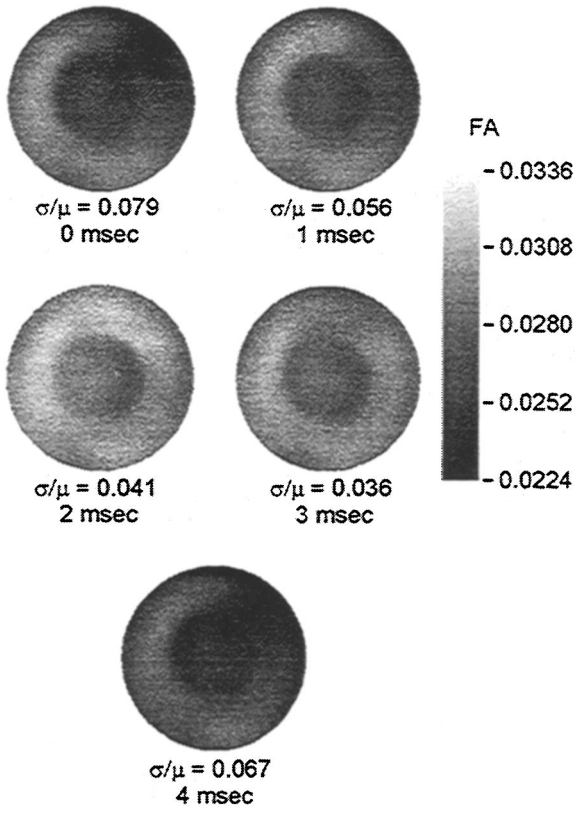

Fig. 10 Phase-averaged fuel/air concentration profiles and unmixedness at premixer exit for 2-Hz modulation of fuel injection using configuration 4

to 7.9 percent during the cycle, indicating that reasonably good mixing was being maintained throughout. The average acetone concentration changed by +/−7 percent during a cycle, compared to the command variation of +/−10 percent. These tests demonstrated the ability of injector configuration 4 to control the temporal character of the fuel/air ratio at the exit of the premixer without excessively degrading the spatial fuel/air mixing at any point in time.

Combustion Results

Each of the control fuel injection concepts was tested in the single-nozzle combustor under controlled and uncontrolled conditions. During uncontrolled operation, fuel was delivered through the control fuel circuit at the same mean flow rate as was used in the controlled tests. This was necessary to truly isolate the true effect of the unsteady aspect of the fuel injection.

All three of the ''spoke'' injection concepts showed increased NO_x and CO levels (relative to baseline levels) during operation with steady, nonmodulated flow through the control fuel system. These levels did not change appreciably when control was applied (for the same mean flow through the control fuel system). In general, the level of NO_x increase that was observed correlated with the degree of unmixedness that was observed.

For each of the spoke injection configurations a ''piloting'' effect on the instability was also observed. When a constant fuel flow was delivered through the control fuel system, the local enrichening resulted in an attenuation of the pressure fluctuations. This behavior is similar to that observed when a diffusion-flame pilot was applied to the system. When piloted, the pressure fluctuation levels were reduced, but at the expense of higher NO_x emissions.

Configuration 4, in which the control fuel was delivered through a portion of the main fuel injection array, showed no difference in either pressure fluctuations or emissions between the baseline case and the case in which steady fuel flow was delivered through the control fuel system (as expected).

Figure 12 shows that the level of reduction in the amplitude of the dominant instability mode correlated with the mixing performance, when measured at the optimal control delay for each configuration. Better-mixing injection schemes provided significantly better actuation authority, with configuration 4 producing a 16 dB (6.3×) reduction.

Figure 13 shows a comparison between the uncontrolled and controlled combustor pressure spectra for configuration 4. The amplitude of the instability near 200 Hz was reduced from just over 12 psi to less than 2 psi. The harmonic observed near 380 Hz in the uncontrolled spectrum was also eliminated. Under control, the frequency of the remaining pressure oscillations was slightly higher. No other modes were excited above their baseline levels

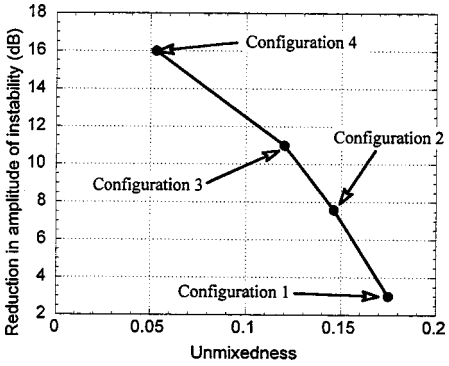

Fig. 12 The effect of steady-state fuel/air mixing on actuator authority in combustion tests for four different actuated fuel injection configurations

under controlled conditions. The broadband RMS pressure fluctuation level in the 0–2 kHz band was reduced by a factor of 2.4 with control.

Fuel concentration measurements reported by Lee and Anderson ([10]) using this combustor with actuation configuration 4, showed that the actuation system directly affected the unsteady component of the fuel/air ratio at the exit of the premixing nozzle. Their measurements showed large variations in equivalence ratio when the control system was used to drive the instability, and negligible variations when the control system was used to attenuate them. It is possible that residual equivalence ratio fluctuations still existed under attenuating conditions, but that they were not measurable using this instrument. This diagnostic technique was not applied to combustion tests using the three other actuation system configurations.

One of the more interesting observations was that both NO_x and CO emissions were improved under controlled conditions for configuration 4. NO_x emissions were reduced by 27 percent and CO emissions were reduced by 54 percent. This trend is consistent with observations made by Cohen et al. ([2]). It is most likely that the control system, by reducing equivalence ratio fluctuations, also reduced temporal ''hot spots'' and ''cold spots,'' thus decreasing the production of NO_x and CO, respectively.

Summary and Conclusions

The design of this actuation system followed from the conceptual model of the instability as being driven by equivalence ratio fluctuations. The ability of the fuel injection actuator to reduce these equivalence ratio fluctuations was tied to its ability to mix the control fuel flow in a way that provided a more spatially and temporally uniform fuel/air distribution at the premixer exit. It is likely that the instantaneous deficits/excesses in equivalence ratio were spatially uniform at the premixer exit plane, given the nature of the acoustic mode through which they were created (a uniform-pressure Helmholtz mode) and the intent of the premixer design (to achieve good spatial mixing). The effect of actuation should, then, also be spatially uniform in order to compensate for these variations and interfere with the heat-release/acoustic coupling process.

The results presented here illustrate that the authority of an active-control actuator used to attenuate instabilities by reducing or canceling equivalence ratio fluctuations can be improved by optimizing its mixing characteristics. This was systematically demonstrated through a series of mixing and controlled combustion experiments. An improved actuation injection system enabled an active instability control system which reduced pressure fluctuations by 16 dB, NO_x emissions by 27 percent and CO emissions by 54 percent at realistic operating conditions.

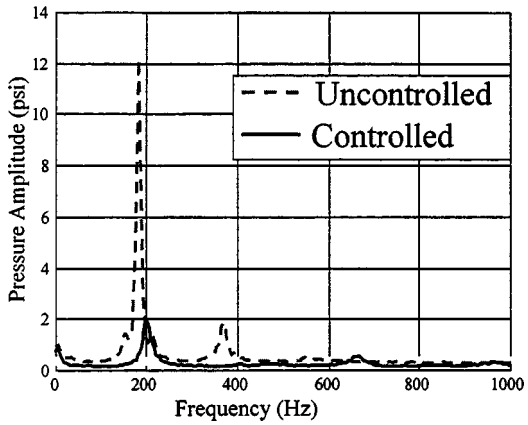

Fig. 13 Comparison of uncontrolled and controlled combustor pressure spectra for control with main fuel array actuation (configuration 4)

Acknowledgments

The authors are greatly indebted to the following persons for their efforts in this study: Mr. Joseph Poplawski, Mr. Skip Maciolek, Mr. Jeffrey Walker, and Mr. John Miano. Mrs. Nancy Rey provided expertise in design of the fuel modulation system. Drs. Clas Jacobson and Andrzej Banaszuk provided insight on the dynamic nature of the control system. The support of Drs. Thomas Rosfjord and Alan Eckbreth is also greatly appreciated. This study was funded by the United Technologies Research Center internal research program.

References

[1] Hibshman, J. R., Cohen, J. M., Banaszuk, A., Anderson, T. J., and Alholm, H. A., 1999, ''Active Control of Combustion Instability in a Liquid-Fueled Sector Combustor,'' ASME Paper 99-GT-215, International Gas Turbine and Aeroengine Congress & Exposition, Indianapolis, IN, June.

[2] Cohen, J. M., Rey, N. M., Jacobson, C. A., and Anderson, T. J., 1999, ''Active Control of Combustion Instability in a Liquid-Fueled Low-NO_x Combustor,'' ASME J. Eng. Gas Turbines Power, **121**, No. 2, pp. 281–284.

[3] Seume, J. R., Vortmeyer, N., Krause, W., Hermann, J., Hantschk, C.-C., Zangl, P., Gleis, S., Vortmeyer, D., and Orthmann, A., 1997, ''Application of Active Combustion Instability Control to a Heavy Duty Gas Turbine,'' ASME Paper 97-AA-119, ASME Asia '97 Congress and Exhibition, Singapore, Oct.

[4] Hoffmann, S., Weber, G., Judith, H., Hermann, J., and Orthmann, A., 1998, ''Application of Active Combustion Instability Control to Siemens Heavy Duty Gas Turbines,'' Symposium of the AVT Panel on Gas Turbine Engine Combustion, Emission, and Alternative Fuels, Lisbon, Portugal, Oct.

[5] Paschereit, C. O., Gutmark, E., and Weisenstein, W., 1999, ''Control of Combustion Driven Oscillations by Equivalence Ratio Modulations,'' ASME Paper 99-GT-118, International Gas Turbine and Aeroengine Congress & Exposition, Indianapolis, IN, June.

[6] Richards, G. A., Yip, M. J., Robey, E., Cowell, L., and Rawlins, D., 1995, ''Combustion Oscillation Control by Cyclic Fuel Injection,'' ASME Paper 95-GT-224, International Gas Turbine and Aeroengine Congress & Exposition, Houston, TX , June.

[7] Sattinger, S. S., Neumeier, Y., Nabi, A., Zinn, B. T., Amos, D. J., and Darling, D. D., 1998, ''Sub-scale Demonstration of the Active Feedback Control of Gas-Turbine Combustion Instabilities,'' ASME Paper 98-GT-258, International Gas Turbine and Aeroengine Congress & Exposition, Stockholm, Sweden, June.

[8] Peracchio, A. A., and Proscia, W., 1999, ''Nonlinear Heat-Release/Acoustic Model for Thermoacoustic Instability in Lean Premixed Combustors,'' ASME J. Eng. Gas Turbines Power, **121**, No. 3, pp. 415–421.

[9] Lieuwen, T., Torres, H., Johnson, C., and Zinn, B., 1999, ''A Mechanism of Combustion Instability in Lean Premixed Gas Turbine Combustors,'' ASME Paper 99-GT-3, International Gas Turbine and Aeroengine Congress & Exposition, Indianapolis, IN, June.

[10] Lee, D. S., and Anderson, T. J., 1999, ''Measurements of Fuel/Air—Acoustic Coupling in Lean Premixed Combustion Systems,'' AIAA Paper AIAA-99-0450, AIAA Aerospace Sciences Meeting, Reno, NV, Jan.

[11] Stufflebeam, J. H., Kendrick, D. W., Sowa, W. A., and Snyder, T. S., 1999, ''Quantifying Fuel/Air Unmixedness in Premixing Nozzles Using an Acetone Fluorescence Technique,'' ASME Paper 99-GT-399, International Gas Turbine and Aeroengine Congress & Exposition, Indianapolis, IN, June.

Y. Yoshida
Engine and Environmental Research Division,
Japan Automobile Research Institute, Inc.,
Tsukuba, Ibaraki, Japan

K. Oyakawa
Advanced Power System Research Division,
Japan Automobile Research Institute, Inc.,
Tsukuba, Ibaraki, Japan

Y. Aizawa
Central Technical Research Laboratory,
Nippon Mitsubishi Oil Company,
Yokohama, Kanagawa, Japan

H. Kaya
Human Resources Development Office,
Tonen Company,
Tokyo, Japan

A High-Temperature Catalytic Combustor With Starting Burner

A catalytic combustion system has high potential to achieve low NO_x emission level. When this combustion system is applied to a gas turbine, the required combustor performance must be maintained over a wide range of operating conditions. These conditions range from cold starting to steady-state operation. Particularly during the initial stage of cold starting when the catalyst is not yet activated, the catalyst must be heated by some means. This study proposes a new concept of a catalytic combustor with a direct heating system using vaporizing tube for starting burner in order to downsize the combustor and reduce the warm-up time during cold starts. The effectiveness of this concept is experimentally verified. Furthermore, NO_x, CO, and HC emissions during startup can be reduced to a low level so as to achieve ultra-low pollution of the catalytic combustion over a wide range of operating conditions from cold start to steady-state operation. This paper outlines the operation concept covering cold start, verification of the concept through the experiments with flame visualization in the combustor, spray characteristics, construction of the combustor, and combustion characteristics that show low pollution in various operating conditions of the catalytic combustor. [DOI: 10.1115/1.1373397]

Introduction

A catalytic combustion system reduces NO_x emission levels below those of conventional systems such as diffusion combustion or premixed combustion ([1]). It is thus a low-pollution combustion system with excellent features that enables using various types of fuels without regard to specifications such as octane number or cetane index. In the project to develop a 100 kW ceramic gas turbine for automobiles, a catalytic combustor that allows raising the combustor outlet temperature to 1473 K was investigated ([2]). When this catalytic combustor is mounted on an engine, the required combustor performance must be maintained over a wide range of operating conditions. These conditions range from cold starting to steady-state operation. Particularly during the initial stage of cold starting when the catalyst is not yet activated, the catalyst must be heated by some means.

Various methods for enabling cold starting, such as installing a preburner in the upper stream of the catalytic combustion section ([3]) and initially employing a starting burner then using a bypass valve to switch after the combustion warms up ([4]), have been developed. These complex structures have such shortcomings as emitting more NO_x during startup as the combustor becomes larger.

This study proposes a new concept of a catalytic combustor with a direct heating system in order to downsize the combustor and reduce the warm-up time during cold starts. This new concept employs a vaporizing tube that mixes gas and functions as a starting burner. The effectiveness of this concept is experimentally verified. This combustor concept not only enables the combustor to be downsized but also reduces the time for warm up because the catalyst can be heated quickly. Furthermore, NO_x, CO, and HC emissions during startup can be reduced to a low level so as to achieve ultra low pollution of the catalytic combustion over a wide range of operating conditions from cold start to steady-state operation.

This paper outlines the operation concept, covering cold start, verification of the concept through the experiments with flame visualization in the combustor, combustion characteristics and low pollution in various operating conditions of the catalytic combustor, including startup, transition, and steady state.

Concept of the Combustor

The operational concept of the catalytic combustor is shown in Fig. 1. This concept includes three phases, (1) cold startup, (2) transition from startup to steady state, and (3) steady state. The combustor outlet temperature is specified to 1473 K or higher. The catalytic combustor consists of a variable swirler, air-assist fuel nozzle, vaporizing tube, ignition plug, a first-stage catalyst with a heat resistance of 1273 K and high activity at lower temperatures, and second-stage and third-stage catalysts with heat resistances of 1473 K or more. Inflow ports are provided in the liner between the first-stage and second-stage catalysts so as to allow combustion gas flow into the high-temperature mixing zone from outside of the liner, in the event of excessively high swirl strength. Combustion gas is forced to move outer direction by the momentum of the gas with high swirl strength. A large amount of the gas passes through the slit section, and a large circulation flow is formed that passes through the first-stage catalyst and the vaporizing tube. The slit is opened always. As a result of this design, the high-temperature flame cannot directly heat the first-stage catalyst during the startup phase with high swirl strength. One feature of this concept is that the phase switching from startup to transition and from transition to a steady state can be accomplished smoothly by adjusting the swirl strength of the combustion air or the atomizing air flow rate of the fuel nozzle. Thus the size of the structure can be reduced. These operation phases are described below.

1 Startup. Cold combustion air is swirled by the variable swirler and flows into the vaporizing tube. The fuel spray injected by the fuel nozzle is ignited by the ignition plug to form a swirling flame in the vaporizing tube, which assumes the function of the starting burner. A large circulation flow is formed that passes through the central portion of the vaporizing tube and the first-stage catalyst; the flame cannot directly contact the first-stage catalyst, but rather the first-stage catalyst is heated by the circulation of the burning gas that flows into the high-temperature mixing zone. This burning gas that flows into the high-temperature mixing zone passes through the second and third-stage catalysts to heat them and it is then exhausted, after burning the unburned CO and HC components completely through catalytic reactions.

Contributed by the International Gas Turbine Institute (IGTI) of THE AMERICAN SOCIETY OF MECHANICAL ENGINEERS for publication in the ASME JOURNAL OF ENGINEERING FOR GAS TURBINES AND POWER. Paper presented at the International Gas Turbine and Aeroengine Congress and Exhibition, Munich, Germany, May 8–11, 2000; Paper 00-GT-087. Manuscript received by IGTI Oct. 1999; final revision received by ASME Headquarters Oct. 2000. Associate Editor: D. Wisler.

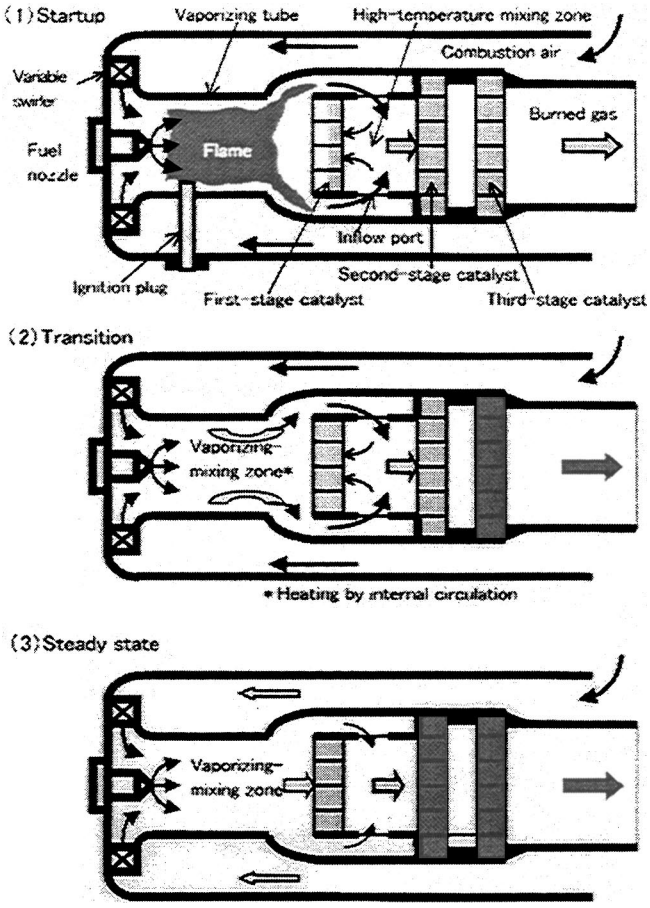

Fig. 1 Concept of operation

2 Transition. The first-stage catalyst is heated rapidly after startup, and the temperature of the catalyst will rise above the ignition temperature (473 K), at which time it becomes active; the temperature of the first-stage catalyst further increases by receiving radiation heat from the second-stage catalyst. This concept assumes the use of a heat exchanger that recovers waste heat of the exhaust, and switching to the transition phase occurs when the combustor inlet air temperature has been raised by the heat exchanger. The flame of the starting burner is supported near the inner wall of the vaporizing tube; the starting burner is extinguished by increasing the atomizing air flow rate so that the well-atomized spray doesn't reach the vaporizing tube wall because of the reduced penetration. The starting burner will be extinguished after this stage, and catalytic combustion alone will remain. If the temperature of the combustion air is below the level required for complete evaporation of the liquid fuel, the vaporizing gas will be heated by the reversed reacting gas from the first-stage catalyst and thus the internal circulation heating in the vaporizing tube is maintained. In this way, the high temperatures required for catalytic combustion of the second-stage and succeeding catalyst are maintained and catalytic combustion will continue.

3 Steady State. A steady-state operation begins when the combustion air has been preheated by a heat exchanger to above the required temperature. Ordinary catalytic combustors operate under these conditions. Switching from the transition to a steady state is accomplished by adjusting the swirl strength of the combustion air.

Experimental Verification of the Starting Burner

A combustor with visible internal structures comprised of quartz glass cylinders for the vaporizing tube section and a catalyst liner section (Fig. 2) was used in the experiments to verify the concept of the starting burner. The structure of the combustor is such that a slit is provided upstream of the first-stage catalyst to allow part of the burning gas flow into the peripheral section of the catalyst liner during startup. Burning gas is thus supplied from the inflow ports provided in the catalyst liner to the high-temperature mixing zone, which is located between the first-stage and second-stage catalysts. This high-temperature mixing zone also promotes homogenization of the burning gas if some heterogeneity of the premixed gas exists during steady state.

The dimensions of the vaporizing tube are inner diameter of 70 mm at the inlet, 90 mm at the outlet, length of the straight tube portion of 100 mm from inlet, and length of the tapered tube portion of 130 mm. Inflow ports are provided in the catalyst liner in radial directions at a distance of 20 mm from the outlet end of the first-stage catalyst, where 12 ports with diameters of 12 mm are arranged at equal intervals in a circle. The slit widths we adopted are 12 mm from the outlet of the vaporizing tube to the

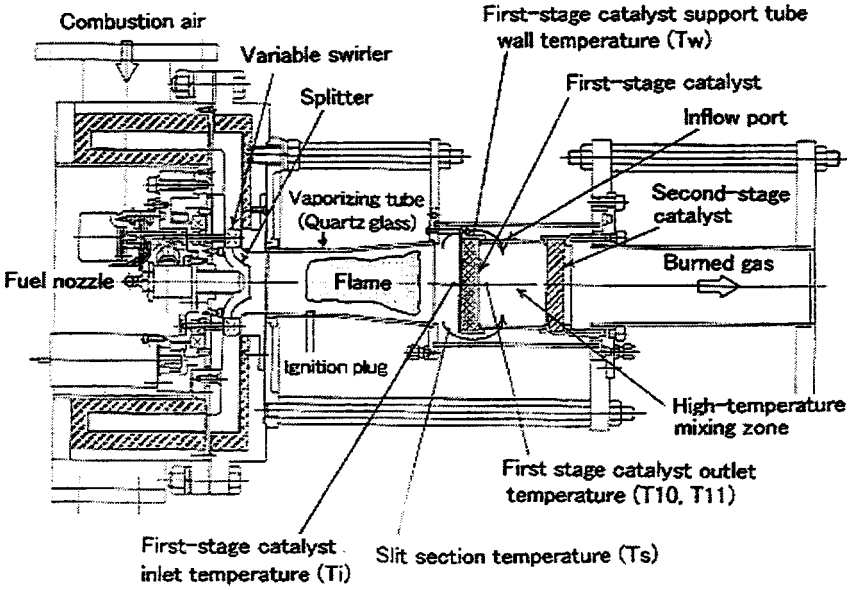

Fig. 2 Construction of the flame-visualized combustor

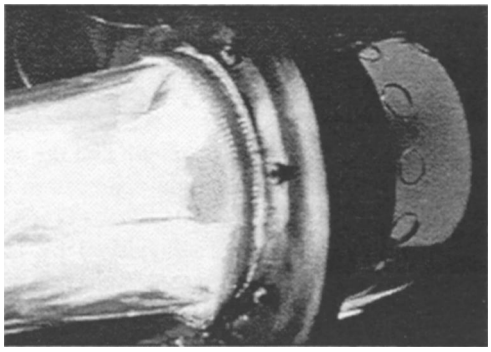

Fig. 3 Flame behavior of the starting burner

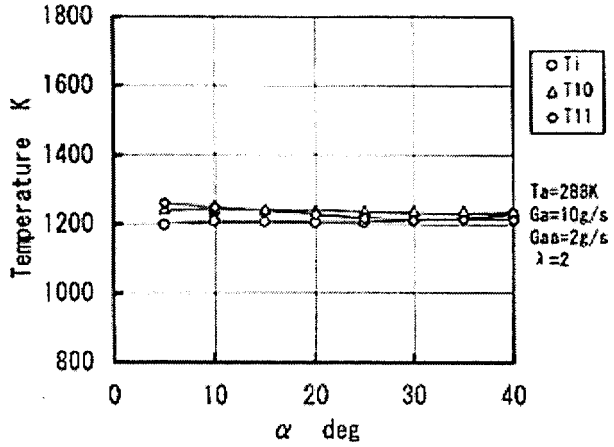

Fig. 5 Temperature characteristics around the first-stage catalyst (*Ga*=10 g/s)

first-stage catalyst and an interval of 60 mm between the first stage and second stage. These were selected because they provide good combustion conditions for the starting burner and steady-state catalytic combustion.

An air-assist fuel nozzle was used for supplying liquid fuel and a splitter with a split ratio ([outlet diameter of the splitter/inlet diameter of the vaporizing tube]^2) of 0.25 was used to adjust the combustion air velocity distribution.

A conventionally used honeycomb catalyst made of Pd/Al_2O_3/cordierite with a heat resistance of 1273 K and high activity at low temperatures was used for the first-stage catalyst in this experiment. Experiments were conducted primarily to clarify the temperature characteristics and flame behavior around the first-stage catalyst. A honeycomb body made of aluminum titanate with a heat resistance of 1773 K was used for the second-stage catalyst. Both have an outer diameter of 100 mm, a thickness of 20 mm, and number of cells of 200 cells/in^2. The temperatures were measured using R type of thermocouples to determine the first-stage catalyst inlet temperature (*Ti*), the gas temperature in the slit section (*Ts*), the first-stage catalyst support tube wall temperature (*Tw*), the first-stage catalyst outlet temperature at radii of 0 mm and 20 mm (T_{10},T_{11}), and the second-stage catalyst inlet temperature at each position (T_{20},T_{21}). A variable swirler was used so that the swirl strength of the combustion air, which influenced the ignitability and combustion state, could be varied continuously. Kerosene was used for fuel.

Ignition was performed by the ignition plug provided in the vaporizing tube. The ignition time and the temperature of each part were measured with varying the swirl angle of the swirler, and behavior of the flame and state of each part of the catalyst were also observed.

An experiment of the ignition time while supplying cold air and varying the swirl angle indicated an ignition time of 1 sec or less at swirl angles between 15 deg and 30 deg, and thus good ignitability was confirmed.

The combustion state at a swirl angle (α) of 35 deg, a combustion air flow rate (*Ga*) of 10 g/s, and an air excess ratio (λ) of 2, functioning as the starting burner, is shown in Figs. 3 and 4. Figure 3 shows the flame behavior flowing into the slit section without flowing into the first-stage catalyst. Figure 4 shows the state after ten minutes operation where the first-stage catalyst and the second-stage catalyst are heated by burned gas. These photographs enabled to clarify the combustion state of the starting burner.

The gas temperatures on the front and rear portions of the first-stage catalyst, measured while varying the swirl angle under the above-mentioned burning conditions, are shown in Fig. 5. Even if a flame is formed, both gas temperatures on the front and rear portions of the catalyst are suppressed to below 1273 K of the heat resistance temperature of the catalyst. These temperatures do not vary much if the swirl angle is varied, because almost all combustion is completed in the vaporizing tube when *Ga* is 10 g/s. The temperature of each part around the first-stage catalyst when *Ga* is increased to 20 g/s is shown in Fig. 6. When α is 5 deg to 10 deg, other measurement of the distribution of flow velocities which is not shown here indicate that no circulation flow zone is formed in the central portion of the vaporizing tube because of weak swirl strength. In this case, according to visual observations, the annular flame supported on the inner wall of the vaporizing tube extends

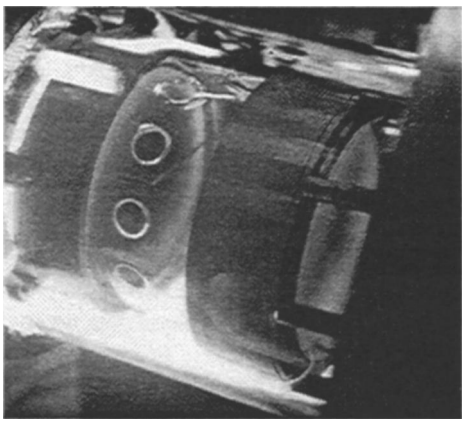

Fig. 4 Catalysts heated by burning gas

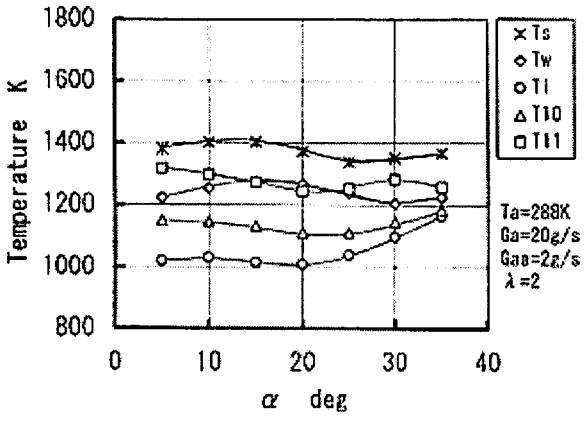

Fig. 6 Temperature characteristics around the first-stage catalyst (*Ga*=20 g/s)

to the downstream side by passing through the slit section and the peripheral section of the first-stage catalyst. The flame temperature in the slit section is 1373 K and wall temperature of the first-stage catalyst support tube is approximately 1273 K. While the first-stage catalyst inlet temperature (at a radius of 20 mm) is 1023 K, the corresponding outlet temperature (at a radius of 20 mm) is approximately 1323 K. As the α increases, the volume of the burning gas that flows into the slit section increases, and the volume of the gas flowing into the high-temperature mixing zone also increases. It results in the higher penetration of the inflow gas. A circulating flow passing through the first-stage catalyst and vaporizing tube is also formed by high swirl strength. As a result, as α is increased, homogenization of the temperatures of Ti, T_{10}, and T_{11} will advance to within the range of 25 deg to 30 deg. At α=20 deg, the wall temperature becomes the highest and the first-stage catalyst inlet and outlet temperatures become the lowest. The validity of the concept of the starting burner shown in Fig. 1, phase (1) is verified by these flame behaviors and temperature measurements.

Spray Characteristics

An air-assist nozzle was used to control the spray characteristics such as drop size and dispersion by varying the atomizing air flow rate to the appropriate operating condition of the catalytic combustor. For the drop size measurement, phase doppler particle analyzer (PDPA) system was utilized with arrangement as shown in Fig. 7. The distribution of liquid within a spray was measured radially using sampling probes with inner diameter of 6 mm set to 100 mm downstream apart from the fuel nozzle defined as *Lpv* in Fig. 7. The diameter of the cylindrical tube for injecting fuel is 70 mm. Kerosene was used for the fuel.

Figure 8 shows the effect of the atomizing air flow rate on the distribution of the mean drop size indicated by the Sauter mean diameter d_{32} at the radial location. When the atomizing air flow rate is reduced, much larger d_{32} appeared at larger radial locations because of the reduced atomizing energy. As the result, higher penetration of the drops was obtained at smaller atomizing air flow rate. In contrast, weak penetration can be obtained by increasing the atomizing air flow rate.

The distribution of the measured spraying mass flux q_1 is shown in Fig. 9. The profiles at Gaa=1 and 2 g/s show that the larger mass of fuel exists outside of a cross-sectional area at Lpv =100 mm. And small mass of fuel exists outside at Gaa=3 g/s. These characteristics of spray are available when the starting burner is extinguished for changing the operating condition from startup to transition.

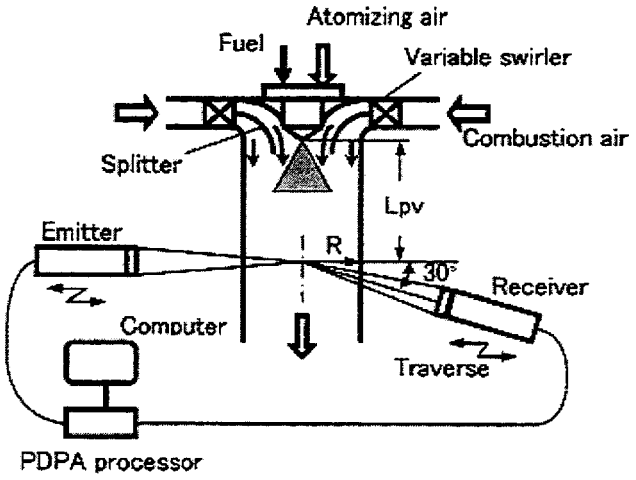

Fig. 7 Schematic diagram of spray measurement apparatus

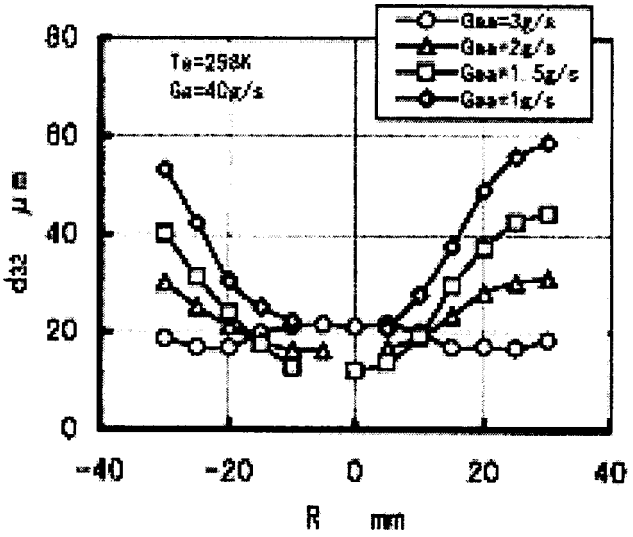

Fig. 8 Distribution of the Sauter mean diameter in radial direction

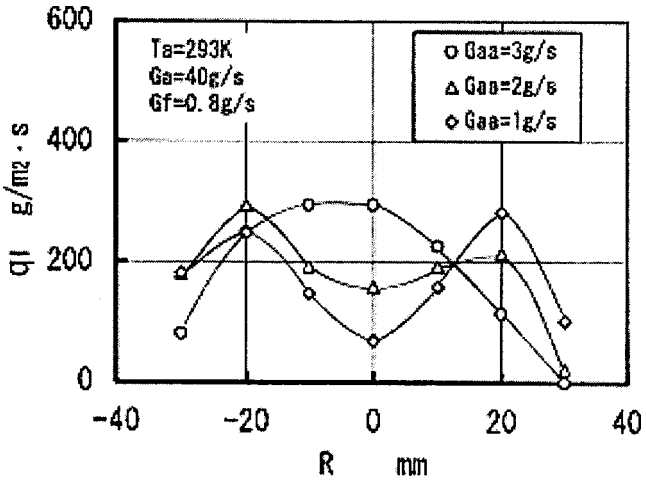

Fig. 9 Distribution of spraying mass flux in radial direction

Combustion Characteristics

Construction of the Combustor. Construction of a combustor that can be installed on a gas turbine was considered. A test catalytic combustor as shown in Fig. 10 was designed and tested to evaluate combustion characteristics and the functions of the operating concept. Combustor inlet temperatures between the atmospheric temperature and 973 K and combustor outlet temperatures of more than 1473 K were specified as operating conditions. The fuel nozzle, variable swirler, splitter, and ignition plug were the same as those used for the flame-visualized combustion tests mentioned above. The form of the vaporizing tube was also similar, except that the length of the straight tube portion was 150 mm and the length of the tapered tube portion was 40 mm. The same material was used for the first-stage catalyst as for the flame-visualized combustion tests, with a diameter of 100 mm and a thickness of 12 mm. A material based hexaaluminate, with a diameter of 100 mm, thickness of 20 mm, and heat resistance of 1473 K, was used for the second and third-stage catalysts. The diameter of the flow path in these catalysts are 90 mm. Twelve ports with diameters of 10 mm were provided for inflow ports, and the distance between the first-stage and the second-stage catalysts was set to 50 mm.

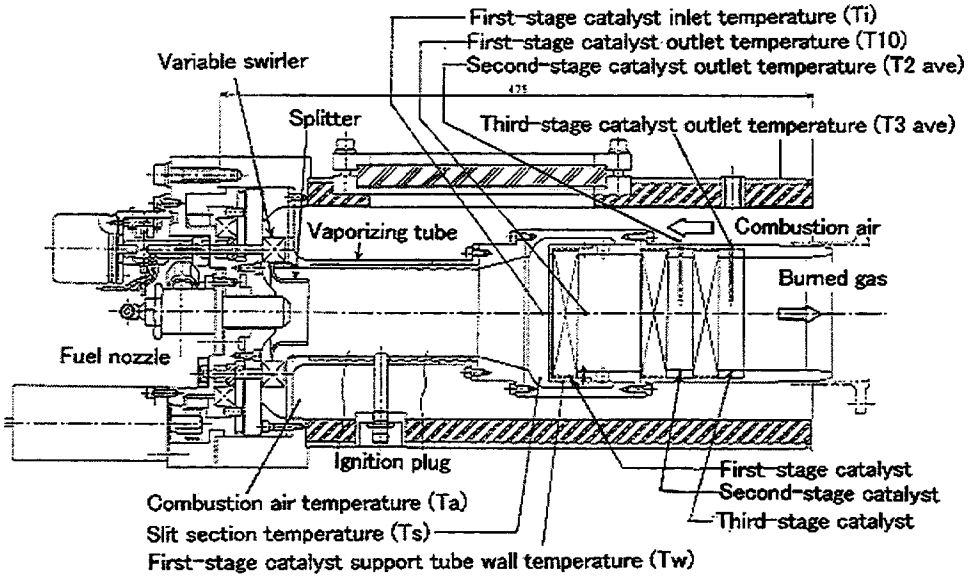

Fig. 10 Construction of the catalytic combustor

Experimental Procedure. Following ignition tests to confirm well ignitability, combustion tests were performed under operating conditions corresponding to the startup, transition, and steady state shown in the concept of operation in Fig. 1. Tests were performed with the combustion air flow rate $Ga=5$ to 60 g/s, the atomizing air flow rate $Gaa=1$ to 3 g/s, the combustion air temperature between the atmospheric temperature and 973 K, and the combustor pressure setting to atmospheric pressure. Kerosene was used for fuel. The temperature was measured around the first-stage catalyst at the same points as in the visible-flame combustion tests. Further, measurements were performed in the cross sections every 10 mm downstream from the second and third-stage catalysts, at five points arranged in a radial direction at intervals of 20 mm in the sections. The combustor outlet temperature was measured 150 mm downstream from the combustor outlet. Exhaust gases were sampled at 200 m, downstream (position 1) and 1.5 m downstream (position 2) from the combustor outlet using water cooled multiholes probes, and were analyzed using an exhaust gas analyzer for automobiles.

Results and Discussion. The temperature and exhaust characteristics of the catalytic combustor were examined for each of the operating conditions shown in Fig. 1.

Startup. Ignition of the starting burner is completed at $Ga=5$ g/s. The combustion air flow rates are maintained at 10, 20, and 30 g/s after ignition. Those were burned at a constant condition of $\lambda=2$ (at an adiabatic flame temperature of 1503 K), and investigated how the temperature of each part and the exhaust gas varied as time elapses. The time-series variation of the temperatures of each part when $Ga=10$, 20, 30 g/s are shown in Figs. 11, 12, and 13. In the figures, T_{10} represents the gas temperature at the center of the outlet of the first-stage catalyst, and T_{2ave} and T_{3ave} represent the average of the temperatures of five points at the outlets of the second and third-stage catalysts. Figure 11 indicates that the temperatures of each part around the catalyst section rose rapidly to the level of 1073 K to 1273 K within two minutes after ignition. It is possible in this state to switch to the transition operation shown in Fig. 1. Further, though combustion air of $Ta=298$ K is fed, it will be heated by the liner due to the counter-flow type construction and thus the *Ta* will rise as time elapses. Figure 12 shows that temperature *Ts* is the highest up to 20 minutes after ignition; thereafter, the temperature at the outlet of the second-stage catalyst becomes the highest temperature. Therefore, we assume that complete combustion occurs at the second-stage catalyst after 20 minutes. Even after 40 minutes, the temperatures at the inlet and outlet of the first-stage catalyst are maintained at

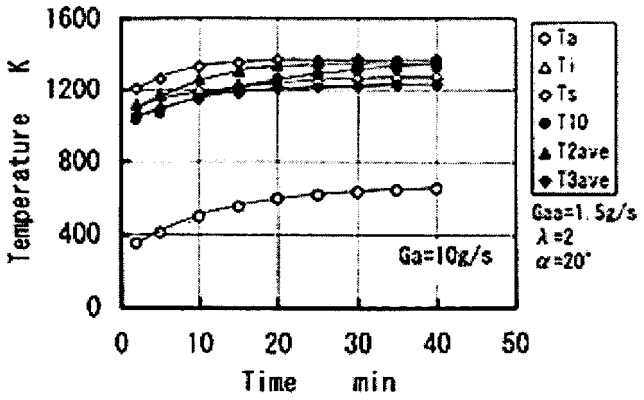

Fig. 11 Temperature characteristics with burning time at *Ga*=10 g/s

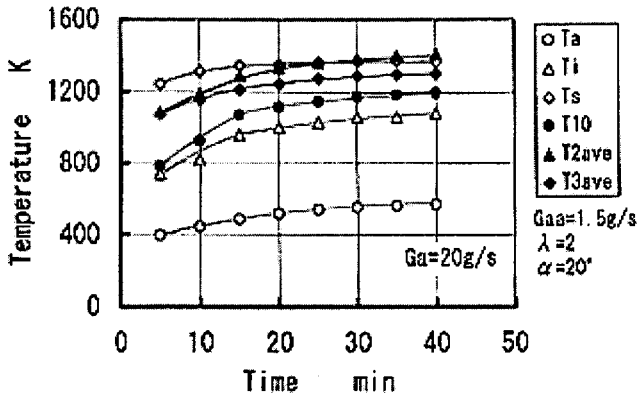

Fig. 12 Temperature characteristics with burning time at *Ga*=20 g/s

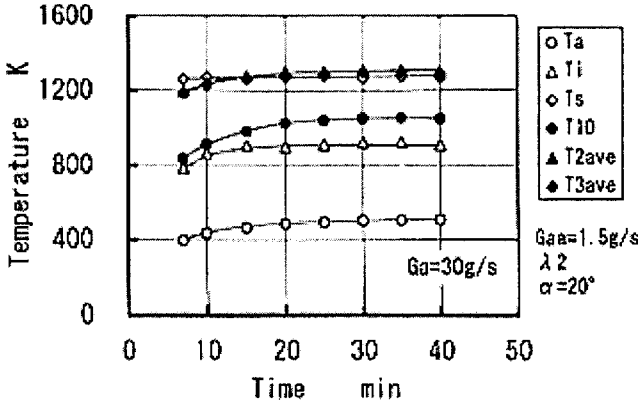

Fig. 13 Temperature characteristics with burning time at *Ga*=30 g/s

1083 K and 1193 K, below the heat resistance temperature of the catalyst. Figure 13 shows that Ts, T_{2ave}, and T_{3ave} have similar time-series variations. This indicates that the reaction does not finish at the second-stage catalyst but combustion continues up to the third-stage catalyst.

A time-series variation of the NO_x emission index at sampling position 2 when $Ga=10$, 20, and 30 g/s are shown in Fig. 14. The NO_x increases as time elapses when $Ga=10$ g/s and 20 g/s. It is supposed that this is because combustion with the flame mainly occurs in these cases and the combustion temperature rises as the *Ta* rises. In contrast, when $Ga=30$ g/s, the NO_x emission is kept almost constant at a low value even after time has elapsed. This means that the ratio of the catalytic combustion to diffusion combustion increases as the air flow rate increases.

Conventional starting burners primarily use diffusion combustion, resulting in a high level of NO_x emission. However, the starting burner in this study can reduce the emission level of NO_x during the cold startup. Also unburned emissions such as CO, HC are reduced when the catalysts are heated. This combustion system can achieve low-pollution combustion even during the cold startup phase, because it uses a combination of diffusion and catalytic combustion.

Transition. Transition is the operating condition that the starting burner has been extinguished and catalytic combustion alone occurs until entering into the steady state. Transition was achieved when the starting burner was extinguished by increasing the atomizing air flow rate to weaken the penetration of the spray as shown in Fig. 9, and after the extinction the atomizing air flow rate was returned. To investigate the combustion characteristics

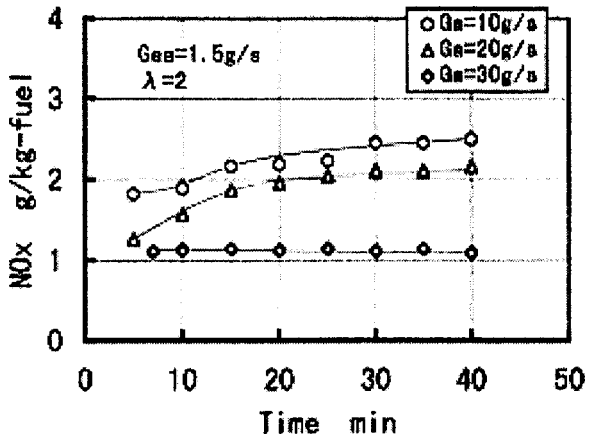

Fig. 14 NO_x emission index during start-up

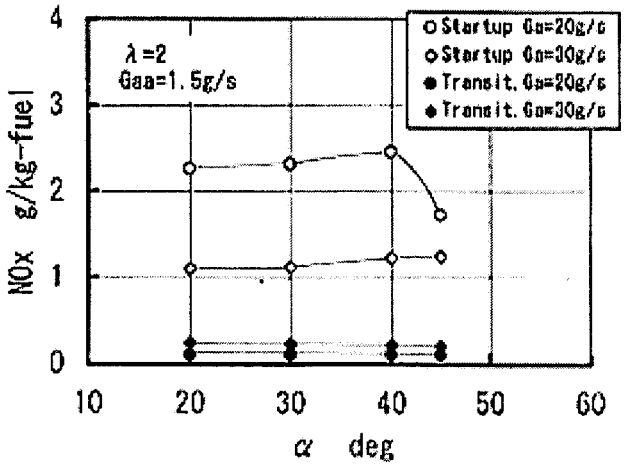

Fig. 15 Comparison of NO_x emission index between startup and transition

under these operating conditions, the starting burner was operated for 40 minutes at $Ga=20$ and 30 g/s until the temperature of each part had become stable, and the NO_x, HC, CO emissions were then measured when catalytic combustion alone was occurring. Starting burner was extinguished by increasing the atomizing air flow rate from 1.5 g/s to 3 g/s. The flow rate was immediately returned after catalytic combustion.

The combustor inlet temperature of *Ta* was controlled by electric heater between 523 K and 573 K during transition phase so that it was corresponded to the conditions of the starting burner after 40 minutes. The NO_x and HC emission indices obtained while varying the swirl angle from 20 deg to 45 deg are shown in Figs. 15 and 16. Figure 15 shows that the NO_x emission index decreases to a very low value of 0.1 to 0.24 g/kg-fuel after entering the transition phase with catalytic combustion alone. The HC emission index is also extremely low levels shown in Fig. 16.

Steady State. The results of the emission characteristics of catalytic combustion defined as steady state while varying the swirl angle at $Ta=773$ K and 973 K are shown in Fig. 17. Combustor outlet temperature was kept from 1453 K to 1474 K in both cases to compare the effect of the combustor inlet temperatures on emissions. The figure shows that the emission indices of NO_x, CO and HC can be reduced to a very low level by catalytic combustion even if the combustor inlet temperature is raised.

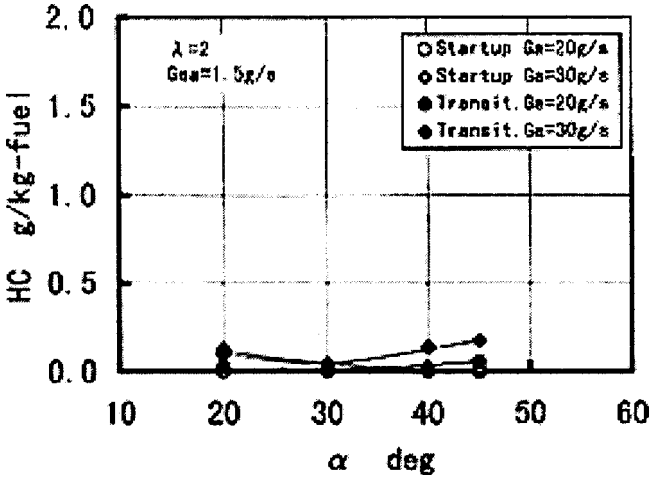

Fig. 16 Comparison of HC emission index between startup and transition

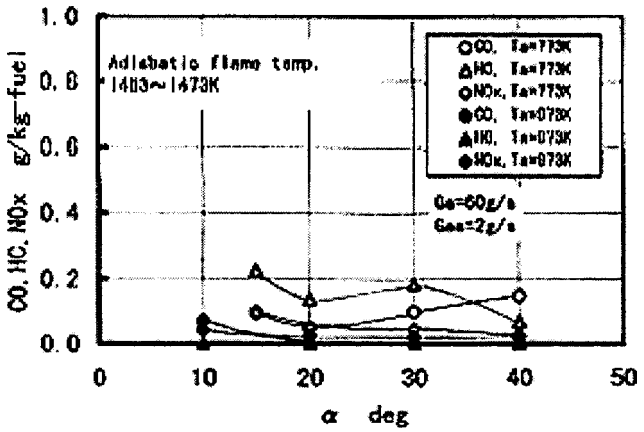

Fig. 17 NO_x emission index at steady state

The combustor outlet temperature was restricted by the heat resistance of the catalyst to 1474 K in this study. However, it can be raised further if the heat resistance of the catalyst can be improved.

Summary

Experiments were performed to verify a new concept of a catalytic combustor with starting burner enabling low pollution combustion from startup to steady state, and the following results were obtained:

- Possibility of a compact catalytic combustor using a vaporizing tube with function as starting burner was verified.
- Although a little high NO_x is emitted in the lower combustion flow rate of the startup, it was the lower level than that of the conventional pre-burners using diffusion combustion. In increasing the combustion air flow rate, NO_x emission was reduced because the rate of catalytic combustion increases as the air flow rate is increased.
- It has been also found that NO_x emission can be reduced significantly by changing from the startup phase to the transition phase, consisting of catalytic combustion alone.

The development of catalysts with a higher heat resistance is necessary to further raise the combustor outlet temperature and the reliability of the catalytic combustor. It has been proceeded to the concurrent development of high-temperature catalysts and catalytic combustors.

Acknowledgment

The work was performed as a part of a 100 kW automotive CGT development program of the Petroleum Energy Center supported by the Agency of Natural Resources and Energy of MITI.

References

[1] Handa, H., and Yoshida, Y., 1996, ''Research and Development of Catalytic Combustion System for Automotive Ceramic Gas Turbine (CGT),'' 26th International Symposium on Combustion, Work-In-Progress Posters, p. 463.
[2] Kaya, H., 1997, ''Catalytic Combustion Technologies,'' J. Gas Turbine Soc. Jpn. **25**, No. 98, pp. 48–51.
[3] Kitajima, J., and Kajita, S., 1989, ''Catalytic Combustor for Small Gas Turbine: Combustor Development,'' ASME Paper 89-GT-265.
[4] Lundberg, R., and Gabrielsson, R., 1995, ''Progress on the AGATA Project—A European Ceramic Gas Turbine for Hybrid Vehicles,'' ASME Paper 95-GT-446.

Field Demonstration of a 1.5 MW Industrial Gas Turbine With a Low Emissions Catalytic Combustion System

D. Y. Yee

K. Lundberg

C. K. Weakley

Catalytica Combustion Systems, Inc.
430 Ferguson Drive
Mountain View, CA 94043-5272

An electric utility grid connected test facility has been established at Silicon Valley Power (SVP) in Santa Clara, California to validate the reliability, availability, maintainability, and durability (RAMD) of a commercial-ready catalytic combustor system (XONON). Installed in the Silicon Valley Test Facility (SVTF) is a 1.5MW Kawasaki MIA-13A gas turbine fitted with a catalytic combustor. The gas turbine package is controlled by a Woodward MicroNet control system. The combustor utilizes a two stage lean premix preburner system to obtain the required catalyst inlet temperatures and low NO_X over the operating load range. The fuel-air mixer incorporates counter rotating swirlers to mix the catalyst fuel and air to achieve the desired uniformity. The patented catalyst design is composed of specially coated metal foils. Overall engine performance was measured and the emissions were continuously monitored. As of Dec. 1999, emissions of $NO_X < 2.5$ ppmv and CO and UHC<6 ppmv have been maintained at 100 percent load for over 3700 hours of operation on the utility grid. The turbine continues to operated 24 hours a day, 7 days per week with commercial levels of unit availability. [DOI: 10.1115/1.1374199]

Introduction

Several groups have adapted catalytic combustion systems onto gas turbine engines. Kajita and co-workers reported the development and engine demonstration of a catalytic combustor for a 170 kW Kawasaki S1A-02 gas turbine ([1–3]). These authors concluded that the catalyst deactivated after 200 hours of operation and further catalyst development was needed. Subsequent work was done by Sadamori and co-workers utilizing a new catalyst material and module design applied to the same Kawasaki combustor and gas turbine system ([4]). The gas turbine was operated for 220 hours at full load with NO_X emissions in the range of 11 to 17 ppmv (at 15 percent O_2). CO emissions started at <1 ppmv but rose to 265 ppmv at the end of the 220 hours of operation ([5]). O'Brian described a catalytic combustion system on a 50 kW gas turbine that was operated for eight hours with emissions of 6 ppmv NO_X, 97 ppmv CO, and 0 ppmv UHC, all at 15 percent O_2 ([6]). All of these early demonstration tests required full fuel conversion within the catalyst and required the catalyst to operated in the 1000 to 1200°C range.

In a more recent test, Dalla Betta and co-workers reported on the development and field testing of a catalytic combustor for a 1.5 MW Kawasaki M1A-13A gas turbine ([7]). Their work demonstrated 1000 hours of operation on a dynamometer test facility with reported emissions of $NO_X < 3$ ppmv and CO and UHC<5 ppmv. Their catalyst system only required partial fuel conversion within the catalyst with the remaining fuel combusted homogeneously just downstream of the catalyst ([8]). This approach allows lower catalyst operating temperatures and therefore catalyst durability was not an issue.

In the work described in this report, a test facility with access to the electric utility grid was constructed. A 1.5 MW Kawasaki M1A-13A gas turbine was fitted with a commercial-ready catalytic combustor (XONON) using the catalyst system similar to the one described by Dalla Betta [7]. The gas turbine was installed into the test facility to demonstrate reliability, availability, maintainability, and durability.

Field Test Facility

The Silicon Valley Test Facility (SVTF) is located at the Gianera Generating Station of Silicon Valley Power, a municipally owned electric utility serving the City of Santa Clara, California. The Gianera station hosts two 25 MW General Electric Frame 5 gas turbines running simple cycle and used for peak power applications. The SVTF is situated on land rented from the city of Santa Clara. Under the arrangement with Silicon Valley Power, the utility hosts the XONON catalytic combustor equipped gas turbine system, purchasing its output and delivering it to the utility grid.

The SVTF consists of two elements; the engine/generator enclosure and the control trailer (Fig. 1). The enclosure houses the

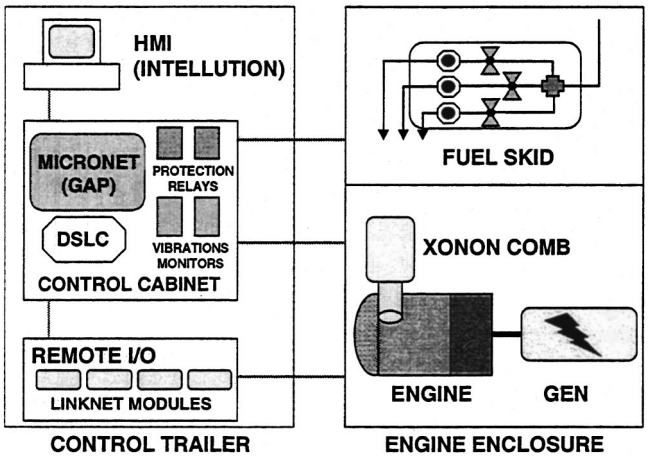

Fig. 1 Schematic of key elements of the Silicon Valley Test Facility (SVTF)

Contributed by the International Gas Turbine Institute (IGTI) of THE AMERICAN SOCIETY OF MECHANICAL ENGINEERS for publication in the ASME JOURNAL OF ENGINEERING FOR GAS TURBINES AND POWER . Paper presented at the International Gas Turbine and Aeroengine Congress and Exhibition, Munich, Germany, May 8–11, 2000; Paper 00-GT-088. Manuscript received by IGTI Oct. 1999; final revision received by ASME Headquarters Oct. 2000. Associated Editor: D. Wisler.

engine, gearbox, generator, utility breaker, electrical relays, and fuel skid. The engine is a simple-cycle model M1A-13 gas turbine made by Kawasaki Heavy Industries (KHI) upgraded to an M1A-13A configuration. The engine is attached to a Toyo Seimitsu Zohki reduction gearbox and drives a Kato 480 V three-phase generator—the entire assembly is rated to a maximum power output of 1570 kW under ISO conditions. The fuel skid is manufactured by Woodward Governor Company (WGC) and consists of three natural-gas fuel circuits with remotely actuated control valves, shutoff valves, flowmeters, and associated electronics.

The catalytic combustor mounts to the engine onto the same, unmodified flange as the original diffusion combustor. The only modification made to the engine to accommodate the catalytic combustor was the installation of a ''low-flow'' transition scroll between the combustor outlet and turbine inlet. The scroll is termed ''low-flow'' since the transpiration cooling flow requirements is reduced over the standard scroll. This item is manufactured by KHI for their dry low-NO_X combustor hardware and is not unique to the catalytic combustor hardware.

Control System. The control system filled two functions, first as the control system for the gas turbine system and second acting as the data acquisition system for the additional data inputs required for a portion of the development program. The control system was a WGC MicroNet system that handled all of the gas turbine, generator, and package control functions.

For the control system, critical control inputs requiring rapid update rates such as fuel valve position, rotor speed, exhaust gas temperature, etc., were connected directly to the MicroNet input bus through field terminal modules. These inputs provide update rates as fast as 5 ms. Less critical inputs that did not require rapid update rates such as interlocks, enclosure temperature, generator temperature, and ambient temperature were routed to WGC LinkNet modules. These modules are interfaced to the MicroNet CPU through a serial twisted pair cable. The LinkNet module provides lower cost data input with a slower update rate, typically 200 ms.

The control system for the engine/generator and XONON combustion system consists of three elements: the remote input/output (I/O) system, control cabinet, and human/machine interface (HMI). The remote I/O system is a data multiplexer/distributed I/O system, and consists of four networks of WGC LinkNet modules, each of which can accept 16 discrete inputs or six 4–20 mA, resistance temperature detectors (RTD), or thermocouple inputs. Each network consists of multiple modules connected with a single twisted-pair wire, which allows the SVTF remote I/O system to interface with 206 separate data channels over four twisted-pair wires.

The control cabinet is located in the trailer, and contains the heart of the control system: the WGC MicroNet. The MicroNet Control System is a digital control system consisting of a versomodule eurocard (VME) rack with a central processing unit (CPU) module, nonvolatile memory module, and various input/output modules. The MicroNet provides an environment for programming through WGC-proprietary Graphical Application Programmer (GAP). The MicroNet Operating System, together with GAP, produces the control and data processing environment. The MicroNet/GAP unit autonomously performs system sequencing, operation, and monitoring with minimum operator intervention, including engine start and grid synchronization, XONON combustor operation as load and speed change, routine system shutdown and purging, and system shutdown and safeguarding in the event of out-of-specifications operations. In addition to the MicroNet unit the control cabinet also contains electronics for the generator protection relays and engine/gearbox/generator vibration monitors, and also hosts the Digital Synchronizer and Load Control (DSLC) unit. When actuated by MicroNet the DSLC performs automatic grid synchronization and bus closure, as well as automatic load control. The DSLC can also be operated manually from the control cabinet, as can the MicroNet for simple commands such as engine stop/start.

While manual control is possible from the control cabinet the primary operator interface is through the HMI system. This consists of a Windows-NT PC running Intellution's FIX32 control and data automation software. FIX32 provides a graphical user interface and a supervisory control and data acquisition (SCADA) environment, and performs monitoring and control, data collection and graphic display, historical trending, alarming, data archiving, and security. The HMI system communicates directly with the MicroNet/GAP controller, and displays data and status information while sending operator commands. It also continuously archives all monitored data in a compressed file format, and includes a report generator to create data files for off-line analysis. The HMI system also incorporates a remote paging system, which issues a page when critical control parameters go out of specification to an off-site operator, therefore enabling the SVTF to operate completely unmanned for extended periods. In fact, an operator is rarely present on the site during normal operation.

Added Data Acquisition Capability. The data acquisition system was designed to handle the extensive data collection requirements for new combustor design testing. The basic requirements were

- 200 thermocouple inputs,
- 20 differential pressure inputs,
- 4 absolute pressure inputs,
- 4 fast dynamic signal inputs, and
- Infrared imaging system.

To provide this capability, the SVTF has five data acquisition capabilities, which are illustrated by Fig. 2. The first is an expanded LinkNet system, which includes 120 thermocouples, 6 differential pressures, 4 absolute pressure, and other inputs. This system records this data on the Woodward HMI archiving system every second.

Additional thermocouple and differential pressure monitoring was accomplished through an auxiliary data acquisition system (ADAS) and consists of a pressure scanner and thermocouple input panel. The pressure scanner is an integrated self-calibrating multi-channel intelligent system with 80 differential pressure channels. The thermocouple panel has 96 thermocouple inputs connected to a multiplexer chassis. Both the scanner and thermocouple panel are connected via RS482 serial communication cable to a PC-based data acquisition system running LabView for data analysis and display.

Two data systems not shown in Fig. 2 are the combustion dynamics and IR thermal imaging system. The combustion dynamics system mounts highly sensitive dynamic pressure transducers

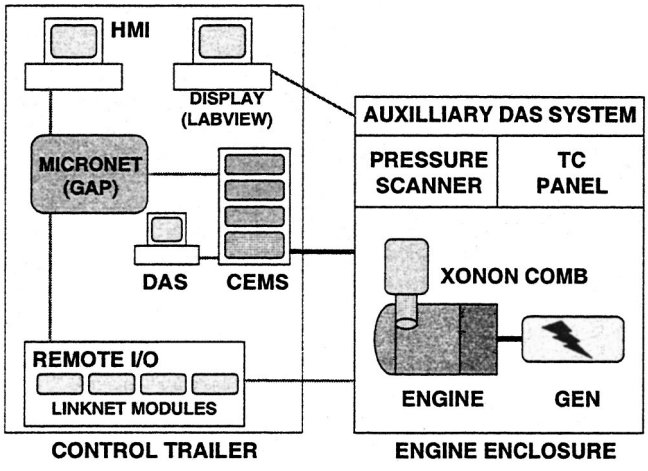

Fig. 2 Schematic of Silicon Valley Test Facility's (SVTF) data acquisition capabilities

on probes extending into a reaction zones in the combustor. The transducer outputs go to an analog device which outputs hard root-mean-squared (RMS) signals to the remove I/O system. The outputs also go to a Macintosh-based data acquisition system which performs a fast Fourier transform (FFT) on the signals and stores selected samples. Finally, the transducer signals are monitored in real time by an oscilloscope and recorded by a DAT recorder.

The IR thermal imaging system uses a water and air-cooled infrared imaging camera mounted on the combustor and focused on the catalyst outlet. The resulting calibrated image shows catalyst temperatures across the entire catalyst outlet face and is used to assess catalyst temperature uniformity as well as absolute outlet temperatures, which are also measured at discrete points by thermocouples.

The final data acquisition element serves a continuous emissions monitoring system (CEMS). This is a Monitor Labs ML 661 integrated system, and includes a sample train with a heated and filtered sample probe in the exhaust stack, a heated sample line, pump, and sample dryer. The sample train incorporates a backflush system and a zero/span gas inlet at the sample probe. The CEMS has five analyzers for the following species (with the analyzer type in parentheses): CO (nondispersive infrared), total hydrocarbons (flame ionization detector), oxides of nitrogen (chemilluminescence), CO_2 (nondispersive infrared), and dry O_2 (magnetodynamic paramagnetic). A programmable logic controller (PLC) handles system timing and alarm and data processing. Raw emissions data is transmitted directly from each analyzer to the MicroNet/GAP controller and archived by the HMI system. The PLC performs one minute averages of the raw emissions and transmits the averages to a CEMS Data Acquisition and Handling System (DAHS) through a serial data link. The DAHS stores the data, performs final data reduction, and formats the data into reports required by the local air quality agency.

The performance specifications of the CEMS are functionally equivalent to those required under 40 CFR part 60 Appendix B. The CEMS is operated in a manner consistent with the principles of the quality assurance and quality control requirements of Appendix F. An initial Relative Accuracy Test Audit (RATA) was performed. Quarterly gas audits are being conducted and annual RATAs are planned.

Combustor Design

The catalytic combustor, shown in Fig. 3, comprises three main components to ensure optimum performance over the load range:

1 preburner,
2 catalyst fuel/air mixer, and
3 catalyst system.

In the Kawasaki M1A-13A application, the combustor is mounted in a vertical configuration on top of the entire pressure vessel, bolting onto the same, unmodified flange as the original equipment manufacturer (OEM) diffusion combustor. Compressor discharge air enters into an outer, narrow annulus. This annulus continues around the burnout zone liner and is used to convectively cool the liner wall. The air then discharges into an annular plenum outboard of the catalyst case before entering the preburner. The preburner discharges into an annular channel, which then reverses the flow into a diffuser leading the hot gas into the catalyst. A catalyst fuel/air mixer system comprising a radial swirler and 24 fuel pegs is located in the radial portion of the turn. The catalyst is 38.1 cm (15 inches) in diameter and comprises two stages. Immediately following the catalyst is the burnout zone, which is essentially a straight duct providing the required residence time to burn out hydrocarbons and CO.

Preburner Design. The purpose of the preburner is twofold:

1 To provide the main source of heat during engine starting and
2 To optimize operating conditions for the catalyst over the load range.

Concept. The preburner is an annular two-stage design. It wraps around the diffuser in the catalyst fuel/air mixer. The two stages uses 254 mm ID (1 in.) tubes for mixing fuel and air, the primary stage has six tubes and the secondary 12. Both primary and secondary tubes feed the fuel/air mixture through the outer preburner liner. The secondary tubes are straight with slotted exits. The slots are angled sideways to promote mixing with the hot gases emanating from the primary stage. The primary tubes have an axial inlet, but incorporate a 90-deg turn to accommodate a tangential entry into the primary stage. The swirling motion of the primary stage enables the use of a single igniter and is also intended to improve the exit temperature uniformity. The primary premixing tubes also have a flange at the inlet to accommodate a metering plate. This has been used to fine tune the air flow to the primary stage, based on its lean blow-out performance, required operating range as dictated by the catalyst and NO_X emissions. Fuel is injected at the inlet to the premixing tubes through annular manifolds that wrap around the tubes and inject the fuel through orifices in the tube wall. This concept was chosen to minimize the risk of flame holding in the fuel rich wake behind the orifice, as there are no mechanical means of flame holding present. Fuel injectors and fuel manifolds are entirely self-contained inside the combustor and there are only two fittings through the combustor case, supplying fuel to each of the two stages.

Both primary and secondary stages are used during the start transient, at full-speed-no-load (FSNL) and up to some intermediate load point, depending on ambient conditions. At higher loads, only the primary stage is needed to provide the required catalyst inlet temperature. The primary stage typically provides a temperature rise from about 330°C to 475°C at base load, i.e., a rise of about 145°C (261°F). To accomplish this, the primary stage takes about 8.3 percent of the total preburner air flow. The primary stage comprises an impingement cooled heat shield that requires about 15.8 percent air for cooling. The secondary stage takes 14.3 percent and the remaining 60 percent of the air is channeled through the aft dilution holes.

Rig Testing. Extensive rig testing has been carried out on this preburner design. Atmospheric testing has been conducted at Catalytica's facility in Mountain View, CA. Due to the inability to run these tests nonvitiated, they have focused on lean blow-out mapping, linear wall temperatures, and preburner exit temperature profile. For the latter, an instrumentation ring comprising 23 rakes was used, covering the full 360-deg sector. Nine rakes had five radially spaced thermocouples installed while the remaining had a single TC measuring the temperature at the center of the flow channel. The atmospheric test also enabled visual examination of the flame stability in the primary stage as well as the interaction between the two stages. This provided very valuable information, particularly at low secondary stage fuel/air ratios.

High pressure testing was conducted at Caterpillar's test facility in Peoria, IL. This testing incorporated emissions measurements and lean blow-out mapping at correct engine conditions. NO_X emissions correlated reasonably well with the literature ([9]) as shown in Fig. 4. In this figure, Wf,pil refers to pilot burner fuel flow.

Other aspects that were investigated were flashback propensity into the premixing tubes, pilot burners and primary stage flame holding. The lean blow-out performance of the primary stage is close to the optimum value as suggested by Lefebvre [10], illustrated in Fig. 5.

The preburner rig was equipped with a view port at the exit, enabling view to the primary stage showing the flame front of one burner. This was an excellent way to verify both ignition and lean blow-out, in addition to examining the pilot operation and the mode of flame stabilization.

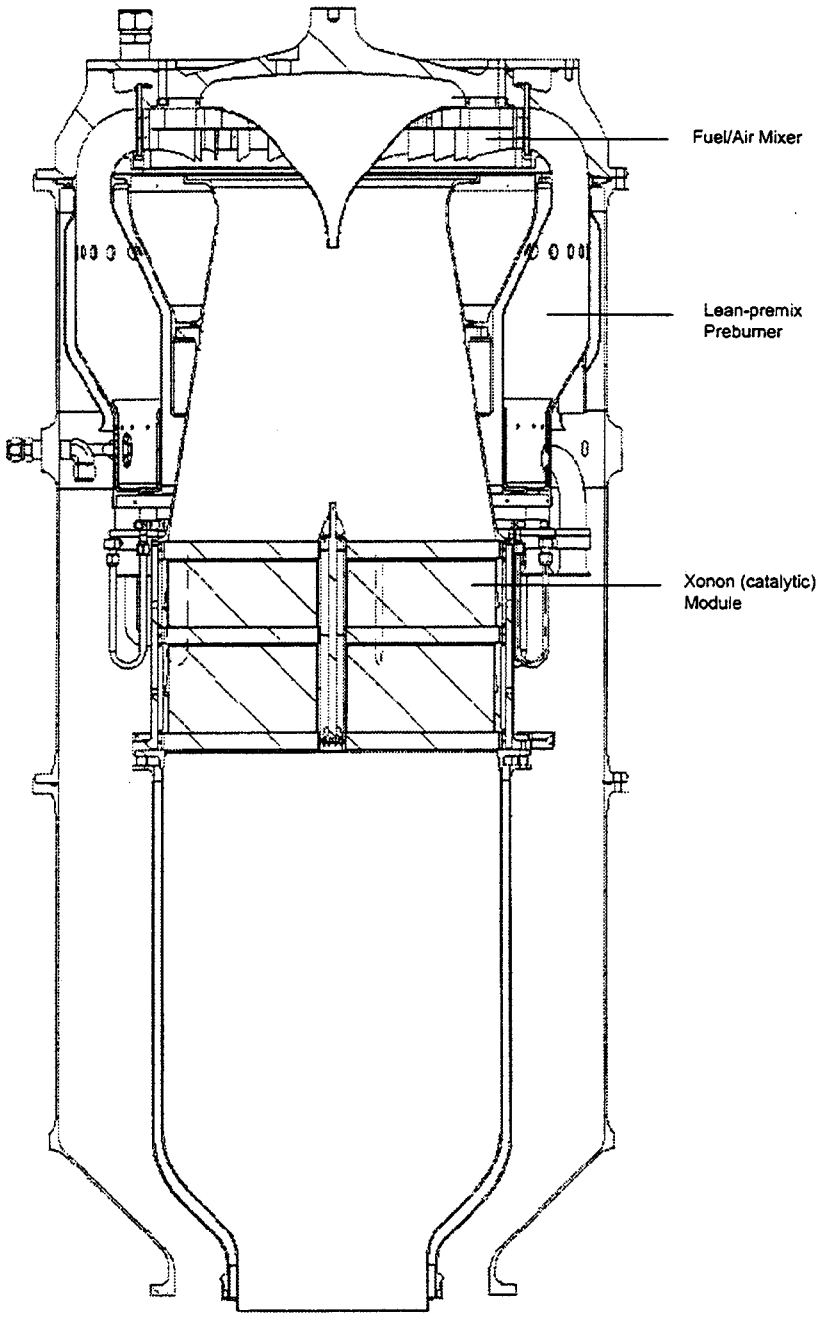

Fig. 3 Schematic of catalytic combustor

Computational Fluid Dynamics (CFD). The preburner has been studied using nonreactive flow CFD using the Star-CD code (version 3.050A) [13]. This study has included both two-dimensional and three-dimensional models. The purpose of the study was to improve the understanding of the flow field within the combustor, in particular to see how the primary and secondary stages interact. The study also included the fuel injector, where potential for recirculation and thus flame holding was investigated. This led to a redesign of the metering plates at the primary fuel/air mixing tubes.

Catalyst Fuel/Air Mixer Design. The catalyst fuel air mixing system has three main components:

1 the *fuel pegs*, where the location and quantity of fuel injection orifices contribute to the high fuel uniformity at the catalyst inlet,
2 the *swirler*, which provides mechanical mixing of the fuel with the incoming air, and
3 the *flowpath*, which directs the fuel and air to the catalyst with a minimum loss while providing turbulent mixing downstream of the swirler.

CFD. The fuel air mixer has been extensively analyzed in CFD, using both two-dimensional and three-dimensional models. The two-dimensional models have to a large extent used parametric variation to find the most viable flowpath design. This has then been carried to a three-dimensional model. This CFD modeling provided the optimized design for the counter rotating swirler pack including flow splits and vane angles. Modeling also pointed to the need of optimizing the flow field to avoid vortex breakdown downstream of the throat. Reducing the swirl angle of the swirler nearest the outer wall eliminated flow separation at the wall. Fuel

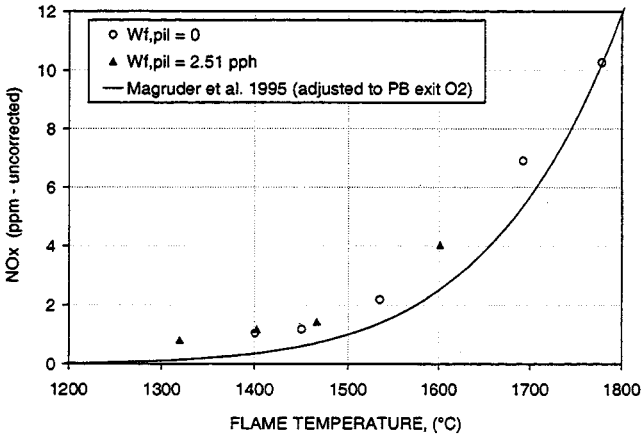

Fig. 4 Preburner NO_X emissions comparison to Magruder et al. [9]

air mixing is driven by the shear between the counter rotating flows and one design objective was to maximize momentum in the counter rotating flows and then achieve nearly complete cancellation of the momentum and maximum mixing at the catalyst inlet position. The fuel flow distribution along the fuel pegs was optimized in atmospheric tests.

Performance. The fuel-air mixing system was designed to achieve better than ±2 percent uniformity at the catalyst inlet. This requirement is necessary to maximize the catalyst operating window ([11]). The performance of the fuel-air mixing system was measured at the catalyst inlet face in the engine using an array of 20 sample tubes. These small diameter tubes were connected through a multiport valve and then to a percent-range hydrocarbon analyzer. The catalyst inlet fuel-air mixture uniformity at 1250 kW is shown on Fig. 6. The fuel-air ratio varies from +0.88 percent to −0.71 percent about the mean. This data shows that the catalyst fuel injection and mixing system produces a very uniform mixture at the catalyst.

The performance of the fuel-air mixing system and the catalyst was measured at the catalyst outlet face using a thermal imaging system. The thermal imagine camera is mounted on the outside of the combustor pressure case and views the catalyst outlet face through an air-cooled quartz view port located in the homogeneous burnout zone. The catalyst's thermal uniformity at 1250 kW is shown in Fig. 7. The thermal uniformity is consistent with the measured fuel-air uniformity.

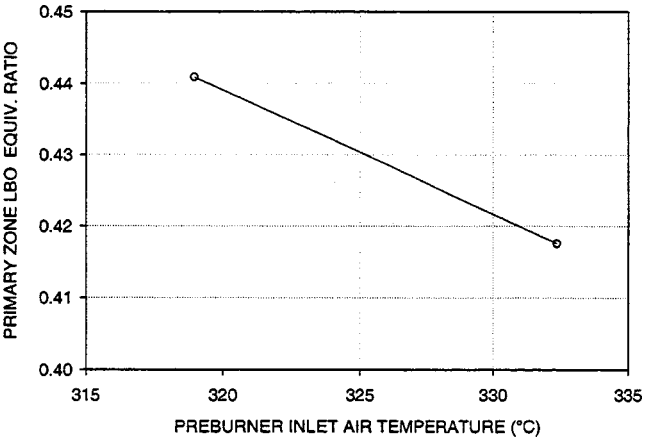

Fig. 5 Primary stage lean blowout versus preburner inlet temperature

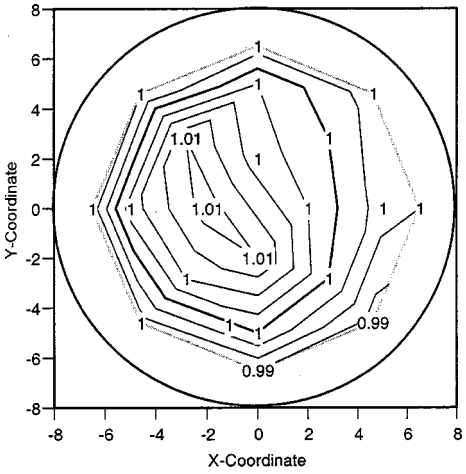

Fig. 6 Relative fuel concentration at the catalyst inlet face with the engine operating at 1250 kW and with an average fuel composition of 3.5 percent methane

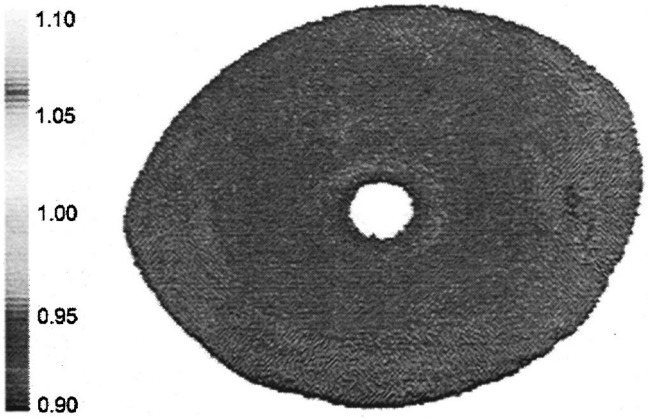

Fig. 7 Thermal uniformity of catalyst outlet face with the engine operating at 1250 kW and with an average fuel composition of 3.5 percent methane

Catalyst System Design. The catalytic combustor system described in this report is illustrated in Fig. 8. The catalyst system is designed to combust only a portion of the fuel in the catalyst with the remaining fuel combusted homogeneously just downstream of the catalyst ([8]) in the post-catalyst burnout zone (BOZ).

The catalyst core has sufficient activity to react with a portion of the incoming fuel and achieve a sufficiently high outlet gas temperature to sustain the homogeneous combustion reaction within the BOZ residence time. The catalyst core is divided into two stages sandwiched between supporting structures design to withstand the axial load resulting from the pressure drop across

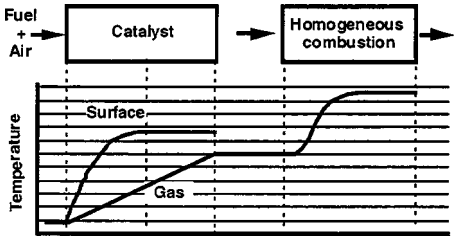

Fig. 8 Schematic of catalytic combustion process with partial fuel combustion in the catalyst

the catalyst. Each catalyst stage is composed of a patented catalytic washcoat deposited on a corrugated metal substrate.

Structural Analysis. Structural analysis using ANSYS (rev. 5.5) ([14]) has been done in two phases. During initial conceptual and mechanical design, preliminary structural analysis was done using estimated loads, pressure drops, materials temperatures, and temperature gradients. Structural analyses based on these operating conditions were used in the mechanical design of the prototype parts for rig and engine testing.

Rig tests at full pressure and engine tests included temperature measurement at critical components via thermocouples and thermal paint tests to establish actual operating temperatures. In addition, thermal transients and thermal gradients in some parts were estimated from measured gas temperatures, mass flow rates and estimated heat transfer coefficients. These analyses have included steady-state thermal stress, cyclic stress induced during the start and load transient, vibration mode analysis, pressure-induced load and gravity load. Some of these analyses are described below.

- Computed axial displacement of the bonded metal monolith (BMM) catalyst support structure. This displacement is a result of the pressure drop across the catalyst module. The catalyst consists of three BMM wafers, each operating at different temperature depending on its location.
- Preburner fuel injectors were analyzed due to the thermal stresses originating from cold fuel on one side and hot air on the other. LCF was calculated to be in excess of 10,000 cycles based on 304SS fatigue data.
- The preburner heat shields have been analyzed for LCF. The preburner has also been analyzed for gravitational stresses, as it is a vital part of the load path that supports the internal components of the combustor.
- The preburner fuel manifolds have been analyzed for vibratory stresses.
- The swirler mixer has also been extensively analyzed and consequently redesigned to reduce local thermal stresses during the start transient and engine loading. The swirler has a very low thermal inertia compared to the neighboring components. This has required added features to ensure an adequate cycle life.

Operational Expectations

Operational expectations for the SVTF included demonstrating operability of the XONON system on a utility grid, provide an environment for development and optimization of the catalytic combustion system, implementing a RAMD program (reliability, availability, maintainability, and durability), and addressing additional operational issues such as load shedding and turbine wash.

The first expectation was met when the SVTF first went on the electrical grid in late 1998. Catalytic successfully demonstrated that the a catalytic combustion system could provide reliable electrical power in a utility setting. Secondly, the SVTF was successfully used for an initial shakedown program for the prototype commercial XONON combustion system and optimization of the control system prior to the start of round-the-clock system operation.

As part of the continuous operation phase, Catalytica instituted a RAMD program, where the goal is to track and identify parts or control practices leading to outages or out-of-specifications operation. Fixes could then be designed and installed and their long-term performance monitored.

Finally, the SVTF is an ideal platform to continue development of the commercial XONON system to increase its operational flexibility and durability. This includes evaluating the performance of a XONON-equipped utility station under off-normal operating conditions, such as turbine wash, load shedding and part-load operations. The design of the facility and the control and data acquisition systems allow testing programs to be prepared and implemented quickly and the results incorporated efficiently into ongoing operations.

Operation Experience

A control strategy was developed to reproducibly start and accelerate the turbine to full-speed-no-load (FSNL), then synchronize with the utility grid and load the turbine to base load conditions. When base load conditions are achieved, the turbine operates unattended 24 hours a day, 7 days a week.

Typical Start and Acceleration Sequence. The acceleration of the turbine to FSNL is accomplished through a fixed schedule of fuel flows and preburner discharge temperature versus turbine speed. In the start sequence, a starter motor is used to purge the turbine for 45 seconds to ensure there is no residual fuel within the combustor. After the purge, the turbine is allowed to coast down to ignition speed. The preburner's primary tubes are ignited at this stage. Upon confirmation of ignition, the starter motor accelerates the turbine on a fixed schedule of preburner discharge and combustor fuel-to-air ratio (F/A) versus turbine speed. This sequence is illustrated on Fig. 9.

The short dwell at 6400 rpm is referred to as the ''warm-up'' where the combustor internal components are preheated prior to fueling the catalyst. At the end of the ''warm-up,'' the catalyst fuel is introduced and preburner discharge is ramped down as the starter motor continues to accelerate the turbine. At 14,000 rpm, the starter motor is disengaged. There is sufficient thermal energy to continue the acceleration without the starter motor and the turbine quickly accelerates to FSNL.

Once at FSNL, the DSLC adjusts the turbine speed and generator voltage and then automatically closes the breaker to connect the generator to the utility grid.

Typical Generator Loading Sequence. A typical load cycle is shown on Fig. 10. After the breaker closes, the control system automatically ramps the load to 300 kW. A manual input by the operator is required to further increase the generator load. In this example, the operator chose to ramp the load to 1200 kW before ramping to base load.

As the generator load is increased, preburner discharge and combustor F/A is controlled by a fixed schedule. This is illustrated on Fig. 10. Preburner discharge is held constant at the lower generator load range but as load increases, preburner discharge is lowered. The preburner discharge schedule is determined by the catalyst operating window ([11,12]) to maximize catalyst durability and the operating range with low emission conditions.

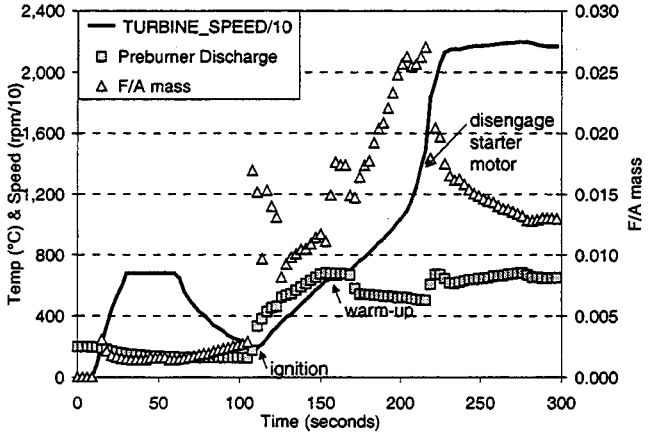

Fig. 9 Start sequence illustrating the fixed schedule of preburner discharge, combustor fuel to air (F/A) and turbine speed

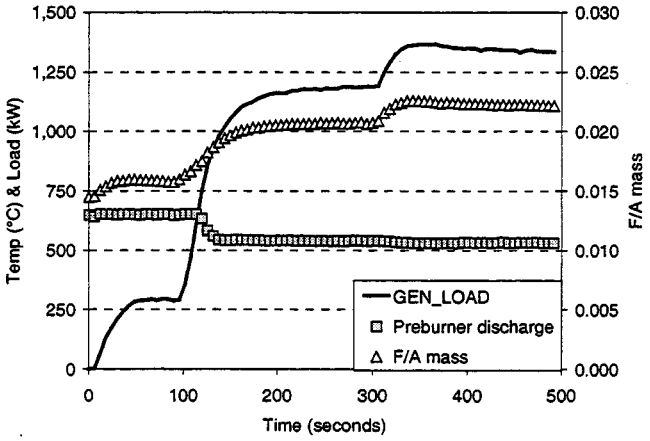

Fig. 10 Fixed schedule of preburner discharge and catalyst fuel to air (F/A) while ramping generator load

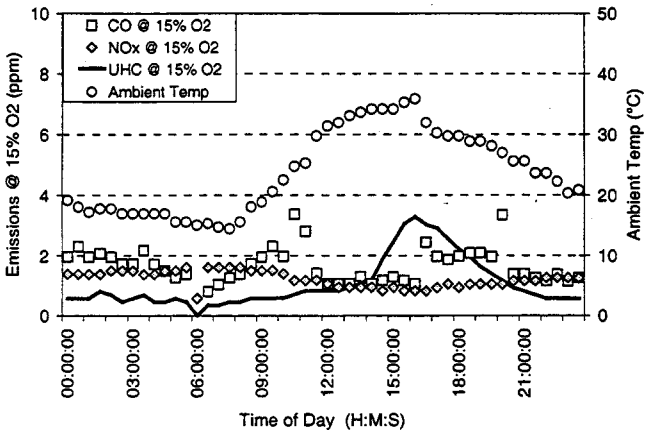

Fig. 12 Emissions (corrected to 15 percent O_2) during a 24-hour period

Typical Full Load Performance. The catalytic combustor equipped gas turbine at SVTF operates at base load conditions 24 hours a day, 7 days a week. Emissions are monitored by a continuous emissions monitoring system (CEMS). The site has been permitted to 5 ppmv NO_X and 10 ppmv CO and UHC. Typical emissions have been $NO_X < 2.5$ ppmv, and CO and UHC<6 ppmv. Figure 11 illustrates the average emissions at 18°C ambient during the first 3700 hours of operation. Each data point represents an average over a 10-minute period.

Typical emissions during a 24-hour period is shown on Fig. 12. During this particular 24-hour period, the ambient temperature varied from 14°C to 37°C. Since the source of NO_X in this catalytic combustor is from the preburner and the preburner temperature rise varies with ambient, the higher NO_X emission at the lower ambient temperature is expected.

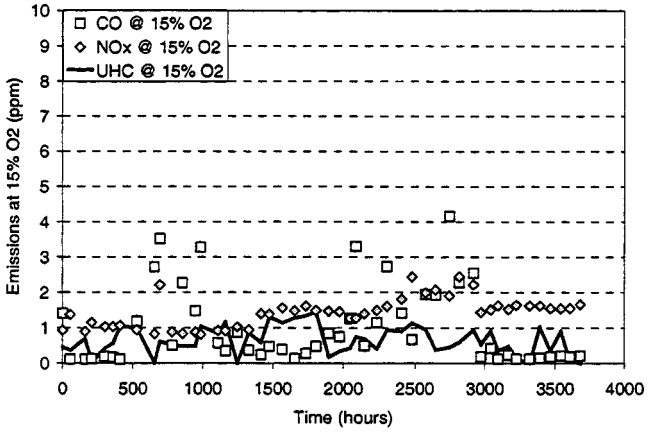

Fig. 11 Typical emissions (correcetd to 15 percent O_2) at 18°C ambient

Summary

A commercial-ready catalytic combustion system (XONON) has been demonstrated on a 1.5 MW gas turbine engine connected to an electric utility grid. The system operates at base load conditions unattended, 24 hours a day, 7 days a week. The emissions are continuously monitored by a CEMS and low emissions, $NO_X < 2.5$ ppmv, and CO and UHC<6 ppmv, have been consistently demonstrated during base load operations.

References

[1] Kajita, S., Tanaka, Y., and Kitajima, J., 1990, ''Evaluation of a Catalytic Combustor in a Gas Turbine-Generator Unit,'' ASME Paper No. 90-GT-89.

[2] Kitajima, J., and Kajita, S., 1989, ''Catalytic Combustor for Small Gas Turbines: Combustor Development,'' ASME Paper No. 89-GT-265.

[3] Hoshino, A., Kajita, S., Hagiwara, Y., Fujimoto, K., and Kitajima, J., 1987, ''Preliminary Tests of Catalytic Combustion in a Small Gas Turbine,'' ASME Paper No. 87-GT-100.

[4] Sadamori, H., Tanioka, T., and Matsuhisa, T., 1994, ''Development of a High Temperature Combustion System and Prototype Catalytic Combustor Turbine Test Results,'' *Proceedings of the International Workshop on Catalytic Combustion*, H. Arai, ed., Tokyo, Japan, Apr. 18–20, Catalysis Society of Japan, Tokyo, p. 158.

[5] Sadamori, H., 1994, reported in the presentation at the International Workshop on Catalytic Combustion, Tokyo, Japan, Apr. 18–20.

[6] O'Brian, 1998, ''Development of a 50 KW, Low Emissions Turbogenerator for Hybrid Electric Vehicles,'' ASME Paper No. 98-GT-400.

[7] Dalla Betta, R. A., Nickolas, S. G., Weakley, C. K., Lundberg, K., Caron, T. J., Chamberlain, J., and Greeb, K., 1999, ''Field Test of a 1.5 MW Industrial Gas Turbine with a Low Emissions Catalytic Combustion System,'' ASME Paper No. 99-GT-295.

[8] Dalla Betta, R. A., Schlatter, J. C., Nickolas, S. G., Yee, D. K., and Shoji, T., 1994, ''New Catalytic Combustion Technology for Very Low Emissions Gas Turbines,'' ASME Paper No. 94-GT-260.

[9] Magruder, T. D., McDonald, J. P., and Mellor, A. M., 1995, ''Engineering Analysis for Lean Premixed Combustor Design,'' AIAA Paper No. 95-3136.

[10] Lefebvre, A. H., 1983, *Gas Turbine Combustion*, Taylor & Francis, London.

[11] Schlatter, J. C., Dalla Betta, R. A., Nickolas, S. G., Cutrone, M. B., Beebe, K. W., and Tsuchiya, T., 1997, ''Single-Digit Emissions in a Full Scale Catalytic Combustor,'' ASME Paper No. 97-GT-57.

[12] Dalla Betta, R. A., Schlatter, J. C., Nickolas, S. G., Cutrone, M. B., Beebe, K. W., Furuse, Y., and Tsuchiya, T., 1996, ''Development of a Catalytic Combustor for a Heavy-Duty Utility Gas Turbine,'' ASME Paper No. 96-GT-485.

[13] Star-CD version 3.050A, 1998, ADAPCO, Ltd., Melville, NY.

[14] ANSYS rev. 5.5, 1998, Swanson Analysis Systems, Houston, PA.

Prediction and Measurement of Thermoacoustic Improvements in Gas Turbines With Annular Combustion Systems

U. Krüger[1]
J. Hüren

B&B-AGEMA,
Gesellschaft für Energietechnische
Maschinen und Anlagen,
Aachen, Germany

S. Hoffmann
W. Krebs
P. Flohr

Siemens AG,
Power Generation Group KWU,
Mülheim, Germany

D. Bohn
Institute of Steam and Gas Turbines,
Aachen University of Technology,
Aachen, Germany

Environmental compatibility requires low emission burners for gas turbine power plants. In the past, significant progress has been made developing low NO_x and CO burners by introducing lean premixed techniques in combination with annular combustion chambers. Unfortunately, these burners often have a more pronounced tendency to produce combustion-driven oscillations than conventional burner designs. The oscillations may be excited to such an extent that the risk of engine failure occurs. For this reason, the prediction of these thermoacoustic instabilities in the design phase of an engine becomes more and more important. A method based on linear acoustic four-pole elements has been developed to predict instabilities of the ring combustor of the 3A-series gas turbines. The complex network includes the whole combustion system starting from both compressor outlet and fuel supply system and ending at the turbine inlet. The flame frequency response was determined by a transient numerical simulation (step-function approach). Based on this method, possible improvements for the gas turbine are evaluated in this paper. First, the burner impedance is predicted theoretically and compared with results from measurements on a test rig for validation of the prediction approach. Next, the burner impedance in a gas turbine combustion system is analyzed and improved thermoacoustically. Stability analyses for the gas turbine combustion system show the positive impact of this improvement. Second, the interaction of the acoustic parts of the gas turbine system has been detuned systematically in circumferential direction of the annular combustion chamber in order to find a more stable configuration. Stability analyses show the positive effect of this measure as well. The results predicted are compared with measurements from engine operation. The comparisons of prediction and measurements show the applicability of the prediction method in order to evaluate the thermoacoustic stability of the combustor as well as to define possible countermeasures.
[DOI: 10.1115/1.1374437]

Introduction

One of the key issues of the development and design of modern gas turbine combustion systems are combustion-driven oscillations. The problems with these self-excited oscillations, which can reach high amplitudes, arise in aero-derivative as well as in heavy duty gas turbines. In order to reach the aspired levels of NO_x and CO and to minimize the risk of engine failure and increased wear and tear, these oscillations have to be avoided.

Different approaches to limit self-induced oscillations are known:

- avoiding the set-off disturbance that initiates the beginning of the self-excited oscillations.
- augmenting damping by (passive) dissipative means in order to suppress the starting oscillation or to limit the amplitude of the running combustion-driven oscillation.
- reducing or suppressing the oscillation by active control, e.g., by introducing small quantities of additional fuel, and
- avoiding combustion-driven oscillations by tuning the interaction of all relevant components of the combustion system in an appropriate way.

Considering that a very small disturbance in the system can be the starting point for the buildup of the oscillation, it is almost impossible to realize the first approach in turbulent premixed combustion. The turbulent flow as well as small inhomogeneities in the fuel/air mixture are always possible sources of a setoff disturbance.

For the other approaches, investigations on test rigs or realizations in commercial gas turbines are known from literature.

Putnam [1] already showed the effects of passive acoustic dampers (Helmholtz resonators and quarter-wave tubes) on combustion-driven oscillations at different test rigs. Nowadays, Helmholtz resonators are considered a useful measure for the damping of (self-excited) combustion oscillations ([2]). Helmholtz resonators or quarter-wave tubes are implemented in some commercial aero-derivative gas turbines ([3,4]).

Active control became an important issue in recent years for the limitation of combustion-driven instabilities ([5,6]). Possible control mechanisms are cyclic out-of-phase injection of small amounts of additional fuels in order to counteract the oscillation. This effect was demonstrated on different test rigs by Hibshman et al. [7], McManus et al. [8], Paschereit et al. [9,10], or Richards et al. [11] for example, and on a heavy duty gas turbine by Hermann et al. [12]. Also, simple injection of additional fuel has been found to be an appropriate measure for the reduction of combustion dynamics ([4]). An active control strategy using counter pressure from loudspeakers was examined by Mahmoud et al. [13] on

[1]Presently a Behr GmbH & Co., Stuttgart, Germany.

Contributed by the International Gas Turbine Institute (IGTI) of THE AMERICAN SOCIETY OF MECHANICAL ENGINEERS for publication in the ASME JOURNAL OF ENGINEERING FOR GAS TURBINES AND POWER. Paper presented at the International Gas Turbine and Aeroengine Congress and Exhibition, Munich, Germany, May 8–11, 2000; Paper 00-GT-095. Manuscript received by IGTI Oct. 1999; final revision received by ASME Headquarters Oct. 2000. Associate Editor: D. Wisler.

test rigs or modifying the upstream boundary condition to get a fluctuating mass flow ([14]), but is not considered to be a realistic alternative for commercial engines.

Finally, combustion-driven oscillations can be reduced or avoided by designing the combustion system such that the acoustic interaction of all relevant parts is detuned and oscillations cannot build up.

Therefore, Straub and Richards [15] experimentally investigated the impact of the swirl vane location on combustion dynamics and Steele et al. [16] demonstrated the effect of the axial gas spoke location in the fuel injector in experiment and numerical simulation respectively.

Like those, this paper refers to possible improvements in the thermoacoustic characteristics of a gas turbine combustor system detuning the interaction of the different acoustic parts. This detuning can be realized by (small) changes in geometry or some additional components.

This approach is advantageous because the costly implementation of damping devices (with additional changes in geometry) or active control systems only becomes reasonable following optimization of the acoustic interaction (by simple measures).

Some authors emphasize the influence of burner impedance for thermoacoustic instabilities, i.e., the impedance in the outlet plane of a burner describing the acoustic behavior of the upstream part ([17,18]). The burner impedance is *not* a characteristic parameter of a burner itself, but a characteristic value at the specific position of the burner outlet in the acoustic system of a combustor.

Considering a thermoacoustic analysis of the combustion chamber, the burner impedance can be used as a boundary condition at the burner outlet plane representing the acoustic properties of all parts upstream of the burner outlet.

Unsteady heat release in the initial stage of combustion-driven oscillations may have two origins. First, unsteady heat release may be caused by a fluctuating equivalence ratio. Second, the unsteady heat release results from acoustic forcing whereby flame front surface fluctuations are induced by an oscillating burner outlet velocity. In order to suppress acoustic forcing, the burner impedance should be very high. Thus, acoustic particle velocity is small compared to acoustic pressure. With the reasonable assumption that the flame reacts mainly to acoustic particle velocity, unsteady heat release becomes smaller the lower the acoustic particle velocity.

Considering this, the paper will demonstrate the influence of the burner impedance on the combustion system of a gas turbine. Therefore, the burner impedance in a test rig is determined experimentally and by prediction in the first part of the paper. With the comparison of the results, the acoustic modeling is validated for the prediction of in-duct properties such as burner impedance. Then, the burner impedance in the gas turbine combustor model developed in previous work ([19]) is obtained. The burner impedance is improved following the arguments presented above and the effect on system stability is analyzed.

Simple modifications in geometry (cylindrical burner outlets, CBO) were implemented at some burners in the annular ring combustor of Siemens 3A-series gas turbines. This nonregular arrangement of burners in circumferential direction of the combustion chamber led to a significant improvement in thermoacoustic stability ([20]). In the second part of the paper, these arrangements were modeled and investigated by the acoustic stability prediction as well. The predictions were compared with measurements and experience from engine operation.

Acoustic Analysis Model

Transfer Matrices. The propagation of acoustic waves in most components of gas turbine combustion systems can be treated as one-dimensional because the cross sections of the relevant components is small compared to the wavelength of the low-frequency oscillations.

Therefore, sound propagation is fully determined by the acoustic pressure (p) and the acoustic particle velocity (u). The time dependence is given by $e^{i\omega t}$, and the well-developed four-pole theory of linear one-dimensional wave propagation (see, for example, [21]) can be used to describe the acoustics of a combustion system upstream and downstream of the flame. The entire system of interest is divided into simple geometrical units of known acoustical behavior and 2×2-transfer matrices are provided which describe the change in the acoustic quantities p, u within this unit. As a result, the change in p and u over the whole area considered is given by multiplication of the transfer matrices (Fig. 1).

Standard four poles can be used to build up the entire system for a complex gas turbine. Analytical formulations for those exist in literature, for example, [21,23–25].

The advantage of modeling the acoustics in this way and the network concept used is the possibility of incorporating not only the analytical elements described but also additional information derived from either experimental or numerical sources. This is essential for the modeling of real gas turbine combustion systems. Only by this means numerically determined flame frequency responses—which describe the flame behavior of complex gas turbine flames best—can be implemented.

With p and u known at all parts of the system, the local impedances can be calculated simply following the definition:

$$z=\frac{p}{u}. \tag{1}$$

Starting at the boundary at the inlet and multiplying the transfer matrices leads to the local impedance describing the acoustic behavior of the part upstream of the position examined. By multiplying the transfer matrices starting at the other end of the system, the local impedance that includes the acoustic behavior of the downstream part is determined.

Stability Criterion. If the transfer matrices are calculated from experimental data, no complex frequencies can be introduced. Complex eigenfrequencies of the system can only be used if analytic solutions for the transfer matrices are given. Thus, a new formulation of a stability criterion developed by Bohn and Deuker [25] is used that does not make use of complex frequencies. As a result, experimental or numerical data for the transfer matrices can be easily incorporated.

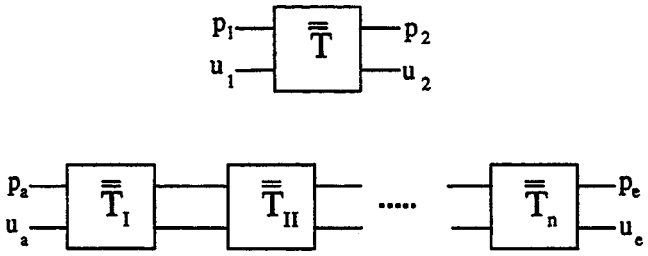

Fig. 1 Transfer matrices

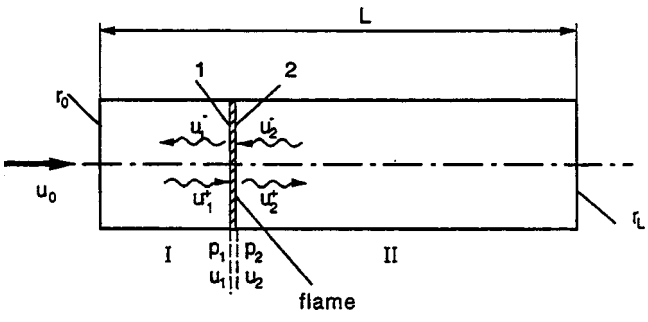

Fig. 2 Wave propagation in a tube including a flame

Consider a single pipe with a flame at some specific position (Fig. 2): A wave u_2^+ starting downstream of the flame travels to the end of the pipe, is reflected and comes back to the flame (u_2^-), travels through the flame (u_1^-) to the other end, is reflected again, comes back to the flame (u_1^+) and finally passes the flame and returns to the point of its beginning. If the phase angle after this cycle is zero and the amplitude has increased, amplification of the original perturbation takes place. The amplitude will grow continuously in time limited only by nonlinear effects and strong oscillations will result. This formulation of a stability criterion is comparable to the Nyquist-criterion from control engineering.

The mathematical formulation is

$$\begin{aligned} F_0 &= |F_0| \cdot e^{i\varphi} \\ &= F_{II} \cdot F_{fl}^- \cdot F_I * F_{fl}^+ \\ &\text{with} \begin{cases} |F_0| < 1 & \text{for } \varphi = 0 \rightarrow \text{damped oscillation} \\ |F_0| > 1 & \text{for } \varphi = 0 \rightarrow \text{amplified oscillation} \end{cases} \end{aligned} \tag{2}$$

with the partial frequency responses given by

$$F_I = \frac{u_1^+}{u_1^-} = \frac{(\rho_0 a_0)_I + z_1}{(\rho_0 a_0)_I - z_1} \quad F_{fl}^+ = \frac{u_2^+}{u_1^+} = \frac{F_{fl} + \dfrac{z_1}{(\rho_0 a_0)_{II}}}{1 + \dfrac{z_1}{(\rho_0 a_0)_I}} \tag{3}$$

$$F_{II} = \frac{u_2^-}{u_2^+} = \frac{(\rho_0 a_0)_{II} - z_2}{(\rho_0 a_0)_{II} + z_2} \quad F_{fl}^- = \frac{u_1^-}{u_2^-} = \frac{1 - \dfrac{z_1}{(\rho_0 a_0)_I}}{F_{fl} - \dfrac{z_1}{(\rho_0 a_0)_{II}}}.$$

Note that the partial frequency responses can also be developed for p instead of u without F_0 being changed.

The equations above do not change for more complex geometries. The acoustical behavior of the part upstream of the flame is represented by z_1, and the downstream part is represented by z_2. The values for z_1, z_2 can either be obtained from numerical or experimental analysis or from analytical equations ([26]).

The beginning of a self-excited combustion oscillation can be characterized as a linear process (see Fig. 8 in [13] or refer to [27]). A small starting disturbance introduces oscillations that can grow by unsteady heat release to high amplitudes only limited by nonlinear effects. Thus, the approach of linear transfer elements and the stability criterion can be used to evaluate the principle stability of the system and to determine the critical starting frequency of the instability. The absolute amplitude of the on-going unstable oscillation and possible (small) shifts in frequency through nonlinear effects can not be governed by this approach. However, the approach is a suitable aid in analyzing combustion systems' stability and demonstrating possible improvements.

Acoustic Model for 3A-Series Gas Turbine

In previous work ([19]) an acoustic model for the Siemens 3A-series gas turbine was developed and a stability analysis was performed. Frequencies of thermoacoustical instabilities could be predicted well with this model. The same model is used herein for the stability analyses in order to evaluate the thermoacoustic improvements proposed. Therefore, the model used will be described again in brief.

Figure 3 shows the combustion system of the Siemens Vx.3A-series gas turbine family. It is characterized by an annular combustion chamber with 24 identical hybrid burners for gas and oil.

The complete combustion system starting at compressor outlet, ending at the turbine inlet and including the gas fuel supply is transferred to an acoustic network using four-pole elements. The detailed description of this transfer is presented by Krüger et al. [19].

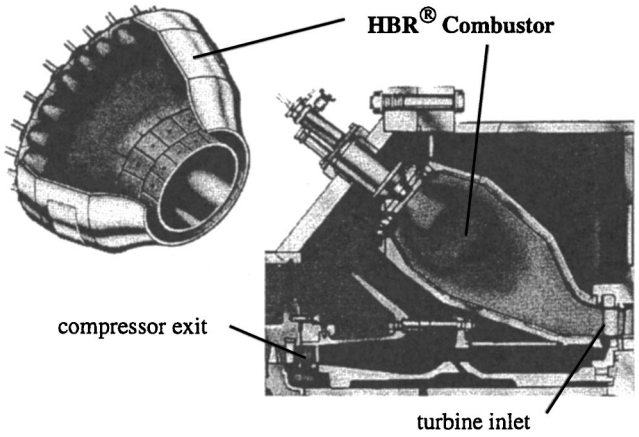

Fig. 3 Siemens 3A-Series HBR® turbine combustor

As long as no two-dimensional waves have to be taken into account, two main oscillation directions in principle have to be considered for this kind of ring combustor: the circumferential and the axial direction. Basically, the four-pole elements are one-dimensional with the result that the stability analysis has to be split off into the circumferential direction and the axial direction. This procedure affects all transfer elements downstream of the burner, namely the flame, the combustion chamber and the boundary condition and they are modeled in a different way for each direction.

The combustion chamber itself is modeled by tubes whose summed-up length corresponds to eigenfrequencies of the respective direction determined by a numerical analysis of the annular ring. The boundary conditions represent the turbine inlet for the axial direction and the periodicity of the annular ring for the circumferential direction, respectively. The most important element of the thermo-acoustic network is the matrix that describes the dynamic behavior of the flame. The transfer element of the flame is calculated by a transient numerical prediction of the combustion and flow field ([19,28]). It makes use of the step-function approach that was validated in previous work for turbulent diffusion flames ([29]), for laminar premixed flames ([30]), for turbulent premixed flames ([31]), and finally used for a swirled, turbulent premixed gas turbine flame ([18,27]).

The most complex network system occurs for the circumferential direction as shown in Fig. 4. All 24 burner systems are taken into account to represent the annular combustor. The system is closed with a periodic boundary condition.

Using this model, a stability analysis has been performed ([19]) and the main critical frequencies have been determined. They correspond well with the frequencies observed during gas turbine operation. All subsequent stability analyses are compared to these ''original'' results. As the circumferential direction is of main interest, the following analyses are restricted to this direction.

Influence of Burner Impedance

The impedance at the burner outlet plane has an important impact on the thermoacoustic behavior of combustion systems. At the burner outlet plane the impedance can be formulated in two different ways: the first describing the acoustic behavior of the system upstream of the burner (i.e., burner, plenum, diffusor, fuel supply), the second describing the acoustic behavior of the downstream system (mainly the combustion chamber). Depending on the formulation of the impedance at the burner outlet, different characteristics are preferable.

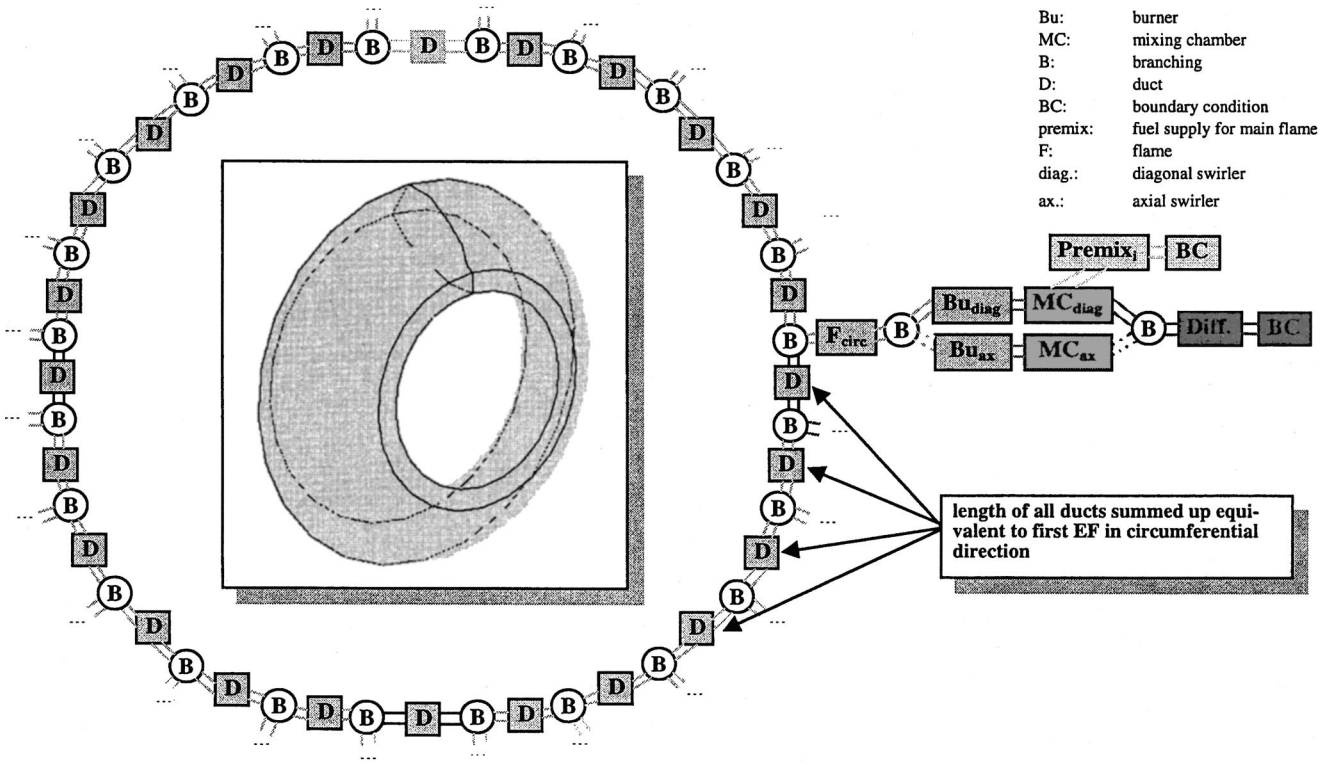

Fig. 4 Acoustic network for combustion chamber in circumferential direction in detail

Considering the acoustic system composed of burner and plenum (i.e., the ''upstream'' part), the impedance at the burner outlet plane could be taken as boundary at the downstream end of this system. In this case, it describes the behavior of the acoustic components downstream of the burner, i.e., mostly the combustion chamber. The unsteady heat release from the flame introduces an unsteady volume oscillation resulting in an augmentation of acoustic particle velocity. Thus, it is preferable to have a combustion chamber in which a high increase in acoustic particle velocity results in a comparably small increase in acoustic pressure. High acoustic particle velocity leading to low-pressure amplitudes means that the impedance describing the downstream part (combustion chamber) should be low (realised perhaps by acoustic dampers).

Considering the acoustic propagation in the combustion chamber, the impedance at the burner outlet plane represents the complete acoustic system upstream of the burner exit. This is called the *burner impedance*. The pressure oscillation in the combustion chamber introduces an acoustic particle velocity in the upstream part that itself influences the flame and the unsteady heat release. Thus, the pressure amplitudes in the combustion chamber must be prevented from resulting in high acoustic particle velocities upstream of the flame. Consequently, the impedance describing the acoustics of the upstream part should be high. Similar arguments can be found in ([17,18]).

With this background, following a validation of the prediction method for in-duct acoustic properties, the burner impedance should be improved theoretically and its positive impact on the combustion system dynamics should be shown by a stability analysis.

Measurement and Prediction of the Impedance

H-Burner. A Siemens H-burner was chosen for the comparison of measurements on the test rig and corresponding theoretical prediction of the burner impedance.

Some details of the hybrid burner are shown in Fig. 5. The main air enters the burner through a perforated plate and flows through the outer so-called diagonal swirler where the premixing of fuel and air takes place. Fuel is injected through small holes in the premix gas pipes upstream of the swirl vanes. Additional air enters through the central so-called axial swirler and (if necessary) a pilot flame is produced in order to stabilize the main flame. Fuel for diffusion flames can also be injected in the axial swirler. A

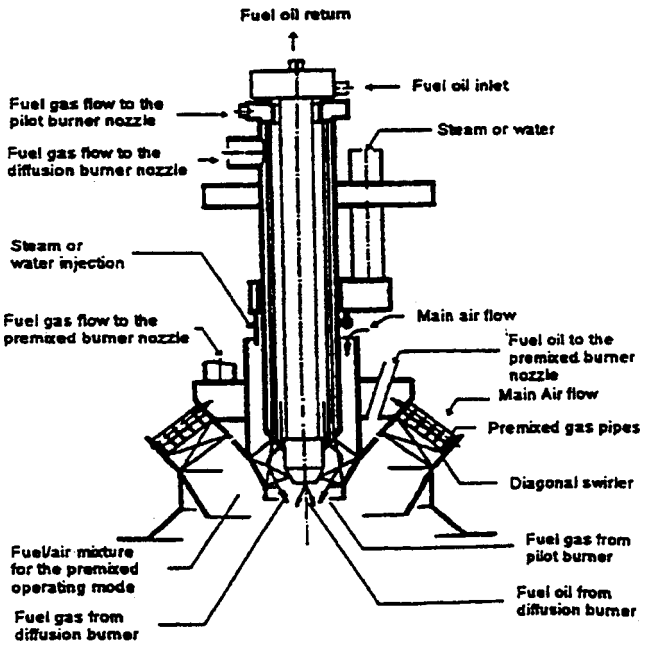

Fig. 5 Hybrid burner ([35])

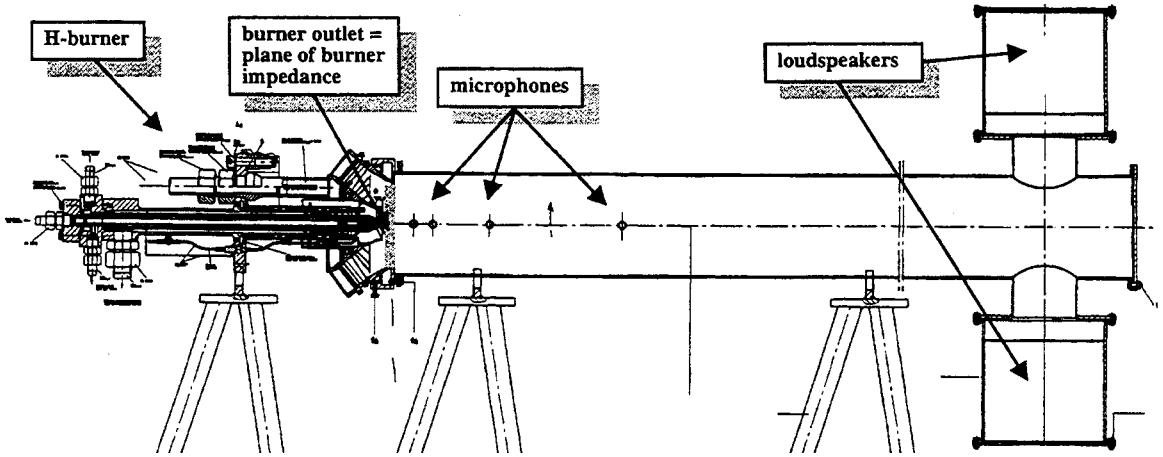

Fig. 6 Test rig for the measurement of the burner impedance

special oil nozzle is implemented in the middle for the oil operation mode but this is replaced by a dummy for the measurements performed.

Test Rig for the Measurement. The H-Burner is mounted on a tube of 2-m length. At one end two loudspeakers can excite acoustic waves (Fig. 6). Considering the dimensions of all components, the waves are one-dimensional up to a frequency of about 500 Hz for atmospheric pressure and temperature. The tube is closed at the other end. The burner impedance (the reflection coefficient, respectively) is determined using the two microphone approach proposed by Chung and Blaser [32] and Bodén and Abom [22].

Plane waves are excited by the loudspeakers. The acoustic pressure is recorded at two different microphone locations. Following Chung and Blaser [32] the impedance at an arbitrary position in the test tube can be calculated for excitation with plane waves by

$$\frac{z}{\rho a} = j\,\frac{H_{12}\cdot\sin(kl)-\sin[k(l-s)]}{\cos[k(l-s)]-H_{12}\cdot\cos(kl)} \quad \text{with} \quad k=\frac{\omega}{a} \tag{4}$$

where ρ is the density and a the speed of sound, respectively. While l corresponds to the distance from the first microphone to the plane of interest, s is the distance between the microphones. H_{12} is the transfer function from microphone 1 to microphone 2 derived from the pressure measurements.

The detailed derivation of this method is presented by Chung and Blaser [32]. Finally, the area discontinuity between burner outlet and tube has to be considered in order to determine the impedance at the burner outlet plane, i.e., the burner impedance.

This burner impedance describes the acoustic behavior of the system upstream of the burner outlet. The behavior of the upstream acoustic system includes the propagation of an incident wave upstream, the reflection at the perforated plate and the propagation back. Thus, the burner impedance is a boundary condition for the wave propagation inside of the tube representing the upstream acoustics.

The test rig and the measurement method have been tested for the simple case of an unflanged tube end. The comparison with results from Levine and Schwinger [33] showed good agreement with the measurements at the test rig ([34]).

All measurements for the determination of the burner impedance were conducted without mean flow for an atmospheric pressure of 1 bar and a temperature of 293 K.

Acoustic Model for the Prediction. For an accurate prediction of the burner impedance the whole burner has been modeled in a manner as detailed as possible. Figure 7 gives an overview of the acoustic decomposition of the burner. There are two main branches: the part of the diagonal and of the axial swirler.

While most of the elements of the main branches already correspond to acoustic four-pole elements, ''premix gas,'' ''diffusion gas,'' ''pilot gas,'' and ''oil burner'' represent branches that are

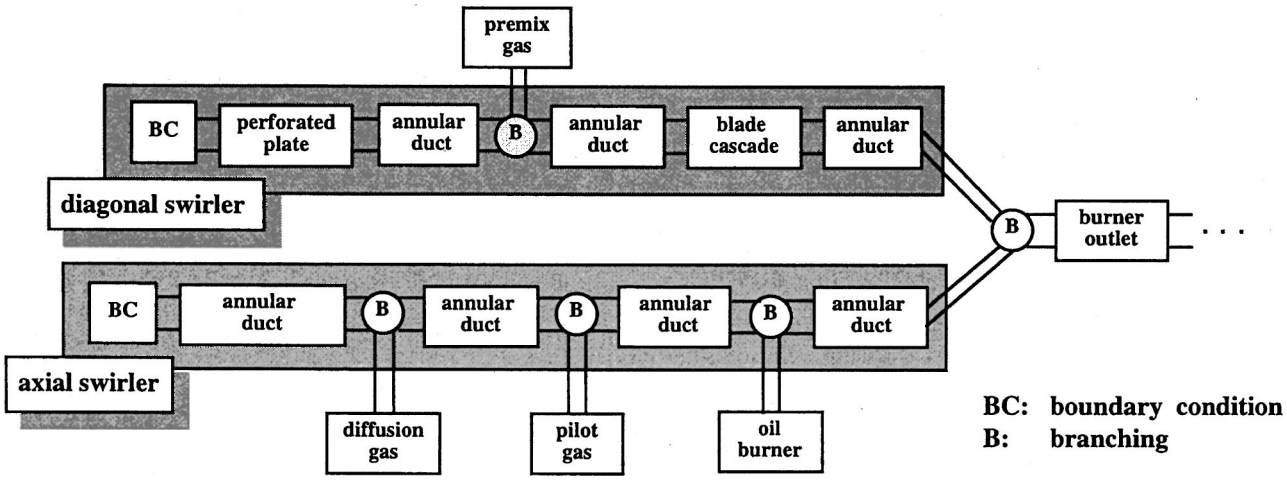

Fig. 7 Acoustical model for the prediction of the burner impedance

modeled in detail with a multitude of four-pole elements themselves. The perforated plate is modeled as 1599 small parallel ducts with a short length.

Downstream of the merging of the branches corresponding to axial swirler and diagonal swirler, a small geometrical part remains for completing the whole acoustic system from the entry up to the plane of the burner outlet.

Letting the boundary condition at the small holes of the perforated plate be an open duct end, all impedances starting at this boundary impedance can be calculated by multiplying the transfer matrices. Corresponding to the nomenclature of the experiment the acoustic particle velocity is set to be positive in the direction upstream of the burner.

First, the configuration corresponding to the experiment (pressure of 1 bar, temperature of 293 K, no mean flow) has been investigated.

However, the great advantage of the prediction method is that also mean flows, pressures and temperatures that can not be realised in the test rig can be modeled in a simple way.

In order to demonstrate the influence of mean flow, an additional mean flow is chosen that leads to a mean axial velocity in the burner port of 20 m/s.

Results From Prediction and Measurement. The first aim of the comparison between prediction and measurement was evaluating the reliability of the prediction method. As in real engine operation, only system characteristics (humming/no humming, frequency, intensity, geometric wave structure) can be measured, the test rig was used for checking the prediction of acoustic in-duct properties.

Figure 8 shows prediction and measurement of the burner impedance. The frequency of the measurements is limited to a range of 50 to 500 Hz. The loudspeakers were not able to excite frequencies lower than 50 Hz with sufficient intensity. For frequencies higher than 500 Hz, two-dimensional effects influence the measurements as the cutoff frequency for circumferential waves is crossed.

Looking at the measured results, the gain rises continuously from about 100 to 1000. The phase remains constant at 90 deg up to 200 Hz and then starts to shift slightly. At about 430 Hz a characteristic shift of gain and phase appears. Although this frequency corresponds quite well with a (higher) natural frequency of the acoustic system of the test rig, the shift should result from a characteristic length of the burner.

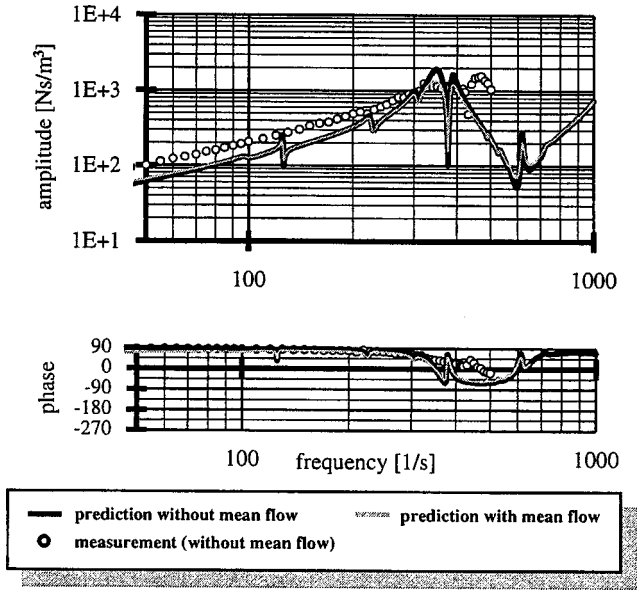

Fig. 8 Burner impedance in the test rig

Two predictions are shown in Fig. 8. First, the prediction of the burner impedance using the acoustic system presented above without mean flow and secondly, with mean flow resulting in a mean velocity in the burner outlet of 20 m/s in axial direction. The characteristics of both predictions are mostly the same. The slopes correspond well with the measurements. The gain of burner impedance is a little bit lower for the predictions and the phase shifts slightly stronger for frequencies higher than 300 Hz. Some characteristic shifts in phase and gain can be noticed as well. The main shift that corresponds to the measurement is at about 380 Hz.

One reason for the differences between the measurement and prediction results are the difficulties in prescribing the boundary condition at the perforated plate at the inlet regarding the acoustic radiance. Another reason may be the description of the acoustic transfer behavior of the swirl vanes (especially of the narrowly staggered vanes of the axial swirler).

The prediction with mean flow differs only in the phase for low frequencies from the one without mean flow. The phase is slightly lower in that frequency range. Additional damping due to turbulence or the swirling flow may influence the burner impedance with mean flow, but was not yet taken into account for the prediction.

Summing up, the measurements and the prediction are in satisfactory agreement. The acoustic behavior of a system described by its internal acoustic properties such as the impedance at a certain location can be analyzed by the prediction.

Application to a Gas Turbine Acoustic System

Burner Impedance in the Gas Turbine System. The prediction of the burner impedance in a acoustic system has been validated in a test rig configuration. Next, the burner impedance in the complete acoustic network of a gas turbine combustion system can be analyzed. Thus, using the validated methods outlined in the previous sections, burner modifications can be evaluated in terms of their acoustic impedance in the complete gas turbine system.

As pointed out before, a high impedance upstream of the flame is preferable in order to avoid high acoustic particle velocity in the mixture supply that excites the flame.

Figure 9 shows the impedance at the burner outlet in the gas turbine combustion system described above (Vx.3A with HBR-

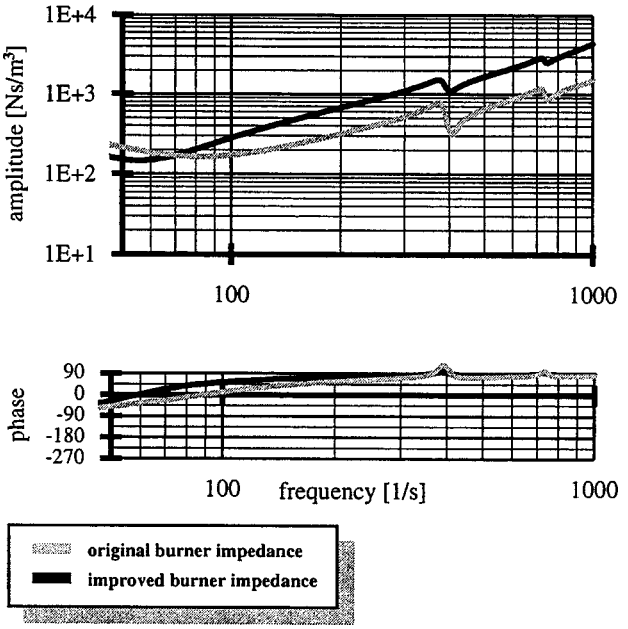

Fig. 9 Original and improved burner impedance in the gas turbine combustion system

burners). It describes the acoustic behavior of the burner itself and the parts upstream of the burner, namely the plenum and the diffusor.

As the plenum behaves like a large volume and is oscillating itself, the ''boundary condition,'' i.e., the impedance at the inlet of the burner differs from the test rig condition. Thus, the burner impedance cannot be compared with the one measured on the test rig. Of course, temperature and pressure differ as well.

Nevertheless, the burner impedance in the gas turbine combustion system shows similar behavior to the burner impedance in the test rig. The gain is rising continuously with an obvious shift at about 400 Hz, resulting from the behavior of the diffusor. The phase is close to 90 deg; it is only shifting for lower frequencies. The burner impedance is mostly influenced by the plenum in this case.

Figure 9 shows also the burner impedance when a small geometric change is implemented at the burner inlet. By lengthening the duct upstream of the diagonal swirler, the burner impedance can be increased/almost doubled.

A detailed thermoacoustic stability analyses of the gas turbine combustion system have been performed in order to show the impact of the different burner impedances on combustion oscillations.

Stability Analysis With Improved Burner. The original stability analysis was presented and described by Krüger et al. [19]. As pointed out by Krüger et al. [28], the frequency response of the swirled flame calculated is different for each direction of wave propagation in the annular combustion chamber. Thus, there are two flame frequency responses for the circumferential direction in the combustion chamber: one in clockwise direction and one in counterclockwise direction. Consequently, two stability analyses were performed, namely for the clockwise and for the counterclockwise direction.

Figure 10 shows the frequency response F_0 of the system of the original stability analysis and the new one with the improved burner impedance for the clockwise direction. According to the stability criterion discussed above, the prediction indicates humming if the phase equals zero for a frequency and the gain is higher than 1.

One main humming frequency of the system could be found in the prediction at about 185 Hz (for details refer to [19]). The augmentation of the burner impedance leads to a much better slope of the phase in that frequency range. The phase does not shift that strongly anymore. The humming frequency at 185 Hz vanishes. This improvement in the range of 185 Hz is paid for with a rise in gain at about 350 Hz, the second frequency at which humming is indicated. The phase slope remains unchanged but the gain is increased.

Figure 11 shows the stability analysis for the counterclockwise direction. Once again, the original stability analysis shows a stronger phase shifting at about 165 Hz, but no zero phase frequency. A peak in the gain is also present at this frequency range. The first frequency at which the phase becomes zero is 345 Hz with a gain of slightly higher than 1 indicating humming. The improved burner impedance reduces the phase shift in the range of 165 Hz making it appear more stable. The humming frequency of about 345 shifts slightly to lower frequencies but the gain remains almost unchanged.

The higher frequencies with a zero phase appearing in both analyses are not to be seen as critical because damping may be underestimated in this range and they were not observed in engine operation.

Summing up, augmentation of the burner impedance realised by a simple geometric change at the burner leads to a significant improvement in the thermoacoustic stability in the prediction. An improvement could not be found for higher frequencies.

Detuning the System. In the original configuration, the annular ring combustor is equipped with 24 identical burners. A possible measure to detune the interaction of the different acoustic parts is to change the burner impedance dependent on the circumferential direction. As described by Berenbrink and Hoffmann [20], exactly this kind of detuning has been examined experimentally and later implemented in the gas turbine system. As the prediction method was developed later, it should be evaluated whether the effects of this detuning could be grasped by the acoustic analyses as well.

20 of the 24 burners in the annular combustion chamber are supplied with Cylindrical Burner Outlets (CBO), i.e., cylindrical extensions at the burner nozzle (see Fig. 12 for example).

Figure 13 once again shows the acoustic model of the combustion system for the circumferential direction. At the branchings (B), the parts of the network with the flame, burner and the up-

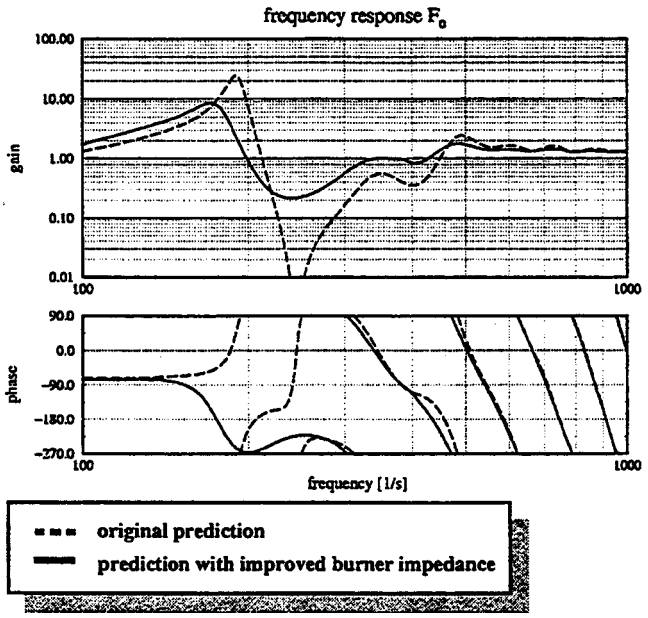

Fig. 10 Stability analysis with improved burner impedance (clockwise direction)

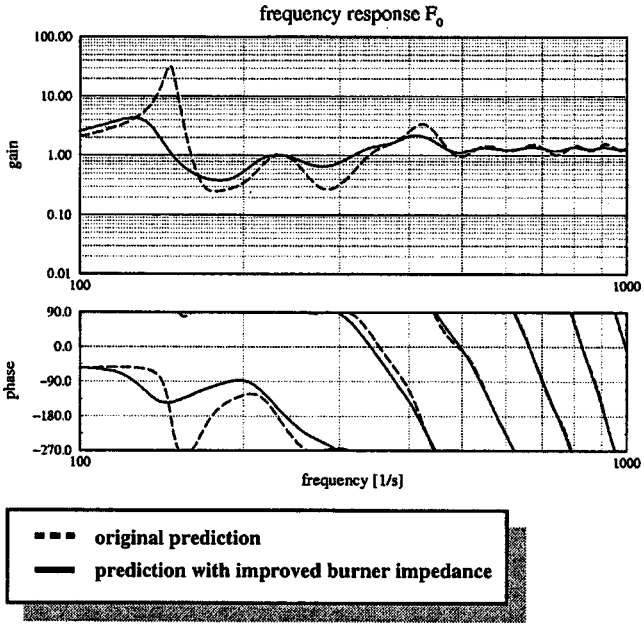

Fig. 11 Stability analysis with improved burner impedance (counterclockwise direction)

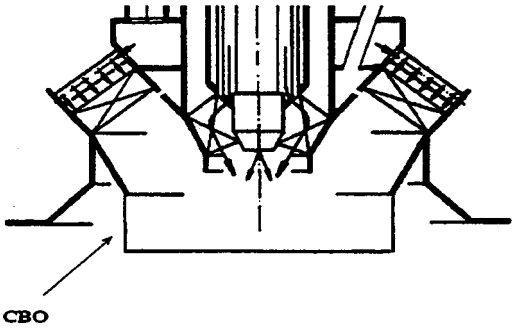

Fig. 12 Schematic of cylindrical burner outlet (CBO) layout (Berendbrink and Hoffman [20])

stream part are linked. In Fig. 13, the locations of the burners with CBO in the annular ring combustor are marked by ''dark'' branchings.

The CBOs can effect the acoustic interaction in two ways. First, they change the impedance at the burner outlet similarly like the improvements presented in the last section. Furthermore, the flame response may change due to a different velocity profile in the burner exit or a shift of the flame position in downstream direction. This second effect is part of on-going work and is not pursued herein. Only the first effect is taken into account in the following paragraphs.

Stability Analysis for Detuned System. Once again both possibilities for the circumferential direction (clockwise and counterclockwise) were examined.

The results are similar to those with improved burner impedance. For the clockwise direction (Fig. 14), the phase is not shifting strongly in the range of 160 to 250 Hz and the humming frequency at about 185 Hz vanishes. All the other critical frequencies remain unchanged.

For the counterclockwise direction (Fig. 15), the phase is also not shifting strongly in the range of 160 to 200 Hz anymore. In the

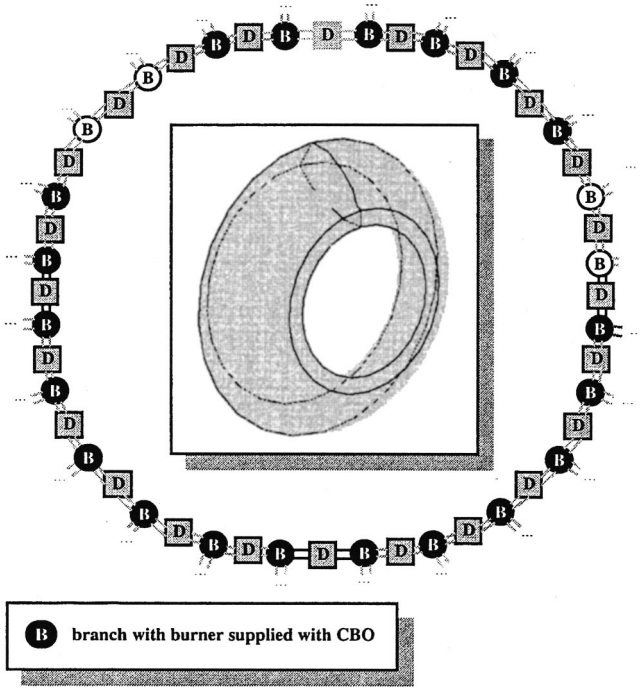

Fig. 13 Acoustic network for the detuned system

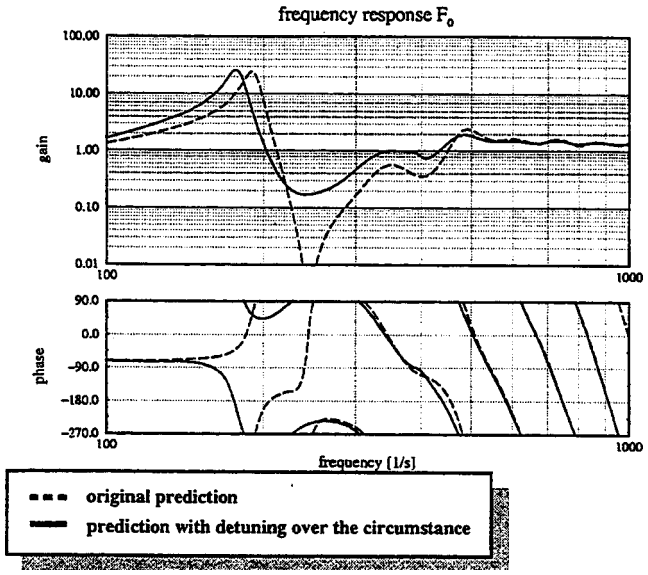

Fig. 14 Stability analysis for the detuned system (clockwise direction)

range between 300 to 350 Hz, the zero crossing of the phase is shifted slightly towards lower frequencies for the detuned system. The higher zero phase frequencies are not considered as critical for the reasons presented above.

The analyses for the detuned configuration indicate an improvement in the thermoacoustic stability in the range of 160 to 200 Hz. For the second critical range of 340 to 350 Hz no significant improvement can be deduced. Nevertheless, the prediction indicates a considerable improvement in thermoacoustic stability.

Figure 16 shows data from engine operation. The power output could be increased by nine percent to the baseline by implementing 20 H-burners with a CBO in the annular combustion chamber. These data demonstrate the positive impact of the CBOs on the system stability.

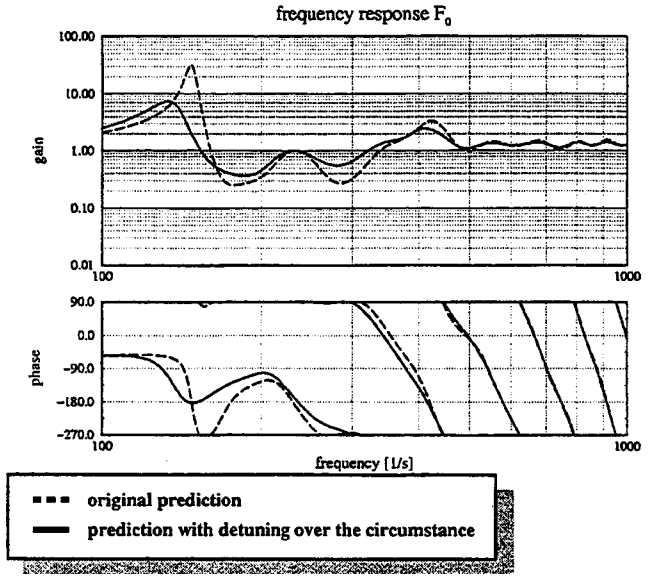

Fig. 15 Stability analysis for the detuned system (counterclockwise direction)

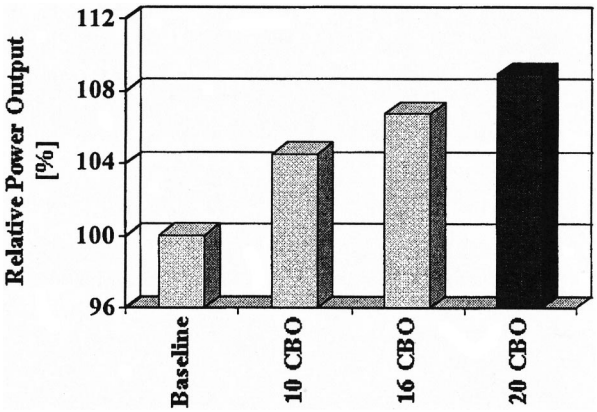

Fig. 16 Stability limits for different cylindrical burner outlet (CBO) configurations (Berendbrink and Hoffman [19])

The data from engine operation confirm the results of the stability analyses performed on the gas turbine system presented. Both, measurements and prediction show a considerable improvement in the thermoacoustic stability.

Summing up, the experience of engine operation can be grasped by the stability analyses of the detuned system. One reason for the improved thermoacoustic stability of the detuned system can be found in the change of the burner impedance at the modified burners. Investigations of other possible reasons, such as a change in the flame response due to the CBO, are part of current work.

Summary and Conclusion

Different approaches to avoiding or minimizing the occurrence of thermoacoustic oscillations are possible. Before applying active measures or additional damping devices, it is reasonable to design the acoustic interaction of all relevant components of the combustion system such that these oscillations are minimized.

The analyses presented pointed out the influence of the impedance at the burner outlet. The higher this impedance at the burner outlet the smaller the acoustic particle velocity oscillations that excite the flame.

As a validation for the prediction of in-duct acoustic properties using the modeling approach developed, the burner impedance for a test rig has been measured and predicted. Measurement and prediction are in good agreement although some characteristic frequencies do not correspond exactly.

With this positive validation in mind, the burner impedance in the complete combustion system was determined from the prediction. The burner impedance turned out to be rather low. Thus, with some geometric changes, the gain of the impedance was almost doubled.

Stability analyses with this new burner impedance in the system led to a significant improvement in stability in the frequency range of about 185 Hz in the prediction. Initially expected improvements in other critical frequencies, especially the second range of interest at about 350 Hz, could not be demonstrated.

Similar results were obtained for the stability analyses for a detuned system where some of the burners are supplied with cylindrical burner outlets (CBO). The improvement predicted can also be explained by the change in burner impedance.

Changes in the flame frequency response have not yet been considered for the CBOs. The implementation CBOs may influence the velocity profile at the burner outlet or may shift the flame in downstream direction. Thus, the flame shape or position in the combustion chamber may be changed, possibly leading to shifts in the characteristic frequencies of the dynamic flame response. Consequently, this aspect is part of current work. The procedure to determine the flame frequency response of a gas turbine flame, the step-function approach (see [28]), will be applied to the burner equipped with a CBO. Thus, the accuracy of the prediction should be improved.

Nevertheless, the analyses presented show that simple changes of geometry or a detuning of the acoustic system of the gas turbine combustor can be evaluated theoretically. Comparisons with data from engine operation confirm the results of the prediction. This demonstrates that evaluations of improvements by implementation of additional measures can be derived well. Thus, the prediction method presented is a helpful tool for understanding complex acoustic systems (such as gas turbine combustors) and finding (in advance) combustor system configurations that best fulfil the requirements for thermoacoustic stability.

Nomenclature

a = speed of sound
F = frequency response
f = frequency
H = transfer function
k = wave number ($=\omega/a$)
$\dot{m}$ = mass flow rate
p = acoustic pressure
r = reflection coefficient
$\underline{T}$ = temperature
T = transfer matrix
u = acoustic particle velocity
z = acoustic impedance ($=p/u$)

Greek

φ = phase angle
ρ = density
ω = angular frequency

Subscripts

ax = axial swirler
circ = circumferential direction
diag = diagonal swirler
Fl = flame
0 = steady-state quantities

Superscripts

$+$ = wave traveling in downstream direction
$-$ = wave traveling in upstream direction

References

[1] Putnam, A. A., and Dennis, W. R., 1955, ''Suppression of Burner Oscillations by Acoustical Dampers,'' Trans. ASME, **77**, pp. 875–883.
[2] Gysling, D. L., Copeland, G. S., McCormick, D. C., and Proscia, W. M., 1998, ''Combustion System Damping Augmentation with Helmholtz Resonators,'' ASME Paper No. 98-GT-268.
[3] Schlein, B. C., Anderson, D. A., Beukenberg, M., Mohr, K. D., Leiner, H. L., and Träptau, W., 1998, ''Development History and Field Experience of the First FT8 Gas Turbine with Dry Low NO_x Combustion System,'' ASME Paper No. 99-GT-241.
[4] Pandalai, R. P., and Mongia, H. C., 1998, ''Combustion Instability Characteristics of Industrial Engine Dry Low Emission Combustion Systems,'' Paper No. AIAA 98-3379.
[5] Candel, S. M., 1992, ''Combustion Instabilities Coupled by Pressure Waves and Their Active Control,'' The Twenty-Fourth (International) Symposium on Combustion, The Combustion Institute, Pittsburgh, PA, pp. 1277–1296.
[6] McManus, K. R., Poinsot, T., and Candel, S. M., 1993, ''A Review of Active Control of Combustion Instabilities,'' Prog. Energy Combust. Sci., **19**, pp. 1–29.
[7] Hibshman, J. R., Cohen, J. M., Banaszuk, A., Anderson, T. J., and Alholm, H. A., 1999, ''Active Control of Combustion Instability in a Liquid-Fueled Sector Combustor,'' ASME Paper No. 99-GT-215.
[8] McManus, K. R., Magill, J. C., and Miller, M. F., 1998, ''Combustion Instability Suppression in Liquid-Fueled Combustors,'' AIAA 98-0642.
[9] Paschereit, C. O., Gutmark, E., and Weisenstein, W., 1999, ''Suppression of Acoustically Excited Combustion Instability in Gas Turbines,'' Paper No. AIAA-99-1986.
[10] Paschereit, C. O., Gutmark, E., and Weisenstein, W., 1999, ''Control of Combustion-Driven Oscillations by Equivalence Ratio Modulations,'' ASME Paper No. 99-GT-118.
[11] Richards, G. A., Yip, M. J., Robey, E., Cowell, L., and Rawlins, D., 1997,

''Combustion Oscillation Control by Cyclic Fuel Injection,'' ASME Paper No. 95-GT-224.
[12] Hermann, J., Hantschk, C. C., Zangl, P., Gleis, S., Vortmeyer, D., Orthmann, A., Seume, J. R., Vortmeyer, N., and Krause, W., 1997, ''Aktive Stabilitätskontrolle an einer 170 MW Gasturbine,'' 18, Deutsch-Niederländischer Flammentag 97, Delft, VDI-Berichte 1313, pp. 337–344.
[13] Mahmoud, H., Fleifil, M., Ghoneim, Z., and Ghoniem, A. F., 1997, ''Active Control of Thermoacoustic Instability Using LQR-Techniques,'' *ASME Joint Power Generation Conference 1997*, Vol. 1, ASME, New York, pp. 299–307.
[14] Bloxsidge, G. J., Dowling, A. P., Hooper, N., and Langhorne, P. J., 1989, ''Active Control of Reheat Buzz,'' AIAA J., **26**, No. 7.
[15] Straub, D. L., and Richards, G. A., ''Effect of Axial Swirl Vane Location on Combustion Dynamics,'' ASME Paper No. 99-GT-109.
[16] Steele, R. C., Cowell, L. H., Cannon, S. M., and Smith, C. E., 1999, ''Passive Control of Combustion Instability in Lean Premixed Combustors,'' ASME Paper No. 99-GT-052.
[17] Kremer, H., 1979, ''Schwingungen in Feuerräumen,'' Gas Wärme International, **28**, No. 8.
[18] Schimmer, H., and Vortmeyer, D., 1977, *Selbsterregte Schwingungen in Brennkammern*, Nr. 286, VDI-Berichte, pp. 21–28.
[19] Krüger, U., Hüren, J., Hoffmann, S., Krebs, W., and Bohn, D., 1999, ''Prediction of Thermoacoustic Instabilities With Focus on the Dynamic Flame Behavior for the 3A-Series Gas Turbines of Siemens KWU,'' ASME Paper No. 99-GT-111.
[20] Berenbrink, D., and Hoffmann, S., 2000, ''Suppression of Combustion Dynamics by Active and Passive Means,'' ASME Paper No. 2000-GT-0079.
[21] Munjal, M. L., 1987, Acoustics of Ducts and Mufflers, John Wiley and Sons, New York.
[22] Bodén, H., and Abom, M., 1986, ''Influence of Errors in the Two-Microphone Method for Measuring Acoustic Properties in Ducts,'' J. Acoust. Soc. Am., **79**, pp. 541–549.
[23] Meyer, E., and Neumann, E. G., 1967, ''Physikalische und technische Akustik,'' Vieweg-Verlag, Brauschweig, Germany.
[24] Heinig, K. E., 1983, ''Sound Propagation in Multistage Axial Flow Gas Turbine Engines,'' AIAA J., **21**, pp. 98–105.
[25] Bohn, D., and Deuker, E., 1993, ''An Acoustical Model to Predict Combustion Driven Oscillations,'' 20th International Congress on Combustion Engines (CIMAC), London.
[26] Faber, Ch., 1991, ''Entwicklung eines Rechenmodells zur Vorausberechnung des Stabilitätsverhaltens von Brennkammersystemen,'' internal report, Institute of Steam and Gas Turbines, RWTH Aachen.
[27] Baade, P. K., 1974, ''Selbsterregte Schwingungen in Gasbrennern,'' *Klima, Kälte, Anlagenbau*, Vol. 57, pp. 167–176.
[28] Krüger, U., Hüren, J., Hoffmann, S., Krebs, W., and Bohn, D., 1999, ''Combustion-Driven Oscillations: Numerical Prediction of Dynamic Behavior of Gas Turbine Flames,'' AIAA Paper No. 99–1910.
[29] Bohn, D., Deutsch, G., and Krüger, U., 1996, ''Numerical Prediction of the Dynamic Behavior of Turbulent Diffusion Flames,'' ASME Paper No. 96-GT-133.
[30] Bohn, D., Li. Y., Matouschek, G., and Krüger, U., 1997, ''Numerical Prediction of the Dynamic Behaviour of Premixed Flames Using Systematically Reduced Multi-Step Mechanisms,'' ASME Paper No. 97-GT-265.
[31] Krüger, U., Hoffmann, S., Krebs, W., Judith, H., Bohn, D., and Matouschek, G., 1998, ''Influence of Turbulence on the Dynamic Behavior of Premixed Flames,'' ASME 98-GT-232.
[32] Chung, J. Y., and Blaser, D. A., 1980, ''Transfer Function Method of Measuring In-Duct Acoustic Properties: I, Theory; II, Experiment,'' J. Acoust. Soc. Am., **68**, pp. 907–921.
[33] Levine, H., and Schwinger, J., 1946, ''On the Radiation of Sound From an Unflanged Circular Pipe,'' Physical Review, **73**, pp. 383–406.
[34] Flohr, P., 1999, internal report, Siemens KWU.
[35] Prade, B., Streb, H., Berenbrink, P., Schetter, B., and Pyka, G., 1996, ''Development of an Improved Hybrid Burner-Initial Operating Experience in a Gas Turbine,'' ASME Paper No. 96-GT-045.

Experimental and Theoretical Studies of a Novel Venturi Lean Premixed Prevaporized (LPP) Combustor

N. A. Røkke

A. J. W. Wilson

Rolls-Royce,
Ulstein Turbine AS,
N-5811 Bergen, Norway

A new gas turbine engine using a unique layout patented in Norway has a low-emission combustion system under development. The gas generator uses entirely radial rotating components and employs a dual entry LP radial compressor, a radial HP compressor, and a radial HP turbine. The power turbine is of a two-stage axial design, coupled to an epicyclical gear embedded in the exhaust duct. Several combustor concepts have been tested and evaluated during the development of the engine. The engine is targeted for marine, power generation, and train propulsion. For the marine and train application liquid fuel operation is needed, thus the primary focus in the development has been for a lean premixed prevapourised system. An interesting concept utilizing two venturi premixers has been studied intensively. By utilizing venturi premixers the following advantages can be achieved: (1) low overall pressure drop but high injector pressure drop and velocities in the mixing region (throat region), (2) high shear forces and drag imposed on the droplets enhancing droplet shedding and evaporation, and (3) excellent emission behavior at designated load conditions. Although these advantages can benefit gas turbine low-emission combustion, the challenges in using venturi premixers are: (1) venturis are susceptible to separation and thus flame stabilization within the venturi which is detrimental and (2) inlet flow disturbances enhance the tendency for separation in the venturis and must be minimized. Studies were launched to investigate a proposed combustor configuration. These studies included analytical studies, computational fluid dynamics (CFD) calculations of isothermal and combusting flow inside the combustor together with rig tests at atmospheric, medium, and full pressure. Finally, engine tests within the full operating range were conducted with very favorable emission figures for lean premixed prevaporized (LPP) operation. The system was capable of running at below 20 ppm NO_x and CO, at elevated power for liquid fuel. Control of part load performance and emissions is by variable fuel staging of the two venturi stages. The paper highlights the features of the venturi combustor development and discusses the characteristics in terms of flow conditions and droplet motion, heat transfer, ignition delay time, and emissions. [DOI: 10.1115/1.1377008]

Introduction

Low-emission combustion has become a common demand for large power-generating gas turbines in most countries in the world. The term ''low emissions'' usually refers to emissions of nitrogen oxides—NO_x($NO+NO_2$), carbon monoxide—CO and unburned hydrocarbons (UHC). Additional species/pollutants may be particulate matter, sulphur oxide, methane (due to greenhouse effect contribution), and trace species (dioxins, metals, and heavy ring-structured hydrocarbons). Legislation is also emerging for offshore and marine applications world wide.

The traditional challenge has been to combine low emissions of NO_x with low emissions of CO over the useful power range of the engine. Several techniques are developed to control this by keeping the equivalence ratio within a range that gives reaction temperatures in the range of 1650–1900 K. Below this range the oxidation of CO becomes too slow and above this range the temperature becomes high enough to produce thermal NO_x through the high activation energy Zel'dovich mechanism. Lean, high-pressure premixed combustion also produces NO_x through the nitrous oxide (N_2O) mechanism ([1]) the study suggests that this dominates NO_x production for lean premixed prevaporized (LPP) conditions.

Temperature and thus emissions control can be achieved by parallel staging of the combustor, utilizing several burners that can be put into/out of operation, separately or in groups. Series staging means feeding a constant temperature stage into a hot consecutive stage for load variations so that adequate time and temperature is achieved for burnout of the partly nonoxidized exhaust gas. Thirdly, variable geometry can be used for regulating the air flow through the combustor, through zones of the combustor or through the compressor. All these techniques are based on lean premixed combustion and are mainly developed for gaseous fuels.

Other techniques include the rich-quench-lean (RQL) technique, which is hampered by the rapid mixing needed and the inherent problems of wall cooling and soot control. Lean direct injection is an emerging technique, which is problematic due to the very rapid mixing times needed to be able to mix before chemical reaction takes place ([2]). Catalytic combustion, which has the promise of giving below 5 ppm emissions of both CO and NO_x, has been proven in the field to some extent. For new engines this technology is limited too, as the increasing turbine inlet temperature for higher efficiency will be too high for the catalysts we know today.

Contributed by the International Gas Turbine Institute (IGTI) of THE AMERICAN SOCIETY OF MECHANICAL ENGINEERS for publication in the ASME JOURNAL OF ENGINEERING FOR GAS TURBINES AND POWER. Paper presented at the International Gas Turbine and Aeroengine Congress and Exhibition, Munich, Germany, May 8–11, 2000; Paper 00-GT-110. Manuscript received by IGTI Oct. 1999; final revision received by ASME Headquarters Oct. 2000. Associate Editor: D. Wisler.

Table 1 Engine characteristics—at ISO condition

Combustor inlet temperature (K)	720
Combustor inlet pressure (Bar)	17
Combustor mass flow (kg/s)	1.7
Combustor pressure drop (%)	3.5
Temperature pattern factor $(T_{max}-T_{average})/(T_{average}-T_{inlet})$ (%)	15
Fuel/air ratio (−)	.018
NO_x @15% O_2 (ppmvd)	<45
CO @15% O_2 (ppmvd)	<40
O_2 (Vol %)	~16
UHC (ppmvd) as C_1	<5

The ruling technology is thus lean premixed combustion by using some kind of staging technology. Although this is well known for gas fired engines, less work and effort have been directed to LPP systems for smaller engines.

Smaller engines running with liquid fuels pose a large challenge for low-emission requirements. They are often limited in size for the combustor system and development costs are relatively high. The latter precludes the use of complicated staging techniques.

The Engine Concept

The engine is a two-shaft simple cycle gas turbine, comprising an all-radial gas generator, a two-stage axial power turbine and an integral reduction gearbox. The gas generator section consists of two centrifugal compressor stages, the first of which has a double entry. A single-stage radial inflow turbine drives both stages. The power turbine is a two-stage axial design.

The combination of individual components in the gas generator with optimum ''specific speeds'' provides an important basis for the engine cycle. The combination of a double-entry first-stage compressor and a single-entry second-stage compressor, together with a radial inflow turbine allows each component to operate at the peak of its efficiency. Due to the high tip speed of the radial turbine it is possible to operate at a high pressure-ratio and adequate firing temperature without the need for internal cooling.

The Table 1 shows some important engine data at base load conditions running with diesel fuel. The engine has fulfilled 250 hrs sea tests in a large passenger catamaran with the described combustor system with diesel as fuel without any structural damage to the combustor parts. The combustor TBO is targeted to 9000/20,000 hrs for liquid and gas operation, respectively.

Combustor System

During the development of the engine, focus has been on marine propulsion, i.e., a liquid fueled combustor. Additionally a low-emission system had to cope with both liquid and gas, as power generation is a required application.

The system reported on here is a multi-venturi system, as depicted in Fig. 1. The combustors are of a reverse flow type. Reference is made to Fig. 1. Air enters the combustor at (A), where dilution air is fed, the remaining portion (approx. 60 percent) flows further up the cooling jacket. The combustor is fully convection cooled and internally TBC coated. From exiting the cooling jacket at (C), the air is further distributed up to the primary venturi (F) and to the secondary venturi at (D). Fuel and air is mixed in the venturi throats by an adequate fuel injector taking benefit from the high air velocity in the throat. Air-assisted injectors have been utilized. The mixture is then fed to the combustor at the exit of each venturi. For the secondary venturi, the mixture is fed to the bulk flow through a perforated cone. The combustor is also fitted with a start-up torch (5); this is only in-operation during start-up. The engine has six combustors, each combustor consisting of two premixing venturis. These are staged so that the tangentially entering venturi (primary venturi-PV) supplies energy

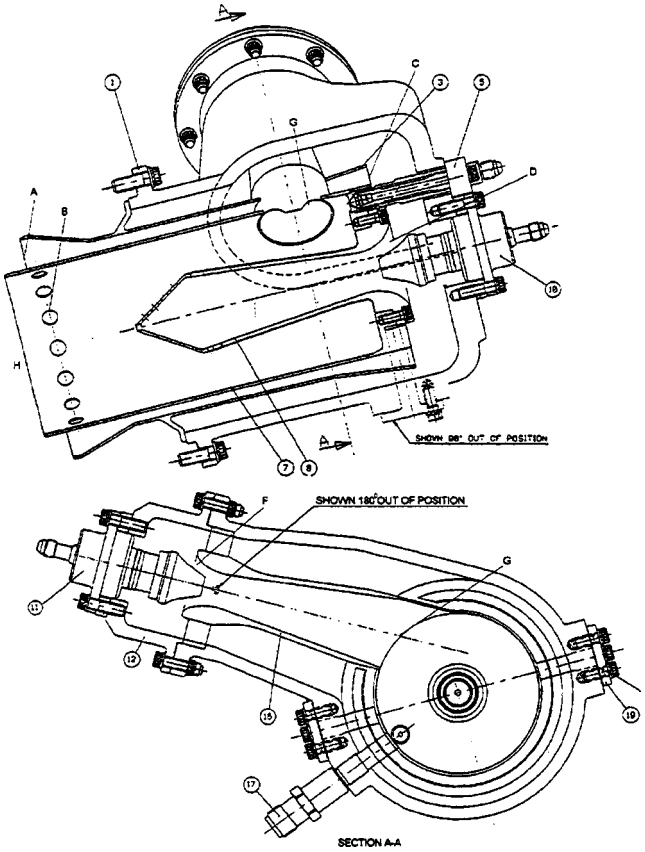

Fig. 1 Combustor assembly

to the engine at idle and low-power operation, whereas the secondary venturi is put into operation at higher speeds.

At full load the two venturis run at the same equivalence ratio. A general view of the fuel schedule is shown in Fig. 2. Figure 3 shows the adiabatic flame temperature range for the two combustor venturis. The mix temperature for the two venturis will be approximately the weighted mean of these two temperatures.

During the course of the development, much effort has been put into optimizing the combustor for good stability margins, low emissions, and acceptable wall temperatures. The clue to the successful operation of such a combustor is the venturi characteristics.

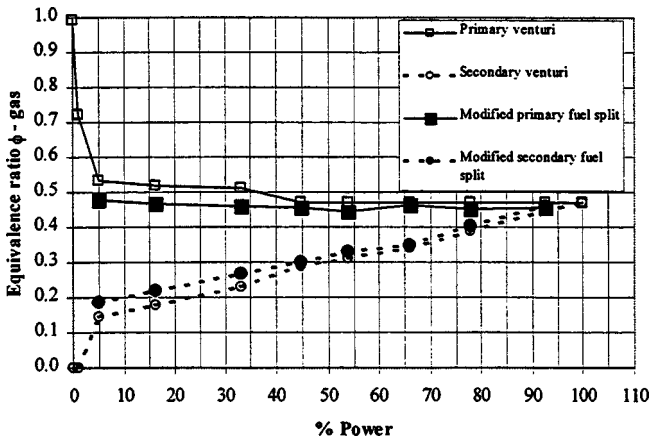

Fig. 2 Fuel schedule

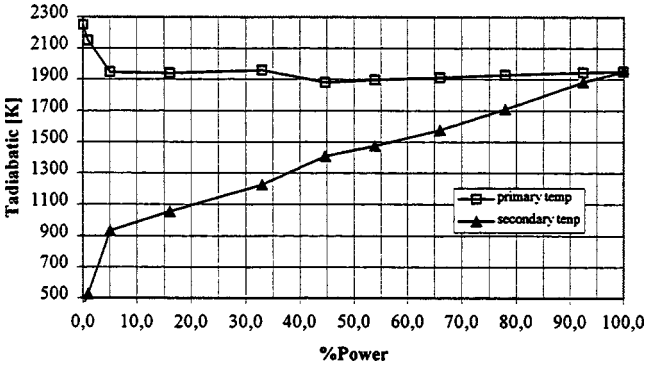

Fig. 3 Temperature schedule

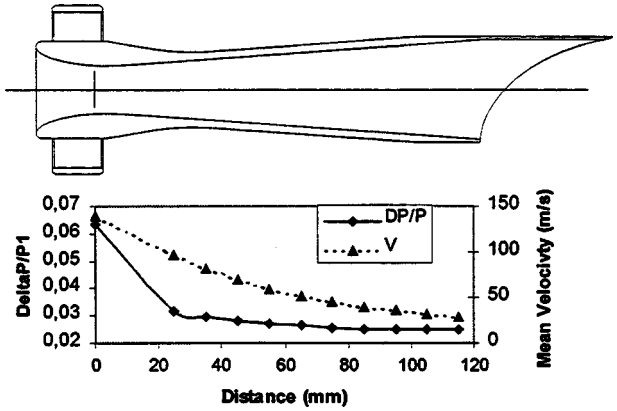

Fig. 5 Venturi pressure drop and velocity

The Venturi Premixer

The reasons for using venturis for premixing are:

- low pressure in the venturi throat which can be used for getting good atomization performance (analogy to carburettor throats),
- very good discharge coefficients of the venturi throats and good pressure recovery, geometric and effective areas virtually identical,
- reliable measuring devices for actually measuring the air flow in the different stages, and
- the changing air velocity in the venturi and the near constant absolute slip velocity between air and droplets enhance droplet-shedding evaporation.

Venturi Characteristics

Typical venturi performance is shown in Fig. 4, depicting the profiles of static properties along the venturi length.

This shows the favorable conditions for droplet atomization/evaporation. First the high velocity at the throat increases turbulence and mixing. The high-velocity air accelerates the droplets and we can in theory achieve a constant slip velocity $u_s = |V - u_{\text{droplet}}|$ for the droplets. This is good for droplet shedding so that a very small stable droplet size can be achieved; thus efficient mass diffusion to the bulk flow can be achieved.

The venturi characteristics have been mapped through measurements and calculations. Figure 5 shows the pressure profile through the venturi actually used in the engine.

Venturi angles (half-angles) ranging from 3 deg to 6.5, deg have been used with different L/d_{throat}. The pressure recovery of the venturi provides the advantage of high velocities with lower overall pressure loss. This enables a lower pressure at the fuel nozzle outlet, which provides for a good flow of air through the nozzle swirler and thus better atomisation.

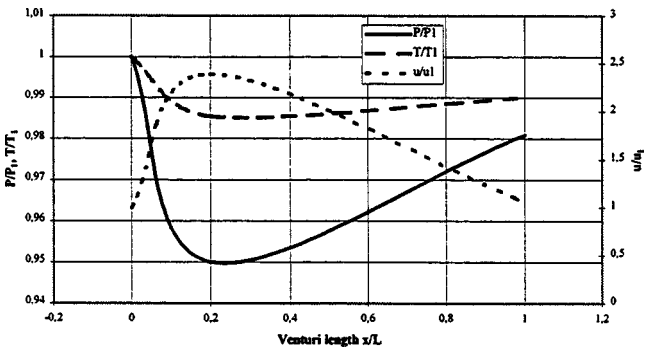

Fig. 4 Venturi characteristics

Figure 5 shows the measured static pressure variation in the venturi and the mean velocity calculated from continuity. An ''isentropic'' velocity can be calculated from the dynamic pressure assuming no loss in total pressure and this velocity will be somewhat higher. From the measured static pressure and the velocity calculated from continuity one can obtain an indication of the variation in total pressure loss.

A one-dimensional model of the venturi flow was combined with a droplet evaporation model. Motion is controlled by the drag in the air stream and thus the diameter, diminishing as the mass-diffusion transports vapours from the droplet surface. The actual evaporation conditions in the primary venturi are depicted in Fig. 6 for full load conditions. The graph depicts the $(d_p/d_{p0})^2$ versus the venturi length for different initial droplet sizes. As can be seen the droplets have an initial heat-up period (no change in diameter), a boiling point where mass loss becomes increased, and then a more or less constant evaporation gradient. The latter region is known as the d^2 region $((d_p^2 - d_{p0}^2) = -\lambda t$, t=time). The figure shows the above-mentioned features of acceleration and deceleration, being more pronounced as the droplets are bigger. The results show that droplets of marine diesel being less than 40 μm can be evaporated before the mixture enters the flametube, given a residence times of 2–2.7 ms for the primary and secondary venturi.

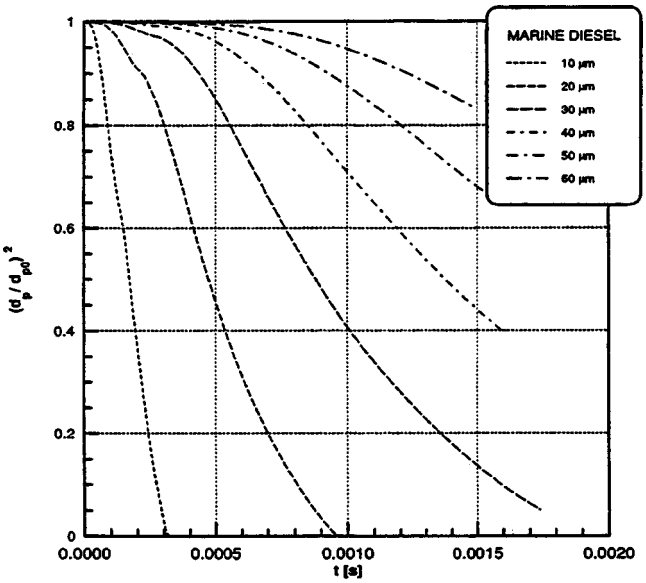

Fig. 6 Droplet evaporation

The simplified one-dimensional analysis describes an ideal situation; however, the flow situation is highly complex as the fuel flow is swirled and the airflow has high turbulence from bends, pressure drop devices, and diffusers. The airflow is thus highly three-dimensional also caused by the flow obstacle constituted by the fuel nozzle. The computational fluid dynamics (CFD) discussion shows how the real effects affect the fuel placement necessary to achieve a homogeneous mixture.

Autoignition Limits and Margins

Based on the studies by Spaddacini and TeVelde [3], an estimate for the ignition delay time is derived which depends on inlet temperature and pressure. Calculations have shown that the most critical case appears for a ''hot day'' since temperature has a more pronounced impact on autoignition than does pressure. The secondary venturi is most susceptible to autoignition, having the longest transport time and being subjected to additional heat transfer from the primary flame. For the design point of the combustor it is fair to assume a pressure of 17 bar and air temperatures of 720 K at the inlet to the cooling jacket and approximately 760 K at the combustor top (venturi entrance). This gives an ignition delay time of 7.5 ms. If we take 45°C as ambient temperature for a hot day the venturi inlet temperature would typically be 780 K and the pressure 16.5 bar, which yields an ignition delay time of 3.9 ms. Assuming the average fuel drop velocity equals the mean air velocity ($V_{in}+V_{out}/2=42$ m/s), the residence time is approximately 2.7 s.

Figure 7 below shows the ignition delay time (ms) as a function of temperature for pressures from 14 bar to 20 bar. The data depicted uses the correlation:

$$\tau = \frac{2.43\cdot 10^{-9}}{p^2}\cdot e^{209915/T}(\text{ms})$$

derived from the reports by Spadaccini and TeVelde [3].

The findings by Spadaccini and TeVelde must, however, be considered as indicative as more and more combustor experimental findings show stable nonburning flow conditions well within the autoignition envelope described by the preceding correlation. This is for instance shown in Ripplinger et al. [4] However, using the preceding, correlation, the margins for autoignition is acceptable (1.4–2.8 in safety margin). Tests have been performed at increased pressure and temperature together with an increased residence time to assess the limits of the system. Tests at the indicated condition in Fig. 7 at 20.5 bar could be run without autoignition. For this test a delay time of 2.5 ms is predicted whereas the condition was 3.2 ms. It can thus be concluded that the autoignition margins are comfortable for this configuration.

Autoignition has never been experienced in engine operation even under most arduous conditions, which verifies the above conclusion. For gas operation the autoignition times are much longer and are not reported here. Other flame stabilization/creep back mechanisms are not discussed here, boundary layer flame creep or separation are other modes that must be avoided in venturi design.

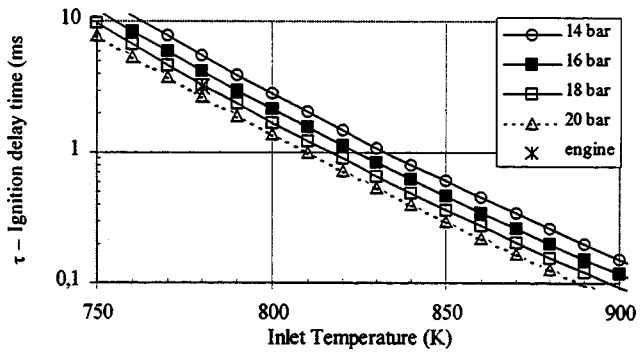

Fig. 7 Delay time versus temperature and pressure

Heat Transfer

Cooling of hot components is of crucial importance for long service life. The challenging parts of this combustor are the convection cooling of the flametube and the secondary venturi that is inside the reaction zone. For both areas, analysis using empirical correlations and CFD has been utilized to lower the temperature level and thermal stress level.

Flametube. The flametube, as depicted in Fig. 1, is cooled by a high-velocity airflow on the outside and thermally insulated on the inside by a thermal barrier coating with a low conductivity. By this simple cooling configuration heat transfer coefficients on the cooling side can be as high as 1200 W/m^{2}K. Due to the swirling flow of the primary venturi, the heat impact on the flametube will also be affected by the swirling flow thus giving temperature gradients circumferentially and axially. Alternatives to the TBC coating have been considered as the TBC layer has a cumbersome application process. External circumferencial and axial ribs have been considered, and these can match the TBC layer in terms of wall temperature, but at a higher pressure loss for the combustor. The TBC coating reduces the material temperature by approximately 40 K. In Fig. 8 and Fig. 9 a comparison between an engine test with thermal paint and a CFD calculation is shown. The CFD calculation is performed using detailed chemistry and a computer code named ''Spider'' as described in Gran and Magnussen [5]. The pattern shown from these calculations is in good agreement with thermal paint test results from the engine.

As the venturi flow is deflected by the liner wall it follows the wall around and meets the outflow from the venturi opening. It

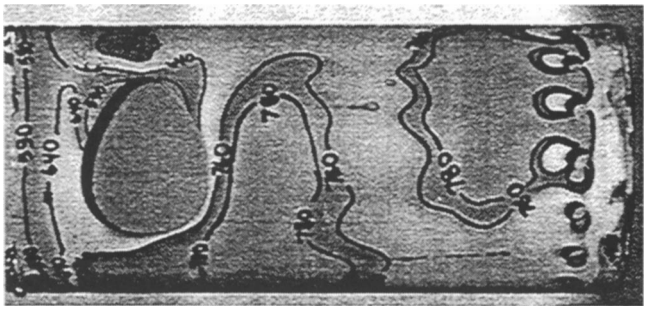

Fig. 8 Flametube thermal paint pattern—diesel fuel

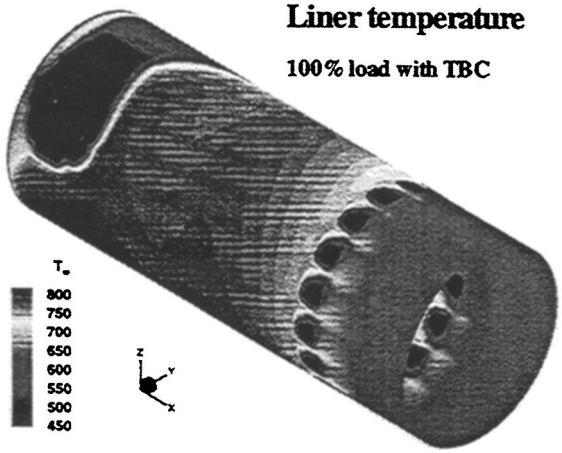

Fig. 9 Wall temperatures from computational fluid dynamics (CFD) calculation including reaction, methane

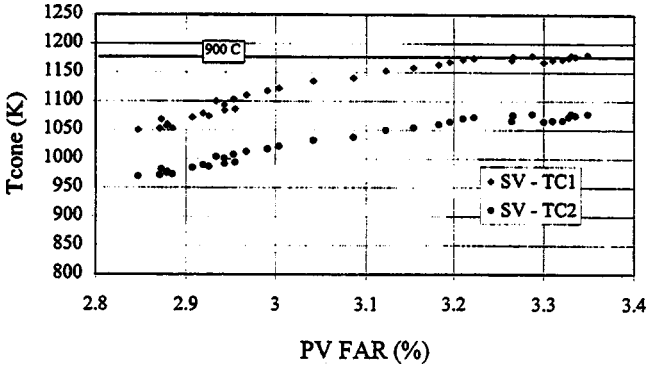

Fig. 10 Secondary venturi cone temperature

then has to deflect and in this region very high turbulence and intense combustion is achieved. A ''flame tongue'' originating from the swirling combustion flow can be seen in both the calculation and in the actual thermal paint test.

Secondary Venturi. The secondary venturi is covered on the outside with a TBC coating identical to the flametube internal coating. The actual heat pick-up for the secondary venturi due to heat transfer from the primary flame to the secondary venturi is rather low and below 10 K when coated. The secondary cone is, however, not coated and is subjected to high temperatures on the outside and is cooled by the outflowing fuel and air mixture.

Figure 10 shows measured temperatures in the secondary venturi (SV) as function of the primary venturi (PV) fuel/air ratio (FAR). The temperature is measured by two thermocouples (TC1 and 2) positioned between two hole rows in the perforated cone, 180 deg offset. The temperature difference is due to the swirling flow on the outside. The metal temperature is clearly dependent on the primary venturi FAR and a good fuel control system is needed for transient operation of the combustor. The engine is managed by a digital electronic control unit (DECU) which enables accurate and advanced control of the running conditions.

Computational Fluid Dynamics Calculations of Detailed Combustor Flow

Analysis of the secondary venturi cone wall temperatures led us to suspect an uneven distribution of cooling inside the cone. A reason for this could be an uneven flow distribution caused by the effect of blockages in the supply air. CFD analysis was carried out to examine the effect of such flow distributions. Calculations were performed with the CFX-TASC flow V.2.9 code using the standard $k-e$ turbulence model. The fluid was defined to be compressible for all calculations and a second-order discretisation scheme was applied. The complete model had 1.6 million grid nodes. The model was run with the uniform inlet conditions prescribed to the inlet of the secondary venturi, without swirl, although the model contained the complete geometry definition otherwise. The model was run without combustion. Two configurations were investigated: with venturi half-angles of five degrees then three degrees. The result of the three degree calculation is summarized in Fig. 11. It can be seen that even with the three-degree venturi a region of low velocity exists at the venturi wall, especially at the exit where the velocity is 20–30 m/s and the tendency towards separation is high. In the center the velocities are also lower and a region of reverse flow exists at the venturi exit before the cone.

A model was then run with the actual complete geometry, also without combustion and for the same two venturi angles. The result of the three-degree calculation is summarized in Fig. 12 for comparison with Fig. 11. In this case the tendency for separation at the wall was reduced. The nonuniform inlet conditions have

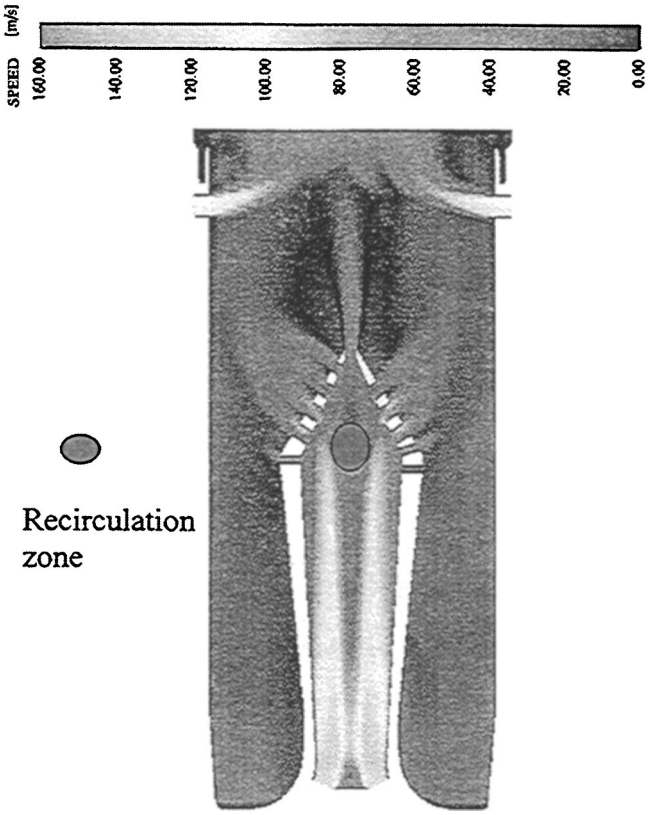

Fig. 11 Computational fluid dynamics (CFD) calculation with symmetrical inlet conditions

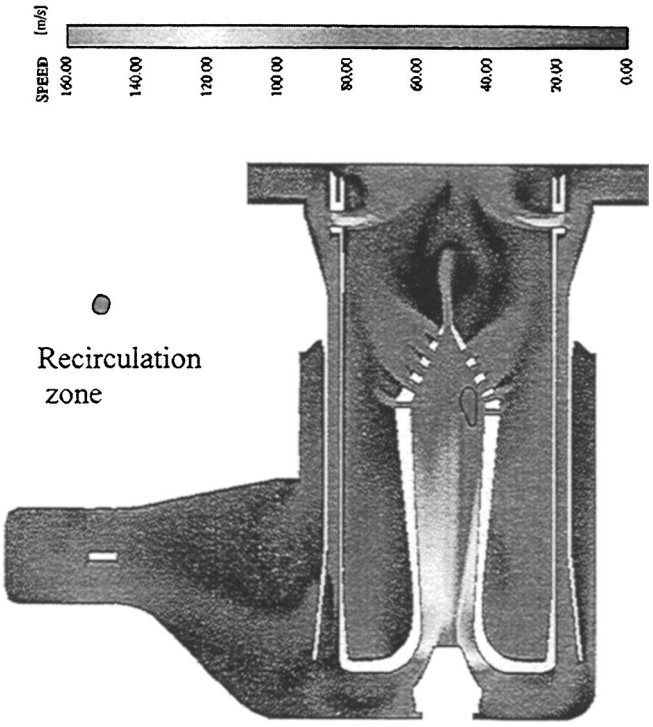

Fig. 12 Complete combustor computational fluid dynamics (CFD) analysis, swirl effect

two effects. There is a large blockage due to the presence of the primary venturi in the cooling channel and there is some residual swirl after the air has split to the primary and secondary venturis. The swirl component creates centrifugal forces, which reduce the tendency for separation on the walls of the diffuser. However, due to the inlet pressure gradient caused by the blockage effects, of both the fuel nozzle and of the primary venturi, a larger recirculation zone in the center at the venturi exit is noticed. To reduce the danger of this causing autoignition and to improve cooling of the cone by ensuring higher internal velocities a shorter venturi has been produced but not yet been analyzed. The key to clean flow in the venturis will, however, be controlled by the ability of making a fuel nozzle that produces as little disturbance to the flow in the inlet and throat region as possible.

Emissions Behavior

Testing has been conducted both in rigs and in the engine for gaseous emissions sampling and analysis. The bulk of the experiments and tests have been run with liquid fuel.

Figure 13 depicts the emission curves for an engine test covering the whole operating envelope of the engine. To understand this behavior it is necessary to examine the data in conjunction with the standard fuel split schedule in Fig. 2.

Two curves are shown, with the standard fuel split and a modified fuel split schedule. At idle the equivalence ratio is near stoichiometric and this gives acceptable CO emissions. As idle speed is a given mechanical speed independent of ambient conditions, the mixture can also burn rich which was the case for these tests. As load is increased, the secondary venturi is brought into operation with a fairly low equivalence ratio. This poses a problem for fuel burnout, which causes fuel fragments (UHC's) and CO in the exhaust gas if no other means are utilized (variable geometry, switching strategies). For the high power range, emissions of both NO_x and CO are reduced as the primary equivalence ratio is reduced and the secondary equivalence ratio is increased giving more favourable conditions for CO oxidation through OH. In general it will be beneficial for the combustor to run with as high secondary equivalence ratio as possible, limited by the flameholding characteristics of the primary venturi and the overall engine operating line, limited to a flame temperature of, say, $1950 \pm k$. For very low loads this will not be possible as the secondary equivalence ratio will still be too low to give realistic characteristic oxidation times for CO. This strategy can be seen in the figure. More fuel was directed to the secondary through the engine range except for idle and above 88 percent load where the fuel valve control posed a limit for changes in the distribution at that time. The results were, however, very good with near single-digit emissions of NO_x for liquid fuel at 16 bar. The NO_2/NO_x ratio

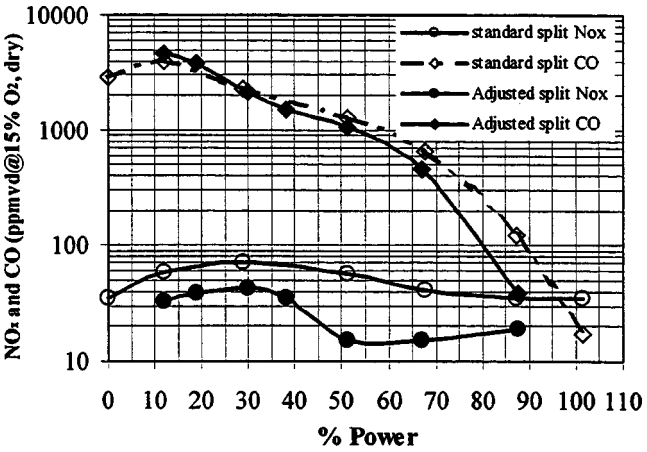

Fig. 13 Engine emission test results, diesel fuel

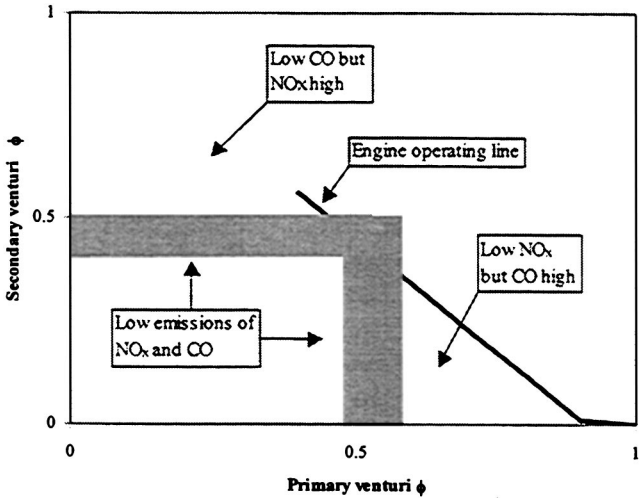

Fig. 14 Schematic view of low emissions range

proves to be inversely proportional to the load, low powers give high ratios (0.5) whereas high loads give ratios in the region of 0.1, in line with the findings of Røkke et al. [6].

Rig testing with natural gas and liquid fuel has revealed the same characteristics as the engine. Gas development has been challenging due to combustion generated pulsations. This can be controlled to very low levels using a stable venturi design (opening angle) and by minimizing flow disturbances to the venturi inlet. Decoupling of the fuel transport time and the natural frequencies of the system has also proved important.

Rig tests have also shown that the contribution from the two stages in terms of NO_x and CO is very dependent on the equivalence ratios of the two stages. Figure 14 shows this principle. Rig test have also revealed that there is a reburning effect of the two stages as the emissions of NO_x from the first stage is equal or more than that of the two stages when run at the same primary equivalence ratio. It should also be noted that gas and liquid operation at elevated pressure (10 bar) in rig has given single-digit NO_x levels for a narrow band of operating conditions.

Fuel injector development for mixture homogeneity (importance given for instance by [7]) has also played an important factor in the system development. Local hot spots caused by variations in FAR from inhomogenity causes higher local reaction temperatures and high NO_x production and contribution. This is still under development and is of particular importance for liquid fuel.

Lean Blow-Out Limits

The combustor does not have any diffusion flame pilot to support stability. This is done on purpose not to compromise on emissions.

Transient operation of the engine has necessitated accurate control of the combustor fuel schedule as inlet temperatures and lower equivalence ratios must be coped with. This has been achieved by the development of an intelligent transient control loop which ensures a near-constant blow-out margin during acceleration/deceleration by adjusting the primary fuel flow when the inlet temperature differs from steady state conditions. Overall combustor blow-out figures of 166 in AFR (Air to Fuel Ratio) have been achieved and recent configuration changes have given promise for figures in the region of 200 (AFR).

Summary and Conclusions

A new LPP combustor concept is described utilizing venturi premixers. The combustor architecture has been studied in rig and engine tests together with analytical studies and CFD modeling.

Venturi premixers can be utilized within safe operation for LPP combustion up to the pressure ratio utilized in this engine ($r = 17$). Venturi premixers offer the advantage of good mixing and atomization/evaporation behavior. Care must be taken to avoid separation in the diffuser region and it is of utmost importance that the venturi and fuel injector is regarded as a single mixing unit. Their performance and design cannot be separated.

No problems with autoignition have been experienced even for the arduous running conditions that have been used in the development program.

Heat transfer calculations for the flametube wall showed good agreement with thermal paint results of the flametube during engine tests. This is utilized further for cooling optimization.

Rig tests with instrumented secondary venturi cones revealed elevated material temperatures, these temperatures are dependent on the primary venturi equivalence ratio.

The full CFD calculation of the combustor revealed that very important information can get lost by running uncoupled calculations of the inner (inside flametube) and outer flow (cooling annulus) of the combustor. It also revealed that the venturi flow pattern can benefit from a slight swirl, giving a more even axial velocity field in the presence of a injector given that the pressure along the venturi centerline is not too low to cause flow reversal.

Emissions can be controlled to a low level with this combustion system and engine tests have shown 15 ppmvd of NO_x at elevated load with liquid fuel. As for most LPP systems this combustor also exhibits load dependent CO emission levels as the two-staged design does not give enough possibilities for keeping the reaction temperature within a narrow band of 200 K. Complexity and price precludes the use of multiple burner arrangements for optimum temperature control for engines in this power range.

Further developments of such a concept should include:

- exotic heat resistant materials in the venturi cone to maintain structural strength over service time in an oxidizing atmosphere;
- possibilities of an active fuel switching/staging system to keep within the CO and NO_x ''window of opportunity'' in terms of temperature. Preliminary tests have shown a good effect of this approach; and
- optimization of a venturi/injector mixer to allow homogeneous mixing conditions over the engine operating range.

Acknowledgments

The authors would like to acknowledge the CFD modeling and work of I. R. Gran for the thermal behavior of the flametube and the detailed combustion chemistry modeling. Furthermore, the CFD work utilizing Tascflow by T. Ripplinger and N. Zarzalis of MTU.

Nomenclature

FAR = fuel-to-air ratio (mass)
d = diameter (m)
p = static pressure (Pa)
r = pressure ratio
T = temperature (K)
t = time (s)
u_s = slip velocity (m/s)

Greek

ϕ = equivalence ratio
λ = evaporation constant (m^2/s)
τ = ignition delay time (ms)
ρ = density (kg/m^3)

References

[1] Nicol, D. G., Malte, P. C., and Steele, R. C., 1994, ''Simplified Models for NO_x production Rates in Lean-Premixed Combustion,'' ASME paper 94-GT-432.
[2] Correa, S. M., 1992, ''A Review of NO_x Formation Under Gas Turbine Combustion Conditions,'' Combust. Sci. Technol., **87**, pp. 329–362.
[3] Spadaccini, L. J., and TeVelde, J. A., 1982, ''Autoignition Characteristics of Aircraft-Type Fuels,'' Combust. Flame, **46**, pp. 283–300.
[4] Ripplinger, T., Zarzalis, N., Meikis, G., Hassa, C., and Brandt, M., 1999, ''NO_x Reduction by Lean Premixed Prevaporized Combustion,'' NATO-RTO/MP/14-paper #7.
[5] Gran, I. R., and Magnussen, B. F., 1996, ''A Numerical Study of a Bluff-Body Stabilised Diffusion Flame. Part 2, Influence on Combustion Modelling and Finite Rate Chemistry,'' Combust. Sci. Technol., **19**, pp. 191–217.
[6] Røkke, N. A., Hustad, J. E., and Berg, S, 1993, ''Pollutant Emissions From Gas Fired Turbine Engines in Offshore Practice–Measurements and Scaling,'' ASME paper 93-GT-170.
[7] Leonard, G., and Stegmaier, J., 1993, ''Development of an Aeroderivative Gas Turbine Dry Low Emissions Combustion System,'' ASME paper 93-GT-288.

M. Y. Leong[1]
Graduate Researcher

C. S. Smugeresky
Graduate Researcher

V. G. McDonell
Senior Research Scientist

G. S. Samuelsen[2]
Professor

UCI Combustion Laboratory
University of California
Irvine, CA 92697-3550

Rapid Liquid Fuel Mixing for Lean-Burning Combustors: Low-Power Performance

Designers of advanced gas turbine combustors are considering lean direct injection strategies to achieve low NO_x emission levels. In the present study, the performance of a multipoint radial airblast fuel injector Lean Burn injector (LBI) is explored for various conditions that target low-power gas turbine engine operation. Reacting tests were conducted in a model can combustor at 4 and 6.6 atm, and at a dome air preheat temperature of 533 K, using Jet-A as the liquid fuel. Emissions measurements were made at equivalence ratios between 0.37 and 0.65. The pressure drop across the airblast injector holes was maintained at 3 and 7–8 percent. The results indicate that the LBI performance for the conditions considered is not sufficiently predicted by existing emissions correlations. In addition, NO_x performance is impacted by atomizing air flows, suggesting that droplet size is critical even at the expense of penetration to the wall opposite the injector. The results provide a baseline from which to optimize the performance of the LBI for low-power operation. [DOI: 10.1115/1.1362318]

Introduction

The goal of the next generation of gas turbine combustors is to reduce NO_x emissions to meet regulatory levels that cannot be attained with present-day conventional combustors. In conventional gas turbine combustors, thermal NO_x is one of the major contributors to overall NO_x production. Thus, the reduction of NO_x is mainly accomplished by lowering the reaction temperature, which itself can be achieved by operating the combustor under fuel-lean conditions. The attainment of a lower level of NO_x production by these lean-burning, advanced gas turbine combustors primarily depends on the preparation of the fuel-air mixture by fuel injectors. NO_x production increases with fuel-air unmixedness in both spatial (Lyons [1]) and temporal domains (Fric [2]). Although the mixture may be overall lean, a wide distribution of local equivalence ratios that bracket the stoichiometric condition will encourage thermal NO_x production. These lean-burning, low-NO_x combustion concepts, though, are not without disadvantages. For example, operating near the lean flammability limit runs the risk of combustor blow out or combustor instability. In addition, the levels of carbon monoxide (CO), unburned hydrocarbons (UHC), and air toxics (e.g., aldehydes) may increase to unacceptable levels. Low-NO_x combustion methods that burn fuel-lean must overcome these challenges in order to become a viable technology.

One low-NO_x lean combustion concept—the lean-premixed-prevaporized (LPP) combustor—involves the introduction of a uniformly lean mixture of fuel vapor and air into the dome region of a combustor. Low NO_x levels can be achieved by burning the fuel in its vapor phase rather than as droplets (Lefebvre [3]). The low-NO_x potential of LPP combustion has led to studies characterizing the effect of mixing on combustion instability and emissions (e.g., Shih et al. [4]; Dutta et al. [5]). However, the premixed state of the fuel and air makes LPP combustion prone to autoignition and flashback. In addition, the stability limits of the LPP combustor tend to fall in a narrow range, and ignition of the mixture may be difficult.

Another fuel preparation concept for lean-burning combustors is lean direct injection (LDI), in which fuel is injected immediately upstream of the reaction zone, thereby reducing the potential for autoignition and allowing for smaller overall combustion system dimensions. The low-NO_x potential of the LDI has mainly been demonstrated for gaseous fuel injection (Tacina, [6]), but the challenges of atomizing and vaporizing liquid fuel sufficiently for low-NO_x, LDI combustion have been met with the lean burn injector (LBI). The LBI nozzle prepares a vaporized fuel-air mixture (as in the LPP concept) for combustion in the confines of a contracting mixing section. Developed by Shaffar, Sowa, and Samuelsen [7], the LBI assembly consists of a fuel tube centerbody, swirler, and venturi mixing section that is also referred to as a ''quarl'' (Fig. 1). Rapid mixing of liquid fuel and air is achieved by injecting spray jets of fuel radially from the center body, into a swirling crossflow of air. The sprays are formed by airblast atomization, which allows for higher fuel turndown ratios compared with pressure-swirl atomizers. The fuel sprays mix with the swirling air in the contracting venturi section. The fuel-air mixture is subsequently ejected out of the venturi section and into the primary dome of the combustor. The swirling component in the fuel-air mixture induces the recirculation zone that anchors the combustion process. As noted by Shaffar and Samuelsen [8], combustion stabilizes downstream of the venturi throat, which also helps to prevent flashback. The quarl section, serving as both a fuel-air premixing section and as a flame arrestor, is the main novel feature of the LBI injector assembly.

The LBI concept can be applied to aeroengine and industrial engine, and to conventional as well as to the next generation of low-NO_x combustors. However, the thrust of the current development involves investigating the performance of the LBI for a low-NO_x aeroengine application. Shaffar and Samuelsen [8] demonstrated low NO_x performance with NO_x EI less than 9 for a condition of 5 atm. 700 K preheat, between $\phi=0.45–0.70$. To prove the potential utility and versatility of the injector across the entire aeroengine duty cycle, a baseline survey of LBI performance must be established. The objective of the present study is to evaluate the robustness of the LBI design for low-NO_x combustion, primarily at low-power conditions where low preheat temperatures and pressures may not fully atomize and vaporize drops before the mixture exits the quarl mixing section. The effect of spray atomi-

[1]Presently at United Technologies, Research Center, East Hartford, CT 06188.
[2]Corresponding author: gss@uci.edu

Contributed by the International Gas Turbine Institute (IGTI) of THE AMERICAN SOCIETY OF MECHANICAL ENGINEERS for publication in the ASME JOURNAL OF ENGINEERING FOR GAS TURBINES AND POWER. Paper presented at the International Gas Turbine and Aeroengine Congress and Exhibition, Munich, Germany, May 8–11, 2000; Paper No. 00-GT-116. Manuscript received by IGTI Feb. 2000; final revision received by ASME Headquarters Jan. 2001. Associate Editor: M. Magnolet.

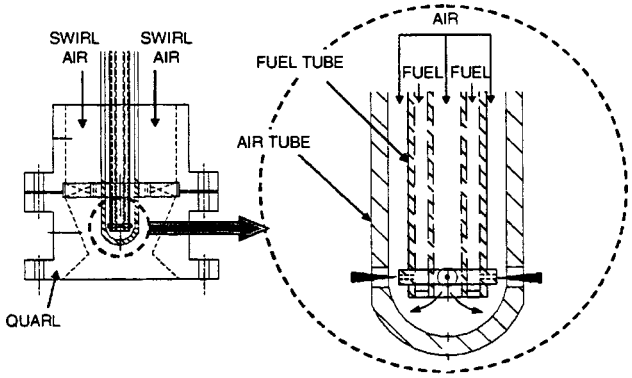

Fig. 1 LBI injector, swirler, and quarl assembly

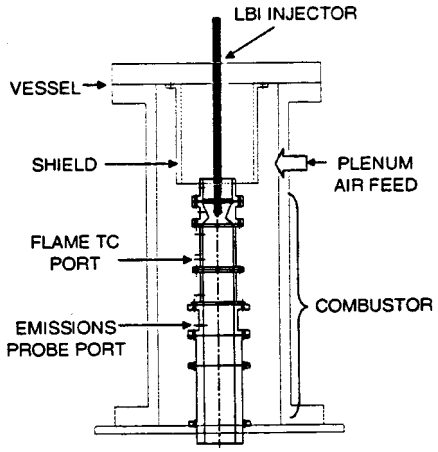

Fig. 2 LBI injector, combustor in elevated pressure facility

zation on combustion performance is evaluated by varying the atomizing air supply to the injector. Emissions measurements are primarily used to assess combustion performance in terms of low-NO_x and high combustion efficiency, and are compared with the predictions of existing correlations.

Experiment

LBI Injector. The LBI assembly (Fig. 1) consists of an eight-port injector, a production cast swirler with a swirl number of 2.2, and a quarl. The LBI injector used in the combustion tests employs the same design used by Shaffar and Samuelsen [8]. The injection lance is comprised of a fuel tube and an outer air tube. The fuel tube itself is comprised of two concentric tubes with the tip of the annular region welded shut so that fuel can only exit through eight holes that are 0.66 mm diameters each, drilled radially through the tube and an outer ring welded on to the outside of the tube. The atomizing air (9–15 percent of the mass flow of dome air) flows through the center of the fuel tube as well as through the annulus formed by the outer fuel tube and the inner air tube. The airblast-atomized spray emerges from holes drilled in the outer air tube. The total effective area of all eight air orifices is 36.1 mm^2. The injection point occurs 19.1 mm downstream from the swirler vanes, and 18.5 mm upstream of the quarl contraction.

The main difference between the present injector and the injector used by Shaffar and Samuelsen lies in the dimension of the fuel hole diameter, which was enlarged to preclude potential coking issues for the range of operating conditions considered. The enlargement does not impact the basic behavior of the spray as indicated by the study of Lorenzetto and Lefebvre [9], which found that initial fuel stream diameter has little effect on the spray behavior of low viscosity liquids atomized by plain-jet airblast atomizers.

Elevated Pressure Facility for Combustion Tests. The LBI combustor tests are conducted in a pressure facility designed primarily for reacting experiments (Fig. 2). The LBI injector is installed in a model 80 mm ID can combustor assembly that is downward fired. The combustor is bolted to the bottom flange of the pressure vessel. The cylindrical vessel has an inside diameter of 0.30 m and a height of 0.86 m. Four 152 mm diameter ports along the circumference of the vessel provide optical access as well as an opening for the insertion of an emissions probe. Smaller ports are also available in the vessel wall for thermocouples and pressure taps. The top of the vessel is a blind flange through which the LBI injector tube passes. The injection tube is secured to the vessel after it is inserted into the combustor assembly. The products of this down-fired combustion rig pass through a water quench section before exhausting. Vessel pressure is regulated by a control valve downstream of the water quench system.

The facility utilizes two separately metered air circuits—a high flow line to feed the plenum of the pressure vessel, and a low flow line to supply the atomizing air. The air flows are controlled by a system of thermal mass flow meters and electropneumatic control valves. Both air circuits can be heated by electric circulation heaters. However, in this experiment, the injector atomizing air was not heated in order to establish a baseline condition for future tests involving the effect of airblast air temperature on fuel-air mixing and combustion performance.

Measurements. Emissions samples were obtained 271 mm downstream of the quarl throat. At this point, the calculated bulk residence time of the combustion products is 8 msec. The emissions sampling system utilized the pressure differential between the experiment and the exhaust at atmospheric pressure to drive the sample through the probe. A multiport water-cooled probe 12.7 mm in diameter was designed to yield area-weighted emissions across the combustor can.

The sampling procedure involved individual, independent measurement of emissions at each port. The gas sample was sent through an ice water bath to condense the water in preparation for the analyzers, which measure dry gas sample concentrations. The residence time of the sample from the probe to the ice bath was approximately 1 sec. Any condensate forming in this section of the line was filtered at the water dropout station immediately downstream of the ice water bath. The possibility of NO_2 dissolving in the condensate existed, but the loss was presumed minimal because of the short residence time that the sample gases were in contact with the water.

With the sample gas venting to an exhaust hood, a pump in a sampling unit (Horiba ES-510) drew a slip stream of gas. The sample was then split and sent to two units for analysis. The total unburned hydrocarbon concentrations were measured by a flame ionization analyzer (Horiba FIA-510) while CO, CO_2, O_2, and NO_x were measured by a portable gas analyzer (Horiba PG-250). The portable gas analyzer employs non-dispersive infrared (NDIR) methods to measure CO and CO_2, a galvanic cell to measure O_2, and chemiluminescence to measure NO_x. The uncertainty associated with the analyzers is within 1 percent of the full scale reading.

The analog signals from the emissions analyzers were collected through an 8-channel, 16-bit analog input board (National Instruments FP-AI-110), which was connected to a computer through an RS-485 network interface board (National Instruments FP-1001). A routine written in the software program that accompanied the boards (LABVIEW 5.0, National Instruments) recorded and processed the signals. The signals from the analyzers were sampled at a rate of 2 Hz, for a duration of 50 sec. The mean emissions data exhibited a stationary temporal distribution. Temporal signal fluctuations only contributed up to 1 percent of the overall uncertainty.

Table 1 Operating conditions for the LBI low-power tests

Case name	P_3 (kPa)	m_{air} (kg/sec)	$m_{airblast}$ (kg/sec)	$\Delta R_{airblast}$ (%)
4 atm/8 DP	412	0.15	0.021	8
4 atm/3 DP	412	0.15	0.014	3
6.6 atm/7 DP	670	0.24	0.035	7
6.6 atm/3 DP	670	0.24	0.023	3

Table 2 Lean blow-out levels for the various tests

Condition	LBO
4 atm/8 DP	0.42
4 atm/3 DP	0.41
6.6 atm/7 DP	0.43
6.6 atm/3 DP	0.36

The computerized data acquisition system also sampled thermocouple readings at the same rate. Type-K chromel-alumel thermocouples were used to measure the temperature of the preheated dome air prior to its passage through the swirler, as well as the temperatures of the nozzle air, fuel, and combustor skin. A type-B platinum-rhodium thermocouple monitored the bulk reaction temperature 106 mm downstream from the quarl throat. The shielded 1.59 mm OD type-B thermocouple was also sheathed with a 3.18 mm OD alumina ceramic cover to protect the thermocouple from the harsh turbulent and reacting environment. The reported temperatures were corrected for radiation heat loss. The uncertainty associated with the temperature measurements were as high as 2 percent of the corrected values.

Test Matrix. To assess the utility of the LBI injector in aeroengine applications, the injector is tested at practical conditions. The flow rates in these tests are comparable to the low-power regime of ground idle and subsonic cruise conditions. The four cases and their main operating parameters are listed in Table 1. Two ambient pressure cases were tested: 412 kPa (4 atm) and 670 kPa (6.6 atm). The overall mass flow of air m_{air} through the combustor, which is the sum of the swirl and atomizing air mass flow rates, was determined by the combustor pressure drop, which was maintained at 4 percent. For each ambient pressure condition, the atomizing air flow was set at two pressure drops that bracketed the typical range of air pressure drops available in aeroengine combustors (4–7 percent, according to Lefebvre [3]). The airblast velocity remained constant at a given pressure drop condition, for different ambient pressures.

While the overall air mass flow rate was kept constant, the fuel-air equivalence ratio was changed by varying the fuel flow rate of Jet-A (Unocal). Measurements were begun at an equivalence ratio between 0.55 and 0.65. Emissions concentrations were measured after lowering the equivalence ratio in increments of 0.05. After attaining the desired condition, the system was given 5–10 min to thermally stabilize before measurements were obtained. For all of the tests, a fuel air ϕ as low as 0.45 was reached. After attaining the $\phi=0.45$ level, the equivalence ratio was decreased further by increments of 0.01 until LBO occurred. In three of the cases. LBO occurred between 0.41 and 0.43 (see Table 2). At the 6.6 atm/3 percent dp condition, LBO occurred at $\phi=0.36$.

Results and Discussion

Combustion Product Uniformity. A radial profile of emissions samples was obtained for each case to yield an area-weighted average. The area-weighted average CO_2 and O_2 concentrations were compared with their respective equilibrium values calculated at corresponding equivalence ratio conditions. The emissions measured for the 4 atm cases agreed well to within 2 percent of predicted values, whereas the emissions for the 6.6 atm cases varied up to 15 percent of predicted values.

Radial profiles for the measured species concentration samples are presented in Fig. 3 for the 4 atm/8 percent dp case. The uniform radial profiles of CO_2 and O_2 seen in this case at the different equivalence ratios were also typical of the other three cases.

The CO, UHC, and NO_x radial concentration profiles in this 4 atm/8 percent dp case were also uniform at equivalence ratios ranging from 0.50 to 0.65. The magnitude of the profiles decreased as ϕ decreased from 0.65 to 0.50. At $\phi=0.45$, the leanest equivalence ratio that was measured in this case, the radial profile was uniform for NO_x, but nonuniform for the CO and UHC emissions.

Figure 4 presents a condensed depiction of the radial profile uniformity, as represented by the standard deviation of the concentrations measured at each condition. Only the profiles for CO_2, NO_x, and CO are shown for clarity, since the trends for O_2 mirrored those for CO_2, and since the trends for UHC closely followed those for CO.

The standard deviations for each test case are plotted with respect to equivalence ratio. Lower standard deviation values correspond to a more uniform radial concentration profile. The shape of the curve indicates how the degree of uniformity changes with respect to equivalence ratio.

The standard deviation values for the 4 atm/8 percent dp case summarize the observations made in Fig. 3 for the case. For example, uniform CO_2 profiles at each equivalence ratio, observed in Fig. 3, are represented by the low standard deviation values in Fig. 4. The small degree of variation in the curve for CO_2 reflects the uniformity in profiles at the different ϕ. The nonuniform CO profile obtained at $\phi=0.45$ in this case (see Fig. 3) is reflected by a high standard deviation value at that equivalence ratio (see Fig. 4).

In all of the cases tested, the radial profile of concentrations became more uniform as leaner equivalence ratios were attained. Two exceptions to this point are found in the CO profile measurement. As discussed earlier, the 4 atm/8 percent dp case produced a highly nonuniform CO profile at the $\phi=0.45$ condition. Likewise, the 6.6 atm/3 percent dp condition produced a similar result near the lean blow-out limit, at $\phi=0.37$. Similar high CO standard deviation values in the 4 atm/3 percent dp and 6.6 atm/7 percent dp cases would probably have been achieved if emissions measurements had been made near the LBO limit.

Bulk reaction temperatures were measured nearly halfway between the quarl throat and the emissions probe, where the thermocouple protruded 25 mm into the combusting flow. The temperatures shown in Fig. 5 represent time-averaged values across the sampling duration of emissions at the particular equivalence ratio condition.

At a given equivalence ratio, the bulk reaction temperature should be the same. Figure 5, however, shows some deviation in the measured temperatures, particularly for the equivalence ratios from 0.45 to 0.55. The 4 atm/8 percent dp case produced temperatures that were significantly higher than those from the other 3 cases, which amongst themselves registered temperatures within an experimental uncertainty of ± 20 K. The differences in reaction temperature between the cases show that, though uniform flow may have been achieved at the plane of the emissions probe, uniform flow may not have yet been attained at the plane of the thermocouple.

Combustion Performance. Two parameters used to assess combustion performance are the combustion efficiency and the production of pollutant emissions. The gas turbine combustor should operate at a high efficiency while forming minimal levels of pollutants.

The combustion efficiency η, calculated from the CO and UHC emissions, indicates the degree to which complete combustion products is attained. As seen in Fig. 6, the LBI injector combustion efficiency is above 99.90 percent for every condition except

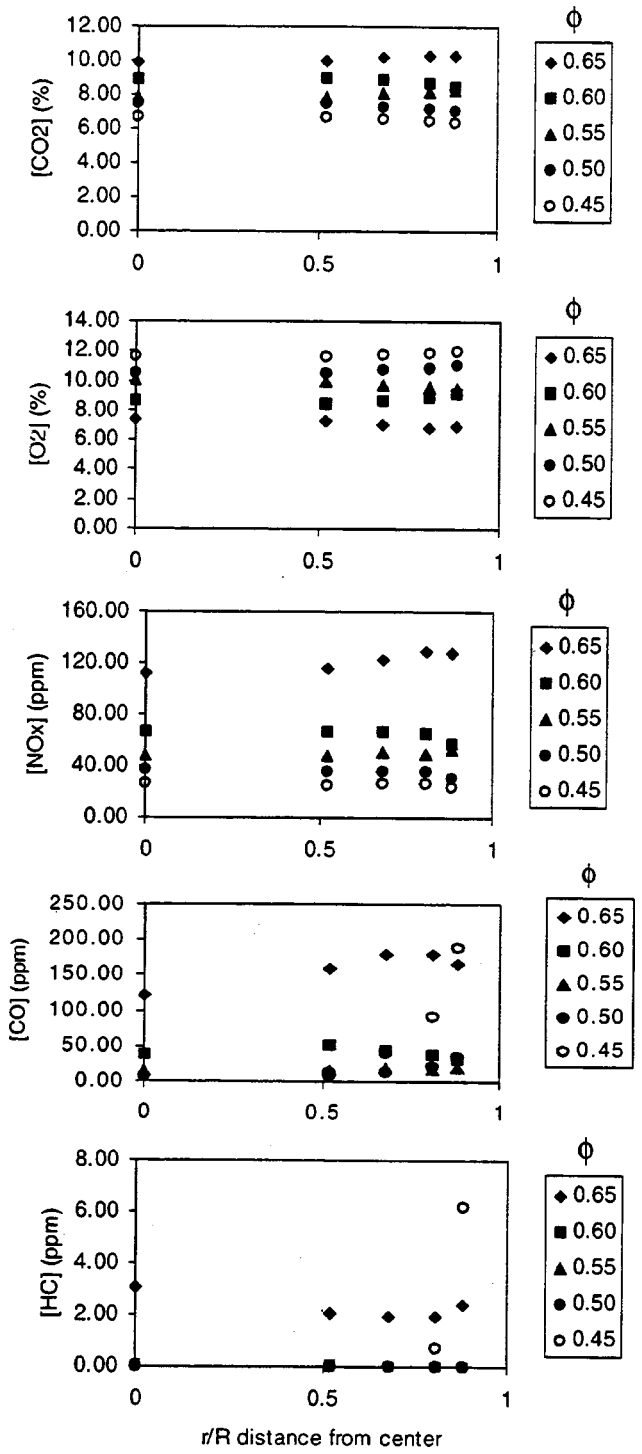

Fig. 3 Radial emissions profile for the 4 atm/8 percent DP case

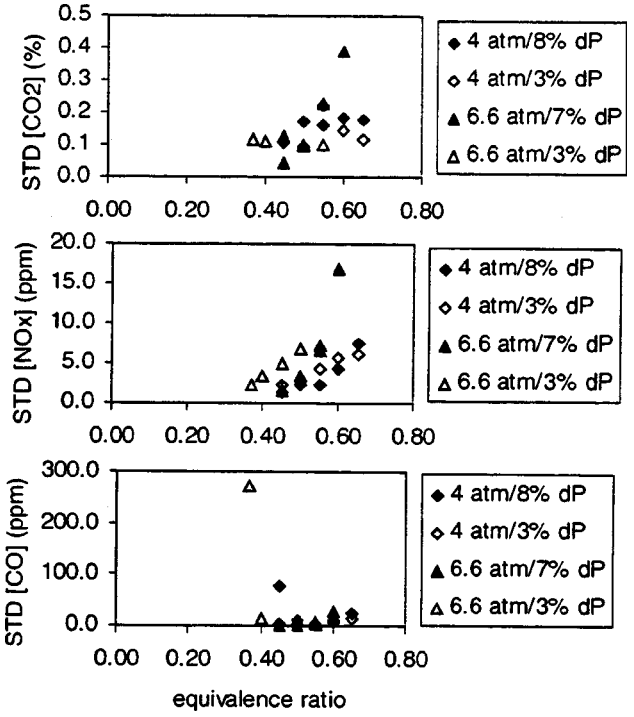

Fig. 4 Standard deviation values indicating radial profile uniformity at different equivalence ratios

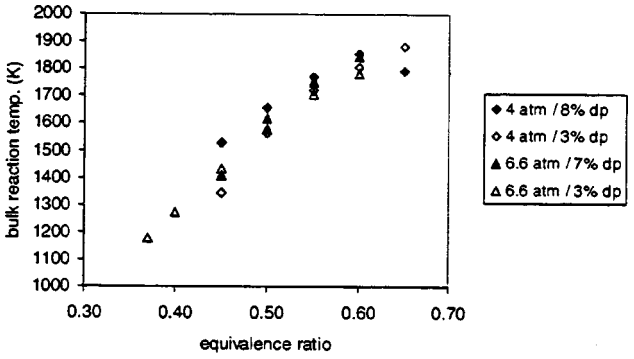

Fig. 5 Bulk temperature measured 106 mm downstream of quarl throat

the 6.6 atm/3 percent dp case where emissions obtained at $\phi=0.37$ near the LBO limit led to a 99.57 percent efficiency (not shown in the figure). In general, at each pressure condition, higher efficiencies are obtained for the 7–8 percent airblast pressure drop condition than for the corresponding 3 percent pressure drop case.

Pollutant emissions are often represented by emission indices (EI), which cast the volumetric measurements of the emissions onto a mass basis. Figure 7 shows the NO_x EI across the range of equivalence ratios tested in each case. The NO_x EI measured are all below 5, which can be attributed to the low reaction temperatures seen in Fig. 5. With overall reaction temperatures reaching at most 1800 K, the steep exponential NO_x formation rate associated with the thermal mechanism is avoided (Samuelsen [10]; Lefebvre [3]).

For a given airblast pressure drop, a direct comparison can also be made between different ambient pressure conditions because the ALRs were also kept constant at each equivalence ratio. In cases with similar airblast pressure drops, an increase in ambient pressure generally led to an increase in the NO_x EI.

Existing emissions correlations were compared with measured NO_x and CO concentrations to determine their applicability to the LBI combustion process. NO_x and CO correlations developed by Lefebvre [11] and by Rizk and Mongia [12] were applied. Lefebvre's correlations are primarily used for conventional spray combustors, but can be applied to LPP combustion with a suitable temperature variable substitution. The correlations of Rizk and Mongia [12] include the effects of spray evaporation and mixing on combustion emissions production.

When applied to the LBI data, the ''spray version'' of the Lefebvre [11] correlation and the Rizk and Mongia [12] correlations produced NO_x and CO trends that were inversely proportional to

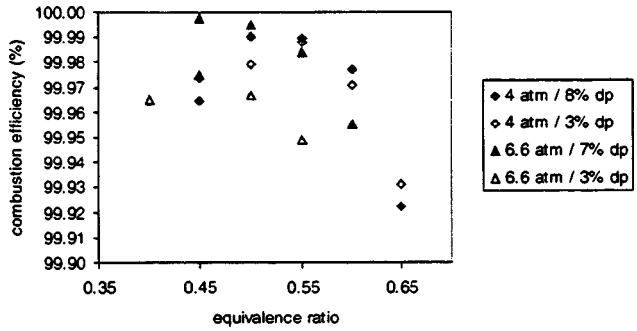

Fig. 6 LBI combustion efficiencies at the various operating conditions

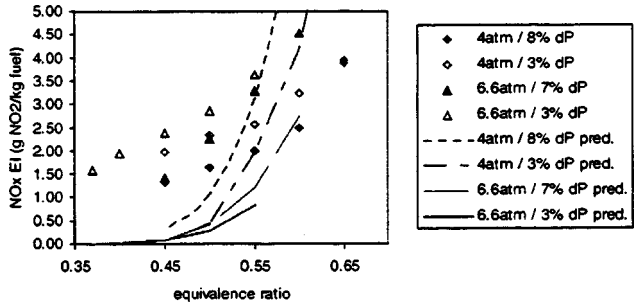

Fig. 7 Spatially averaged NO_x emission indices overlaid with LPP predictions from Lefebvre [10]

the measured values. The ''LPP version'' of the Lefebvre correlation predicted NO_x EI and CO EI trends that were similar to the measured data, but were also unsatisfactory in their accuracy.

The NO_x curves predicted by the ''LPP version'' of the Lefebvre correlation, shown overlaid on the NO_x EI plot in Fig. 7, illustrate the lack of fit to the data. As seen in Fig. 7, the curves follow the decreasing NO_x with decreasing ϕ data trend. However, the NO_x EI curve for the 7–8 percent airblast dp cases are higher than the corresponding 3 percent cases for each pressure condition. For the constant overall air flow rates at the 4 and 6.6 atm cases, the predicted curves should coincide for these pressure conditions. In addition, the 4 atm cases are predicted to produce higher NO_x EI than the 6.6 atm cases. The main parameters that vary in the Lefebvre correlation are pressure and the primary zone temperature, and since the measured reaction temperatures, depicted in Fig. 5, were already shown to deviate at each ϕ condition, the NO_x EI predictions were also similarly affected. In any case, this insufficient fit by the LPP-based Lefebvre correlation and by the spray combustor model of Rizk and Mongia points toward the need to measure and model the fuel-air mixture characteristics in and immediately downstream of the quarl so that the model can accommodate the mixing features of the LBI injector.

Spray Atomization and Penetration. To explain the combustion performance in relation to fuel atomization and mixing, spray droplet size and penetration correlations were utilized. The droplet size of interest in combusting flows is D_{32}, which represents the ratio of the total volume to the total surface area of the spray droplets. The D_{32} values of the sprays produced in this experiment were calculated using the Lorenzetto and Lefebvre [9] correlation for plain-jet airblast atomizers, which according to Shaffar and Samuelsen [8] satisfactorily predicted the droplet size of sprays from the LBI injector.

Figure 8 shows the predicted droplet sizes for the conditions tested, as well as for the LBO limits. The similar D_{32} values obtained at the same airblast pressure drop conditions reflect the similar airblast air to liquid mass flow ratios (ALR) used in these cases.

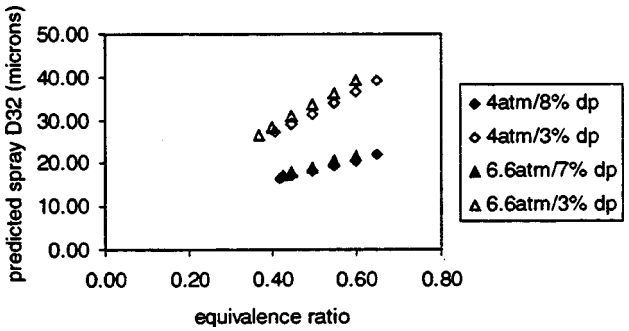

Fig. 8 Droplet D_{32} as predicted by the Lorenzetto and Lefebvre correlation [9]

As the fuel flow is lowered to decrease ϕ, the ALR increases. Higher airblast pressure drops, which increase the relative velocities between the atomizing air and fuel stream also lead to higher ALRs. In airblast sprays higher ALRs result in smaller D_{32} (Lefebvre [13]). Smaller droplets vaporize faster than larger droplets, resulting in faster fuel vapor mixing with air. Thus, at higher airblast pressure drops, one expects lower NO_x emissions resulting from smaller droplet sizes, as the data in Fig. 7 depict. Risk and Lefebvre [14] also observed this relationship between decreasing droplet size and lower NO_x emissions in their study.

In relation to the uniformity of the emission fields, decreasing D_{32} values corresponded to increasingly uniform emissions fields at lower equivalence ratios up until the point when LBO is reached (see Fig. 4). The higher combustion efficiencies obtained with increased airblast pressure drop also correlated to the smaller droplet D_{32} values that occur here at the lower ϕ (see Fig. 6).

Despite the small droplet D_{32} produced by airblast atomization, the conditions of the tests did not induce full vaporization of the spray by the quarl exit plane. The droplet evaporation times calculated for the given operating conditions and droplet sizes were at least four times greater than the calculated residence time of the spray from the point of injection to the quarl exit (0.75 msec), suggesting that droplets persisted in the dome region.

The penetration of the spray into the swirling dome air can be predicted by a modified correlation describing the maximal spray surface trajectory into the crossflow. Leong et al. [15] derived a correlation from images captured, in an experiment modeled after the LBI hardware, of a single spray jet injected into a uniform crossflow. Although the trajectory analysis neither accounts for the highly nonuniform velocity profile in the quarl contraction nor for droplet vaporization, the correlation can give a general estimate of spray penetration into the quarl.

In the spray correlation of Leong et al. [15], images were obtained at ambient pressures of 1, 3, and 5 atm, at different airblast pressure drops. The trajectory of maximum penetration was described by an equation that incorporated a jet-to-crossflow momentum-flux ratio. For a single phase jet, the momentum-flux ratio is clearly defined, but for a two-phase flow, such as the airblast spray jet, the momentum-flux ratio must incorporate the momentum of both liquid and airblast air streams. The following definition was developed in the 1998 work to describe the two-phase momentum-flux ratio q_2:

$$q_2 = \{[(\rho V^2 A)_{\text{fuel}} + (\rho V^2 A)_{\text{airblast}}]/A_{\text{jet}}\}/(\rho V^2)_{\text{crossflow}}, \quad (1)$$

where A_{airblast} is the annular area corresponding to A_{jet} minus A_{fuel}, and $V_{\text{crossflow}}$ corresponds to the bulk crossflow velocity at the point of injection. The derived correlation described the upper surface trajectory well at the 3 atm case, but underpredicted the spray trajectories at the 1 atm condition, and overpredicted the trajectories at the 5 atm condition.

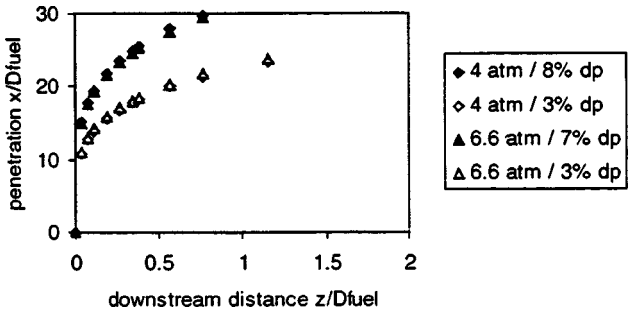

Fig. 9 Upper spray penetration predicted by modified correlation of Leong et al. [15]

One reason for the insufficient fit lies in the lack of a term to account for the atomization quality of the spray. Adding the factor (D_{32}/D_{fuel}) to the curve fit of Leong et al. [15] to account for the droplet size greatly improved the correlation. A least squares analysis performed with the additional factor resulted in the following curve fit which describes the upper surface penetration x/D_{fuel}:

$$x/D_{\text{fuel}} = (A1)*q_2^{A2}*(z/D_{\text{fuel}})^{A3}*(D_{32}/D_{\text{fuel}})^{A4}, \qquad (2)$$

where z/D_{fuel} represents the downstream distance, and constants $A1=13.8$, $A2=0.67$, $A3=0.22$, and $A4=0.39$.

The q_2 values ranged between 28–29 for the 7–8 percent airblast pressure drop cases, and between 12–13 for the 3 percent dp cases. Varying the liquid fuel flow to achieve different equivalence ratios does not significantly impact the value of q_2. The result of applying the modified correlations of Leong et al. using the q_2 values for the present test conditions is shown in Fig. 9.

At the point of spray injection, the distance between the LBI injection tube to the quarl wall is 16 mm. Furthermore, the continued contraction of the quarl section narrows the gap between the injector and the quarl wall. Thus, to avoid wall impingement, the spray trajectory should, at a minimum, penetrate no farther than $x/D_{\text{fuel}}=27$. The plot in Fig. 9 shows that all of the cases produce sprays that can impinge on the quarl wall. The 3 percent airblast dp sprays reveal relatively more bending into the cross flow with a reduced possibility of quarl impingement.

The calculated time that it would take for the spray to travel the distance from the injection point to the quarl wall, based on the bulk relative velocity of the droplets, varies from 0.14 to 0.23 msec, which is an order of magnitude less than the estimated total vaporization time of the droplets. This suggests that wall impingement most likely occurs, with the droplets either flash vaporizing upon collision with the wall, or possibly reatomizing after the impacted fluid shears off the lip of the quarl throat.

Summary and Conclusions

The LBI injector, which combines the direct injection principle with a short mixing section, was tested under various ambient pressures and with different atomizing air flows to assess its performance at low-power engine conditions. Radial profiles of species concentrations were generally uniform, with increasing spatial uniformity occurring as leaner equivalence ratios were attained, up until a point near lean blow out.

The atomization quality of the spray is primarily affected by the pressure drop of the atomizing air as well as the atomizing air to liquid mass flow ratio (ALR). A high airblast pressure drop (7–8 percent) and a high ALR (achieved in this experiment at leaner equivalence ratios), correspond to a decrease in D_{32}. This in turn produces a lower NO_x EI and higher combustion efficiencies. The improvement continues up to an equivalence ratio in the near vicinity of lean blow out. Despite achieving finer droplets, it is probable that the spray droplets persist in the flow at the relatively low air preheat temperature associated with low power operation.

We conclude the following.

1 The LBI is an attractive strategy for the introduction of fuel and the promotion of rapid mixing. At low power conditions, attention must be directed to the identification of design and operation parameters that minimize (and preclude) the penetration of liquid fuel to the quarl wall.

2 The crossflow injection of evaporating droplets presents novel challenges for existing penetration and emissions correlations. The effects of pressure, air preheat, initial spray characteristics (e.g., size distribution, component of swirl), atomizing air properties, and fuel properties), and secondary atomization have particular significance in crossflow configurations.

Acknowledgments

The authors would like to acknowledge the following people for their assistance with the LBI experiment: S. W. Shaffar for the design of the emissions probe and for discussions regarding the LBI operation and R.L. Hack, J. Auckland, and R. Pessa for their help with integrating the experiment into the high pressure facility. This research program was funded by the NASA John H. Glenn Research Center at Lewis Field under Contract No. NCC3-412, with R. R. Tacina and J. D. Holdeman serving as program monitors.

Nomenclature

ALR = airblast air to liquid mass flow ratio
D_{32} = total droplet volume to total droplet surface area ratio
EI = emission index, (g emission)/(kg fuel)
LBO = equivalence ratio at which lean blow-out occurs
q_2 = two-phase jet to crossflow momentum-flux ratio
ϕ = fuel-air equivalence ratio

References

[1] Lyons, V. J., 1981, ''Fuel/Air Nonuniformity—Effect on Nitric Oxide Emissions,'' AIAA J., **20**, pp. 660–665.
[2] Fric, T. F., 1993, ''Effects of Fuel-Air Unmixedness on NO_x Emissions,'' J. Propul. Power , **9**, pp. 708–713.
[3] Lefebvre, A. H., 1999, *Gas Turbine Combustion*, 2nd ed., Taylor and Francis, Philadelphia, PA.
[4] Shih, W. P., Lee, J. G., and Santavicca, D. A., 1996, ''Stability and Emissions Characteristics of a Lean Premixed Gas Turbine Combustor,'' *Twenty-Sixth Symposium (International) on Combustion*, pp. 2771–2778.
[5] Dutta, P., Gore, J. P., and Sojka, P. E., 1997, ''Emissions Characteristics of Liquid-Fueled Pilot Stabilized Lean Premixed Flames in a Tubular Premixer-Combustor,'' J. Eng. Gas Turbines Power, , **119**, pp. 585–590.
[6] Tacina, R. R., 1990, ''Low-NO_x Potential of Gas Turbine Engines,'' AIAA Paper 90–0550.
[7] Shaffar, S. W., Sowa, W. A., and Samuelsen, G. S., 1995, ''Lean Burn Injector for Gas Turbine Combustor,'' U.S. Patent No. 5,477,685, 26 December.
[8] Shaffar, S. W., and Samuelsen, G. S., 1998, ''A Liquid Fueled, Lean Burn, Gas Turbine Combustor Injector,'' Combust. Sci. Technol. **139**, pp. 41–57.
[9] Lorenzetto, G. E., and Lefebvre, A. H., 1977, ''Measurements of Drop Size on a Plain Jet Airblast Atomizer,'' AIAA J., **15**, pp. 1006–1010.
[10] Samuelsen, G. S., 1975, ''The Combustion Aspects of Air Pollution,'' in *Advances in Environmental Science and Technology*, John Wiley & Sons, New York, Vol. 5. pp. 219–322.
[11] Lefebvre, A. H., 1984, ''Fuel Effects on Gas Turbine Combustion—Liner Temperature, Pattern Factor, and Pollutant Emissions,'' J. Aircr., **21**, No. 11, pp. 887–898.
[12] Rizk, N. K., and Mongia, H. C., 1993, ''Semi-analytical Correlations for NO_x, CO, and UHC Emissions,'' J. Eng. Gas Turbines Power, **115**, pp. 612–619.
[13] Lefebvre, A. H., 1992, ''Twin Fluid Atomization: Factors Including Mean Drop Size,'' Atomization Sprays **2**, pp. 101–119.
[14] Rink, K. K., and Lefebvre, A. H., 1989, ''The Influence of Fuel Composition and Spray Characteristics on Nitric Oxide Formation,'' Combust. Sci. Technol. **68**, pp. 1–14.
[15] Leong, M. Y., McDonell, V. G., and Samuelsen, G. S., 1998, ''Effect of Ambient Pressure on an Airblast Spray Injected into a Crossflow,'' AIAA Paper 98-3903.

Experimental and Numerical Investigation on the Evaporation of Shear-Driven Multicomponent Liquid Wall Films

M. Gerendas
e-mail: gerendas@its.uni-karlsruhe.de

S. Wittig

Institut für Thermische Strömungsmaschinen,
Universität Karlsruhe,
76128 Karlsruhe, Germany

The presented work is concerned with two-phase flows similar to those in prefilming airblast atomizers and combustors employing film vaporization. Correlations for the multicomponent mixture properties and models for the calculations of the multicomponent evaporation were implemented in a well tested elliptic finite-volume code GAP-2D (S. Wittig et al., 1992, ''Motion and Evaporation of Shear-Driven Liquid Films in Turbulent Gas,'' ASME J. Eng. Gas Turbines Power ***114****, pp. 395–400) utilizing time-averaged quantities, k,ε turbulence model, wall functions, and curve-linear coordinates in the gas phase, adiabatic or diabatic conditions at the film plate, partially turbulent velocity profile, uniform temperature, and a rapid mixing approach in the wavy film. This new code GAP-2K was tested for stability, precision, and grid independence of the results by applying it to a turbulent hot air flow over a two-component liquid film, a mixture of water and ethanol in different concentrations. Both simulations and experiments were carried out over a wide range of inlet conditions, such as inlet pressure (1–2.6 bar), inlet temperature (298–573 K), inlet air velocity (30–120 m/s), initial liquid flow rate (0.3–1.2 cm^2/s), and initial ethanol concentration (20–75 percent mass). Profiles of temperature, gas velocity, and concentration of the evaporating component normal to the film, and the development of the film temperature, the static pressure, the liquid flow rate, and the liquid compound along the film plate have been measured and compared with the simulation, showing a good match.* [DOI: 10.1115/1.1362663]

Introduction

Knowledge of the parameters influencing the heat, mass, and momentum transfer of wavy liquid films driven by the shear of a turbulent air flow is of dominant interest in various practical engineering applications. In extending our earlier experimental and computational studies of prefilming airblast atomizers ([1–4]) experimental and numerical tools for the examination of two-phase flows with wavy multicomponent liquid films have been developed. At the Institute of Thermal Turbomachinery at the University of Karlsruhe these tools are also used for the examination of film vaporization in combustors and the flow in curved intake pipes of internal combustion engines. Therefore this work is not solely focused on airblast atomizer's.

At elevated temperatures the two-phase flow inside the nozzle is characterized by a coupled momentum, heat, and mass exchange of the different phases and the unknown coupling conditions at the liquid/gas interface (Fig. 1).

Additional difficulties arise from the correct description of the coupling conditions for the momentum, the heat, and the mass transfer at the phase interface. For different kinds of airblast atomizers the film can be heated only by the gas phase or both directly by the gas and through the film plate.

For a prediction of the complex multiphase multicomponent flow in practical engine design a variety of simplifications is necessary. In the study presented here, suitable simplifications are discussed and examined by a comparison of theoretical results with detailed experiments.

Contributed by the International Gas Turbine Institute (IGT) of THE AMERICAN SOCIETY OF MECHANICAL ENGINEERS for publication in the ASME JOURNAL OF ENGINEERING FOR GAS TURBINES AND POWER. Paper presented at the International Gas Turbine and Aeroengine Congress and Exhibition, Munich, Germany, May 8–11, 2000; Paper 00-GT-136. Manuscript received by IGTI February 2000; final revision received by ASME Headquarters January 2001. Associate Editor: M. Magnolet.

Calculation Procedure

The flow within the gap is a highly unstationary two-phase flow pattern with a moving, wavy film of significant height and strongly coupled heat, mass, and momentum transfer. As earlier studies pointed out, reasonable results can be obtained using time-averaged calculational procedures ([2,4–6]). Therefore, the calculation of the gas phase flow is based on the Reynolds-averaged Navier-Stokes equations with additional equations for energy and species transport. All properties of the gas phase are calculated as functions of temperature, pressure, and concentration, assuming ideal gas behavior. Despite the well-known problems associated with the modeling of near wall turbulence, a standard k,ε turbulence model is used for the gas phase. Since modified wall functions based on the well-known logarithmic law of the wall are

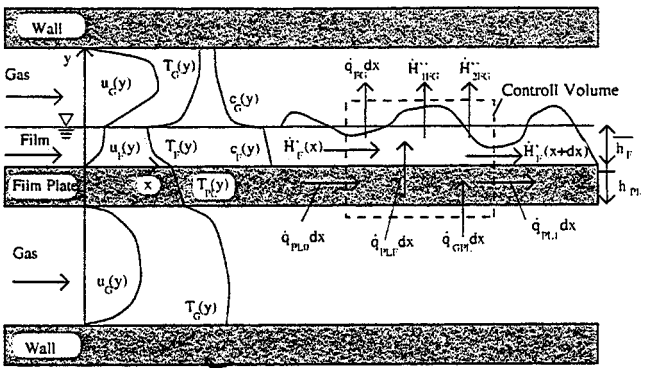

Fig. 1 Two-phase flow in prefilming gap

used in the near wall region with $y^+<30$, more sophisticated turbulence models do not promise significant advantages for the present investigation.

A priori neither the local film mass flux, the local film compound, nor the local film temperatures are known, and therefore the film thickness and the film velocity distribution are unknown. Since the blockage of the gap by the film cannot be neglected, the exact shape of the computational domain near the lower wetted surface is unknown. Body-fitted coordinates are used to steadily adapt the computational grid to the newly calculated location of the film surface. The computational domain starts 20 mm upstream of the film former (see also Fig. 2) and ends at the atomizing edge. Although the additional capabilities of an elliptic code over a parabolic code are not used in this study, the single-component version GAP-2D was already successfully used to compute the flow in the curved intake pipe of a SI engine ([3]).

The boundary conditions near the phase interface are described by a sand grain approach,

$$k_s=\psi_\tau \overline{h_F}, \quad \psi_\tau=1.47+0.01851\tau_W, \tag{1}$$

where k_s is the sand grain roughness and ψ_τ the roughness factor, which relates the film thickness to the roughness of the film surface.

Sattelmayer and Wittig [2] found this correlation for the roughness factor ψ_τ to give good results for the velocity profile in the gas phase in combination with the following logarithmic law of the wall. It is based on measurements of the turbulent boundary layer over liquid films with various properties, and measurements of the film thickness:

$$u^+=\frac{1}{\kappa'}\ln y^+ + C(\mathrm{Re}_{k_s}) \tag{2}$$

with

$$u^+=\frac{u}{u_\tau}=u\sqrt{\rho_p/\tau_W}, \quad y^+=\frac{y u_\tau}{\nu_p}, \quad \mathrm{Re}_{k_s}=\frac{u_\tau\cdot k_s}{\nu_p}$$

Re_{k_s} is the roughness Reynolds number and it is used to calculate the roughness coefficient $C(\mathrm{Re}_{k_s})$, which is given by

$$C(\mathrm{Re}_{k_s})=\begin{cases} 5.15 & \text{if } \mathrm{Re}_{k_s}<5 \\ 1.5497+19.1lg\,\mathrm{Re}_{k_s}-\dfrac{1}{\kappa'}\ln\mathrm{Re}_{k_s}-14.433lg^2\,\mathrm{Re}_{k_s} & \\ \quad +3.308lg^3\,\mathrm{Re}_{k_s} & \text{if } 5\leqslant\mathrm{Re}\leqslant 70 \\ 8.5-\dfrac{1}{\kappa'}\ln\mathrm{Re}_{k_s} & \text{if } 70<\mathrm{Re}_{k_s} \end{cases}. \tag{3}$$

In conjunction with the standard k,ε turbulence model, the following wall functions result for the calculation of the momentum transfer in the gas phase:

• Shear stress and velocity at the grid point P adjacent to the film surface:

$$\frac{u_t,p}{\tau_W/\rho_p}C_\mu^{0.25}k_p^{0.5}=\frac{1}{\kappa'}\ln\left(\frac{e^{C(\mathrm{Re}_{k_s})\kappa'}\Delta n C_\mu^{0.25}k_p^{0.5}}{\nu_p}\right). \tag{4}$$

• Turbulent kinetic energy and dissipation rate:

$$k_p=\frac{\tau_W/\rho_p}{C_\mu^{0.5}}, \quad \varepsilon_p=\frac{C_\mu^{0.75}k_p^{1.5}}{\kappa'\Delta n}. \tag{5}$$

In order to reduce effects of the nonisothermal boundary layer flow with spatially varying vapor concentration, and therefore changing local fluid properties, the grid for the gas phase was steadily optimized to fulfill the following condition for the grid point nearest the wall:

$$y_p^+=30\pm 5. \tag{6}$$

To take into account effects of pressure gradients and of the mass flow normal to the film surface, which results from the evaporation, an averaged shear stress calculated from

$$\overline{\tau}=\tau_W+\frac{\Sigma\dot{m}''_{i,W}u_p}{[1+((\tau_W/(\rho u^2)_p)^{0.5})/\kappa']}+0.5\Delta n\frac{dp}{dx} \tag{7}$$

was used instead of τ_W in the wall functions. A similar procedure was proposed by Spalding [7].

For prediction of the heat and mass transfer processes the well-known standard wall functions for the stagnation temperature and the vapor concentrations ([7]) are used. However, as earlier experiments in our Institute show ([8]), the roughness of the wavy liquid film has only a minor effect on the heat and mass transfer in comparison to the momentum transfer. Therefore, an empirical correlation is used in the numerical code for the gas phase to relate the enhancement of heat transfer by roughened surfaces to the increase of momentum transfer:

$$\eta_{\dot{q}}=\left(\frac{\mathrm{St}}{\mathrm{St}_o}\right)\Big/\left(\frac{c_f}{c_{f,0}}\right)=\eta_{\dot{q}}(\mathrm{Re}_{k_s},\mathrm{Pr}) \tag{8}$$

with

$$\eta_{\dot{q}}=\log\left(\frac{\mathrm{Pr}^{0.33}}{\mathrm{Re}_{k_s}^{0.243}}\right)-0.32\times10^{-3}\,\mathrm{Re}_{k_x}\log(\mathrm{Pr})+1.225. \tag{9}$$

The aforementioned correlation was developed by Burck [9] based on heat transfer measurements on roughened surfaces without evaporating liquid and extended by Sill [8] for evaporating water films. By introducing the stagnation enthalpy the following formulation of the wall function for the heat transfer with evaporating wavy film surfaces results:

$$\mathrm{St}^*=\frac{-\dot{q}w}{\rho_P u_{t,P}[h_{t,P}-h_{t,w}-(1-\mathrm{Pr}_t)u_{t,P}^2/2]}=\frac{\eta_{\dot{q}}c_f^*}{\mathrm{Pr}_t(1+P\sqrt{\eta_{\dot{q}}c_f^*})} \tag{10}$$

with

$$c_f^*=\frac{\overline{\tau}}{\rho_P u_{t,P}^2}, \quad P=9{,}0\left(\frac{\mathrm{Pr}}{\mathrm{Pr}_t}-1\right)\left(\frac{\mathrm{Pr}_t}{\mathrm{Pr}}\right)^{0.25}.$$

First the fully known right side of Eq. (10) is used to calculate the local Stanton number of the heat transfer, then the left side is solved for the heat $\dot{q}_w$ transferred to the film. The corresponding wall function for the mass transfer of the ith component is

$$\mathrm{St}^*_{\dot{m},i}=\frac{-\dot{m}''_{i,w}\beta_{\mathrm{Stefan}}(1-c_{i,w})}{\rho_P u_{t,P}(c_{i,P}-c_{i,w})}=\frac{\eta_{\dot{m}}c_f^*}{\mathrm{Sc}_t(1+P_{\dot{m}}\sqrt{\eta_{\dot{m}}c_f^*})} \tag{11}$$

with

$$\beta_{\mathrm{Stefan}}=\frac{\ln\{[p-p_i(y)]/(p-p_{i,w})\}}{[p_i(y)-p_{i,w}]/(p-p_{i,w})}. \tag{12}$$

It is obtained from the assumption that the effect of roughness on the mass transfer can be described in similarity to the heat transfer, by replacing the Prandtl number by the Schmidt number. The Stefan flux correction β_{Stefan} Eq. (12), is used to compensate the errors introduced during the deduction of Eq. (11). Again, in a first step the completely known right side of Eq. (11) is used to calculate the local Stanton number of the mass transfer of each single component. Then the left side is solved for the evaporation mass flux $\dot{m}''_{i,w}$. The partial pressure of a component at the phase interface has to take the temperature and film compound dependent activity coefficient $\gamma(X_i,T_I)$ into account and is calculated using

$$p_{s,i}=X_i\gamma(X_i,T_I)p_{s,0,i}(T_I). \tag{13}$$

With the equations given above, only the gas flow over liquid films can be calculated. With the shear stress derived from the

calculation of the gas phase and the conservation of mass for the film, the local film thickness and velocity can be calculated using an assumption for the turbulent viscosity distribution in the film. Earlier studies often used either completely laminar or fully turbulent velocity profiles ([4]). But measurements showed that neither approach gave a precise prediction. Glahn and Wittig [11] and Elsäßer et al. [10] performed Laser Doppler anemometry (LDA) measurements inside the shear-driven liquid film and film thickness measurements. They found the best fit of measured and calculated values using the partially turbulent correlation, Eq. (14), for the turbulent viscosity distribution in the film. It was first published by Deissler [12] and Dukler [13]:

$$\frac{\nu_t}{\nu_F} = n^2 \mu_F^+ y_F^+ \{1 - e^{-n^2 u_F^+ y_F^+}\} \tag{14}$$

with

$$n = 0.109, \quad 0 \leqslant y_F^+ \leqslant \overline{h}_F^+, \overline{h}_F^+ \leqslant 27.$$

The calculational procedure for the film temperature is dominated by a balance of heat and mass transfer at the film surface as shown in Fig. 1. The heat of evaporation $\dot{m}''_{1,I}(h_{1,I} - h_{F,I})$ is determined under the assumption of thermal equilibrium at the phase interface ($T_{F,I} = T_{G,I}$), taking into account the enthalpy transported by the film itself. Thus, the heat transferred from the gas phase can be written as

$$\dot{q}_{G,I} = -\rho \, \mathrm{St}^* u_{t,P} \left[h_{t,P} - h_{t,I} - (1 - \mathrm{Pr}_t) \frac{u_{t,P}^2}{2} \right], \tag{15}$$

$$\dot{q}_{Pl} = \alpha (T_{G,L} - T_F) dx. \tag{16}$$

This leads to the following equation using the uniform temperature approach:

$$\dot{q}_{PI} - \dot{q}_{G,I} + \dot{m}'_{F,x} c_p T_x - \dot{m}'_{F,x+\Delta x} c_p T_{x+\Delta x} - \sum_i \dot{m}''_{i,I} (h_{i,I} - h_{i,F,l}) = 0. \tag{17}$$

In Eq. (17) $\dot{q}_{Pl}$ represents the heat transferred from the gas in the lower channel (see Fig. 1), through the film plate, to the film in the upper channel in case of a diabatic boundary condition at the film plate. The heat transfer coefficient α and the bulk temperature of the gas in the lower channel are stored in a file from a previous calculation using GAP-2K without a liquid film. Dimensionless values cannot be used, since the properties of the flow are later no longer available to the program. At the outside channel wall not wetted by the film, measured temperature distributions are used.

Based on the conditions on the phase interface the local film mass flux in a distance l from the film inlet is calculated by

$$\dot{m}'_{x=l} = \dot{m}'_{x=0} - \sum_{i=1}^{k} \int_{x=0}^{x=l} \dot{m}''_{i,w} dx. \tag{18}$$

The local concentration of each component in a distance l from the film inlet in the film is given by

$$c_{i,x=l} = \left[(c_i \dot{m}')_{x=0} - \int_{x=0}^{x=l} \dot{m}''_{i,w} dx \right] \frac{1}{\dot{m}'_{x=l}}, \quad i = 1, \ldots, k. \tag{19}$$

The properties of the mixture are based on the properties of the pure components and mixing rules following the recommendations of Reid et al. [14]. The properties of the components are third order polynomials fitted to values listed in ([15]), not allowing a higher root mean square than 1 percent. The set of mixing rules for the liquid phase used in this study is displayed in Table 1. For the density of the mixture, Eq. (20) was used:

$$\rho = (c_1 \rho_1 + c_2 \rho_2)(-\psi c_2^2 + \psi c_2 + 1), \quad \psi = 0.0878. \tag{20}$$

Table 1 Mixing rules for the liquid phase

Property	Model	Fitted to
Activity coefficient	Margules (1895)	Kirschbaum (1939)
Density	eq. (20)	Kreitling (1892)
Dynamic viscosity	Teja, Rice (1981)	Kay, Broadwater (1979)
Heat conductivity	Li (1976)	Li (1976)

References cited in table are Refs. ([16–21]).

The precision of all mixing rules for the liquid phase was checked against published measurements (see Table I), not allowing a higher root mean square than 2 percent.

For the calculation of the multicomponent diffusion coefficient, the Stephan-Maxwell equation was solved ([22]):

$$An \nabla Y_i = \sum_{j=0}^{k} \frac{1}{D_{i,j}} (Y_i \dot{N}_j - Y_j \dot{N}_i) \tag{21}$$

with

$$\dot{N} = \sum_{j=0}^{k} \dot{N}_j, \quad \dot{N}_j = \frac{\dot{m}''_j A}{M_j}, \quad n = \sum_{j=0}^{k} n_j, \quad n_j = \frac{c_j \rho}{M_j}, \quad Y_j = \frac{n_j}{n}.$$

The multicomponent diffusion coefficient is defined by

$$D_{i,\mathrm{mix}} = \frac{\dot{N}_i - \dot{N} Y_i}{An \nabla Y_i}, \tag{22}$$

leading to the following equation for the multicomponent diffusion coefficient in program-compatible quantities:

$$D_{i,\mathrm{mix}} = \frac{(\dot{m}''_i / M_i) \Sigma_{j=0}^{k} c_j / M_j - (c_i / M_i) \Sigma_{j=0}^{k} n''_j / M_j}{\Sigma_{j=0}^{k} (1/D_{i,j})(c_i / M_i)(\dot{m}''_j / M_j) - (c_j / M_j)(m''_i / M_i)}. \tag{23}$$

With the equations given above, the two-phase flow of turbulent hot air over evaporating wavy multicomponent liquid films can be calculated with limited numerical effort.

The first test case for the new code was the reproduction of simulations carried out with the predecessor ([23]) for selected conditions with pure water as evaporating single-component liquid, leading to a very good match. Differences were found only in cases where the limited grid resolution of the predecessor with 44×20 grid point: led to difficulties, compared to a variable grid size set to 88×20 of the new code. The computation time increased only by 9 percent due to the dramatic improvement of the grid configuration, also expressed by a slightly reduced number of grid adaptations during the simulation and a strongly increased stability. A further refined grid did not gain comparably.

The presented numerical procedure is based on a large number of assumptions and simplifications in order to develop a system that is fast and compact enough to be used for parameter studies in engine design. Therefore the program GAP-2K is used to predict a large number of cases (see Table 3 below), which are compared with measurements in order to check the validity of the assumptions and simplifications the code is based on. The next section describes the experimental setup, which is used to collect the data base for this comparison.

Experimental Setup

The setup is a combination of design elements found in prefilming airblast atomizers and combustion chambers employing film evaporation. The film plate is longer than in usual atomizers

to provide enough length for a significant evaporation and vapor diffusion. In the first half of the test section, the vapor is found only very close to the film surface. Film/probe interaction and droplets generated at the film surface prohibit measurements in close proximity to the film. The amount of liquid evaporated in the usual atomizer length is not sufficient to lead to significant liquid or gas property changes. Therefore, the most important information for this type of application is the temperature and film thickness development, which are documented over the complete length of the test section (see Figs. 8 and 13 below).

The test section (Fig. 2) has a primary cross section of 83×60 mm^2, converging to a cross section of 13×60 mm^2. Wittig et al. [4] characterized the turbulent intensity by TI=5 percent and an integral length scale of 5 percent of the gap height $h_{S,0}$.

With the film plate for the liquid film along the centerline of the channel, two gaps of 3.9 mm height are formed. Other gap heights can be generated, but are not part of this study. Trip wires of 0.3 mm diameter are positioned at the upper and lower walls at the gap entrance and on the half-elliptic nose of the film plate, in order to avoid effects of laminar-turbulent transition, which are not the subject of the present study. The liquid film is formed by a row of 0.5 mm holes, which are 0.8 mm apart. The liquid is fed into the film plate through the sidewall by two separate pipes with 2.5 mm inner diameter.

The test section provides six measurement planes, 80 mm apart. The first plane is 20 mm downstream of the end of the half-elliptic nose of the film plate, which is the start of the computational domain. If conditions with heat transfer through the wetted wall to liquid film are chosen, the liquid is only supplied to one side of the plate. Under these conditions the film plate is heated by the flow in the second gap without film. For adiabatic wall conditions, the film is supplied to both sides of the film plate.

To measure the velocities and the temperatures of the gas phase, pitot tubes of 0.6 mm outside diameter with integrated thermocouples of 0.25 mm diameter are used. The temperatures of the prefilming plate and the upper channel wall are determined with thermocouples of 0.25 mm diameter, which are soldered into the surface before roughening the film surface with the sandblast unit. The static pressure taps at the channel wall have a diameter of 0.3 mm. The pressure measurement hoses are connected to a 48-channel Scanivalve and a magnetic valve array. Pressure measurements use an absolute pressure transducer (0–6.7 bar) and a differential pressure transducer ($\pm$172 mbar). The reference pressure is the static pressure upstream of the test section. The pressure transducer with the higher precision for the respective pressure measurement is automatically selected by the controlling computer program. All thermocouple voltages and the outputs of the pressure transducers are routed through a 256-channel multiplexer to a digital voltmeter with 30-bit resolution.

The film is drained in measurement plane 5 (MP5) over a certain time in order to measure the film volume flux and the compound. The volume, weight, and temperature of the film sample are determined and the compound is calculated using the inverse function of Eq. (20). The vapor concentration profiles are measured by taking gas samples through a probe employing isokinetic suction. The gas sample is first cooled down in a condenser to 273 K. Then the compound of the condensate is analyzed in the same way as the drained film. The vapor concentration in the gas phase of the condenser is calculated by Eq. (13) based on the condensate compound and the measured pressure and temperature in the condenser. This leads in conjunction with the measured volumetric flow rate of the saturated air behind the condenser and the related pressures and temperatures to an overall mass flow rate of the dry air and each component. The ratio of the mass flow rate of each component and the dry air represents the mass concentration of the vapor component at the probe tip. The uncertainties related to the different sources and the calculated quantities are displayed in Table 2.

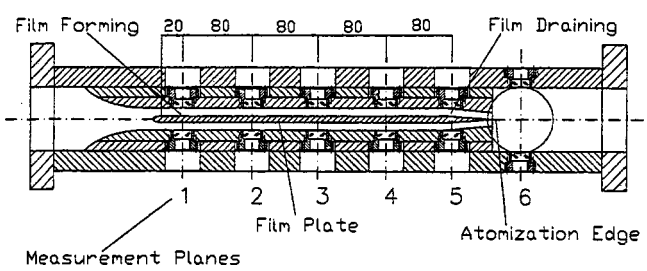

Fig. 2 Test section (dimensions in millimeters)

Table 2 Uncertainties

Measured Quantity	p	T	Weight	Volume
Primary uncertainty [%]	0.5	0.065	0.5	1.3
Calculated Quantity	U_{Gas}	$\dot{V}_F/B$	Conc. in film	Conc. in gas
Related uncertainty [%]	1.4	2.3	6.3	8.5

In order to check the measurement equipment and procedures, selected measurements with pure water were performed, showing a very good match with data taken in the past ([23]). Only after that state was reached were measurements with the two-component liquid carried out.

Results

In order to check the numerical procedure presented here, a comparison of measured and calculated values is made. The liquid used in the experiments is a mixture of distilled water and ethanol. The comparison is carried out over a wide range of inlet and boundary conditions, as displayed in Table 3. The parameters in brackets were used only for stability checks and no data for these cases are presented here, since the test rig does not allow measurements at, for example, 800 K with ethanol in a safe manner. Table 4 shows some liquid properties for $T_F=315$ K and $c_{\text{ith}}=50$ percent.

The velocity profile in the gap at elevated pressure in the measurement plane 4 (MP4), displayed in Fig. 3, shows a fully turbulent but asymmetric shape. This is due to the order-of-magnitude higher roughness of the wetted wall, compared to the dry opposite side. Additionally, the gas near the lower wall is cooled by the film, thereby increasing the density and decreasing the velocity of the gas.

Table 3 Varied system parameters

Parameter	Variants				
Gas velocity in m/s	30	60	90	120	
Gas temperature in K	297	573	(800)		
System pressure in bar	1.1	2.6	(4)		
Film volume flux in cm^2/s	0.1	0.3	0.6	0.9	1.2
Mass ratio Water : Ethanol	(1:0)	1:1	4:1	1:3	

Table 4 Liquid mixture properties (T_F=315 K, c_{Eth}=50 percent, p=1.1 bar)

Quantity	ρ	μ	λ
Value	$900\frac{kg}{m^3}$	$0.0016\frac{Ns}{m^2}$	$0.180\frac{W}{mK}$
Quantity	c_p	$p_{s,1}$	$p_{s,2}$
Value	$3.44\frac{kJ}{kg}$	8140 Pa	19700 Pa

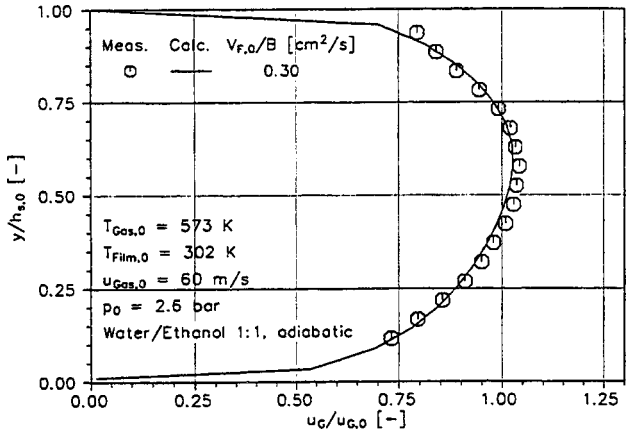

Fig. 3 Velocity profile at elevated pressure in MP4

This cooling of the gas by the film is visible in the temperature profile in the gap in the measurement plane 4 (MP4), displayed in Fig. 4. The match between the measured and the calculated values for velocity and temperature is very good. The straight part close to both walls of the line representing the numerical simulation marks the distance that is bridged by the wall functions. The wall function used near the wetted surface does not end at the channel wall, but on the film surface.

The concentration profiles of both evaporating components, displayed in Fig. 5, shows a minimum near the dry top wall and an increase with decreasing distance from the film. The difference between the measurements and calculation increases noticeably when the probe approaches the wetted wall. Close to the film surface, no measurements were performed due to the disturbance of the film by the suction probe and the increasing droplet density. The difficulties due to the impact of droplets onto the probe are also visible at lower pressure (see Fig. 6). But still these deviations do not indicate a fault in the code, since droplets are not part of the model.

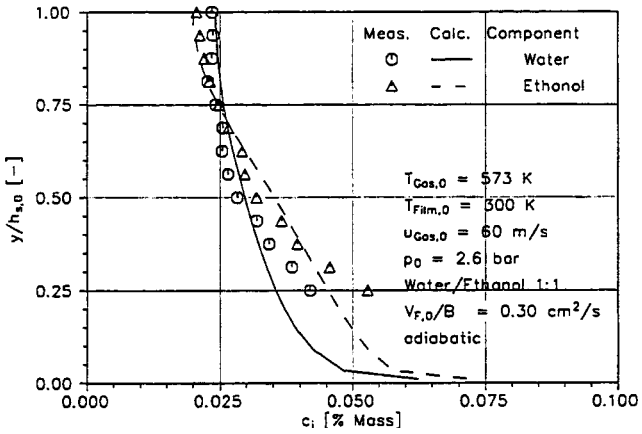

Fig. 5 Concentration profiles at elevated pressure in MP4

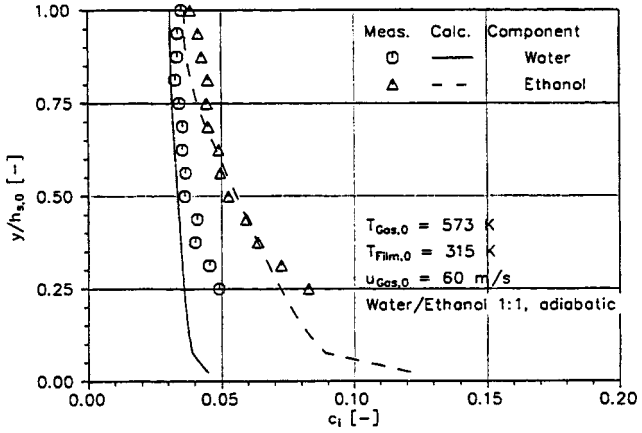

Fig. 6 Concentration profiles at p_0=1.1 bar in MP4

Profiles of velocity, temperature, and compound normal to the film surface are very important indicators for the quality of the simulation, but there are also other considerations to make. A quite important one is the precision of the prediction of the pressure loss through the gap. In the real application of an airblast atomizer, this determines how much air will flow though the nozzle into the combustion chamber and how much through air holes in the combustor liner. As visible in Fig. 7, this important

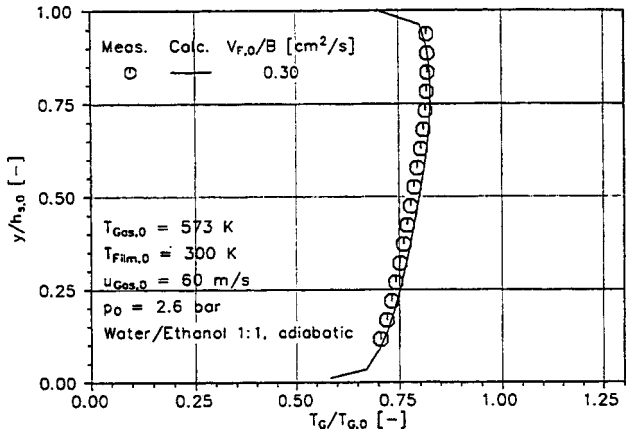

Fig. 4 Temperature profile at elevated pressure in MP4

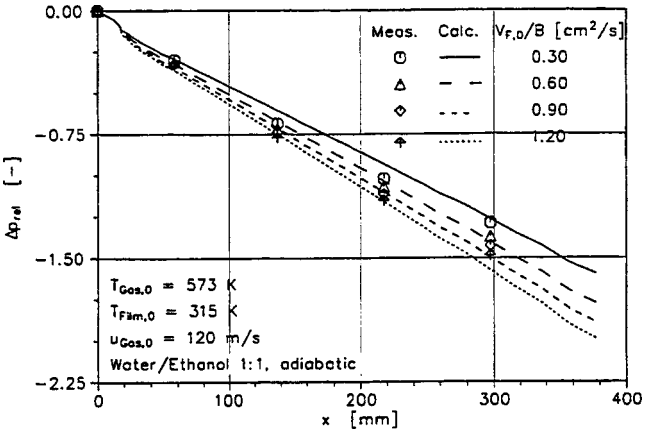

Fig. 7 Pressure drop along the gap

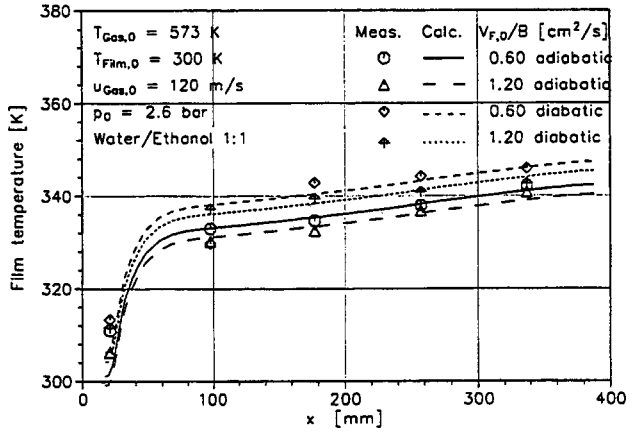

Fig. 8 Film temperature along the film plate at elevated pressure and temperature

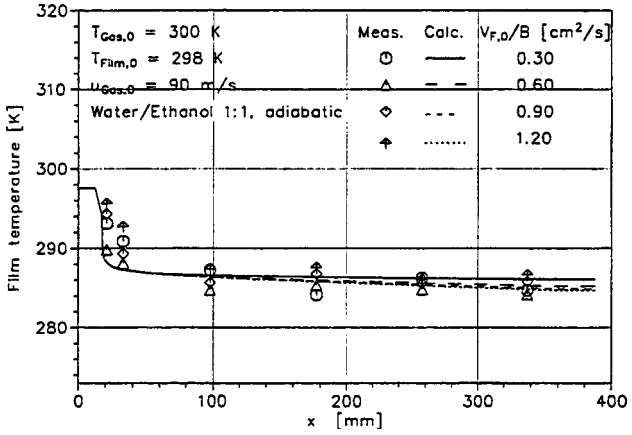

Fig. 9 Film temperature along the film plate at low pressure and temperature

prediction is quite accurate. The identical values for the first 20 mm of the simulation for all liquid flow rates and the strong pressure drop at this location indicate the position of the film forming device. The static pressure drops due to the acceleration of the flow by the reduced gap free gap height at the film entrance. Downstream of this location, the influence of the different liquid flow rates becomes visible.

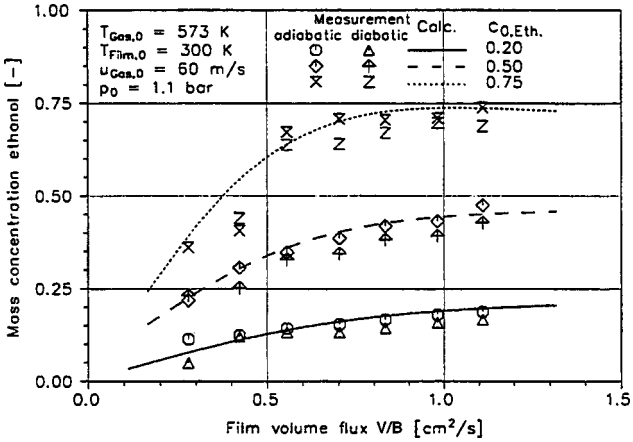

Fig. 10 Ethanol concentration in the film in MP5

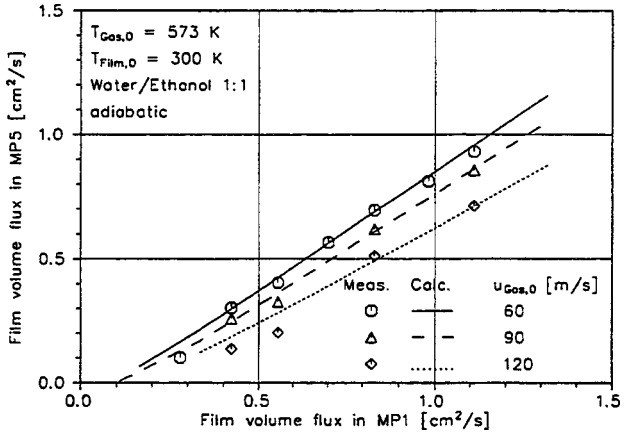

Fig. 11 Film volume flux with adiabatic film plate in MP5

One reason to calculate the flow through a prefilming airblast atomizer is to calculate the film temperature at the atomizing edge, because it determines the liquid properties in conjunction with the compound. The numerical prediction for the film temperature for different liquid flow rates and different thermal boundary conditions at the film plate is compared with measurements in Fig. 8. After a strong increase in the first quarter of the gap, the temperature climbs only slightly over the remaining part of the film plate. If the latent heat of evaporation is large compared to the heat transferred to the film, the temperature should drop after the film forming device until equilibrium is reached. This is the case for an initial gas temperature of 300 K (see Fig. 9).

As mentioned above, the next important information about the film at the atomizing edge is the compound, displayed in Fig. 10 as mass concentration of the alcohol by variation of the initial film flow rate and concentration. At very high film flow rates, the concentration of ethanol at the measurement plane 5 is nearly the initial one. If the initial wall film flux gets smaller, then the ethanol concentration drops down more rapidly. The effect gets larger with increasing initial ethanol concentration.

The reduction of the local film volume flux along the film plate in the test section is stronger than in a typical prefilming airblast atomizer, where it can usually be neglected. But for a prevaporizing combustion chamber employing film evaporation, this is the performance determining quantity. The film volume flux in measurement plane 5 as a function of the initial film volume flux is shown in Fig. 11 for an adiabatic boundary condition at the film plate and in Fig. 12 for diabatic boundary condition. The relation

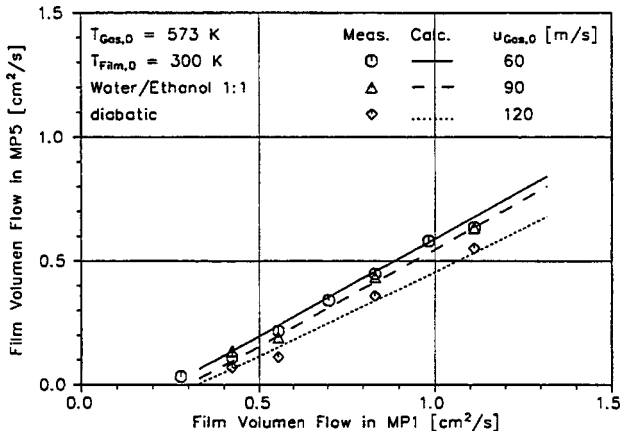

Fig. 12 Film volume flux with diabatic film plate in MP5

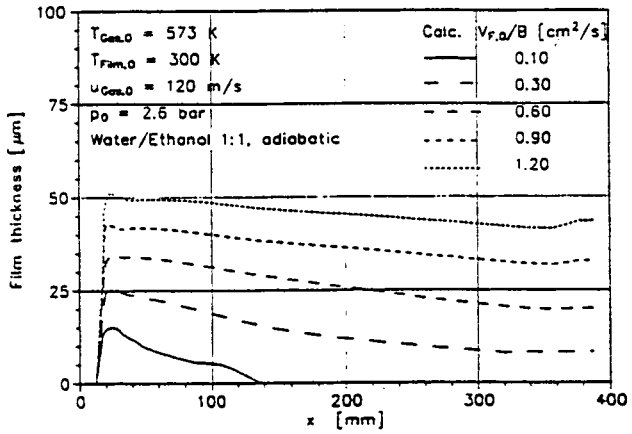

Fig. 13 Film thickness development along the film plate

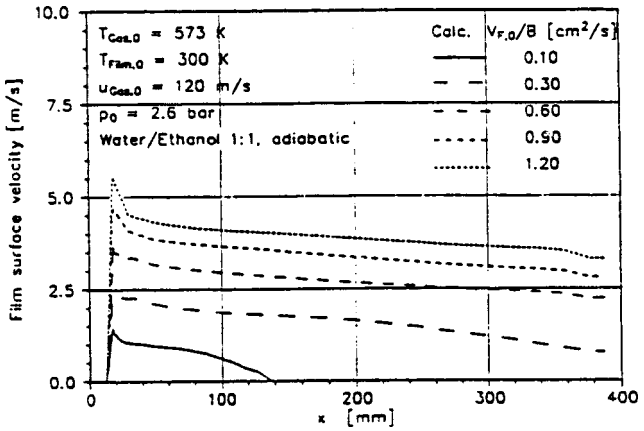

Fig. 14 Film surface velocity development along the film plate

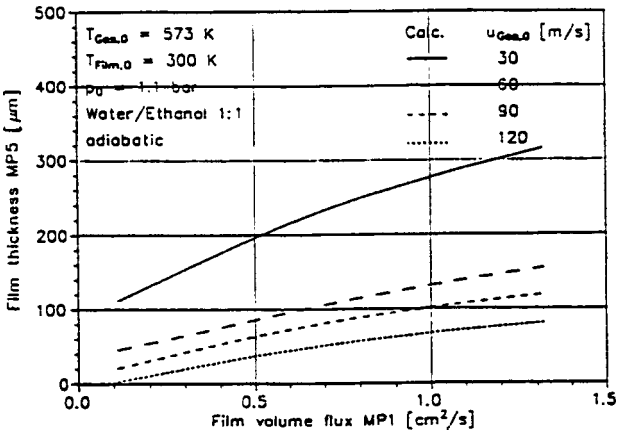

Fig. 15 Film thickness in MP5

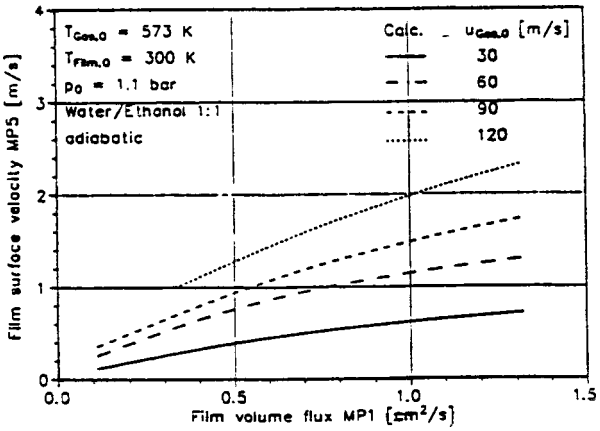

Fig. 16 Film surface velocity in MP5

between the remaining and initial film volume flux is practically linear in both cases. The intersection of this linear relation and the ordinate marks the initial film volume flux, which dries completely before it reaches measurement plane 5.

The parameters that are most difficult to determine are the film thickness and the film velocity, described here in terms of surface velocity. Since the film thickness/compound/velocity measurement device under development (based on [4]), has until now not reached a sufficient speed to resolve the film thickness and compound at gas velocities up to 120 m/s, only calculated values are shown.

The film thickness depends mainly on the phase interface shear stress and the film volume flux, but also on the viscosity, which is itself a function of temperature and compound. The shear stress decreases along the film plate due to the growth of the boundary layer. The film volume flux gets smaller due to the evaporation. The resulting film thickness development along the plate at an elevated pressure and temperature level is displayed in Fig. 13. The film thickness has its maximum at the film forming device and decreases afterward. For a very small initial film volume flux, the film dries completely before it could reach the atomizing edge. A similar development is visible in the film surface velocity plot (Fig. 14). Generally speaking, a thinner film moves more slowly. Additionally, for a very thin film, the partial-turbulent velocity profile is reduced to a laminar one ($u^+ = y^+$). Twice the initial film volume flux (1.2 cm^2/s instead of 0.6 cm^2/s) leads only to a 35 percent increase in velocity (3.1 m/s to 4.2 m/s), but to a 41 percent growth in film thickness (34 μm to 48 μm) in a plane 40 mm downstream of the film forming device. At the location were the film plate starts to reduce its thickness toward the atomizing edge, an additional effect becomes visible (mainly at a high film volume flux). The slight turn of the flow leads to a reduction in surface shear stress and surface velocity, and therefore to an increasing film thickness.

A variation of the gas velocity and the initial film volume flux near ambient pressure leads to a film thickness and film surface velocity in measurement plane 5 as displayed in Figs. 15 and 16. The film thickness in measurement plane 5 at high initial film volume flux is reversely proportional to the gas velocity. At lower initial film volume flux, a stronger influence of the evaporation is visible. The film surface velocity in measurement plane 5 scales at high initial film volume flux nearly linearly with gas velocity with the same effect of evaporation at lower initial film volume flux. A film with an initial volume flux of 0.1 cm^2/s evaporates completely before reaching measurement plane 5 at 120 m/s gas velocity; therefore no film surface velocity is given in this case.

Conclusion

Turbulent two-phase flows with wavy multicomponent liquid films can be described with good accuracy by employing time-averaged numerical procedures, a partially turbulent film velocity profile, and a uniform temperature/rapid mixing approach in the film. Considering the results presented, the two-phase flow with wavy multicomponent liquid film is well predicted for a wide range of gas temperatures and flow conditions. It is concluded that the momentum, heat and multicomponent mass transfer between

the film and the gas phase is modeled with sufficient precision, despite the large number of simplifications used in the deduction of the model. The calculational procedures presented can be incorporated into available numerical codes with a limited effort, in order to predict the flow for numerous other configurations in practical engineering problems with satisfactory accuracy.

Acknowledgments

The present study was supported by a grant from the Sonderforschungsbereich SFB 167 (High Intensity Combustors) of the Deutsche Forschungsgemeinschaft (DFG). Additionally, a helpful discussion of multicomponent evaporation and diffusion with Professor Dr. Ing. H. Martin is gratefully acknowledged.

Nomenclature

A = Area (m^2)
C = Constant in the logarithmic law of the wall
c_p = Specific heat (J/kg K)
c_i = Mass concentration of a vapor component
$D_{i,j}$ = Binary diffusion coefficient (m^2/s)
$D_{i,\mathrm{mix}}$ = Multicomponent diffusion coefficient (m^2/s)
h_t = Stagnation enthalpy (J/kg)
$h_{s,0}$ = Gap height without film (m)
$(h_{i,l}-h_{i,F,l})$ = Latent heat of evaporation (J/kg)
H'_F = Enthalpy flux of the liquid per unit width (W/m)
$\overline{h_F}$ = Time-averaged film thickness (m)
k_s = Equivalent sand roughness (m)
M = Molar mass (kg/kmol)
$\dot{m}$ = Mass flux (kg/s)
$\dot{N}$ = Molar flux (kmol/s)
n = Molar density ($kmol/m^3$)
p = Pressure (N/m^2)
Pr = Prandtl number
$\dot{q}$ = Heat flux per unit area (W/m^2)
Re = Reynolds number
Sc = Schmidt number
T = Temperature (K)
u = Gas velocity (m/s)
u_F = Film velocity (m/s)
u_τ = Shear stress velocity (m/s)
u^+ = Nondimensional velocity
v_i = Velocity of component i
$\dot{V}_F/B$ = Liquid volume flux per unit width (m^2/s)
X_i = Molar concentration of ith component
x = Coordinate in axial flow direction (m)
Y = Mole faction
y = Coordinate in vertical direction (m)
y^+ = Nonwall distance
α = Heat transfer coefficient (W/m^2 K)
β_{Stefan} = Stefan flux correction
Δ_n = Normal distance from wall (m)
Δp_{rel} = Relative pressure drop $\Delta p_{\mathrm{rel}}=(p-p_{x=0})/[(\rho G/2)/u_G^2]_{x=0}$
γ_i = Activity coefficient of the ith component
κ' = von Karman constant
λ = Thermal conductivity (W//m K)
μ = Dynamic viscosity (N s/m^2)
ν = Kinematic viscosity (m'/s)
ψ_τ = Roughness factor of film
ρ = Density (kg/m^3)
τ = Shear stress (N/m^2)
∇ = $\nabla \equiv i(\partial/\partial x)+j(\partial/\partial y)+k(\partial/\partial z), i,j,k$ tensor indices

Subscripts

F = Film, liquid
G = Gas
I = Interface gas-liquid
i = ith component of the mixture
L = Lower channel
0 = Value at gap entrance, single component
P = Grid point adjacent to the wall
PL = Film plate
U = Upper channel
s = Saturation
t = Stagnation, turbulent, tangential
W = Wall
1 = Water
2 = Ethanol
$'$ = Per unit width, turbulent variation
$''$ = Per unit area

References

[1] Sattelmayer, Th., and Wittig, S., 1986, ''Internal Flow Effects in Prefilming Airblast Atomizers: Mechanisms of Atomization and Droplet Spectra,'' Trans. ASME (86-GT-150).
[2] Sattelmayer, Th., and Wittig, S., 1989, ''Performance Characteristics of Prefilming Airblast Atomizers in Comparison with other Airblast Nozzles,'' *Encyclopedia of Fluid Mechanics*, Vol. 8, Golf Publishing Company, Houston, pp. 1091–1141.
[3] Wittig, S., Noll, B., Himmelsbach, J., Hallmann, M., and Samenfink, W., 1991, ''Experimentelle und theoretische Untersuchung der Strömung und des Filmverhaltens in den Saugrohren von Ottomotoren,'' Forschungsvereinigung Verbrennungskraftmaschinen (FVV), Informationstagung Motoren, Heft R 463.
[4] Wittig, S., Himmelsbach, J., Noll, B., Feld, H. J., and Samenfink, W., 1992, ''Motion and Evaporation of Shear-Driven Liquid Films in Turbulent Gas,'' ASME J. Eng. Gas Turbines Power, **114**, pp. 395–400.
[5] Whalley, P. B., 1987, *Boiling, Condensation and Gas-Liquid Flow*, Clarendon Press, Oxford.
[6] Sattelmayer, Th., 1985, ''Zum Einfluß der ausgebildeten, turbulenten Luft-Flüssigkeitsfilm-Strömung auf den Filmzerfall und die Tropfenbildung am Austritt von Spalten geringer Höhe,'' dissertation, Universität Karlsruhe, Germany.
[7] Spalding, D. B., 1977, *Genmix—A General Computer Program for Two-Dimensional Parabolic Phenomena*, Pergamon Press, Oxford.
[8] Sill, K. H., 1982, ''Wärme- und Stoffübergang in turbulenten Strömungsgrenzschichten längs verdunstender welliger Wasserfilme,'' Dissertation, Universität Karlsruhe, Germany.
[9] Burck, E., 1969, ''Der Einfluß der Prandtl-Zahl auf den Wärmeübergang und Druckverlust künstlich aufgerauhter Strömungskanäle,'' Wärme-Stoffübertrag., **2**, pp. 87–98.
[10] Elsäßer, A., Samenfink, W., Wittig, S., Ebner, J., and Dullenkopf, K., 1996, ''Velocity Profiles in Shear-Driven Liquid Films: LDV Measurements,'' 8th Int. Symposium on Applications of Laser Technique to Fluid Dynamics, 8–11, July, 1996, Lisbon, Portugal, Paper No. 25.2.
[11] Glahn, A., and Wittig, S., 1996, ''Two-Phase Air/Oil Flow in Aeroengine Bearing Chambers—Assessment of an Analytical Prediction Method for the Internal Wall Heat Transfer.'' 6th Int. Symposium on Transport Phenomena and Dynamics of Rotating Machinery (ISROMAC-6), Honolulu, Hawaii.
[12] Deissler, R. G., 1954, ''Heat Transfer and Fluid Friction for Fully Developed Turbulent Flow of Air and Supercritical Water with Variable Fluid Properties,'' Trans. ASME, **76**, pp. 73–85.
[13] Dukler, A. E., 1960, ''Fluid Mechanics and Heat Transfer in Vertical Falling-Film Systems,'' Chem. Eng. Prog., Symp. Ser., **56**, pp. 1–10.
[14] Reid, R. C., Prausnitz, J. M., and Polling, B. E., 1988, *The Properties of Gases and Liquids*, 4th international edition, McGraw-Hill, New York.
[15] VDI-Wärmeatlas, 1997, *Berechnungsblätter für den Wärmeübergang*, Springer, Berlin.
[16] Margules, M., 1895, S.-B. Akad. Wiss. Wien, math.-naturwiss. K1. II., **104**, pp. 1234 (see also [24]).
[17] Kirschbaum, E., and Gerstner, F., 1939, Z. VDI Beiheft Verfahrenstechnik 10, VDI-Verlag.
[18] Kreitling, W., 1892, ''Die Ausdehnung des Wassers, des absoluten Alkohols und der Mischungen beider,'' Dissertation, Universität Erlangen, Germany.
[19] Teja, A. S., and Rice, P., 1981, ''Generalized Corresponding States Method for the Viscosities of Liquid Mixtures,'' Ind. Eng. Chem. Fundam., **20**, pp. 77–81.
[20] Kay, R. L., and Broadwater, T. L., 1976, ''Solvent Structure in Aqueous

Mixtures: III. Ionic Conductances in Ethanol-Water Mixtures at 10 and 25°C,'' J. Solution Chem., **5**, pp. 57–76.
[21] Li, C. C., 1976, ''Thermal Conductivity of Liquid Mixtures,'' AIChE J., **22**, pp. 927–930.
[22] Cussler, E. L., 1976, *Multicomponent Diffusion*, Elsevier Scientific, Oxford.
[23] Himmelsbach, J., 1992, ''Zweiphasenströmungen mit schubspannungsgetriebenen welligen Flüssigkeitsfilmen in turbulenter Heißlufströmung—Meßtechnische Erfassung und numerische Beschreibung,'' Dissertation, Universität Karlsruhe, Germany.
[24] Gmehling, J., Onken, U., and Arlt, W., 1981, ''Vapor-Liquid Equilibrium Data Collection, Aqueous-Organic Systems,'' DECHEMA Chemistry Data Series, Vol. 1, Part 1a, DECHEMA, Frankfurt/Main.

J. H. Kim
Researcher,
Turbo and Power Machinery Research Center,
Seoul National University,
Seoul 151-742, Korea

T. W. Song
Graduate Student,
School of Mechanical Engineering,
Seoul National University,
Seoul 151-742, Korea

T. S. Kim
Assistant Professor,
Department of Mechanical Engineering,
Inha University,
Inchon 402-751, Korea

S. T. Ro
Professor,
Fellow ASME,
School of Mechanical Engineering,
Seoul National University,
Seoul 151-742, Korea

Model Development and Simulation of Transient Behavior of Heavy Duty Gas Turbines

This paper describes models for the transient analysis of heavy duty gas turbines, and presents dynamic simulation results of a modern gas turbine for electric power generation. Basic governing equations have been derived from integral forms of unsteady conservation equations. Mathematical models of each component are described with the aid of unsteady one-dimensional governing equations and steady-state component characteristics. Special efforts have been made to predict compressor characteristics including the effect of movable vanes, which govern the operating behavior of a whole engine. The derived equation sets are solved numerically by a fully implicit method. A controller model that maintains constant rotational speed and target temperature (turbine inlet or exhaust temperature) is used to simulate practical operations. Component models, especially those of the compressor, are validated through comparison with test data. The dynamic behavior of a 150 MW class engine is simulated. The time-dependent variations of engine parameters such as power, rotational speed, fuel, temperature, and guide vane angles are compared with field data. Simulated results are fairly close to the operation data. [DOI: 10.1115/1.1370973]

Introduction

Gas turbines suffer transient operation during startup, load change and shutdown as well as under abnormal conditions such as emergency. During the transient operation, system response time should be as short as possible and temporal peaks of main parameters such as turbine inlet temperature and rotational speed should not exceed certain reference values required for safe and reliable operation. Therefore, a precise prediction of the transient behavior of gas turbine engines is very important for stable operation, fault diagnosis, controller design, and so on.

Analytical and experimental investigations of the transient behavior of gas turbines began around early 1950s. Several models and methods for predicting the transient behavior of gas turbines have been proposed and applied in analyzing system dynamic characteristics. In the early stages of those works, the gas turbine was approximated a first-order system with the response of rotor speed to a step change on fuel flow being a simple lag ([1]). These models have been used and modified for designing a speed controller with a frequency domain analysis ([2,3]). Recently, dynamic simulations have been executed in the time domain introducing conservation equation sets ([4–6]).

In this study, models have been developed to describe the transient behavior of gas turbines, and applied to the dynamic simulation of a real engine. The mathematical model describing system dynamics is derived on the basis of unsteady one-dimensional conservation equations and steady state characteristics of components. Special efforts have been made to develop a compressor model based on a modified stage stacking method, which includes the simulation of modulating the variable inlet guide vane (VIGV) and the variable stator vanes (VSV) and conforms to the implicit numerical scheme. Transient behavior of a 150 MW class heavy-duty gas turbine during load variations is investigated and compared with field data.

Contributed by the International Gas Turbine Institute (IGTI) of THE AMERICAN SOCIETY OF MECHANICAL ENGINEERS for publication in the ASME JOURNAL OF ENGINEERING FOR GAS TURBINES AND POWER. Paper presented at the International Gas Turbine and Aeroengine Congress and Exhibition, Munich, Germany, May 8–11, 2000; Paper 00-GT-548. Manuscript received by IGTI Oct. 1999; final revision received by ASME Headquarters Oct. 2000. Associate Editor: D. Wisler.

Dynamic Model Overview

Dynamic behavior of a system that consists of working fluid and rotating parts can be described by conservation laws and the equation of motions. For a thorough analysis of the dynamic characteristics of gas turbines, unsteady three-dimensional calculations may be used. It is, however, inefficient to apply the unsteady three-dimensional simulation that requires a great computational effort for an entire engine volume, given that only the overall system dynamic characteristics will be obtained. It has been acknowledged that the unsteady one-dimensional simulation gives sufficiently accurate results for integral engine simulation purposes ([5–7]). In previous studies, ordinary differential equations describing system dynamics were usually derived from the partial differential equations by means of spatial discretization. Since the partial differential equations originate from an infinitesimal volume analysis, careful attention should be paid in their derivation when they are applied to a finite volume such as compressor, turbine, combustor, etc. Actually, the force and shaft power terms do not appear explicitly in partial differential forms of conservation equations.

In this study, to avoid such complexity in deriving the basic governing equations, the integral forms of conservation equations are used. This method is more intuitive and easier to understand than those used in previous studies. Regardless of the difference in the origination, the final ordinary differential equations are identical in both cases. The integral forms of conservation equations are

Continuity equation:

$$\int \left[\frac{\partial \rho}{\partial t} + \nabla \cdot (\rho \mathbf{u})\right] dV = 0 \tag{1}$$

Momentum equation:

$$\int \left[\frac{\partial (\rho \mathbf{u})}{\partial t} + \nabla \cdot (\rho \mathbf{u}\mathbf{u})\right] dV = -\int_S p\,\mathbf{n}\,dS + \mathbf{F} \tag{2}$$

Energy equation:

$$\int \left[\frac{\partial(\rho \hat{e})}{\partial t} + \nabla \cdot (\rho \hat{e} \mathbf{u}) \right] dV = \dot{Q} - \dot{W}_s - \dot{W}_p \tag{3}$$

where

$$\hat{e} = e + \frac{1}{2}(\mathbf{u} \cdot \mathbf{u}).$$

The ordinary differential equations describing the unsteady behavior of each component are obtained by integrating the above equations over the control volume. The variables in the storage terms are represented by the control volume exit values. The obtained ordinary differential equations can be solved numerically with the prescribed initial and boundary conditions. The derived basic governing equations are as follows:

Continuity equation:

$$V \frac{d\rho_{i+1}}{dt} = -\dot{m}_{i+1} + \dot{m}_i \tag{4}$$

Momentum equation:

$$V \frac{d(\rho u)_{i+1}}{dt} = -(\dot{m}_{i+1} u_{i+1} - \dot{m}_i u_i + p_{i+1} A_{i+1} - p_i A_i) + F \tag{5}$$

Energy equation:

$$V \frac{d}{dt}(\rho H - p)_{i+1} = -(\dot{m}_{i+1} H_{i+1} - \dot{m}_i H_i) + \dot{Q} - \dot{W}_s . \tag{6}$$

These equations are applied to each component with suitable F, $\dot{Q}$, and $\dot{W}_s$, which must be specified in each time step, i.e., given as input values. The force and shaft power in the governing equations are determined by steady-state characteristics, which can be derived from either characteristic maps or steady state off-design models. Once inlet conditions are given, the outlet conditions, which usually refer to total pressure and total temperature, can be determined by a steady-state analysis. Eventually, the force and shaft power terms in the governing equations are evaluated by the following equations:

$$F = \dot{m}^*_{i+1} u^*_{i+1} - \dot{m}_i u_i + p^*_{i+1} A_{i+1} - p_i A_i \tag{7}$$

$$\dot{W}_s = \dot{m}_i (H_i - H^*_{i+1}) \tag{8}$$

where ''*'' denotes the steady-state outlet conditions for the given inlet conditions at each time-step.

Component Models

Inlet and Exhaust Duct. There is no shaft work and heat transfer in these components, i.e., $\dot{Q}=0$ and $\dot{W}=0$. The total pressure loss in transient operations is corrected by the following equation ([8]):

$$\frac{(\Delta P/P_{\text{in}})}{(\Delta P/P_{\text{in}})_d} = \frac{(\dot{m}\sqrt{T}/P)^2_{\text{in}}}{(\dot{m}\sqrt{T}/P)^2_{\text{in},d}} \frac{R}{R_d}. \tag{9}$$

Compressor. Multistage axial flow compressors of heavy-duty gas turbines are usually equipped with VIGV for a stable startup and enhancement of exhaust heat recovery at part-load in the combined cycle plant. In some engines, VSVs are equipped as well. In addition, air bleeding from intermediate stages is performed to prevent surge and to supply coolant for turbine blades. As such, the operating characteristics of modern compressors are too complicated to be handled by conventional prediction methods, which generate a performance map first and utilizes it in engine simulation.

Accordingly, a novel method is proposed in this study. In order to simulate the interstage bleeding and VIGV and VSV modulation, a stage-by-stage calculation is executed. The whole performance of a compressor can be evaluated by stacking stage performances. Consequently, the method looks similar to the conventional stage-stacking method ([9] for example). However, the present method is different from the previous one in that it requires thermodynamic state variables rather than airflow rate as boundary conditions. This enables simultaneous calculations of all interstage variables, which avoids much iteration needed in the conventional sequential scheme. In the conventional method, air mass flow is first assumed and then calculation is executed until the given exit stage such as total pressure is obtained. It has an intrinsic problem in predicting the near-choke operation because even a slight change of mass flow results in a drastic change in pressure ratio. When pressure is used as boundary conditions as in the present method, the severity of the problem will be much alleviated. In the simultaneous calculation, static pressure, temperature and axial velocity are variables. Therefore, all of $3(n+1)$ variables exist for n stages. Three of them are given as boundary conditions (inlet temperature, inlet pressure, and exit pressure). Consequently, $3n$ variables are obtained since we have equal number $(3n)$ of equations (continuity, momentum, and energy for n stages). The multivariable Newton-Raphson method is used to solve the equation set.

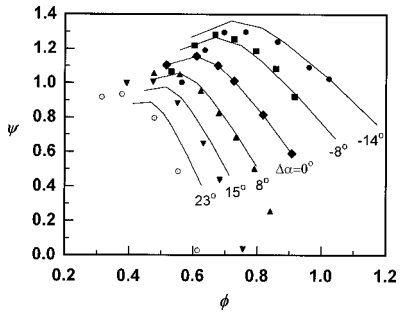

Fig. 1 Comparison of corrected stage characteristics by Eq. (10) with experimental data (lines: prediction, marks: experimental data from [16])

The generalized characteristic curves based on experimental data are used to predict stage performances ([10]). The stage characteristics are represented by nondimensional parameters such as flow coefficient (ϕ), pressure coefficient (ψ), and isentropic efficiency (η). The present method is easily extended to the variable geometry. In that case, a modification is made in evaluating the stage characteristics at different vane setting angles. If it is assumed that the stage efficiency, axial velocity ratio, and rotor discharge angle are primarily a function of rotor-incidence angle, the operating points with the same rotor incidence angle lie along the line ψ/ϕ = constant ([11]). This means that stage efficiency is constant along the line of constant ψ/ϕ. At a constant rotor-inlet angle, the change in flow coefficient associated with a given change in an upstream stator discharge angle (or rotor inlet flow angle) is found from the following equation:

$$d\left(\frac{1}{\phi}\right) = d(\tan \alpha). \tag{10}$$

The corrected flow coefficient at different vane setting angles can be found from a design point angle setting and flow coefficient. The pressure coefficient and stage efficiency are also determined from the corrected flow coefficient with the relation ψ/ϕ = constant at constant stage efficiency. To demonstrate the validity of the foregoing method, comparison with test results of a single stage compressor is presented. As shown in Fig. 1, the stage characteristics at different vane setting angles are well corrected by Eq. (10).

Shown in Fig. 2 is an example of the characteristics of a 12-stage axial flow compressor with fixed geometry. Since the flow

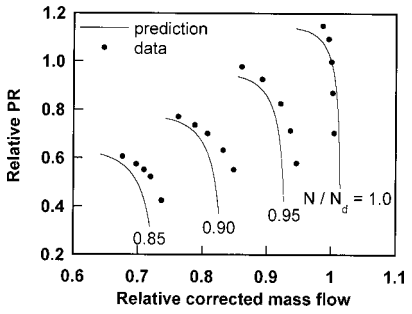

Fig. 2 Predicted characteristics of an axial flow compressor with fixed geometry (data from [17])

path geometric data are not given, they are presumed on the basis of general design criteria of modern compressors. Though a slight difference is found between the predicted and experimental data, results are satisfactory enough. If the exact geometric data of the compressor were known, results would be much closer to the experimental data. Estimated overall performance of a 17-stage variable geometry axial flow compressor is shown in Fig. 3. The characteristics predicted with assumed VIGV and VSV setting angles at each RPM (increase of vane closing with decreasing rotational speed) are presented together with those predicted with fixed geometry. It is clear that the predicted results with closing VIGV and VSV setting angles show closer coincidence with experimental data than those with fixed geometry do. This calculation confirms that the experimental map is generated with rpm-dependent vane setting angle.

Air bleed at the exit of a stage reduces the mass flow at the next stage, which influences the stage characteristics and ultimately changes overall compressor characteristics. In this study, since the stage-by-stage calculation method is introduced, the effect of interstage air bleed can be easily estimated by taking into account the flow rate of the extracted air in the stage-based governing equations.

From steady-state characteristics evaluated in the foregoing manner, stage exit variables in Eq. (7) and Eq. (8) are obtained, which are used to calculate the force and power required in the dynamic equations of Eq. (5) and Eq. (6).

Combustor. The amount of heat transfer in the energy equation is as follows:

$$\dot{Q} = \eta_{\text{comb}} \dot{m}_f (\text{LHV} + \Delta \text{H}_{T_0 \to T_f}). \tag{11}$$

The subscript 0 indicates a reference point where the lower heating value (LHV) is defined. η_{comb} is combustion efficiency. Total pressure loss in the combustor is also considered in the same manner as in duct model. The fuel flow rate that enters into the combustor must also be included in the continuity equation. Changes in gas components and thermodynamic properties after combustion are also considered.

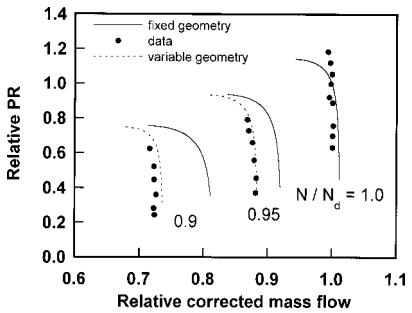

Fig. 3 Predicted characteristics of an axial flow compressor with variable geometry (data from [18])

Turbine. The turbine model is basically similar to the compressor model. The only difference lies in the method for evaluating steady-state characteristics. With given inlet conditions, expansion pressure ratio is obtained by the following Stodola equation:

$$\frac{\dot{m}_{\text{in}} \sqrt{T_{t,\text{in}}}}{P_{\text{in}}} = K \sqrt{1 - \left(\frac{P_{\text{out}}}{P_{\text{in}}} \right)^2} \tag{12}$$

where K is calculated from design point values. As mentioned above, the air extracted from the compressor is entrained to turbine blade rows for cooling and influence stage characteristics. Therefore, the effect of coolant flow must be considered in evaluating stage characteristics. To obtain stage performance, a row-by-row prediction method for cooled turbines, proposed by Kim and Ro [12], is used and a model of pressure loss caused by mixing is modified based on the model proposed by Kim et al. [13].

The amount of the coolant flow entrained to the turbine blade rows during transient operations is determined by the following equation:

$$\dot{m}_c = K_c p_c \sqrt{\frac{2(1 - p_t / p_c)}{R T_c}}. \tag{13}$$

The coolant flow is driven by static pressure differences between points where the coolant is extracted and injected. K_c is obtained from design conditions and p_t is static pressure at row inlet and exit for nozzle and rotor, respectively. The energy and mass flow rate of the coolant is included in the energy and continuity equations.

Rotating Shaft. The rotational motion of the shaft can be presented by the following equation:

$$I \frac{d\omega}{dt} = G_t - G_c - G_l. \tag{14}$$

The first two terms in the right-hand side refer to ''developed torque.'' In any steady operation of a generator driving gas turbine, the developed torque must be balanced with load torque (the last term) determined by the required power. During transient operations, when the load torque changes, imbalance between the load torque and the developed torque occurs, resulting in a change in the rotational speed.

Control Unit. In most generator driving gas turbines, the rotational speed is controlled at constant value, as they are required to produce constant frequency (50 or 60 Hz) electricity. The function of speed control is assigned to fuel control which performs its task by modulating fuel flow rates. Turbine exhaust temperature (TET) is usually controlled at its highest level during its transient operations if the load varies within an assigned range where TET control is possible. This is performed by controlling compressor inlet airflow using VIGV and VSV setting angle modulation. In many researches, various kinds of control logic have been proposed such as PID control, state space control, etc. As the object of this study, however, is not the controller design itself, a typical control unit model adopted in real engine control ([14]) is utilized. This model has also been used in other simulation studies with minor modifications ([3,15]).

The control unit is represented by the combination of a governor, an actuator, and a measurement system. The block diagram for the control unit is shown in Fig. 4. The control system includes speed control, temperature control, VIGV control, acceleration control, and upper and lower fuel and VIGV angle limits. The

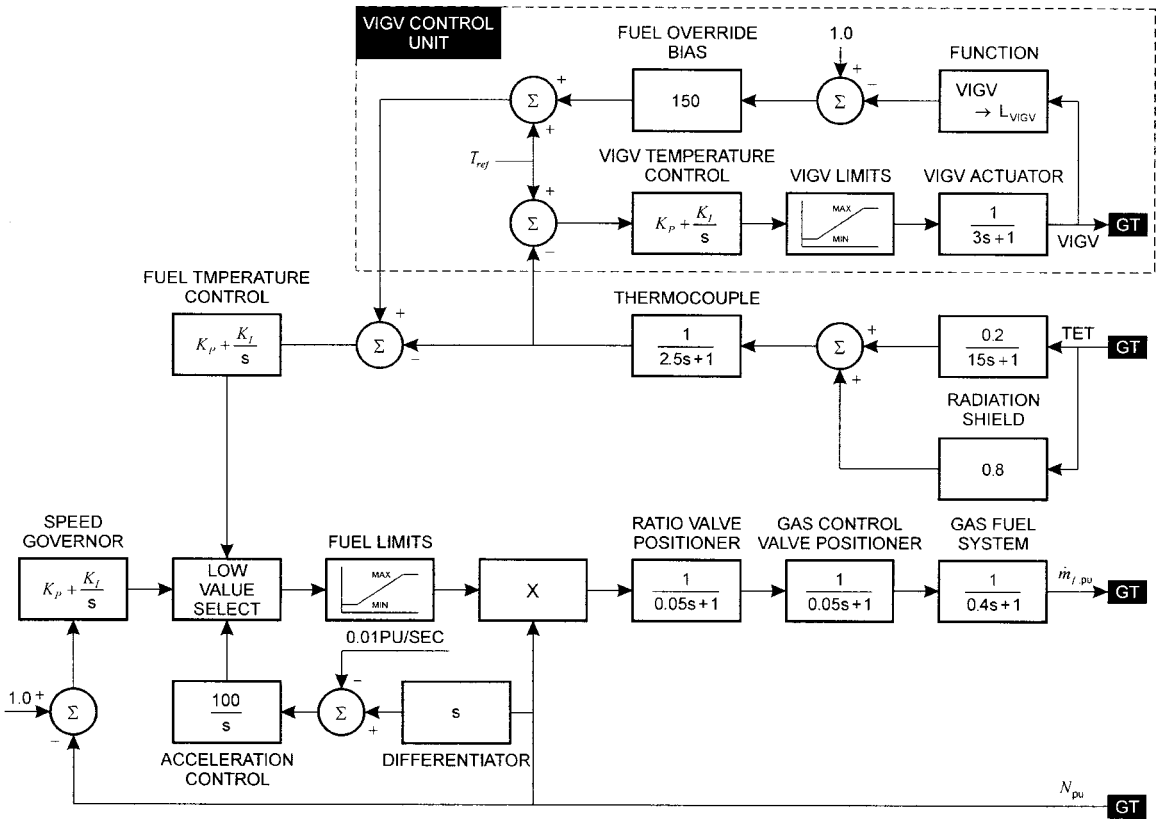

Fig. 4 Block diagram for the speed and target temperature control

governors are designed based on PI control logic and the fuel override bias is provided at partially closed VIGV to allow transient overfiring.

Since the simulation is executed in the time domain, the block diagram representation needs to be converted into the time-dependent equation forms. As a result, the control unit is described by first-order ordinary differential and algebraic equations. The fuel flow rate and VIGV angle are determined by solving these equations with given speed and TET at each time-step.

Numerical Treatment

Component mathematical models result in a system of ordinary differential equations. Simulating engine transient behavior means solving these equation sets numerically with the prescribed initial and boundary conditions. The gas turbine system can be divided into two modules from the viewpoints of numerical calculations: the uncontrolled gas turbine module and the control unit module. The control unit module of Fig. 4 determines the fuel flow and VIGV angle at each time-step based on the output data (speed and TET) of the uncontrolled gas turbine module of which component models have been explained in the previous section. Similarly, the characteristics of the uncontrolled gas turbine can also be calculated using the outputs of the control unit module (fuel flow and VIGV setting angle) as system inputs. Since each module needs only outputs of the other, two modules can be treated independently in the numerical calculation. In the uncontrolled gas turbine module, a fully implicit method is introduced for the sake of numerical stability and compatibility with a steady-state off-design performance prediction. The independent variables are static pressure, static temperature, velocity, and rotational speed. The system boundary conditions are total pressure and temperature at engine inlet and static pressure at engine exit. In the control unit module, the fourth-order Runge-Kutta method is adopted.

Results and Discussion

Accurate predictions of the steady-state characteristics must be the first step for accurate dynamic simulation. To validate the proposed model, steady-state off-design performance is predicted for a representative heavy-duty gas turbine (Siemens V64.3) and compared with operation data provided by the manufacturer. The steady performance can be predicted by the foregoing simulation method with transient terms neglected. Since full engine specifications, especially geometric data, are not given, they are complemented with the aid of a design point analysis of this work using appropriate assumptions. The design point analysis is executed based on the previous work ([12]). The design specifications are shown in Table 1. V64.3 engine has a 17-stage axial flow compressor with VIGV and four stages of VSVs. TET remains constant up to 50 percent load reduction. The design point VIGV and VSV angles are assumed to be 15 deg. It is further assumed that VSV angles are assumed to be linked linearly with the VIGV angle. The predicted results are shown in Fig. 5. System parameters describing steady-state characteristics show good agreements

Table 1 Design specifications of the V64.3 engine

System	SIEMENS V64.3	
Speed, rpm		5400
Electrical power, MW		61.5
Cycle efficiency, %		35.8
Compressor	17-stage axial	
Inlet air flow, kg/s		185
Pressure ratio		15.6
Combustor	Can type	
Turbine	4-stage axial	
Inlet temperature, °C		1250
Exit temperature, °C		534

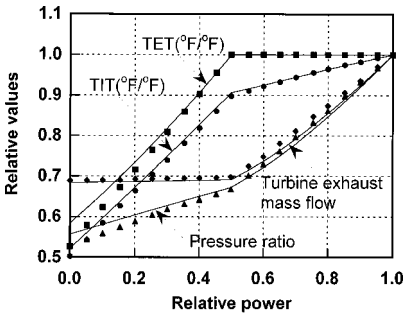

Fig. 5 Predicted off-design performance data compared with engine data for part-load operation of V64.3 (lines: prediction, marks: data from [19])

with manufacturer's data. This successful calculation indicated that the present component models, especially those of a variable geometry compressor, simulate the practical operation well enough.

For a modern 150 MW class heavy-duty gas turbine (GE 7F), the dynamic simulation is executed and compared with field data measured in a power plant. The 18-stage axial flow compressor is equipped only with VIGV for TET control. The design specifications are described in Table 2. This engine adopts VIGV control based on measured TET, but firing temperature (TRIT) instead of TET maintains its maximum value from 100 percent to 80 percent load. Thus, TET increases while load decreasing from the design point to 80 percent load. This is for the maximum heat recovery in the combined cycle plant. Since the firing temperature is not directly measured during the real field operation, its value for the temperature control feedback must be predicted. In most power plants, it is usually estimated from measured TET and compressor discharge pressure (CDP). In this study, however, firing temperature is presumed to be measured (a calculated value from the uncontrolled gas turbine module is used for this purpose) because the practical TRIT prediction method based on TET and CDP is not known explicitly. This pseudo-measured firing temperature is compared with a reference temperature, and error is estimated to

Table 2 Design specifications of the GE 7F engine

System	GE 7F	
Speed, rpm		3600
Electrical power, MW		150
Cycle efficiency, %		34.5
Compressor	18-stage axial	
Pressure ratio		13.5
Combustor	Reverse flow type	
Turbine	3-stage axial	
Exhaust air flow, kg/s		419
Firing temperature, °C		1260
Exit temperature, °C		600

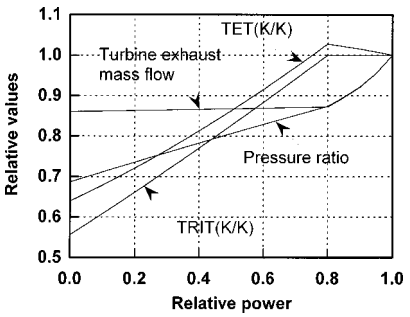

Fig. 6 Predicted off-design performance data of GE 7F engine

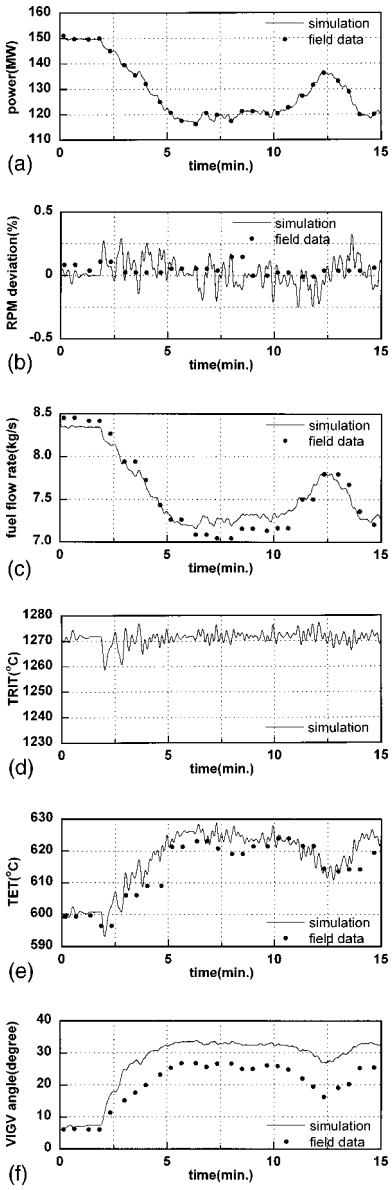

Fig. 7 Comparison of simulated transient behavior of GE 7F engine with real operation data: (*a*) developed power, (*b*) rpm deviation, (*c*) fuel flow rate, (*d*) firing temperature, (*e*) turbine exhaust temperature, (*f*) VIGV angle

activate VIGV setting control. The steady part-load performance under TRIT control predicted by the present calculation is shown in Fig. 6. These steady state off-design values are used to get the reference firing temperature (effectively the same as design temperature from 100 percent to 80 percent load).

Under variations of demanded load, transient characteristics are simulated and compared with field data. The field data are sampled for every 10 seconds during 15 minutes. The control gains provided by Rowen [14] are used with slight changes in the integral gain of the fuel control to prevent system instability. As control signal is usually updated for every 0.1–0.2 second, the simulation is executed with 0.1 second time-step. The simulated dynamic characteristics are shown in Fig. 7. As shown in Fig. 7(*a*) and (*d*), the rotational speed and TRIT are controlled at their desired value by modulating fuel flow rate and VIGV. The overall predicted data are in good agreement with the corresponding field data. Since demanded load is obtained for relatively long sampling time and the control gains are not known exactly, high-

frequency deviation can be seen in the simulation results. The difference in VIGV angles between prediction and measurement is mainly due to ambiguity in defining angles. No clear definition of measured angle is given. It could be either guide vane exit metal angle or any other nominal setting angle such as blade stagger angle. In the present simulation, VIGV angle is deduced from rotor inlet flow angle for the typical blade geometry data and no flow deviation is assumed. Detailed information on guide vane geometry and angle definition would improve the coincidence. As of now, however, in view of predicting overall engine performance behavior, the exact simulation of the absolute value of the VIGV angle is not critical. What is important is the precise prediction of compressor inlet airflow rate, which are believed to be well predicted considering the good agreements with field data of other performance parameters such as temperatures and power.

Conclusion

A dynamic simulation model for heavy duty gas turbines is proposed and applied to the simulation of a real engine. Every component is modeled on the basis of common ordinary differential formulations. Special efforts have been made to model operating characteristics of multistage axial flow compressors with variable vane setting angles and interstage bleeding. A novel stage-stacking method characterized by simultaneous calculation of all interstage variables is introduced and its validity is exemplified. The intensive cooling of turbine blades is also modeled. Since accurate prediction of steady-state characteristics is required for dynamic simulations, steady-state off-design operation is first predicted. The predicted results are in good agreements with real engine data. Appropriate control logic is introduced to predict practical engine transient behavior. Dynamic simulation of a modern 150 MW class heavy duty gas turbine is carried out through the combination of a gas turbine simulation routine and a control unit model, which are represented by sets of ordinary differential equations and algebraic equations. Transient behaviors during variation of demanded load are fairly close to field data. It is concluded that the proposed simulation model are suitable for predicting both the steady-state off-design performance and the dynamic behavior of heavy-duty gas turbines.

Acknowledgment

This work was supported by the Brain Korea 21 Project.

Nomenclature

A = area
e = internal energy per unit mass
F = force
$\mathbf{F}$ = force vector
G = torque
H = total enthalpy
I = polar moment of inertia
$\dot{m}$ = mass flow rate
$\mathbf{n}$ = surface normal unit vector
N = rotational speed
P = total pressure
p = static pressure
PR = total to total pressure ratio
$\dot{Q}$ = heat transfer rate
R = gas constant
S = surface
t = time
T = total temperature
TET = turbine exhaust temperature
TIT = turbine inlet temperature
TRIT = turbine rotor inlet temperature
u = axial velocity
$\mathbf{u}$ = velocity vector
V = volume
VIGV = variable inlet guide vane
VSV = variable stator vane
$\dot{W}_s$ = shaft power
$\dot{W}_p$ = pressure work
α = rotor inlet flow angle
ρ = density
ω = angular velocity

Subscripts

c = compressor or coolant
d = design point
f = fuel
i = control volume index
in = inlet
l = load
out = outlet
t = turbine

References

[1] Fawke, A. J., and Saravanamuttoo, H. I. H., 1971, ''Digital Computer Methods for Prediction of Gas Turbine Dynamic Response,'' SAE Paper 710550.
[2] Rowen, W. I., 1983, ''Simplified Mathematical Representations of Heavy-Duty Gas Turbines,'' ASME J. Eng. Power, **105**, pp. 865–869.
[3] Crosa, G., Ferrari, G., and Trucco, A., 1995, ''Modeling and Recoupling the Control Loops in a Heavy-Duty Gas Turbine Plant,'' ASME Paper 95-GT-61.
[4] Korakianitis, T., Hochstein, J. I., and Zou, D., 1993, ''Prediction of the Transient Thermodynamic Response of a Closed-Cycle Regenerative Gas Turbine,'' ASME Paper 93-GT-136.
[5] Schobeiri, M. T., Attia, M., and Lippke, C., 1994, ''GETRAN: A Generic, Modularly Structured Computer Code for Simulation of Dynamic Behavior of Aero- and Power Generation Gas Turbine Engines,'' ASME J. Eng. Gas Turbines Power, **116**, pp. 483–494.
[6] Crosa, G., Pittaluga, F., Trucco, A., Beltrami, F., Torelli, A., and Traverso, F., 1998, ''Heavy-Duty Gas Turbine Plant Aerothermodynamic Simulation Using Simulink,'' ASME J. Eng. Gas Turbines Power, **120**, pp. 550–556.
[7] Badmus, O. O., Eveker, K. M., and Nett, C. N., 1995, ''Control-Oriented High-Frequency Turbomachinery Modeling: General One-Dimensional Model Development,'' ASME J. Turbomach., **117**, pp. 320–335.
[8] Cohen, H., Rogers, G. F. C., and Saravanamutto, H. I. H., 1996, *Gas Turbine Theory*, 4th Ed., Longman Group Limited, U.K.
[9] Stone, A., 1958, ''Effects of Stage Characteristics and Matching on Axial-Flow-Compressor Performance,'' Trans. ASME, **80**, pp. 1273–1293.
[10] Muir, D. E., Saravanamuttoo, H. I. H., and Marshall, D. J., 1989, ''Health Monitoring of Variable Geometry Gas Turbines for the Canadian Navy,'' ASME J. Eng. Gas Turbines Power, **111**, pp. 244–250.
[11] Klapproth, J. F., 1958, discussion in Stone, [9].
[12] Kim, T. S., and Ro, S. T., 1995, ''Comparative Evaluation of the Effect of Turbine Configuration on the Performance of Heavy-Duty Gas Turbines,'' ASME Paper 95-GT-334.
[13] Kim, J. H., Kim, T. S., Lee, J. S., and Ro, S. T., 1996, ''Performance Analysis of a Turbine Stage Having Cooled Nozzle Blades with Trailing Edge Ejection,'' ASME Paper 96-TA-12.
[14] Rowen, W. I., 1992, ''Simplified Mathematical Representations of Single Shaft Gas Turbines in Mechanical Drive Service,'' ASME Paper 92-GT-22.
[15] Hannett, L. N., and Khan, A., 1993, ''Combustion Turbine Dynamic Model Validation from Tests,'' IEEE Trans. On Power Systems, **8**, No. 1, pp. 152–158.
[16] Cyrus, V., 1994, ''Separated Flows in Axial Flow Compressor with Variable Stator Vanes at Positive Incidence Angles,'' ASME Paper 94-GT-480.
[17] Iwamoto, T., Ikesawa, K., Kanayama, T., Nagai, K., Yukinari, A., and Nakagawa, T., 1991, ''Development of a High-Pressure Ratio Axial Flow Compressor,'' *Proceedings of the 1991 Yokohama International Gas Turbine Congress*, Vol. II, Gas Turbine Society of Japan (GTSJ), pp. 79–86.
[18] Kashiwabara, Y., Matsuura, Y., Katoh, Y., Hagiwara, N., Hattori, T., and Tokunaga, K., 1986, ''Development of a High-Pressure-Ratio Axial Flow Compressor for a Medium-Size Gas Turbine,'' ASME J. Turbomach., **108**, pp. 233–239.
[19] Jansen, M., Schulenberg, T., and Waldinger, D., 1992, ''Shop Test Result of the V64.3 Gas Turbine,'' ASME J. Eng. Gas Turbines Power, **114**, pp. 676–681.

An International Electronic and Interactive Teaching and Life-Long Learning Platform for Gas Turbine Technology in the 21st Century

T. H. Fransson
Professor, Fellow ASME
e-mail: fransson@egi.kth.se

F.-X. Hillion
Graduate Student
e-mail: fxh@egi.kth.se

E. Klein
Graduate Student
e-mail: eloi@egi.kth.se

Royal Institute of Technology,
Division of Heat and Power Technology,
100 44 Stockholm, Sweden

An interactive learning platform which sets a new standard for electronic learning of gas turbine technology in a global life-long learning perspective is presented (Fig. 1). The platform contains a theoretical section in the form of several pages for each chapter available, with a significant number of related interactive simulations, movies, animations, virtual laboratory exercises, virtual study visits and realistic case studies. A significant background information related to historical development in the field, a display of existing components, nomenclature, multi-lingual dictionary and keywords, as well as questions for self-assessment and exams, an electronic communication group and a database of the user's ''successes and failures,'' enhance the learning process in a significant way. The program is intended as a platform for an international collaboration on learning heat and power technology. It can be used both in the classroom as well as for self-studies and is as such well adapted for both university and post-university learning, both on and off campus. Tools to facilitate the introduction of new material exist. It is thus hoped that teachers at different universities can join forces and in a noncompetitive way introduce material which can be shared, instead of developing similar simulations with somewhat different interfaces. The long-term goal of the learning platform is of course that users worldwide will have the possibility to access the best teaching material available from any specialist, and that this material will contain supplementary pedagogical information which will enhance the learning both at a university and a post-university level. [DOI: 10.1115/1.1367341]

Introduction and Objectives

The classroom is at many universities today almost like it was in the beginning of the 20th century. The teaching is often done the same way and the students are supposed to learn the same way, although much more material is today presented to them. Of course, some technical issues have been changed with the appearance of the slide projectors for photos and overhead slides, as well as with movie and video projectors and with computers. Teachers often enhance the teaching with illustrations using these media, and then the students are expected to grasp the full implications of the shown material immediately, as they do not have the possibility to repeat the experience at their own learning speed (mostly while studying for the exam!). Similar with laboratory exercises and study visits. These very often pass by the students as a nice but not very exciting experience in which the students often copy material from colleagues to get it over with as soon as possible. All these various teaching environments are of course essential and good, and enhance the *teaching* to a large extent, but the *learning* aspects are usually much less improved. An important aspect is that the ''learning by repetition'' can not be achieved as the students often only see some highly interesting material once.

Since the personal computer entered into the university environment in the early 1980s, teachers with futuristic views have tried to use this technology as part of their teaching/learning material. Other teachers have totally avoided this new media. The limited experience available related to the use of computers in teaching technical subjects at a university level has shown that the students have probably not learned more than in the classical way. As a matter of fact, the experience of using computers in the classroom has often been fairly frustrating for the teacher as they spend a lot of time in preparing the material, which the students thereafter do not use and, moreover, do not at all appreciate the significance of. The fact that most classrooms are not equipped for teaching with the aid of computers is certainly another contributing factor to the many failures in ''electronic learning.''

The classical textbook on basic engineering subjects should be considered from a similar perspective as the classroom: It looks

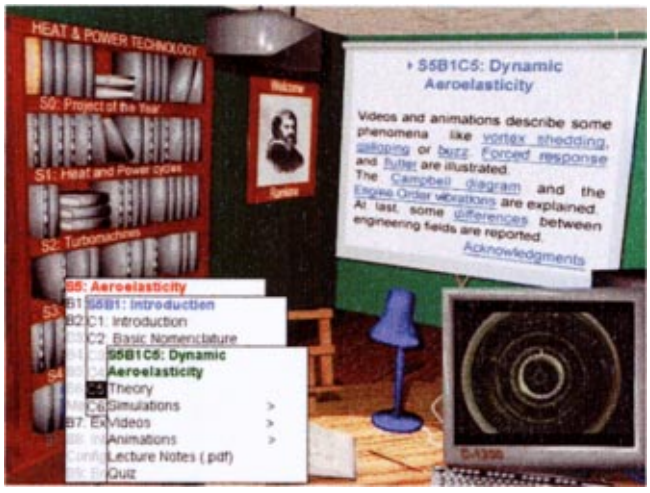

Fig. 1 The bookcase gives the main interface of the platform

Contributed by the Advanced Energy Systems Division of THE AMERICAN SOCIETY OF MECHANICAL ENGINEERS for publication in the ASME JOURNAL OF ENGINEERING FOR GAS TURBINES AND POWER. Manuscript received and accepted by the AES Division, Dec. 2000. Editor: H. D. Nelson.

almost the same as it did in the beginning of the 20th century. Of course, many more textbooks exist today, covering the scientific and technical progress (but are all much better?) and the most recent books present a limited number of computer simulations in electronic form. The textbook is of course an essential material in the learning process, but it is today possible to enhance this learning with animations, simulations, movies, virtual laboratory exercises, case studies, etc., in a way which greatly surpasses what any printed textbook can offer. Perhaps the time has come when electronic material should be the basis for the learning process, and the printed textbook the appended material?

The main objective of the model presented is to, for the first time in turbomachine related teaching, *establish a comprehensive combined learning and teaching tool* which from the start has been established as fully electronic, such that it covers all the necessary aspects which are perceived to belong to learning in a modern environment. The secondary objective is to present a tool which can be used as *an international platform for a global learning space*, in which teachers from different universities work together with the goal to in a common way enhance learning for students anywhere in the world: a tool to be used any time and any place.

Fig. 2 Typical page from the chapter ''Introduction to Turbomachines''

General Layout of the Platform

Several computerized simulations have been developed for classroom use over the last 20 years in the field of gas turbine technology. Among the most recent ones can be mentioned Benson et al. [1–4], Bölcs [5] and Mattingly [6]. An excellent calculation program which can be recommended also for teaching purposes is developed by Kurzke [7]. A first preliminary attempt of a universal educational platform was presented by Léotard et al. [8]. Many computer programs for research have derivatives that the researcher has transformed into teaching material. Each one of these attempts is generally good and brings home a specific message to the students. Because of the large cost involved in developing electronic course material, individual efforts have however often been concentrated on isolated spinoff simulations from research topics, and entered into the ''classical'' teaching material as an attachment. In most cases the students have not been as enthusiastic about the added *teaching* value as the researcher, and their *learning* has not been enhanced the way the teacher might have imagined. As far as the present authors are aware the platform presented here is, however, the first electronic attempt to more completely cover the material a student would use during the learning process of heat and power technology.

This platform collects the theory for courses in the form of overhead pages (which can be used both for lectures and self-studies), interactive simulations, virtual laboratory exercises, virtual study visits, and selected case studies. Additional information is provided by a toolbar, and classical ''lecture notes'' are as well included (to be read on the screen or printed). Of course, access to vast stores of information by itself does not guarantee broad educational benefits, as pointed out by Boyle [9]. As a matter of fact, the role of computer software is to create an effective environment for learning. Therefore particular attention has been paid to structure the information aiming at more coherence and to enhance interactivity. First, the complete material is organized as a ''bookcase'' (Fig. 1): a shelf gathers the information about a general subject, which is divided into books, which are divided into chapters (Figs. 1 and 2). Secondly, according to Laurillard's [10] advice, all the chapters share the same buildup: The first page in each chapter gives an introduction, the second one defines which knowledge the student has to acquire, and the last one sums up the key points. The main text is limited to keywords or short sentences, but a lot of supplementary information is available as ''pop-up'' by clicking on underlined blue words (Fig. 3). The student who attended the lecture will benefit from this synthetic presentation but, of course, the one who did not may sometimes have trouble in understanding the points. Therefore such students will enjoy an automatic mode to follow vocal explanations by a guide. This feature is both practical (easy to use, speedily illuminating) and attractive to learners for its efficiency and its motivating ''human touch.''

The simulations are the next appealing aspect of the platform. They enable the learners to familiarize themselves with the topic and highlight the key parameters as well as their influence (Fig. 4). Moreover, in each of these simulations, a ''guide'' gives advice to the students of how to use the simulation in the most effective way. This guide ''simulates'' the teacher during the student's home studies, but is not intended to ever replace the interaction with the teacher during normal lectures. Yet, the simulations are flexible enough to let any teacher illustrate their main interest. These simulations constitute a second way to learn, based on discovery and experience and then, as such, are another major asset of the platform.

Besides, deeming the invaluable ergonomics of a book, the programming tries to enhance the freedom of the user. The bookcase enables to flip through the whole material as the topic of each chapter is automatically displayed on the ''white board'' (Fig. 1). The contents of each chapter are also available. The user can take notes, bookmark pages as he bookmarks web pages, and go back to any previous page. Teachers can preselect pages for their own

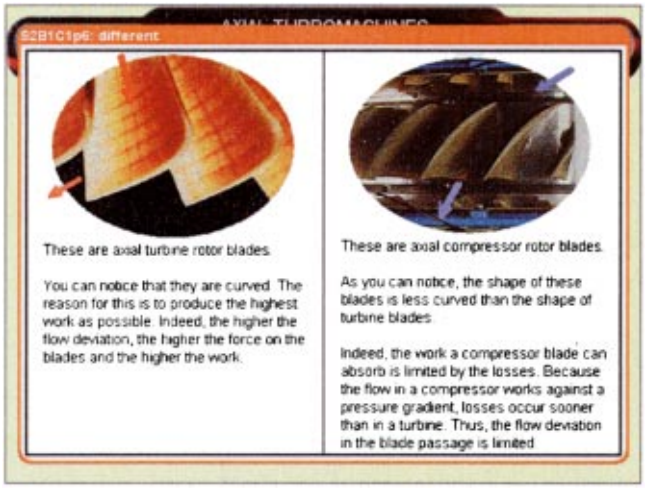

Fig. 3 The underlined words, ''pop-up,'' provide further information

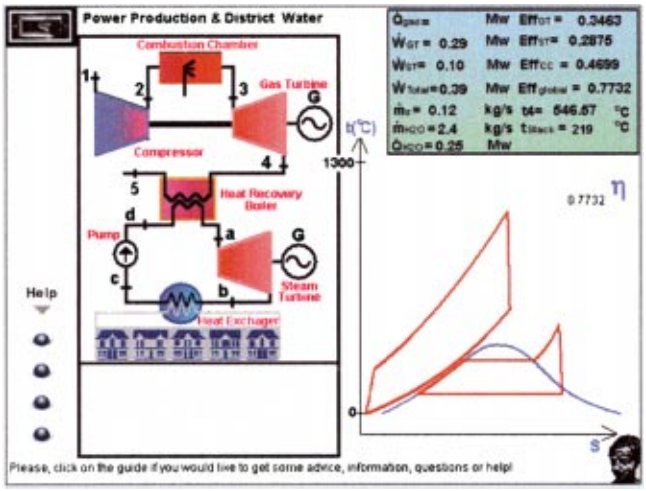

Fig. 4 Simulation of ''Combined Cycle Power Production and District Heating.'' The guide is seen in the bottom right corner.

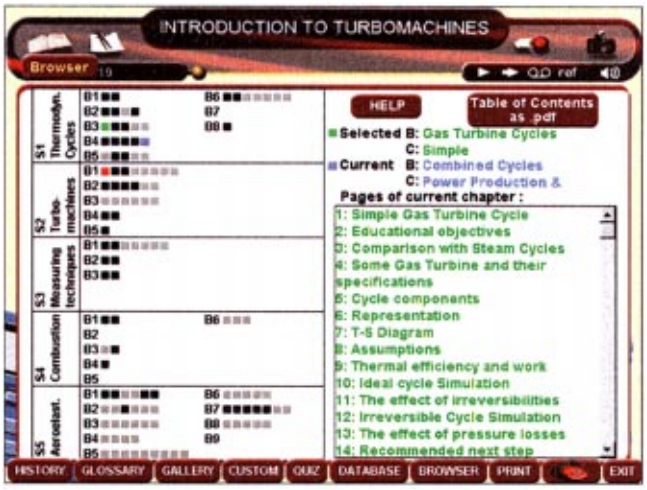

Fig. 6 The browser is one of the several navigation tools in the platform, it enables one to reach any page

individual lectures (Fig. 5). As such it is possible to use other media to present the basic background (blackboard, overhead projector . . .) and directly jump back and forth with the preselected material from the platform. A browser gives a complete view of all the detailed ''pages'' and enables to reach any one in a very easy way (Fig. 6). These various tools are designed to meet the different needs of teachers and students. Even a teacher who does not want to use the existing theoretical section is still able to navigate easily and employ the more advanced learning tools available.

As courses do not make up the whole material by themselves, the authors want to broaden the education to the history of the related fields as well as to specific knowledge of technical choices for the design of today's machines. These are part of other significant utilities presented in the form of a ''toolbar'' at the bottom of the screen (Fig. 6). The historical section gives the main tendencies, in a fairly detailed way, of the turbomachinery development (Fig. 7), as well as an indication to scientists and engineers who have made significant contributions to the field. A gallery gives a significant amount of sketches and photos of different gas turbines, steam turbines, and boilers, together with detailed facts related to the scale of the machine, pressure ratio, temperature, number of stages, etc. (Figs. 8, 9). This kind of information is of interest to anyone who tries to learn differences between machines, or just want to get a general overview of existing components.

A glossary is introduced to solve comprehension issues related to terminology. It proposes a list of keywords to find the exact definition of most terms used inside the platform (Fig 10), a list of all symbols employed, a list of the units employed throughout the program. Finally, the students who do not have English as mother tongue will enjoy a multi-language dictionary translating specific engineering terms into German, French, Italian, Spanish, Hungarian, and Swedish (Fig. 11). A search engine allows the user to click on many terms and be directed to the page where the subject is treated more in detail.

In any classical textbook the exercises available play a significant role in the student's learning process. Books often state a problem and then possibly the final answer, and leave the student completely in the dark about how to solve the problem. In the present platform the approach is to specify the problem in a similar way as in a classical textbook, but then to allow the students to ''buy hints'' from a ''guide'' about how to solve it. A score of one to ten points (depending on the complexity of the problem) is obtained in the case the student solves the complete problem, without any help, by clicking on the correct multichoice answer.

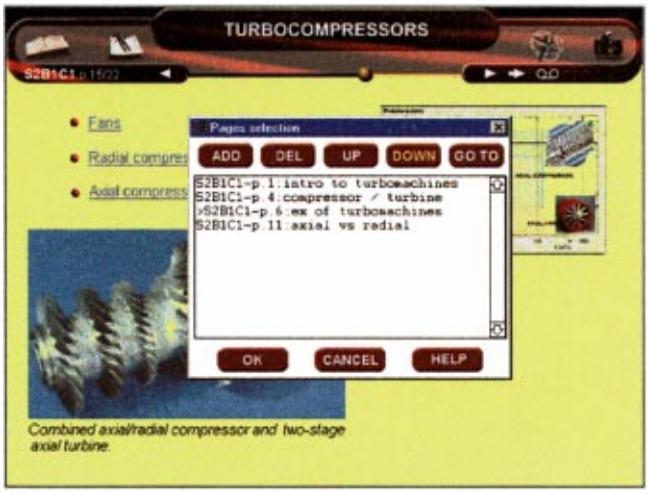

Fig. 5 Teachers can pick up the elements they want for their lecture by preselecting their pages

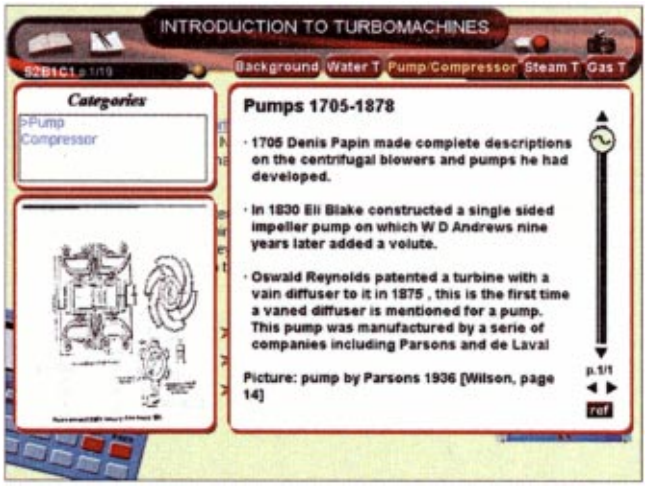

Fig. 7 Snapshot of the historical content

Fig. 8 Example of overall information contained in the ''Gallery''

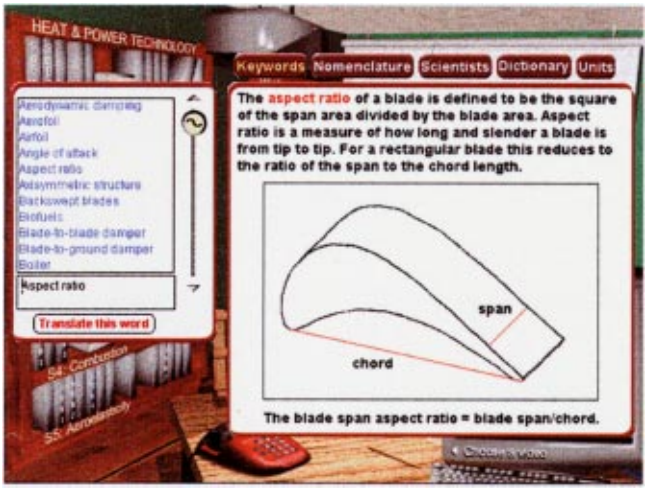

Fig. 10 The glossary defined keywords, relying heavily on illustration and referring to books and articles

Along the way one to five ''hints'' can be bought. For each help bought, the students final score for this exercise is reduced by one (or more) point(s).

As the main goal for several students during their studies seem to be ''pass the exam,'' a self-assessment quiz has been added (Fig. 12). This allows the student to check the personal progress and easily to go back to the material which has perhaps not been assimilated and accommodated as well as it should. The questions are of a multiple-choice character with seven possible answers to reduce the chance of getting a good score by random guessing to less than 15 percent. Ten questions are presented in each quiz session, selected from ten different categories, and both the questions and the answers are presented randomly, giving a large number ($=10*7$) of variations even if exactly the same ten questions would be used more than once. With a growing number of questions in each chapter, it will be possible to use these same questions also as exam questions. As a supplement to the quiz a database, which keeps track on what the student has looked at and achieved, is present (Fig. 13). It gives the student the total score achieved throughout the learning process. This database can also, if wished, be used by the teacher as a mean to follow up on the progress of an individual student. Each quiz question has a certain score to it (as with the classical exercises discussed above), and an electronic scoreboard is available in which the students can continuously compare their score against each other.

The individual teacher has a possibility to establish own quiz questions with the ''quiz-creator.'' The so-established questions will override, or complement, the original questions in the platform. In such a way, by means of this tool and the ''page selector'' (Fig. 5), the students will primarily follow the teacher's material and only use the platform as a secondary learning source.

The use of the worldwide web has recently been introduced into the platform. Before the first lecture, the students must answer a prerequisite test in the form of ten multiple-choice questions on the program web page. This preliminary examination aims at targeting the right level of teaching. In the future, these tests will be part of the CD-ROM and access to a chapter will require good results to the corresponding test. Besides, an electronic discussion group has been established to facilitate communication between and among teachers and students at the same or different universities. The teacher can provide additional material to the whole group or set important dates. The student who has problems somewhere can ask for help from the other persons, and not get into disarray. It also has a social purpose since the person who answers becomes an adviser. If necessary students can ask a teacher, but in the developers' vision they must first look by themselves. A ''Frequently Asked Questions'' database will be available for all the

Fig. 9 Detailed information gives the key parameters

Fig. 11 Glossary: multi-language dictionary

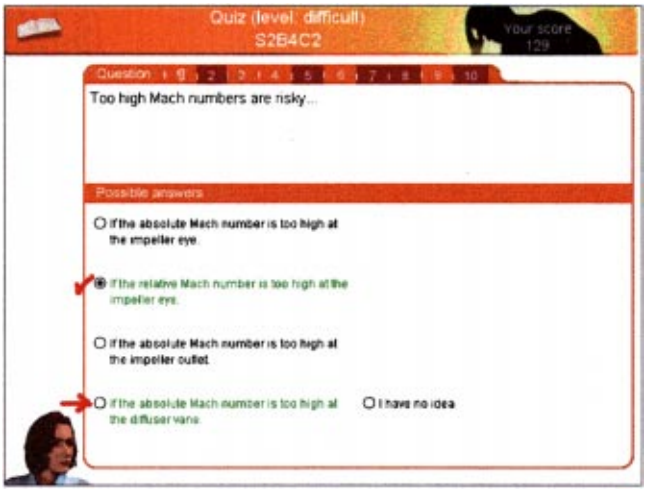

Fig. 12 Quiz for self-assessment, the correct answers are the second and fourth listed. Clicking on them leads to the page in the theoretical part where further explanations be found.

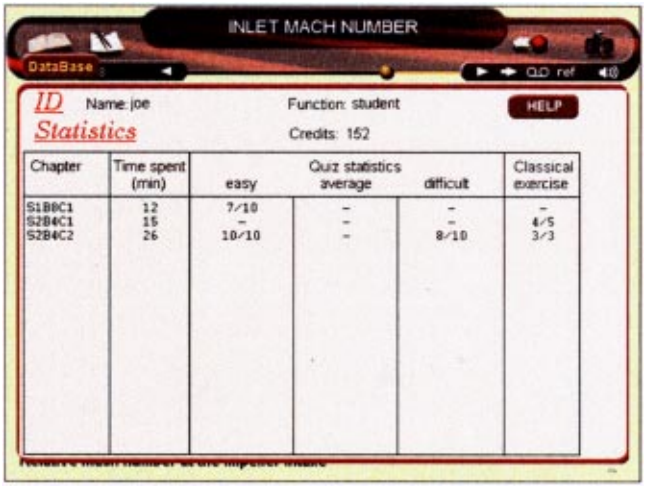

Fig. 13 The database collects the results of the quiz and classical exercises for both the students and the teacher. These results are prepared by the platform developers to the time spent in order to improve the material.

students: Everyone will be able to profit from the experience of the others. Private companies have the possibility to introduce company proprietary material. These will not be part of the global platform and will need specific user names and passwords.

Specific Technical Content of the Platform Presently

The platform is in no way intended to leave the impression of being complete at the present time, although there is already a significant amount of material included. It is instead thought of as a start for joint educational collaboration in the field of heat and power technology, with the aim that teachers worldwide will add material which they consider to be good and unique. In such a way the content will be extended over the next few years. Presently the main emphasize has been put on the following courses (or ''bookshelves''):

- heat and power cycles
- turbomachinery
- combustion
- measuring techniques
- aeroelasticity

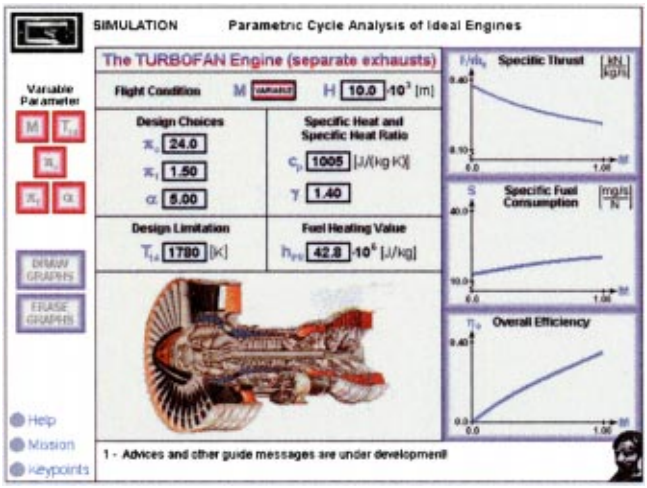

Fig. 14 Simulation of an ideal turbine

with the upper shelf (Fig. 1) giving supporting material of various kind, among these specifically the ''projects of the year.'' These latter rely on the concept of ''project based learning'': the students have to, as a team, complete a one academic year-long project. They learn by themselves while being supervised by a ''design review team'' consisting of professors and engineers the traditional matters through the project difficulties (Svensdotter et al., [11]). The intent is that students from different universities in the future will work together on such projects as multinational teams.

The ''*project of the year*'' shelf collects the reports of previous ''project of the year'' studies, which keep track of the progress and the motivation for choices at each milestone. The 98/99 KTH students had to design a power plant (Svensdotter et al. [11]) and the 99/00 KTH students have found inside the platform the technical specifications, the process overview, the feasibility study, the layout and general design, the component design, and finally the commissioning of this plant. It is believed that the students will benefit from the experience of their predecessors when they will work on their own ''project of the year.''

The content of the *heat and power cycle shelf* gives the students a basic repetition of thermodynamic cycles, and concentrates thereafter on various steam and gas turbine cycles, covering the basic Rankine and Brayton cycles. Passing by aspects like regenerating, inter-cooling, reheat, as well as the combined gas and steam cycle (Fig. 4), the steam-injected gas turbine and more advanced cycles like the humid air turbine, Kalina cycle and air bottoming cycle, as well as some propulsion cycles, are described to the students, illustrated with information from some existing power plants, together with a significant number of interactive simulations. In some chapters a spoken text is introduced into the program, again with the idea to enhance the student's learning capabilities during the off-campus studies. As part of the *propulsion cycles*, simulations related to the ramjet as well as the turbofan, turboprop, and turbojet (all with/without afterburner) cycles can be employed (Fig. 14). On this shelf, as well as on the others, the detailed material is not yet complete, but it is still believed to be of such quality that it will be a significant positive added value to courses in the field at most universities.

On the *turbomachinery shelf* the user is introduced to the components of a gas and steam turbine, the definitions of the fundamental equations, the two-dimensional velocity triangles, design parameters, and cascade flow. Several simulations (Fig. 15) and animations are available inside this shelf. As there is not yet any discussion related to the three-dimensional flow in this part of the platform, this shelf can be considered to represent an introductory turbomachinery course.

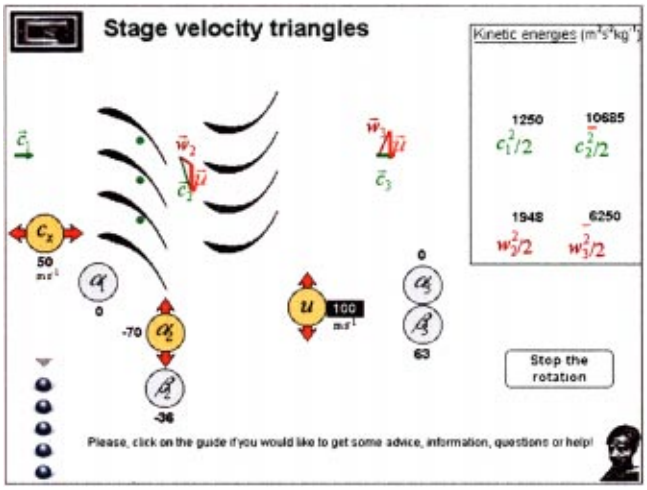

Fig. 15 One of the simulations related to the velocity triangles

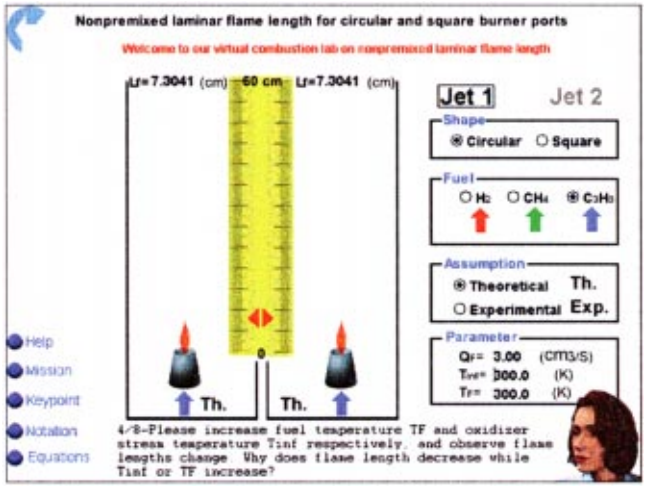

Fig. 16 Virtual laboratory exercise on ''Laminar Flames Length''

The *combustion shelf* is presently very basic and covers only an introduction to general combustion as well as a ''virtual laboratory exercise'' dealing with laminar flame lengths (Fig. 16). These ''virtual laboratory exercises'' are intended as a pre-laboratory experience for the students to prepare themselves for a more effective ''real'' hands-on laboratory exercise, and serve also as an extremely useful tool for the students when they prepare themselves for the exam.

On the *measuring techniques shelf* a few experimental techniques of relevance to turbomachinery are introduced. First of all the students are given background material to how to perform an experiment, and thereafter material related to pressure, velocity, mass flow, and temperature measurements are presented, along with some basic visualization techniques. Both theoretical aspects as well as some ''virtual laboratory exercises'' (Fig. 17) are present. For this shelf complete lecture notes (both in English and French) in a written form exist so that the user can study these on the monitor, or print them out for more ''classical'' reading.

The *aeroelasticity in turbomachines shelf* is today the last information available. It covers presently a very detailed introduction to the field as well as detailed terminology and nomenclature. There are several animations and simulations present, each covering some essential features for a physical understanding of the phenomena (see Figs. 18, 19). As for the measuring techniques shelf, written lecture notes are included for a few chapters.

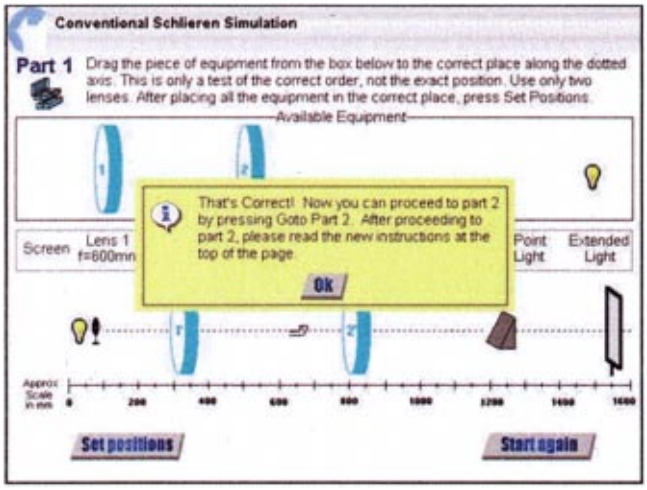

Fig. 17 Virtual laboratory exercise on ''Schlieren Visualization''

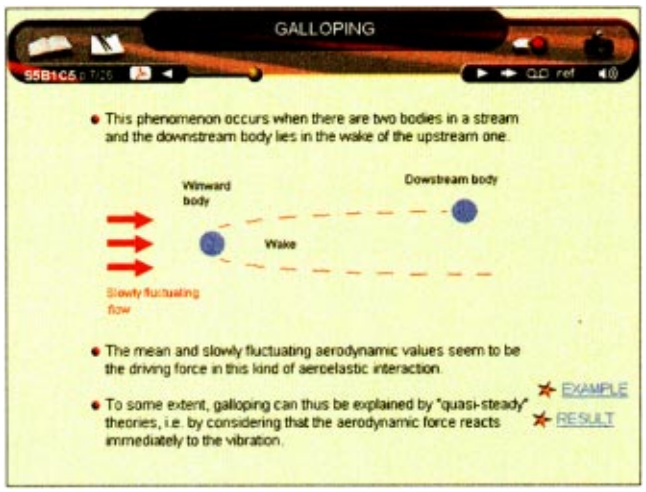

Fig. 18 Animation explaining galloping

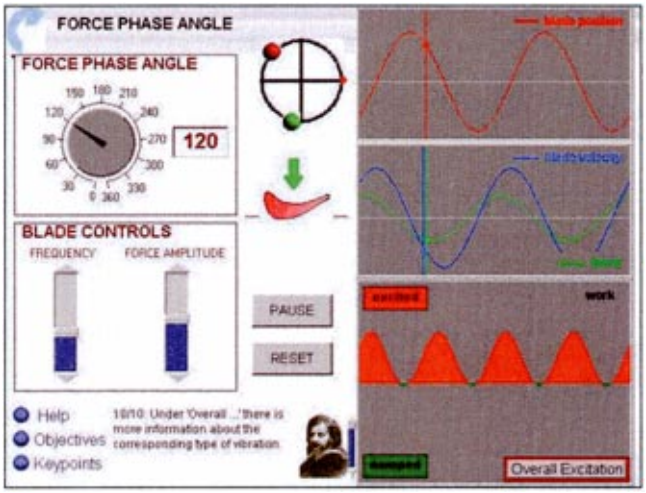

Fig. 19 Simulation of the force phase angle of the unsteady flow on a vibrating blade

With the content on these five shelves it is believed that the curriculum at most universities who teach the subject of heat and power technology or air-breathing propulsion will find something useful inside the platform. Of course, it will not be possible (and is not the intention) for one university to completely fill such a broad field. It is instead hoped that the present content can give a flavor of what is possible with today's electronic means, and that a joint collaboration in the future will allow for an increase of material, as well as for an improvement of the existing parts, with the objective to increase the users' learning speed and understanding depth.

Teachers' Concern: ''Why Should This Electronic Learning Tool Succeed as so Many Others Have Failed?''

Any kind of change from the traditional educational way is, rightly, treated with a large degree of skepticism: Many attempts have been made aiming for significant improvements, with a few successes and many failures. Thus many concerns of various importance have been expressed during the development of the proposed teaching and learning platform. A few of these will be mentioned in this section, together with some ideas of why the present platform can be considered to be more adapted to ''electronic learning'' than previous attempts in similar directions, and why an ''electronic learning'' platform can enhance the learning process.

Tried It Before and It Did Not Work. Many attempts towards using computers in education have been performed over the last 10–20 years. Almost all have failed as the students have not been as enthusiastic as the researcher/teacher was. The main reason for this lack of enthusiasm from the students can, the present authors believe, probably be attributed to the fact that the students are very goal-oriented in their studies. However, often this goal (=pass the exam) is not the same as the teacher's goal (=learn the subject as well as possible). In almost all attempts the present authors have seen related to computerized education the emphasize has been put on a specific simulation/calculation the students should perform. The basic connection to the underlying theory and, more specifically, to the exam, has been missing. The present platform is established to connect all the essential ingredients into a linked package so that the students see the connection between all the different parts of the curriculum and the knowledge to be obtained (i.e., how to pass the exam).

Not Invented Here. This is a teacher, not a student, syndrome. The present authors believe that the basic reason why there are so many different textbooks in certain areas with only small differences is related to the fact that each teacher has his own individual way of presenting a specific material. A teacher might be happy with certain chapters in a specific book, but not with others. Individually written lecture notes are thus perceived as something essential, to a large degree as students cannot be expected (=refuse?) to collect material from several textbooks. Over the years small changes in the lecture material make the teacher to take the decision to go ahead and write a full textbook.

The remedy to this problem in the present platform is to realize that the main importance of the platform is not the way the theory is presented by the individual teacher. It is instead related to the physical understanding by interactive simulations, animations, movies, etc., as well as to the completeness of the lecture material, as prepared by many different teachers, in one volume. Each individual teacher can thus use their own theory for any specific chapter in the way he or she would like (as blackboard, overhead slides, lecture notes, etc.), and they may or may not choose to include this material in the platform or to distribute it to the students. Of course, if a teacher thinks that nothing inside the existing platform is of any interest whatsoever, the authors can only conclude that this teacher must have an excellent material available, and would hope that it can be made available to a larger audience immediately.

I Want to Use My Own Material. No problem of course. Any teacher should use the own material as long as it is better than what is offered. The cost for developing a complete learning material will however prevent most teachers from developing anything better than what can be done in the form of a consortium. The ''page'' and ''quiz creators'' can be used to include own material in different ways. Easy jumps between any part of the platform to the teachers own PowerPoint (or other) files give an increased flexibility for the teacher to improve the lecture material.

''Many Students Do Not Speak English Well Enough'' and ''Teachers Want to Preserve Their Own Language''. The most important aspects of the platform are the simulations, the animations, and especially the pedagogical and other ''added-value'' links. It is believed that these in the long-term perspective will be of enough value to teachers and students to compensate for the lack of material in the students own language. Furthermore, although the material in the program is in English, it is, of course, normal that the teacher during the lectures speaks the language that would be spoken without the existence of the proposed platform, and also that the teachers under certain circumstances may offer some material in the platform in another language than English (as an example, the lectures notes of several ''books'' on ''The Measuring Techniques'' are both in English and French). With the growing number of foreign exchange students at many universities worldwide it may actually be beneficial for many students to have some reference material also in English.

I Like to Browse the Book. This is a very important factor, and it can, of course, not be done on a computer in the same relaxed way as with a traditional book. The platform tries to be flexible on this issue: First of all the navigation inside the platform is easy and user-friendly, and secondly all the material is offered also as a printed version, if anyone would select to use the material in such a way. Furthermore, printing utilities, such that the user can print anything from the platform, have been included.

I Can Bring the Book Everywhere. This is of course, an important aspect. However, the present authors consider it highly likely that there, within a few years, will be ''reading computers'' of low weight and long battery life. The weight and length of a ''study session'' will thus probably not be of any concern in a few years, especially not as the students do not have to carry with them several kilos of books anymore.

It is Difficult to Concentrate as Long on a Computer as in a Book. This is a very valid concern, which the present authors fully agree with. It is thus of high importance that any electronic learning tool will have a significant amount of diversification incorporated to avoid loss of concentration. Still, it is likely that a ''learning session'' will be shorter with electronic learning than in the case a classical textbook is used. Furthermore, one of the main reasons for the electronic learning is to reduce the learning time which then of course justify the shorter ''learning sessions.'' In the present program the number of pages per chapter is limited to 10–15, with a significant amount of diversity inside each page.

Will This Platform Replace the Teacher. This is absolutely not the intent! However, it is hoped that through the fact that many persons are involved in the effort the material included will make it possible for an interaction teacher↔student on a higher intellectual level than what sometimes can be possible in the classical teaching environment. This may very well put a larger burden on teachers as more students may have more of the complicated questions that traditionally only a few exceptional students have come up with. But this must be regarded as a positive problem by any teacher!

All Students Everywhere Shall Not be Presented With the Same Material. This is again a very valid argument which has to be addressed by individual teachers. The presented platform can serve as a base for a faster and more thorough learning of a significant amount of material, but it is also intended to arise the students' intellectual curiosity. The student↔teacher interaction at a higher physical understanding level, as well as the fact that the material in the platform will be presented by several person (while still in a similar framework), will thus be the main catalyst for the students ''out-of-the-box-futuristic'' thinking.

Will This Platform Replace the Book. Again, this is absolutely not the intent! However, it could very well be imagined that a material as presented in the platform in the future will reduce the number of similar undergraduate (and beginning graduate) textbooks on an identical subject. There will also in the foreseeable future still be a large need for high-level textbooks on special scientific topics. But today's emphasize on ''printed book with accompanying electronic simulations'' will probably be changed towards ''electronic simulations with accompanying printed material''?

How Can the Student Take More Serious Notes Than Just Text. As in the classical learning environment, any student or teacher can make notes on paper and keep or submit these to the teachers. In the present platform, there is a possibility to write in plain text as comments but there is not yet a way to make personalized comments in electronic graphical form inside the ''notes'' package. However, when more computers will have received touch screens for writing such an option can without problem be introduced. Nevertheless, the program offers a printing command which exports all pages of a chapter (including the popups if wished) as pictures and generates an html file making them up as a handout for students.

It is Not Possible to Assess the Students Knowledge With Computerized Multiple-Choice Exams. This is a concern for many teachers, as they consider multiple-choice questions to be much too simplistic. It is true that a computerized exam with multiple choice questions can not replace an *oral* exam, with the student/teacher interaction. However, the present authors maintain that most *written* exam questions can be replaced by electronic multiple-choice questions, without the fear that the student can pass the exam by just guessing. Guessing can, of course, never be excluded but with seven possible answers and a negative score for wrong answers the probability of successfully passing the exam in this way becomes very low. The other fear is of course that the students can pass the exam by solving the problems correctly but without acquiring the fundamental physical understanding of the material which the teacher intended. This concern has to be taken care of by sophisticated multiple-choice questions. Such pedagogical tools are already common in various exam forms.

A Teacher Would Like to Use His Own Exam Questions as the Emphasis on the Lecture Material From Various Teachers are Different. This is of course no problem. The platform is conceived such that new quizzes can easily be added, and that individual questions can override the ones presently in the platform. It is however believed, and hoped, that most teachers would not have anything against that their students also test the knowledge against questions established by other teachers. This can nothing but improve the students understanding. Furthermore, if a certain number of teachers would like to eliminate certain questions from the platform this will of course also be possible. In general new questions from different teachers will however probably be added instead and thus enhance the value of the platform.

Why Should the Student Use This Program as They Still Need a Textbook. The need for a textbook will depend on the teacher and the specific chapters. Presently there are lecture notes of, it is believed, sufficient quality in some chapters, and these can be printed by the students if they so would like. As time goes on it is hoped that different teachers would work together to establish a common text for each individual chapter which many instructors would be comfortable with. Of course, every time a teacher would have a new text, this can be put into the program so that students can have access to it. Thus, it is not a problem to have several complete, but somewhat different, textbooks for a specific chapter available inside the platform if this would be necessary! It is, however, rather probable that most teachers would like to make only minor adjustments to a common text. The advantage would be that the teachers can still use the chapters from the ''electronic platform'' which they would be comfortable with, and can thus concentrate upon improving certain chapters instead of writing a full textbook. With this system the total cost for the lecture material would, in a fairly short time perspective, be reduced for the student, as all the material needed for basic studies of heat and power technology would be directly available from the platform.

There is Too Much Material in the Program. The Students Will be Overwhelmed. The classical approach for most teachers is to guide the student through the material which should be covered during a specific course by indicating which pages should be read in which chapter in which book, which pages are for learning and which are for browsing, etc. This procedure is exactly the same in the present ''electronic platform.'' The teacher will in an individually prepared accompanying information indicate to the students which parts of the platform are of highest interest for this teacher's specific course. Furthermore, a teacher can of course, select to present the different subjects in separate ''platforms'' (i.e., in different ''bookcases''), although some of the advantages with a common platform for the entire subject of heat and power technology would then be lost.

The Students Should Not Get Everything Served Inside One Book. They Should Learn to Find Material at Other Places. This is of course also a very valid comment. The reason why there are so many textbooks with similar basic engineering material is, however, as the lower classes of undergraduate students generally do not accept to receive materials from different sources (different notations, high costs, . . .). For these students there would be no change in the working habits. For the senior years the only change is that the students have a significant larger amount of material available in the ''electronic book'' than in a ''classical textbook,'' but it is in no way perceived that all the material a students would need to solve a real-life problem will be present in the ''e-book.'' There will thus not be any significant change in the student's working habit with the appearance of ''electronic books.''

All Students Do Not Have Access to an Appropriate Computer at Home. As seen from the preliminary evaluation discussed below, this fact was some sort of surprise to the authors since KTH had made some deliberate efforts a few years ago to allow students to acquire home computers inexpensively. Yet it is believed that, as time goes on, less and less students will be in this situation. Otherwise the student will have to study the material on the campus computers, much the way that most students today not buy all textbooks but instead go to the library to study these.

Difficult to Communicate Among Teachers at Different Universities. The initiator of the platform dares to put forward the statement that there unfortunately in a ''normal'' teaching environment is hardly any exchange between teachers at different universities! Any kind of collaboration would thus be a progress. In the platform the following electronic communication groups are offered:

- students and teachers discussing technical aspects of the platform,
- students and teachers discussing the solution to specific problems in the platform,
- ''frequently asked questions'' group which anyone can consult,

- students sending individual comments to the platform developers, and
- teachers sending individual comments to the platform developers.

In the two last cases the caretaker of the discussion groups will judge if the comment is of such a general interest that it should be added to the ''frequently asked questions'' group.

Virtual Laboratory Exercises and Study Visits Can Never Replace a ''Hands-On'' Experiment. Of course, this is not the purpose. However, a virtual exercise or study visit will allow the students to better prepare themselves beforehand, and will also allow a detailed repetition of the material afterwards. The learning process of the student will thus be improved.

Preliminary Assessment

It is not expected that teachers or students will embrace the presented platform fast or fully. The promises and expectations expressed in the previous section of this paper have to be investigated and evaluated in detail in the future. It is also recognized that detailed assessments have of course to be performed related to both the way the user perceives the technical issues of the platform as well as, more importantly, how the students learning process is improved with the tool.

Various preliminary versions of the platform have been employed in a course in the fourth-quarter teaching at KTH for the last three years. During this time both the platform interface and the course material has evolved. It is, however, still important to note that only about 10–15 percent of the teaching material in the division of heat and power technology (which covers about 400 hours in total) is presently imported into the platform. The first year the tool was only used as a teaching tool (i.e., by the teachers) in the third year (of a four-year curriculum). It was perceived that the students had better assimilated the material related to velocity triangles than previous years. The second year the platform was made available to students in the form of a CD-ROM as well as on the local network at KTH, but ridiculous technical problems appeared (there were no-CD-ROM readers in the PC rooms at KTH, and the students did not have access to the network on which the program was installed.) Before these problems were solved more than half of the quarter was gone, and the assessment by the students was (rightly) very critical. The ''lessons learned'' was of course that in order to keep the students' interest there can be absolutely no flaws in the access to the program! The third year an evaluation related to the ease of use of the software was performed and the students appreciation of the media showed a very high (70 percent and above) appreciation rate. However, not enough care had been put on the correlation between the exam questions and the material in the program, and as such a complete evaluation of the students knowledge could not be performed.

The program has also been used on a much smaller scale at universities in Finland, Switzerland, and the USA. All the comments obtained from the colleagues at these universities have been worked into the platform.

The evaluation will continue during the future academic years in a more precise pedagogical, as well as technical, manner.

Conclusions

An electronic learning and teaching platform for the field of heat and power engineering is presented. It is believed to be the first complete electronic textbook in the field which covers the main essential ingredients in a modern educational environment, such as:

- presentation of the basic theory in an electronic, interactive form together with printed versions of the material in the classical form,
- ''pop-up'' for further very detailed information,
- interactive simulations with guided messages,
- movies and animations,
- virtual laboratory exercises,
- virtual study visits,
- case studies,
- polyvalent glossary,
- pre-requisite test in the web,
- electronic discussion groups, and
- interactive exercises and exam questions.

This type of new electronic learning platform can hopefully serve as a base for a better teaching and learning environment in a global life-long education in the field of transforming chemically bound energy to heat and power in the future.

Future Work

The latest navigation and customization tools must be evaluated during the next academic years. Comments from students and teachers will yield considerable corrections.

Presently the information available in the platform is related to the thermo and aerodynamics of gas turbines, it would be highly appreciated to have collaboration in material science and in maintenance of machines in order to improve these aspects.

The platform is currently available to teachers for testing on a common CD-ROM. In the future, it is intended to be available directly on internet.

A consortium related to the future development of the educational material inside the program is planned. Industry and academia will then work together to improve/expand the material over the next few years. The reader is invited to contact the development team if he or she would be interested to participate in this process.

The core of the platform is more or less independent of the topic. It is scheduled to excerpt it in order to provide the background programming to the one who wish to develop course on another topic.

Acknowledgments

The platform presented has been developed with funding partly from the Council of Renewable Education in Sweden (B. Jalling), together with the School of Mechanical and Material Engineering at KTH (Prof. M. Hansson), Birka Energi (J. Alsparr), and the Division of Heat and Power Technology. The ideas expressed are the authors alone and do not necessarily correspond to the ones of the sponsoring organizations. A significant number of undergraduate and graduate students at the KTH have been involved in the project. Their work is acknowledged in detail inside the program.

A special thanks goes also to the colleagues with whom the first author has discussed many pros and cons of an electronic learning platform over the years.

References

[1] Benson, T. J., 1994, ''On the Use of Computers for Teaching Fluid Mechanics,'' NASA Technical Memorandum 106587.
[2] Benson, T. J., 1995, ''An Interactive Educational Tool for Turbojet Engines,'' AIAA 95-3055.
[3] Benson, T. J., Trefny, C. J., and Walker, J. F., 1997, ''Interactive Design Tool for Turbine Based Combine Cycle Engines,'' AIAA 97-3160.
[4] Benson, T. J., 1998, ''Using Computers in Fluids Engineering Education,'' NASA TM-1998-208810.
[5] Bölcs, A., 1990, private communication, EPF-Lausanne, Switzerland.
[6] Mattingly, J. D., 1999, ''New Software to Support System Approach to Conceptual Design of Aircraft Engines,'' AIAA 99-2849.
[7] Kurzke, J., 1998, ''Gas Turbine Cycle Design Methodology: A Comparison of Parameter Variation with Numerical Optimization,'' ASME Paper 98-GT-343.
[8] Léotard, P. Roy, S., Gaulard, F., and Fransson, T. H., 1998, ''Computerized Educational Program in Turbomachinery,'' ASME Paper 98-GT-415.
[9] Boyle, T., 1997, *Design for Multimedia Learning*, Prentice-Hall, Englewood Cliffs, NJ.
[10] Laurillard, D., 1993, ''Program Design Checklist for Making the Most of the Medium,'' http://iet.open.ac.uk/h802/2/sup/DesignCheckList.html.
[11] Svensdotter, S., Almkvist, P., and Fransson, T., 2000, ''Introduction of Project Based Learning for Designing a Heat and Power Plant into the Last Year Curriculum,'' ASME Paper 2000-GT-0583.

Measurement and Visualization of Leakage Effects of Rounded Teeth Tips and Rub-Grooves on Stepped Labyrinths

D. L. Rhode

B. F. Allen

Mechanical Engineering Department,
Texas A&M University,
College Station, TX 77843

The effect of rounded labyrinth teeth tips and worn abradable lands has been found to give substantially increased leakage, which is well known to give reduced machine efficiency. Very little information concerning this exists, and some of the first measurements and visualization movies for stepped labyrinths are provided here to give an enhanced understanding of this phenomenon. A unique, very large-scale seal test facility was used. Glitter, and alternatively fluorescein dye, was employed as the flow tracer material. The flow visualization movies were digitally stored on the hard drive of a computer. Large decreases of leakage resistance due to the presence of worn teeth as well as rub-grooves were found. For the cases considered, the leakage resistance decrease for the large step height configurations were 85 percent, 55 percent, and 70 percent for the small, medium, and large pre-rub clearances, respectively. It was also found that the resistance varied with wear geometry, in order from highest to lowest resistance, as (a) ungrooved-unrounded-teeth, (b) ungrooved-rounded-teeth, (c) grooved-unrounded-teeth and (d) grooved-rounded-teeth. Further, a substantial tooth tip recirculation zone was visually observed only for the grooved-unrounded-teeth cases, and it was shown to be the mechanism by which the unrounded teeth give this configuration a higher resistance than do the rounded teeth. [DOI: 10.1115/1.1377873]

1 Introduction

A decrease in overall efficiency results from fluid leakage through noncontacting seals inside many turbomachines; the higher pressure drop values found in more modern gas/steam turbines, as well as centrifugal compressors, generally yields increased leakage. The advantages of labyrinth seals are primarily their reliability and simplicity, as well as their forgiveness when radial misalignment of the rotor and casing centerlines occurs. In addition they are easy to manufacture and are advantageous over an extremely wide speed, temperature, and differential pressure range. For example, Zimmermann et al. [1] discuss the advantages of labyrinths over other sealing alternatives for high temperatures and high centrifugal speeds. Also Sneck [2], for example, discusses the comparative advantages of labyrinths.

Labyrinth seals satisfy different requirements, depending on the application. Often they either minimize the leakage between high and low pressure regions, or they maintain a desired leakage to provide thermal reliability. Each throttling tooth in a labyrinth of any configuration provides a locally high kinetic energy at the throttle, a portion of which is dissipated. The portion which is not dissipated is either diffused or constitutes the kinetic energy carryover that reaches the subsequent tooth; this latter quantity is generally approximated as zero for a stepped seal.

Although present in essentially all product testing, the effect of tooth tip wear and rub-grooves on abradable labyrinth performance has rarely been investigated; rather, seal test rigs and design models have ignored these effects. The results shown herein demonstrate that a very substantial increase in leakage (decrease in leakage resistance) occurs due to the presence of rub-grooves and/or the presence of tooth tip wear. Because new machines must have higher efficiency and reliability, they are generally being designed for higher temperatures and/or pressures, which require more careful design analysis of challenging problems. Thus designers need a better cause-and-effect understanding of worn teeth and rub-grooves on labyrinth leakage.

Choice of Leakage Parameter. Leakage data for gas labyrinths has been conveniently presented as the well-known flow parameter ϕ, which is the mass flow per unit area for an ideal gas. However, when obtaining flow visualization data, water gives very large advantages over air, and the flow parameter is not allowed because of its ideal gas requirement. A further complication in the present work is that measurements clearly show a significant Re dependence for a given actual (minimum-distance) tooth clearance ''c_a'' which for the groove-centered tooth location considered, is the ungrooved clearance ''c'' plus any groove depth. This effect has apparently been unknown (or at least unreported) until recently ([3]). The leakage Reynolds number is defined as $\mathrm{Re}_{2ca}=\rho V_{ca}(2c_a)/\mu$, which is proportional to the mass flow rate, i.e., $m=\mathrm{Re}_{2ca}\mu\pi D/2$. In order to separate the Reynolds number effect from that of geometry, Re_{2ca} should be plotted against the pressure drop for each seal geometry. The dimensionless pressure drop can be defined as $K_{ca}=\Delta P/(0.5\rho V_{ca}^2)$, and (assuming c_a/R_{sh} is small) the mass flow is obtainable therefrom as $m=[2\rho]^{0.5}[\Delta P/K_{ca}]^{0.5}[\pi D c_a]$.

However, comparison of a configuration with and without a rub-groove cannot be easily shown on a single figure when using quantities defined in terms of the actual clearance c_a. Further, due to thermal mismatch and rotor centrifugal growth, the labyrinth teeth undergo significant axial and radial movement relative to the stator seal surface. Thus, at some operating conditions the actual clearance is sometimes the diagonal distance between the downstream corner of the tooth tip and the downstream *exterior* corner

Contributed by the International Gas Turbine Institute (IGTI) of THE AMERICAN SOCIETY OF MECHANICAL ENGINEERS for publication in the ASME JOURNAL OF ENGINEERING FOR GAS TURBINES AND POWER. Paper presented at the International Gas Turbine and Aeroengine Congress and Exhibition, Indianapolis, IN, June 7–10, 1999; ASME Paper 99-GT-377. Manuscript received by IGTI, Mar. 1999; final revision received by the ASME Headquarters, Aug. 2000. Associate Editor: D. Wisler.

of the rub-groove. Alternatively, the actual minimum-distance clearance is sometimes the *axial* distance from the tooth tip to an ''end-wall'' of the rub-groove.

To allow the leakage of all rub-groove depths for a given pre-wear clearance to be easily compared on a single figure, the pre-groove radial clearance ''*c*'' is being employed as a *reference clearance* in defining K and Re again in the present work. Hence, the reference quantities, based on the reference clearance ''*c*,'' are $V_c = m/(\rho a)$, $K = \Delta P/(0.5\rho V_c^2)$, $\mathrm{Re} = \rho V_c(2c)/\mu$ and $m = [2\rho]^{0.5}[\Delta P/K]^{0.5}[\pi Dc]$. It is easily observed that such use of a fixed reference clearance allows grooved and ungrooved configurations, for any particular ''*c*'' category, to be easily compared on a single figure. Specifically, for a given ΔP, the higher K value in such a comparison indicates the lower mass leakage. Thus K is considered to be the *leakage resistance coefficient* similar to the pipe flow friction factor. Note that a plot of the similar quantity involving the actual clearance, i.e., K_{ca} defined above (rather than the reference clearance, i.e., K), causes confusion because a higher K_{ca} value indicates a higher mass leakage [i.e., $K_{ca} = K(c_a/c)^2$].

The following section gives the objective. Next is a brief review of the most relevant previous work. Subsequently, the facilities and then the tooth wear and rub-groove configurations are described. Finally the results and then a summary are given.

Objective

Almost all current seal design methods do not attempt to account for the effect of rounded teeth tips (herein referred to as ''worn'') or of rub-groove wear. These types of wear are commonly found in abradable labyrinths (including honeycomb labyrinths). ''Rounding'' of the sharp tooth tip edges is particularly found for unhardened teeth such as those of teeth-on-stator (aluminum-teeth) labyrinths commonly found in centrifugal compressors, for example. Because very little information concerning these effects on labyrinth leakage exists, especially for stepped seals, little design progress in this area can currently be made. The objective of this investigation is to obtain an improved understanding of the effect of tooth wear and rub-groove wear on leakage resistance. This is to be accomplished by obtaining and analyzing leakage resistance measurements as well as corresponding visualization movies.

For the wear-in type of labyrinth there exists an extremely wide range of (*a*) pre-rub clearances (perhaps 0.051 mm (0.002 in.) to 0.254 mm (0.01 in.)), (*b*) rotor centrifugal growth, and (*c*) rotor thermal axial growth. Thus the current work attempts to provide a generalized insight for a broad range of groove and tooth cases with applicability to most types of turbomachinery, including centrifugal compressors.

Previous Work

Flow visualization techniques, although providing very insightful understanding, have been used only occasionally for labyrinth seals. Stocker [4], for example, used a ''two-flat-plates'' water flow visualization tunnel to obtain a preliminary assessment (Phase 1) of numerous designs. Air bubbles were injected into the flow, and design candidates were judged on bubble concentration density, recirculation zone velocity, and leakage measurements. In a later phase, the better configurations were tested in a rotating air rig.

In another case, Jerie [5] used flow visualization photographs of simulated labyrinth seals that were also in a two-flat-plates water channel. Jerie considered only straight-through configurations because of their simplicity and cost-effectiveness. He attributed the discrepancies between his data and that of Egli [6] to Egli's inability to accurately measure the smaller tooth throttle clearances in his smaller test rig. Jerie observed varying diffusion effects on leakage as the clearance-to-pitch ratio varied for very low Re from 1500 to 2000.

A very large-scale ''two-flat-plates'' water rig for visualization/leakage measurements was developed by Rhode et al. [3] that allowed almost any stepped, interlocking, or straight-through configuration to be quickly altered from outside the test rig. Because of its uniquely large degree of scale-up, it allowed small details (i.e., tooth throttling) to be easily photographed. The very complicated geometry-leakage relationship was determined by simultaneously adjusting various aspects of a given seal configuration and comparing the relative levels of turbulence and leakage. The result was that, in some situations, an unexpected change in leakage occurred. In other situations a large change in configuration gave a negligible change of leakage.

The flow visualization of the very large-scale test facility described above was upgraded and used to study ([7,8]) novel design features for stepped labyrinths. The upgrade incorporated an 8-mm camcorder with a 12-X zoom lens that interfaced to a pentium computer, which captured the digital images on the hard drive. Tiny plastic glitter particles were injected into the water as tracer particles. A new design with a strategic annular groove, for which flow visualization movies were available, gave a 26 percent leakage reduction over the standard design. Much greater leakage reductions were also found, but complete visualization was unavailable for those.

Static Testing Effects. Waschka et al. [9] found that the effect of shaft speed on leakage, at realistic Re greater than about 10^4, is negligible. The limiting Re above which shaft speed has a negligible effect depends on the tooth clearance, and larger clearances give larger Re. Thus since most turbomachines exhibit labyrinth Re above 10,000 there is little concern of shaft speed.

Labyrinth Wear Effects. Teeth tip ''wear'' (rounding) occurs sometimes for non-wear-in labyrinth designs and always for light-wear-in designs, whereas heavy-wear-in designs often use a hardness coating that is initially quite rounded at the tip and changes little with rubbing. Succintly stated, currently operating gas turbines have many coated, i.e., ''worn-teeth'' seals. Almost without exception, labyrinth seal test specimens from which rig data have been collected for developing design leakage correlations have generally not included any wear effects. Moreover, design method development and validation efforts (typically proprietary) have generally not accounted for the effects of tooth tip wear and rub-groove wear. A contributing reason for this is apparently that wear-in labyrinths throughout turbomachinery products encompass a wide range of pre-rub clearance, rotor centrifugal growth and rotor thermal axial growth. Hence, considering turbomachinery in general, there appears to be no ''typical'' groove shape or size (for further details see ''Parameters and Conditions''). However, there are a few published studies that have considered the effects of wear. Specifically, a commercial CFD code was utilized by Zimmermann et al. [1] to examine the effects of worn abradable coatings and worn (rounded) tooth tips on the discharge coefficient of straight-through and stepped labyrinths. The primary wear geometry that was considered typical for their product range was a rectangular groove shape with: (a) an axial width of 0.075 cm (0.03 in.), (b) a radial depth of 0.02 cm (0.008 in.) (c) pre-rub clearances of 0.02 cm (0.008 in.) and 0.04 cm (0.016 in.), and (d) (uncoated) tooth tips that were quite rounded. They found, for their operating conditions, that such rub-grooves can increase the leakage by varying substantial amounts for the stepped seal.

Secondly, Stocker et al. [10] tested primarily straight-through labyrinths with solid, abradable and honeycomb surfaces. The few tests involving rub-grooves were for straight-through abradable labyrinths. The rub-grooves considered representative for their product range (aircraft engines) were nearly rectangular in cross section with a radial depth of 0.025 cm (0.01 in.). The groove width was 0.06 cm (0.024 in.) at the land surface and narrowed to a width of 0.051 cm (0.2 in.) at the groove bottom. The tooth clearances investigated were 0.013 cm (0.005 in.), 0.025 cm (0.01

in.), and 0.051 cm (0.02 in.). In this case the grooves reduced the leakage; however, this anomaly was attributed to the fact that fabrication of the grooves appeared to close off the pores in the abradable material. Thus the leakage was considered reduced by that portion of the leakage that would otherwise have passed through the pores.

For straight-through labyrinths, the leakage effect of rub-grooves with unworn (i.e., perfectly hardened) teeth was determined by Rhode and Allen [11]. As the first flow visualization study of labyrinth rub-grooves, they discovered (and showed how) that the leakage resistance decrease due to the presence of rub-grooves in straight-through seals was as much as 70 percent.

Experimental Facility

The very unique and very large-scale test specimens with a tooth clearance of 2.54 cm (1.0 in.) represent, for example, a 100-X enlargement of a prototype (actual-size) labyrinth seal with a tooth radial clearance of 0.0254 cm (0.01 in.). Or, for example, they represent a 50-X enlargement of a prototype with a tooth radial clearance of 0.051 cm (0.02 in.). Previous flow visualization rigs were approximately a 10-X enlargement, which did not allow tooth tip and rub-groove details to be properly visualized. The second unique feature is that a wide variety of bolt-on, acrylic building block modules can be immediately attached to the test section framework shown in Figs. 1 and 2 to construct a wide range of stepped and straight-through labyrinth configurations. Another unique capability is immediate adjustment from outside the rig of the pre-rub clearance, the step height and/or the ''axial'' position of the rotor relative to the stator (simulating axial thermal expansion). Observe that the ''two-flat-plates'' arrangement, instead of the ''circumferentially around the shaft'' arrangement, used for previous flow visualization rigs has also been utilized here to facilitate an easy change of configuration. In support of this approach, Waschka et al. [9], Rao and Narayanamurthi [12], and many other investigators have found that shaft speed has a negligible leakage effect for typical leakage Re (i.e., Re $>$10,000 approximately).

A Hastelloy-X containment vessel, which measures 0.914 m$\times$0.914 m$\times$2.43 m (3 ft$\times$3 ft$\times$8 ft), houses the test section shown in Fig. 2. The test section consists of a very unique framework of simulated ''rotor'' and ''stator'' surfaces that are each composed of several seal elements made from acrylic. A system of ''push-rods'' allows the step height (s) and the tooth ''radial'' clearance (c) to be quickly adjusted from outside the test rig. The push-rods extend from the seal element attachment point, through the containment vessel vertical wall, to the point where they are connected to an adjustable screw mechanism.

The test facility is one component of a closed-loop water system with a 2.84 m^3 (750 gallon) outdoor reservoir. A 10.16 cm (4 in.) flange tap orifice meter was located well downstream of the test rig to measure the leakage flow rate. Validyne model DP-15 variable reluctance pressure transducers were used to measure the pressure differential across the orifice plate and across the test section.

Flow Visualization. Several acrylic windows in the containment vessel shell allow flow visualization. A bank of 150 W halogen lamps produced a sheet of light passing through the vertical window of the test section. Plastic clear glitter was found to be the best flow tracer particle, except that for the magnified images of the tooth tips, injected fluorescein sodium dye was preferred. The largest dimension of the glitter particle is only about five percent of the tooth clearance, and they are effective in reflecting sufficient light to the 8 mm RCA camcorder. The fluorescein dye was illuminated by a thin sheet of light from a 5W Argon-ion laser. The camcorder had a 12-X zoom lens and was operated in the fully automatic mode. The framing rate in this mode was 60 frames per second. The digital movies were imported to a pentium computer that had a digital video capture board. The computer was a 90 MHZ pentium with 32 MB of RAM storage and a 2.05 GB hard disk. The video capture board was capable of capturing 30 frames per second, depending on the image viewing size.

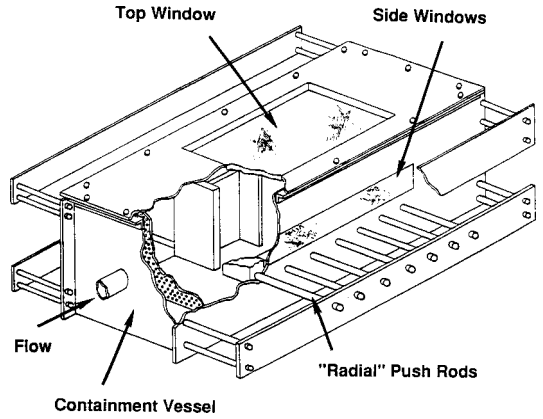

Fig. 1 Cutaway view of the very large-scale test section showing the flow visualization windows

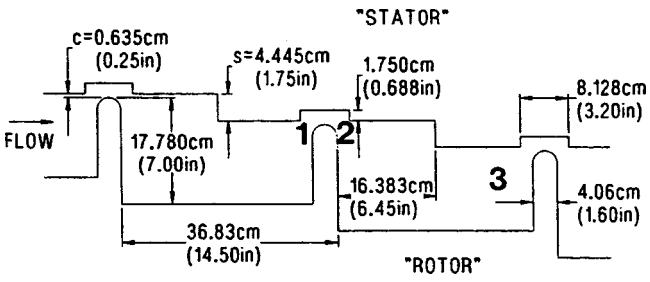

Fig. 2 Test seal for the grooved-worn-teeth case of small clearance $c=0.064$ cm (0.25 in.) and small step height $s=4.45$ cm (1.75 in.)

Discussion

Parameters and Conditions. To obtain an enhanced understanding of labyrinth seal leakage, it is preferred to use the Reynolds number $\mathrm{Re}=\rho V_c(2c)/\mu$ to quantify the leakage, where V_c is the bulk axial velocity based on the pre-rub tooth radial ''reference clearance c'' (see Choice of Leakage Parameter). The labyrinth pressure differential is best quantified for liquids by the leakage resistance coefficient $K=2\Delta P/(\rho V_c^2)$, which was also discussed in the Choice of Leakage Parameter section. The leakage resistance coefficient represents the energy losses in a labyrinth seal and is identical to the minor loss coefficient used to represent mechanical energy losses in pipe elbows, for example. Note that the resistance coefficient for two labyrinth configurations, with different tooth reference clearances ''c'' for a given Re, are not to be compared. This is best understood from the expression $K=(a/\mathrm{Re})^2c^2[\Delta P]$, where $a=2[2\rho]^{1/2}/\mu$. It is seen that K varies quadratically with c, but only linearly with ΔP. Thus the smaller clearance labyrinth gives a lower value for K, even though it has the higher pressure drop. Thus, as found for the pipe flow friction factor, even though the smaller clearance labyrinth exhibits a lower K value at a given Re, it will give lower leakage for a given pressure drop.

Water was used in this study because it greatly facilitates obtaining flow visualization movies of important details. Also, it was found in every case of the first author's previous labyrinth leakage work with many different configurations that the best seals when flowing water are also the best with air. Moreover, compared to standard labyrinths, it was found that advanced labyrinths giving, for example, 50 percent leakage reduction flowing water also give

approximately 50 percent leakage reduction flowing air. For high pressure drop situations with air labyrinths, caution should be exercised in utilizing the K values obtained from water, especially for labyrinths with Mach number greater than about 0.4.

Figure 2 shows the test section configuration for the smallest clearance and smallest step height case. Three-teeth stepped seals were tested in the very large-scale facility. The flow visualization movies and subsequent images were recorded for the cavity between the second and the third teeth. The seals tested were not optimized for minimum leakage, although the authors have had substantial success at such optimizing. The quantitative data currently presented was obtained for fixed values of all geometric dimensions (see Fig. 2) except for the pre-rub clearance, the step height, and the particular groove/tooth-tip combination details which are given for each case.

The first author has observed varying degrees of rounded corners, rather than square corners, at the base (i.e., bottom) of the rub-grooves in turbines and compressors being upgraded. In the current work the essentially rectangular shape and the ratio of groove-width to pre-rub clearance (the most important geometrical parameters) was chosen so as to encompass the values used in the work of Zimmermann et al. [1] and Stocker et al. [10]. Specifically, a rectangular (cross section) rub-groove shape and a completely rounded rub-groove shape were initially considered. The rounded shape was fabricated from a large-diameter pipe wall giving the same groove depth and width. The rounded groove gave slightly increased leakage resistance values over that of the rectangular groove only for Re generally less than 2.0×10^4. Thus the rounded grooves were discontinued in favor of other configurations. Further, the worn teeth tips were simulated as completely rounded, as this was approximately the case found for gas turbines (Zimmermann et al. [1]) when no hardness had been applied. This tooth tip was easily fabricated by attaching an acrylic rod of round cross section, which had been cut along its longitudinal axis, to each tooth tip of the seal elements shown in Fig. 2.

The rub-grooves initially considered here exhibited rectangular shaped grooves of width 4.064 cm (1.60 in.), 8.128 cm (3.20 in.), and 16.26 cm (6.40 in.). The narrow width groove was initially considered only because it is the limiting case of a very thin tooth, i.e., a tooth without a hardness coating. Narrow groove data is not shown because it is too idealized to be of practical interest. The widest groove gave almost the same resistance values as did the medium width groove, and thus it was discontinued. The simulated rub-grooves had a fixed depth of 1.746 cm (0.688 in.). The dimensions of the seal configurations are shown in Fig. 2. The pre-rub tooth clearances (i.e., excluding the groove depth) included are 0.635 cm (0.25 in.), 1.91 cm (0.75 in.), and 2.54 cm (1.0 in.). All rub-grooved lands were tested with the teeth centered on the grooves.

As a brief review, Fig. 2 shows where the throughflow jet accelerates (location 1) to provide high tooth tip kinetic energy and turbulence, and subsequently high dissipation near location 2. If all of the kinetic energy has been dissipated between locations 2 and 3, maximum sealing effectiveness, i.e., ideal labyrinth performance, has been attained.

Note that the length of a particle trajectory indicates particle velocity in the flow visualization figures. Further, the varying degree of particle darkness is simply due to glare from the sheet of light. Also, dark lines have been sketched, using the commercial software PhotoShop, based on many observations of the digital movie to show the approximate time-averaged throughflow jet boundaries. Unfortunately, an unavoidable shadow occurred in a portion of the tooth tip region, rendering the particles invisible there.

Uncertainty Analysis. The experimental uncertainty of measuring the Re and K was recently estimated using the Kline-McClintock method ([13]). The uncertainty in the resistance coefficient was calculated to be 3.4 percent, for example.

Results

As mentioned earlier, heavy-wear-in labyrinth designs have quite rounded tooth tips due to the presence of the hardness coating. The reference to ''unworn'' (sharp tip edges) versus ''worn'' (rounded tips) evolved from noncoated labyrinths.

Small Pre-Rub Clearance. As mentioned above, almost the same leakage resistance was generally found for (a) the present medium width rectangular groove, (b) the wider (doubled) width rectangular groove, and (c) the rounded, medium width groove. Thus, it was decided that additional medium-width groove cases would be tested instead of rounded-groove and wide-groove cases.

Large Step. For the small pre-rub clearance $c=0.064$ cm (0.25 in.) and large step height $s=8.26$ cm (3.25 in.), the variation of leakage resistance with leakage Reynolds number is shown in Fig. 3. Note that both the ungrooved-worn-teeth case, as well as the ungrooved-unworn-teeth case, have much higher leakage resistance (near $K=1.0$) than do the corresponding grooved cases. Because of the insensitivity of leakage resistance to groove shape, a number of currently operating abradable stepped labyrinths are represented by the grooved-worn-teeth case. Fortunately the K values are fairly constant with Re, and the value at $\mathrm{Re}=2.0\times10^4$, for example, is approximately 0.16.

Observe that the effect of the worn land and teeth is generally to decrease the resistance by about 85 percent. Further, Fig. 3 shows that if a perfectly sharp tooth tip could be achieved, i.e., resulting in the grooved-unworn-teeth case, a K increase from 0.16 to 0.35 would be obtained for a 120 percent increase of resistance over the grooved-worn-teeth case. Alternatively, if the location of the rotor and stator seal surfaces of a new machine could be continuously adjusted to maintain the small pre-rub clearance (perfect control of thermal/centrifugal growth) to give the ungrooved-unworn-teeth case, a leakage resistance gain from 0.16 to 0.95 (at $\mathrm{Re}=2.0\times10^4$) is expected, representing a 500 percent resistance increase. Further, if a new abradable surface and perfect clearance control were installed during retrofit (ungrooved-worn-teeth), a K value of 1.05 representing a 550 percent increase at $\mathrm{Re}=2.0\times10^4$ is expected.

The cavity flow pattern for the grooved-worn-teeth case is shown in the instantaneous digital image of Fig. 4. The heavy dark lines illustrate the authors' approximation of the time-mean throughflow jet boundaries from viewing the glitter digital movies. They were sketched using the commercial software package

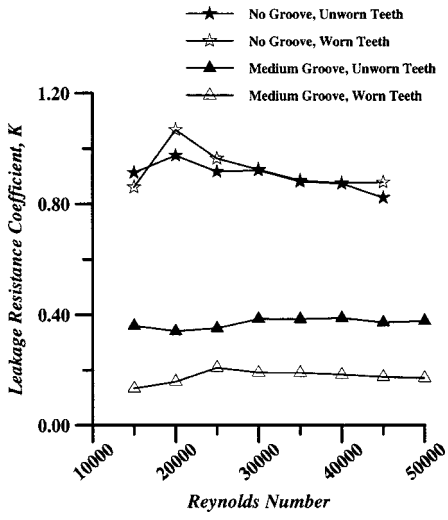

Fig. 3 Leakage resistance coefficient versus Re; small clearance $c=0.064$ cm (0.25 in.) and large step height $s=8.26$ cm (3.25 in.)

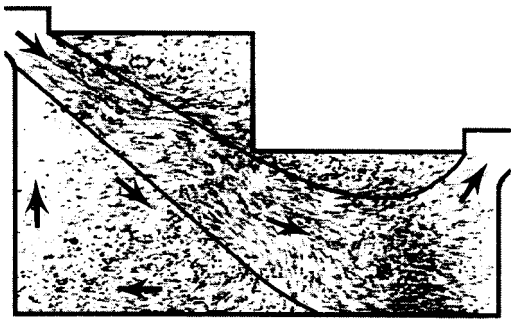

Fig. 4 Digital image of grooved-worn-teeth case; small clearance $c=0.064$ cm (0.25 in.) and large step height $s=8.26$ cm (3.25 in.)

PhotoShop on the pentium computer. The tracer particles are clear plastic glitter, and the length of a particle trajectory line indicates particle velocity. Unfortunately an unavoidable shadow occurred in a portion of the tooth tip region so that particles there are essentially invisible. Note that the still images shown here are not capable of indicating the degree of particle wiggling seen in the movies, which approximately indicates the chaotic nature of the turbulence. In particular, the region of the jet downstream of a tooth throttling exhibits a high degree of particle wiggling, which is where previous investigations have shown that a high level of turbulence intensity exists. Figure 4 shows an unexpected flow pattern such that, upon exiting the tooth throttling, the jet is immediately deflected toward the toothed surface giving a large cavity entrance angle. This large angle is attributed to the large stagnation pressure at the downstream end-wall of the groove, located slightly downstream of the tooth. Observe that the time-mean jet slightly bypasses the step corner and gives a highly nonperpendicular impingement on the toothed surface. Further, the jet apparently exhibits a minimized kinetic energy carryover coefficient, which was described by Vermes [14] for example, and produces three fairly large recirculation zones of low turbulence intensity.

Magnified views of the tooth throttling region of the grooved-worn-teeth case and the grooved-unworn-teeth case are found in Figs. 5 and 6, respectively. Here fluorescein dye was injected into the groove and was illuminated by the Argon ion laser. Observe in Fig. 5 that the rounded edges of the tooth tip produce no appreciable recirculation zone there to reduce the effective jet throttling clearance. Thus the effective jet throttling clearance in this case equals the actual (minimum-distance) clearance, which is the ''radial'' distance to contact between the tooth tip and groove bottom. Also shown is the large jet cavity entrance angle immediately downstream of the tooth. Figure 6 shows that the presence of the sharp tooth tip edges produce a recirculation zone on the tooth tip that results in a jet throttling clearance that is reduced significantly from that seen in Fig. 5. The decrease of K for the grooved-worn-teeth case compared to the grooved-unworn-teeth case is primarily attributed to this reduction in effective throttling clearance.

Fig. 5 Magnified digital image of grooved-worn-teeth tips; small clearance $c=0.064$ cm (0.25 in.) and large step height $s=8.26$ cm (3.25 in.)

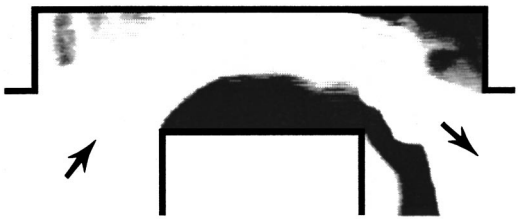

Fig. 6 Magnified digital image of grooved-unworn-teeth tips; small clearance $c=0.064$ cm (0.25 in.) and large step height $s=8.26$ cm (3.25 in.)

The overall cavity flow pattern for the ungrooved-worn-teeth case is shown using glitter particles in Fig. 7. The cavity entrance angle is essentially zero, and the jet impacts directly on the vertical surface of the land step. A perpendicular impingement of the jet on the toothed surface is found here. This flow pattern yields a desirable very long distance for traversing a cavity. The resulting two large recirculation zones are relatively slow with lower turbulence intensity than that found in the jet at the cavity entrance. Further, the overall cavity flow pattern for the other high resistance configuration, i.e. the ungrooved-unworn-teeth case, is nearly identical and thus is not shown. However, the cavity flow pattern for the grooved-unworn-teeth case is somewhat similar to that for the grooved-worn-teeth case of Fig. 4 and is shown in Fig. 8. Note that this configuration produces a jet trajectory that has a slightly larger cavity entrance angle than that of Fig. 4, but is otherwise very similar. In summary, the leakage resistance decrease for the two grooved cases is primarily attributed to: (a) the increased time-mean, effective throttling clearance of the through-flow jet and (b) the reduced energy losses due to the altered cavity flow pattern.

For the present small clearance with both large and small step heights, the unexpected increase of K for the ungrooved-worn-

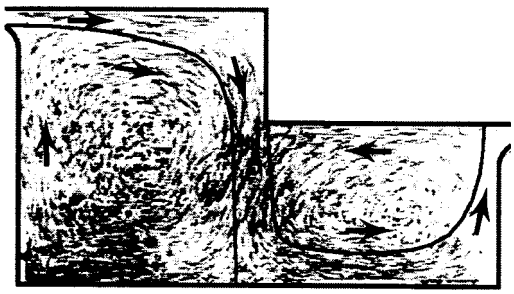

Fig. 7 Digital image of ungrooved-worn-teeth case; small clearance $c=0.064$ cm (0.25 in.) and large step height $s=8.26$ cm (3.25 in.)

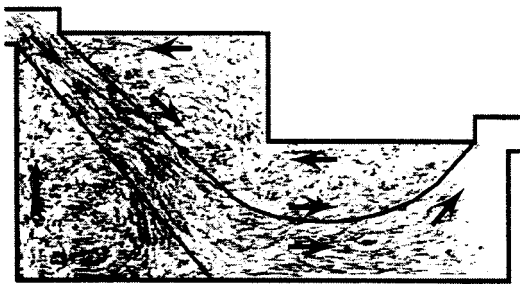

Fig. 8 Digital image of grooved-unworn-teeth case; small clearance $c=0.064$ cm (0.25 in.) and large step height $s=8.26$ cm (3.25 in.)

teeth case over the ungrooved-unworn-teeth case for Re$<3.0\times10^4$ is contrary to the observation of flow separation over the unworn teeth of Fig. 6 versus the worn teeth of Fig. 5. This particular anomaly is not attributed to an oscillatory or unstable throughflow jet flow pattern, as this basic configuration and operating condition is in the ''nonbifurcated'' flow regime ([15]). It seems likely that a difference of cavity flow pattern (i.e., cavity resistance), such as the difference between Fig. 7 and Fig. 4, is the cause.

Small Step. Leakage resistance values for the small pre-rub clearance $c=0.064$ cm (0.25 in.) and the small step $s=4.45$ cm (1.75 in.) configurations are shown in Fig. 9. The results are somewhat similar to that for the large step configurations with both ungrooved cases exhibiting much higher resistance than both grooved cases. The much higher resistance for the ungrooved cases is attributed once again to the smaller effective jet throttling clearance for the ungrooved cases and to the altered cavity flow pattern. The grooved-worn-teeth case, which is similar to currently operating abradable seals of this configuration, gives $K=0.25$ at Re$=2.0\times10^4$ versus $K=0.16$ for the corresponding large step configuration. The effect of the small step height on the worn land and teeth here is to increase K by about 56 percent. If a perfectly sharp tooth tip could be achieved, resulting in the grooved-unworn-teeth configuration, a K increase from 0.25 to 0.35 would be obtained at Re$=2.0\times10^4$; this represents a 40 percent increase of resistance. If a perfect clearance control system for thermal and centrifugal effects could be installed at assembly to give the ungrooved-unworn-teeth configuration, $K=0.73$ would result; this gives a 192 percent increase from the grooved-worn-teeth case.

Further, if a new abradable surface with perfect thermal/centrifugal clearance control were installed upon retrofit, the ungrooved-worn-teeth case would result with $K=0.78$; this represents a 210 percent increase of resistance over the current grooved-worn-teeth case. In addition, comparing resistances of the corresponding small step versus large step cases (Figs. 9 versus 3) reveals that the grooved-worn-teeth case with the small step gives the (slightly) higher resistance, whereas for both the ungrooved cases the large step gives the higher value. Flow visualization is not included for the Fig. 9 cases for brevity reasons, as the flow patterns are nearly the same as for the large step cases.

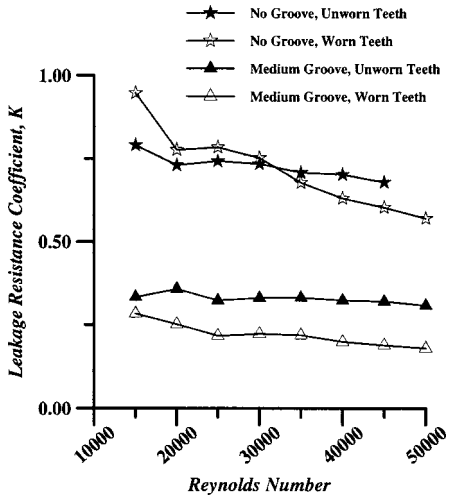

Fig. 9 Leakage resistance coefficient versus Re; small clearance $c=0.064$ cm (0.25 in.) and small step height $s=4.45$ cm (1.75 in.)

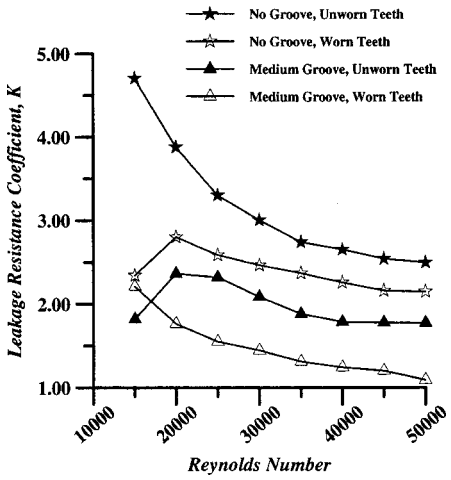

Fig. 10 Leakage resistance coefficient versus Re; medium clearance $c=1.91$ cm (0.75 in.) and large step height $s=8.26$ cm (3.25 in.)

Medium Pre-Rub Clearance

Large Step. The resistance values for the medium pre-rub clearance cases (i.e., $c=1.91$ cm (0.75 in.)) and large step height are shown in Fig. 10. The results for Re$>3.0\times10^4$ have generally similar trends to the above small clearance configurations (Fig. 3), however, the potential resistance improvement is much smaller here when expressed as a percentage increase over the grooved-worn-teeth case.

Once again the ungrooved cases have higher resistance for the same reasons as for the small clearance categories above, and the ungrooved-unworn-teeth case has the highest values. It is surprising that at Re$=1.5\times10^4$, both the ungrooved-worn-teeth and the grooved-unworn-teeth cases exhibit a substantial reduction in K. Further, the grooved-unworn-teeth case is worse here than even the grooved-worn-teeth case. The flow visualization movies indicate that this finding seems attributable to the overall flow pattern, which is more like the highly dissipative one seen in Fig. 7. Also, the ungrooved-unworn-teeth curve is surprisingly steep at this Re. Note that currently operating abradable labyrinths of this category at Re$=2.0\times10^4$ have $K=1.75$. For this category the reduction of K due to the worn land and teeth is about 55 percent. Further, the grooved-unworn-teeth, the ungrooved-unworn-teeth and the ungrooved-worn teeth cases give resistances of 2.3, 3.85, and 2.8, respectively; these values represent an increase over the grooved-worn-teeth case of 31 percent, 120 percent, and 60 percent, respectively. The flow visualization images are not shown for this category of configurations. Both grooved flow patterns are very similar to that of Figs. 4 and 8, while both ungrooved flow patterns are similar to that of Fig. 7.

Small Step. Figure 11 shows the resistance values for the $s=4.45$ cm (1.75 in.) and $c=1.91$ cm (0.75 in.) category. For Re $>3.0\times10^4$, as found for the large step cases in Fig. 10, the ungrooved-unworn-teeth case gives the highest K value, and the grooved-worn-teeth case gives the lowest value. Also like Fig. 10, the ungrooved-worn-teeth case gives a sharp drop in K at low Re. However, one distinction is that the expected (laminar-like) rise in K, as found for Moody's well known pipe friction factor, does not appear here unless the lower Re of about 1.5×10^4 occurs. The K value for currently operating abradable labyrinths, i.e., the grooved-worn-teeth case, at the present clearance and step values is 1.7 at Re$=2.0\times10^4$. The presence of the rub-grooves and worn teeth is to decrease K by about 38 percent. The K values at Re $=2.0\times10^4$ for the grooved-unworn-teeth case, the ungrooved-unworn-teeth case and the ungrooved-worn-teeth case are 1.8,

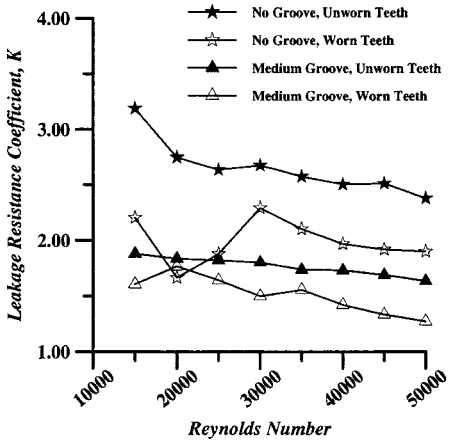

Fig. 11 Leakage resistance coefficient versus Re; medium clearance $c=1.91$ cm (0.75 in.) and small step height $s=4.45$ cm (1.75 in.)

Fig. 12 Digital image of grooved-worn-teeth case; medium clearance $c=1.91$ cm (0.75 in.) and small step height $s=4.45$ cm (1.75 in.)

2.75 and 1.6, respectively; these values represent an increase over the grooved-worn-teeth case of 6 percent, 62 percent and −6 percent, respectively. For this pre-rub clearance and step height, both grooved cases exhibit a flow pattern that is similar to that of Fig. 4. One distinction between these grooved cases, however, is that the small step height does not deflect medium-clearance cavity flow as much as the large step height deflects the small-clearance cavity flow. Specifically, Fig. 12 illustrates the grooved-worn-teeth cavity flow pattern, which exhibits (a) a smaller cavity entrance angle and (b) a resulting shorter jet trajectory.

Large Pre-Rub Clearance

Large Step. The K values for the large $c=2.54$ cm (1.0 in.) and large $s=8.26$ cm (3.25 in.) category are shown in Fig. 13. The trends of the four configurations shown are similar to that of the medium clearance category of Fig. 10, except that the Fig. 13 K values are generally higher. One distinction from the medium clearance category of Fig. 10 is that the ungrooved-worn-teeth values of Fig. 13 are lower than expected and are nearly identical to that of the grooved-unworn-teeth case. This is attributed to the cavity flow pattern, which is somewhat similar to that of Fig. 12 such that it has a shortened jet trajectory. The currently operating grooved-worn-teeth abradable labyrinths of this category have a K value of 1.95 at $\mathrm{Re}=2.0\times10^4$. For this category the reduction of K due to the worn teeth and land is about 70 percent. The grooved-unworn-teeth, the ungrooved-unworn-teeth and the ungrooved-worn-teeth cases exhibit K values of 2.3, 6.6, and 3.0, respectively; these values represent an increase over the grooved-worn-teeth case of 18 percent, 238 percent, and 54 percent, respectively.

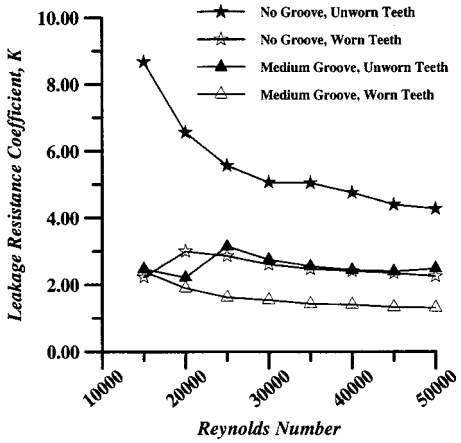

Fig. 13 Leakage resistance coefficient versus Re; large clearance $c=2.54$ cm (1.0 in.) and large step height $s=8.26$ cm (3.25 in.)

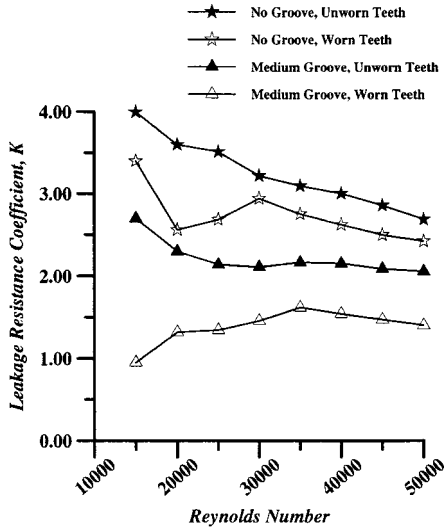

Fig. 14 Leakage resistance coefficient versus Re; large clearance $c=2.54$ cm (1.0 in.) and small step height $s=4.45$ cm (1.75 in.)

Small Step. Resistance for the large clearance and small step category is shown in Fig. 14. Here the rank ordering and the trends of the four cases in terms of the K value are very similar to that of the medium clearance category of Fig. 11, except that the Fig. 14 values of K are generally higher (especially at low Re). Also, the same fairly sharp decrease, and then increase, in the ungrooved-worn-teeth curve occurs here near $\mathrm{Re}=2.0\times10^4$ as found in Fig. 11. The currently operating grooved-worn-teeth abradable labyrinths of this category have $K=1.3$ at $\mathrm{Re}=2.0\times10^4$. Here the presence of the rub-groove and worn teeth decreases K by about 64 percent. The resistance values at this Re for the grooved-unworn-teeth, the ungrooved-unworn-teeth and the ungrooved-worn-teeth cases have K values of 2.3, 3.6, and 2.55, respectively; these values represent resistance increases of 77 percent, 177 percent, and 96 percent, respectively.

Summary

A seal test facility with unique capabilities was used, allowing for the first time, clear and detailed visualization movies of important tooth throttling and labyrinth cavity mixing phenomena to be obtained. One of the unique capabilities is the much greater degree of enlargement of the actual seal than was obtainable with

previous seal visualization rigs; this allows more clear and detailed magnified views of the important tooth throttling region in particular. The second unique capability is immediate adjustment from outside the rig of the pre-rub clearance, the step height and/or the ''axial'' position of the rotor relative to the stator (simulating axial thermal expansion). Third is the capability of immediately attaching, in ''building-block'' fashion, easily fabricated acrylic pieces to easily construct almost any seal configuration. For example, the rectangular rub-grooves were simulated by simply attaching acrylic plates separated by a space equaling the width of the rectangular rub-groove opposite from each tooth.

From examining the digitally stored (computer hard drive) movies in conjunction with the resistance measurements, an improved understanding of the cause-effect relationships of worn versus unworn teeth and of rub-grooves versus no rub-grooves, was obtained. For the cases considered, with grooves and clearances which may not be typical for the entire range of wear-in labyrinths throughout turbomachinery applications, it was determined that

(a) the leakage resistance generally varied among the cases, in order from highest to lowest resistance, as (i) ungrooved-unworn-teeth, (ii) ungrooved-worn-teeth, (iii) grooved-unworn-teeth, and (iv) grooved-worn-teeth.

(b) for the large step height, for example, the resistance decrease due to the presence of a worn land and teeth was 85 percent, 55 percent, and 70 percent for the small, medium, and large pre-rub clearances, respectively.

(c) a substantial tooth tip recirculation zone was observed in the movies only for the grooved-unworn-teeth cases; the recirculation zone acts to constrict (i.e., reduce) the effective tooth throttling clearance. The digital images explain how the unworn teeth for these cases give higher resistance than do worn teeth, even though the higher stagnation pressure on the downstream end-wall of the groove gives a greater deflection of the jet and thus a somewhat less frictional (i.e., less turbulent) flow pattern via departure from the four 90-deg flow turns.

(d) the decrease of leakage resistance due to the presence of a rub-groove is primarily attributed to (i) the increased effective throttling clearance of the throughflow jet and (ii) the reduced energy losses of the deflected-jet cavity flow pattern.

It is easily concluded that, because machine efficiency is reduced by labyrinth tooth wear and/or rub-grooves, design procedures should be extended to account for these based on experience.

Acknowledgments

The authors are grateful for the financial support from the NASA CSP and from the Texas Advanced Technology Program.

Nomenclature

c = pre-rub clearance between a tooth and land (excludes any groove depth) (cm)
c_a = actual (minimum-distance) tooth clearance (includes any groove depth) (cm)
D = diameter of seal rotor (cm)
K = leakage resistance coefficient $(2\Delta P/(\rho V_c^2))$
m = mass leakage flow rate (kg/s)
ΔP = pressure drop across the test seal (kPa)
Re = Reynolds number based on pre-rub clearance $(\rho V_c(2c)/\mu)$
s = step height of stepped seal (m)
V_c = bulk fluid velocity based on pre-rub clearance (m/s)
μ = dynamic fluid viscosity (N-s/m^2)
ρ = fluid density (kg/m^3)

References

[1] Zimmermann, H., Kammerer, A., and Wolff, K. H., 1994, ''Performance of Worn Labyrinth Seals,'' ASME Paper 94-GT-131.
[2] Sneck, H. J., 1974, ''Labyrinth Seal Literature Survey,'' Journal of Lubrication Technology, **96**, pp. 579–582.
[3] Rhode, D. L., Broussard, D. H., and Veldanda, S. B., 1993, ''Labyrinth Seal Leakage Resistance and Visualization Experiments in a Novel, Variable-Configuration Facility,'' Tribol. Trans., **36**, pp. 213–218.
[4] Stocker, H. L., 1975, ''Advanced Labyrinth Seal Design Performance for High Pressure Ratio Gas Turbines,'' ASME Paper 75-WA/GT-22.
[5] Jerie, J., 1948, ''Flow Through Straight-Through Labyrinth Seals,'' *Proceedings of the Seventh Annual International Congress for Applied Mechanics*, Vol. 2, ASME, New York, pp. 70–82.
[6] Egli, A., 1935, ''The Leakage of Steam Through Labyrinth Seals,'' Trans. ASME, **57**, pp. 115–122.
[7] Rhode, D. L., Johnson, J. W., and Broussard, D. H., 1997, ''Flow Visualization and Leakage Measurements of Stepped Labyrinth Seals; Part 1: Annular Groove,'' ASME J. Turbomach., **119**, pp. 839–843.
[8] Rhode, D. L., Younger, J. S., and Wernig, M. D., 1997, ''Flow Visualization and Leakage Measurements of Stepped Labyrinth Seals; Part 2: Sloping Surfaces,'' ASME J. Turbomach., **119**, pp. 844–848.
[9] Waschka, W., Wittig, S., and Kim, S., 1992, ''Influence of High Rotational Speeds on the Heat Transfer and Discharge Coefficients in Labyrinth Seals,'' ASME J. Turbomach., **114**, pp. 462–468.
[10] Stocker, H. L., Cox, D. M., and Holle, G. F., 1977, ''Aerodynamic Performance of Conventional and Advanced Design Labyrinth Seals With Solid-Smooth, Abradable, and Honeycomb Lands,'' NASA CR-135307, Detroit Diesel Allison, Indianapolis, IN.
[11] Rhode, D. L., and Allen, B. F., 1998, ''Visualization and Measurements Of Rub-Groove Leakage Effects On Straight-Through Labyrinth Seals,'' ASME Paper 98-GT-506.
[12] Rao, C. K. V., and Narayanamurthi, R. G., 1973, ''An Experimental Study of Performance Characteristics of Labyrinth Seals,'' Mech. Eng. (Am. Soc. Mech. Eng.), **53**, pp. 277–281.
[13] Kline, S. J., and McClintock, F. A., 1953, ''Describing Uncertainties in Single-Sample Experiments,'' Mech. Eng. (Am. Soc. Mech. Eng.), **75**, pp. 3–9.
[14] Vermes, G., 1961, ''A Fluid Mechanics Approach to the Labyrinth Seal Leakage Problem,'' ASME J. Eng. Gas Turbines Power, **83**, pp. 161–169.
[15] Rhode, D. L., Johnson, J. W., and Allen, B. F., 1997, ''Effect of Flow Instabilities and Self-Sustained Oscillations on Labyrinth Seal Leakage Resistance,'' ASME Paper 97-GT-214.

Negative Stiffness Coefficients for Magnetic Actuators Using Laplace's Equation

L. S. Stephens
Assistant Professor,
Department of Mechanical Engineering,
University of Kentucky,
Lexington, KY 40506-0108
e-mail: stephens@engr.uky.edu

M. A. Casemore
Research Assistant,
Mechanical Engineering Department
Louisiana State University,
2508 CEBA
Baton Rouge, LA 70803

Magnetic bearings offer high speed and low power losses as compared to film riding and rolling element bearings. Significant efforts are underway to apply magnetic bearings to gas turbines and jet aircraft engines. Negative stiffness coefficients for magnetic actuators can have a significant impact on shaft rotordynamics. These coefficients are typically computed as the sensitivity of a magnetic force expression derived from a lumped parameter reluctance network. However, as the complexity of magnetic actuator designs increases, the reluctance network method may become impractical for, or even incapable of, coefficient determination. In this paper, an alternative method is presented for determination of negative stiffness coefficients for a large class of magnetic actuators. The method solves the Dirichlet boundary value problem for the magnetomotive force in the actuator air gap, subject to periodic boundary conditions that can be represented by Fourier series. A conformal transformation to bipolar coordinates is used that results in a boundary value problem that is solvable using separation of variables. Negative stiffness coefficients are presented and the method is benchmarked against well-known solutions using the reluctance network method. [DOI: 10.1115/1.1377874]

Introduction

Advances in high temperature, high strength ferromagnetic materials and ceramic-coated copper wire have made magnetic bearings an attractive alternative for gas turbine applications ([1–3]). Of significant interest in these applications is rotordynamic performance of the shaft/wheel/bearing system, which is characterized for magnetic bearings using the closed-loop controller gains and the open-loop current gain and negative stiffness. More generally, magnetic actuators find use in all types of high speed rotating machinery as bearings, motor drives, dampers, and more recently, self-bearing motors. The bias portion of the magnetic flux in each of these actuators produces a negative stiffness and correspondingly a side-pull force if the shaft is displaced from the centered position.

Magnetic actuators generate bias flux by distributing magnetomotive force sources (electromagnet coils or permanent magnets) periodically about the actuator circumference. Figure 1 illustrates three such actuators. Figure 1(*a*) shows a typical eight-pole heteropolar magnetic bearing with N-S-N polarity on adjacent stator teeth. This bearing uses electromagnet coils as the magnetomotive force source to generate a bias flux density between the stator teeth and the journal. The bias flux linearizes the bearing force and provides for an adequate bearing force slewrate. This is the most common magnetic bearing configuration and has been studied extensively including solutions for the negative stiffness coefficient ([4]). This actuator is included in this paper for the purposes of benchmarking the proposed method.

Figure 1(*b*) shows a DC motor that uses permanent magnets on the journal as the magnetomotive force source to generate a bias flux that links with the stator winding current to produce motoring torque. Such designs are common in a variety of servomotor and low torque motor applications. The same general construction is used even if the PM DC motor is used as a self-bearing motor ([5,6]). In that case attempts are made to produce a purely sinusoidal PM flux by techniques such as using layered PM arcs ([5]).

Figure 1(*c*) illustrates a heteropolar, PM-biased, radial magnetic bearing with a cylindrical radial flux return path on a separate axial plane. This design is for low power losses and high speed such as required for gas turbine applications and is similar to that analyzed by Maslen [7]. Radial flux return paths also occur in homopolar designs ([8]) and thrust bearing designs ([9]). The cylindrical radial return path is used for the PM bias flux to complete its path through the actuator resulting in lower power losses ([7]). A method to compute the negative stiffness coefficient for a cylindrical radial flux return path was studied by Knospe and Stephens [9]. That method solved Laplace's equation using an assumed solution form that is particular to problems with constant boundary conditions. The method proposed in this paper is sufficiently general so that it is applicable to a wide range of actuator designs with complex flux paths and distributions.

Each of the designs detailed above has the property that the reluctance seen by the bias flux density as it crosses the radial air gap from the magnetomotive force source to the opposing surface, is constant about the circumference when the journal is centered. This is so in all toothless actuator designs and in most toothed designs where the magnetomotive force source is on the same surface as the teeth. An example of where this assumption breaks down is a PM motor with teeth spaced far apart on the stator and PM's on the journal. (The PM's then oppose either a tooth or a slot depending upon journal orientation, thus the magnetomotive force source sees a variable reluctance about the circumference.) The method detailed in this paper is limited to actuators with constant reluctance. A second limitation of the method is that it neglects the reluctance of the iron and is therefore more accurate for large air gap machines.

Another approach to computing negative stiffness is the use of finite element and/or boundary element methods. These methods can handle complex geometry including both iron and air flux paths in the same model, and can account for flux leakage and fringing effects. The method in this paper neglects these effects and therefore overpredicts any measured negative stiffness values. The finite element and boundary element methods typically re-

Contributed by the International Gas Turbine Institute (IGTI) of THE AMERICAN SOCIETY OF MECHANICAL ENGINEERS for publication in the ASME JOURNAL OF ENGINEERING FOR GAS TURBINES AND POWER. Paper presented at the International Gas Turbine and Aeroengine Congress and Exhibition, Munich, Germany, May 8–11, 2000; Paper 99-GT-179. Manuscript received by IGTI Oct. 1999; final revision received by ASME Headquarters Oct. 2000. Associate Editor: D. Wisler.

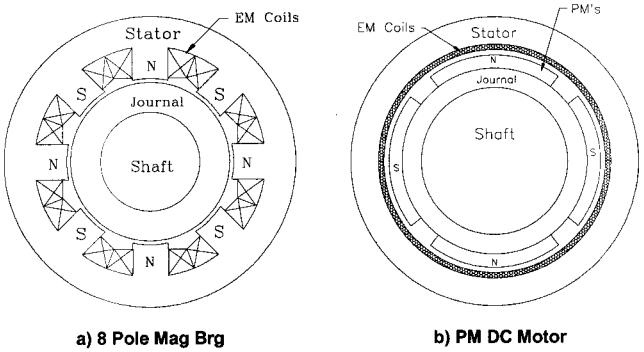

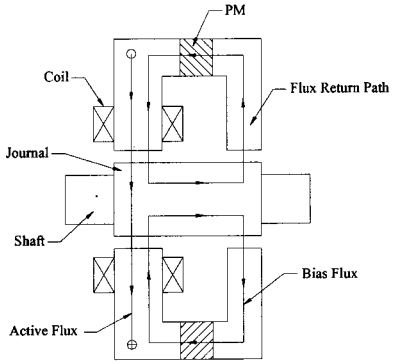

Fig. 1 Typical magnetic actuators

quire expensive software and/or extensive programming as compared to the proposed method which can be implemented using simple programming techniques.

Assumptions and Approach

For the actuators in Fig. 1, the geometry of the air gap can be represented as shown in Fig. 2, where b is a small perturbation in the negative x-direction. Due to symmetry in the actuators $K_{xx}=K_{yy}$ and $K_{xy}=K_{yx}=0$, therefore, perturbations in the x-direction alone are considered without loss of generality. It is assumed that this problem is magnetostatic. This assumption is valid even if an active flux component crosses the air gap because the negative stiffness is defined in the limit as the active flux components tend towards zero. This analysis also assumes that saturation does not occur. Therefore the actuators are operating well below their peak force or torque capabilities. It is also assumed that there is no axial component of flux in the air gap, which is valid for small radial air gaps. Finally, it is assumed that the reluctance of the air

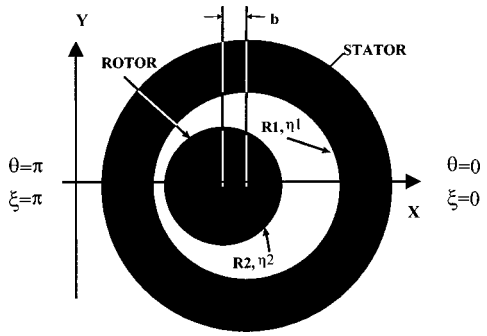

Fig. 2 Annular magnetic actuator air gap region

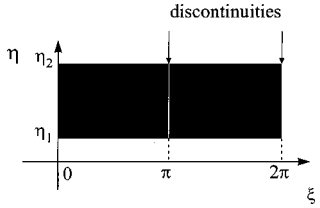

Fig. 3 Bipolar coordinate transformation of air gap

gap is much greater than that of the magnet iron. Under these assumptions, the magnetomotive force distribution in the low permeability air gap region satisfies Laplace's equation ([11]).

The method of solution proceeds by computing the magnetomotive force in the air gap using Laplace's equation subject to the periodic boundary conditions on the journal-air and/or stator-air interfaces. In order to compute the negative stiffness coefficient the rotor position is perturbed to an eccentric location. To accommodate the eccentricity a conformal mapping to bipolar coordinates is used such that Laplace's equation is still valid and solvable by the separation of variables approach. The flux distribution in the air gap is computed as the gradient of the magnetomotive force. The resulting Maxwell force is then computed using the flux density at the rotor surface. Computing the sensitivity of this force to small perturbations of the rotor, b, finally characterizes the negative stiffness of the actuator.

Analytical Solution—Laplace's Equation

The boundary value problem on the eccentric annulus is quite complex and cannot be solved analytically using Cartesian or Polar coordinates. A conformal mapping is used to simplify the problem such that it is transformed to bipolar coordinates η and ξ from Cartesian coordinates x and y using the following transformations from Happel and Brenner [12]:

$$x = C\frac{\sinh(\eta)}{\cosh(\eta)-\cos(\xi)} \tag{1}$$

$$y = C\frac{\sin(\xi)}{\cosh(\eta)-\cos(\xi)} \tag{2}$$

$$C = \frac{\sqrt{R_1^4+R_2^4-2R_1^2R_2^2-2b^2(R_1^2+R_2^2)+b^4}}{2b} \tag{3}$$

where C is the pole location of the bipolar coordinate system in the x-direction, and is solely dependent upon geometry. Under this transformation the air gap geometry in Fig. 2, which represents the physical coordinates, is transformed to that in Fig. 3 in bipolar coordinates. Note that there are discontinuities in this mapping at $\xi=0$ and $\xi=\pi$. This is due to the symmetry in the geometry above and below the x-axis. Since the boundary conditions are not necessarily symmetric about this axis, the problem must be solved piecewise over the intervals $0<\xi<\pi$ and $\pi<\xi<2\pi$.

The stator and rotor surfaces in the (η,ξ) coordinates are given by $\eta=\eta_1$ and $\eta=\eta_2$. Under this mapping, the radii R_1 and R_2 and the displacement b are given by the following relations obtained from Happel and Brenner [12]

$$R_1 = C\,\mathrm{csch}(\eta_1) \tag{4}$$

$$R_2 = C\,\mathrm{csch}(\eta_2) \tag{5}$$

$$b = C[\coth(\eta_1)-\coth(\eta_2)]. \tag{6}$$

Note that with this mapping, a positive displacement b is in the negative x-direction. Under this transformation Laplace's equation in bipolar coordinates governing the magnetomotive force in the air gap is given on both piecewise intervals as

$$F_{\xi\xi}+F_{\eta\eta}=0 \tag{7}$$

and is subject to the boundary conditions on the journal-air interface and the stator-air interface. (This is identical to Laplace's equation in x-y coordinates, except that x replaces ξ and y replaces η.) The boundary conditions are given below in a general form as

$$F(\eta_1,\xi)=F_1(\xi) \tag{8}$$

$$F(\eta_2,\xi)=F_2(\xi) \tag{9}$$

where $F_1(\xi)$ and $F_2(\xi)$ must be derived for each actuator type. (These boundary conditions are reduced to functions of a single variable using the transformation. In Cartesian or Polar coordinates these boundary conditions are difficult functions of two variables.) One key to formulating the boundary conditions correctly is the relationship between the angular coordinate in the physical coordinates, θ, and the bipolar coordinates, ξ and η. Since the bipolar coordinate system is approximately centered about ordinate C for $\eta>1$, and since there is a discontinuity in the transformation at $\xi=\pi$, the following relations hold:

$$x-C=\begin{cases} r\cos(\theta) & 0<\xi<\pi \\ r\cos(2\pi-\theta) & \pi<\xi<2\pi \end{cases} \tag{10}$$

$$r=\sqrt{(x-C)^2+y^2}. \tag{11}$$

Equation (10) is solved for $\theta(\eta,\xi)$ using Eqs. (1), (2), and (11) as

$$\theta(\eta,\xi)=\begin{cases} \cos^{-1}\left(\left(\dfrac{C}{r(\eta,\xi)}\right)\left(\dfrac{\sinh(\eta)}{[\cosh(\eta)-\cos(\xi)]}-1\right)\right) \\ \quad 0<\xi<\pi \\ 2\pi-\cos^{-1}\left(\left(\dfrac{C}{r(\eta,\xi)}\right)\left(\dfrac{\sinh(\eta)}{[\cosh(\eta)-\cos(\xi)]}-1\right)\right) \\ \quad \pi<\xi<2\pi \end{cases} \tag{12}$$

where

$$r(\eta,\xi)=\frac{C}{\cosh(\eta)-\cos(\xi)}\sqrt{\sinh^2(\eta)+\sin^2(\xi)}. \tag{13}$$

The transformations of Eqs. (12) and (13) are then used to formulate the boundary conditions of Eqs. (8) and (9) in bipolar coordinates (this is done for the actuators of Fig. 1 in Table 1). In addition to the specified boundary conditions, the following natural boundary conditions arise due to periodic circular symmetry:

$$F_\xi(\eta,0)=0 \tag{14}$$

$$F_\xi(\eta,\pi)=0. \tag{15}$$

Table 1 Actuator boundary conditions

Case	Description	Boundary Conditions	
		Stator ID $F_1(\xi,\eta)$	Journal OD $F_2(\xi,\eta)$
1	8 pole Mag. Brg.	$\sum_{n=1}^{\infty} A_n \cos\left(\frac{2n\pi\theta(\xi)}{T}\right)$	0
2	4 pole PM motor	0	$\sum_{n=1}^{\infty} A_n \cos\left(\frac{2n\pi\theta(\xi)}{T}\right)$
3	4 Pole PM sinewave motor	0	$F_m \cos(\omega t - 2\theta(\xi))$
4	Low Power Loss Mag. Brg.	F_m	0

The solution is obtained using separation of variables which yields a series solution. This solution is valid on both piecewise intervals and is given by

$$F(\eta,\xi)=a_0+b_0\eta+\sum_{n=1}^{\infty}[(a_n e^{n\eta}+b_n e^{-n\eta})\cos(n\xi) + (c_n e^{n\eta}+d_n e^{-n\eta})\sin(n\xi)] \tag{16}$$

where the Fourier coefficients a_0, b_0, a_n, b_n, c_n, and d_n are found by solving the following six equations simultaneously:

$$a_0+b_0\eta_1=\frac{1}{2\pi}\int_0^{2\pi}F_1(\xi)d\xi \tag{17}$$

$$a_0+b_0\eta_2=\frac{1}{2\pi}\int_0^{2\pi}F_2(\xi)d\xi \tag{18}$$

$$a_n e^{n\eta_1}+b_n e^{n\eta_1}=\frac{1}{\pi}\int_0^{2\pi}F_1(\xi)\cos(n\xi)d\xi \tag{19}$$

$$a_n e^{n\eta_2}+b_n e^{n\eta_2}=\frac{1}{\pi}\int_0^{2\pi}F_2(\xi)\cos(n\xi)d\xi \tag{20}$$

$$c_n e^{n\eta_1}+d_n e^{n\eta_1}=\frac{1}{\pi}\int_0^{2\pi}F_1(\xi)\sin(n\xi)d\xi \tag{21}$$

$$c_n e^{n\eta_2}+d_n e^{n\eta_2}=\frac{1}{\pi}\int_0^{2\pi}F_2(\xi)\sin(n\xi)d\xi \tag{22}$$

and where $F_1(\xi)$ and $F_2(\xi)$ are the associated boundary conditions evaluated piecewise over the intervals $0<\xi<\pi$ and $\pi<\xi<2\pi$. Once the magnetomotive force is found, the flux density in the air gap is calculated using

$$\mathbf{B}=-\mu_0\nabla F \tag{23}$$

where the gradient for the conformal mapping is given by

$$\nabla=h\left[\boldsymbol{\eta}\frac{\partial}{\partial\eta}+\boldsymbol{\xi}\frac{\partial}{\partial\xi}\right]. \tag{24}$$

The metrical coefficient for the conformal mapping is given by

$$h=\frac{1}{C}\{\cosh(\eta)-\cos(\xi)\}. \tag{25}$$

The Maxwell force on the rotor is found by evaluating the following integral over the entire surface, S, of the rotor

$$\mathbf{f}=\frac{1}{2\mu_0}\int_S|\mathbf{B}|^2\mathbf{n}dS \tag{26}$$

where $\mathbf{n}$ is the area unit vector which points outward from the rotor surface. Since the sign convention for the flux is positive for flux leaving the stator and entering the rotor, then $\mathbf{n}=-\boldsymbol{\eta}$. The following relation defines the differential surface area in the bipolar coordinate system:

$$dS=\frac{L}{h}d\xi \tag{27}$$

and the unit vector $\boldsymbol{\eta}$ is computed as

$$\boldsymbol{\eta}=h\left(\frac{\partial x}{\partial\eta}\mathbf{i}+\frac{\partial y}{\partial\eta}\mathbf{j}\right). \tag{28}$$

Noting that there is no component of force in the y-direction for this case, the force expression reduces to

$$f_x=-\frac{L}{2\mu_0}\int_0^{2\pi}|\mathbf{B}|^2\frac{\partial x}{\partial\eta}d\xi \tag{29}$$

with the partial of x with respect to η found using Eq. (1). Computing the sensitivity of this force as a function of displacement b gives the negative stiffness coefficient, K_{xx}, as

$$K_{xx}=\left.\frac{\partial f_x}{\partial x}\right|_{b\to 0}. \tag{30}$$

Boundary Conditions

Using the three actuator designs shown in Fig. 1, four different cases are presented in the results. These cases are summarized and their boundary conditions given in Table 1.

Case 1 is the eight-pole heteropolar radial magnetic bearing with N-S-N polarity. The bias flux between the stator teeth and the journal is generated by magnetomotive force provided by a bias current in the electromagnetic coils on the stator inner diameter. No magnetomotive force source exists on the journal outside diameter. Therefore, the magnetomotive force source on the stator inside diameter is a square wave that can be approximated using a Fourier series. This approximation is given in Table 1, where A_n in that table is given by

$$A_n=\frac{4F_m(w_s+w_t)}{Tn\pi}\left[\begin{array}{c}-\sin(n\pi)+\\ \sin\left(\frac{n\pi w_t}{2(w_t+w_s)}\right)\cos\left(\frac{n\pi w_s}{(w_t+w_s)}\right)+\\ \sin\left(\frac{n\pi w_s}{(w_t+w_s)}\right)\cos\left(\frac{n\pi w_t}{2(w_t+w_s)}\right)+\\ \sin\left(\frac{n\pi w_t}{2(w_t+w_s)}\right)\end{array}\right] \tag{31}$$

and where w_s and w_t are the slot width and tooth width, respectively, T is the period, and F_m is the maximum value of the magnetomotive force. Figure 4(a) illustrates the Fourier series approximation of this boundary condition. Note the zero magnetomotive force between the poles of the squarewave. This is due to the slots between the teeth.

Case 2 is a PM DC motor with four permanent magnets of equal strength constructed on the journal outside diameter as the magnetomotive force source to provide the bias flux density. This magnetomotive force source is also a square wave with zero magnetomotive force at the slot locations. This magnetomotive force is represented by the Fourier series given in Table 1, where the coefficients, A_n, are again given by Eq. (31). While windings are present on the stator inside diameter, they do not contribute to the bias flux density in the actuator air gap, therefore, when computing the negative stiffness coefficient the magnetomotive force on the stator inside diameter is taken as zero. Figure 4(b) illustrates the Fourier series approximation of the magnetomotive force on the journal outside diameter. Note that in terms of magnetomotive force, Case 2 is essentially the same problem as Case 1, notwithstanding the number of poles in each actuator.

Case 3 is another four pole PM DC motor except that the permanent magnets have been arranged to give an ideal approximation of a sinusoidal flux distribution on the journal outside diameter. This is frequently done in motor designs to produce a smoother angular velocity profile for precision applications. The boundary condition for magnetomotive force on the journal outside diameter is an ideal sinewave as given in Table 1 and shown graphically in Figure 4(c).

Case 4 is the cylindrical radial flux return plane of the PM-biased heteropolar bearing shown in Figure 1(c). This bearing is a low power loss design and targeted towards application in gas turbines and other high speed machines. (The axial plane with the electromagnet coils has discrete pole pieces and is the same as Case 1 in this paper. The overall negative stiffness for this bearing is the sum of the negative stiffness of these two planes.) For Case 4, the bias flux is generated by permanent magnets that are typically far removed from the air gap boundaries in the circuit. Thus the flux spreads out evenly about the air gap circumference of the radial flux return path. Assuming the flux moving inward from the stator to the journal is positive, the magnetomotive force distribution at the gap is a positive constant and is illustrated in Fig. 4(d) and given in Table 1.

Finally, it should be noted that many other particular actuator designs can be analyzed using this method as long as the boundary conditions on one or both of the air gap boundaries can be represented by Fourier series. This includes motors with several overlapped phases and complicated winding schemes. In those cases the boundary conditions take the form of the sum of several Fourier series approximations to each phase in the actuator.

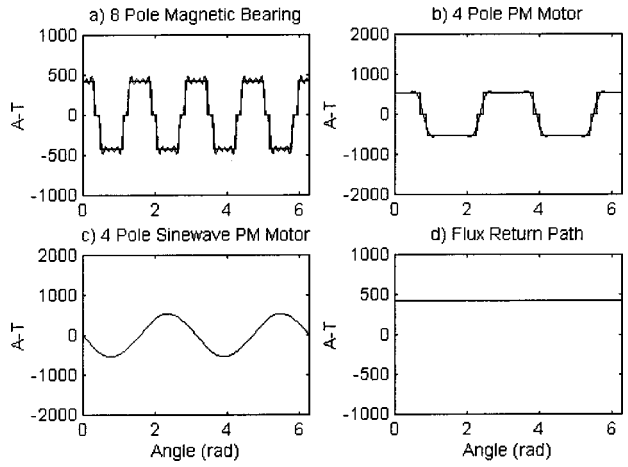

Fig. 4 Graphical representation of boundary conditions

Results and Discussion

Table 2 lists the parameter values for each of the actuator Cases 1–4. The actuators are assumed to be constructed of silicon iron which has a practical saturation flux density of 1.6 Tesla. For each of the magnetic bearing Cases (#1 and #4) the bias flux density is assumed to be half the saturation flux density or $B_b=0.70$ Tesla. For a radial air gap of $g_o=0.75$ mm in each of these actuators the peak value of magnetomotive force on the stator is 426.8 A-Turns. For each of the PM motor Cases (#2 and #3) the bias flux density is taken as $B_b=0.9$ Tesla. For a radial air gap of $g_o=0.75$ mm and a PM radial thickness of $t_m=2.54$ mm in each of the motors, the

Table 2 Properties for each magnetic actuator design

Parameter	Symbol (units)	Case 1 8-Pole Mag. Brg.	Case 2 4-Pole Motor	Case 3 Sinewave Motor	Case 4 Cylindrical Flux Path
Actuator Length	L (mm)	25.4	25.4	25.4	25.4
Stator Inner Radius	R_i (mm)	63.5	63.5	63.5	63.5
Radial Air Gap	g_o (mm)	0.75	0.75	0.75	0.75
PM Radial Thickness	t_m (mm)	N/A	2.54	2.54	N/A
Peak MMF On Journal	F_m (A-T)	N/A	535.1	535.1	N/A
Peak MMF on Stator	F_m (A-T)	426.8	N/A	N/A	426.8
Peak Bias Flux Density	B_b (Tesla)	0.7	0.9	0.9	0.7
Saturation Flux Density	B_{sat} (Tesla)	1.6	1.6	1.6	1.6

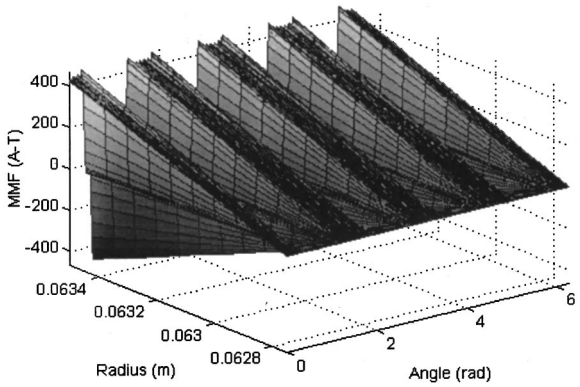

Fig. 5 Magnetomotive force for centered journal: Case 1

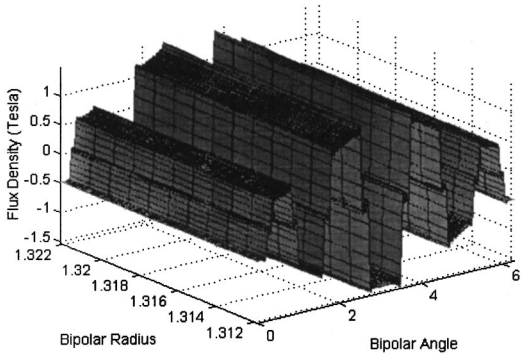

Fig. 7 Flux density for eccentric journal: Case 1

peak value of magnetomotive force on the journal is 535.1 A-Turns. In all cases the stator inside radius is taken as 63.5 mm and the actuator length is taken as 25.4 mm.

Case 1: Eight-Pole Heteropolar Magnetic Bearing. Figure 5 shows the resulting magnatomotive force in the radial air gap for the eight-pole magnetic bearing with the journal in the centered position. Note the approximate square wave on the stator inside diameter and the linear gradient to the zero magnetomotive force on the journal outside diameter. To achieve these results the first 75 terms of the Fourier series approximation were used in the solution. Figure 6 shows the resulting flux distribution in the air gap which indicates that the flux is concentrated beneath each of the stator teeth. Since the journal is centered the flux density at each tooth is equal to that of the other teeth as expected.

When the journal is displaced to an eccentric position the bias flux is then distorted as shown in Fig. 7. As the air gap reluctance is decreased on one side of the journal and increased on the other side, the flux density beneath the stator teeth increases on one side and decreases on the other, respectively. This results in a side pull force, and hence a negative stiffness. The side pull force is quadratic and the linear portion about zero displacement is used to compute the negative stiffness.

Results were computed for the negative stiffness coefficient for a range of radial air gaps and source magnetomotive forces. These results are benchmarked against the well-known closed-form solution for negative stiffness based on the reluctance network method. From the reluctance network method the negative stiffness coefficient for the eight-pole magnetic bearing is

$$K_{xx,r}=\frac{4\mu_o(NI)^2A}{g_o^3}. \tag{32}$$

Figure 8 shows the resulting negative stiffness coefficient for the eight-pole magnetic bearing computed by the two methods. The figure indicates almost identical results and successfully benchmarks the method presented in this paper.

Case 2: PM DC Motor. Case 2 is essentially the same as Case 1 except that a four-pole PM configuration generates the magnetomotive forces. Figure 9 shows the resulting flux density for the PM motor with the journal in an eccentric position. Again, due to this eccentricity, a side pull force and negative stiffness results. Figure 10 gives the resulting negative stiffness coefficient for the PM DC motor from using the PDE method in this paper. This is compared to the coefficient from the reluctance network method, which is given by Eq. (32) with an equivalent magneto-

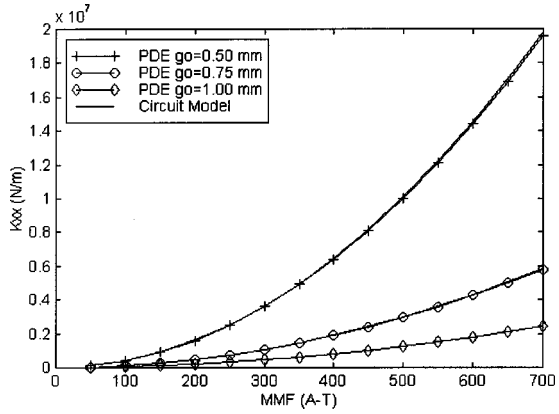

Fig. 8 Negative stiffness coefficient: Case 1

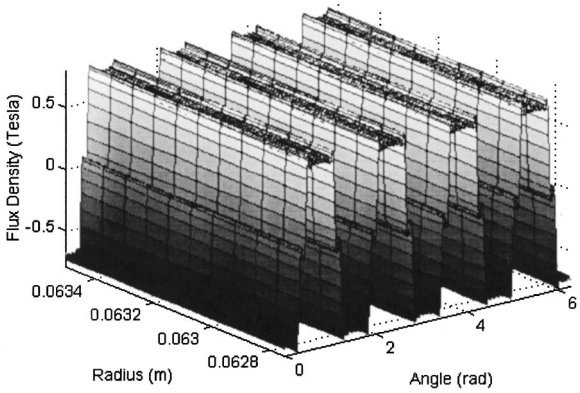

Fig. 6 Flux density for centered journal: Case 1

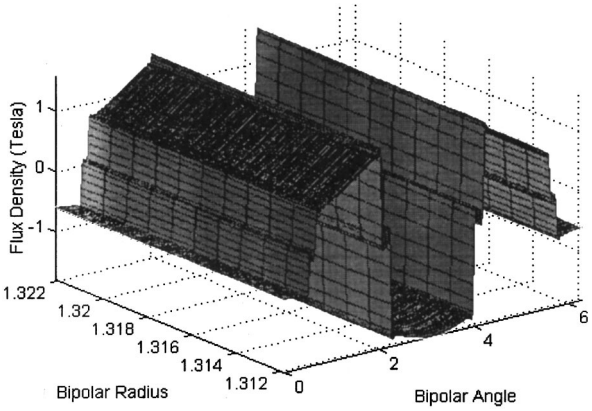

Fig. 9 Flux density for eccentric journal: Case 2

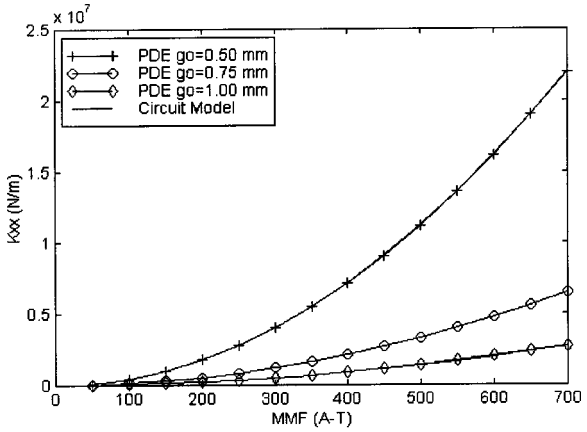

Fig. 10 Negative stiffness coefficient: Case 2

motive force replacing (NI) in that equation. Again, this figure indicates almost identical results and serves as a second benchmark of the proposed method.

Case 3: Sinewave PM Motor. The sinewave PM motor generates a sinusoidal bias flux in the air gap as shown in Fig. 11. This figure is for the journal in an eccentric position, $x=-b$ which corresponds to a bi-polar angle of $\xi=\pi$. As expected the magnitude of the flux density at this location increases from the bias value, and that at $\xi=0$ decreases from the bias value. This

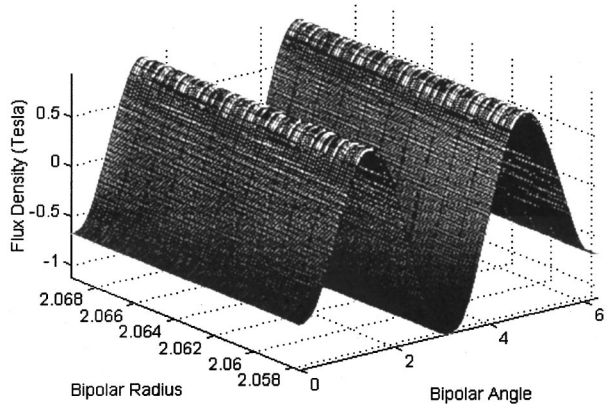

Fig. 11 Flux density for eccentric journal: Case 3

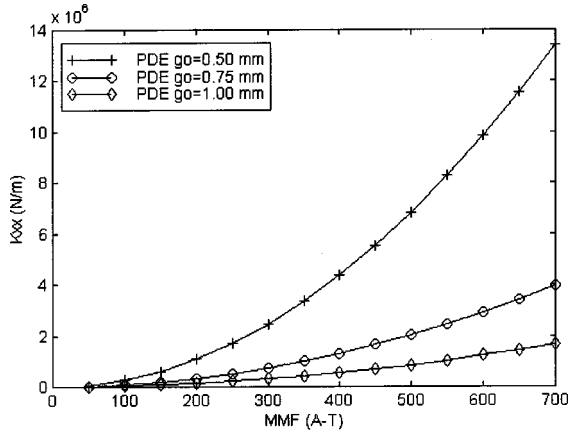

Fig. 12 Negative stiffness coefficient: Case 3

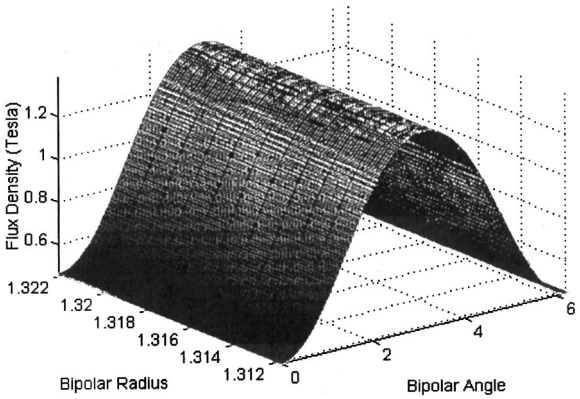

Fig. 13 Flux density for eccentric journal: Case 4

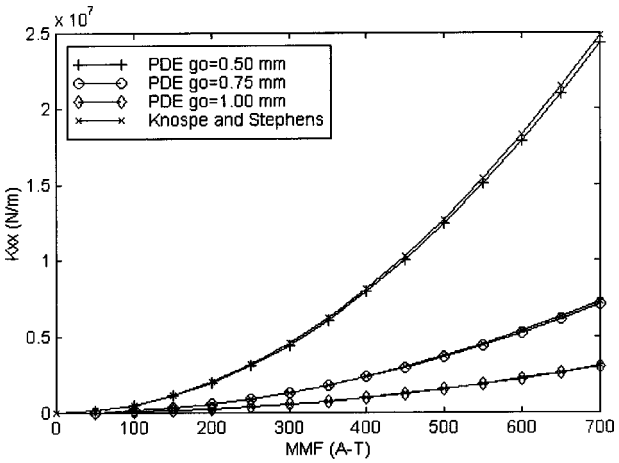

Fig. 14 Negative stiffness coefficient: Case 4

results in a side pull force and a negative stiffness. The resulting negative stiffness coefficient is shown in Fig. 12 for different combinations of radial air gap and MMF values.

Case 4: Cylindrical Radial Flux Return Path. The resulting flux density for the centered cylindrical radial flux return path is a constant value of 0.71 Tesla. As expected for this design the flux density is independent of radial and angular coordinates for a centered journal. When the journal experiences a displacement to an eccentric position, the flux density increases on one side and decreases on the other, resulting in a flux distribution as shown in Fig. 13. This flux distribution results in a side pull force and negative stiffness. Figure 14 gives the negative stiffness coefficient for this actuator for different combinations of radial air gap and magnetomotive force values. This value is compared to that resulting from the work of Knospe and Stephens [10] which used an alternative solution technique for the negative stiffness coefficient in cylindrical radial flux return paths. These two solutions are seen to agree well.

Conclusions and Summary

Advances in high temperature, high strength magnetic actuator materials have prompted their use in many high speed turbomachinery applications including gas turbine bearings. The negative stiffness of these actuators can have a significant effect on rotordynamic performance. An alternative method to compute the negative stiffness coefficient for these actuators was presented and benchmarked against other known solutions. The method solves Laplace's equation on the eccentric annulus for actuators with magnetomotive force boundary conditions that can be represented

by Fourier series approximations. The method is limited to actuators in which the reluctance seen by the magnetomotive force source is independent of the angular coordinate when the journal is centered. This includes most toothless and many toothed actuator designs. The method is sufficiently general to handle a large number of common magnetic actuator designs with complex flux paths. Results were presented for several actuator designs, including a low power loss magnetic bearing design targeted towards gas turbine application. Good agreement was seen between the method and the benchmark solutions. This method is another useful tool for evaluating the effects of magnetic actuators on shaft rotordynamics.

Nomenclature

A = pole area
A_n = Fourier series coefficient
B = flux density
B_b = bias flux density
C = constant in conformal mapping
F = magnetomotive force
F_1 = magnetomotive force distribution at stator inner radius
F_2 = magnetomotive force distribution at rotor outer radius
I = current
K_{xx} = x-direction negative stiffness
K_{xy} = cross-coupled stiffness
K_{yy} = y-direction negative stiffness
L = length of actuator in z-direction
N = number of turns
R_1 = inner radius of stator
R_2 = outer radius of rotor
S = surface area of rotor
T = waveform period
b = minus x displacement of rotor
f = rotor force vector
f_x = x-direction force on rotor
g_o = radial air gap
h = metrical coefficient for conformal mapping
$\mathbf{n}$ = area unit vector for rotor surface
t_c = radial thickness of copper windings
t_m = radial thickness of permanent magnets
w_s = slot width
w_p = pole (tooth) width
μ_0 = permeability of free space $=4\pi\times10^{-7}$ W/A-m
η = bipolar coordinate
η_1 = value of bipolar coordinate corresponding to stator inner radius
η_2 = value of bipolar coordinate corresponding to rotor outer radius
ξ = bipolar coordinate

References

[1] Schultz, R. R., Bornstein, K. R., Jayawant, R. C., and Leung, R., 1995, ''Applications of Active Magnetic Bearings to High Speed Turbomachinery with Aerodynamic Rotor Disturbance,'' *Proceedings of Mag '95*, Technomic, Lancaster, PA, pp. 14–23.
[2] Iannello, V., 1995, ''Magnetic Bearing Systems for Gas Turbine Engines,'' *Proceedings of Mag '95*, Technomic, Lancaster, PA, 1995, pp. 77–86.
[3] Kelleher, W. P., and Kondoleon, A. S., 1997, ''A Magnetic Bearing Suspension System for High Temperature Gas Turbine Applications,'' *Proceedings of MAG '97*, Technomic, Lancaster, PA, pp. 15–24.
[4] Maslen, E. et al., 1989, ''Practical Limits to the Performance of Magnetic Bearings: Peak Force, Slew Rate, and Displacement Sensitivity,'' ASME J. Tribol., **111**, pp. 331–336.
[5] Okada, Y., Miyamoto, S., and Ohishi, T., 1996, ''Levitation and Torque Control of Internal Permanent Magnet Type Bearingless Motor,'' IEEE Trans. on Control Systems Technology, **4**, No. 5, pp. 565–571.
[6] Bischel, J., 1991, ''The Bearingless Electrical Machine,'' *Proceedings of the International Symposium on Magnetic Suspension Technology '91*, NASA Langley Research Center, p. 561.
[7] Maslen, E. et al., 1996, ''Magnetic Bearing Design for Reduced Power Consumption,'' ASME J. Tribol., **118**, pp. 839–845.
[8] Meeks, C., 1993, ''Magnetic Bearing Structure Providing Radial, Axial, and Moment Load Bearing Support for a Rotating Shaft,'' U.S. Patent No. 5,216,308.
[9] Sortore, C., Allaire, P., Maslen, E., Humphris, R., and Studer, P., 1990, ''Permanent Magnet Biased Magnetic Bearings—Design, Construction, and Testing,'' *Proceedings of 2nd International Symposium on Magnetic Bearings*, Tokyo, July 12–14, University of Tokyo, Tokyo.
[10] Knospe, C. R., and Stephens, L. S., 1996, ''Side-Pull and Stiffness of Magnetic Bearing Radial Flux Return Paths,'' ASME J. Tribol., **118**, pp. 98–101.
[11] Walowit, J. A., and Pinkus, O., 1982, ''Analytical and Experimental Investigation of Magnetic Support Systems. Part 1: Analysis,'' ASME J. Lubr. Technol., **104**, pp. 418–428.
[12] Happel, J., and Brenner, H., 1986, *Low Reynolds Number Hydrodynamics*, Matrinus Nijhoff, Boston, pp. 474–499.

Swirl Effects on Combustion Characteristics of Premixed Flames

A. K. Gupta

M. J. Lewis

M. Daurer

The Combustion Laboratory,
Department of Mechanical Engineering,
University of Maryland,
College Park, MD 20742

The effect of radial distribution of swirl has been examined on the thermal behavior of two different premixed flames using a double concentric premixed swirl burner. The double concentric swirl burner allowed systematic variation in the radial distribution of swirl (both co- and counter-) between the inner and outer annulus of the burner. The burner had two annular jets and a central nozzle. Information on the thermal field in two flames formed by co- or counter-swirl in the outer annulus and co-swirl in the inner annulus has been examined. Specifically mean and fluctuating temperatures, integral and micro thermal time scales, and probability density distribution of temperatures have been determined at various spatial positions in the flames. The micro-thermocouple output was compensated to provide high-frequency (about 1 kHz) response of the thermocouple. Direct flame photographs were taken to provide information about the global features of flames and flame stability. The global and thermal characteristic data presented here provided a complete insight on the thermal behavior of co- and counter-swirl flames. The results show that the direction of swirl (co- or counter-) used to stabilize a flame from annular jets provides a great influence on flame symmetry. The simultaneous combination of co- and counter-swirl in the burner showed a very nonsymmetrical behavior of the flame. The global and thermal data presented here confirmed these findings. The results suggest significant effect of co- and counter-swirl distribution in flames on the NO_x emission levels. [DOI: 10.1115/1.1339987]

Introduction

The use of lean premixed combustion in a gas turbine combustor has been preferred over nonpremixed combustion by gas turbine manufacturers for achieving low NO_x emission. Lean premixed combustion reduces the peak flame temperature at the fuel–air interface in the traditional diffusion flame-type combustor. The degree of premixing determines the thermal field uniformity of the flames. In all premixed combustor configurations the fuel and air are premixed upstream of the swirler. The swirl is used for the stabilization of the flame. This stabilization is accomplished by transporting hot and chemically active combustion species from the downstream region of the flame to the root of the flame. A thermal nonuniformity is created between these recirculated hot gases and the relatively cold gases flowing into the combustor from upstream of the swirler and flame zone.

The extent of thermal nonuniformity in premixed flames is poorly characterized but can be expected to depend upon the combustor configuration, the degree and distribution of swirl in the combustor, and other input and operational parameters of the combustor [1]. The nonuniformity in the thermal field can have an influence on the efficiency of the combustor as well as on the emission levels, including NO_x [2].

Significantly different combustion characteristics have been obtained by altering the radial distribution of swirl in a burner [3]. Marshall and Gupta [4] determined thermal characteristics of diffusion flames performed through various combinations of swirl and axial inlet momentum distributions in a double concentric swirl burner. Fluctuating temperature measurements were obtained from several flames at various spatial positions in the flames, including the recirculation zone, shear layer, and post-combustion region. By maintaining a constant equivalence ratio, a comparison of the dimensions and distribution of temperatures for different flames was achieved. These results provided information on the important role of radial distribution of swirl and jet axial momentum on the flame thermal characteristics.

In this present paper, the effect of radial distribution of swirl, obtained by changing the swirl flow direction in the outer annular of the burner while maintaining the inner swirl direction fixed, has been obtained for premixed swirling flames. Information on the flame shape, mean and fluctuating temperatures, spatial distribution of probability density of temperatures, and integral and micro thermal time scales is examined. These time scales provide information on the large and small thermal eddies present in the flame, which subsequently affects NO_x emission.

Experiment Facility and Investigation Methodology

A schematic diagram of the experimental double concentric swirl burner is given in Fig. 1. The burner consists of a central nozzle surrounded by two concentric annuli. Each annulus of the burner can be given any desired degree of swirl (either co- or counter-swirl) so that the flame can have either co-swirl in the two annuli or co- and counter-swirl between the inner and outer annulus of the burner. The co- and counter-swirl refer to the flow direction in the clockwise or counter-clockwise direction, respectively, when viewed from the top into the burner. Premixed mixture at the desired mixture ratio can be introduced into any annulus or central nozzle of the burner. The burner is mounted vertically upwards and the flame formed is confined in an enclosure. Details on the burner and the experimental facility are provided in Refs. [3,4]. The experimental conditions used here are given in Table 1. The o.d. of the burner was 65 mm.

High-frequency temperature measurements have been taken with an R-type (Pt/Pt-13 percent Rh) micro-thermocouple probe. The wire diameter of thermocouple was 50 μm. Thermocouple junction is suspended between two 1.6 mm insulated stainless steel supports. The wire diameter is small enough not to cause any significant interference on the flame structure while maintaining structural rigidity of the thermocouple. The thermocouple output is compensated to high frequencies (about 1 kHz). At every probe

Contributed by the Fuels and Combustion Technology Division of THE AMERICAN SOCIETY OF MECHANICAL ENGINEERS for publication in the ASME JOURNAL OF ENGINEERING FOR GAS TURBINES AND POWER. Manuscript received by the FACT Division, August 12, 2000; final revision received by the ASME Headquarters, November 15, 2000. Associate Editor: H. D. Nelson.

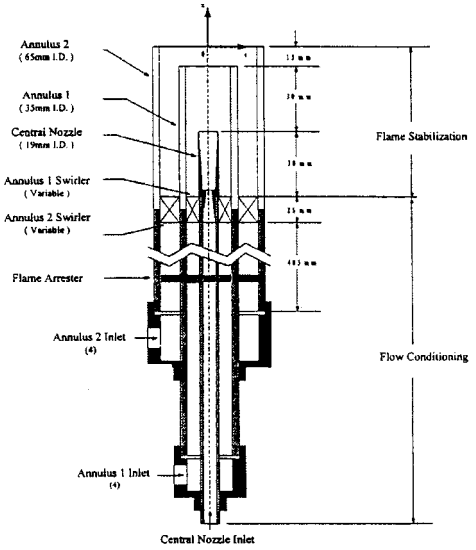

Fig. 1 Schematic diagram of the premixed burner

location in the flame the signal of the thermocouple is amplified and digitized at 10 kHz for a total of 300,000 samples. The sampling time was therefore 30 s. The high sampling frequency is used to resolve small thermal time scales that may occur in flames. The resulting long sampling time of 30 s allows averaging over low-frequency temperature fluctuations to assure a good statistical representation of the thermal field. At any location in the flame, large variations in temperature were found. The distribution of temperature at a given location allowed evaluation of statistical properties in the flame.

Previous studies have shown temperature fluctuations of several kHz in strongly swirling flames [5–10]. The frequency response of the thermocouple depends on wire diameter, flow velocity, and temperature, among other parameters. Without compensation the response time of the thermocouples of usable size is very small (of the order of few Hz). Even with micro-thermocouples with bead diameter of 50 μm, detection of temperature fluctuations higher than 50 Hz is not possible. The small size thermocouples used alone do not inadequately resolve the flame thermal behavior at high frequencies. PLIF diagnostics in premixed flames have revealed significant effect of swirl and flow distribution in the burner on the flame characteristics [11].

In order to extend the frequency response of thermocouples to high frequencies, compensation to the thermocouple output must be made. This compensation requires determination of the time constant that depends on flow velocity and temperature. The time constant therefore varies at different spatial positions of the flame. The time constant is measured at various spatial locations in the

Table 1 Test conditions

Case	''Co''	''Counter''
Fuel	Propane	Propane
Swirler: Annulus 1	30°	30°
Swirler: Annulus 2	50°	−50°
Swirlnumber: Annulus 1	0.3849	0.3849
Swirlnumber: Annulus 2	0.794	0.794
Equivalence Ratio (all)	0.625	0.625
Axial Momentum: Central pipe lbm*ft/min2	300	300
Axial Momentum: Annulus 1 lbm*ft/min2	1500	1500
Axial Momentum: Annulus 2 lbm*ft/min2	2163	2163
Momentum Ratio	0.693	0.693

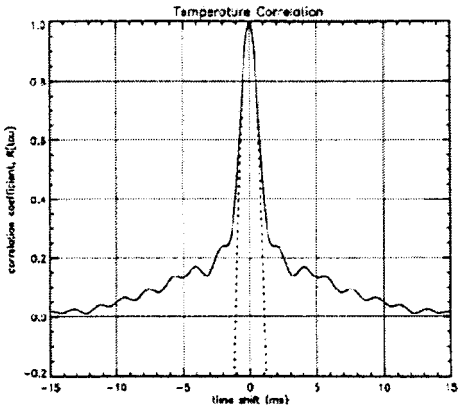

Fig. 2 Auto-correlation function

flame by electrically heating the wire to some higher temperatures and noting the signal decay as a function of time. Due to the fluctuation of temperatures in the flame, the process is repeated up to 300 times at each measurement location. The resulting temperature decay curves are averaged to obtain a smooth decay curve. A time constant τ is determined as the value at which the overheat temperature ΔT has decreased by the factor $1/e$. This time constant is used to compensate the thermocouple output for determining the true high-frequency data. Details on the response of the thermocouples to high frequencies as well as the methodology used to determine the thermal time scales and probability density function of temperature are given in Ref. [7].

The auto-correlation coefficient of temperature $R(\Delta t)$, see below, is calculated for different locations within the flame:

$$R(\Delta t)=\frac{\int [(T'(t)-T_{\text{mean}})\cdot(T'(t+\Delta t)-T_{\text{mean}})]dt}{[T_{\text{fluct}}]^2}$$

where

T' = instantaneous temperature
T_{mean} = mean temperature
T_{fluct} = fluctuating temperature
Δt = time shift

The above equation is used during the post-data-processing for calculating the micro thermal time scales (t_{mic}). It is defined as

$$t_{\text{mic}}=\left(\frac{-2}{d^2R(\Delta t)/d^2\Delta t}\right)^{0.5}$$

t_{mic} = micro time scale

The information on integral time scales (t_{int}) is calculated from

$$t_{\text{int}}=\int_0^{\infty} R(\Delta t)d\Delta t$$

Figure 2 presents a typical auto-correlation function that is calculated at every measured point in the flame. The micro time scales represent the characteristic sojourn times of big and small eddies. Knowledge of this information therefore allows one to conclude about the microstructure of the flames. A small value of micro thermal time scale indicates that the flow movement and thus the fluctuations in the flame are very fast. In contrast, a bigger one represents a slow movement.

After the compensation and data processing, one can obtain information on the distribution of mean temperatures, fluctuating temperatures, thermal time scales, and the probability density distribution of temperatures at a given location in the flame. The accuracy on the reported data is estimated to be about ten percent.

In a former study only measurements of half planes were taken and results were mirrored for the other half [3]. In order to obtain more information about flame symmetry, measurements of the whole flame plane have been taken at 207 points (23 radial loca-

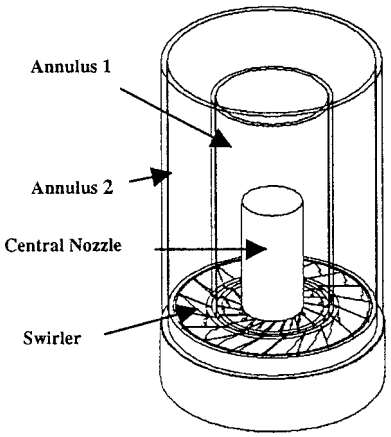

Fig. 3 Flame stabilization zone

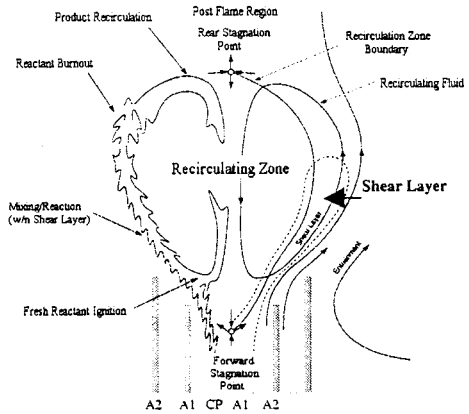

Fig. 4 Sketch of swirling flow field [7]

tions at 0.25-in. intervals and 9 vertical locations at 0.75-in. intervals) by moving the thermocouple with respect to the burner. The value of time constants, τ, is measured at 55 locations in the flame (every other measurement point).

Two premixed flames have been investigated in this study. These flames were produced from the change of swirl direction between the inner and outer annulus. In both cases a +30 deg swirler was used for annulus 1. For outer annulus 2 either +50 deg or −50 deg swirler was used. The arrangement that had both swirlers in the same direction is called the ''co-swirl'' flame. However, the flame formed with +30 deg swirler in annulus 1 and −50 deg swirler in annulus 2 is called the ''counter-swirl'' flame. A sketch of the burner outlet section, shown in Fig. 3, provides the geometry of the flame stabilization zone. The sketch of the swirling flow field, presented in Fig. 4, shows the characteristic regions of a swirl-stabilized premixed flame [7].

Results and Discussion

CCD Flame Photographs. The negative images of the CCD photographs in Fig. 5 show the approximate size of the flame in proportion to the burner. The grid shown between the two flames shows the measurement location for the temperature measurement. Each cell size in the grid is uniform having dimensions of 0.25 in. in the radial direction and 0.75 in. in the vertical direction.

The dark sections in the flame represent very luminous regions. These luminous regions indicate the reaction/combustion area. A comparison of the negative photographs as well as the time-averaged CCD photographs of the co- and counter-swirling flames, shown in Fig. 6, show a very nonsymmetrical nature of the counter-swirling flame. Upon closer observation, in particular the post-flame region and the upper region of the flame, the co-swirling flame also shows nonsymmetrical behavior. However, the asymmetry for the co-swirling flame is much less than the counter-swirling flame.

All CDD images of the counter-swirling flame show a wide and flat shear layer towards the left side and a steep and long shear layer towards the right side of the flame. Another observation is the gap in the lower region of the right shear layer. This region does not show any sign of combustion, and may be caused by the asymmetry of the counter-swirling flame. A possible reason for this may be the presence of three-dimensional instability in swirl flows. The counter-swirl condition, although useful for very intense mixing, leads to amplification of this instability due to the opposing motion of the flow in the flame. It is conjectured that the two instabilities are displaced in the radial direction at different instants of time in the flow. This then leads to more nonsymmetrical nature of the counter-swirling flame.

Temperature Data. Different types of temperature maps are presented to gain an understanding of the thermal and local structure of the swirling flames. The raw temperature data has to be compensated for radiative losses and thermal inertia effects of the

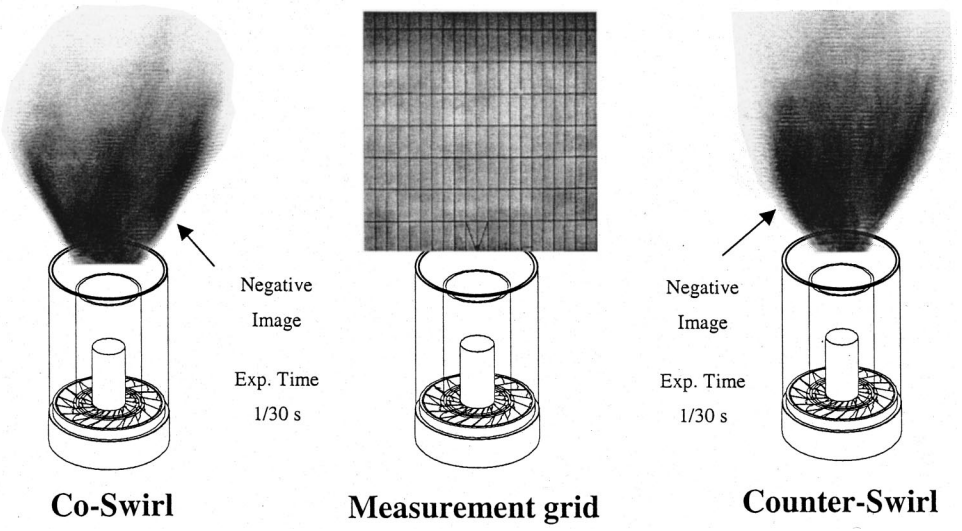

Fig. 5 Size of CCD flame photographs (negative images)

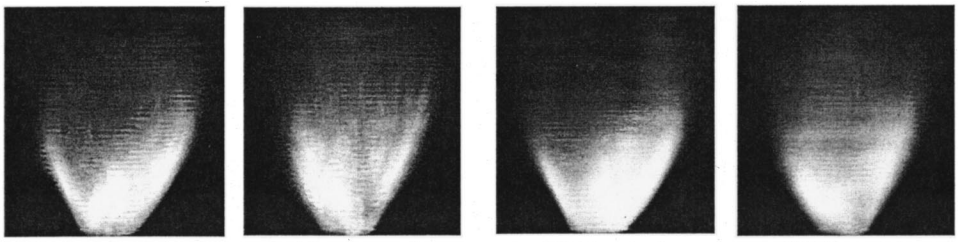

Fig. 6 CCD photographs and average of 50 images

thermocouple. These radiative losses can be significant, in particular at high temperatures. Similarly, the level of temperature fluctuations obtained without compensating the thermocouple output can be significant. A comparison of the uncompensated and compensated thermocouple output has been shown in one of our previous publications [3]. The results showed that fluctuating temperatures are much lower (as much as 250°C at some locations in the flame) without compensation. The mean temperatures are similarly affected without any compensation. The corrections were significant for both the co- and counter-swirling flames examined here. A comparison between the uncompensated and compensated data of the mean temperature data reveals that the calculated temperature difference can be up to 300 K at the same location in the flame. The corrected mean and fluctuating temperature contours shown in Figs. 7 and 8 are for the co- and counter-swirling flames, respectively. Therefore, the importance of the compensation technique for mean and fluctuating temperature measurement can be recognized when it is desired to determine NO_x emission levels from the temperature data. The importance of accurate temperature data can also be recognized when estimating other pollutants emission and heat transfer characteristics of the flame.

Mean Temperatures. The compensated mean temperature maps, shown in Fig. 7, show big differences between the left and right sides of the flame for the case of counter-swirling flame. The map also shows a flat hot shear layer at the left side (temperatures higher than 1700 K). The right side has a shear layer that is steeper but not as hot as on the left side ($T_{\text{Mean}} \approx 1500$ K). By comparing the mean temperature map of the counter-swirling flame with the co-swirling flame one can confirm the nonsymmetrical behavior of the counter-swirling flame. In the post-flame regions (and at axial location of $r/D > 1.2, \ldots, 1.5$) there is a significant difference between the mean temperatures on both sides ($\Delta T_{\text{Mean}} > 200$ K). The results of the co-swirling flame confirm this unsymmetrical behavior; only the shear layer region is more symmetrical. A direct comparison of mean temperatures with the co-swirling case shows negligible differences in mean temperatures. However, the co-swirling flame is wider.

The reaction gap in the counter-swirling shear layer, observed in the CCD photographs, cannot be confirmed with the mean temperatures. It is, however, possible that the regions close to the shear layer have similar temperatures without any reaction which may be caused by heat conduction and heat convection of the hot burned gases.

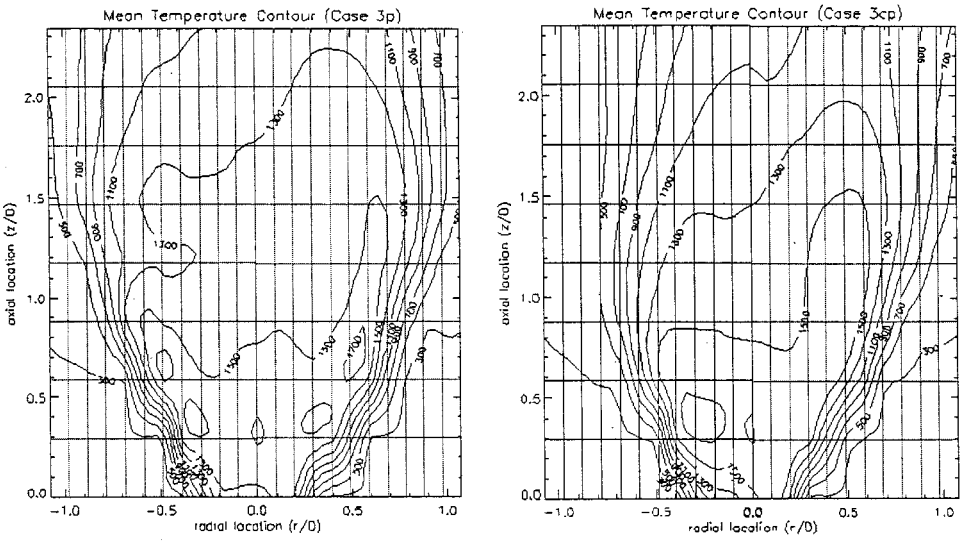

Fig. 7 Compensated mean temperatures maps

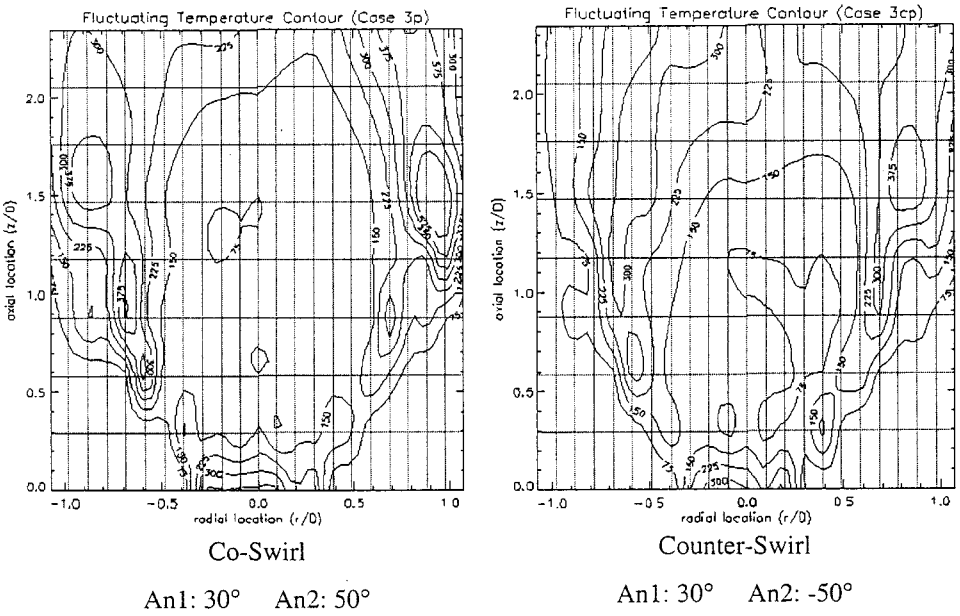

Fig. 8 Compensated fluctuating temperatures maps

Fluctuating Temperatures. The contours of fluctuating temperature, shown in Fig. 8, confirm the unsymmetrical behavior of both co- and counter-swirl flames. Two regions can be seen with extraordinarily high fluctuating temperatures for the co-swirl flame case. The right-hand side of the flame has fluctuating temperatures up to 525 K whereas the left-hand side zone has only up to 375 K. The map of the counter-swirl flame shows only one such region on the right side of the flame shown in Fig. 8. This confirms the general observation of a very unsymmetrical flame with counter-swirl arrangement in the burner.

To understand the process within the flame, a combination of fluctuating, mean temperatures and other thermal physical characteristics are necessary. In the following, thermal correlation between various parameters are described.

Correlations. The combination of mean and fluctuating temperature maps (Fig. 9) makes it possible to locate the combustion area, the recirculation zone, and the post-flame region. Outside and above the shear layer regions the flame shows higher fluctuating temperatures ($T_{\mathrm{Fluc}} = 150$ to 450 K) than in the recirculation zone ($T_{\mathrm{Fluc}} < 75$ to 150 K). These regions of low fluctuations are caused by continuous combustion and represent the region of burned gases within the recirculation zone. Very high temperature fluctuations outside of the combustion zone are caused from mixing between the hot reaction products and the surrounding air. This is confirmed from Fig. 9, which shows a high temperature fluctuation zone on the right side in the measured plane for the co-swirling flame. The change of distribution for temperature probability density functions from outside to inside, at an axial position of 4.5 in. downstream from the burner exit, is shown in Fig. 10. These results show the evolution of the mean temperatures as well as the fluctuating temperatures. The probability density functions at the location of 09/06 and 08/06 show the simultaneous presence of warm and hot burned gases at the same location in the flame. This distribution indicates a mixture of simultaneous ambient air and combustion products. The areas of high fluctuating temperature suggest a stream of ambient air entrained towards the flame that is caused by the recirculation zone of the swirling flow field.

In general, the combined temperature maps (Fig. 9) show that the hottest regions are not the regions of the high temperature

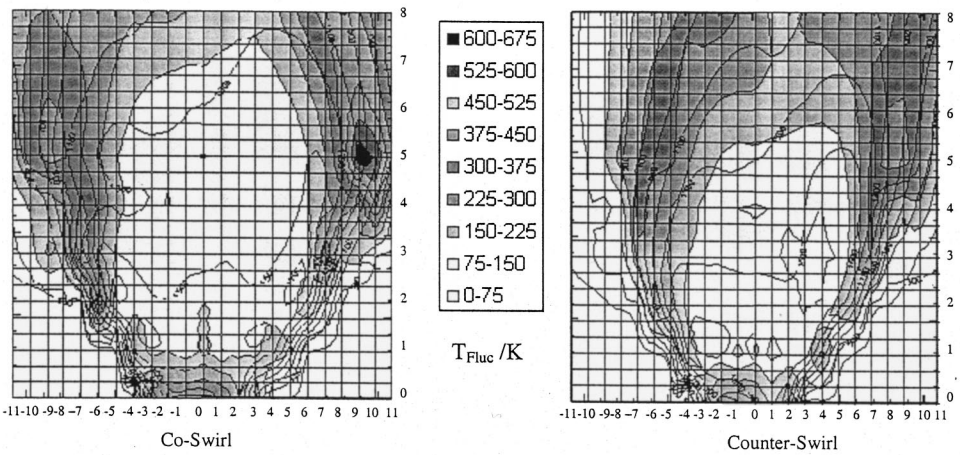

Fig. 9 Combination of fluctuating (colors) and mean temperature maps

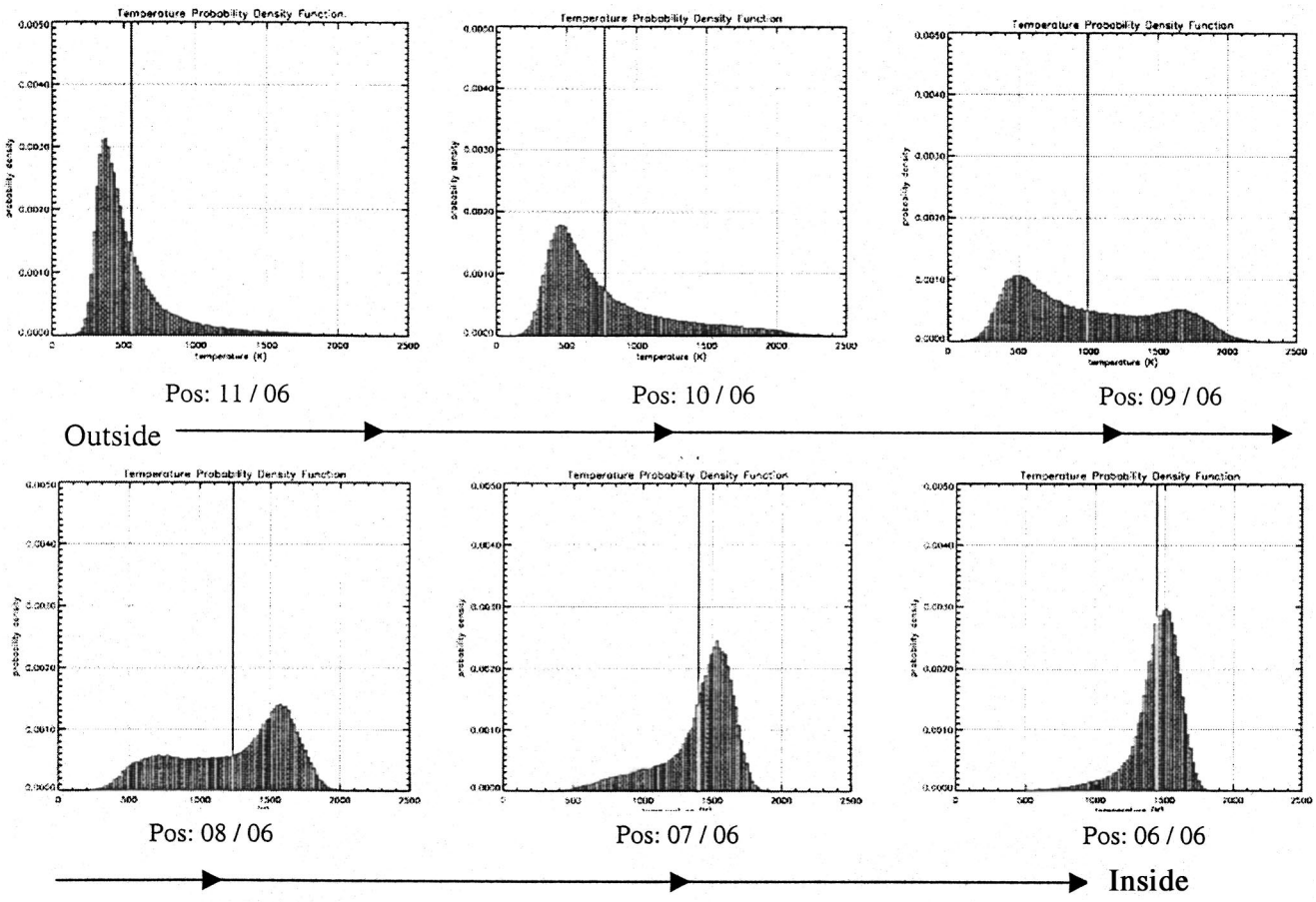

Fig. 10 Temperature probability density functions/Cut through right high fluctuating temperature section in the co-swirling flame

fluctuations. The regions of the high temperature fluctuations are outside the hot regions. The hot regions in the flame correspond to the location of low temperature fluctuations. The hot regions appear to separate the regions of high temperature fluctuations outside of flame from those with low temperature fluctuations inside of the flame. The hot regions themselves show only moderate levels of fluctuating temperatures ($T_{\mathrm{Fluc}} \approx 150$ K).

The comparison of both cases shows an area of very low temperature fluctuations for the counter-swirling flame on the right side of the recirculation zone (at a radial location of $r/D \approx 0.1-0.4$ and axial location of $r/D \approx 0.3-1.2$). In contrast, the co-swirling flame shows a wider and larger area of lower fluctuations ($T_{\mathrm{Fluc}} = 75$ to 150 K). This behavior seems to be caused by the reaction zones of the flames. The extent of the co-swirling flame combustion area is wider than that of the counter-swirling flame case, so that it is apparent that the low temperature fluctuation areas are caused by the reaction zones and behave in a similar fashion. Generally, it can be said that the wider reaction zone for the co-swirling flame case causes a wide and long area of low temperature fluctuations. However, the thin but intense reaction zone in the counter-swirling flame case causes nonsymmetrical temperature fluctuations in the flame and in a smaller area. This observation will be confirmed with the thermal micro time scales of the flames, described in the following section.

Thermal Micro Time Scales. Figure 11 shows the distribution of the thermal micro time scales for both the co- and the counter-swirling flames for the whole flame. The results for both flames show low values of thermal micro time scales outside the shear layer region (shown as white regions in the figures) and higher thermal time scales in the recirculation zone (shown as dark regions in the figure). Within the combustion zone, which can be located in the combined mean and fluctuating temperature maps (see Fig. 9), the thermal micro time scales decrease rapidly from inside to outside of the flame. This leads to the conclusion that there are high temperature fluctuations outside the shear layer region and lower fluctuations in the recirculation zone of the flame. This can also be seen in the combined mean and fluctuating temperature contours shown in Fig. 10.

The combined thermal micro time scale maps and fluctuating temperature maps (Fig. 11) show that the regions of low micro time scales correspond to high fluctuations. Since only small differences are observed, a direct comparison would be more appropriate. Figure 12 shows the differences between the co- and counter-swirling cases. In this figure the thermal micro time scales of the counter-swirl case are subtracted from the thermal micro time scales of the co-swirl case. The positive results indicate lower temperature fluctuations for the co-swirl case (light region shown in Fig. 12) and negative results show lower temperature fluctuations for the counter case (dark region shown in Fig. 12). Regions near zero show no significant differences between the co- and counter-swirling cases.

The results presented in Fig. 12 show that the co-swirling flame has higher thermal micro time scales within the flame. The thin and long region in the middle of the flame indicates higher thermal micro time scales for the counter-swirling flame. Thus, it appears that the fluctuation levels in the center of the counter-swirling flame (see dark regions shown in Fig. 12) are lower than that for the co-swirling flame (see light regions shown in Fig. 12). This observation is also confirmed by comparing the fluctuating temperature contours, shown in Fig. 9, which show lower fluctuating temperatures in the center of the counter-swirling flame.

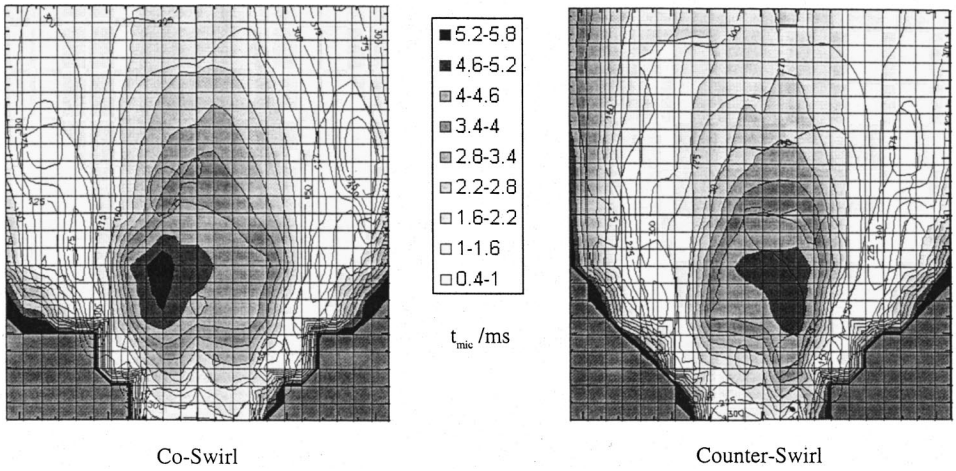

Fig. 11 Combined fluctuating temperature map (isothermal lines) and thermal micro time scales map (colors)

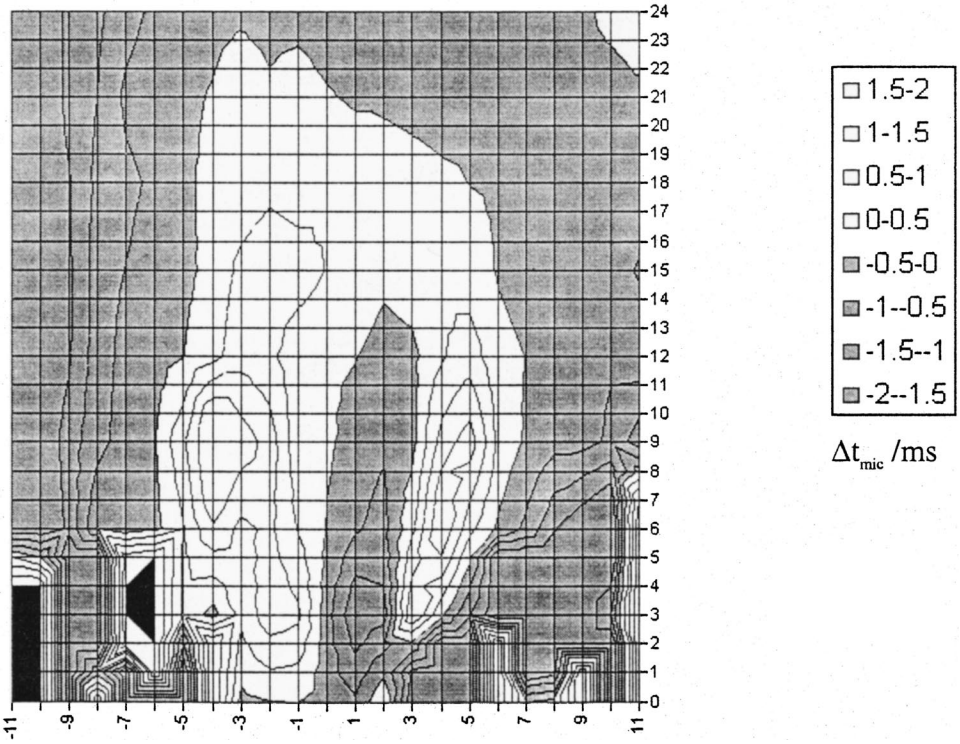

Fig. 12 Difference between micro time scales

The distributions of the thermal integral time scales were also observed and they showed no differences in the distribution.

Conclusions

An experimental investigation has been carried out on premixed flames to determine the influence of co- and counter-swirl distribution in a burner on the flame thermal characteristics. An experimental facility including a burner and thermal signature detection of flames at high frequencies was designed and built for this purpose. Compensated micro thermocouples were used for temperature measurements in order to provide detailed information on the thermal characteristics of the premixed swirling flames.

Information on mean temperatures and fluctuating temperatures has been obtained from co- and counter-swirling flames. The results show significant differences between the co-and counter-swirl cases. The temperature probability density functions at multiple locations provided information on the fate of local gas/air mixture in the swirling flow field. The direct comparisons of mean temperatures, fluctuating temperatures, thermal micro time scales, and also the flame photographs allowed conclusions to be made about the ongoing processes in the premixed flames. The compensated mean temperature maps and the CCD photographs showed that the counter-swirling flames are very unsymmetrical. The wider reaction zone for the co-swirling flame case causes a wide and long area of low temperature fluctuations. However, the thin but intense reaction zone in the counter-swirl case causes nonsymmetrical temperature fluctuations in a smaller area in the flame. The change in swirl combination is expected to have a significant influence on NO_x emission. The results have clearly shown that the influence of asymmetry is larger than anticipated for the

counter-swirl case. The swirler geometry and configuration provides an important role on this unsymmetrical behavior. The radial distribution of swirl in a burner has an important effect on the temperature fluctuations and flame instability.

Acknowledgments

The US DoE, via the South Carolina Institute of Energy Studies, Clemson University, supported the research; program manager Mr. Dan Fant. The help provided by Michael Heim is much appreciated.

References

[1] Gupta, A. K., Lilley, D. G., and Syred, N., 1984, *Swirl Flows*, Abacus Press, Tunbridge Wells, England.
[2] Reese, J. L., 1994, State of the Art of NO_x Emission Control Technology, ASME Paper No. 94-JPGC-EC-15.
[3] Qi, S., Gupta, A. K., and Lewis, M. J., 1997, ''Effect of Swirl on Temperature Distribution in Premixed Flames,'' 35th AIAA Aerospace Sciences Meeting, Paper No. 97-0373.
[4] Marshall, A. W., and Gupta, A. K., 1996, ''Effects of Jet Momentum Distribution on Thermal Characteristics of Co-Swirling Flames,'' 34th AIAA Aerospace Sciences Meeting, Paper No. 96-0404.
[5] Gupta, A. K., Syred, N., and Beer, J. M., 1975, ''Fluctuating Temperature and Pressure Effects on the Noise Output of Swirl Burners,'' *Proc. 15th Symposium (intl.) on Combustion*, The Combustion Institute, Pittsburgh, PA, 1975, pp. 1367–1377.
[6] Lockwood, F., and Odidi. A. O. O., 1975, ''Measurement of Mean and Fluctuating Temperature and of Ion Concentration in Round Free-Jet Turbulent Diffusion Flames,'' *Proc. 15th Symposium (intl.) on Combustion*, The Combustion Institute, Pittsburgh, PA, pp. 561–571.
[7] Marshall, A. W., 1996, Ph.D. thesis, University of Maryland, College Park, MD.
[8] Marshall, A. W., and Gupta, A. K., 1996, ''Effects of Jet Momentum Distribution of Thermal Characteristics of Co-Swirling Flames,'' AIAA 34th Aerospace Sciences Conference, Reno, NV, Jan. 15–18, AIAA Paper No. 96-0404.
[9] Qi, S., Gupta, A. K., and Lewis, M. J., 1997, ''Effect of Swirl on Combustion Characteristics in Premixed Flames,'' 1997 IGTI Conference, Orlando, FL, June 2–6, ASME Paper No. 97-GT-276.
[10] Daurer, M., Gupta, A. K., and Lewis, M. J., 1998, ''Swirl Effects on Combusion Characteristics of Premixed Flames,'' *Proc. Intl. Joint Power Generation Conference*, Baltimore, MD, Aug., ASME FACT-Vol. 22, ASME, New York, pp. 573–578.
[11] Birouk, M., and Gupta, A. K., 1998 ''Swirl Distribution Effects on the Structure of Lean Premixed Flames Using PLIF Diagnostics,'' ASME J. Heat Transf., **120**, p. 541.

A Mixing Based Model for Di-methyl Ether Combustion in Diesel Engines

B. H. Bek

S. C. Sorenson

Department of Energy Engineering,
Technical University of Denmark,
Building 403,
DK-2800 Lyngby, Denmark

A series of studies has been conducted investigating the behavior of di-methyl ether (DME) fuel jets injected into quiescent combustion chambers. These studies have shown that it is possible to make a good estimate of the penetration of the jet based on existing correlations for diesel fuel, by using appropriate fuel properties. The results of the spray studies have been incorporated into a first generation model for DME combustion. The model is entirely based on physical mixing, where chemical processes have been assumed to be very fast in relation to mixing. The assumption was made on the basis of the very high Cetane number for DME. A spray model similar to that proposed by Hiroyasu et al. [11] has been used, with the assumption that rapid combustion occurs when the local mixture attains a stoichiometric air fuel ratio. The spray structure is based on steady-state spray theory, where the shape of the spray has been modified to match the measured spray penetration rates. The spray theory and experimentally determined penetrations implicitly determine the rate of air entrainment into the spray. The results show that the combustion rates calculated during the mixing controlled portion of combustion agree well with experimental measurements from a previous study, without additional adjustment. [DOI: 10.1115/1.1362665]

Introduction

Since its presentation as a low emission alternative to diesel fuels (Sorenson and Mikkelsen [1], Hansen et al. [2], Fleisch et al. [3], and Kapus and Ofner [4]), additional studies have substantiated the desirable performance of di-methyl ether (DME) (Kapus and Cartellieri [5], Sorenson, and Mikkelsen [6], Christensen et al. [7], and Rhee et al. [8]). Some initial studies of spray behavior in DME injection systems have also been performed (Glensvig et al. [9], and Sorenson et al. [10]). These results have shown that in general it is possible to predict DME injection penetration rates using previously developed methods for diesel spray (Hiroyasu [11]). It has also been shown that cavitation is likely in the flow through the injection nozzle (Kapus and Ofner [4]). The ignition characteristics of DME have also been examined. To date, however, there have been no attempts to model the combustion of DME in diesel engines. Therefore, in order to further investigate the combustion of DME and the possibilities of calculating the performance of DME engines, the current study was initiated to develop a first combustion rate model for DME.

Due to its low ignition temperature (high cetane number) (Edgar et al. [12]), DME ignition occurs shortly after injection with a low initial combustion rate (Sorenson and Mikkelsen [1], Kapus and Ofner [4], Christensen et al. [13]) resulting in low engine noise. The high cetane number suggests that chemical prosecute may play a lesser role in the total combustion process than with diesel fuels. In keeping with this concept, a first combustion model for DME has been developed, based on limitations due to fluid mixing alone. This is based on a series of studies previously conducted into the behavior of a jet of DME during the injection process. In particular, spray penetration rates and spray angles have been determined for high-pressure injections of DME into Nitrogen.

Contributed by the Internal Combustion Engine Division of THE AMERICAN SOCIETY OF MECHANICAL ENGINEERS for publication in the ASME JOURNAL OF ENGINEERING FOR GAS TURBINES AND POWER. Manuscript received by the ICE Division Dec. 6, 2000; final revision received by the ASME Headquarters Dec. 7, 2000. Associate Editor: D. Assanis.

Spray Model

Due to the high vapor pressure of DME and the above-mentioned cavitation in the nozzle exit, it seems reasonable, at least in this initial model, to treat treat DME as a gas once it leaves the injector.

Hence, the basis for the combustion simulation is the turbulent fluid dynamic jet theory (Turns [14]). The jet of injected fuel is considered to be an axisymmetric turbulent, quasi-steady-state jet. The geometry of the jet is shown in Fig. 1.

The jet is assumed to leave the orifice with a uniform velocity profile and an exit velocity given by the Bernoulli equation. Flow differences due to density were corrected using a scaling parameter of $(\rho_{inj}/\rho_{amb})^{(0.5)}$. This gives an effective radius that can be used instead of the actual physical nozzle radius.

$$R_e = R\sqrt{\frac{\rho_{inj}}{\rho_{amb}}} \tag{1}$$

For turbulent flow, the conservation of mass is given by

$$\frac{\partial(\bar{v}_r r)}{\partial x} + \frac{\partial(\bar{v}_r r)}{\partial r} = 0 \tag{2}$$

Similarly, using the concept of a turbulent viscosity, the conservation equation for the axial momentum is

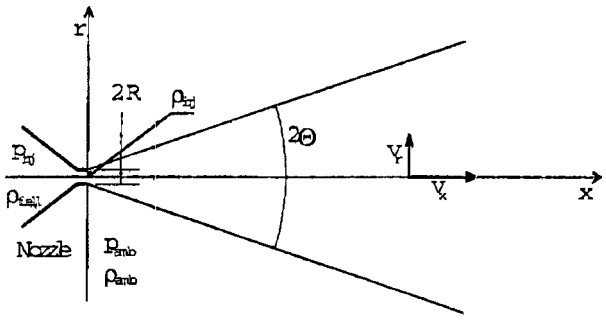

Fig. 1 Spray properties and geometry

$$\overline{v}_x\frac{\partial(\overline{v}_x)}{\partial x}+\overline{v}_r\frac{\partial(\overline{v}_r r)}{\partial r}=\frac{1}{r}\frac{\partial}{\partial r}\left(r\varepsilon\frac{\partial\overline{v}_x}{\partial r}\right) \tag{3}$$

The use of the turbulent viscosity alone is justified since it in much larger than the laminar viscosity for the flow conditions in the jets studied.

Prandtl's mixing length hypothesis is used and applied to the turbulent free flow of the jet:

$$\mu_{\text{turb}}=\rho\varepsilon=c_1\rho l_m(\overline{v}_{x,\max}-\overline{v}_{x,\min}) \tag{4}$$

For a free axisymmetric jet, $l_m=0.075\,r_{\text{jet}}$, where r_{jet} is the radial distance from the centerline to the point where v_x has decayed to 1 percent of its centerline value.

It has also been shown (Schlicting [15]) that

$$r_{\text{jet}}\propto x,\quad \overline{v}_{x,0}\propto x^{-1} \tag{5}$$

Combining this with Eq. (4) gives

$$\varepsilon=cr_{\text{jet}}\overline{v}_{x,0}=\text{const.} \tag{6}$$

where $c=c_1l_m$. For a constant turbulent viscosity, Eqs. (2) and (3) can be integrated to give

$$\overline{V}_x=\frac{3}{8\pi}\frac{J_{\text{exit}}}{\varepsilon x}\left(1+\frac{\xi^2}{4}\right)^{-2} \tag{7}$$

$$\overline{v}_r=\sqrt{\frac{3J_{\text{exit}}}{16\pi}}\frac{1}{x}\frac{(\xi-\xi^3/4)}{(1+\xi^2/4)^2} \tag{8}$$

where $J_{\text{exit}}=\pi v_{\text{exit}}^2R_e^2$, and

$$\xi=\sqrt{\frac{3J_{\text{exit}}}{16\pi}}\frac{1}{\varepsilon}\frac{r}{x} \tag{9}$$

The axial velocity can then be determined

$$\frac{\overline{v}_x}{v_{\text{exit}}}=\frac{3}{8}\frac{v_{\text{exit}}R_e}{\varepsilon}\frac{R_e}{x}\left(1+\frac{\xi^2}{4}\right)^{-2} \tag{10}$$

and the centerline velocity is

$$\frac{\overline{v}_{x,0}}{v_{\text{exit}}}=\frac{3}{8}\frac{v_{\text{exit}}R_e}{\varepsilon}\frac{R_e}{x} \tag{11}$$

Setting $\overline{v}_x/\overline{v}_{x,0}=0.01$ and solving for $r=r_{\text{jet}}$, the jet radius is obtained as a function of distance.

$$r_{\text{jet}}=\frac{24}{\sqrt{3}}\frac{x\varepsilon}{v_{\text{exit}}R_e} \tag{12}$$

Substituting Eqs. (11) and (12) into Eq. (6), the eddy viscosity, centerline decay, and spreading rate are obtained:

$$\varepsilon=\sqrt{27}cv_{\text{exit}}R_e \tag{13}$$

$$\frac{\overline{v}_{x,0}}{v_{\text{exit}}}=\frac{1}{c\sqrt{192}}\frac{R_e}{x} \tag{14}$$

$$r_{\text{jet}}=72cx \tag{15}$$

The latter three quantities are all determined by the value of the constant c for the turbulent viscosity.

Air Distribution

Within the jet itself, it is important to determine the air distribution, since this determines the local stoichiometry of the jet. It can be shown that the volumetric flow rate in a laminar jet as a function of distance can be given by the following (Schlicting [15]).

$$\dot{Q}=8\pi vx \tag{16}$$

Using the above equation,

$$\dot{Q}=24\sqrt{3}\pi v_{\text{exit}}R_ex \tag{17}$$

Since the injected volume is much smaller than the entrained volume, it is acceptable to approximate the entrained volume flow with the total volume flow (14). Then for the entrained mass

$$m_{\text{ent}}=\dot{Q}_{\text{ent}}\rho_{\text{amb}}=24\sqrt{3}\pi c\rho_{\text{amb}}v_{\text{exit}}xR_e \tag{18}$$

The entrained mass is assumed to be equally distributed over the cross section of the jet, which gives the density of the entrained air across the jet as

$$\rho_{\text{ent}}=\frac{\dot{m}_{\text{ent}}}{\Delta x\pi r_{\text{jet}}^2}=24\sqrt{3}\frac{cxR_e}{r_{\text{jet}}^2}\frac{v_{\text{exit}}}{\Delta x}\rho_{\text{amb}} \tag{19}$$

Fuel Distribution

In an axisymmetric jet, the fuel distribution throughout the jet is subject to a series of conditions.

First, the fuel density must be zero at the edge of the jet

$$\rho_{\text{fuel}}=0,\quad r=r_{\text{jet}} \tag{20}$$

Due to symmetry, the gradient of the fuel density in the radial direction must be zero at the center of the jet:

$$\frac{\partial\rho_{\text{fuel}}}{\partial r}=0,\quad r=0 \tag{21}$$

And finally, since no fuel leaves the jet,

$$\int_A\rho_{\text{fuel}}\overline{v}_x(x,r)\,dA=\dot{m}_{\text{fuel}} \tag{22}$$

Given that there are three conditions to be fulfilled, a second-order distribution of the fuel density as a function of the radius was arbitrarily assumed. Applying the three conditions to the jet, the radial distribution of the fuel in the jet is found to be

$$\rho_{\text{fuel}}=a(r_{\text{jet}}^2-r^2) \tag{23}$$

where

$$a=\frac{\dot{m}_{\text{fuel}}}{13\,824\sqrt{3[9-\ln(10)]}\pi v_{\text{exit}}R_ec^3x^3} \tag{24}$$

Given the distribution of the fuel and the entrained air, the mass fraction of fuel throughout the jet can be obtained as

$$f(x,r)=\frac{a(r_{\text{jet}}^2-r^2)}{a(r_{\text{jet}}^2-r^2)+24\sqrt{3}c_s\dfrac{cxR_e}{r_{\text{jet}}^2}\dfrac{v_{\text{exit}}}{\Delta x}\rho_{\text{amb}}} \tag{25}$$

Correlation With Experimental Spray Results

Under the assumptions made above, it was found that the jet geometry can be described with the empirical parameter, c. This must be determined by comparison with experimental spray observations. The observations of DME sprays given in Glensvig et al. [9] and Sorenson et al. [10] were used for this purpose. The method used was to find a value of the spray constant c, which agrees with the experimentally observed spray penetration rates. This was done by integrating the equation for the centerline velocity and solving for the tip position x_{tip}:

$$x_{\text{tip}}=\sqrt{\frac{2}{c\sqrt{192}}v_{\text{exit}}R_et} \tag{26}$$

This equation is assumed to be valid only after the breakup time of the spray with diesel fuel. Before the breakup, the tip position is proportional to the time. That is there is assumed to be a constant velocity before spray breakup. Hiroyasu et al. [11] found spray breakup to be given by the following relationship:

Table 1 Spray parameters for DME injection into Nitrogen

Opening pressure—bar	Chamber pressure—bar	t_{break} ms	$c\times10^3$
130	15	0.327	1.71
130	25	0.265	2.91
120	40	0.221	2.29
180	40	0.251	2.76
200	40	0.261	2.28
240	40	0.280	2.34
200	55	0.234	3.85

$$t_{break}=28.65\frac{2\rho_{inj}R_e}{\sqrt{\rho_{amb}(p_{inj}-p_{amb})}} \tag{27}$$

The spray tip position before the breakup is then assumed to follow:

$$x_{tip}=\sqrt{\frac{v_{exit}R_e}{25\sqrt{3}c}}t \tag{28}$$

In using Eq. (27) with DME, there is some question as to what value to use for ρ_{inj}. There is evidance that there can be a significant mount of cavitation during DME injection (Kapus and Ofner [4]). Hence, an estimate was made of the injection density using the ideal gas law for DME at the injection pressure and fuel temperature. There are no data to substantiate this assumption other than the bench flow results of Kapus and Ofner [4].

The spray constant was then determined by the following procedure from the photographic observations of the DME spray:

1 Estimate the breakup time from Eq. (27)
2 Plot the square of the penetration as a function of time for $t>t_{break}$
3 Find the slope of the line using linear regression
4 Determine c from Eq. (26).

For a series of sprays from Glensvig et al. [9] and Sorenson et al. [10], the results obtained are shown in Table 1. There appears to be a slight dependence of the injection constant, c, on the ambient pressure of the injection chamber. A linear fit to the data of Table 1 gives

$$c=1.152\times10^{-9}\ p_{amb} \tag{29}$$

As an example of the modeled spray structure, the calculated spray is shown in Fig. 2. The calculations were performed for injection into a chamber with constant pressure and temperature for the conditions shown in Table 2.

According to the quasi-steady jet theory applied here, the half-width spray angle is given by

$$\theta=\tan^{-1}(72c) \tag{30}$$

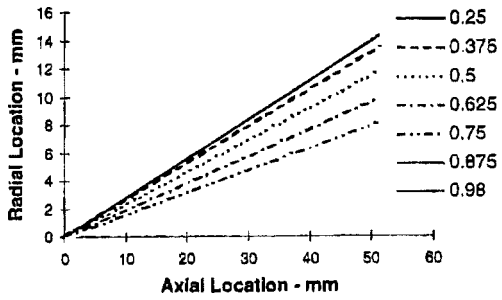

Fig. 2 Relative fuel concentrations as a function of location for the jet model

Table 2 Conditions for spray simulation shown in Fig. 2

Injection Pressure	100 bar
Fuel Temperature	298 K
Chamber Pressure	38 bar
Chamber Temperature	800 K
Elapsed time	4 ms

For the conditions shown, the half-angle is 17.5 deg. The edges and therefore the angles of the experimental sprays are difficult to determine precisely using reflected light. Accepting these difficulties, the experimental spray angles measured in Glensvig et al. [9] are in the range of 15 to 20 deg. Thus, by correlating the penetration rates of the initial portion of transient sprays to a quasi-steady structure, the correct jet shape is also determined.

Combustion Model

The basis of the combustion model is the formulation of Hiroyasu [11]. As fuel enters the combustion chamber, the new fuel spray portion is divided in 10 packets in the radial direction, each packet comprising 180 deg of spray. In this initial version of the model, the effects of swirl are not considered. With the division of the spray packets used, it is intended to include swirl effects by making the spray nonsymmetrical. This was not implemented in the current model, and the division used corresponds to a series of five axisymmetrical packets. The schematic of the model spray structure is shown in Fig. 3.

Should a packet hit the cylinder wall before combustion, it is assumed to travel along the wall with a speed of one jet radius per crank angle degree. The air entrainment rate is then corrected with a factor of 1.5, as suggested by Hiroyasu [11]. When the fuel injection process ends, the spray motion is assumed to continue unchanged, but all packages then inserted into the spray contain no fuel. The injection pressure is considered to be constant at the average injection pressure.

The stoichiometry of each packet is determined by the fuel and air distributions, as described in the previous sections. Combustion is assumed to occur at the time when the fuel air ratio in a given packet becomes equal to the stoichiometric value. The reactions leading to the ignition of the fuel have been assumed to be very fast in relation to the mixing processes. This is obviously an over simplification, but is partially justified by the low ignition temperature. Similarly, fuel evaporation processes are not considered. The cylinder pressure is close to, or above the DME's critical pressure of 54.7 bar, and the fuel temperature is near the critical value of 127°C after passage through the fuel injection nozzle. This, in combination with the tendency of DME to cavitate when flowing out of the orifice, reduces the importance of evaporative processes with DME combustion.

The spray model is used to calculate the rate of heat release for the integration interval. The cylinder conditions are then calculated using a single zone combustion model, as used by Assanis and Heywood [16].

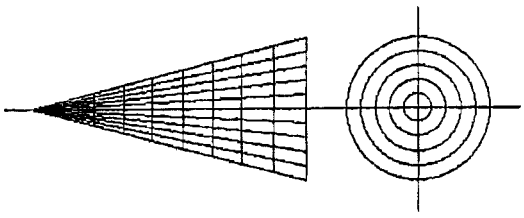

Fig. 3 Schematic diagram of the spray division

Results

The combustion model was used in connection with a standard diesel cycle simulation for the single cylinder, naturally aspirated diesel engine used in Christensen [7], and Christensen et al. [13]. Its specifications are given in Table 3.

The cycle simulation uses the Woschni correlation for the cylinder heat transfer (Woschni [17]). It is assumed that the products of combustion are in chemical equilibrium and the equilibrium calculation procedure of Olikara and Borman [18] is used to determine the equilibrium composition.

Figure 4 shows the calculated combustion rate for an engine speed of 2000 rpm and a brake mean effective pressure of 680 kPa, along with the measured values from Christensen [7]. The calculated heat release-time curve shown is irregular in nature. This is due to the finite size of the fuel packets, and the fact that within the integration step size of one crank angle degree, one or more packets may achieve a stoichiometric mixture. All of this energy is then released at the end of the interval instead of being distributed throughout it. A division of the spray into smaller packets, or decreasing the step time, would give smoother curves. Thus it is the average of the heat release through time, which should be compared to engine data.

Another thing that should be noted is that there is a ''spike'' in the heat release curve near the start of the combustion. This is due to the size and number of packets releasing energy at this time, and is not related to any chemical delay, since this has not been considered in the model.

Of primary interest in the heat release diagrams is that the maximum rates of heat release predicted by the simple jet model agree well with those measured in the engine. In addition, the general duration of the calculated heat release periods are similar to the measured values, although the ends of the calculated heat release profiles are more abrupt than the experimental values.

At the end of the combustion process, the experimental results show an additional heat release. This is due to after injections because of the large pressure oscillations in the injection line with DME (Sorenson et al. [10]). This was not included in the model calculations.

The effect of injection timing on the heat release rate is shown in Figs. 5 and 6, which are for similar conditions to those of Fig. 4, but with injection timings of 6 and 3 deg BTDC respectively. In the experimental and model results, there is not a large effect of the timing on the general shape of the heat release, and there is a reasonably good agreement between the general shape and the maximum rate of heat release during the middle and latter stages of the combustion.

In all of the model results, there is a tendency for an initial large rate of heat release, as the first element or elements reach a stoichiometric mixture. This agreement may to be fortuitous, since there are no chemical reactions included in the model. However, mixing and jet related processes are important in determining the initial mixing and heating rates of the fuel, even though the initial combustion appears to be with much richer mixtures (Dec. 1997). In the later stages, where the combustion process has been shown to be controlled by mixing in a diffusion flame, there is good agreement between the general shape of the model prediction and experimental results, as well as between the maximum heat release rates.

For the same injection timing, the model predicts an ignition at an earlier time than that shown in the experimental results. For the conditions shown in Figs. 4–6, the experimental ignition delay was nearly constant at a value of about 8CA deg, while the model predicted a value of about 4CA deg. This is not unreasonable, since the model does not consider the chemical processes leading to ignition.

The effect of load was also investigated, and the results are shown in Figs. 7 and 8 for half and quarter load, respectively. At part load, the model predicts a faster burning rate than the experimental results. In particular, the predicted combustion ends much sooner than the experiments. As was the case with full load timing

Table 3 Engine specifications

Bore	85 mm
Stroke	85 mm
Connecting Rod Length	160 mm
Compression Ratio	18.5:1
Nozzle orifice diameter	0.24 mm
Nozzle holes/cylinder	4
Intake air	naturally aspirated
Injection type	direct injection

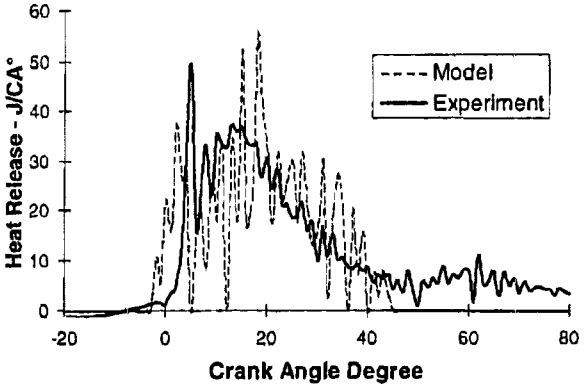

Fig. 5 Comparison of experimental and predicted rate of heat release at 1988 rpm, 634 kPa BMEP, injection at 6 deg BTDC

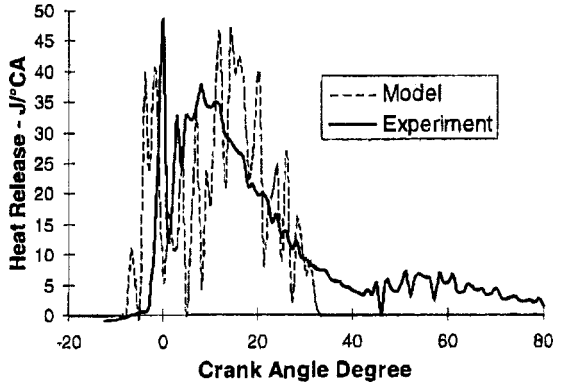

Fig. 4 Comparison of experimental and predicted rate of heat release at 2010 rpm, 643 kPa BMEP, injection at 12 deg BTDC

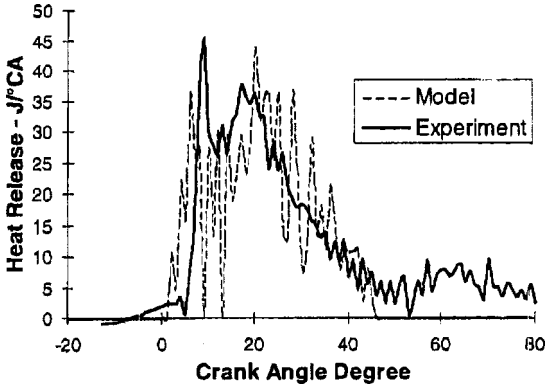

Fig. 6 Comparison of experimental and predicted rate of heat release at 1989 rpm, 638 kPa BMEP, injection at 3 deg BTDC

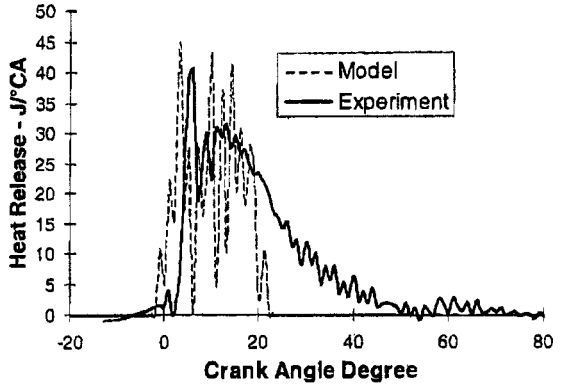

Fig. 7 Comparison of experimental and predicted rate of heat release at 1986 rpm, 359 kPa BMEP, injection at 6 deg BTDC

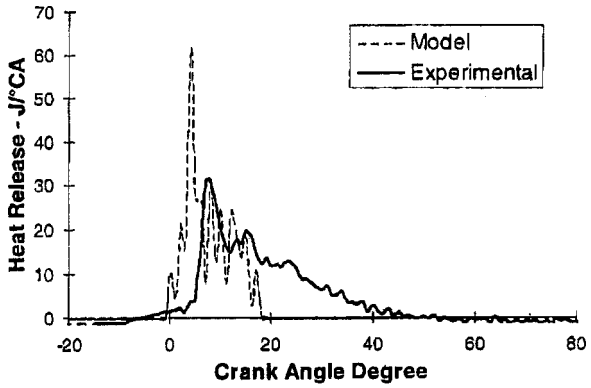

Fig. 8 Comparison of experimental and predicted rate of heat release at 2022 rpm, 183 kPa BMEP, injection at 6 deg BTDC

results, the ignition delay predicted by the model is shorter than the experimental results; for these runs as well, the predicted delay was about 5 deg CA shorter than the experiments.

The general tendencies of the model and experimental heat release curves are similar. At part load, the high initial combustion rates predicted by the model are even more pronounced than at full load. It is of interest to note that at the light loads, the heat release rates in the later stages of combustion are lower than at full load, and that the model predicts the appropriate combustion rate at this time.

As stated in the introduction, the model should be regarded as an initial modeling attempt for DME powered engines. It is recognized that a more complete model should include the effects of reaction chemistry on ignition delay. Nevertheless, the predictions of the fairly simple model are seen to give reasonable combustion rates, particularly for the portions of combustion, which are expected to be mixing controlled. In this regard, the model can be considered to be a successful first step in the development of a more comprehensive combustion model for DME powered engine. It can also be considered to be a promising link between investigations of spray behavior under controlled injection conditions and actual engine combustion.

Conclusions

A simple mixing based model has been presented for the combustion of DME in direct injection diesel engines. The model is based on simple steady-state jet theory, where the jet penetration has been fit to match experimental penetration data. The predicted spray angles agree with the experimental values determined by direct lighting methods in previous work.

The model predicts combustion rates, which are in reasonably good agreement with experimentally determined values. The model predicts the high rate of heat release commonly observed in direct injection diesel engines, even though the effects of chemical reactions on ignition delay are not considered. The model predicts appropriate heat release rates for the diffusion flame controlled portion of the combustion process, where it is expected that the assumptions of the model are most valid.

Nomenclature

Symbols:

A = Area
c = The spray constant
c_a = Correction factor for wall impingement
J = Momentum flux
l_m = Prandtl mixing length
p = Pressure
Q = Volume of entrained air
R = Nozzle radius
R_e = Effective nozzle radius
r = Radial coordinate
t_{break} = Break up time of spray
V_x = Velocity in x-direction
V_r = Velocity in r-direction
x = Axial coordinate
x_{tip} = Spray penetration
ε = Kinematic viscosity
$\theta_{1/2}$ = Half width angle of spray
ν = Laminar viscosity

Subscripts:

amb = Ambient conditions
e = Effective
ent = entrainment
exit = Nozzle exit plane
inj = Upstream of injection nozzle
jet = Related to the jet
turb = Turbulent conditions
0 = Local upstream stagnant conditions

References

[1] Sorenson, S. C., and Mikkelsen, S.-E., 1995, ''Performance and Emissions of a 0.273 Liter Direct Injection Diesel Engine Fueled with Neat Dimethyl Ether,'' SAE Paper 950964.
[2] Hansen, J. B., Voss, B., Joensen, F., and Sigurdardóttir, D., ''Large Scale Manufacture of Dimethyl Ether—a New Alternative Diesel Fuel from Natural Gas,'' SAE Paper 950063.
[3] Fleisch, T., McCarthy, C., Basu, A., Udovich, C., Charbonneau, P., Slodowske, W., Mikkelsen, S.-E., and McCandless, J., 1995, ''A New Clean Diesel Technology: Demonstration of ULEV Emissions on a Navistar Diesel Engine Fueled with Dimethyl Ether,'' SAE Paper 950061.
[4] Kapus, P., and Ofner, H., 1995, ''Development of Fuel Injection Equipment and Combustion System for DI Diesels Operated on Dimethyl Ether,'' SAE Paper 950062.
[5] Kapus, P., and Cartellieri, W., 1995, ''ULEV Potential of a DI/TCI Diesel Passenger Car Engine Operated on Dimethyl Ether,'' SAE Paper 952754.
[6] Mikkelsen, S.-E., Sorenson, S. C., and Hansen, J. B., 1996, *Dimethyl Ether as an Alternate Fuel for Diesel Engines, Application of Powertrain and Fuel Technologies to Meet Emissions Standards*, Institution of Mechanical Engineers, London, pp. 289–298.
[7] Christensen, R., 1996, ''DME as a Fuel in a DI Diesel Engine,'' MS thesis, Report ET-EP 96-24, Dept. of Energy Engineering, Technical University of Denmark. (In Danish).
[8] Katijani, S., Chen, Z. L., Kono, M., and Rhee, K. T., 1997, ''Engine Performance and Exhaust Characteristics of a Direct-Injection Diesel Engine Operated with DME,'' SAE Paper 972973.
[9] Glensvig, M., Sorenson, S. C., and Abata, D. L., 1996, ''High Pressure Injection of DME,'' in Alternative Fuels, Vol. 27-3, ASME Internal Combustion Engine Division, p. 57.
[10] Sorenson, S. C., Glensvig, M., Abata, D. L., 1998, ''Dimethyl Ether in Diesel Fuel Injection Systems,'' SAE Paper 981159.
[11] Hiroyasu, H., Kadota, T., and Arai, M., 1983, ''Development and use of a Spray Combustion Modeling to Predict Diesel Engine Efficiency and Pollutant Emissions, Parts 1 & 2. Bulletin of the ASME, Vol. 26, papers 214–12 and 214–15.

[12] Edgar, B. L., Dibble, R. W., and Naegli, D. W., 1997, ''Autoignition of Dimethyl Ether and Dimethoxy Methane sprays at High Pressures,'' SAE Paper 971677.
[13] Christensen, R., Sorenson, S. C., Jensen, M. G., and Hansen, K. F., 1997, ''Engine Operation on Dimethyl Ether in a Naturally Aspirated, DI Diesel Engine,'' SAE Paper 971665.
[14] Turns, S. R., 1996, ''Introduction to Combustion, Concepts and Applications,'' McGraw-Hill, NY.
[15] Schlicting, H., 1960, *Boundary Layer Theory*, McGraw-Hill, NY.
[16] Assanis, D., and Heywood, J. B., Jr., 1986, ''Development and use of a Computer Simulation of the Turbocompounded Diesel System for Engine Performance and Component Heat Transfer Studies, SAE paper 860329.
[17] Woschni, G., 1967, ''A Universally Applicable Equation for the Instantaneous Heat Transfer Coefficient in the Internal Combustion Engine,'' SAE Paper 670931.
[18] Olikara, C., and G. L. Borman, 1974, ''A Computer Program for Calculating Properties of Equilibrium Combustion Products with Some Applications of IC Engines,'' SAE paper 740468.

Design of Capacitance Probes for Oil Film Thickness Measurements Between the Piston Ring and Liner in Internal Combustion Engines

D. O. Ducu
Detroit Diesel Corporation,
13400 Outer Drive, West,
Detroit, MI 48239-4001

R. J. Donahue
Mercury Marine,
W6250 Pioneer Road,
Fond du Lac, WI 54936-1939

J. B. Ghandhi
University of Wisconsin-Madison,
1500 Engineering Drive,
Madison, WI 53706

Measurement of the capacitance formed between the piston ring and a probe mounted in the cylinder liner provides an accurate means of determining the oil film thickness provided that the region between the ring and probe is flooded with oil and the dielectric constant of the oil is known. All aspects of the design, construction, installation of capacitance probes, and analysis of the resulting measurements are reviewed in this paper. Biases introduced due to the fringing of the electric field, curvature of the ring face profile, roughness of the ring profile, and the tilt angle of the ring face are analyzed, and correction algorithms are proposed. Errors associated with the proposed algorithms are gauged through comparisons to finite difference solutions. Shielding the sensing electrode is found to eliminate fringing effects and also stray capacitance which can affect the signal. A rectangular probe design with a high aspect ratio is suggested as an optimum. The small axis of the probe provides high spatial resolution, while the longer length, which is in the circumferential direction, provides a sufficient surface area to ensure sufficient signal strength. A design procedure which allows for the sizing of probe dimensions for a given level of allowable error and capacitance measuring circuitry is developed. [DOI: 10.1115/1.1368116]

Introduction

The interaction of the piston ring with the cylinder liner plays a critical role in the determination of frictional losses and mechanical wear of internal combustion engines. In addition, concern for the environment has led to increasingly more stringent pollution legislation. Relevant to engine pollution is the fact that the lubricating oil which is consumed can account for a significant fraction of the soluble fraction of the particulate emissions from Diesel engines ([1]). This is especially problematic under light load operation. In order to address these issues, the ring-linear interface has been studied extensively both experimentally ([2]) and analytically ([3]). The primary objective of these studies has been the determination of the minimum oil film thickness between the piston ring and cylinder liner. However, as reduced oil consumption becomes a more significant constraint on the engine design, the transport of oil within the ring pack will become a more relevant performance metric.

There are a variety of methods which have been used for measuring the minimum oil film thickness in operating engines, but the capacitance technique has been found to produce the most quantifiable results. The objective of this paper is to discuss the necessary criteria for the design, installation, and calibration of capacitance gauges for use in the measurement of minimum oil film thickness in firing internal combustion engines. First, a theoretical description of the capacitance technique will be provided with special attention to phenomena that make the output deviate from the basic parallel plate formula. A series of formulas for correcting the errors that are due to the probe and ring parameters will be given. Errors associated with the proposed algorithms are gauged through comparisons to finite difference solutions. Second, the electronic circuitry required to measure the capacitance level will be briefly discussed. Several probe designs, which maximize the spatial resolution while keeping the errors to a minimum (via active shielding and appropriate geometry), will then be discussed. Finally, the complete calibration of a sample measurement will be discussed to illustrate the application of the approach. The intent is to provide guidelines for the use of the capacitance technique.

Background

A variety of methods have been employed to investigate the oil film thickness in internal combustion engines utilizing both electrical and optical methods ([4]). Optical methods which rely on laser-induced fluorescence of the oil, with or without dye added to the oil, allow the behavior of the oil to be studied over the entire engine stroke. Excellent spatial resolution can be achieved through the use of fiber optics, and photomultiplier tubes provide excellent temporal resolution for the optical methods. However, the accurate calibration of the fluorescence technique is difficult due to the dependence of the optical properties of the fluorescent components on temperature. The most promising method for overcoming this effect is the direct calibration of the fluorescence data with a simultaneous, independent measure of the oil film thickness made using the capacitance technique ([5]).

The electrical techniques which have been employed are: measurement of the electrical resistance of the oil film, measurement of the inductance change of a coil as the metallic piston ring passes in front of the coil, and measurement of the capacitance formed between a probe surface and the piston ring with oil serving as the dielectric material ([4]). All of these techniques have been implemented by mounting the transducers in the liner to directly measure the ring-wall distance, and in the ring gap to measure the changes in the ring circumference from which the ring-wall distance can be inferred.

Contributed by the Internal Combustion Engine Division of THE AMERICAN SOCIETY OF MECHANICAL ENGINEERS for publication in the ASME JOURNAL OF ENGINEERING FOR GAS TURBINES AND POWER. Manuscript received by the ICE Division Aug. 2000; final revision received by the ASME Headquarters Dec. 2000. Editor: D. N. Assanis.

The resistance method has been found to be ineffective for ring-wall measurements because of frequent short-circuiting of the ring and liner. The primary advantage of the inductance method is that it is insensitive to the presence, or lack, of oil in the ring-wall gap. To limit the temperature dependence observed when using a single coil, dual coil mutual inductance probes are preferred. Still, temperature dependence can occur under engine operating conditions. Additionally, the spatial resolution of inductance probes is poor (approx. 1 mm). Finally, inductance probes are sensitive to magnetic run-out, a measurement error caused by nonuniform magnetism in magnetic target materials. This nonuniformity causes large variances in the permittivity of the magnetic field into the target surface and contributes noise to the output signal. The remainder of the discussion focuses on the capacitance method.

Fundamentals of Capacitance

When two electrodes separated by an insulator have different electric potentials, charge is stored on the surface of both electrodes and capacitance forms. The capacitance is given by Eq. (1).

$$C = \frac{\Sigma q}{\Delta V} \tag{1}$$

where Σq is the total charge on one of the electrode's surfaces, and ΔV is the potential difference. The system made of the electrodes (plates) and insulator (dielectric) is called a capacitor. For two infinite parallel plates, the capacitance can be calculated using the following analytical expression often referred to as the parallel plate formula

$$C = \frac{\varepsilon A}{d} \tag{2}$$

which shows that the capacitance, C, is directly proportional to both the permeability, ε, of the insulator, and the area of the plate, A, while inversely proportional to the separation distance, d, between the plates.

In an engine, a capacitor can be formed between the piston ring and an electrode installed flush with, but electrically insulated from, the cylinder liner. When the ring passes in front of the electrode, the capacitance generated between the electrode and piston ring can be used to calculate the separation distance using the parallel plate equation. It is assumed that the piston ring is grounded, the electrode is insulated from the grounded engine block, and the region between the liner and the ring is fully flooded, i.e., the gap between the ring and the wall is filled completely with oil.

The assumption that the piston ring is grounded is valid even if there is no electrical contact between the ring and the grounded piston. This is true because the area of the ring facing the piston is substantially larger than the area of the probe facing the ring. The total capacitance, C_{tot}, between the electrode and the grounded piston is the sum of the capacitors in series,

$$\frac{1}{C_{\text{tot}}} = \frac{1}{C_{\text{probe-ring}}} + \frac{1}{C_{\text{ring-piston}}}. \tag{3}$$

Using the parallel plate equation, the capacitance between the ring and piston will be much greater than the capacitance between the probe and the ring, and thus can be neglected in Eq. (3). Furthermore, if the piston is assumed not to be electrically grounded, the same philosophy can be used between the piston and connecting rod. By continuing this thought process, it becomes apparent that the piston, connecting rod, crankshaft, and block may all be considered to be at a ground potential.

Since in firing engines the piston rings operate under starved (not fully flooded) conditions ([6]), the dielectric medium between the probe face and the ring may be comprised of oil, air, or a combination thereof. The dielectric constant of the oil varies for the particular type of oil used and should be measured, but on average the dielectric constant of oil and air differ by a factor of about 2.1. Separation of the oil from the ring face is not likely with the favorable pressure gradient present in the convergent section of the ring-wall gap. Therefore, at the end of the convergent section where the minimum oil film thickness occurs, fully flooded conditions should prevail, and the dielectric constant of the pure oil can be used with a high level of confidence. Hence, the capacitance technique is only capable of accurately measuring the minimum oil film thickness, and is not suitable for characterizing the ring shape in the running engine.

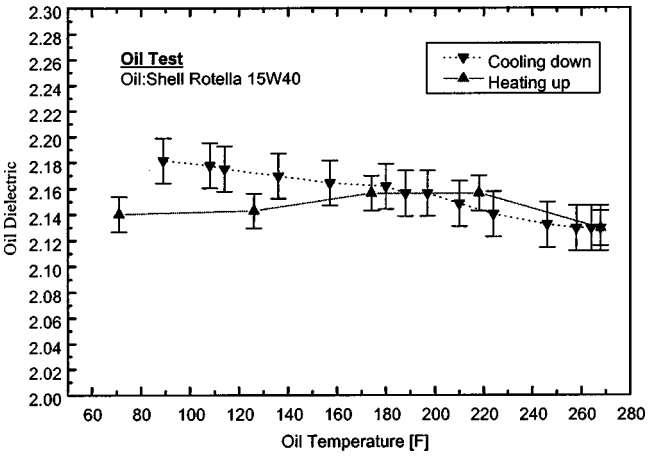

Fig. 1 Variation of oil dielectric constant with oil temperature

Another factor related to the dielectric material is the possibility that the dielectric constant can be a function of other properties, especially temperature. Tests in our laboratory have indicated that the dielectric constant of engine oil is independent of temperature up to a temperature of 150°C ([7]), see Fig. 1. To measure the oil dielectric versus temperature great care was taken to ensure the test set-up was insensitive to thermal expansion effects, vapor bubbles, and nonuniform heating of the oil. Ceramic spacers were used to ensure a constant separation distance between the capacitor's electrode and the target plate. The capacitor was placed in a thermostatically controlled oil bath that was stirred to ensure a uniform temperature throughout the bath. In order to allow flow of the oil between the plates, a large plate area was used to permit a large plate separation. The plates were placed on an incline to ensure that any bubbles which formed were evacuated. At temperatures above 150°C excessive bubble formation occurred and the tests were ceased. The test apparatus was verified using air as the dielectric.

Parallel Plate Deficiencies. The parallel plate formula given by Eq. (2) provides the major functional relationships for determining distance from the measured capacitance. There are, however, several real effects, which must be accounted for in order to achieve a high level of accuracy. In this section, methods to estimate the errors that are introduced will be presented. As discussed in more detail later, these relations can be used in the design process or they can be used to retroactively correct measurements.

Fringing of the Electric Field. The parallel plate relationship was developed for infinite plates, so the fringing of the electric field at the edges of the plates was neglected. In reality, all parallel plate capacitors have finite dimensions and exhibit fringing effects. To quantify the effect of fringing, Laplace's equation was solved numerically to determine the electric field between an electrode and the target ([8]). Figure 2 shows lines of constant potential calculated for a probe with a rectangular electrode which is insulated from the grounded cylinder liner. The fringing effect can be observed as the curvature of the constant potential lines near the edge of the electrode plate.

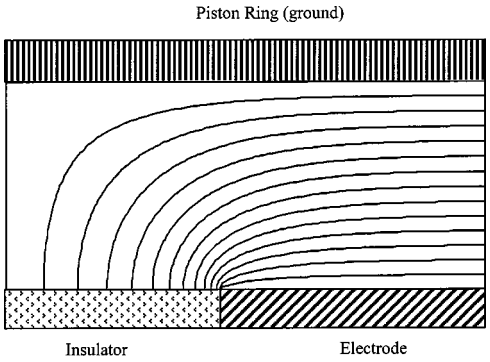

Fig. 2 Constant potential lines between the capacitance probe electrode and the piston ring (due to symmetry, only the half left of the probe's axis of symmetry is shown)

Integrating the charge on the electrode surface provides the actual capacitance of this system, from which a distance can be calculated using the parallel plate equation. Figure 3 shows the effect of fringing for two rectangular probes of width 63.5 and 127 μm, respectively. As demonstrated in this figure, fringing causes the film thickness to be underpredicted. Furthermore, the error associated with fringing increases as the probe area decreases or the film thickness increases. In order to maintain less than one percent error due to fringing effects, the ratio of the plate diameter or minimum side to the separation distance should be larger than 130.

The most effective means of reducing the effects of fringing is to completely surround the electrode by a shield driven at the same potential as that of the probe. Fringing of the electric field would then occur mainly over the shielded section, leaving the center electrode unaffected by fringing. Shielding will be discussed in more detail in a subsequent section.

Plate Effects. A fundamental assumption of Eq. (2) is that the ring face is perfectly parallel to the electrode surface. In reality, there are a variety of factors which cause the geometry to be nonparallel in the engine. These factors can be grouped into three major categories as shown in Figs. 4(*a*) to (*c*); the curvature which is defined by the average shape of the ring profile; the surface roughness of the ring profile; and the angular misalignment caused by ring twist, piston secondary motion, ring motion, and the ring profile. These effects have been modeled as a parabolic ring profile, a flat plate with surface roughness, and a nonparallel flat plate, respectively.

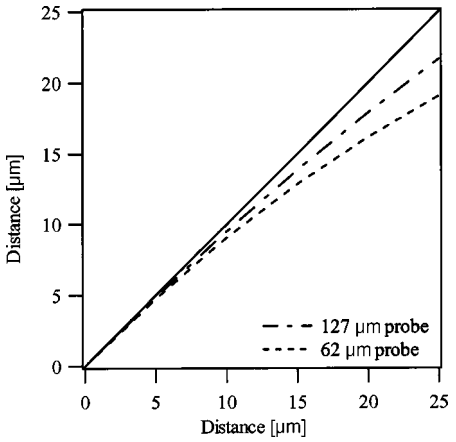

Fig. 3 Error in the parallel plate equation due to neglecting fringing effects for rectangular probes of 62 and 127-μm width

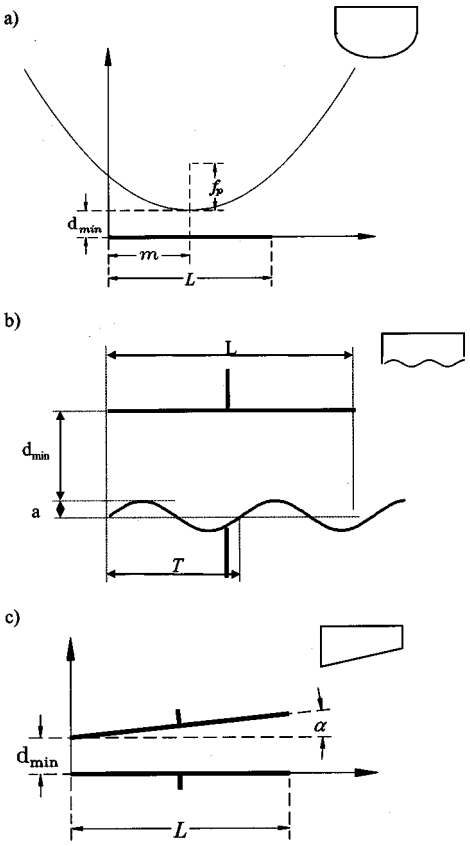

Fig. 4 Geometry used to investigate plate effects, (*a*) ring profile curvature, (*b*) surface roughness, (*c*) nonparallel plates

Analytical relations have been developed to approximate the measured capacitance, C_{meas}, for each of the previous effects. Furthermore, the relative error, δ, associated with applying the parallel plate equation to these nonparallel geometries was determined from

$$\delta = \frac{d_{meas}}{d} \tag{4}$$

where d is the characteristic separation distance which will be defined separately for each correction technique, and d_{meas} is the distance calculated from the capacitance, C_{meas}, by applying the parallel plate formula. All equations shown were derived using Cartesian coordinates for a rectangular probe having the length, L, and width, W, where $W > L$. These equations were developed by piecewise integration of the parallel plate equation along the probe's length with the assumption that the fringing of the electric field at the edges of the probe can be neglected. See Appendix A for details. To retain the dimensionless form of the results, the capacitance will be reported as

$$\tilde{C} = \frac{C_{meas}}{C_{ideal}} = \frac{C_{meas}}{\dfrac{\varepsilon(WL)}{d}}. \tag{5}$$

Additionally, the finite difference program used to evaluate the fringing was also applied to analyze the plate effects. These results are included in Figs. 5–7 as open symbols and, in general, verify the analytically derived solutions.

Correction for Ring Profile Curvature. The shape of the barrel ring face is modeled as a parabola with focal length, f_p. The

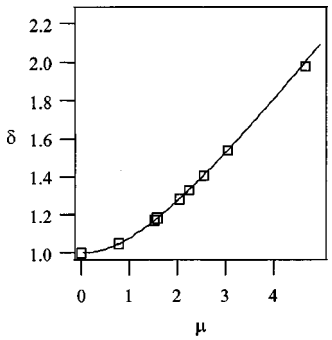

Fig. 5 Relative error due to ring profile curvature, β=0.5. Solid line (Eq. (7)), open symbols derived from numerical solution.

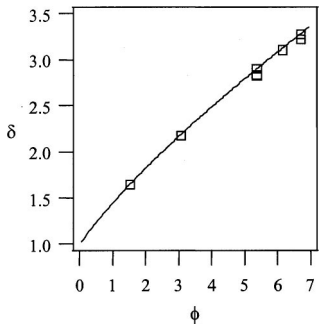

Fig. 7 Relative error due to a nonparallel geometry. Solid line, Eq. (18), open symbols derived from numerical solution.

characteristic separation distance is the minimum separation distance $d_{\min}$. The x-coordinate of the parabola focal point is given by m as seen in Fig. 4(a).

As the parabolic ring slides in front of the flat probe, the system's capacitance changes. The effect of ring curvature is isolated when the center of the probe aligns with the ring focal point, or when m is half the plate length L. At other times the curvature is superimposed on a nonparallel geometry. The equations for the capacitance and relative error are

$$\tilde{C}=\frac{1}{\mu}[\tan^{-1}(\mu-\mu\beta)-\tan^{-1}(-\mu\beta)] \tag{6}$$

$$\delta=\frac{\mu}{\tan^{-1}(\mu-\mu\beta)-\tan^{-1}(-\mu\beta)} \tag{7}$$

where

$$\mu\equiv\frac{L}{2\sqrt{d_{\min}f_p}}(\text{dimensionless}) \tag{8}$$

$$\beta\equiv\frac{m}{L}(\text{dimensionless}). \tag{9}$$

Figure 5 shows the effect of the profile curvature at the position where β equals 0.5, or when the probe is centered with the barrel shaped ring. The error is seen to increase as the value of μ increases, where μ is inversely related to the radius of curvature (the focal length of the parabola). As expected, at large curvatures the ring looks like a flat plate, and the parallel plate formula is recovered. In general, small errors are obtained with small probes and large separation distances and radii of curvature. There is excellent agreement between the finite difference solution (symbols) and the analytical solution (solid curve).

A one percent error corresponds to a μ value of 0.35 (and β equal to 0.5). For a typical barrel-faced top ring with a width of 3 mm and a 15-μm peak in the face profile, the parabola focal length is 32,700 μm. For a probe length L of 125 μm, typical of those used in our lab, errors larger than one percent are achieved for distances less than 1 μm. As the ring profile wears and the ring face become flatter, this distance will decrease. The rails of the oil control ring will have a smaller radius of curvature, which will cause higher levels of curvature-induced error in the capacitance measurements of the film thickness. Significant errors can also result from large probes located near top dead center where the film thickness is expected to be minimal.

The capacitance probes should be flush with the cylinder liner. However, with inadequate polishing or honing techniques, the probe surface may exhibit a curvature. If this is the case, the parallel plate equation should also be corrected for the probe's profile in the same way in which the barrel profile was corrected. As an example, a finished rectangular capacitance probe in our engine exhibited a parabolic profile with a 324-μm focal length (corresponding to just a 3-μm maximum height above the liner). This poorly finished probe had a resulting μ value of 1.55 for a 5-μm thick film, corresponding to an error of 17.5 percent.

Surface Roughness Correction. The surface roughness was modeled as a one-dimensional sinusoidal surface with an amplitude, a, and period, T, as shown in Fig. 4(b). The sine wave is shown in the L direction in Fig. 4(b), but its orientation can be rotated 90 deg, so that it is aligned with the W direction, with no loss of generality. The results shown need only be modified by substituting the variables W and L for each other. The characteristic distance is the average distance, $d_{\text{ave}}=a+d_{\min}$. The one-dimensional geometry is assumed since the general two-dimensional rough ring case does not lend itself to a simple analytical solution. As a first approximation the two-dimensional effect can be estimated using the square of the one-dimensional results, δ^2, although this is only an approximation due to the nonlinearity of the process.

The equations derived for the capacitance and relative error are

$$\tilde{C}=\frac{1}{\omega\pi\sqrt{1-\lambda^2}}\left\{n\pi+\tan^{-1}\left[\sqrt{\frac{1-\lambda}{1+\lambda}}\tan(\omega\pi)\right]\right\} \tag{10}$$

$$\delta=\omega\pi\sqrt{1-\lambda^2}\frac{1}{\left\{n\pi+\tan^{-1}\left[\sqrt{\frac{1-\lambda}{1+\lambda}}\tan(\omega\pi)\right]\right\}} \tag{11}$$

where

$$\omega\equiv\frac{L}{T};\quad \omega\neq\frac{(2k-1)}{2},\quad k=1,2,3,\ldots\quad(\text{dimensionless}) \tag{12}$$

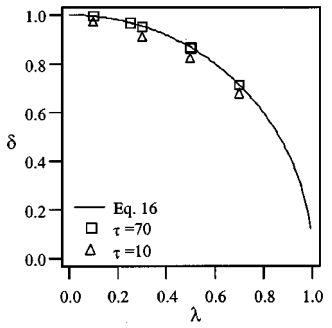

Fig. 6 Relative error due to ring roughness. Solid line, Eq. (16), open symbols derived from numerical solution.

$$\lambda \equiv \frac{a}{d_{\text{ave}}} \leqslant 1 \quad \text{(dimensionless)} \tag{13}$$

$$n \equiv 1 + \text{int}\left(\frac{L}{T} - 0.5\right) = 1 + \text{int}(\omega - 0.5). \tag{14}$$

When the value of ω is not an integer, fractional orders of the sinusoidal profile are observed by the probe and anomalous results are obtained. However, the rectangular probe geometry is typically chosen so that L is small (for high spatial resolution), and W is large (for sufficient signal strength). Even if fractional periods of the asperities are observed in the L direction, the probe will be integrating over a large number of asperities in the W direction. Therefore, as a first approximation, the two-dimensional probe can be modeled by choosing the larger of W or L as the principle sinusoidal axis, i.e., ω is large. Under this assumption, Eqs. (10) and (11) can be simplified since the bracketed terms account for the effect of integrating over a fractional period and for a large number of periods, n, the fraction of a period remaining has a small effect on the total capacitance. This is also equivalent to having an integral value of ω (all integral values of ω give the same result). Under these assumptions, Eqs. (10) and (11) become

$$\tilde{C} = \frac{1}{\sqrt{1-\lambda^2}} \tag{15}$$

$$\delta = \sqrt{1-\lambda^2}. \tag{16}$$

The effect of the surface roughness can be observed in Fig. 6 for the one-dimensional case described above. As the relative surface roughness λ increases, the measured capacitance will under predict the film thickness. This is due to the nonlinear inverse dependence of the capacitance on distance, which biases the measurement towards the smaller distances. The finite difference results (open symbols in Fig. 6) indicated that another dimensionless parameter, $\tau \equiv T/a$, affects the results. This parameter is a measure of the curvature of the sinusoidal surface, where small values indicate high levels of curvature. Since Eq. (16) was derived using the parallel plate equation, deviations between the finite difference and analytical solutions are observed at the lower values of τ. At high values of τ excellent agreement is observed between the finite difference and analytical solutions for all values of λ. In light of the other assumptions in the roughness analysis, Eq. (16) is considered to provide a sufficient representation of the roughness effects. It should be noted that for small probes (those with *both* dimensions on the order of the period of the roughness) fractional orders will be observed by the probe and random errors will be introduced to the measurements since the phasing of the roughness will vary from cycle to cycle.

From Fig. 6, a one percent error is obtained for a value $\lambda = 0.14$. For a ring with an amplitude, a, of 0.2 μm, greater than one percent errors will occur for separation distances less than 1.4 μm. Corrections to the measured values can be obtained from Fig. 6 provided that the ring roughness is known. Again, as the rings wear these errors will decrease. It is recommended to measure the roughness any time the cylinder kit is removed.

Correction for Nonparallel Flat Plates. The effect of nonparallel surfaces was modeled as a tilted pad as shown in Fig. 4(*c*). The characteristic distance is the minimum separation distance d_{min}.

The equations for the capacitance and relative error are

$$\tilde{C} = \frac{\ln(1+\phi)}{\phi} \tag{17}$$

$$\delta = \frac{\phi}{\ln(1+\phi)} \tag{18}$$

where

$$\phi \equiv \frac{L \tan(\alpha)}{d_{\text{min}}} \text{(dimensionless)}. \tag{19}$$

The angle between ring face and the probe, α, is required. The taper angle should be measured rather than taken from the print where possible. Additionally, the twist angle of the ring and the tilt angle of the piston can be determined computationally.

The resulting error from the tilted plate geometry is shown in Fig. 7 for both the analytical expression and the finite difference result. Excellent agreement is observed between the two methods. As the value of ϕ increases, the minimum separation distance is overpredicted. This is due to the fact that the mean plate separation distance is greater than the minimum distance, reducing the capacitance. A one percent error corresponds to a ϕ value of 0.02. If a probe of length $L = 125$ μm were used with a minimum separation distance of 5 μm, this would be just a 0.046 deg allowable tilt angle. For larger values, higher errors in the minimum distance will occur. Typical heavy-duty engines feature second rings with a taper angle of approximately 15 deg. For the probe geometry and separation distance just described, the value of ϕ is 6.7 and an error of 320 percent is incurred in the minimum film thickness.

Electronics

The goal of the electronic circuitry is to generate a voltage signal which is directly proportional to film thickness. Thus, a signal proportional to capacitive reactance, X_c

$$X_c = \frac{1}{2\pi f C_{\text{meas}}} \tag{20}$$

is desired because reactance is inversely proportional to capacitance and hence, directly proportional to film thickness. Such a signal can be generated by measuring the impedance of the capacitance probe, since the resistance of the oil film is much larger than the capacitive reactance.

Two circuit techniques which allow the reactance to be measured are frequency modulation and amplitude modulation. With frequency modulation, a carrier signal's frequency changes with the capacitance of the probe. This frequency is then converted, or demodulated, into a voltage signal. For amplitude modulation, a carrier signal's amplitude changes with the capacitance of the probe. The RMS value of the amplitude is then converted to a voltage signal. Frequency demodulation is less susceptible to noise than amplitude modulation, but it has other drawbacks.

Frequency modulation is accomplished by measuring the change in the resonance frequency of an RC-type oscillator formed with the capacitance probe. The dynamic range of these systems is limited, and the circuits are unstable when shorted. Amplitude modulation is accomplished by one of three circuit designs: AC current source applied directly to the probe, AC voltage source applied to a series RC circuit, and AC voltage source applied to a series RLC circuit. Details of the measurement characteristics of each design are provided in Appendix B. An AC voltage source circuit operating between 100 kHz and 1 MHz was used in this work, but an AC current source is recommended due to its excellent linearity.

Shielding. As discussed previously, the use of a conductive shield surrounding the sensing electrode, and driven at the same potential as the electrode, can eliminate the effect of fringing on the sensor. In addition, the lack of a voltage gradient between the shield and the electrode also serves to completely eliminate the static capacitance of the probe and susceptibility to extraneous capacitive noise from the environment. Static capacitance formed between the electrode and environment, and not associated with the target surface, causes all of the previously mentioned circuits to be nonlinear with respect to film thickness. Furthermore, a static capacitance will decrease the dynamic range of the measurement. The shield must be driven with the modulated signal com-

ing from the electrode of the capacitance probe. To drive the shield, an Op-Amp with a very low input capacitance configured for unity gain should be used.

There are two important details for shield design: the probe should be completely surrounded with the shield, and the shield should be placed as close as possible to the center electrode. However, it has been our experience that if the shield is placed too close to the electrode or the liner the shield may short circuit to either the probe or liner when honed, or when wear occurs during engine operation. With this constraint, a distance of 75 μm should be allowed between shield and center of the probe.

Probe Design

Probe Shape. To maximize spatial resolution, the probe size should be as small as possible. However, small probes yield small capacitance values which limits the measurement range. An optimal probe would be rectangular with a large aspect ratio, having the smaller length in the direction where high spatial resolution is required, and the length in the transverse direction chosen to maximize total plate surface area. For equivalent plate areas, a circular probe will be less affected by fringing than a rectangular probe; however, with proper shielding techniques, the effect of fringing will be negligible. Fully shielded circular probes are easier to construct than fully shielded rectangular probes.

Rectangular probes with the shorter length parallel to the axis of the liner have been utilized in this study. This results in higher spatial resolution in the direction of the ring profile, and minimizes the effect of curvature. In addition, the rectangular probe is relatively insensitive to the error caused by the end-gap of the ring moving in front of the probe, due to its increased length perpendicular to the axis of the liner. The length of the probe in the circumferential direction is, however, limited by the desired resolution. Overly long probes will include the effect of bore distortion in the measurements. Therefore, the width of the probe should be limited to the minimum length which provides sufficient signal strength.

Design Procedure. Based on the analysis presented in the Plate Effects Section, a design procedure for rectangular capacitance probes is proposed. The procedure is shown graphically in Fig. 8. Initially, the desired error is selected and the expected separation distance is estimated. As the roughness analysis is independent of probe dimensions, it should be used as a correction factor for post-processing data rather than for sizing the probe. Since the probe location on the liner is an important factor for estimating the film thickness, it may be possible to select an alternative location for the probe based on the calculated roughness parameter λ, to obtain the desired error. The correction equations for ring profile curvature and tilt should then be applied to deter-

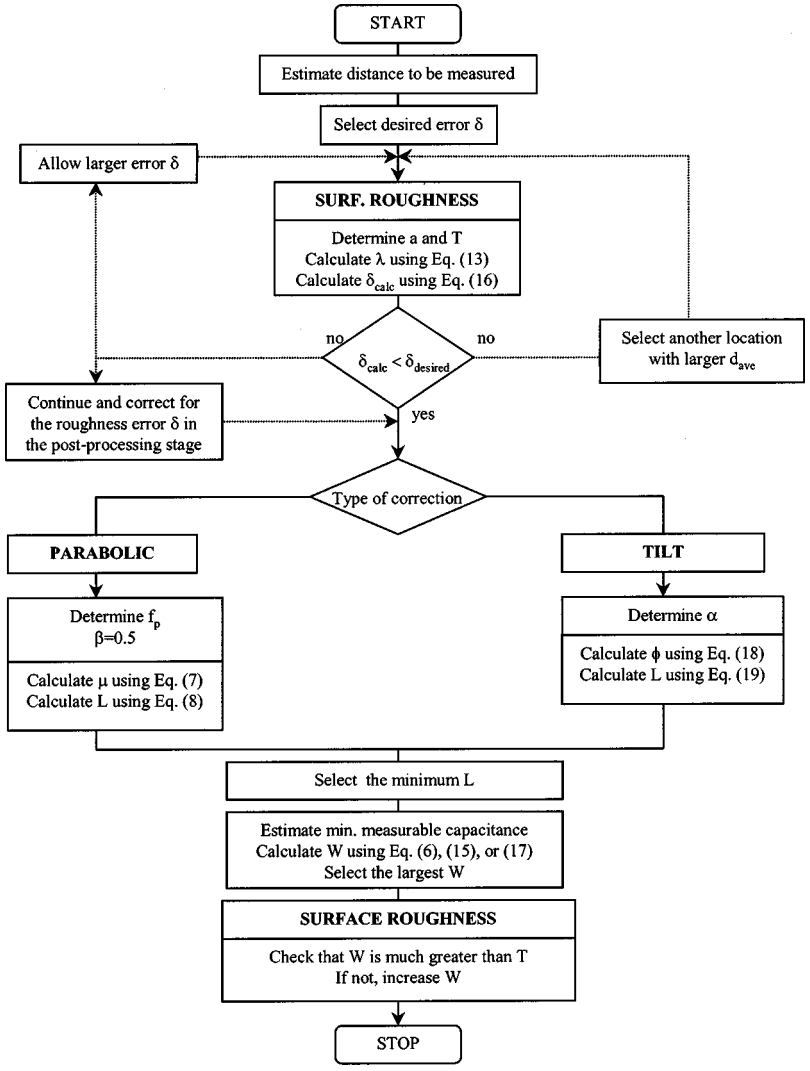

Fig. 8 Procedure for designing a rectangular capacitance probe

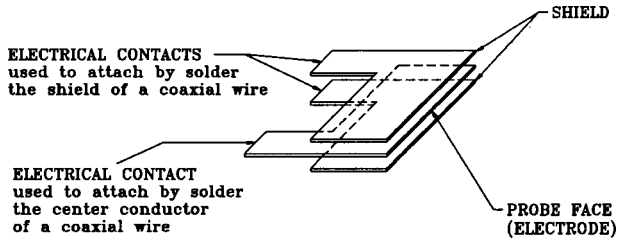

Fig. 9 Rectangular capacitance probe

mine the required minimum probe length, *L*. The minimum capacitance measurable by the electronic circuitry then defines the probe width, *W*.

Construction. To simplify the design and fabrication of the rectangular capacitance probes, the sides of the electrodes used in this study were not shielded. In doing this, rectangular probes can be manufactured by simply stacking thin pieces of sheet metal separated by an insulator, as shown in Fig. 9. Because the sides of the electrodes were not shielded, a static capacitance of approximately 10 to 15 pF was generated by the probe and will be discussed in regard to the calibration of the circuit.

Several different methods have been used to construct the rectangular probes using the plate geometry shown in Fig. 9. The first technique used a jig to hold the thin pieces of sheet metal parallel to each other and separated by the desired distance. The spaces were then filled with a high temperature epoxy which served structural and electrical purposes. The second technique was introduced to keep the plates as parallel as possible. Thin layers of mica were stacked between the thin pieces of sheet metal. The mica ensured the plates would be insulated from each other and would be parallel. High temperature epoxy was used to seal the probe. The third technique was introduced because there was a concern the probe would lose integrity due to the mica delaminating. Slits were machined in a single piece of Celazole® (a high temperature polymer) in which the thin pieces of sheet metal were inserted. High temperature epoxy was then applied around the probe to hold it together. Because delamination of the mica never occurred, and because the machining of the Celazole® was complex, the second technique, using mica, was determined to be superior.

Installation. To install the rectangular capacitance probes in the liner, rectangular slots were machined into the liner using an electro-discharge machine (EDM). The assembled capacitance probes and slots were coated with a high temperature epoxy, and the probes were installed with their faces protruding into the interior of the liner. After the epoxy was allowed to cure, the probes were polished flush with the liner inner surface.

To polish the probes, 25-μm-thick steel shim stock was used to mask the liner surface surrounding the probe. The shim stock was held in place with masking tape. 400 grit sandpaper was wrapped around a steel bar 2.5-cm diameter by 3-cm long, and was used to sand down the probe. The shim stock provided a stop for the sanding process. After the sanding was repeated with 600 grit sandpaper, the shim stock was removed, and the remaining 25 microns was carefully polished down to approximately 6 microns using small pieces of sand paper wrapped around the blunt end of a small wooden dowel in a dental mill. Finally, to make the probes flush with the liner surface, the liner was honed. Further details can be found in reference [9].

Calibration

There are two methods through which the capacitance probes mounted in the liner can be calibrated.

Direct Calibration. In the direct calibration method, the voltage output from the circuit versus separation distance to a target is measured using a test rig or a micrometer. Extreme care must be taken in fabricating the experimental setup so that offset errors and plate tilt effects are avoided. Additionally, it is difficult to obtain sufficient resolution of the calibration in the range of interest (0–10 μm) for ring-wall measurements. Further, if the target is not an actual ring, corrections must be made a posteriori for the barrel profile and surface roughness. For the stated reasons a direct calibration was not performed.

Indirect Calibration. In the indirect calibration method, first the voltage output from the circuit is measured using various fixed capacitors inserted in parallel with the capacitance probe. Then, the parallel plate equation, and appropriate corrections for fringing and real geometry are used to determine the distance from the measured capacitance. The values of the fixed capacitors should be measured before the indirect calibration method is applied. These capacitance values are difficult to measure because of their small magnitudes. To obtain accurate values for these capacitors, three different measurement devices were used, the measurements were repeated, and a statistical mean was determined.

Static Capacitance. If the probe is inadequately shielded, a static capacitance will act in parallel with the desired capacitance developed between the ring and the probe. The total capacitance measured with the probe will be the sum of these capacitances, and therefore, capacitive reactance and film thickness will no longer have a linear relationship. The equations developed in the Appendix B must be adjusted accordingly to account for this nonlinear relationship.

The effect of static capacitance drift with operating temperature, and hence clearance distance, has been determined to be very small if the probe is completely shielded. The measured drift for the partially shielded probe shown in Fig. 9 was less than 1 pF. However, if the quality of the capacitance probes and the shielded circuit are less than ideal, drift can occur when the engine warms up.

For an RC or RLC circuit, when nothing is placed in front of the probe, the output voltage corresponding to the static capacitance can be measured. The effect of the static capacitance change with ambient temperature can be quantified by measuring the output voltage with the engine hot and at room temperature. In both cases, the rings, piston, or skirt should not face the probe. Using this voltage difference, an effective distance corresponding to the static capacitance change can be calculated. When the calibration equations are applied, all distances should be offset from this effective distance.

Experimental Data

In this section, the methodology presented in this paper is used to calibrate a capacitance probe signal. For this example, the rectangular probe shown in Fig. 9 was used, and was driven with an RC-type circuit. This circuit and probe were used to measure film thickness on the liner of a Cummins L-10 diesel engine [7,8]. Sample data will be provided for a single operating condition, 1300 rpm and 40 percent load, for a probe located 120 deg ATDC relative to the top compression ring, or 123 mm from the top of the cylinder liner to demonstrate the measurement procedure. The engine had a single-piece aluminum piston with a dual Ni-resist insert in the ring groove region. The ring pack consisted of a no-twist barrel-faced top ring, a positive twist scraper ring, and a two piece oil control ring. Shell Rotella 15W40 oil was used.

First, an indirect calibration was performed on the circuit. The results of this calibration are shown in Fig. 10. Since the rectangular probe used with this circuit was partially unshielded, a static capacitance was present and acted in parallel with the added capacitance used in the calibration of the circuit. The fit equation is the result of a voltage divider applied to the RC circuit with a static capacitance in parallel with the probe and adjustable offset and gain. Note that the voltage output corresponding to just the static capacitance was −4.55 VDC.

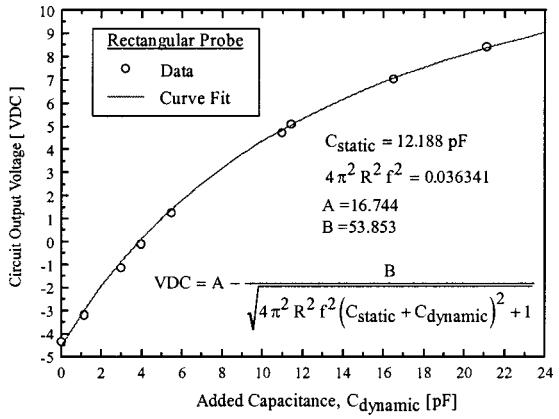

Fig. 10 Calibration of the RC voltage source circuit

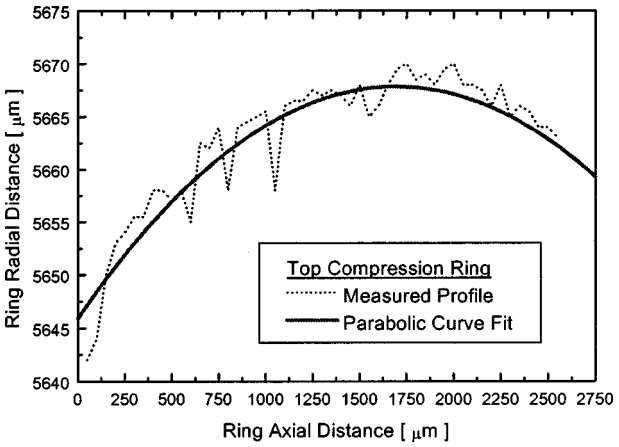

Fig. 12 Measured surface profile of the top compression ring

After completing the circuit calibration, data from the engine were then obtained. An example of the raw voltage output from the firing engine is shown in the upper half of Fig. 11. Notice that when no rings were in front of the probe, the measured voltage was −3.82 VDC. This voltage corresponds to the static capacitance when the engine is warmed up. Using this voltage, a new static capacitance of 12.696 pF was calculated by backtracking through the circuit calibration shown in Fig. 10. With this particular probe, the static capacitance drift between when the engine was cold and when the engine was warmed up, was only 0.51 pF.

With the circuit calibration adjusted for the new static capacitance caused by the elevated temperatures of the running engine, the dynamic capacitance caused by the piston rings moving past the probe could now be calculated. Shown in the lower half of Fig. 11, is the film thickness calculated by applying the parallel plate equation. Since the extent to which the ring is wetted by oil is unknown, the minimum film thickness measurements are the most reliable. The minimum film thickness for the top ring was 1.22 μm.

To correct the minimum film thickness measurements for the barrel shape of the top compression ring, the ring profile was measured, as shown in Fig. 12, using a profilometer. A parabolic curve fit through the profile using a least-squares regression technique was used to determine a focal length of 32,700 μm. Using the dimensions of the rectangular probe (center electrode, 127 μm by 7620 μm), the dimensionless number, μ, equal to 0.318 was determined. The error ratio, δ, corresponding to this calculation was only 1.008 (assuming $\beta = 0.5$). The corrected minimum oil film thickness was 1.21 μm.

Finally, to correct the minimum film thickness measurements for the surface roughness of the top compression ring, the measured ring profile displayed in Fig. 12 was estimated to have a roughness amplitude of 1.5 μm. This amplitude was much larger than typical values because the rings had a special lapped finish. Equation (16) was solved to determine an error ratio, δ, equal to 0.63 at λ equal to 0.78 (assuming $d_{meas} = 1.21\ \mu$m). The determined average minimum oil film thickness was 1.93 μm.

In the case of the second ring, calculations were performed for the narrow face of the tapered ring, which features a shallow parabolic profile with 14,633 μm focal length. The voltage measured at the minimum separation distance was 1.4 VDC, which corresponds to a capacitance of 5.5 pF, according to the circuit calibration curve associated with the appropriate probe. Assuming the minimum separation gap is completely filled with oil at less than 150°C, the parallel plate equation and correction for field fringing yields a minimum distance of 4.12 μm. Measurements of the ring face indicated a surface roughness which can be approximated with a sine curve having the amplitude and period of 0.5 μm and 77 μm, respectively. The correction for roughness is carried out using the Eq. (16), where the dimensionless coefficient, λ, is 0.1212. The error ratio, δ is 0.9926, and the corrected minimum oil film thickness is 4.15 μm.

Finally, to correct the minimum oil film thickness measurements for the narrow face parabolic profile, the dimensionless parameter μ of 0.25768 is used in Eq. (7) to calculate the error ratio δ of 1.0055. The determined average minimum oil film thickness under the second ring is 4.13 μm.

During this work, a fixed geometry capacitor was used to measure the oil dielectric, ε. In this fashion, changes in ε due to oil contamination were monitored in real time and results fed into calculations. The location of the monitoring capacitor is not influenced by oil temperature as long as its value is below 150°C ([7]).

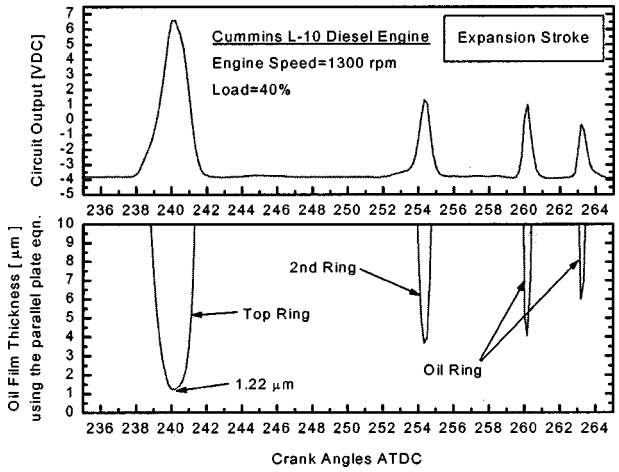

Fig. 11 Capacitance probe data, upper graph raw voltage data, lower graph, uncorrected oil film thickness

Summary

The capacitance technique provides an accurate means of measuring the minimum oil film thickness under the piston ring in a firing internal combustion engine. However, to perform measurements with a high level of accuracy the probes must be designed and installed correctly, and the detection circuitry must be properly matched to the probe. Potential biases and noise sources in the measurements are the static capacitance of the probe, fringing of the electric field, ring profile curvature, ring surface roughness, nonparallel geometry and probe mounting offsets.

The effects of static capacitance and fringing can be eliminated by completely shielding probes, i.e., surrounding the sensing elec-

trode with a metal shield which is driven at the same potential as that electrode. If complete shielding can not be accomplished, a nonlinear relationship between film thickness and capacitive reactance will exist, and the effects of the static capacitance drift must be accounted for. Furthermore, the static capacitance will significantly decrease circuit sensitivity.

The effects of ring profile curvature, surface roughness and a nonparallel geometry have been modeled and the errors that are incurred have been assessed. Analytical estimates of the errors have been derived and compared favorably to finite difference models for each geometry investigated. The effect of ring profile curvature is to overpredict the minimum film thickness, with large errors associated with large probe sizes, small ring-liner distances, and small radii of curvature. The effect of ring surface roughness is to underpredict the average ring-liner separation distance for large probes (defined as having a large ratio of the largest probe dimension to the period of the roughness). Probes for which the largest dimension is of the same order as the period of the disturbance will produce anomalous results and should be avoided. The effect of a nonparallel geometry is to overpredict the minimum ring-liner distance. The error increases with increased probe size, an increased angle between the plates and decreased ring-liner distance.

A design procedure has been developed to determine the required probe dimensions for an allowable level of error. If an acceptable design can not be established, the above models can be used to correct the measured capacitance for the nonideal effects. In our experience a rectangular probe shape has proven to be optimal. A high aspect ratio is chosen with the smaller dimension normal to the engine cylinder axis. The small dimension in the direction of the ring profile affords high spatial resolution while not incurring large errors due to ring profile curvature or nonparallel effects. The large dimension in the circumferential direction provides a large area to enhance the signal strength, while reducing the uncertainties associated with ring roughness.

Circuits employing amplitude modulation are preferred over those using frequency modulation due to their superior characteristics. For optimal linearity, an AC current source-type circuit should be used with amplitude modulation.

The use of a fixed geometry capacitor to monitor oil dielectric constant is recommended.

Acknowledgments

The authors would like to acknowledge the many useful discussions with Emeritus Prof. G. L. Borman and the assistance of Dr. M. Allie of Cummins Engine Co. and Emeritus Prof. R. Greiner in the analysis of the electronic circuits. Support for this work was provided by the Army Research Office under Grant Nos. DAAH04-94-G-0328 and DAAHL03-92-0122, and the Cummins Engine Company.

Appendix A

Development of Analytical Capacitance Equations. The capacitance of a capacitor with the plate area $W\,dx$ and separation distance $y(x)$ can be expressed using the parallel plate formula, with the assumption that the fringing of the electric field at the edges of the probe can be neglected. This differential area produces a capacitance

$$dC=\frac{\varepsilon W dx}{y(x)}. \tag{A1}$$

The total capacitance of a capacitor of a given geometry can be found by integrating over the entire sensor face

$$C=\int\int_{\text{Area}} dC=\int_0^L \frac{\varepsilon W dx}{y(x)}. \tag{A2}$$

The separation distance $y(x)$ depends on the particular geometry. The distance function and resulting integral are shown below for the three geometries investigated. The results are left in their dimensional form.

Surface Roughness

$$y(x)=d_{\text{ave}}+a\cos\left(\frac{2\pi x}{T}\right) \quad \text{with} \quad d_{\text{ave}}>a \tag{A3}$$

$$C=\int_0^L \frac{\varepsilon W dx}{d_{\text{ave}}+a\cos\left(\frac{2\pi}{T}x\right)} = \frac{\varepsilon WL}{d}\frac{T}{\pi L\sqrt{1-\lambda^2}}\left\{n\pi+\tan^{-1}\left[\sqrt{\frac{1-\lambda}{1+\lambda}}\tan\left(\pi\frac{L}{T}\right)\right]\right\} \tag{A4}$$

where

$$\lambda=\frac{a}{d_{\text{ave}}}<1; \quad n=\text{int}\left(\frac{aL}{2\pi}\right)$$

Nonparallel Flat Plates

$$y(x)=d_{\min}+L\tan\alpha \tag{A5}$$

$$C=\int_0^L \frac{\varepsilon W dx}{d_{\min}+L\tan\alpha}=\frac{\varepsilon W}{\tan\alpha}\ln\left(\frac{d_{\min}+L\tan\alpha}{d_{\min}}\right) \tag{A6}$$

Ring Profile Curvature

$$y(x)=d_{\min}+\frac{(x-m)^2}{4f} \tag{A7}$$

$$C=\int_0^L \frac{\varepsilon W dx}{d_{\min}+\frac{(x-m)^2}{4f}}=\frac{2\varepsilon W}{\sqrt{\frac{d_{\min}}{f}}}\left[\tan^{-1}\left(\frac{L-m}{2\sqrt{d_{\min}f}}\right)-\tan^{-1}\left(\frac{-m}{2\sqrt{d_{\min}f}}\right)\right] \tag{A8}$$

Appendix B

Amplitude Modulation Circuit Characteristics. Amplitude modulation is accomplished by supplying a sine wave carrier to the capacitance probe. As the capacitance changes, the impedance of the probe will change, causing a voltage change in the amplitude of the carrier signal. Three circuits which can be used with amplitude modulation are an AC current source applied directly to the probe, an AC voltage source applied to a series RC circuit, and an AC voltage source applied to a series RLC circuit.

AC Current Source. For an AC current source applied directly to the probe, the voltage across the probe can be represented as follows:

$$\tilde{V}_{\text{probe}}=\frac{\tilde{I}_0}{2\pi f C_{\text{meas}}}. \tag{B1}$$

Substituting the parallel plate relationship into Eq. (*B*1) yields

$$\tilde{V}_{\text{probe}}=\left(\frac{\tilde{I}_0}{2\pi f A\varepsilon}\right)(d_{\text{meas}}) \tag{B2}$$

which shows that the output voltage is linearly proportional to the film thickness. Since a current source behaves ideally with low impedances, this circuit will be linear at small film thickness. However, at large film thickness the current source will eventually reach the limit of its compliance. Once this happens, the voltage output will be limited. This does not pose a problem, it only limits

the measurement range. The range can be extended by increasing the probe dimensions and/or carrier frequency, but only at the expense of decreased circuit sensitivity.

AC Voltage Source on an RC Circuit. For an AC voltage source applied to a series RC circuit, the voltage across the probe can be represented as follows:

$$\tilde{V}_{\text{probe}} = \frac{\tilde{V}_0}{\sqrt{\left(\frac{f}{f_c}\right)^2 + 1}}. \tag{B3}$$

This series RC circuit behaves as a first-order low-pass filter with a corner frequency, f_c

$$f_c = \frac{1}{2\pi R C_{\text{meas}}}. \tag{B4}$$

For a first-order low-pass filter, a unity gain pass band exists below the corner frequency. A stop band with a -6 dB per octave slope exists above the corner frequency starting at a frequency approximately twice the corner frequency. When the sine wave carrier frequency supplied to the circuit is greater than approximately twice the corner frequency, Eq. (*B*3) can be approximated with the following simpler equation:

$$\tilde{V}_{\text{probe}} = \left(\frac{f_c}{f}\right)\tilde{V}_0 = \frac{\tilde{V}_0}{2\pi f R C_{\text{meas}}}. \tag{B5}$$

Combining with the parallel plate relationship gives

$$\tilde{V}_{\text{probe}} = \left(\frac{\tilde{V}_0}{2\pi f R A \varepsilon}\right)(d_{\text{meas}}) \tag{B6}$$

which again demonstrates a linear relationship between the sine wave amplitude and the film thickness. This desirable linear relationship will always exist at small film thickness, because the large capacitance generated at small film thickness will force the corner frequency to be very low relative to the set modulation frequency. However, for large film thickness, the corner frequency may eventually become large enough to cause nonlinearity between the sine wave amplitude and the film thickness. Therefore, to ensure linearity to the desired film thickness, the value of series resistance and operating carrier frequency must be chosen correctly for a given capacitance probe design. Note that, as with the constant current design, the disadvantage of extending the linear range of the circuit is that the sensitivity of the circuit will decrease.

AC Voltage Source on an RLC Circuit. For an AC voltage source applied to a series RLC circuit, the voltage across the probe can be represented as

$$\tilde{V}_{\text{probe}} = \frac{\tilde{V}_0}{\sqrt{\left(1 - \left(\frac{f}{f_n}\right)^2\right)^2 + \left(\frac{f}{f_n}\right)^2\left(\frac{1}{Q}\right)^2}}. \tag{B7}$$

This series RLC circuit behaves as a second-order low-pass filter. In Eq. (*B*7), f_n is the resonant frequency,

$$f_n = \frac{1}{2\pi\sqrt{L' C_{\text{meas}}}}. \tag{B8}$$

The term Q from the Eq. (*B*7) is related to the damping coefficient, ζ, and can be represented as a function of the electrical components in the circuit as follows:

$$Q = \frac{1}{2\zeta} = \left(\frac{1}{R}\right)\sqrt{\frac{L'}{C_{\text{meas}}}}. \tag{B9}$$

If the Q term is assumed to be high, and if the frequency supplied to the circuit is greater than approximately twice the resonance frequency, Eq. (*B*7) can be approximated with the following simpler equation:

$$\tilde{V}_{\text{probe}} = \left(\frac{f_n}{f}\right)^2 \tilde{V}_0 = \frac{\tilde{V}_0}{(2\pi f)^2 L' C_{\text{meas}}}. \tag{B10}$$

Substituting the parallel plate relationship yields

$$\tilde{V}_{\text{probe}} = \left(\frac{\tilde{V}_0}{(2\pi f)^2 L' A \varepsilon}\right)(d_{\text{meas}}) \tag{B11}$$

which again shows a linear relationship between sine wave amplitude and film thickness. Therefore, there is no improvement with a second-order system relative to the first-order system. The disadvantage of this second-order system is that it is more susceptible to nonlinearity because of its second-order terms.

It is important to realize that with high carrier frequencies (e.g., on the order of 1 MHz), nonideal behavior of the first-order RC circuit may occur, thereby causing the natural inductances within the wires to become significant. This will effectively make the first-order system act as a second-order RLC circuit. To eliminate this potential problem, the carrier frequency should be kept low. However, the carrier frequency must be high enough to allow low-pass filters to reasonably attenuate the carrier signal from the modulated signal during demodulation.

Nomenclature

a = surface roughness amplitude (m)
A = plate area (m^2)
AC = alternating current
C = capacitance (farads)
$\tilde{C}$ = ratio of measured capacitance to capacitance calculated by applying the characteristic distance to the parallel plate equation (dimensionless)
C_{meas} = measured capacitance (farads), the capacitance between the electrode and the ring
d = characteristic separation distance [m] for a given plate geometry (either d_{min} or d_{ave})
d_{ave} = average separation distance (m) corrected for plate effects
d_{meas} = distance (m) calculated from C_{meas} using the parallel plate equation (no corrections for plate effects were applied)
d_{min} = minimum separation distance (m) corrected for plate effects
EDM = electro-discharge machining
f = frequency of AC signal
f_c = cutoff frequency for RC-type circuit
f_n = resonant frequency for RLC-type circuit
f_p = focal length of parabolic profile (m)
I_o = AC current source
L = length of the probe plate (measured along the engine cylinder axis) (m)
L' = inductance (henry)
m = position from the edge of the probe plate of the parabolic ring profile local minimum (m)
n = an integer coefficient (dimensionless)
Σq = total electric charge (coulomb)
Q = damping ratio for 2nd order electrical circuits
R = resistance (Ω)
RC = a circuit with a resistor and capacitor
RLC = a circuit with a resistor, inductor, and capacitor
T = surface roughness period (m) $\tilde{V}_o$ AC voltage source
$\tilde{V}_{\text{probe}}$ = AC voltage across a capacitance probe
ΔV = potential voltage difference (volts)
W = width of the probe plate (m)
X_c = capacitive reactance (Ω)

α = plate tilt angle (radians)
β = dimensionless position relative to the probe plate of the parabolic ring profile local minimum relative error, the ratio of d_{meas} to the characteristic separation distance (dimensionless)
ε = permeability, for vacuum $\varepsilon = 8.858\text{E-}6$ pF/μm (typically for oil, $\varepsilon_{oil} \cong 2.12\varepsilon_{vacuum}$)
ϕ = dimensionless number for plate tilt effects
λ = dimensionless surface roughness amplitude
μ = dimensionless numbers for the parabolic profile
ω = dimensionless length for the surface roughness correction
τ = dimensionless number for the surface roughness correction
ζ = damping coefficient (dimensionless)

References

[1] Ariga, S., ''Observations of Transient Oil Consumption with In-Cylinder Variables,'' SAE Paper 961910, 1996.

[2] Hamilton, G. M., and Moore, S. L., 1974, ''The Lubrication of Piston Rings,'' Proc. Inst. Mech. Eng., **188**, pp. 253–268.

[3] Furuhama, S., 1959, ''A Dynamic Theory of Piston-Ring Lubrication,'' Bull. JSME, **2**, p. 423.

[4] Sherrington, I., and Smith, E. H., 1985, ''Experimental Methods for Measuring the Oil-Film Thickness Between the Piston-Rings and Cylinder-Wall of Internal Combustion Engines,'' Tribol. Int., **18**, No. 6, pp. 315–320.

[5] Stiyer, M. J., and Ghandhi, J. B., 1997, ''Direct Calibration of LIF Measurements of the Oil Film Thickness Using the Capacitance Technique,'' SAE paper 972859.

[6] Moore, S. L., and Hamilton, G. M., 1978, ''The Starved Lubrication of Piston Rings in a Diesel Engine,'' Journal Mechanical Science, **20**, No. 6, pp. 345–352.

[7] Donahue, R. J., 1997, Experimental Studies on Ring Pack Design Parameters and the Analysis of Radial Ring Collapse, Ph.D. thesis, Department of Mechanical Engineering, University of Wisconsin-Madison, 1997.

[8] Ducu, D. O., 1996, Calibration of the Laser-Induced Fluorescence Technique Applied to Oil Film Thickness Measurements on a Diesel Engine Cylinder Liner by Using Capacitance Gauges, Ph.D. thesis, Department of Mechanical Engineering, University of Wisconsin-Madison.

[9] Ostroski, G. M., 1998, The Use of a Dual-Fiber Probe and the Laser-Induced Fluorescence Technique to Study Oil Consumption in a Diesel Engine, M.S. thesis, Department of Mechanical Engineering, University of Wisconsin-Madison.

Performance Characteristics of a Low Heat Rejection Direct-Injection Military Diesel Engine Retrofitted With Thermal Barrier Coated Pistons

P. Schihl

E. Schwarz

W. Bryzik

U.S. Army TACOM R&D Center,
Propulsion Laboratory,
Warren, MI 48397-5000

A special two-cylinder military specific power plant was employed to evaluate the effect of thermal barrier coated pistons on overall engine performance at simulated low heat rejection-type operating conditions. This study focused on three combustion systems including a noncoated baseline ductile iron piston along with zirconia and chrome-oxide sealed zirconia coated analogs. For the test matrix encompassing ten full and half-load operating conditions, both coated piston combustion systems yielded a detrimental effect on fuel economy in comparison to the baseline combustion system at constant fueling and air consumption rates. These performance differences were attributed to a combination of combustion phasing modulations, injection timing discrepancies, and sluggish combustion associated with the zirconia coated piston configurations. [DOI: 10.1115/1.1370372]

Introduction

Typical U.S. military combat and tactical vehicle propulsion specifications are focused on high power density power plants that must meet stringent under hood or under hood or under armor volume requirements. Traditionally these objectives are met for tactical vehicles and specific combat vehicles through implementation of commercial high output two-stroke truck (diesel) engines. Due to market forces, it has become apparent that future upgraded tactical and combat vehicle power plants will consider including military adapted commercial four-stroke diesel engines. Potential power plant modifications will focus on reducing coolant system size and thus improving overall power plant power density through various strategies that could include thermal barrier coated combustion chamber components, synthetic high temperature lubricants, near stoichiometric combustion system designs, highly flexible injection systems, variable rate coolant handling systems, and variable rate boost systems.

Past efforts by the U.S. Army and others have encompassed some of these potential technological approaches. Nearly 20 years ago, Hoppie [1] and Schwarnwebber [2] investigated the applicability of hypergolic (high temperature) injection for controlling combustion through injection rate. Modern unit injector technology has vastly improved since this particular study and is more capable of controlling combustion in comparison to available injection technology in the early 1980s. A current U.S. military effort aimed at better controlling combustion in direct injection diesel engines has focused on implementing piezo-technology for augmented injector needle lift control ([3]). A more historical technological area revolves around the employment of various coating types for insulating the combustion system. The U.S. military has investigated this particular area of interest throughout the past three decades for tactical and combat vehicle applications ([4–13]) while others have investigated this technology for either potential commercial applications or as a tool to gain better understanding of low heat rejection combustion systems ([14–20]). The results of these numerous studies from a U.S. military perspective have been inconclusive based on available contradicting data sets.

The U.S. military and its partners have also performed various investigations in the area of high temperature lubrication. These efforts have focused on achieving oil sump temperatures approaching 170°C ([21–24]). Other low heat rejection topics of interest have included air-gap insulated pistons ([25–27]), high pressure fuel injection, near stoichiometric combustion systems ([28–30]), and oxygen enrichment for burst power application ([31,32]).

The focus of this study was to examine the global effect of operating an existing military-type power plant in low heat rejection mode by insulating the piston crown with various thermal barrier coatings and simulating both projected appropriate coolant and lubrication boundary conditions while maintaining constant air-fuel ratio at a specific targeted operating condition.

Experimental Setup

The engine employed in this particular study was a Cummins VTA903 modified for single cylinder operation by elimination of the rear six cylinders. Only one of the remaining two cylinders was operational while the other cylinder included a specially modified piston that provided the necessary balancing without developing compression pressure. The front end of the engine, crankshaft, camshaft, and cylinder head were redesigned to accommodate single cylinder operation and also incorporate both injector rocker arm force and in-cylinder pressure measurements at a resolution of 0.2 crank angles. This arrangement included external coolant, lubrication, and fuel handling systems that allowed for temperature and flow rate control through appropriate steam/water heat exchangers and variable bypass pump elements. Turbo-charging was simulated by using compressed shop air and a variable displacement exhaust restriction device in-conjunction with an electric heater located upstream of the intake manifold surge tank. Engine specifications are included in Table 1. (Additional specifications are given by Schwarz et al. [11] and Schihl [33].)

Three separate ductile iron pistons were evaluated over a variety of near full and half load conditions that encompassed a total

Contributed by the Internal Combustion Engine Division of THE AMERICAN SOCIETY OF MECHANICAL ENGINEERS for publication in the ASME JOURNAL OF ENGINEERING FOR GAS TURBINES AND POWER. Manuscript received by the ICE Division Apr. 2000; final revision received by the ASME Headquarters Jan. 2001. Associate Editor: D. Assanis.

Table 1 Engine specifications

Number of active cylinders	1
Displacement, L	1.85
Bore, mm	140
Stroke, mm	121
Geometric compression ratio	12.5
Injection system	Cummins PT*
Injector, number of orifices x diameter, mm	7 x 0.190

* Pressure-time unit injector

Table 2 Targeted engine operating condition parameters

Engine speed, RPM	Manifold Temperature, °C	Desired Torque, N-m	Desired Air/Fuel Ratio
1600	60 , 107	78.0 , 156.0	32.5 , 20.5
1800	60 , 107	81.3 , 162.3	33.0 , 22.0
2100	60 , 107	85.4 , 170.8	33.0 , 23.5
2300	60 , 107	87.5 , 175.0	34.0 , 24.0
2600	60 , 107	85.4 , 170.8	35.0, 25.0

of 46 test points. Two of the three pistons included zirconia or chrome-oxide sealed zirconia coatings (both 0.510 mm thick) in the corresponding bowl regions. Both the baseline and the zirconia coated pistons were evaluated at 20 different operating conditions while the chrome-oxide sealed zirconia coated piston was only evaluated at six operating conditions due to a premature and irreparable injector failure. Both the liner and the piston rings were coated with a thin chrome-oxide film as part of the high temperature tribology strategy.

All operating conditions included in this study employed low heat rejection cooling strategy by maintaining coolant and lubricant supply temperatures near 138°C. The lubricant was a synthetic Stauffer SDL-1 blend while the coolant mix was 100 percent ethylene glycol. Two levels of aftercooling were simulated by maintaining an intake manifold temperature of either 60°C or 107°C. In total, five different engine speeds were evaluated at half and full loads with two levels of aftercooling for both the baseline and zirconia coated pistons. (As noted beforehand, the chrome-oxide sealed zirconia coated piston endured only six full load operating conditions.) Full and half load operating conditions were defined according to fuel maps and other available data for the 373 kW Cummins VTA903 V-8 engine. A summary of the test plan is given in Table 2 and includes both half and full load conditions for each specific engine speed. For example, half load at 1600 RPM includes both 60°C or 107°C manifold temperatures, a desired torque of 78 N-m and a targeted air/fuel ratio of 32.5 while full load at 1600 RPM includes the same two manifold temperatures, a desired torque of 156 N-m and a targeted 20.5 air-fuel ratio.

In order to maintain constant air-fuel ratio for both the baseline and coated piston test conditions, the level of boost was adjusted by regulating the shop air supply. In similar fashion, fueling rate was held relatively constant through incremental adjustments in the fuel supply pressure as indicative of the Cummins PT injection system control strategy. Injection timing was held nearly constant for each particular operating condition by properly adjusting and monitoring injector lash throughout the entire test plan based on the measured injector push rod force-time history.

Experimental Results

The test strategy outlined for this project is more focused on determining perturbations in fuel economy (BSFC) and brake mean effective pressure (BMEP) based on nearly constant air-fuel ratio and injection timing at a specific operating condition for each of the three similar combustion systems. In order to ensure a reasonable comparison between each system, it is important to maintain adequate semblance of peak cylinder pressure at a particular operating condition. As shown in Fig. 1, both coated piston arrangements maintained comparable or lower peak values in comparison to the baseline condition and furthermore, never exceeded the maximum rate value of 130 bars. Injection timing did vary for each combustion system as shown in Fig. 2. At half load and most of the full load conditions, it appears that the start of injection was retarded from 0.5 deg to 1.0 deg for the porous zirconia coated piston in comparison to the baseline piston. The sealed chrome-oxide zirconia coated combustion system injection timing was nearly identical to the porous zirconia coated piston. It was difficult to determine the *exact* cause of the larger discrepancies (1.0 deg), but a few different phenomena might help to explain this observation.

Injection Timing Discrepancies. First, start of injection was determined by comparing a particular operating condition rocker arm force measurement with its motoring analog. There are obvious differences in each trace throughout the injection event and thus referencing the firing data against the motoring data provides an estimate of start and end of injection in-conjunction with peak injection pressure. As recommended by Cummins Engine Company [34], the start of injection is estimated for the PT system by comparing slopes of the motoring and firing traces. The accuracy of such a method is contingent on encoder resolution and individual interpretation. In the worst-case scenario, this potential source of error may be responsible for a maximum of approximately three encoder counts, i.e., 0.6 deg.

Second, all testing was conducted from a low heat rejection perspective and thus the cylinder head was subjected to large thermal loads. Higher overall engine temperatures did result in changes to the injector plunger/cup seating process as evidenced by measured rocker arm force-time histories. In particular, the seating force tended to decrease with higher temperature operating conditions regardless of incidental injector lash differences. For example, simply increasing intake manifold temperature and boost during adjacent test condition operating points exhibited this type of behavior. Given the PT system is a mechanical unit injector design, it is possible that both the start and end of injection could change with expansion of critical seating areas and is evident by comparing the two levels of simulated aftercooling test conditions (see Schihl [33]).

Third, injector lash setting has a large impact on the injection event and more predominately on start of injection and the peak injection pressure. For example, an increase in lash of 0.050 mm resulted in such noticeable changes in comparison to the standard setting of approximately 5.46 mm (see Schihl [33]). Once again, it is difficult to assess the quantitative influence of this initial condition on start of injection without taking a dynamic measurement which was not feasible for this particular study.

Nevertheless, each of these three phenomena contributed toward the discrepancies noticed in start of injection between the three combustion systems. Due to the inherent nature of each effect, it is very difficult to quantitatively assess the most and least

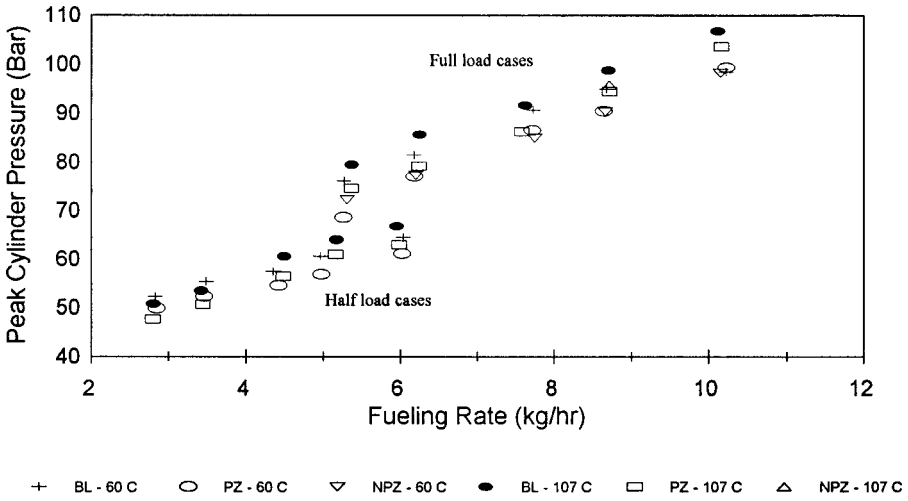

Fig. 1 Peak cylinder pressure trends for various combustion systems. The number following the combustion system designator represents intake manifold temperature in centigrade, i.e., BL-60°C is the baseline combustion system at 60°C intake manifold temperature.

dominant phenomena. Regardless, such injection timing variances alone do not completely explain the overall behavioral differences between the three combustion systems. Again, the resultant injection timing differences for each combustion system is shown in Fig. 2.

Fuel Economy and Power Density. As given by Fig. 3, the brake specific fuel consumption (BSFC) was higher for both coated piston arrangements at both half and full load operating conditions. (*It is important to note that BSFC and BMEP are defined according to the dynamometer measured load and thus do not account for required fuel, lubricant, and coolant system pumping work.*) The baseline combustion system exhibited the best overall fuel consumption at both the full and half load operating conditions. Larger amounts of aftercooling were more effective at half load operating conditions compared to full load operating conditions for the baseline combustion system. This full load trend is especially noteworthy given the aftercooled fuel consumption calculations fail to account for any required work associated with cooling post compressor charge air.

Correspondingly, the baseline combustion system in general yielded higher BMEPs throughout the test plan. Additionally, as noted in Fig. 4, neither aftercooling strategy demonstrated advantageous behavior over the entire test plan in comparison to its counterpart for the baseline combustion system. This trend does not absolutely coincide with fuel consumption trends noted in the previous discussion and is explained based on injected fuel quantity variances. The desired test plan did focus on attempting to keep both injection timing and quantity constant at a specific operating condition, but such an approach was difficult due to the inherent nature of the PT injection system. Measured fueling rates did vary at a specific operating condition from 0.5 percent to 2.0 percent between the baseline and coated combustion systems and thus do account for discrepancies between fuel consumption and measured BMEP. This observation is also applicable when comparing the two levels of aftercooling at common speed and load points for a particular combustion system.

These trends are difficult to explain with one simple parametric correlation and thus such an explanation will not be offered in this

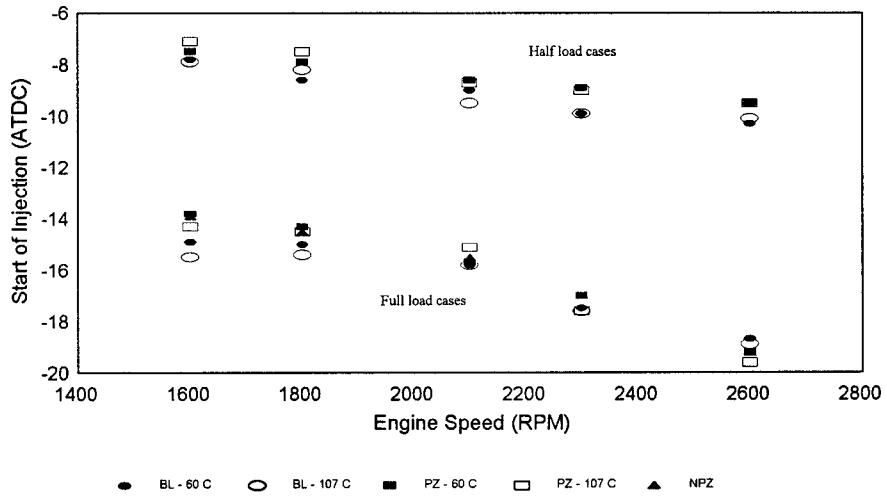

Fig. 2 PT fuel injection system delivery performance. The number following the combustion system designator represents intake manifold temperature in centigrade, i.e., BL-60°C is the baseline combustion system at 60°C intake manifold temperature. NPZ data includes both 60°C and 107°C manifold conditions.

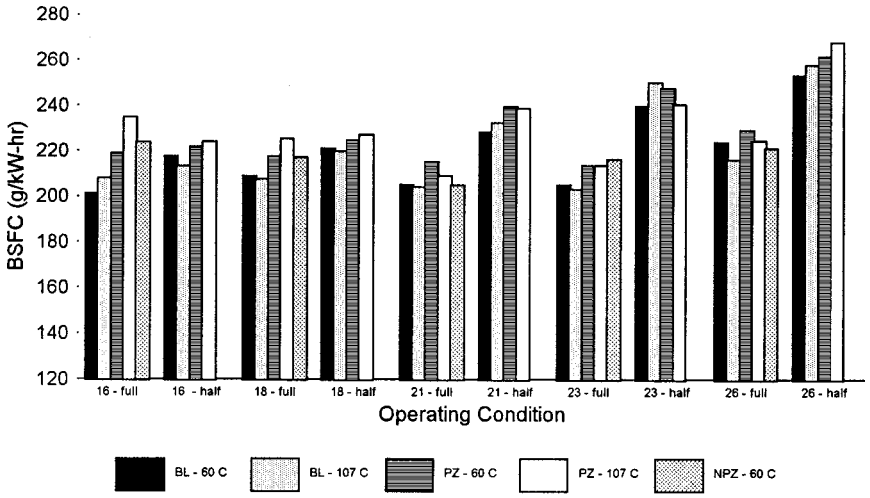

Fig. 3 The influence of combustion system design on indicated fuel economy. The number following the combustion system designator represents intake manifold temperature in centigrade, i.e., BL-60°C is the baseline combustion system at 60°C intake manifold temperature while the column descriptor has the format given by engine speed-load, i.e., 16-full is 1600 RPM at full load.

paper. Instead, a number of observations were made that might help differentiate between performance differences offered by each combustion system over segments of the test plan. These observations are based on measured cylinder pressure, mean mixing rate and combustion phasing, and indirectly measured bulk net heat release rate profiles. Additionally, the coated pistons exhibited exhaust temperatures ranging from 5°C to 20°C higher in comparison with the noncoated baseline piston and thus provided some level of reduced in-cylinder heat transfer for some cases. This effect in general will be implicitly incorporated into subsequent discussions concerning ignition delay and associated compression work changes.

Meaning Mixing Rate. One potential indicator of overall diesel engine performance is the measured peak cylinder pressure and its corresponding location (LPP—location of peak pressure). For the engine employed in this study, LPP varied from 7 deg to 12 deg after top dead center (ATDC) and also provided a reasonable indicator of the midpoint in the accumulated heat release profile. For all test cases, the elapsed time between start of injection (SOI) and LPP is arguably defined as an accumulation of a chemical induction time (ignition delay), a mean flame spread time (premixed phase burn), and a mean bulk mixing time. This total time is defined as a characteristic combustion time (CCT) given by τ_C.

For the full load cases, the ignition delay was nearly constant and the associated net heat release rate profiles were predominately in the mixing controlled phase. Thus, the variance in CCT for these full load cases over the speed range included in this study was primarily due to the heat release profile and in particular, differences between the fraction of premixed versus mixing controlled burn. Increasing engine speed at full load exhibited slightly smaller ignition delays but higher injection pressures with the net result yielding a shorter effective mixing time, i.e., the combination flame spread and bulk mixing time scale decreased

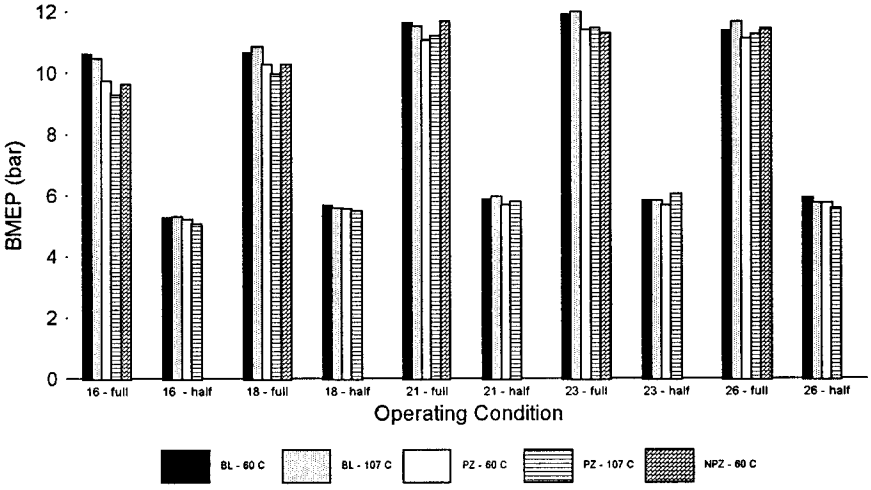

Fig. 4 The influence of combustion system design on indicated work output. The number following the combustion system designator represents intake manifold temperature in centigrade, i.e., BL-60°C is the baseline combustion system at 60°C intake manifold temperature while the column descriptor has the format given by engine speed-load, i.e., 16-full is 1600 RPM at full load.

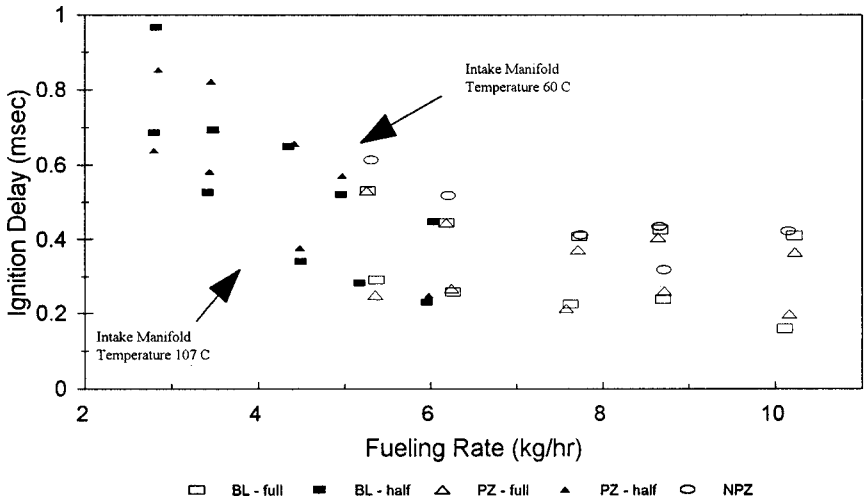

Fig. 5 Ignition delay trends for various combustion system designs. The descriptor following the combustion system designator represents engine load condition.

with engine speed at full load. Such an observation is expected given the higher injection pressures and correspondingly higher mixing rates. Comparison of the baseline and coated piston combustion systems is given by Figs. 5 and 6. It is apparent that at full load the fuel economy tends to diverge at lower speeds and converge at higher speeds (higher injection pressures). Additionally, for CCT values less than approximately 2.2 milliseconds, the fuel economy for each combustion system tends to follow a similar trend.

The half load cases correspond with values of CCT less than approximately 2.0 milliseconds that decrease with increasing engine speed. This behavior is intuitive if the premixed phase burn is interpreted as a flammable spray region whose consumption rate is controlled by the turbulent entrainment rate of a propagating flame. In this sense, the entrained flammable mixture is divided into pockets on the order of the Taylor scale whose consumption rate is dictated by local small scale mixing and local laminar flame speed ([35]). By assuming homogeneous turbulence at a given engine position location, the small scale mixing rate maybe correlated to the large scale mixing rate through a defined turbulent Reynolds number. Though this key assumption is questionable throughout the premixed burn, it does provide an indicator of both the premixed phase burn rate and duration ([33]). Thus, higher half load engine speeds result in faster overall effective mixture mixing rates in comparison to the full load cases. A larger portion of the net heat release rate profiles reside in the premixed phase which has a much shorter time scale in comparison to the mixing controlled phase. For example, the baseline combustion system at full load and 2600 RPM has a mean injection velocity that is approximately 50 percent higher than the half load and 1600 RPM condition, but has a CCT that is 0.2 milliseconds longer for the full load case—the premixed burn fraction is less than ten percent for the full load case and almost 50 percent for the half load case.

The brake fuel economy data does correlate with CCT as shown in Fig. 7 for time scales less than 2.0 milliseconds. This correlation is within four percent of the data as shown by the gray shaded region. For times exceeding 2.0 milliseconds there is a substantial divergence between the three combustion systems. The ceramic coated piston combustion systems tend towards higher fuel consumption with larger CCTs while the baseline combustion system

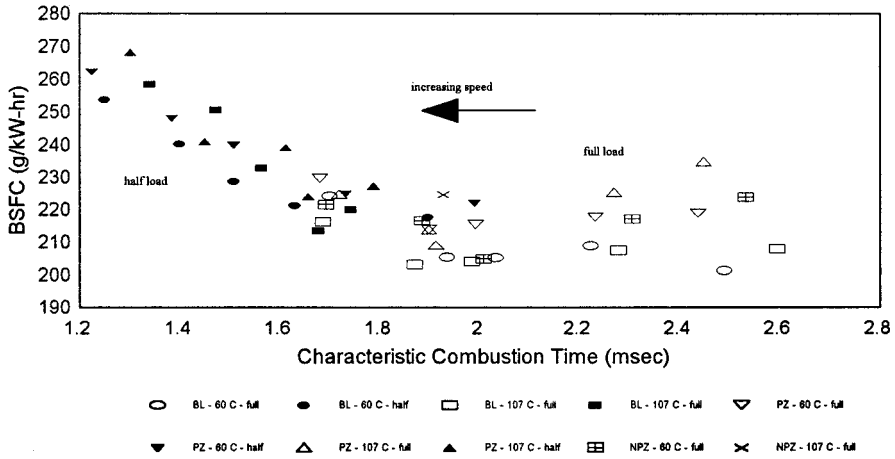

Fig. 6 The influence of representative combustion time on indicated fuel economy. The number following the combustion system designator represents intake manifold temperature in centigrade, i.e., BL-60°C is the baseline combustion system at 60°C intake manifold temperature, while the descriptor following the intake manifold temperature is the engine load condition.

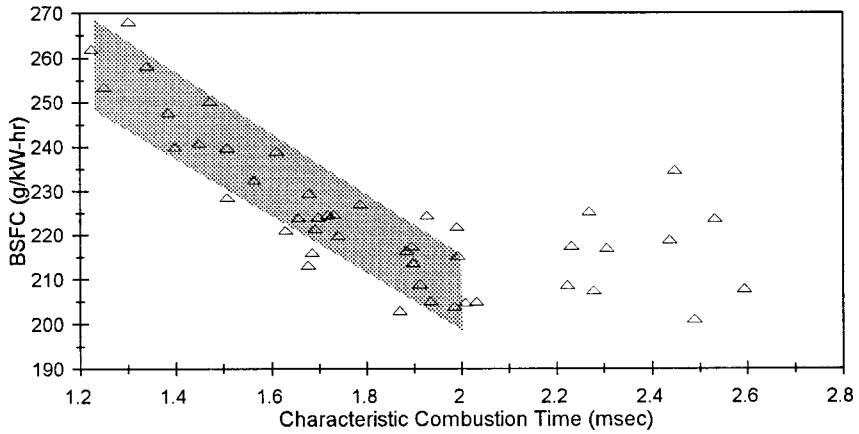

Fig. 7 The role of combustion timing on fuel economy

tends toward some relatively constant value. At this time, the authors cannot offer a general explanation of this divergent behavior.

Combustion Behavior—Half Load Operating Conditions. From an intuitive standpoint, the generalized net heat release profiles provide a good indicator of both BMEP and BSFC. For the *half load cases* (excluding both the baseline and porous zirconia coated combustion systems at 107°C and 2300 RPM—the fueling rates were approximately four percent higher compared to the lower manifold temperature test conditions), variances in fuel economy among combustion systems are readily explained by combustion phasing and timing. For example, at 1600 RPM and the higher manifold temperature (107°C), the baseline combustion system exhibited a shorter ignition delay in comparison to the lesser after-cooling test point (60°C). Ultimately, the pressure rise is less gradual and nearly five degrees closer to TDC with nearly the same peak pressure value as the lower manifold temperature test condition. In general, the porous zirconia combustion system tends to exhibit a more sluggish net heat release profile in comparison to the baseline combustion system and results in both lower peak cylinder pressures and less expansion work.

As noted beforehand, lower speed, half load points for the baseline combustion system exhibited better fuel economy with higher aftercooling while the contrary was true for the higher speed, half load points. This transition is contingent on the tradeoff between expansion and compression work as dictated by the global fuel burning rate profile. The higher manifold temperature conditions required higher boost to maintain a constant air-fuel ratio and thus resulted in both shorter ignition delays and higher required compression work. As timing was advanced with higher engine speed, the resulting pressure rise was continually advanced and eventually settled near TDC for the lower manifold temperature conditions while the higher manifold temperature conditions crossed TDC at 1800 RPM and eventually settled near 4 deg BTDC at 2600 RPM. The fuel economy data for these half load test points reveal the beginning of this transition near 1800 RPM. These same arguments may be applied to the porous zirconia coated piston combustion system (excluding the aforementioned 2300 RPM condition) except that injection timing was retarded 0.5 deg to 1.0 deg.

Combustion Behavior—Full Load Operating Conditions. The baseline and porous zirconia combustion systems exhibited comparable or slightly improved fuel economy with less aftercooling in comparison to more aftercooling at higher engine speeds. Similar to the half load conditions, higher manifold temperatures required higher boost in comparison to the lower manifold temperature conditions with resultant shorter ignition delay, lower premixed spike, and higher required compression work. For both of these combustion systems, the transition point where the expansion work offsets additional required compression work occurs near 1800 RPM, but is much less subtle in comparison to the half load analog.

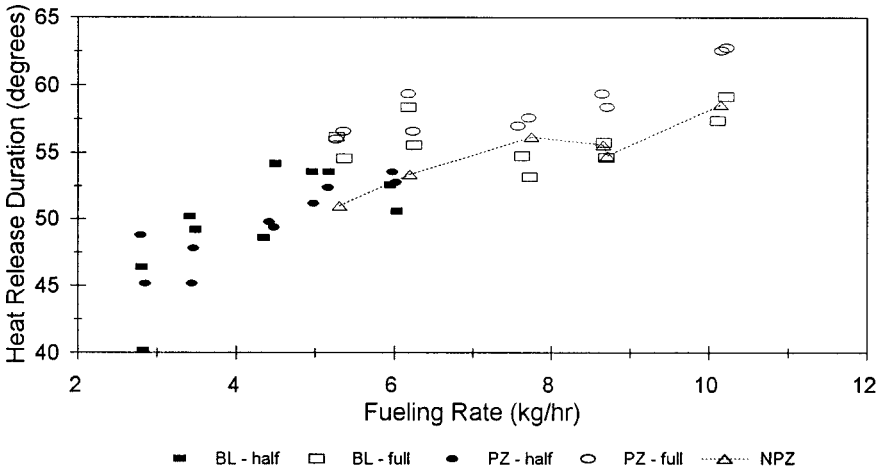

Fig. 8 The influence of combustion system design on the 10 percent to 90 percent burn duration. The descriptor following the combustion system designator is the engine load condition.

For the higher aftercooling cases, the baseline combustion system exhibited better fuel economy in comparison to the porous zirconia coated piston configuration. The two lower speed conditions revealed earlier start of combustion for the baseline system that resulted in both higher peak cylinder pressures and net work created during the compression-expansion stroke. At 2100 and 2300 RPM, these two combustion systems exhibited very comparable start of combustion, but the general heat release rate profile was sluggish for the porous zirconia coated piston configuration and included lower peak cylinder pressures with an accompanying longer burn duration, i.e., time period representing 10 percent to 90 percent of the energy released throughout the combustion event. As previously discussed for other operating conditions, the tradeoff in expansion versus compression work resulted in better fuel economies for the baseline combustion system. At 2600 RPM, start of combustion occurred earlier for the porous zirconia coated piston configuration that resulted in comparable peak cylinder pressures and subsequently similar fuel economies. As given by Fig. 8, the burn duration is shorter for the baseline combustion system and is more divergent with higher speed. This combustion characteristic difference does have ramifications on peak cylinder pressure and thus any tradeoffs in compression versus expansion work. As a final note for this particular manifold and load condition, the sealed zirconia coated piston configuration exhibited fuel economies and net heat release rate profiles that were similar to the porous counterpart. Minor differences in the heat release rate profiles can be attributed to changes in timing and ignition delay. But once again, these differences were minor and had little ramification on overall engine performance.

The lesser aftercooling cases also followed the same trends concerning compression and expansion work tradeoffs based on injection timing and ignition delay for the baseline and porous zirconia combustion systems. In all cases, the baseline system had an advanced start of combustion predominately due to injection timing changes and a comparable or, at higher speeds, shorter burn duration. These differences between the two combustion systems resulted in higher peak cylinder pressures, compression work, and expansion work for the baseline system. Once again, the baseline system exhibited better fuel economy in comparison to the porous zirconia coated piston configuration for the higher temperature manifold conditions.

Conclusions

1 The zirconia coated piston combustion systems demonstrated slightly higher fuel consumption in comparison to the baseline combustion system. This observation was made in light of near constant injection timing and air-fuel ratio.

2 Fuel economy differences between each combustion system were explained according to measured in-cylinder pressure data and indirectly determined net heat release rate profiles. A combination of unintended changes to injection timing, variances in ignition delay, and sluggish combustion at certain operating conditions for the zirconia coated combustion systems resulted in fuel economy trends that were the net result of a tradeoff between compression and expansion work.

3 Generalized fuel economy trends correlated with a representative combustion time scale for most of the half load cases and a portion of the higher speed, full load cases. This characteristic time is comprised of the ignition delay, a premixed flame spread time scale, and a bulk mixing time scale.

4 The 10 percent to 90 percent burn duration for the porous zirconia coated piston configuration was longer in comparison to the baseline combustion system over the full load operating points.

5 The peak cylinder pressure was higher for the baseline combustion system and may be attributed to differences in the applicable heat release rate profiles.

6 Variance in start of injection timing is a factor in assessing potential performance differences between the three combustion systems due to discrepancies in lash setting, the measurement technique, and thermal effects. The ceramic coated combustion systems might require advanced timing compared to the baseline system due to both sluggish combustion and thermal effects on lash setting.

Nomenclature

BL = baseline combustion system
PZ = porous zirconia combustion system
NPZ = nonporous zirconia combustion system

References

[1] Hoppie, L. O., 1982, ''The Influence of Initial Fuel Temperature on Ignition Delay,'' SAE Technical Paper No. 820356.
[2] Scharnweber, D. H., 1984, ''Hypergolic Combustion Demonstration in a Reciprocating Internal Combustion Engine,'' Technical Report No. 13042, U.S. Army TACOM R&D Center, Warren, MI.
[3] U.S. Army, 2000, private communication.
[4] Kamo, R., and Bryzik, W., 1978, ''Adiabatic Turbocompound Engine, Performance Prediction,'' SAE Technical Paper No. 780068.
[5] Kamo, R., and Bryzik, W., 1981, ''Cummins—TARADCOM Adiabatic Turbocompound Engine Program,'' SAE Technical Paper No. 810070.
[6] Bryzik, W., and Kamo, R., 1983, ''TACOM/Cummins Adiabatic Engine Program,'' SAE Technical Paper No. 830314.
[7] Bryzik, W., and Kamo, R., 1984, ''TACOM/Cummins Adiabatic Engine Program,'' SAE Technical Paper No. 840428.
[8] Woods, M., 1984, ''Ceramic Insulating Components for the Adiabatic Engine,'' *The Adiabatic Engine: Past, Present, and Future Developments*, SAE Special Publication PT-28.
[9] Badgley, P., Kamo, R., Bryzik, W., and Schwarz, E., 1990, ''Nato Durability Test of an Adiabatic Truck Engine,'' SAE Technical Paper No. 900621.
[10] Woods, M., Bryzik, W., and Schwarz, E., 1992, ''Heat Rejection from High Output Adiabatic Diesel Engine,'' SAE Technical Paper No. 920541.
[11] Schwarz, E., Reid, M., Bryzik, W., and Danielson, E., 1993, ''Combustion and Performance Characteristics of a Low Heat Rejection Engine,'' SAE Technical Paper No. 930988.
[12] Bryzik, W., Schwarz, E., Kamo, R., and Woods, M., 1993, ''Low Heat Rejection From High Output Ceramic Coated Diesel Engine and Its Impact on Future Design,'' SAE Technical Paper No. 931021.
[13] Schwarz, E., Danielson, E., Bryzik, W., Keelan, T., and Hakim, N., 2000, ''NATO Qualification Test of Detroit Diesel 8V71-TA Engine at 530 BHP With Advanced Ceramic Components,'' SAE Technical Paper No. 2000-01-0524.
[14] Alkidas, A. C., 1987, ''Experiments With an Uncooled Single-Cylinder Open-Chamber Diesel,'' SAE Technical Paper No. 870020.
[15] Alkidas, A. C., 1989, ''Performance and Emission Achievements With an Uncooled, Heavy Duty Single Cylinder Diesel Engine,'' SAE Technical Paper No. 890144.
[16] Assanis, D., Wiese, K., Schwarz, E., and Bryzik, W., 1991, ''The Effects of Ceramic Coatings on Diesel Engine Performance and Exhaust Emissions,'' SAE Technical Paper No. 910460.
[17] Miyairi, Y., Matsuhisa, T., Ozawa, T., Oikawa, H., and Nakashima, N., 1989, ''Selective Heat Insulation of Combustion Chamber Walls for a DI Diesel Engine with Monolithic Ceramics,'' SAE Technical Paper No. 890141.
[18] Ozawa, T., Matsuhisa, T., Miyairi, Y., Oikawa, H., and Nakashima, N., 1990, ''Application of Ceramics to Heat-Loaded Components of Direct Injection Diesel Engine,'' 33rd International FISITA Congress, Torino, Italy, Paper No. 905204.
[19] Kawamura, H., Sekiyama, S., and Hirai, K., 1991, ''Observation of the Combustion Process in a Heat Insulated Engine,'' SAE Technical Paper No. 910462.
[20] Afify, E. M., and Klett, D. E., 1996, ''The Effect of Selective Insulation on Performance, Combustion, and NO Emissions of a DI Diesel Engine,'' SAE Technical Paper No. 960505.
[21] Sutor, P., and Bryzik, W., 1987, ''Tribological Systems for High Temperature Diesel Engines,'' SAE Technical Paper No. 870157.
[22] Sutor, P., Bardasz, E. A., and Bryzik, W., 1990, ''Improvement of High-Temperature Diesel Engine Lubricants,'' SAE Technical Paper No. 900687.
[23] Marolweski, T. A., Slone, R. J., and Jung, A. K., 1990, ''High Temperature Liquid Lubricant for Use in Low-Heat-Rejection Diesel Engines,'' SAE Technical Paper No. 900689.
[24] Yost, D. M., and Frame, E. A., 1995, ''Evaluation of High-Temperature Diesel Engine Liquid Lubricants,'' SAE Technical Paper No. 952544.
[25] Woods, M. E., Glance, P., and Schwarz, E., 1987, ''In-Cylinder Components for High Temperature Diesel,'' SAE Technical Paper No. 870159.
[26] Parker, D. A., and Donnison, G. M., 1987, ''The Development of an Air Gap Insulated Piston,'' SAE Technical Paper No. 870652.
[27] Woods, M., Bryzik, W., and Schwarz, E., 1995, ''Design of High Temperature Engine Components,'' SAE Technical Paper No. 950982.
[28] Gebert, K., Barkhimer, R. L., Beck, N. J., Wickman, D. D., Tanin, K. V., Das, S., and Reitz, R. D., 1998, ''An Evaluation of Common Rail, Hydraulically Intensified Diesel Fuel Injection System Concepts and Rate Shapes,'' SAE Technical Paper No. 981930.

[29] Wickman, D. D., Senecal, P. K., Tanin, K. V., Reitz, R. D., Gebert, K., Barkhimer, R. L., and Beck, N. J., 2000, ''Methods and Results from the Development of a 2600 bar Diesel Fuel Injection System,'' SAE Technical Paper No. 2000-01-0947.
[30] Woods, M., Kamo, R., and Bryzik, W., 2000, ''High Pressure Fuel Injection for High Power Density Diesel Engines,'' SAE Technical Paper No. 2000-01-1186.
[31] Sekar, R. R., Marr, W. W., Assanis, D. N., Cole, R. L., Marciniak, T. J., and Schaus, J. E., 1991, ''Oxygen-Enriched Diesel Engine Performance: A Comparison of Analytical and Experimental Results,'' ASME J. Eng. Gas Turbines Power, **113**, pp. 365–369.
[32] Keating, E. L., and Gupta, A. K., 1994, ''Modes of Oxygen Enrichment in I.C. Engine Indicated Performance,'' *Industrial and Environmental Applications of Fluid Mechanics*, Vol. 186, ASME, New York.
[33] Schihl, P., 1998, ''Development of Global Mixing, Combustion, and Ignition Models for Quiescent Chamber Direct-Injection Diesel Engines,'' Ph.D. thesis, University of Michigan, Ann Arbor, MI.
[34] Hoag, K., 1989, ''Development of a Low Heat Rejection Engine,'' Technical Paper No. 1345, U.S. Army TACOM R&D Center, Warren, MI.
[35] Tabaczynski R., Ferguson, C., and Radhakrishnan, K., 1977, ''A Turbulent Entrainment Model for Spark Ignition Combustion,'' SAE Technical Paper No. 770647.

Dimethyl Ether in Diesel Engines: Progress and Perspectives

S. C. Sorenson
Department of Mechanical Engineering,
Technical University of Denmark,
Building 403, Nils Koppels Allé,
DK2800 Kgs. Lyngby, Denmark
e-mail: scs@mek.dtu.dk

A review of recent developments related to the use of dimethyl ether (DME) in engines is presented. Research work discussed is in the areas of engine performance and emissions, fuel injection systems, spray and ignition delay, and detailed chemical kinetic modeling. DME's properties and safety aspects are discussed. A simplified theoretical explanation of the emissions behavior of DME is presented. A discussion is presented proposing DME as a significant factor in the future international energy picture. Due to its beneficial combustion properties, possibility of production from a variety of sources, and usefulness as a chemical feed stock, DME can be used in a variety of applications in addition to transportation. [DOI: 10.1115/1.1370373]

Introduction

The purpose of this paper is to discuss the status of developments in the use of dimethyl ether (DME) as a clean fuel for diesel engines. Since a major factor concerning DME use is availability, it is also necessary to discuss factors that will aid the introduction of DME into other energy and combustion related areas. It will be proposed that DME is an attractive candidate for participation in the energy supply structure as a fuel that can be produced from a variety of sources and used in a variety of applications.

Background

Dimethyl ether (DME) has been studied in connection with reductions of emissions from diesel engines, especially with regard to particulate emissions. The first diesel engine results presented for DME were in relation to its use as an ignition improver in connection with methanol ([1–4]). In the late 1980s methanol was under consideration as a method to reduce particulate emissions in order to meet the strict EPA particulate emission standards of 0.10 g/hp-hr which had been proposed for city buses in the U.S.A. for 1991. While methanol can burn without producing soot emissions, its low cetane number makes it difficult to ignite in diesel engines. In order to improve the ignition properties of methanol, nitro akyl additives were used as ignition improvers.

At the time of these studies, DME's low self-ignition temperature was known, but based on a somewhat expensive production process for high purity DME based on the dehydration of methanol, DME was basically regarded as a rather expensive chemical. Therefore, it was thought most economically sound to use DME in limited quantities as a fuel additive in order to minimize cost.

Technically, it was found that DME could not really be considered as an additive for methanol. For large amounts of DME in methanol, diesel engine performance on DME/methanol blends could not be regarded as satisfactory. Combustion behavior with these high concentrations of DME still was close to that of methanol, with accompanying problems with ignition and noise. This is illustrated in Fig. 1 showing the results from subsequent studies on neat DME ([5]), showing the region of good ignitiability of DME-methanol-water mixtures in a small DI diesel engine.

Neat DME has good ignition characteristics if it does not contain too much water or methanol. Thus, it might seem more correct to regard methanol as a contaminant that degrades DME ignition, rather than DME as an ignition improver for methanol.

The situation changed in 1995, when several papers were presented concerning (1) low cost production of DME ([6]), (2) single cylinder test studies showing low emissions and noise with good efficiency on neat DME ([5]), (3) the potential of meeting ULEV emissions standards with a seven-liter diesel engine running on neat DME ([7]), and (4) combustion development for low noise and emissions ([8]). The elimination of the soot emissions made possible new tradeoffs in terms of engine optimization, for example optimization with respect to a noise/NO_x emission tradeoff.

Of major importance to the DME situation were the results showing that DME could be produced from natural gas in a process resembling methanol production, but at a lower cost. Thus, it was no longer appropriate to regard DME as a special chemical, but as a potential commodity that could be produced in large quantities at a competitive price. A key point economically was to produce the DME from natural gas that cannot otherwise be economically exploited for use as gas. Such gas is found in many remote places in the world. Excess gas from oil production is often either flared or re-injected into the ground at significant cost and CO_2 emission, since it cannot be used or economically transported to potential users. In the long term, DME can be produced from biomass, although at a higher cost than from natural gas. The low price of the fuel is necessary to compete economically, since DME production facilities must be constructed for future expansion in DME use.

Dimethyl Ether Properties

Although it has very desirable properties in terms of combustion and emissions behavior, DME has physical properties that require changes if it is to be used in traditional diesel fuel injection systems. Experience to date has indicated that the most challenging aspects of DME operation are related to its physical properties, and not to its combustion behavior.

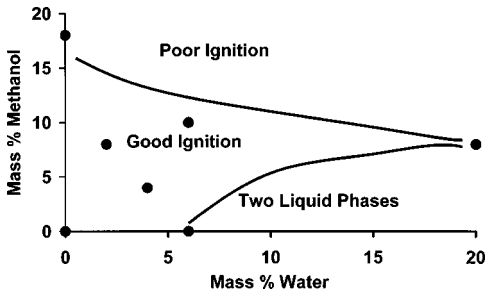

Fig. 1 Regions of good ignition characteristics for dimethyl ether/water/methanol blends [5]

Contributed by the Internal Combustion Engine Division of THE AMERICAN SOCIETY OF MECHANICAL ENGINEERS for publication in the ASME JOURNAL OF ENGINEERING FOR GAS TURBINES AND POWER. Manuscript received by the ICE Division July 2000; final revision received by the ASME Headquarters December 2000. Associate Editor: D. Assanis.

The properties of DME are given in Table 1. Foremost of these properties is its vapor pressure. DME has a boiling point of −24.9°C and a vapor pressure of 5.1 atmospheres at 25°C. The vapor pressure of DME lies between those of propane and butane, which means that its vaporization characteristics are quite close to those of LPG. This is of course means that DME is a gas at standard temperature and pressure, and requires special containment, conventionally in a system similar to those used for LPG.

When compared to diesel fuel, the lower liquid density, lower heating value, and the need for a vapor space above liquid fuel in a DME tank, lead to the requirement of approximately a double-sized fuel tank for an equivalent number of operating hours on DME.

Because of its nearness to the critical state, DME has higher compressibility ([9,10]). This increases the amount of work required to compress the fuel in jerk pump types of systems. Such compression has been named as the source of larger pressure oscillations when DME is used in jerk pump systems. Used in unmodified jerk pump diesel injection systems, the oscillations increased the tendency for after injection of fuel ([10–13]). Studies using jerk pumps to date have been conducted with basically unmodified diesel injection systems. Thus, the delivery valves used were designed for diesel oil. The effects of delivery valve parameters on the injection process of DME in jerk pumps systems have not been investigated.

A second difficulty with the compressibility of DME arises near full load conditions. With the engine at high temperatures, fuel heating can occur, which could result in a decrease in fuel density and increase in compressibility. This is turn would make it more difficult to supply the amount of fuel needed to maintain full power. In this regard, it appears that fuel cooling or temperature control will be advantageous in the DME powered diesel engine.

The viscosity of DME is lower than that of diesel oil by a factor of about 20. This can cause higher rates of leakage through small clearances such as pump plungers and injection nozzles. Leakage is very important in common rail systems, as high flow rates can be required to overcome solenoid leakage, greatly increasing parasitic losses ([14]). In addition to the low viscosity, DME also has a low lubricity, which means that special consideration must be taken with regard to the lubrication of moving parts with DME.

Most of the engine studies to date have used lubricity additives to improve fuel lubricity, decrease pump wear, and prevent seizing of injection system components. In initial studies with DME, a small jerk pump was operated on pure DME for 500 hours before failing, giving some grounds for optimism ([15]). However, in other more sophisticated jerk pump systems, very rapid failures have been observed ([14]), even with the use of lubricity additives and the results of initial study appear to be an exception rather than a rule. Nonetheless, they do give grounds to believe that lubricity problems in a jerk pump can be resolved.

The lubricity additives used to date are typically those developed for low sulfur diesel fuels. One limited study has been performed investigating the wear characteristics of DME fuel additive combinations ([15]) with diesel engine injection system components. The results with commercial jerk pump systems indicate that these additives in amounts recommend for low sulfur diesel fuels would probably not provide adequate long-term protection with DME. This work also demonstrated the need for more fundamental studies of wear, lubricity, and lubricity improving agents under more carefully controlled conditions. Such studies have been initiated in the author's laboratory and include modifications of the commonly used high frequency reciprocating rig (HFRR) to operate with DME under pressurized conditions.

Table 1 Properties of dimethyl ether (DME)

Property	DME
Chemical formula	CH_3OCH_3
Molecular weight	46
Oxygen content—mass %	34.8
Stoichiometric air fuel ratio–kg/kg	9.1
Lower heating value–kJ/kg	28,800
Liquid density–g/ml@15°C	0.668
Boiling point–°C	−24.9
Viscosity–kg/m-s@25°C kg/m-s	est. 0.12–0.15
Vapor pressure@25°C–bar	5.1
Critical pressure–atm	52
Critical temperature–°C	127
Ignition temperature–°C	235

DME is used extensively in the aerosol spray can industry as a replacement for fluorocarbon propellants. This is due primarily to its vapor pressure characteristics and its benign atmospheric behavior. An additional property that makes it attractive for this application is its nature as a strong solvent. Unfortunately, DME's ability to dissolve most organic substances can lead to problems with the use of plastic materials and elastomers in injection systems.

At the present state of knowledge, Teflon compounds are known to be inert to DME, although their stiffness and creep characteristics do not make them well suited for sealing purposes. The substances EPDM and ''KalRez'' a fluorocarbon based polymer, have been used successfully in some applications with DME. Commonly used elastomers have in general not been successful for use with seals in DME applications. Typical DME action on elastomers is to extract the plasticizer from the material, such that it loses its resiliency and no longer is capable of sealing. Some compounds are known to swell up when subjected to a DME environment. In addition, the permeability of the polymer-based materials may be adversely affected by DME. Some work is being conducted with DME in order to develop potential elastomers and other sealing materials, but the topic remains an area where much work is needed. Since the properties of a given type of material can vary, it is essential to evaluate seal material/application combinations carefully in DME systems.

Another property of DME that is not often mentioned in connection with engine emissions is its low reactivity in photochemical reactions. The ozone forming reactivity of DME is among the lowest of organic substances considered for fuel use ([16]). In addition to low ozone forming potential, DME does not form formaldehyde in photochemical reactions in the environment, as do other oxygenated compounds ([17]). Since DME is contained in closed pressurized containers that essentially eliminate evaporative emissions, its impact on urban air should be quite low. The few other organic compounds emitted with DME in diesel engines also have low reactivity ([18]).

Engine Studies

Neat dimethyl ether (DME) has been tested in a number of diesel engines, ranging in size form 273 to 1220 cm^3/cylinder. All of the engines tested have been of the direct injection type. In all of these studies, soot-free operation has been observed. Particulate emissions have been measured at levels that are assumed to those of the lubricating oil contributions.

Low NO_x emission have been reported with DME, especially in initial direct conversion studies of engines with jerk pump systems ([5,11]). Efficiency in these engines was not much affected, even though the injection duration was increased relative to diesel fuel. In both of these naturally aspirated engines, soot emissions were not found with DME.

Subsequent work with DI injection under conditions where the injection timing was carefully monitored and controlled indicate that NO_x emissions from DME can be at similar levels to those of DI engines on diesel fuel with the DME timing advanced, but that there were advantages to reducing the injection timing with DME, since no consideration need be taken of smoke emissions, and NO_x emissions with DME fell faster with timing retard than with diesel fuel ([14,19]). A modified hydraulic electronic unit injection (HEUI) injection system was also successfully used in initial

engine work ([7,8,20]). A smaller turbocharged DI engine was also shown to be well suited to passenger car sized vehicles ([21]).

Heat release profiles in DI engines converted directly to DME operation typically show a lower rate of heat release at the start of combustion, with values approximately half those found with diesel fuel ([8,11]). On the other hand, the second portion of combustion, commonly called the diffusion portion, was longer in duration for DME. Given that injection pumps typically were used without changing the plunger diameter, it was necessary to inject the larger volume of DME required for the same input energy by lengthening the injection duration. This will lengthen the duration of the latter stages of the combustion without appreciably affecting the start of combustion.

Injection Systems

The initial engine studies with jerk pump systems showed that since dimethyl ether (DME) does not form soot during combustion, other considerations determine the injection pressure requirements for DME. DME was shown to operate satisfactorily at much lower injection valve opening pressure than diesel ([5,11]). This suggested the attractiveness of a low-pressure common rail system for DME, and systems of this type have been utilized in the construction of dedicated DME injection ([9,22]).

It has been shown that DME has a higher tendency to form vapor in the fuel system than diesel fuel. This has been demonstrated with a flow model of an orifice ([21]) and with CFD calculations in an injection nozzle ([23]).

Spray Studies

Since dimethyl ether (DME) has such a high vapor pressure, the behavior of a DME spray has been of interest in terms of understanding and improving the combustion process. Studies have been conducted at the University of Hiroshima and the Technical University of Denmark to investigate the overall spray characteristics of shape and penetration ([12,13,24–27]). In addition, the studies at the University of Hiroshima have included ignition behavior.

In terms of the general spray behavior, studies of injection of DME into nitrogen indicate that the spray penetration can be determined by using correlation methods determined for diesel engine sprays ([28]) when consideration is taken of the different physical properties of DME. Other general phenomena were observed in the sprays that are not seen in diesel sprays. The first is that under some conditions, there is a rapid lateral spreading of the spray at the very start of the injection, where after the rest of the spray continues its normal motion. These small ''side jets'' near the nozzle tip evaporate rapidly.

The second process seen is that there are portions of the head of the spray that tend to break off of the spray during the injection process. These chunks of the spray rapidly decelerate and evaporate as the main body of the spray penetrates past them in the usual manner. Neither the reasons for these phenomena nor their importance is known at the present time.

Combustion

Engine Combustion. Several combustion studies have been conducted based on analysis of pressure time diagrams. Results from naturally aspirated engines indicate that the rate of heat release at the start of combustion is much lower for DME than for conventional diesel engines, leading to lower noise ([11,14,19]). In addition, the lower initial heat release rate is expected to contribute to the lower NO_x emissions ([29]). According to these recent results with diesel fuel, NO is only formed in the diffusion portion of the flame in a diesel engine, and the initial heat release plays a significant role in determining the initial temperatures and pressures for the diffusion controlled combustion. As mentioned previously, some of the DME studies have been conducted with a longer period of injection, which also can contribute to lower NO_x emissions.

In studies where similar injection durations were used for both diesel fuel and DME, similar results have been found, but NO_x emissions with DME can be reduced to a greater extent than diesel fuel in a soot free environment when using retarded timing ([14]). By adjusting injection conditions, it has been shown possible to achieve a combustion rate without the traditional ''spike'' at the start of combustion, combustion noise being dramatically reduced in this situation ([8]).

Injection Chambers. The ignition of DME into high temperature and pressure gases has also been studied ([25–27,30]). In this work, ignition delay was determined and compared to diesel fuel. The conditions studied covered a range of temperatures and pressures up to 925 K and 4.1 atm. It was found that for injection into air, the ignition delay of DME was very close to that of diesel, which is surprising, given that DME is generally considered to have a very high cetane number. The cetane number for DME is generally cited as being over 65. In addition, the spray location of the ignition with DME was at the same place as found with diesel fuel. When the oxygen concentration was reduced to ten percent, however, it was found that the ignition delay of DME was shorter than that of diesel fuel. This is interesting with respect to the ability of DME to operate with large amounts of exhaust gas recirculation, as studies have shown that DME can be used with higher amounts of EGR than diesel fuel ([5,7]).

A major difference between the two combustion processes with DME and diesel in the combustion bomb, was the absence of the strong yellow radiation with DME. This is always found in diesel combustion and has its origin in the carbon particles formed in the combustion process. The absence of this radiation is further confirmation of the soot free operation of DME, and shows that the carbon particles are not formed ([27]).

A consistent feature of engine tests has been that DME can be operated with large amounts of EGR as an effective method for NO_x reduction. The absence of soot from the combustion eliminates the problem of excessive particulate emissions, and the shorter ignition delay of DME in a low oxygen environment reduces the deterioration of combustion. The limiting factor with EGR is the formation of unburned fuel ([7]).

In conventional diesel combustion, radiation heat transfer during combustion can account for 30 to 40 percent of the total heat losses in the combustion period and about 20 percent of the total cycle averaged heat transfer ([31]). The absence of the strong radiation should have a beneficial effect on engine efficiency. Although heat transfer in a DME engine has not been measured, the fact that DME efficiencies are comparable to those of diesel fuel, even for long combustion duration suggests that there may be some benefits to be gained here from DME use. The measurement of heat transfer rates in a DME engine compared to a diesel engine presents an interesting opportunity for further study.

Table 2 compares the ignition delays from two constant volume systems with diesel fuel injection for equal temperatures and pressures of comparable level. Since pressures are not identical and

Table 2 A comparison of ignition delays (τ) for two constant volume injection chambers with diesel injection ([27,30])

Study	$10^3/T-K^{-1}$	P–atm	τ–ms
Edgar et al. [30]	1.4	35	12
Wakai et al. [27]	1.4	41	6.3
Edgar et al. [30]	1.2	35	1.2
Wakai et al. [27]	1.2	41	2.3
Edgar et al. [30]	1.4	7	45
Wakai et al. [27]	1.4	11	11
Edgar et al. [30]	1.2	7	9
Wakai et al. [27]	1.2	11	6.5

different injectors were used, the ignition delays are not completely comparable, but they can given an indication of trends. The results of [30] are more sensitive to temperature than those of [27].

Combustion Chemistry. Several studies have been conducted concerning the detailed chemistry of DME. While the scope of this paper is primarily the use of DME in diesel engines, such information is relevant to research studies. Therefore, a few studies will be mentioned, although this does not represent a thorough review. The references cited contain a series of additional references to detailed chemical studies.

A detailed chemical kinetic model has been developed which included 78 species and 336 chemical reactions ([32]). The model was used to compare with experimental data for well-stirred reactors and shock tubes. Good agreement was found between experiments in the literature and calculations for conditions ranging from 650 to 1300 K, 1 to 40 atmospheres, and equivalence ratios from 0.2 to 2.5. Edgar et al. [30] have also compared experimental and theoretical predictions of ignition delay in a constant volume heated chamber with a pintle nozzle. Using a reaction model of 57 species and 178 reactions, they too got good agreement between the calculations and experiments.

Detailed chemical kinetic studies have also been performed for conditions corresponding to exhaust gas ([33]). The mechanism was a modified version of that in a previous study ([32]). DME was found to oxidize readily at temperature above 1000 K. NO and NO_2 were found to enhance the oxidation rate for lean conditions.

Greenhouse Gases

As the local environment improves, more attention is being focused on the global warming. Studies have been conducted concerning the production of greenhouse gases from dimethyl ether (DME) ([20,34,35]). The focus of these studies has bee the use of DME in transport areas, primarily in urban busses. An analysis of the emissions from well to wheel has been performed for several fuels, and results are compared in Table 3. Other applications, such as light duty vehicles, are also attractive for DME, especially in the case where DME replaces gasoline.

In spite of a less favorable CO_2 production per gram fuel, diesel fuel was found to have the lowest emissions of greenhouse gases, basically because of its high in-use efficiency, particularly for part load operation. DME and CNG have both been calculated to have slightly higher greenhouse gas emissions than diesel. They start with natural gas which has a low CO_2 emission per kg fuel. DME loses 29 percent of the energy in the production process, but has low emissions during transport, and then is used in a diesel engine, an application with high efficiency. The engine efficiency with DME has been shown to be at least equal to that of diesel fuel, and actually greater for conditions of very low NO_x emissions ([5]). The production losses essentially negate the low CO_2 fuel emissions.

CNG is also a low CO_2 emission to start with, but has two large losses in the process of being used for transport. The first is the compression of the gas to 200–250 atmospheres, required for a reasonable driving range in buses. The compression work itself constitutes on the order of five percent of the heating value, and if this energy is produced by a heat engine, the compression energy required must be divided by the process efficiency to obtain the total energy required. The second loss is that of operation in a throttled engine. CNG engines have high compression ratios for spark ignited engines, but still suffer from part load throttling losses, important in urban operation. Operating experience with CNG and diesel has shown that in operation, CNG buses require about 14 percent more energy than diesel buses to drive the same distance.

These two losses in essence compensate for the energy losses encountered during the production of DME. Methane losses from pipeline and compression systems contribute to the greenhouse emissions of CNG, but are not well known. LPG and gasoline have considerably higher emissions of greenhouse gases than the other fuels, LPG because of lower efficiency in lower compression SI engines, and gasoline additionally due to unfavorable CO_2 emissions per gram fuel.

In the case where DME is produced by biomass the CO_2 emissions would be much lower, although the price of DME produced from biomass is expected to be considerably higher than that from remote natural gas. It should also be considered that in the comparison of greenhouse gas emission, the natural gas was not assumed to be gas that would otherwise be flared or re-injected in connection with oil production. In either of these cases, the CO_2 produced can be attributed to the production of useful work instead of just being an emission of CO_2. A CO_2 reduction would be obtained in that this work would replace work generated from other CO_2 producing sources. This would significantly improve the greenhouse gas picture previously presented for DME.

Table 3 Relative greenhouse gas emissions for different fuels as used in an urban bus application. Diesel fuel is given a value of 100 ([35]).

Fuel	Relative Value
Diesel	100
DME from natural gas	101
DME from biomass	20
CNG	100–110
LPG	115–120
Gasoline	145

Safety Aspects

Dimethyl ether (DME) has been safely handled in bulk for many years, due to its use as an aerosol propellant, and to date has a good safety record. Handling and safety procedures are similar to those of LPG, since the physical properties of these substances are quite similar. As such there is no fundamentally new technology required for DME use in the energy system. LPG regulations are typically used for DME, but in the event DME becomes a more widespread transport fuel, an evaluation of the safety and handling aspects of DME in this application should be undertaken to see if some modifications should be made.

In the initial DME diesel injection systems built, consideration is taken of the possibility of leakage of DME to the atmosphere when the engine is shut down. The most likely source would be leakage through the closed fuel injectors, but another source could include the volume of fuel in the high pressure common rail. Consequently, two systems have been used to control this. The first uses purging of the high pressure portion of the fuel system into a purge tank. High pressure DME is collected when the engine stops and recycled back to the fuel tank of the engine ([7]). The second system uses an activated charcoal filter, similar to the concept used on gasoline powered passenger cars ([23]). More data must be made available concerning actual rates of leakage and operating experience before a final judgement can be made for the need for eventual requirements of an evaporative emission control system.

Theoretical Considerations

Efforts are being made in connection with improving the understanding of scientific principles behind the behavior of DME. Some initial simplified combustion models have been made. One study was based on a spray model fit to the experimental results from studies of a DME spray, and constructed a model based only on mixing rates from simple jet theory ([36]). Combustion rates calculated during the mixing controlled portion of the combustion were found to agree with measurements from ([11]).

Another simple modeling effort has been developed in order to explain the formation of NO in DME combustion ([19]). They suggested that the mixing of air after diffusion combustion plays a

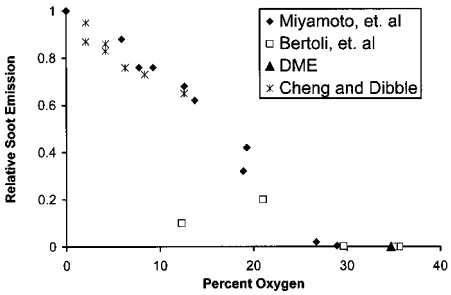

Fig. 2 Relative soot emissions as a function of mass percent oxygen in the fuel for different engine studies in diesel engines

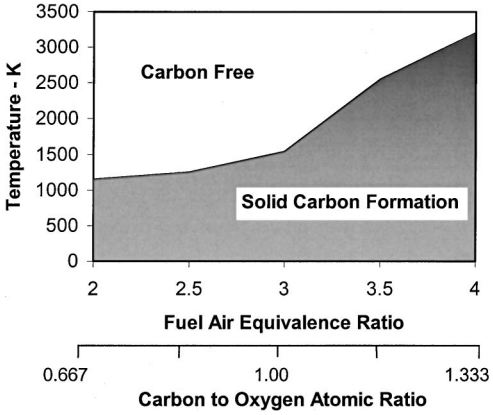

Fig. 3 Temperature above which equilibrium carbon is not formed for C_nH_{2n}, from calculations of Amann et al. [41]

significant role in NO formation, which raises the possibility of using extra turbulence to promote mixing and reduce NO formation. They performed some experiments with a secondary combustion chamber to promote turbulent mixing, but when corrected for the extra amount of fuel needed to generate the turbulence, found that there was not a major effect. Some CFD calculations of DME spray combustion have also been reported ([37]). DME should be simpler than diesel fuel for spray combustion calculations, since it is a single component with a high vapor pressure. It presents an interesting case for development of spray calculations because of these simplifications.

On the basis of new experimental and theoretical results on DME and diesel combustion related processes, it is possible to establish explanations for the combustion phenomena observed with DME. It appears that the soot-free combustion of DME is not necessarily related to the special properties of DME but rather to the presence of the oxygen in the fuel. Figure 2 shows a comparison of the relative reduction in soot or particular emissions compared to pure diesel fuel as a function of oxygen mass percent from three studies of oxygenated diesel fuels ([38–40]).

The results include a variety of pure oxygenated fuels as well as blends of oxygenated compounds in diesel fuel. Given the different base fuels and emission measurements techniques, the results show a good correlation with the oxygen percentage in the fuel. The results indicate that if the oxygen concentration in the fuel is above 30 mass percent, the soot emissions disappear. DME is also shown in the figure as a single point at 34.8 percent oxygen. As pointed out earlier, several studies have shown that there are no soot emissions from DME, and this single data point represents all previous engine studies.

A very simple qualitative explanation for these results can be given by referring to equilibrium calculations. While it is recognized that soot generation is far from an equilibrium process, equilibrium conditions can be used to provide a guideline as to tendencies, as is the case, for example, for NO formation. Calculations of equilibrium tendencies for soot formation have previously been prepared for a pure hydrocarbon fuel ([41]). Their results show a very dramatic dependence of equilibrium soot formation on temperature and equivalence ratio.

Actually it is not the equivalence ratio, *per se* that is needed for equilibrium calculations, but the ratio of the various atoms in the combustion products, in particular the ratio of carbon atoms to oxygen atoms ([42]). That is, combustion products with air are not affected by which fuel created them, but only by the ratios of the atoms of oxygen, nitrogen, carbon, hydrogen, and inert substances.

With pure hydrocarbon fuels, the ratio of carbon to oxygen atoms approaches infinity as the fuel air equivalence ratio approaches infinity. This is not possible with oxygenated fuels. Using DME as an example, the local carbon/oxygen ratio in the combustion products can never be greater than the ratio of these atoms in the molecule, that is two atoms of carbon per atom of oxygen. If one considers a hydrocarbon with a carbon/hydrogen ratio of 1:2, an equivalence ratio of 6 gives the same carbon oxygen ratio found with pure DME. Considering the products of combustion for oxygenated fuels then, no matter what the actual fuel air ratio, the combustion products can never have a higher carbon to oxygen ratio than that corresponding to a hydrocarbon fuel with an equivalence ratio of 6. As the equilibrium calculations show, the tendency to form solid carbon dramatically increases with carbon/oxygen ratio for pure hydrocarbons ([41]).

In the equilibrium calculation for solid carbon, the transition between the presence of solid carbon and its absence is extremely sharp, and for a range of equivalence ratios the results can be referred to in terms of an approximate temperature above which equilibrium carbon does not form. This is shown in Fig. 3.

As an example of the effect of oxygen in the fuel, consider the hydrocarbon-air mixture at an equivalence ratio of 3.0. Then a simple chemical calculation indicates that the carbon/oxygen ratio in the combustion products is 1.0. In order to achieve this same carbon/oxygen ratio, that is the same equilibrium tendency to form soot, a DME-air mixture would have to have an equivalence ratio of 6.0. Or seen from another point of view, a mixture of DME and air at an equivalence ratio of 3.0 would have a carbon/oxygen ratio of 0.667, which corresponds to a much leaner equivalence ratio of 2 in the case of the hydrocarbon fuel with the composition C_nH_{2n}. It can be shown that for any equivalence ratio, DME will always have a lower carbon/oxygen ratio than hydrocarbon fuels and therefore a lower tendency to form soot. The difference between the two substances increases as the mixture becomes richer.

It can be seen that according to the diesel combustion model presented by Dec [43], the first combustion in a diesel engine occurs at an equivalence ratio of 2 to 4, where the fuel is converted to rich combustion products. The soot precursors and soot are formed in the region. By bringing oxygen into this region, oxygenated fuels reduce the tendency towards soot formation on an equilibrium basis, and most likely also on the basis of detailed chemical mechanisms. With DME, for example, the combustion products could never be found in a condition that corresponds to a hydrocarbon fuel richer than an equivalence ratio of 3. In an actual diesel engine situation, the mixture would be leaner due to entrained air. That the initial combustion does not occur at overly lean mixtures is confirmed by the fact that DME in general does not produce higher NO_x emissions than diesel fuel.

The experiments by Dec also indicate that NO formation in diesel combustion only occurs in the diffusion flame surrounding the rich products of combustion in the plume of the burning spray. The initial combustion process in diesel engines plays a significant role in determining the temperature history of the diffusion flame. The higher the initial rate of combustion, the higher the temperature level through the engine diffusion burning portion, and the higher the NO_x emission. This is shown by a good corre-

lation of NO_x emission with either peak cylinder pressure of rate of pressure rise ([44]). This was previously explained as due to an increased amount of initial lean combustion, but the results of Dec offer an alternative explanation based on detailed observations of the NO formation process in a diesel engine.

Future Perspectives

When applied to transport engines dimethyl ether (DME) faces the same problems as all other alternatives to petroleum-based fuels, namely that they must compete with an immense long-established system for providing transport fuels. General resistance to change is well known in this respect, even for liquid fuels such as methanol and ethanol. In addition, major production facilities for DME must be established before it can be considered a practical alternative.

However, the concept of using DME only as a transportation fuel is much too restrictive. There is much more potential in a DME-based system than just its use as a transport fuel. The general concept is illustrated in Fig. 4. DME can be produced from a variety of sources, including natural gas, coal, and different types of biomass. As such, it can be considered as a common product, that is, regardless of the source, one can produce a common fuel.

The flexibility of fuel source is an important issue for the long term. Eventually, production petroleum sources will not be able to keep up with demand, leading to increased prices. In such a scenario, other fuel sources will be needed to become competitive economically, and through the use of a common fuel, effects of changes in fuel supply technology on applications would be reduced. That is, as the fundamental fuel source changes, the fuel could still be the same.

DME as a common fuel can then be used for a variety of applications. An obvious application is that of transport diesel engines, but other applications are equally promising. Gas turbines or stationary diesel engines can use DME, and could provide electrical power, drive pumps, compressors, etc. DME could also be used in rail or marine applications instead of diesel. DME can be used as a replacement for LPG in a variety of applications, where small pressurized tanks of fuel are used in a distributed system for heating purposes, or other forms for energy as is done today. DME can be used as a feed stock for various chemicals. DME can also be used to produce hydrogen for a fuel cell with similar processes as proposed for methanol. It has a slightly higher hydrogen content than methanol. Should fuel cells become common, they represent another potential use of DME. While not all of the above have been demonstrated with DME, it is the intent to indicate that DME can be seen as a potentially useful commodity in many other areas in addition to being an alternative to diesel fuel in transport.

The introduction of DME on a large scale into the international energy supply system would be greatly facilitated in applications involving one or few consumers being supplied from a single source. Contractual, financial, and infrastructure considerations would be much simpler here than in the case of transportation applications. For transportation use, the large number of vehicles, multiple manufacturers and infrastructure in various cites make it difficult to establish the commitments on a time and demand scale necessary for a DME production facility on the order of 5000 tons/day, a size giving economies of scale ([6]). On the other hand, supply to a few customers would improve the availability of DME, which could be made available for special transportation applications, with an originally small demand in a growing market. The flexibility of DME with respect to both source and application increases the attractiveness of DME in the long term.

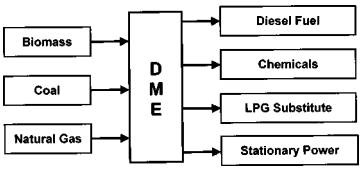

Fig. 4 A schematic diagram of a future fuel system in which dimethyl ether plays a central role for obtaining fuel from different sources for different applications

There are major advantages in terms of establishing an initial production system for DME fuel to supplying a smaller number of very large engines to few customers. It would be easier to conduct agreements with fuel customers, larger stationary applications would be simpler to construct and initially more reliable than a large number of small portable units on vehicles, though the latter is possible as shown by LPG technology. Additionally, the infrastructure would be simpler than with a distributed transport system.

In a practical sense, it is likely that other applications than transport engines will initiate the large scale production of DME. The demonstration of low price availability of DME will provide confidence for developers of initial smaller scale applications, including initial transport uses.

Such efforts have been initiated. The government of India and BPAmoco have announced a joint investigation of the potential use of DME in the Indian energy supply picture ([45]). In this environment, DME represents a potential source of energy for stationary power generation for either Rankine or gas turbine fired units, a replacement for the commonly used fuel LPG, as well as a transportation fuel. This, in connection with close geographic proximity to large amounts of low-priced natural gas, presents a very interesting possibility for the introduction of DME on large scale into the energy supply picture.

Conclusions

Since the presentation of neat dimethyl ether (DME) as a diesel fuel in 1995, several studies have been performed which have improved our understanding of the combustion process with DME. Engine studies over a range of sizes have confirmed the benefits of DME operation in diesel engines. Fundamental studies illuminating the behavior of DME sprays and the ignition delay process have been performed.

Dedicated DME fuel systems have been developed for diesel engines.

Additional efforts are needed to make improvements in sealing materials and the lubricity/wear situation with DME.

The reduction of particulates by DME is consistent with that of other oxygenated fuels, in that other diesel fuels containing more than 30 mass percent oxygen do not produce soot emissions either. Experimental observations and theoretical considerations indicate that carbon particles are not formed in the DME flame.

DME is competitive with diesel fuel and CNG on well to wheel greenhouse gas emissions basis.

DME can play a much larger role in future energy systems than just as a diesel engine fuel for transport applications. The application of DME to large stationary applications with few suppliers and customers would be advantageous in the realization of large scale DME production, and could make DME more readily available for transport applications, or applications where smaller amounts of DME are used.

References

[1] Brook, D. L., Rallis, C. J., Lane, N. W., and Dipolat, C., 1984, ''Methanol with Dimethyl Ether Ignition Promoter as Fuel for Compression Ignition Engines,'' *Proceedings of the 19th Intersociety Energy Conversion Engineering Conference*, pp. 654–658.

[2] Murayama, T., Chikahisa, J., Guo, J., and Miyano, M., 1992, ''A Study of Compressions Ignition Methanol Engine With Converted Dimethyl Ether as an Ignition Improver,'' SAE Paper 922212.

[3] Cipolat, D., Jawurek, H. H., and Rallis, C. J., 1991, ''Methanol/Diethyl Ether Fuelling of a Compression Ignition Engine,'' *Proceedings of the IX International Symposium on Alcohol Fuels*, pp. 411–415.

[4] Guo, J., Chikashisa, T., and Murayama, T., 1994, ''Improvement of Performance and Emissions of a Compression Ignition Methanol Engine with Dimethyl Ether,'' SAE Paper 941908.

[5] Sorenson, S. C., and Mikkelsen, S. E., 1995, ''Performance and Emissions of a 0.273 Liter Direct Injection Diesel Engine Fueled With Neat Dimethyl Ether,'' SAE Paper 950964.
[6] Hansen, J. B., Voss, B., Joensen, F., Sigurdardóttir, I.-D., 1995, ''Large Scale Manufacture of Dimethyl Ether—A New Alternative Diesel Fuel From Natural Gas,'' SAE Paper No. 950063.
[7] Fleisch, T., McCarthy, C., Basu, A., Udovich, Charbonneau, P., Slodowske, W., Mikkelsen, S.-E., and McCandless, J., 1995, ''A New Clean Diesel Technology: Demonstration of ULEV Emissions on a Navistar Diesel Engine Fueled With Dimethyl Ether,'' SAE Paper 950061.
[8] Kapus, P., and Ofner, H., 1995, ''Development of Fuel Injection Equipment and Combustion System for DI Diesels Operated on Dimethyl Ether,'' SAE Paper 950062.
[9] Ofner, H., Gill, D. W., and Kammerdiener, T., 1996, ''A Fuel Injection Concept for Dimethyl Ether,'' *Application of Powertrain and Fuel Technologies to Meet Emissions Standards*, ASME, New York, p. 289.
[10] Sorenson, S. C., Glensvig, M., and Abata, D. L., 1998, ''Dimethyl Ether in Diesel Fuel Injection Systems,'' SAE Paper 981159.
[11] Christensen, R., Sorenson, S. C., Jensen, M. G., and Hansen, K. F., 1998, ''Engine Operation on Dimethyl Ether in a Naturally Aspirated, DI Diesel Engine,'' SAE Paper 971665.
[12] Glensvig, M., Sorenson, S. C., and Abata, D. L., 1996, ''High Pressure Injection of DME,'' *Alternative Fuels*, Vol. 27-3, ASME, New York, p. 57.
[13] Glensvig, M., Sorenson, S. C., and Abata, D. L., 1997, ''An Investigation of the Injection Characteristics of Dimethyl Ether,'' *Engine Combustion, Performance and Emissions*, ICE-Vol. 29-3, ASME, New York, p. 77.
[14] McCandless, J., Teng, H., and Schneyer, J. B., 2000, ''Development of a Variable-Displacement, Rail-Pressure Supply Pump for Dimethyl Ether,'' SAE Paper 2000-01-0687.
[15] Nielsen, K., and Sorenson, S. C., 1999, ''Lubricity Additives and Wear With DME in Diesel Injection Pumps,'' *Emissions, Fuels and Lubricants and HSDI Engines*, ICE-Vol. 33-1, ASME, New York, pp. 145–153.
[16] Bowman, F. M., and Seinfeld, J. H., 1995, ''Atmospheric Chemistry of Alternative Fuels and Reformulated Gasoline Components,'' Prog. Energy Combust. Sci., **21**, pp. 387–417.
[17] Japar, S. M., Wallington, T. J., Richert, J. F. O., and Ball, J. C., 1990, ''The Atmospheric Chemistry of Oxygenated Fuel Additives: t-butyl Alcohol, Dimethyl Ether, and Methyl t-butyl Ether,'' Int. J. Chem. Kinet., **22**, pp. 1257–1269.
[18] Mikkelsen, S.-E., Hansen, J. B., and Sorenson, S. C., 1996, ''Dimethyl Ether as an Alternate Fuel for Diesel Engines,'' *Application of Powertrain and Fuel Technologies to Meet Emissions Standards*, ASME, New York, p. 289.
[19] Konno, M., Kajitani, S., Oguma, M., Iwase, T., and Shima, K., 1999, ''NO Emission Characteristics of a CI Engine Fueled With Neat Dimethyl Ether,'' SAE Paper 1999-01-1116.
[20] Fleisch, T. H., and Meurer, P. C., 1995, ''DME: The Diesel Fuel for the 21st Century?'' presented at the AVL Conference ''Engine and Environment 1995,'' Graz, Austria.
[21] Kapus, P., and Cartellieri, W., 1995, ''ULEV Potential of a DI/TCI Diesel Passenger Car Engine Operated on Dimethyl Ether,'' SAE Paper 952754.
[22] McCandless, J. C., and Li, S., 1997, ''Development of a Novel Fuel Injection System (NFIS) for Dimethyl Ether,'' SAE Paper 970220.
[23] Bek, B. H., Michalek, D. J., Abata, D. L., and Sorenson, S. C., 1999, ''The Onset of Cavitation During Injection of Low Viscosity High Vapor Pressure Fuels,'' *Engine Design, Controls and DI Sprays*, ICE-Vol. 33-2, ASME, New York, pp. 85–91.
[24] Sorenson, S. C., Bek, B. H., Glensvig, M., and Abata, D. L., 1998, ''Dimethyl Ether Injection Studies,'' *Proceedings of the Second International Workshop on Advanced Spray Combustion*, Hiroshima, Japan, Nov. 25.
[25] Wakai, K., Nishida, K., Yoshizaki, T., and Hiroyasu, H., 1998, ''Spray and Ignition Characteristics of Dimethyl Ether Injected by a D. I. Diesel Injector,'' *The Fourth International Symposium COMODIA 98*, JSME, Japan, pp. 537–542.
[26] Wakai, K., Yoshizaki, T., Nishida, K., Hiroyasu, H., and Kawaguchi, Y., 1999, ''Numerical and Experimental Analyses on the Injection Characteristics of Dimethyl Ether With a D. I. Diesel Injection System,'' SAE Paper 1999-01-1122.
[27] Wakai, K., Nishida, K., Yoshizaki, T., and Hiroyasu, H., 1999, ''Ignition Delays of DME and Diesel Fuel Sprays Injected by a D. I. Diesel Injector,'' SAE Paper 1999-01-3600.
[28] Xu, M., Nishida, K., and Hiroyasu, H., 1992, ''A Practical Calculation Method for Injection Pressure and Spray Penetration in Diesel Engines,'' SAE Paper 960642.
[29] Dec, J. E., and Canaan, R. E., 1998, ''PLIF Imaging of NO Formation in a DI Diesel Engine,'' SAE Paper 980147.
[30] Edgar, B. L., Dibble, R. W., and Naegeli, D. W., 1997, ''Autoignition of Dimethyl Ether and Dimethoxy Methane Sprays at High Pressures,'' SAE Paper 971677.
[31] Flynn, P., Mizusawa, M., Uyehara, O. A., and Myers, P. S., 1972, ''An Experimental Determination of the Instantaneous Potential Radiant Heat Transfer Within an Operating Diesel Engine,'' *SAE Transactions*, Paper 720022.
[32] Curran, H. J., Pitz, W. J., Westbrook, C. K., Augaut, P., Boettner, J. C., and Cathonnet, M., 1998, ''A Wide Range Modeling Study of Dimethyl Ether,'' Int. J. Chem. Kinet., **30**, pp. 229–241.
[33] Alzueta, M., Moro, U. J., Bilbao, R., and Glarborg, P., 1999, ''Oxidation of Dimethyl Ether and Its Interaction With Nitrogen Oxides,'' Isr. J. Chem., **39**, pp. 73–86.
[34] Ofner, H., Gill, D. W., and Krotscheck, C., 1998, ''Dimethyl Ether as Fuel for CI Engines—A New Technology and Its Environmental Potential,'' SEA Paper 981158.
[35] Verbeek, R., and Van der Weide, J., 1997, ''Global Assessment of Dimethyl-Ether: Comparison With Other Fuels,'' SAE Paper 971607.
[36] Bek, B. H., and Sorenson, S. C., 1997, ''A Mixing Based Model for DME Combustion in Diesel Engines,'' *Gas Engines and Alternative Fuels*, ICE-Vol. 31-3, ASME, New York, p. 97.
[37] Nordin, N., Golovitchev, V. I., and Chomiak, C., 1998, ''Computer Evaluation of DI Diesel Engine Fueled With Neat Dimethyl Ether,'' presented at the 22nd CIMAC Conference, Copenhagen, May 18–21.
[38] Beatrice, C., Bertoli, C., Del Giacomo, N., and Lazzaro, M., 1996, ''An Experimental Characterization of the Formation of Pollutants in DI Diesel Engines Burning Oxygenated Synthetic Fuels,'' *Application of Powertrain and Fuel Technologies to Meet Emissions Standards*, IMechE, London, p. 261.
[39] Cheng, A. S., and Dibble, R. W., 1999, ''Emissions Performance of Oxygenate-in-Diesel Blends and Fisher-Tropsch Diesel in a Compression Ignition Engine,'' SAE Paper 1999-01-3606.
[40] Miyamoto, N., Ogawa, H., Nurun, N. M., Obata, K., and Arima, T., 1998, ''Smokeless, Low NO_x High Thermal Efficiency, and Low Noise Diesel Combustion With Oxygenated Agents as Main Fuel,'' SAE Paper 980506.
[41] Amann, C. A., Stivender, D. L., Plee, S. L., and MacDonald, J. S., 1980, ''Some Rudiments of Diesel Particulate Emissions,'' SAE Paper 80251.
[42] Streholw, R. A., 1984, *Combustion Fundamentals*, McGraw-Hill, New York.
[43] Dec, J. E., 1997, ''A Conceptual Model of DI Diesel Combustion Based on Laser-Sheet Imaging,'' SAE Paper 970873.
[44] Scholl, K. W., and Sorenson, S. C., 1993, ''Combustion of Soybean Oil Methyl Ester in a Direct Injection Diesel Engine,'' *SAE Transactions*, Paper 930934.
[45] Van Doorn, T., ed., 1999, ''Dimethyl-ether as Automotive Fuel,'' DME Newsletter 3, IEA Newsletter, TNO Automotive.

J. Li[1]
Y. Huang
T. F. Alger
R. D. Matthews
M. J. Hall

Department of Mechanical Engineering,
College of Engineering,
The University of Texas,
Austin, TX 78712-1063

R. H. Stanglmaier
C. E. Roberts

Southwest Research Institute,
San Antonio, TX 78250

W. Dai
R. W. Anderson

Ford Motor Company,
Dearborn, MI 48124

Liquid Fuel Impingement on In-Cylinder Surfaces as a Source of Hydrocarbon Emissions From Direct Injection Gasoline Engines

Hydrocarbon (HC) emissions from direct injection gasoline (DIG) engines are significantly higher than those from comparable port fuel injected engines, especially when ''late'' direct injection (injection during the compression stroke) is used to produce a fuel economy benefit via unthrottled lean operation. The sources of engine-out hydrocarbon emissions for late direct injection are bulk flame quench, low temperatures for post-combustion oxidation, and fuel impingement on in-cylinder walls. An experimental technique has been developed that isolates the wall impingement source from the other sources of HC emissions from DIG engines. A series of steady-state and transient experiments is reported for which the HC emissions due to operation with a premixed charge using a gaseous fuel are compared to those when a small amount of liquid fuel is injected onto an in-cylinder surface and the gaseous fuel flow rate is decreased correspondingly. The steady-state experiments show that wetting any in-cylinder surface dramatically increases HC emissions compared to homogeneous charge operation with a gaseous fuel. The results of the transient fuel injection interrupt tests indicate that liquid-phase gasoline can survive within the cylinder of a fully warmed-up firing engine and that liquid fuel vaporization is slower than current computational models predict. This work supports the argument that HC emissions from DIG engines can be decreased by reducing the amount of liquid fuel that impinges on the cylinder liner and piston, and by improving the vaporization rate of the fuel that is deposited on these surfaces. [DOI: 10.1115/1.1370398]

Introduction

Direct injection gasoline (DIG) engines can offer a substantial improvement in fuel economy and a significant increase in torque in comparison to port fuel injected (PFI) engines. These benefits of DIG engines are well understood ([1]) and have been documented extensively in the past (e.g., Refs. [2–6]). Light-duty vehicles with DIG engines are currently available in the Japanese and European markets.

However, the exhaust emissions from DIG engines are too high to meet the strict U.S. emissions standards to which PFI engines conform. In comparison with similar vehicles equipped with PFI engines, tailpipe emissions of unburned hydrocarbons (HCs) from DIG engine-equipped vehicles operating over the FTP driving cycle have been reported to be two to three times higher and NO_x emissions are four to ten times higher ([3,5]). Stovell et al. [5] report that CO emissions are somewhat lower than for a comparable vehicle with a port fuel injected engine and that particulate emissions are sufficiently low to pass LEV standards but too high to pass LEV II standards. The high tailpipe NO_x emissions stem from the low efficiency of lean NO_x catalysts whereas the high tailpipe HC emissions result from very high engine-out HCs, especially during late injections ([5,6]). Thus, while higher efficiency catalysts may help alleviate the NO_x emissions challenge from future direct injection gasoline vehicles, the HC emissions problems will have to be addressed in-cylinder.

This paper is focused upon the sources of engine-out HC emissions from direct injection gasoline engines.

Hydrocarbon Emissions From Direct Injection Gasoline Engines. At a constant engine speed of 2000 rpm, Matthews and co-workers [6] varied the load of a vehicle with a DIG engine to examine the emissions as the injection timing changed from late (injection during the compression stroke for low and medium loads) to early (injection during the intake stroke at high load). They found that the early-injection mode (near-stoichiometric, nominally homogeneous charge) engine-out HC Emissions Index (grams HCs per kg fuel) was about twice as high as that for a comparable PFI engine. The HC Emissions Index for late injection (lean, stratified charge) was higher still, by a factor of up to four. At the Ford World Wide Mapping Point (WWMP, 1500 rpm, 2.62 bar BMEP), Brehob and co-workers [4] measured the brake specific HCs to be ~25 percent higher when using air-forced early injection (nominally homogeneous charge) than those from the same engine operating with port fuel injection. For late injection, the brake specific HCs increased monotonically with increasing air/fuel ratio, and were about three times higher at 39:1 compared to stoichiometric port fuel injection. These investigators also found that use of EGR with late injection decreased BSHCs, in contrast to the slight increase in BSHCs when EGR is used with port fuel injection. These results are indicative of significant differences in the HC formation mechanisms present in DIG and PFI gasoline engines. Brehob and co-workers also found that the BSHCs were slightly lower at an air/fuel ratio of 20:1 for late injection than for early injection for two different DIG engines. That is, there are also differences in the HC mechanisms between late and early injection for DIG engines. These differences are discussed below.

Early-Injection Hydrocarbon Mechanisms. From an HC emissions standpoint, the only difference between early direct injection and port injection is the mixture preparation process. In port injected engines, most of the vaporization process occurs in the intake port, prior to the fuel entering the cylinder. In a fully

[1]Currently with Cummins Engine Company, 1113-D Thicket Court, Columbus, IN 47201.

Contributed by the Internal Combustion Engine Division of THE AMERICAN SOCIETY OF MECHANICAL ENGINEERS for publication in the ASME JOURNAL OF ENGINEERING FOR GAS TURBINES AND POWER Manuscript received by the ICE Division July 2000; final revision received by the ASME Headquarters Dec. 2000. Associate Editor: D. Assanis.

warmed-up PFI engine, only a small percentage, if any, of the fuel enters the combustion chamber in liquid form. In DIG engines, liquid fuel droplets must vaporize within the cylinder, and some of this fuel inevitably impinges on the cylinder line and/or the piston top. This phenomenon is usually referred to as fuel wall-wetting. All other commonly accepted sources of HCs—including crevices, deposits, and oil films—are thought to be equivalent between homogeneous DI and PFI engines (except that wall-wetting may exacerbate the effect of oil films, deposits, and crevices). Since in-cylinder temperatures are nearly identical, for equal equivalence ratios, post-combustion oxidation rates are also thought to be equal. Thus, it is surmised that wall-wetting is largely responsible for the high HC emissions levels from early-injection, or homogeneous, DIG engines.

Late-Injection Hydrocarbon Mechanisms. There are several potentially significant differences in the HC mechanisms between port-injected and late direct injected gasoline engines:

- Bulk flame quenching may occur as the flame propagates into very lean regions of the combustion chamber. This mechanism is not significant for a homogeneous charge unless it is very lean.
- Lean engine operation results in much lower in-cylinder temperatures, and correspondingly reduced post-combustion oxidation rates during stratified operation. A homogeneous charge cannot operate as lean as a stratified charge, and thus yields higher temperatures for post-combustion oxidation.
- Late fuel injection results in a large reduction in the packing of the top-land crevice with unburned fuel. This crevice has been identified as the principal source of unburned HCs in fully warmed-up homogeneous PFI gasoline engines (e.g., Refs. [7–9]). Unless liquid fuel impacts the liner during late injection, the top land crevice source of HCs should be negligible in comparison to both early injection and PFI engines.
- Late in-cylinder injection causes increased fuel-wall impingement, or wall-wetting, on the piston top and possibly the cylinder liner during stratified operation ([10–12]). This mechanism is thought to increase HC emissions in late-injection DI gasoline engines.

The work presented in this paper concentrates exclusively on investigating the effect of wall-wetting on HC emissions from DIG engines, and the experiments presented here were designed to isolate this HC mechanism from all other effects.

Wall-Wetting in Direct Injection Gasoline Engines. There is considerable computational and experimental evidence of wall-wetting in direct injection gasoline engines. A number of engine simulation codes have been used to predict the mixture preparation process and fuel droplet vaporization rates within DIG engines. These engine simulations range from those with relatively simple drop vaporization models ([13]) to those that incorporate sophisticated spray models ([14–17]). For some operating conditions, these codes predict that as much as 70 percent of the injected fuel mass can impinge on the piston top and cylinder liner. Experimental studies performed in optically accessible engines support these predictions, at least qualitatively ([10–12,17]). The amount and location of wall-wetting depends on the engine geometry and in-cylinder flow, the injection timing, and other engine and control parameters. Late fuel injection timings result in increased wetting of the piston top and a larger overall mass of fuel deposited on the walls. Depending upon the injection timing and bulk flow, early injection can result in wetting of both the piston and the cylinder liner. Dodge [13] asserts that some degree of wall-wetting is unavoidable for all DI gasoline engine operating conditions with the current fuel injector technology.

Given that wetting of the cylinder liner and piston top occurs in DI gasoline engines, the focus of interest becomes determining what transpires with this fuel. Recent engine simulation codes predict that wall-bound fuel drops from a film on the combustion chamber walls and vaporizes rapidly, mostly before the flame passes by its location ([14–17]). However, recent experiments have shown that wall-wetting results in a large increase in HC emissions ([18,19]) and indicate that the vaporization process is slow.

Goals of the Present Study. The objectives of the present work were to (1) study the effect of in-cylinder wall wetting on hydrocarbon emissions compared with inducting the same amount of liquid fuel via port injection and (2) examine the rate of vaporization of liquid fuel from the in-cylinder surfaces of a firing engine.

Engine Experiments

A series of engine tests have been performed in an attempt to elucidate the process by which wall-wetting results in increased hydrocarbon (HC) emissions from spark ignition engines. This work was performed on one cylinder of a four cylinder, four valves/cylinder production port fuel injected (PFI) gasoline engine (a 1992 General Motors Quad-4). A specially designed directional injection probe, capable of injecting a stream of liquid fuel onto any desired surface within the combustion chamber, was used to inject a small amount of liquid fuel into the test cylinder while the engine operated predominately on a gaseous fuel. The details of this injection probe, the test engine, and the experimental procedure have been discussed previously ([18,19]), but a brief review is presented below.

A schematic drawing of the injection probe is shown in Fig. 1. This fuel injection probe is designed to inject a poorly atomized fuel stream, of known mass, onto one of the five locations indicated in Fig. 2: on the piston top and on the liner just under the head and between the two exhaust valves, between the two intake valves, and between the intake and exhaust valves on either side of the cylinder. The probe is mounted on a Champion 304-802 offset electrode spark plug through the hole that is normally used for mounting a cylinder pressure transducer. A fuel pressure of ~930 kPa (120 psig) was used to inject the liquid fuel. The injection probe used in this work does not reproduce the spray characteristics of a DI gasoline injector. However, the fraction of the total fuel deposited on the walls (11–18 percent for most of the present tests) is less than the 30–70 percent predicted for late direct injection ([13–17]). That is, although the film formation dynamics may differ between these experiments and an actual DIG engine, the film mass is much smaller in the experiments than in DIG engines with late injection.

The engine was run on pre-vaporized liquefied petroleum gas (LPG) except for the small amount of liquid fuel (California Phase 2 RFG) deposited on the walls. At atmospheric pressure, the end boiling point for Cal. Phase 2 RFG is almost 180 °C (~450 K). In comparison, simulations for this engine, using Ford's GESIM engine code, with propane fueling and running at this same operating condition revealed a liner temperature of 388 K and a piston temperature of 422 K, as illustrated in Fig. 3.

To minimize the sensitivity of the HC emissions to minor variations in stoichiometry, the excess air ratio was maintained at a constant and slightly lean value before and after depositing the California Phase 2 RFG ($\lambda=1.1$, corresponding to an equivalence ratio $\phi\sim0.9$). During the initial LPG-only operation, the LPG flow rate was adjusted to hold the excess air ratio at $\lambda=1.1$. In the second stage of the procedure, a chosen mass of liquid fuel was injected onto the desired in-cylinder surface using the injection probe. Upon liquid fuel introduction, the overall excess air ratio decreases (the mixture approaches stoichiometric or becomes rich). The overall excess air ratio was then returned to $\lambda=1.1$ by reducing the LPG flow rate, and data were recorded after achieving steady state. Injector interrupt tests were performed by stopping liquid fuel injection but continuing to monitor the excess air ratio using a Horiba Model 101λ wide range lambda sensor.

Two engine operating conditions were studied: 1000 rpm idle and the Ford World Wide Mapping Point (WWMP: 1500 rpm,

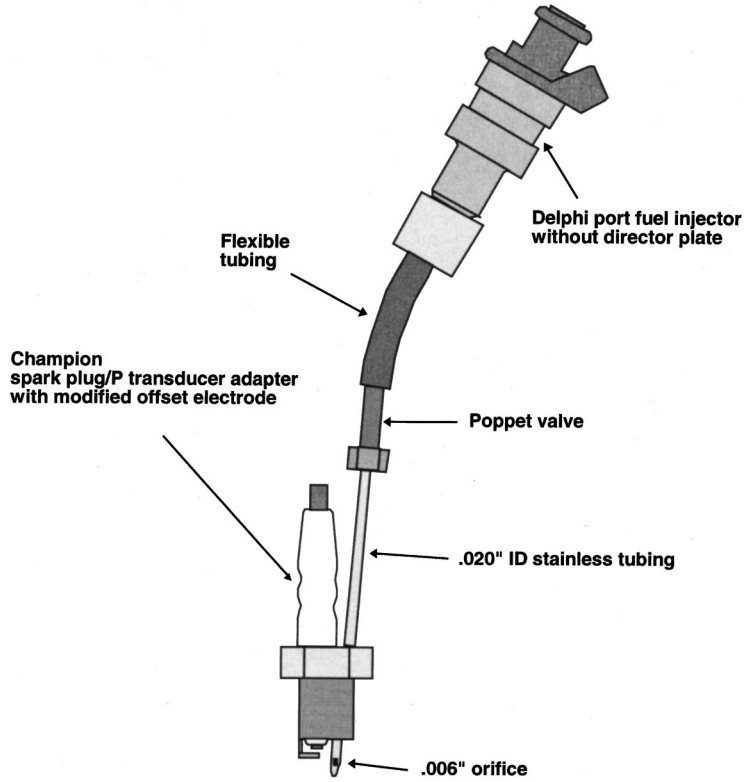

Fig. 1 Directional injection probe used to place liquid fuel on various locations within the combustion chamber

262 kPa BMEP). For most of the tests, 1.5 mg of liquid fuel was injected per cycle. At idle, this is 18 percent of the total fuel mass flow, and 11 percent at the WWMP.

Because the engine is operated predominately on a gaseous fuel with a slightly lean mixture, the bulk quench source and low oxidation temperature source of HC emissions from DIG engines are eliminated. This isolates the wall wetting source from the other two sources of HC emissions for DIG engines with late injection. By comparing the HC emissions when the engine is operating exclusively on LPG to those when operating on LPG plus a small amount of liquid fuel, at equal equivalence ratios, it is possible to examine the HC contribution due to wall-wetting and to measure the percentage of injected liquid fuel that is detected in the exhaust stream.

In the following section, the prior results from this series of experiments are reviewed followed by discussion of new data that is intended to clarify uncertainties from the prior tests. The variables investigated are the effects of fuel injection timing (residence time on the walls), wall-wetting location, coolant temperature, engine operating conditions, and wall wetting amount. The time constant for liquid fuel evaporation is also examined.

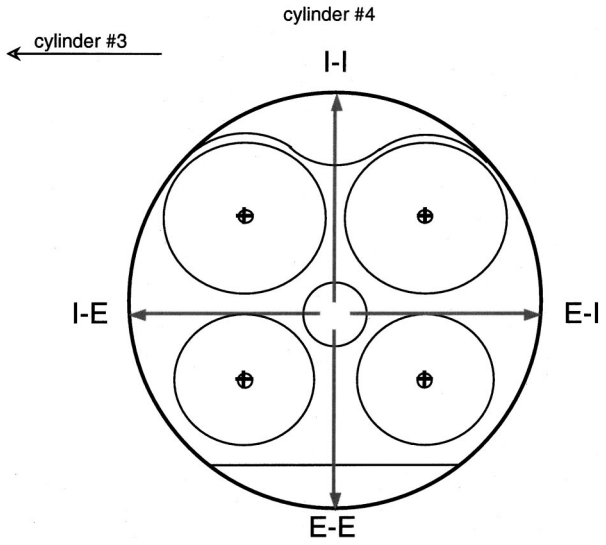

Fig. 2 Engine geometry and wall-wetting locations examined (piston wetting location not illustrated)

Test Results

Figure 4 compares the engine-out HC emissions for all wetting locations and LPG-only at idle, and also illustrates the effects of liquid injection timing. The injection timing has only a slight effect on the HC emissions. That is, varying the residence time of liquid fuel on the walls by changing the injection timing from during the exhaust stroke to during the compression stroke has almost no effect on the HC emissions. These results indicate that the vaporization rate of liquid fuel off the combustion chamber walls is slow compared to the engine cycle, even at 1000 rpm.

Figure 4 also illustrates the effects of wetting location. With 1.5 mg of liquid injected (18 percent of the total fuel mass), wall-wetting resulted in a large increase in the HC emissions for all surfaces examined. The largest increase in HC emissions was obtained for wetting of the cylinder liner under the exhaust ports (E-E), the smallest increase was observed for liner wetting under the intake ports (I-I), and the intermediate liner locations (I-E, and E-I) produced HC emissions between these two extremes. Wetting on the piston top resulted in the second highest increase in HCs, despite the fact that fuel deposited on the piston top cannot be scraped into any crevices or lost to the crankcase. These trends were observed for all coolant temperatures, wetting amounts, and

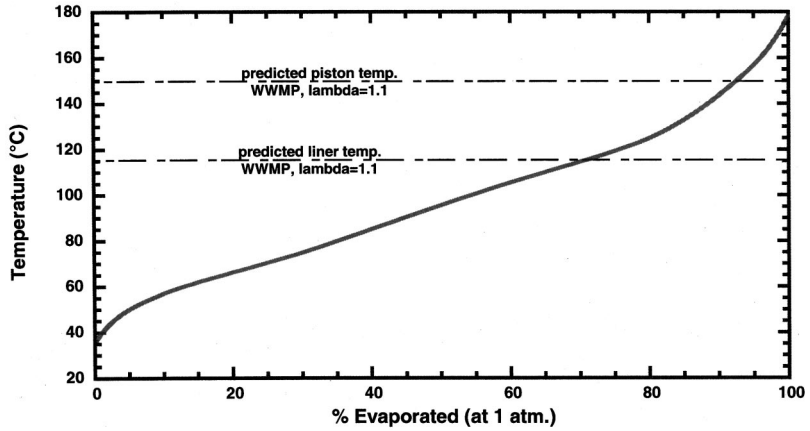

Fig. 3 Atmospheric pressure distillation curve for California Phase 2 reformulated gasoline. GESIM predictions for the piston and linear temperatures for this engine and operating conditions are shown for comparison.

engine operating conditions examined. The effects of wetting location can be explained by considering the physical distance from the wetting location to the exhaust port, which affects both the potential for in-cylinder oxidation and the probability that a portion of the evaporated fuel is retained within the cylinder and burned during the next cycle ([18]). Additionally, liquid fuel on the liner can escape past the rings and into the crankcase whereas liquid impacting the piston has little possibility of escaping into the crankcase. This effect is discussed more with respect to Fig. 5. Time-resolved HC emissions measurements, obtained using a Fast Flame Ionization Detector, were used to further clarify the effects of wall wetting location ([19]). The interested reader is referred to the original reference for details regarding the interpretation of the FFID results.

Some of the liquid fuel that impinges on the cylinder liner is collected in the top land crevice, forced past the piston rings by the cylinder pressure, and lost to the crankcase. This fraction of the liquid fuel does not contribute to engine-out HCs, but is unproductive nonetheless. As explained by Stanglmaier and coworkers [18], measurements of the excess air ratio during liquid fuel injection ($\lambda=1.1$) and following the cessation of liquid fuel injection (leaner than $\lambda=1.1$) can be used to determine the fraction of the liquid fuel injected that can be accounted for in the exhaust. Figure 5 shows the results of such calculations for the same conditions as those used for Fig. 4. Figure 5 shows that virtually all of the liquid fuel injected onto the piston exits the cylinder as either unburned HCs or burned combustion products. For all liner wetting locations, some of the injected liquid fuel was lost to the crankcase. Thus, wall-wetting on the cylinder liner is not only detrimental to HC emissions, but also undoubtedly contributes to oil degradation and increased liner and ring wear rates.

In our previous work we also examined the effects of coolant temperature on the HC emissions due to wall wetting ([18,19]). At both idle and the WWMP, the coolant temperature did not significantly affect the HC emissions for piston wetting, probably because the piston temperature does not change significantly over the range of coolant temperatures examined (40 and 90 °C). For liner wetting, the HC emissions at the WWMP were more sensitive to the coolant temperature than at idle. Increasing the coolant temperature from 40 °C to 90 °C had a larger effect on the HC emissions during LPG-only operation than for any of the wall wetting experiments at idle. That is, the conventional crevice source of HCs (for PFI engines, and for the present gaseous fueling baseline) is more sensitive to coolant temperature than is liner wetting for idle operation. On the other hand, the increase in HC emissions for the liner wetting locations at the WWMP was larger than can be accounted for by the increase in the LPG crevice source when the coolant temperature decreased from 90 °C to

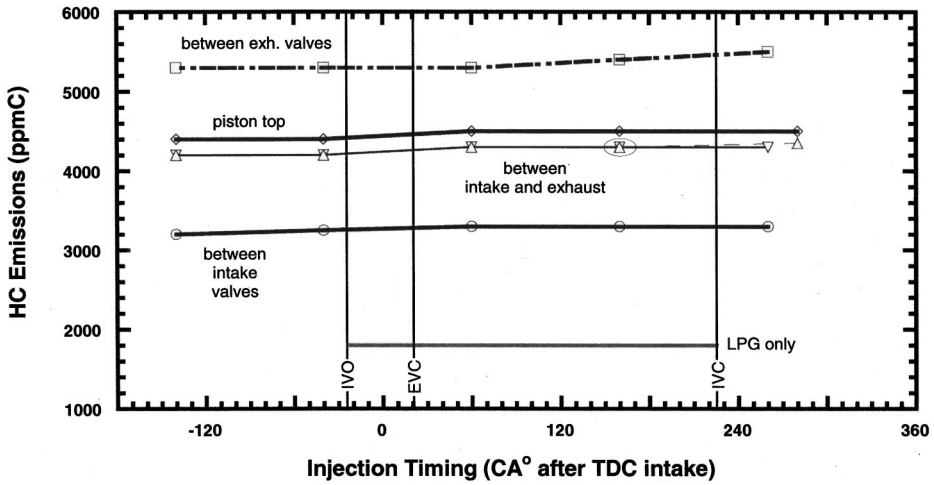

Fig. 4 Effects of wall wetting location and injection timing on HC emissions, from Stanglmaier et al. [18]. (1000 rpm, 32 kPa MAP, 90°C coolant MBT timing ~32 CA deg BTDC, 1.5 mg injected).

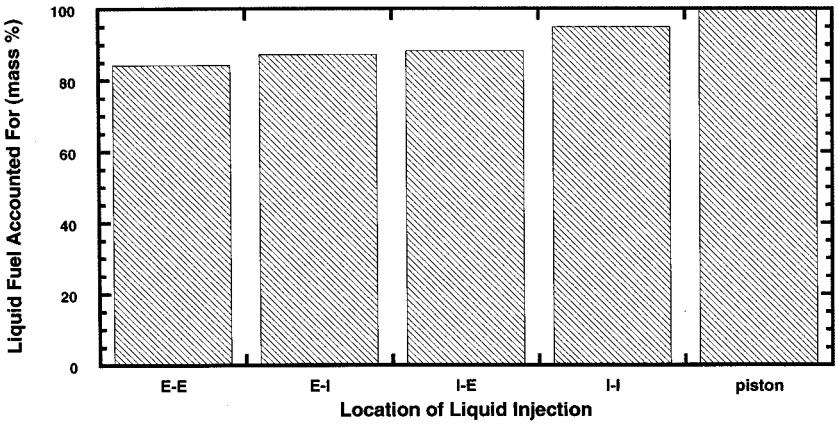

Fig. 5 Fraction of injected liquid fuel that can be accounted for in the exhaust stream, from Stanglmaier et al. [18]. (Same conditions as Fig. 4.)

40 °C. Thus, the coolant temperature does not appreciably affect the HCs due to liner wetting at idle but does affect the HCs due to liner wetting at the WWMP.

We have also examined the effects of engine operating conditions and amount of wall wetting. It was shown that the percent increase in HC emissions, relative to the LPG-only baseline, increased with increasing liquid fuel fraction and that this effect was more pronounced at the WWMP than at idle. However, these experiments pose a question regarding the LPG-only baseline used for the prior experiments. Specifically, it is known that HC emissions are lower for premixed operation with a low molecular weight gaseous fuel, like LPG, than for a higher molecular weight liquid fuel ([20,21]). Thus, because increased HC emissions are expected as the fraction of the higher molecular weight liquid fuel increases even without wall wetting, was our prior observation of increased HC emissions due solely to fuel structure? To address this issue, we operated the engine with a combination of port injection of the liquid fuel plus pre-vaporized LPG introduced (as previously) upstream of the throttle body. The results of these experiments are presented in Fig. 6.

Figure 6 shows that use of only the liquid fuel, introduced via port injection, yields higher HC emissions than when LPG is the sole fuel, as expected. Furthermore, for port injection the HC emissions are dominated by the liquid fuel for high liquid fuel fractions, dominated by LPG for low liquid fuel fractions, and roughly linear in between. Of most importance, piston wetting by the liquid fuel yields much higher HC emissions than when the same liquid fuel fraction is introduced via port injection. The increase in HC emissions is higher at the part load WWMP condition than at idle. For example, 20 percent liquid fuel does not appreciably affect the HC emissions at idle and increases the HC emissions only a few percent at the WWMP with port injection of the liquid fuel, but increases the HC emissions by about 55 percent and 85 percent at idle and the WWMP, respectively, when the liquid fuel is injected onto the piston. At the higher load condition (the WWMP), in-cylinder temperatures are higher, which may be expected to produce greater evaporation rates and higher in-cylinder oxidation rates. However, the engine speed is also higher at the WWMP, which yields less time for evaporation and in-cylinder oxidation. The results in Fig. 6 indicate that the speed effect is more important than the load effect. Additionally, comparison of the PFI results to the piston wetting results at the highest liquid fuel fractions used for piston wetting yields the conclusion that the time available for evaporation is more important than the time available for in-cylinder oxidation. That is, evaporation of the liquid fuel film from in-cylinder surfaces is the limiting process affecting HC emissions due to in-cylinder wall wetting.

Injection interrupt was used in our prior study ([19]) to determine the 1/e time constant for liquid fuel evaporation. Specifically, with 1.5 mg of liquid fuel injected each cycle onto the piston with $\lambda=1.1$ at both idle and the WWMP, injection onto the piston was ceased and a wide range lambda sensor was used to record the change of excess air ratio versus time. The time constant was determined from the relative excess air ratio:

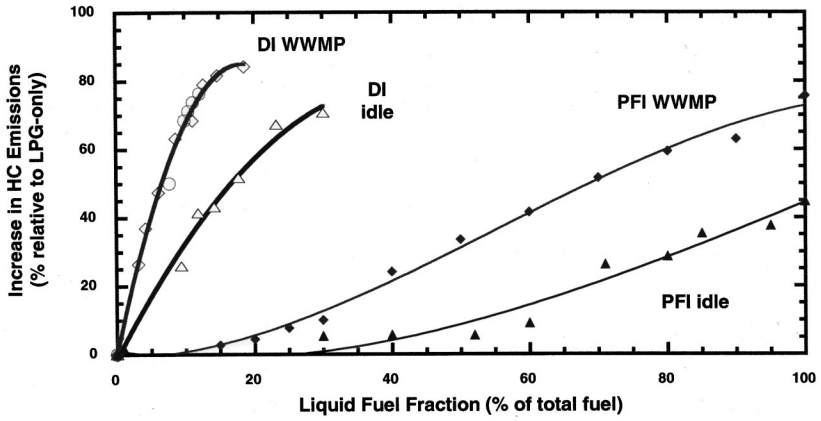

Fig. 6 Effects of the liquid fuel fraction on HC emissions when the liquid fuel is injected onto the piston compared to port fuel injection of the liquid fuel

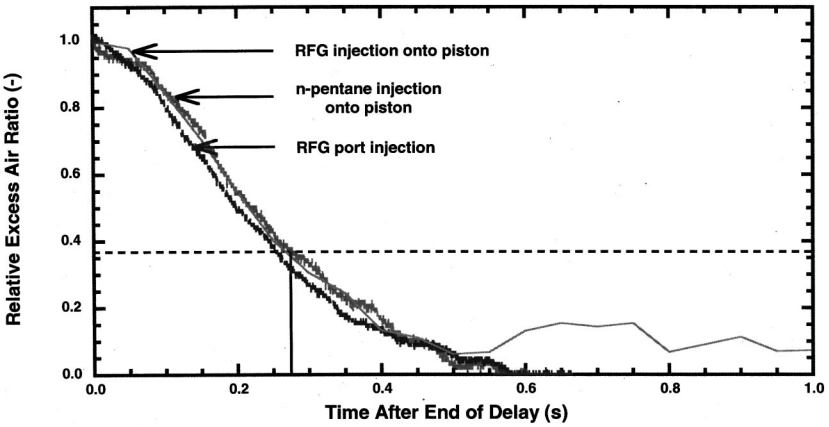

Fig. 7 The 1/e time constant from the wide range lambda sensor output for piston wetting with 1.5 mg of Cal. Phase 2 RFG and also with 1.5 mg of n-pentane, and also for port injection of 1.5 mg of Cal. Phase 2 RFG, all at the WWMP with 40°C coolant

$$\text{relative excess air ratio} = \frac{\lambda_t - \lambda_\infty}{\lambda_0 - \lambda_\infty}, \tag{1}$$

where λ_t is the excess air ratio on each cycle during the transient, λ_0 is the average excess air ratio prior to injector shutoff, and λ_∞ is the average following restabilization.

The engine continues to run on pre-vaporized LPG after liquid injection is ceased in these tests, albeit at a lower fuel/air ratio. Thus, combustion on the cycles following injector shutoff promotes evaporation of any fuel film that may remain on in-cylinder surfaces. At idle, the 1/e time constant for piston wetting was ~0.7 s or ~6 cycles. At the WWMP, the 1/e time constant was ~0.3 s or ~3 cycles. These results are another indication that evaporation is slow compared to engine cycle times. However, the time constant at the WWMP is of the order of the response time of the wide range lambda sensor. That is, the prior injection interrupt results did not prove that evaporation requires more than one cycle at the part load WWMP condition.

To address this uncertainty, additional injector interrupt tests were conducted at the WWMP. The initial tests involving injecting 1.5 mg of a more volatile liquid fuel, n-pentane (for which the boiling point at atmospheric pressure is 36 °C) onto the piston. As shown in Fig. 7, this test produced the same 1/e time constant. However, due to the possibility that the Leidenfrost effect (discussed later) may have influenced the results with the more volatile liquid, injection interrupt tests were again conducted at the WWMP using 1.5 mg of California Phase 2 RFG injected via the port injector. As shown in Fig. 7, these tests again produced the same 1/e time constant. However, because the port injector in this engine is not well targeted, it is possible that a liquid film remains within the intake manifold for these tests. Nevertheless, the results in Fig. 7 strongly indicate that the response time of the wide range lambda sensor is a limiting effect.

Therefore, additional injector interrupt tests were performed with 1.5 mg of Cal. Phase 2 RFG injected onto the piston, but using a different and much faster sensor. Specifically, a Fast-Spec was used to measure the time-resolved hydrocarbon emissions before injector shutoff and during the transient following injector interrupt. The Fast-Spec is a recently developed instrument ([22]) that has the same goal as a fast FID: measurement of the hydrocarbon emissions near the exhaust port as a function of crank angle (or time) throughout the exhaust process. However, rather than using a sampling tube in the exhaust port and a flame ionization detector, the Fast-Spec uses absorption of infrared light that has been multi-passed through the exhaust stream just downstream of the exhaust port. The Fast-Spec eliminates the transport tube delay and possible diffusional mixing in the tube of a fast FID. Additionally, the use of multipass system provides a hydrocarbon measurement that is integrated across the hydrocarbon profile in the exhaust, thereby eliminating the sensitivity to sample tube location of a fast FID ([23,24]).

The HC mole fraction history for an injector interrupt test at idle is provided in Fig. 8. Our previous fast FID results ([19]) showed that the biggest effect of piston wetting was on the final

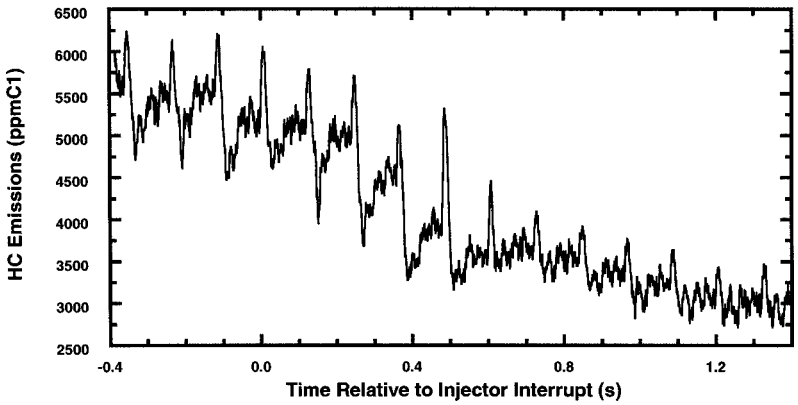

Fig. 8 Fast-Spec results for the HC emissions at idle prior to and following injector shutoff

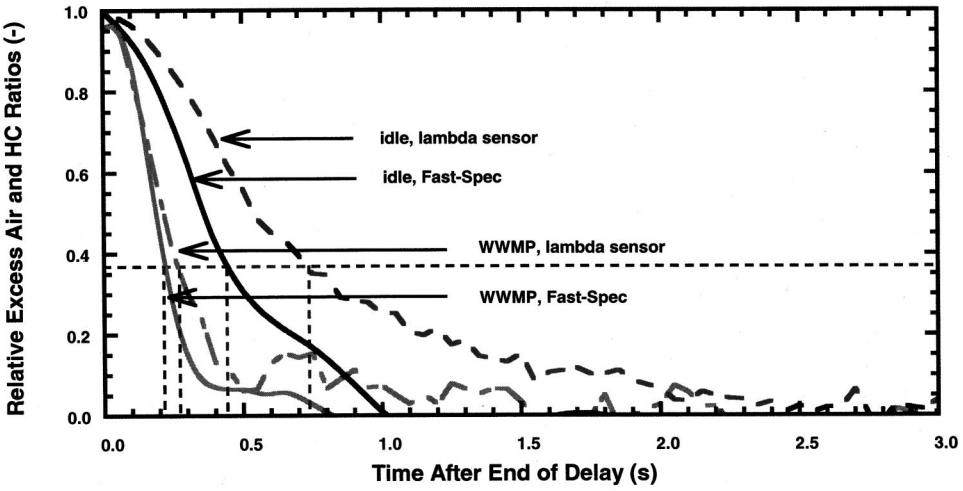

Fig. 9 Relative excess air ratio and relative HC emissions following injector shutoff. Piston wetting with 1.5 mg Cal. Phase 2 RFG.

peak in the HC emissions, near the end of the exhaust stroke, which was much more pronounced for piston wetting than for operation solely on LPG. This peak is evident in Fig. 8 before injector interrupt and during the transient to a new stable state.

Figure 9 compares the results obtained with the Fast-Spec to the results obtained using the wide range lambda sensor. To generate the hydrocarbon curve in Fig. 9, the Fast-Spec results were first integrated over the exhaust process each cycle, and then the relative hydrocarbon emissions were calculated from the HC mole fraction (ppm) on each cycle during the transient (HC_t), the average mole fraction prior to injector shutoff (HC_0), and the average following re-stabilization (HC_∞) via

$$\text{relative HCs} = \frac{HC_t - HC_\infty}{HC_0 - HC_\infty}. \tag{2}$$

As shown in Fig. 9, the 1/e time constant at idle decreased from ~0.7 s or ~6 cycles via the wide range lambda sensor measurements to ~0.4 s or ~3 cycles via the Fast-Spec measurements. However, both indicate that it takes several cycles for the liquid film remaining within the combustion chamber to evaporate to the point that the signal has decreased to ~37 percent of the final stable value. Here, it should be recalled that the results presented in Fig. 5 indicated that 100 percent of the liquid fuel injected onto the piston at idle can be accounted for as either unburned HCs or burned products. Although it may initially seem that the results in Figs. 5 and 9 disagree, in fact these results indicate that a steady state film exists on the piston at idle. That is, although 1.5 mg evaporates during each cycle, a portion of this 1.5 mg was still on the piston from the prior cycle, and the 1.5 mg injected on the current cycle leaves a liquid film of this same magnitude. A similar situation can happen within the intake of PFI and carbureted engines.

As also shown in Fig. 9, the 1/e time constant from the lambda sensor measurements is also larger than the 1/e time constant obtained via the Fast-Spec measurements at the WWMP. However, the change is not as significant at the WWMP as at idle. Specifically, the 1/e time constant of ~0.3 s or ~3 cycles from the lambda sensor decreased to ~0.2 s or two to three cycles via the Fast-Spec. Both measurements indicate that a small amount of liquid remains on the piston past the end of the cycle at the WWMP.

Discussion

The engine test results presented herein have shown that liquid fuel impingement on any surface within the combustion chamber of a DI gasoline engine results in increased HC emissions. Furthermore, these experiments have revealed that the vaporization of wall-bound liquid gasoline is much slower than the engine cycle, and that this fuel can remain within the cylinder for multiple engine cycles. From the present experiments, it is estimated that ~6 percent of the liquid injected contributes to the exhaust HC emissions.

Experimental measurements in a firing optical direct injection gasoline engine ([25,26]) revealed that some of the liquid fuel that impinged on the piston, with a start of injection at BDC of compression, still survived at TDC. Further, these studies showed that later injection resulted in more piston impingement but less liner impingement, and that more liquid survived on the piston to TDC with later injection. How long the liquid on the surfaces survived past TDC was not reported. The authors noted that the surface temperatures in the optical engine are not as high as those in a normal running engine because of the limited time available for firing operation. Nevertheless, these experiments appear to agree with the present results—evaporation of a liquid fuel film on the piston is a relatively slow process.

The multidimensional model developed by Han et al. [14] for rich early injection predicted no more than 18 percent wall impingement (for SOI from 90–180 CA deg ATDC during intake) but that two to seven percent survived to TDC for motoring operation. For late injection (SOI at 60 deg BTDC), Fan et al. [16] predict that less than three percent of the liquid on the in-cylinder surfaces survives to the time of ignition (180 deg BTDC). In contrast, Suh and Rutland [15] modeled early injection in a two-valve engine and found less than ten percent impingement with 100 percent evaporated by TDC in all cases except an SOI of 120 deg ATDC of intake, for which one percent of the liquid survived to TDC. Similarly, Glaspie and co-workers [17] modeled late direct injection with SOI at 80 deg BTDC and predicted 50 percent impingement but that no liquid survived more than 60 CA deg.

The present experiments plus those in the optical engine cited above do not appear to agree with these predictions from multidimensional models of direct injection gasoline engines. Several factors could contribute to this discrepancy. The first factor is the fuel used in the simulations. With the exception of Glaspie et al. [17] who did not specify the fuel modeled, all of the models discussed in the previous paragraph used i-octane. At atmospheric pressure, the boiling temperature of iso-octane is ~100 °C (373 K) whereas the end boiling point for Cal. Phase 2 RFG is almost 180 °C (~450 K) and i-octane is near the T50 point for Cal. Phase 2 RFG. That is, the fuel simulated in the models is more volatile than the gasoline used in the present experiments. The second

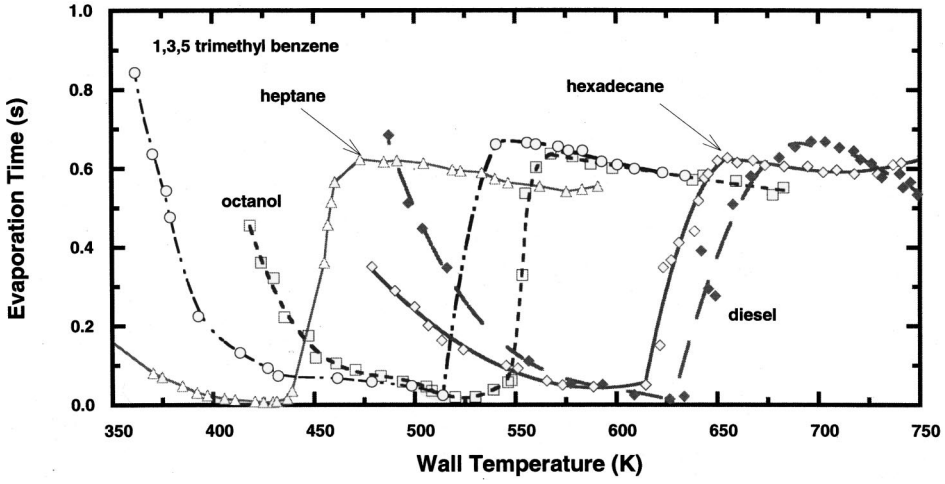

Fig. 10 Vaporization time for a single liquid drop on a hot surface in quiescent surroundings at one bar, from Xiong and Yuen [31]. Initial drop size=0.15 mm, except diesel droplets of 0.19 mm.

factor that may contribute to the apparent disagreement is the film model. Few if any details regarding the film are provided in the references cited in the prior paragraph. However, it is known that the film thickness is important because the temperature of the film surface dictates the vapor pressure of the fuel ([27,28]). In turn, the film surface temperature is determined—at least in part—by conduction from the wall through the liquid. For the early injection cases in the above references, the wall temperatures were well above the atmospheric pressure boiling point of i-octane (liner temperatures from 410–450 K and piston temperatures from 450–516 K, except Glaspie did not provide details regarding wall temperatures). In comparison, the Ford GESIM engine code predicts a liner temperature of 388 K and a piston temperature of 422 K for operation on propane at the WWMP with an excess air ratio of 1.1. The GESIM calculations do not account for cooling of the surface by the liquid, and it is not apparent whether or not the above models account for this important effect. Differences in compression ratio and manifold air pressure (MAP) can contribute to differences between the models and the present experiments because increased pressure inhibits evaporation. The simulations by Fan and co-workers [16] were closest to the present experiments, with the same MAP (40 kPa at the WWMP) and a slightly higher compression ratio (10.5 compared to the present 10). Han and co-workers [14] also had a slightly higher compression ratio (10.5) but a much higher MAP (100 kPa), and Suh and Rutland [15] also had a 100 kPa MAP but a slightly lower compression ratio (9.6) than for the present engine (10.0). The high MAP should inhibit evaporation, but the fuel simulated was more volatile than gasoline. Engine speed affects the time available for evaporation. All of the early injection models used the same 1500 rpm as the present experiments. Glaspie et al. [17] only examined late injection and at a slightly higher speed (1600 rpm), but predicted that all of the liquid on the walls evaporates within 60 CA deg in spite of the shorter time for evaporation.

A final area that might lead to disagreement between the model predictions and the experimental data involves the film evaporation model. This includes not only the film thickness and area, cooling of the wall by the liquid fuel, and conduction through the liquid film to the fuel surface, but might include the Leidenfrost effect (e.g., Refs. [29,30]). The Leidenfrost effect is illustrated in Figs. 10 and 11 for a single drop impacting a hot surface at atmospheric pressure in quiescent surroundings (adapted from Xiong and Yuen [31]). Figure 10 illustrates that if the surface temperature is too far above the boiling point of a fuel, an insulating layer of fuel vapor forms that decreases the evaporation rate by two orders of magnitude or more. This is true not only for the pure

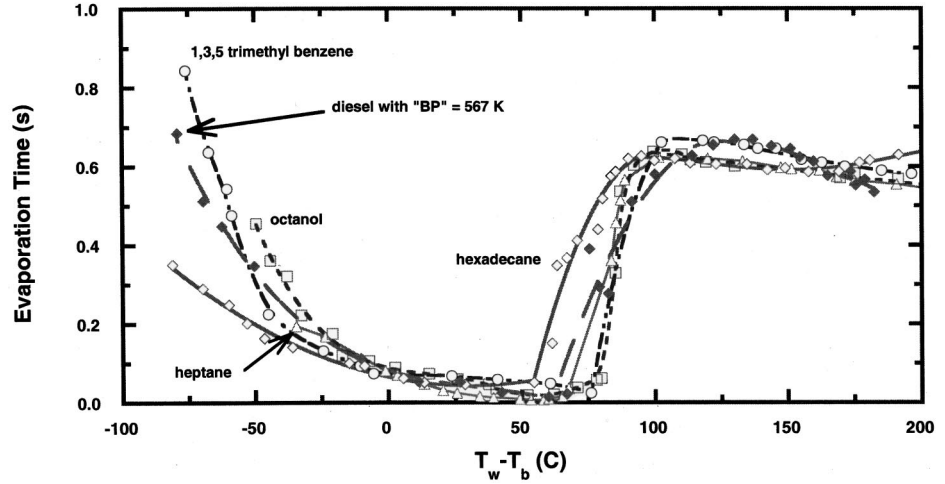

Fig. 11 The results of Fig. 10 in terms of the difference between the wall temperature and the boiling point of the fuel (adapted from Xiong and Yuen [31])

fuels studied by Xiong and Yuen [31] but also for the diesel fuel they examined. Figure 11 shows that the results for all of these fuels are very similar when the evaporation time is shown as a function of the difference between the wall temperature and the boiling temperature (including diesel fuel, if a suitable ''boiling point'' is used). Their results show that if the surface temperature is ~70 K above the boiling point, the evaporation rate decreases significantly (the Nukiyama point). The relevant question is ''Can this occur in engines?'' A study of the fuel vaporization process from the back of intake valves in PFI engines reported the onset of film boiling, and vapor insulation of the liquid layer, at a surface temperature of ~230 °C (503 K), for gasoline on steel ([32]). However, this pressure is low relative to the cylinder pressures during compression, combustion, and expansion. As the pressure increases, so do the Nukiyama and Leidenfrost temperatures [33]. The predicted piston temperature for the present experiments is 422 K and the pressure throughout most of the evaporation process is higher than in the PFI experiments on the Leidenfrost effect. Thus, it does not appear that the Leidenfrost effect is important for the present experiments. However, as the load increases, the surface temperature increases and the increase in pressure results in increases in the Nukiyama and Leidenfrost temperatures. For PFI gasoline engines at full load, the surface temperature of the aluminum piston-crown is reportedly ~555–575 K ([34]), and should be of the same order for a direct injection gasoline engine at full load. The results of Han and coworkers [33] indicate that the Leidenfrost effect may be important for DIG engines at high load but more experimental data are required to determine with certainty whether or not the Leidenfrost effect is important for DIG engines at high load.

Although the Leidenfrost effect does not appear to be important for the conditions of the present experiments, it is clear that evaporation is slower than predicted by the multidimensional engine models. This is due, at least in part, to the simulations using a more volatile, single component fuel and higher surface temperatures than those of the present experiments, and in spite of the fact that most of the models had a higher MAP, which should inhibit evaporation of the liquid film.

Conclusions

Several conclusions can be made from the results obtained in this study:

- Wall wetting on any location within the combustion chamber is detrimental to the HC emissions from DI gasoline engines.
- Wetting on the exhaust side of the liner is worst from an HC standpoint, but all liner locations are probably highly undesirable because of oil-layer dilution.
- HC emissions due to in-cylinder wall wetting by a liquid fuel for an engine operating predominately on a gaseous fuel are much higher than if the liquid fuel is introduced via port injection.
- A steady-state liquid film is formed on the piston for both idle and at the WWMP part load condition, at least for the present experimental setup.
- Wall-wetting results in HC emissions because some of the liquid fuel evaporates from the walls late in the expansion stroke (after in-cylinder temperatures are too low to fully oxidize this fuel) or during the exhaust stroke.
- To accurately reflect the slow evaporation process demonstrated by the present results, it appears that models must adequately account for fuel volatility, surface temperatures (including surface cooling by the liquid), film thickness, and film area.

Acknowledgments

The authors gratefully acknowledge the financial support received for this work from the General Motors Corporation and Ford Motor Company. This research was conducted using the facilities of the General Motors Foundation Combustion Sciences and Automotive Research Laboratories on the campus of The University of Texas.

References

[1] Anderson, R. W., Brehob, D. D., Yang, J., Vallance, K., and Whiteaker, R. M., 1996, ''Understanding the Thermodynamics of Direct Injection Spark Ignition (DISI) Combustion Systems: An Analytical and Experimental Investigation,'' SAE Paper 962018.
[2] Harada, J., Tomita, T., Mizuno, H., Mashiki, Z., and Ito, Y., 1997, ''Development of Direct Injection Gasoline Engine,'' SAE Paper 970540.
[3] Cole, R. L., Poola, R. B., and Sekar, R., 1998, ''Exhaust Emissions of a Vehicle with a Gasoline Direct-Injection Engine,'' SAE Paper 982605.
[4] Brehob, D. D., Fleming, J., Haghgooie, M., and Stein, R. A., 1998, ''Stratified-Charge Engine Fuel Economy and Emissions Characteristics,'' SAE Paper 982704.
[5] Stovell, C., Matthews, R. D., Johnson, B. E., Ng, H., and Larsen, R., 1999, ''Emissions and Fuel Economy of a 1998 Toyota with a Direct Injection Spark Ignition Engine,'' SAE Paper 1999-01-1527.
[6] Matthews, R. D., Stovell, C., Ng, H., Larsen, R., and Johnson, B. E., 1999, ''Effects of Load on Emissions and NOx Trap/Catalyst Efficiency for a Direct Injection Spark Ignition Engine,'' SAE Paper 1999-01-1528.
[7] Thompson, N. D., and Wallace, J. S., 1994, ''Effect of Engine Operating Variables and Piston and Ring Parameters on Crevice Hydrocarbons,'' SAE Paper 940480.
[8] Roberts, C. E., and Matthews, R. D., 1996, ''Development and Application of an Improved Ring Pack Model for Hydrocarbon Emissions Studies,'' SAE Paper 961966.
[9] Alkidas, A. C., 1999, ''Combustion Chamber Crevices: The Major Source of Engine-Out Hydrocarbon Emissions Under Fully Warmed Conditions,'' Prog. Energy Combust. Sci., **25**, pp. 253–273.
[10] Stanglmaier, R. H., Hall, M. J., and Matthews, R. D., 1998, ''Fuel-Spray/Charge-Motion Interaction Within the Cylinder of a Direct-Injected, 4-Valve, SI Engine,'' SAE Paper 980155.
[11] Alger, T. F., Hall, M. J., and Matthews, R. D., 1999, ''Fuel-Spray Dynamics and Fuel Vapor Concentration near the Spark Plug in a Direct-Injected 4-Valve SI Engine,'' SAE Paper 1999-01-0497.
[12] Alger, T. F., Hall, M. J., and Matthews, R. D., 2000, ''Effects of Swirl and Tumble on In-Cylinder Fuel Distribution in a Central Injected DISI Engine,'' SAE Paper 2000-01-0533.
[13] Dodge, L. G., 1996, ''Fuel Preparation Requirements for Direct-Injected Spark-Ignition Engines,'' SAE Paper 962015.
[14] Han, Z., Reitz, R., Yang, J., and Anderson, R. W., 1997, ''Effects of Injection Timing on Air-Fuel Mixing in a Direct-Injection Spark-Ignition Engine,'' SAE Paper 970625.
[15] Suh, E. S., and Rutland, C. J., 1999, ''Numerical Study of Fuel/Air Mixture Preparation in a GDI Engine,'' SAE Paper 1999-01-3657.
[16] Fan, L., Li, G., Han, Z., and Reitz, R. D., 1999, ''Modeling Fuel Preparation and Stratified Combustion in a Gasoline Direct Injection Engine,'' SAE Paper 1999-01-0175.
[17] Glaspie, C. R., Jaye, J. R., Lawrence, T. G., Lounsberry, T. H., Mann, L. B., Opra, J. J., Roth, D. B., and Zhao, F.-Q., 1999, ''Application of Design and Development Techniques for Direct Injection Spark Ignition Engines,'' SAE Paper 1999-01-0506.
[18] Stanglmaier, R. H., Li, J., and Matthews, R. D., 1999, ''The Effect of In-Cylinder Wall Wetting Location on the HC Emissions from SI Engines,'' SAE Paper 1999-01-0502.
[19] Li, J., Matthews, R. D., Stanglmaier, R. H., Roberts, C. E., and Anderson, R. W., 1999, ''Further Experiments on In-Cylinder Wall Wetting in Direct Injected Gasoline Engines,'' SAE Paper 1999-01-3661.
[20] Kaiser, E. W., Siegl, W. O., Henig, Y. I., Anderson, R. W., and Trinker, F. H., 1991, ''Effect of Fuel Structure on Emissions from a Spark-Ignited Engine,'' Environ. Sci. Technol., **25**, pp. 2005–2012.
[21] Kaiser, E. W., Rothschild, W. G., and Lavoie, G. A., 1983, ''The Effect of Fuel and Operating Variables on Hydrocarbon Species Distributions in the Exhaust from a Multicylinder Engine,'' Combust. Sci. Technol., **32**, pp. 245–265.
[22] Mizaikoff, B., Fuss, P., and Hall, M. J., 1998, ''Fast-Spec: An Infrared Spectroscopic Diagnostic to Measure Time-Resolved Exhaust Hydrocarbon Emissions From SI Engines,'' Proceedings of the Combustion Institute, **27**, pp. 2093–2100.
[23] Finaly, I. C., Boam, D. J., Bingham, J. F., and Clark, T. A., 1990, ''Fast Response FID Measurement of Unburned Hydrocarbons in the Exhaust Port of a Firing Gasoline Engine,'' SAE Paper 902165.
[24] Stache, I., and Alkidas, A. C., 1997, ''The Influence of Mixture Preparation on the HC Concentration Histories From an SI Engine Running Under Steady-State Conditions,'' SAE Paper 972981.
[25] Williams, P.A., Davy, M. H., and Brehob, D. D., 1998, ''Effects of Injection Timing on the Exhaust Emissions of a Centrally-Injected Four-Valve Direct-Injection Spark-Ignition Engine,'' SAE Paper 982700.
[26] Davy, M. H., Williams, P. A., and Anderson, R. W., 1998, ''Effects of Injection Timing on Liquid-Phase Fuel Distributions in a Centrally-Injected Four-Valve Direct-Injection Spark-Ignition Engine,'' SAE Paper 982699.
[27] Badillo, E., Assanis, D. N., and Servati, H., 1997, ''One-Dimensional Tran-

sient Dynamics of Fuel Evaporation and Diffusion in Induction Systems,'' SAE Paper 970058.
[28] Stanton, D. W., and Rutland, C. J., 1998, ''Multi-Dimensional Modeling of Heat and Mass Transfer of Fuel Films Resulting from Impinging Sprays,'' SAE Paper 980132.
[29] Mizomoto, M., Hayano, H., and Ikai, S., 1978, ''Evaporation and Ignition of a Fuel Droplet on a Hot Surface (Part 1, Evaporation),'' Bull. JSME, **21**, pp. 1765–1771.
[30] Mach, T. J., Sung, R. L., Liiva, P. M., Acker, W. P., Swindal, J. C., and Chang, R. K., 1993, ''Experimental Determination of Fuel Additive Effects on Leidenfrost Temperature and Deposit Formation,'' SAE Paper 930774.
[31] Xiong, T. Y., and Yuen, M. C., 1991, ''Evaporation of a Liquid Droplet on a Hot Plate,'' Int. J. Heat Mass Transf., **34**, pp. 1881–1894.
[32] Martins, J. J. G., and Finlay, I. C., 1992, ''Fuel Preparation in Port-Injected Engines,'' SAE Paper 920518.
[33] Han, Z., Xu, Z., and Trigui, N., 2000, ''Spray/Wall Interaction Models for Multidimensional Engine Simulation,'' International Journal of Engine Research, **1**, pp. 127–146.
[34] Heywood, J. B., 1988, *Internal Combustion Engine Fundamentals*, McGraw-Hill, New York, p. 700.

Formaldehyde Characterization Utilizing In-Cylinder Sampling in a Large Bore Natural Gas Engine

D. B. Olsen

J. C. Holden[1]

G. C. Hutcherson[1]

B. D. Willson

Engines and Energy Conversion Laboratory,
Mechanical Engineering Department,
Colorado State University,
Ft. Collins, CO 80523

This research addresses the growing need to better understand the mechanisms through which engine-out formaldehyde is formed in two-stroke cycle large bore natural gas engines. The investigation is performed using a number of different in-cylinder sampling techniques implemented on a Cooper-Bessemer GMV-4TF four-cylinder two-stroke cycle large bore natural gas engine with a 36-cm (14-in.) bore and a 36-cm (14-in.) stroke. The development and application of various in-cylinder sampling techniques is described. Three different types of valves are utilized, (1) a large sample valve for extracting a significant fraction of the cylinder mass, (2) a fast sample valve for crank angle resolution, and (3) check valves. Formaldehyde in-cylinder sampling data are presented that show formaldehyde mole fractions at different times during the engine cycle and at different locations in the engine cylinder. The test results indicate that the latter part of the expansion process is a critical time for engine-out formaldehyde formation. The data show that significant levels of formaldehyde form during piston and end-gas compression. Additionally, formaldehyde is measured during the combustion process at mole fractions five to ten times higher than engine-out formaldehyde mole fractions. Formaldehyde is nearly completely destroyed during the final part of the combustion process. The test results provide insights that advance the current understanding and help direct future work on formaldehyde formation. [DOI: 10.1115/1.1363601]

Introduction

Formaldehyde is a toxic emission that is specifically troublesome for natural gas engines because it is a primary combustion intermediate. It falls into a group of pollutants called HAP's (hazardous air pollutants), or air toxics, that will be regulated in the near future. HAP's do not include the criteria pollutants, carbon monoxide (CO), oxides of nitrogen (NO_x), and total hydrocarbons (THC). They include a variety of aldehydes, volatile organic compounds, semivolatile organic compounds, sulfur compounds, and metals. The US Environmental Protection Agency (EPA) is currently developing air toxic regulations for oil and gas production, as described in the 1990 Clean Air Act Amendments. The potential implications of these regulations to large bore natural gas engines used in gas compression and power generation are well documented (Coerr et al. [1], Olsen and Mitchell [2], Kirschner [3], Shareef et al. [4]). The only air toxic emitted in significant quantities from these engines is formaldehyde. The mechanisms of formation for CO, NO_x, and THC have been studied extensively for a wide range of engine designs and fuels. In contrast, little is known about the mechanisms through which engine-out formaldehyde is formed. A thorough understanding of formaldehyde formation will be beneficial as the natural gas industry responds to upcoming EPA air toxic regulations and future revisions to these regulations.

The amount of insight that can be gained from measuring formaldehyde levels in engine exhaust as engine operating parameters are varied is limited. In the interpretation of exhaust emissions one can only speculate as to the events that take place in the cylinder that result in formaldehyde emissions. In-cylinder sampling is a technique that can provide information on events that transpire in the cylinder (LoRusso et al. [5], Tobis et al. [6], Kannappan [7], Booy [8], Houtsma et al. [9], Taylor and Rogowski [10]). Samples are extracted from the cylinder during engine operation then analyzed to determine sample composition. Samples can be removed at different times throughout the engine cycle to measure how composition changes with crank angle in the region being sampled. Samples can also be taken at different locations in the cylinder to acquire information on how composition changes with cylinder location. Three basic types of sample valves are utilized, which are large sample valves (high flow, long duration), fast sample valves (low flow, short duration), and check valves. Each type of valve has advantages, disadvantages and different applications. Large sample valves are intended to remove a relatively large portion of the cylinder mass to determine bulk quantities. Fast sample valves extract a small portion of the cylinder mass over a short duration to provide crank angle resolution of cylinder composition. Check valves are implemented in applications where the pressure profile at the sample location can be utilized to open and close the valve.

Experimental Apparatus and Method

Large Bore Engine Test Bed (LBET). The LBET is housed in the Engines and Energy Conversion Laboratory (EECL) at Colorado State University. At the core of the test bed is a highly instrumented Cooper-Bessemer GMV-4TF engine. A photograph of the engine is shown in Fig. 1. The GMV-4TF is a four-cylinder two-stroke cycle, 36-cm (14-in.) bore, 36-cm (14-in.) stroke, natural gas fired engine. The GMV-4TF has a sea level brake power rating of 330 kW (440 hp) at 300 rpm. The GMV-4TF uses electronic gas admission valves (EGAV), which deliver fuel to each cylinder individually at an injection pressure of about 310 kPag (45 psig). The engine is nominally operated with spark ignition.

The LBET includes a combustion analysis system that uses cylinder pressure profiles to calculate peak pressure, location of peak pressure, misfire frequency, and combustion stability parameters. The test bed has a computer controlled water brake dynamometer for precise load control. A turbocharger simulation package controls intake and exhaust manifold pressures, allowing the

[1]Presently at Enginuity, Inc.

Contributed by the Internal Combustion Engine Division of THE AMERICAN SOCIETY OF MECHANICAL ENGINEERS for publication in the ASME JOURNAL OF ENGINEERING FOR GAS TURBINES AND POWER. Manuscript received by the ICE Division July 11, 2000; final revision received by the ASME Headquarters Dec. 7, 2000. Associate Editor: D. Assanis.

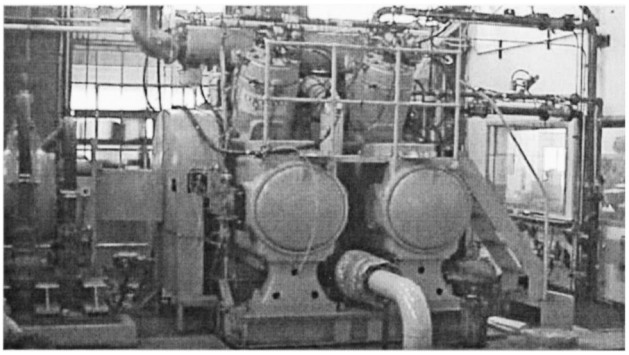

Fig. 1 The Cooper Bessemer GMV-4TF large bore natural gas engine at the EECL

simulation of a wide range of configurations. The turbocharger simulation package is composed of two main components, a supercharger (Roots blower) to pressurize the intake air and a motorized, computer controlled backpressure valve. The test bed also has the ability to control jacket water temperature, air manifold temperature, and air manifold relative humidity. The test bed utilizes a standard five gas analyzer rack for measuring criteria pollutants, O_2, and CO_2, and a Fourier transform infrared (FTIR) spectrometer for examination of a wide range of species including criteria pollutants and formaldehyde.

Figure 2 shows a cross sectional view of a GMV-4TF cylinder and cylinder head with the piston at top dead center (left) and bottom dead center (right). This drawing also shows the location of the air-start, intake, and exhaust ports. The air-start port in the drawing is shown in the same plane with the other features to illustrate the various axial and radial locations. It is actually located at 90 deg to the spark-plug hole, as illustrated in the cylinder head section line. The GMV-4TF is equipped with air-start ports for starting of the engine; however, an externally mounted air starter is installed on the flywheel, making these ports available for diagnostic purposes. Normally piezoelectric pressure transducers are mounted in the air-start ports for real-time cylinder pressure data. For this testing the transducers are located in an alternative port in cylinder #2, allowing sample valve access through the air-start ports. Check valves are placed at two locations in the cylinder. One is installed in the exhaust port (exhaust elbow check valve) and the other is installed in a lube port (midstroke check valve) that normally is not used.

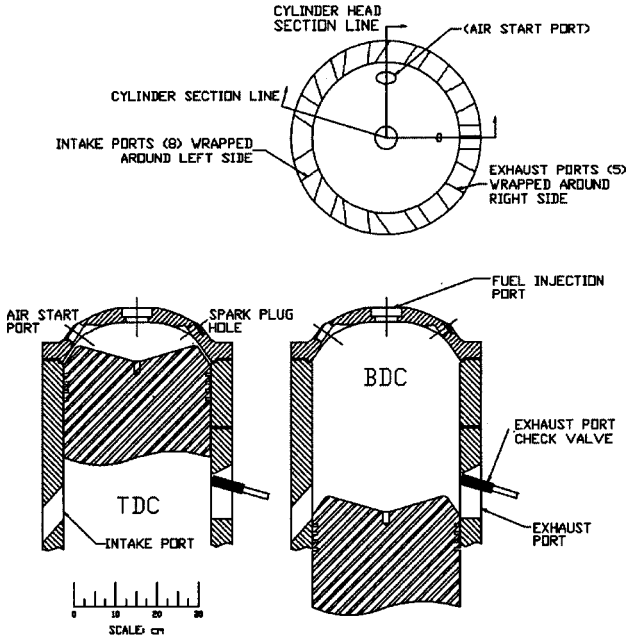

Fig. 2 Piston and cylinder for GMV-4TF showing the spark-plug hole and air-start, intake, and exhaust ports

In-cylinder Sampling Techniques

Large Sample Valve. The large sample valve was operated either during the compression or expansion stroke. The valve was designed to extract as much of the cylinder mass as possible. Consequently, samples extracted with the large sample valve affected engine operation for a short period. This was particularly the case when samples were removed during the compression process. However, it did not affect the composition of the sample because the valve was not actuated until stable engine operation was achieved.

During valve development numerous design and operational issues were addressed, including valve mounting, actuation mechanism, sample storage prior to analysis, and valve mass flowrate. The air-start port diameter defined the maximum envelope for the valve size. This resulted in a 3.2-cm diameter poppet valve. The valve was electrohydraulically actuated and had a 0.97-cm lift. The valve was connected to a 30-liter Teflon lined aluminum sample cylinder by a short section of pipe, approximately 30 cm long. Heated Teflon sample line connected the analyzer to the sample cylinder with a shutoff valve isolating the sample cylinder from the sample line and analyzers. The sample cylinder and short pipe section were wrapped in heat tape and insulation and kept at 380 K to prevent moisture condensation.

A combination of three parameters defined the boundaries for the valve-open duration. They were the crank angle locations of exhaust port open and closure, fuel delivery, and combustion (indicated by valve temperature). To obtain a representative sample during the compression stroke, the sample was extracted after exhaust port closure and fuel admission. The exhaust ports closed at 112 deg BTDC. The fuel valve opened at 120 deg BTDC and closed at approximately 95 deg BTDC. Results from on-engine experimentation determined that a valve opening of 83 deg BTDC allowed for more complete mixing of the fuel and air in the cylinder. High temperatures from combustion dictated the closing crank angle of the valve. Additionally, sampling of combustion products must be avoided, which also impacted the valve-closing angle. For a valve-opening angle of 83 deg BTDC a duration of 80 deg was determined to be optimal.

For sampling during expansion the two main concerns were, opening the valve late enough to prevent high sample valve temperatures and closing it before the exhaust ports open. Combustion was nearly complete by 30 deg ATDC; therefore the sample valve was opened at about 30 deg ATDC. The exhaust ports opened at 112 deg ATDC. The sample valve was closed at 90 deg ATDC to ensure that it was closed before the exhaust ports opened and to prevent backflow from the sample cylinder to the engine cylinder as cylinder pressure is reduced from piston expansion. The sample valve took approximately 9.9 ms to open, or about 18 deg. To close it took approximately 11.9 ms, or about 22 deg.

Figure 3 shows a system schematic for the large sample valve. The valve controller, or INPULSE, provides an electric signal to the valve that controls the hydraulic circuit. Hydraulic pressure actuates the valve head to open or close depending on the electric signal profile. The signal is based on the valve open crank angle location and valve open duration programmed in the INPULSE. The sample cylinder is purged with nitrogen and evacuated before the sample valve is actuated. Typically four to eight sample valve actuations are required to fill the sample cylinder. Engine operation is allowed to stabilize between valve actuations. After the sample cylinder is filled and the temperature has stabilized, the gases are analyzed with the five-gas rack and FTIR spectrometer.

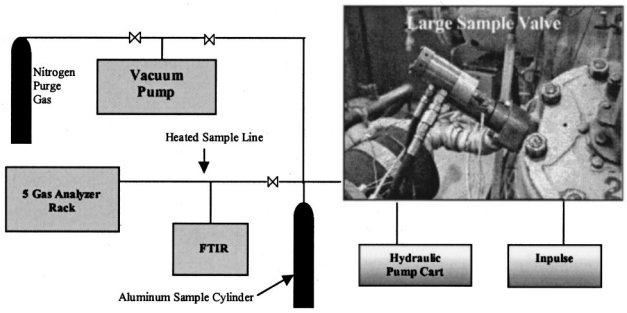

Fig. 3 Large sampling valve system schematic

Fast Sample Valve. The fast sample valve differed from the large sample valve in that it was not designed to remove a sample representative of the complete cylinder mass. The valve extracted a small mass of cylinder gas every cycle near the valve inlet. The valve duration and timing was programmable. Durations as low as five crank angle degrees were possible when cylinder pressure was sufficiently high ($P_{cyl}>1.4$ MPa). As with the large sample valve high temperatures limited its use at certain times during the cycle when combustion was taking place. Though the valve removed a small mass from the cylinder it supplied a significant sample flow to the analyzers because it sampled every cycle. The flow was pulsating near the engine cylinder in the sample line. However, the fluidic capacitance and resistance in the sample line acted to absorb the pulsations and produce a steady flow at the analyzers. It was electrically actuated as opposed to the large sample valve, which was electrohydraulically actuated. The fast sample valve, like the large sample valve, accessed the cylinder through the air start port.

Figure 4 shows the system schematic for the fast sample valve, which incorporates a photograph of the valve. The fast sample valve is an inwardly opening poppet valve as opposed to the large sample valve, which is an outwardly opening poppet valve. There are three radial ports on the valve. The port that exits the upper right of the valve via a heated line is the sample port. There are two identical ports shown at the lower right of the valve. One is for compressed air to cool the valve during operation. The other port is for compressed nitrogen used to apply back pressure on the valve head. The back pressure on the valve head, about 3.2 MPa, is used to keep the valve from opening when it is not being actuated and the cylinder pressure is high.

Check Valve Sampling. Check valve sampling adds a unique sampling alternative to typical in-cylinder sampling valves when extracting samples above certain pressure is desired. Both check valves are designed to open during expansion. The exhaust port check valve is located in the top of the middle exhaust port in cylinder #2. It is intended to extract a portion of the gas that exits the cylinder during blowdown. The check valve is oriented into the flow and as close as possible to the cylinder inner diameter so the dynamic pressure, which is large when the port initially opens, can be recovered and utilized to open the check valve. The check valve is set to open when the pressure is raised above air manifold pressure. This ensures that the check valve is closed during scavenging and when the piston covers the check valve. The check valve has an adjustable spring that changes the pressure at which the sealing face becomes unseated. This is adjusted before installation in the port. An off-engine test stand is used to adjust the spring force. Preliminary testing is performed that assures the check valve only opens during exhaust blowdown and not when scavenging takes place. The exhaust port check valve opening pressure is set at a gage pressure of approximately 68 kPag (20″ Hg).

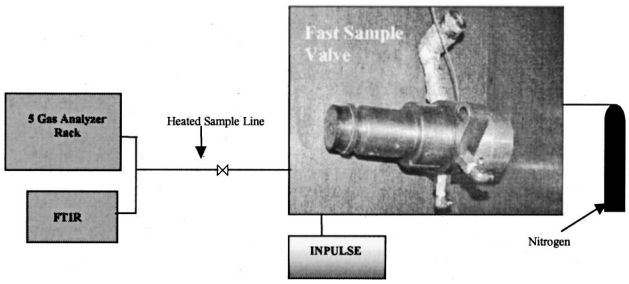

Fig. 4 Fast sampling valve system schematic

One possible error with this technique results from the presence of residual scavenging air from the previous cycle near the port. As the piston uncovers the exhaust port the combustion products begin to exit the cylinder, subsequently raising the pressure in the port. At the same time the flow of combustion products entrains residual scavenging air from the previous cycle. It seems likely that a small portion of the scavenging air will flow through the check valve. This error is reduced by locating the check valve close to the cylinder inside diameter and by setting the check valve to open at pressures slightly higher than intake manifold pressure. With the check valve opening pressure set higher than intake manifold pressure a small delay occurs during blowdown allowing a portion of the residual scavenging air to be swept downstream of the check valve before it opens. Both precautions are taken to ensure the accuracy of the measurements.

The midstroke check valve accesses the cylinder through a lube port, located about half way up the cylinder. It is intended to open during expansion. The midstroke check valve is set to open at pressures higher than the cylinder pressure at the time when the piston ring covers the lube port during compression. Setting the valve-opening pressure this way prevents the valve from opening during the compression process. This check valve is identical to the exhaust port check valve, with the exception of the internal spring. The check valve is set in the same manner the exhaust port check valve is set using an off-engine test stand. The check valve is set to open at 340 kPa (50 psig). It is necessary to have a short length of tubing (about 15 cm) between the cylinder and the check valve to prevent the valve seat from getting too hot.

Results and Discussion

To interpret the formaldehyde sampling results it is necessary to provide additional information on the operation of the sampling valves, much of which comes from test data. There are three basic valve parameters that dictate valve operation. They are (1) valve flow area, (2) valve-open duration, and (3) the crank angle location of the center of duration. There are other factors that are significant such as valve actuation profile and valve flow coefficient, but for the purposes of this discussion these three basic parameters will suffice. Figure 5 illustrates how the various sampling techniques differ in timing and duration. The timing and duration of actuation for the check valves is determined by the physical location in the cylinder, the cylinder pressure profile, and the valve spring tension. The check valve durations are determined by comparing the valve actuation pressure, dictated by valve area and spring force, and the cylinder pressure profile. The large and the fast sample valves are programmable, so the valve-open duration and crank angle location of center of duration are specified parameters. Two examples for each valve are illustrated in Fig. 5. The two profiles shown for the large sample valve are optimal profiles for extracting samples during expansion and compression. The fast sample valve is operated using the shortest duration possible that provides adequate sample flow to the analyzers. At times during the engine cycle when the cylinder pressure is high a 5 deg duration is adequate, shown in Fig. 5 at about 32 deg ATDC. At times during the engine cycle when cylinder

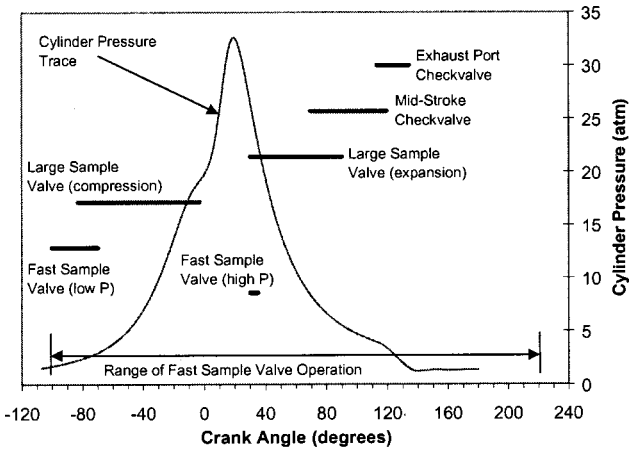

Fig. 5 Sample timing and duration for various sampling techniques

pressure is low, a longer duration is necessary. For example, early in the compression process a 30 deg duration is implemented, at about 90 deg BTDC.

An important aspect of the sampling techniques is the actual amount of gas extracted per cycle. This determines whether the measurement is representative of the bulk cylinder composition, or a localized region near the valve. To evaluate this issue a combination of test data and mass flow calculations are utilized. Table 1 shows some operating characteristics for the various sampling techniques, corresponding to the valve-open profiles in Fig. 5. Based on the differences in flow area of the different valves, it is easy to see that the large sample valve is capable of extracting the largest sample. The flow area in the large sample valve is approximately two orders of magnitude larger than the flow area for the fast sample valve and the check valves.

The mass removed per cycle for the large sample valve reported in the table was calculated from test data. This was carried out by first recording the number of valve cycles and the pressure and temperature in the sample cylinder. The ideal gas law was then used to evaluate the total mass in the sample cylinder. Dividing the total mass by the number of valve cycles yielded the mass extracted per cycle. The mass removed per cycle by the fast sample valve and the check valves was based on test data and compressible flow calculations. The mass flow through an orifice, from Heywood [11], can be expressed as

$$\frac{dm}{dt} = \frac{C_D A_T p_o}{\sqrt{RT_o}} \gamma^{1/2} \left(\frac{2}{\gamma+1} \right)^{(\gamma+1)/2(\gamma-1)}$$

where

dm/dt = mass flow through orifice

Table 1 Sample valve characteristics and performance parameters

Sampling Technique	Valve Flow Area (mm^2)	Duration (degrees)	Approx. Cyl. Mass Removed Per Cycle (%)	Approx. Vol. Removed Per Cycle (STD cc)
Fast Sample Valve (Low Pressure)	9.9	30	0.100	29
Fast Sample Valve (High Pressure)	9.9	5	0.173	50
Large Sample Valve (Compression)	980	113	47	14,000
Large Sample Valve (Expansion)	980	93	15	4,300
Mid-Stroke Checkvalve	7	50	0.30	86
Exhaust Port Checkvalve	7	21	0.078	23

C_D = discharge coefficient
A_τ = minimum throat area
p_o = upstream stagnation pressure
γ = ratio of specific heats
R = gas constant
T_o = upstream stagnation temperature.

This equation was integrated over the valve-open duration to get the mass extracted per cycle. The mass extracted per cycle was then multiplied by the frequency of valve operation yielding a flow rate. The stagnation pressure and temperature were taken from the measured pressure trace and associated bulk temperature, respectively. The gas constant was assumed to be equal to that of air, and a curve fit from Gatowski et al. [12] for the ratio of specific heats that accounts for changes in temperature was implemented. In the low pressure case for the fast sample valve and the exhaust port check valve, the flow to the analyzers was small. It was small enough that the entire sample flowed through the analyzers, whereas the sample flow normally was large enough that a significant fraction bypassed the analyzers. Thus the flow rate measured through the analyzers was the same as the actual flow rate through the valves for the low pressure fast sample valve and exhaust port check valve cases. In these two low flow cases the discharge coefficients were adjusted so that the calculated flow rate matched the measured flow rate. The calculated discharge coefficients were then utilized to evaluate the mass flow through the valves for cases where the flow rate was unknown.

The mass flow per cycle through each valve is presented in Table 1 as a percentage of the trapped cylinder mass for standard operating conditions at 7.5″ Hg of boost. This mass is also expressed on a volumetric basis at standard temperature and pressure. The results show that the large sample valve is the only technique that can give an accurate representation of the average cylinder composition because it removes a significant portion of the cylinder gas. The fast sample valve and the check valves extract less than 0.4 percent of the cylinder contents. However, the fast sample valve and the check valves remove enough mass to represent a significant localized volume. For example, the mid-stroke check valve samples an 86 std. cc volume near the valve inlet.

Variations in CH_2O Level With Crank Angle. The crank angle dependency of formaldehyde formation is investigated using fast sample valve data. Hence, the results reflect formaldehyde formation in the localized region near the fast sample valve inlet. The extracted mass per cycle has a volume of approximately 30–50 cc at standard temperature and pressure. Formaldehyde formation in this region is not likely to be the same as it is elsewhere in the cylinder. However, it is likely to give a general idea of the cycle-resolved behavior of formaldehyde formation in other locations in the cylinder with similar combustion characteristics.

Formaldehyde mole fraction vs. crank angle from the fast sample valve is shown in Fig. 6 for two different boost levels. All data is at 330 kW (440 hp) and 300 rpm. The crank angle that is plotted for each data point corresponds to the center of valve-open duration. The valve-open durations for the data are illustrated with horizontal lines bisecting each data point. Ignition occurs at 10.1 deg BTDC for the 26-kPag (7.5″-Hg) boost case and 11.4 deg BTDC for the 46-kPag (13.5″-Hg) boost case (a common line is used for both on the plot). Both sets of data show an increase in formaldehyde during the compression process and during flame-induced end-gas compression. During the latter part of the compression process, just before spark, for the 26-kPag boost data, a sharp increase in formaldehyde mole fraction is observed. The 46-kPag data show a sharp increase in formaldehyde mole fraction, but not until about 20 deg later in the cycle. This difference can be explained by the decrease in flame speed and increased ignition delay that are typical in leaner mixtures. The mixture is leaner at higher boost because the mass of air inducted into the cylinder during each cycle increases, while fuel flow remains

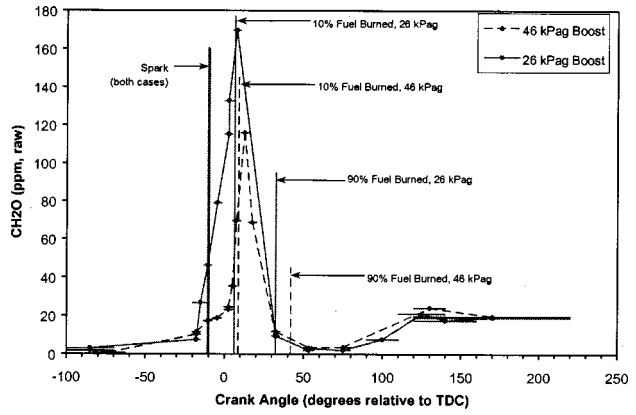

Fig. 6 Fast sample valve formaldehyde measurements vs. crank angle at 330 kW (440 hp) and 300 rpm

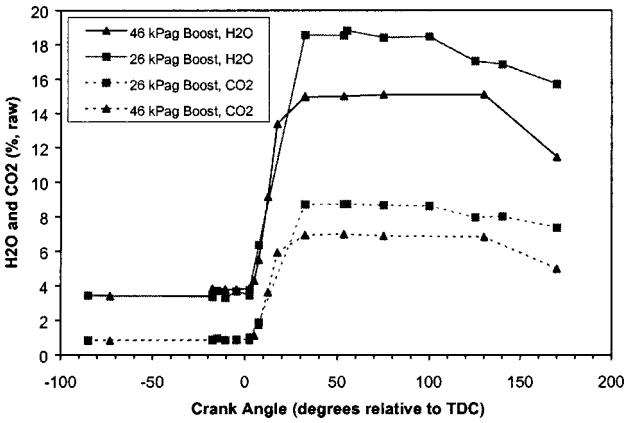

Fig. 7 Fast sample valve CO_2 and H_2O measurements vs. crank angle

roughly the same in order to maintain constant brake power. It is interesting to note that in the 26-kPag boost case rapid formaldehyde formation occurs in the unburned air/fuel mixture before ignition, and after ignition before flame arrival. Karim et al. [13] documents this effect in a paper where chemical kinetic modeling results are presented for a lean burn natural gas engine with diesel pilot injection.

It has been established through the use of a Damköhler map that the most likely combustion regime classification for the GMV-4TF is wrinkled flame sheets (Mitchell and Olsen [14]). Thus, it is appropriate to interpret the fast sample valve data in reference to a flame propagating through the cylinder. A peak in formaldehyde mole fraction is observed for both boost cases just after TDC, though it is much higher for the 26-kPag data. In the 26-kPag boost data the peak occurs at 7.5 deg ATDC, whereas the peak occurs at 12.5 deg ATDC in the 46-kPag boost case. It has been demonstrated through chemical kinetic modeling that formaldehyde peaks in natural gas flames (Ruy [15]). The peaks observed in the data in Fig. 6 can be interpreted as the time in the cycle when the flame is near the inlet of the fast sample valve. The valve is not capable of resolving formaldehyde formation in the flame. There are a couple of reasons for this. First, the valve inlet is about 3X the thickness of a typical flame. Second, based on flame speed estimates, the flame passes the valve inlet in the time corresponding to about one crank angle degree of rotation. This is small in comparison to the smallest fast sample valve duration of five degrees. As a result a sample extracted as the flame propagates through the volume near the valve inlet is likely to represent an average composition of the preflame, flame, and postflame gases. Therefore the highest formaldehyde mole fraction, which exists in the flame, is never detected. This probably explains why peak formaldehyde levels predicted in flames (Ruy [15]) are roughly an order of magnitude higher than peak formaldehyde levels measured with the fast sample valve.

For each boost case the crank angle locations where ten percent and 90 percent of the fuel is burned are labeled in Fig. 6. These values are arrived at from standard heat release analysis of cylinder pressure data. The 10 percent burned location can be viewed as the end of the ignition delay period. The 90 percent burned location can be interpreted roughly as the end of flame propagation. Note that in both boost cases the ignition delay period occurs about five degrees before the peak in formaldehyde is measured. The inlet of the fast sample valve is about 19 cm (7.5 inches) from the spark plug. The flame is still several centimeters away from the fast sample valve inlet after ten percent of the fuel is burned, based on flame font calculations assuming a thin, hemispherical flame front. Thus the early formation of formaldehyde occurs during piston compression and end-gas compression from flame propagation.

After peak formaldehyde values are reached, formaldehyde is quickly and nearly completely destroyed. In both boost cases the formaldehyde mole fraction is reduced from its peak value to less than 4 ppm in 30–50 crank angle degrees. This behavior can be more easily understood when viewed in the context of the evolution of the stable combustion products, CO_2 and H_2O. A plot of CO_2 and H_2O vs. crank angle for the fast sample valve is presented in Fig. 7. In the region sampled by the fast sample valve both constituents begin to increase just after TDC. They are generally formed in the latter stages of the combustion process, and for lean mixtures the production of CO_2 and H_2O indicates the completion of the combustion process. Combustion is complete near the fast sample valve inlet at around 30 deg ATDC, where CO_2 and H_2O reach a relatively constant value. It is in this same time frame, near the end of combustion, when formaldehyde levels are reduced from peak values to minimum values.

The expansion portion of Fig. 6 is perhaps the most applicable to engine-out formaldehyde. That is, formaldehyde formed in the cylinder that is actually emitted from the cylinder into the exhaust system. As combustion is completed in the region sampled by the fast sample valve formaldehyde is nearly completely destroyed. Following this destruction, beginning at about 75 deg ATDC for both boost cases, a gradual increase in formaldehyde mole fraction is observed. The formaldehyde mole fractions for both boost cases continue to increase until values between 20 and 25 ppm are reached at about 125 deg ATDC. Formaldehyde levels are then reduced due, most likely, to scavenging air dilution. Dilution is the likely cause of the reduction in mole fraction because the intake ports open at 123 deg ATDC. This dilution effect is also present in Fig. 7. The maximum formaldehyde levels during expansion are of the same order of magnitude as those emitted from the exhaust stack. In contrast, peak formaldehyde levels that occur during combustion are a factor of five to ten higher than maximum levels measured during expansion.

Two potential mechanisms that could produce formaldehyde during expansion are:

1 formaldehyde produced during piston and end-gas compression and protected from flame propagation in regions such as crevice volumes and wall quench zones emerges during expansion, and

2 unburned hydrocarbons emitted during expansion from regions protected from flame propagation are subsequently oxidized to formaldehyde.

The data from the fast sample valve support both mechanisms. Figure 6 clearly shows formaldehyde being formed during piston and end-gas compression. Since formaldehyde is present prior to flame arrival it is possible that it can survive combustion in regions protected from the flame and then mix with combustion

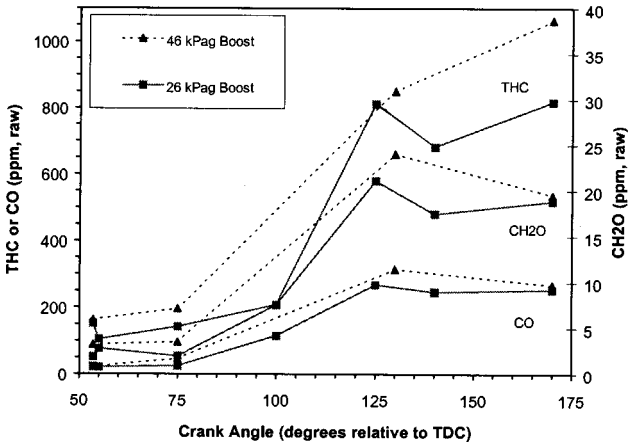

Fig. 8 Fast sample valve measurements of CH_2O, THC, and CO during expansion

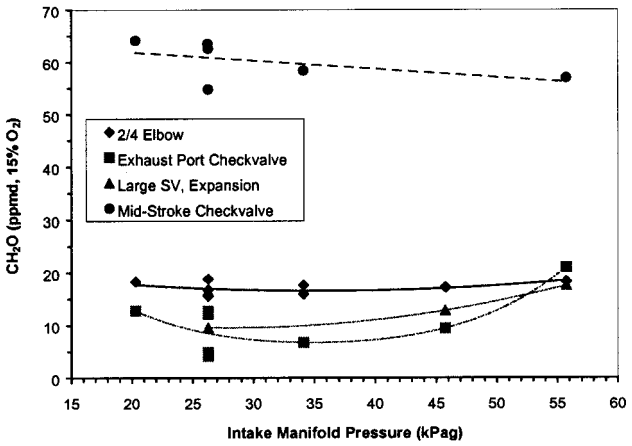

Fig. 9 Formaldehyde measurements for four different sampling techniques

products during expansion. Thus mechanism #1 given above could contribute to the increase in formaldehyde mole fraction during expansion.

Figure 8 shows CH_2O, THC, and CO mole fractions, respectively, from the fast sample valve during expansion. The time frame during expansion where formaldehyde is formed is isolated in the plots by removing the data taken during compression and combustion. All three constituents increase together starting at about 75 deg ATDC. There is very little difference in the formaldehyde data taken during expansion for the two boost cases. However, correcting for dilution would place the 46-kPag boost data significantly higher than the 26-kPag boost data. Formaldehyde and carbon monoxide are products of partial oxidation. In order for products of partial oxidation to form, unburned hydrocarbons and oxygen must be present. The GMV-4TF burns a lean air/fuel mixture, so there is an abundance of oxygen available. The simultaneous increase in unburned hydrocarbons suggests that they are feeding partial oxidation reactions, producing formaldehyde and carbon monoxide. These data provide evidence that mechanism #2 could be an important formation mechanism for formaldehyde.

Variations in CH_2O Level with In-Cylinder Location. The various sampling techniques employed extract samples from different locations in the cylinder. This can be utilized to gain information on the in-cylinder location of formaldehyde formation. The large sample valve is located in the air-start port, sampling the upper portion of the cylinder mass. The midstroke check valve samples a region along the cylinder wall, about half way up the cylinder. When the midstroke check valve initially opens it samples near the crevice volume above the top piston ring, between the piston and the cylinder wall. After the midstroke check valve is fully uncovered it samples gas that is above the piston about 15 cm below the top of the cylinder. The exhaust port check valve samples the blowdown pulse that occurs after the exhaust ports open. Standard exhaust measurements are carried out in the exhaust system, downstream of the exhaust manifold and before the exhaust from the 2-4 and 1-3 banks of the engine come together. There are differences in the piston motions between the 2-4 and 1-3 banks of the engine, which result in different emissions and combustion diagnostic parameters. This is not an issue in interpreting this data because the exhaust measurements are performed on the 2-4 bank, which is where the in-cylinder samples are extracted. The number 2 and 4 cylinders are identical with regard to piston motion and have very similar combustion diagnostic parameters. The combustion products and scavenging air from these two cylinders mix in the exhaust manifold. Consequently, this measurement is considered to be equivalent to a spatial average of the combustion products and scavenging air for cylinder number 2. It is referred to as the 2/4-elbow measurement because the sample tap is located in an elbow just downstream of the exhaust manifold that contains exhaust from cylinder numbers 2 and 4.

Formaldehyde sampling results are presented in Fig. 9 from four different techniques. The data are expressed on a dry, 15 percent O_2 basis to account for varying levels of dilution between the different techniques. The 2/4 elbow data can be viewed as a stack measurement for the 2/4 side of the engine. The data show that in general the different sampling techniques yield different levels of formaldehyde. The most intriguing feature in this data is the high levels of formaldehyde measured with the midstroke check valve. The formaldehyde levels measured with the midstroke check valve are roughly five times higher than the rest of the data. This can be explained by the fact that the midstroke check valve samples near a crevice volume during the latter part of the expansion process. The midstroke check valve data show levels of THC's and CO (not plotted) that are much higher than engine-out levels, particularly THC's. CO levels are about 4X higher than engine-out levels while THC levels are about 40X higher than engine-out levels. The elevated THC levels in this region indicate that combustion is incomplete. Based on these data, high formaldehyde levels are likely in other regions where combustion is incomplete at this time during the cycle. The midstroke check valve, because of the shape of the pressure profile during expansion extracts a high fraction of the total mass sampled right after the piston uncovers it. Based on the mass flow calculations used to determine relative sample sizes (discussed above), about 40 percent of the total mass flow through the midstroke check valve occurs in the first 25 percent of the valve-open duration.

The valve-open durations for the midstroke and exhaust port check valves and the large sample valve-expansion measurements do not coincide exactly in time. Thus the measurements do not give a ''snapshot'' of formaldehyde levels at various locations in the cylinder. However, these three in-cylinder measurements do have a significant amount of valve-open duration overlap. Therefore a certain level of information on the spatial resolution of formaldehyde formation in the cylinder is acquired. Data from the large sample valve-compression measurements are not plotted in Fig. 9. Formaldehyde data from this technique are small, 3–7 ppm for raw measurements, throughout the range of exhaust manifold pressures tested. This formaldehyde most likely originates from formaldehyde contained in the residual fraction and formaldehyde formation during the final part of the compression process.

There are subtle differences in the formaldehyde measurements from the 2/4 elbow, exhaust port check valve, and large sample valve expansion. The 2/4 elbow measurements are, with the ex-

ception of the high boost point, higher than the other two measurements. The 2/4 elbow measurements indicate the spatially averaged engine-out formaldehyde formed throughout the cylinder. This measurement includes contributions from locations where formaldehyde formation is prevalent and from regions of low formaldehyde formation. The midstroke check valve samples from a region where formaldehyde formation is prevalent (discussed above). The large sample valve expansion and exhaust port check valve appear to sample regions in the cylinder where formaldehyde formation is slightly lower than average. The large sample valve removes a significant portion of the cylinder contents when it is actuated. The exhaust port check valve samples a small amount of mass per cycle, but because it is open during the entire blowdown process it is representative of a larger volume of gas. In either case it is difficult to determine where the mass being sampled originated from in the cylinder.

Some insight can be acquired by speculating as to the origin of the gas left behind as opposed to the origin of the gas that flows through the valves. Some of the gas left in the cylinder most likely resides along the walls of the cylinder, cylinder head, and piston. This results from the boundary condition that the gas velocity is zero at the wall. Thus the gas sampled by the large sample valve during expansion and the exhaust port check valve is probably representative of the gas near the center of the cylinder, not contained in the boundary layer. Consequently, this could explain why the formaldehyde mole fractions for these measurements are slightly lower than for the 2/4 elbow data, since the gas in the boundary layer is likely to have a higher mole fraction of formaldehyde. The flow regime near the walls during the sampling process determines the thickness of the boundary layer, which in turn indicates the importance of this effect. More detailed information on the gas flow in the cylinder during the sampling process is required to estimate the thickness of the boundary layer.

Conclusions

Conclusions can be definitively made only for the regions in the cylinder where, and at times in the cycle when, samples were extracted by the valves. These conclusions can most likely be extended to other regions in the cylinder and other times in the cycle that were not sampled, but have similar combustion characteristics.

The test data show that the location in the cylinder where gas is extracted by the fast sample valve experiences relatively complete combustion. Therefore the qualitative behavior of formaldehyde in this region is reflective of other regions in the cylinder that undergo relatively complete combustion. The following observations are made regarding formaldehyde behavior in the region sampled by the fast sample valve:

1 Significant formaldehyde formation occurs during the compression process and in the end-gas during flame propagation and associated compression.
2 Formaldehyde forms in the end gas during flame propagation at mole fractions much higher than engine-out formaldehyde mole fractions.
3 A peak in formaldehyde formation occurs during combustion, which supports the conclusion from other work that formaldehyde peaks early in natural gas flames.
4 Formaldehyde is nearly completely destroyed by the end of the combustion process.
5 Late in the expansion process formaldehyde is formed at levels comparable to those measured in the stack.
6 The rise in formaldehyde mole fraction late in the expansion process is accompanied by increases in CO and THC levels.

The data from several different sampling techniques employed during expansion is presented. These measurements provide information on the location of formaldehyde formation in the cylinder. The midstroke check valve measurements are indicative of formaldehyde behavior during expansion in regions where combustion is incomplete. The following observations are made from the formaldehyde measurements using these techniques:

1 Formaldehyde mole fractions much higher than engine-out formaldehyde mole fractions reside near the wall just above the piston late in the expansion process; CO and THC mole fractions higher than engine-out levels are also found in this region in time and space.
2 Formaldehyde mole fractions slightly lower than engine-out formaldehyde mole fractions are detected with the exhaust port check valve, except at the high boost point.
3 Samples extracted during the expansion process with the large sample valve showed formaldehyde mole fractions slightly lower than engine-out formaldehyde mole fractions for all boost levels tested.

It appears that formaldehyde formed in the bulk charge during the combustion process has little influence on engine-out formaldehyde levels. However, formaldehyde forms during the compression process and in the end gas during flame propagation. This formaldehyde can contribute to engine-out formaldehyde if it is protected from flame propagation. The data indicate that late in the expansion process most engine-out formaldehyde either emerges from quench zones or is formed from unburned hydrocarbons emitted from quench zones.

Acknowledgments

The authors express their appreciation to Kevin Johnson and Stephanie Mick for the important roles that they played in acquiring the test data. This research was sponsored by the Pipeline Research Council International of the American Gas Association and the Gas Research Institute. Enginuity International, Inc., the prime contractor, provided project management. The large and fast sample valves were designed by Optimal Engineering, Inc. and manufactured by the Woodward Governor Company.

References

[1] Coerr, L. F., Coerr, S. P., and Clowney, S. L., 1998, ''EPA's Regulation of Air Toxic Emissions Under the Industrial Combustion Coordinated Rulemaking (ICCR),'' *Proceedings of the 1998 Spring Technical Conference of the ASME Internal Combustion Engine Division*, Vol. 1, Paper No. 98-ICE-79.
[2] Olsen, D. B., and Mitchell, C. E., 1998, ''Factors Affecting Measured CH_2O in Large Bore Natural Gas Engines,'' *Proceedings of the 1998 Spring Technical Conference of the ASME Internal Combustion Engine Division*, Vol. 1, Paper No. 98-ICE-81.
[3] Kirschner, P. K., 1998, ''Formaldehyde Emissions From Caterpillar 3600 Series Engines Utilizing Field Gas as Fuel,'' *Proceedings of the 1998 Spring Technical Conference of the ASME Internal Combustion Engine Division*, Vol. 1, Paper No. 98-ICE-83.
[4] Shareef, G. S., Ferry, K. R., Gundappa, M., Leatherwood, C. A., Ogle, L. D., Campbell, L. M., 1996, ''Measurement of Air Toxic Emissions from Natural Gas-Fired Internal Combustion Engines at Natural Gas Transmission and Storage Facilities, Vol. 1,'' Gas Research Institute, *GRI-96/0009.1*, Chicago, Illinois.
[5] LoRusso, J. A., Kaiser, E. W., and Lavoie, G. A., 1983, ''In-Cylinder Measurements of Wall Layer Hydrocarbons in a Spark Ignited Engine,'' Combust. Sci. Technol., **33**, pp. 75–112.
[6] Tobis, B. J., Meyer, R., Yang, J., Brehob, D. D., and Anderson, R. W., 1994, ''Scavenging of a Firing Two-Stroke Spark-Ignition Engine,'' *Society of Automotive Engineers*, Paper No. 940393.
[7] Kannappan, A., 1964, ''A New Method for Evaluating the Scavenging Performance of Two-Stroke Diesel Engines,'' Society of Automotive Engineers, Paper No. 640370.
[8] Booy, R. R., 1967, ''Evaluating Scavenging Efficiency of Two-Stroke Cycle Gasoline Engines,'' Society of Automotive Engineers, Paper No. 670029.
[9] Houtsma, C. G., et al., 1950, ''Correlation of Scavenging Ratio and Scavenging Efficiency in 2-Stroke Compression-Ignition Engine,'' MIT thesis, Cambridge, Massachusetts.
[10] Taylor, C. F., and Rogowiski, A. R., 1954, ''Scavenging the 2-Stroke Engine,'' *SAE Transactions*, Vol. 62.
[11] Heywood, J. B., 1988, *Internal Combustion Engine Fundamentals*, McGraw-Hill, Inc., New York, New York.
[12] Gatowski, J. A., Balles, E. N., Chun, K. M., Nelson, F. E., Ekchian, J. A., and

Heywood, J. B., 1984, ''Heat Release Analysis of Engine Pressure Data,'' Society of Automotive Engineers, Paper No. 841359.
[13] Karim, G. A., Ito, K., Abraham, M., and Jensen, L., 1991, ''An Examination of the Role of Formaldehyde in the Ignition Process of a Dual Fuel Engine,'' Society of Automotive Engineers, Paper No. 912367.
[14] Mitchell, C. E., and Olsen, D. B., 1998, ''Formaldehyde Formation Mechanisms in Large Bore Natural Gas Engines,'' *ASME-ICE Conference April 1998*, Paper No. 98-ICE 80.
[15] Ruy, C., 1994, ''Zur ReactionKinetik bei der Erdgas/Methan-Verbrennung im Hinblick auf das Zwischenprodukt Formaldehyde,'' *GASWARME International, March 1994*, Vol. 43, No. 3, pp. 102–109.

Fully Coupled Rigid Internal Combustion Engine Dynamics and Vibration—Part I: Model Development

D. M. W. Hoffman[1]

D. R. Dowling

Department of Mechanical Engineering,
The University of Michigan,
Ann Arbor, MI 48109-2121

Robust predictions of engine vibration are important for preliminary design of new engines and new vehicles, and in setting component tolerances. Vibration modeling of internal combustion engines is commonly based on a one-way-coupling assumption between the engine's moving internal components and the vibrating engine block. This assumption causes Coriolis and gyroscopic interactions to be neglected, and leads to a vibration model that does not properly conserve energy. This paper presents a new seven-degree-of-freedom model for low frequency engine vibrations that does not utilize the one-way-coupling assumption. The model is based on fully coupled rigid-body dynamics for the pistons, connecting rods, crankshaft, flywheel, and engine block. Predictions from the new model are compared to those from an equivalent one-way-coupled model for poorly balanced (one-cylinder) and well-balanced (inline six-cylinder) engines. Predicted mount forces are dissimilar for the poorly balanced engine but are nearly the same for the well-balanced engine. In addition, the new model is found to properly conserve energy and account for gravitational forces. [DOI: 10.1115/1.1370399]

1 Introduction

Vibration from piston-driven internal combustion (IC) engines is an important concern for the owners and operators of many different types of vehicles. In addition to potential durability issues, excessive IC engine vibration may lead to quality perception problems for both consumer and commercial vehicles. Thus, effective vibration isolation must be incorporated into vehicle design, especially for the lower frequency range that covers the first several rotational orders of the engine. Naturally, it is best if engine vibration issues are handled in the early stages of design. However, this is only possible if robust predictions of engine vibration levels are possible. This paper describes an efficient engine vibration model suitable for preliminary design work that overcomes inconsistencies in other engine vibration models.

The standard approach to engine vibration modeling is to computationally split the mounted engine into an internal system consisting of the engine's rotating and reciprocating components, and a vibrating engine block supported on resilient mounts. The internal system and the engine block are then coupled through internal forces, but the coupling only occurs in one direction, from the internal system to the block ([1–8]). This one-way-coupled computational approach can be described as follows. The internal system is simulated assuming that all the engine's internal components lie within a perfectly stationary engine structure that is perfectly aligned in the earth's gravitational field via a perfectly rigid mounting system. The reaction forces necessary to constrain the engine's moving internal components are then computed and applied to a resiliently mounted engine block to determine its vibratory motions and the forces delivered to its mounting structure. Thus, the events leading to IC engine power delivery (internal component motion) are presumed to cause the same vibratory excitation of the engine block independent of the block's vibration state.

This approach does not allow for Coriolis or gyroscopic coupling of engine block motions to the rotating and reciprocating internal components of the engine. For example, consider an engine having a crankshaft aligned along the direction of forward travel. A pitch-angle oscillation of this engine will cause the spinning crankshaft-flywheel system to produce a reaction torque leading to a yaw rotation of the engine block. Such coupling effects augment the vibratory excitation of the engine block and are not accounted for in one-way-coupled engine vibration models. Moreover, as shown herein, one-way-coupled models do not properly conserve mechanical energy and may underpredict engine vibration levels for poorly balanced engines.

The key contribution of this paper is the presentation of a fully-coupled seven-degree-of-freedom engine dynamics and vibrations model ([9]) with comparisons to an equivalent, yet simplified, one-way coupled model (OWCM) typical of current practice. Specifically, comparisons are made between computational results from both models for a single-cylinder engine (poorly balanced) and an inline six-cylinder engine (well-balanced). The six-cylinder engine parameters used correspond to the heavy-duty Diesel test engine described in Winton and Dowling [10], Hoffman and Dowling [11], and in a companion paper ([12]). The fully coupled model (FCM) is based on rigid-body dynamics for the engine and its internal components, and linear resilient engine-block mounts. A significant assumption in this study is the exclusion of flexible dynamics of the engine system, which can potentially contribute to select and important frequencies—typically half engine orders—especially at high engine loads ([11]). These previous experiments have shown that the rigid-body assumption is acceptable for low-frequency engine block vibrations across a band of low frequencies up to 200 Hz for this heavy-duty Diesel engine. Therefore, a complete understanding of the engine rigid-body dynamics is a vital first step in understanding overall engine dynamics. The FCM incorporates one rotational degree-of-freedom for the engine's crankshaft and six degrees-of-freedom for the engine's vibratory displacements and rotations. Comparisons of the FCM to experimental measurements are provided in Hoffman and Dowling [12].

The remainder of this paper is divided into four sections. The next section presents the mathematical structure of the FCM and compares it to that of a OWCM. Internal consistency checks for the two models are described in Section 3. Comparisons and predictions based on running engine simulations from both models

[1]nee Winton. Currently at Ford Motor Company.

Contributed by the Internal Combustion Engine Division of THE AMERICAN SOCIETY OF MECHANICAL ENGINEERS for publication in the ASME JOURNAL OF ENGINEERING FOR GAS TURBINES AND POWER. Manuscript received by the ICE Division July 2000; final revision received by the ASME Headquarters Jan. 2001. Editor: D. N. Assanis.

are provided in Section 4. The final section summarizes the work presented herein and provides the conclusions drawn from this study.

2 Model Development

The fully coupled and one-way coupled modeling approaches can be described by the same schematic diagram (see Fig. 1). The models share many similarities, but there is also one important difference. Both models utilize the same inputs: cylinder pressure histories (here, experimentally measured), crankshaft load torque, an empirical friction load torque, engine geometry, and inertial properties of the engine and its components (including engine mount characteristics). Both models divide the simulation effort between the rotational motion of the piston-rod-crankshaft mechanism with one degree-of-freedom (crankangle, θ), and vibratory motion of the engine block with six degrees-of-freedom (three translations and three rotations). Both models are integrated in the time-domain so transient, as well as steady-state simulations, are possible. In both cases, the full nonlinear equations of motion for the piston-rod-crankshaft mechanism are integrated while linearized equations (linearized in block dynamic motion) are solved for the block vibrations. Both models provide predictions of instantaneous crankshaft rotation speed, engine block deflections, and engine mount loads. The difference between the FCM and the OWCM lies in the coupling between the piston-rod-crankshaft mechanism and the engine block. Only the FCM allows block motions to influence the piston-rod-crankshaft dynamics.

2.1 Analytical Formulation. The equations of motion for both the one-way-coupled and fully coupled models were formulated using Kane and Levinson's [13] analytical method for modeling complex dynamic systems (see also [14]). For brevity, only the final vector-matrix equation is provided. A full development of this equation is provided in Hoffman [9].

The coordinate system for the FCM is illustrated in Fig. 2. The FCM equations of motion are developed about an arbitrary reference point of the engine (point O in Fig. 2) that is fixed in the engine-block rigid body. This arbitrary point need not be the center of mass of the system. In fact, because the FCM incorporates a moving engine-system center of mass, a point fixed in the engine block is preferable. The laboratory reference frame, denoted by $\hat{x}$, $\hat{y}$, and $\hat{z}$, is inertial. The engine-block reference frame, denoted by $\hat{a}_1$, $\hat{a}_2$, and $\hat{a}_3$, moves with the vibrating engine. The three-point mount configuration shown in Fig. 2 is used for the single and six-cylinder engines simulated in this study.

The seven degrees-of-freedom are: x, y, and z the translations of the reference point O; q_1, q_2, and q_3 the small-angle engine

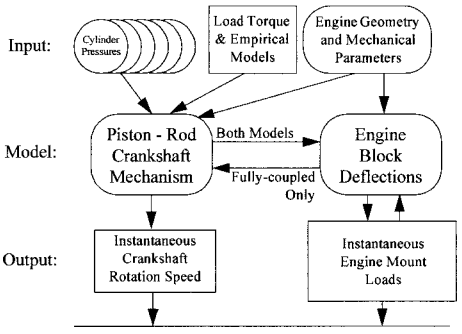

Fig. 1 Schematic diagram of the engine dynamics and vibration modeling. Models are commonly divided into two pieces: one for moving internal components and one for engine block deflections. The fully coupled model (FCM) captures complete coupling between these two model pieces; the one-way coupled model (OWCM) only includes coupling from the piston-rod-crankshaft model to the engine block deflection model.

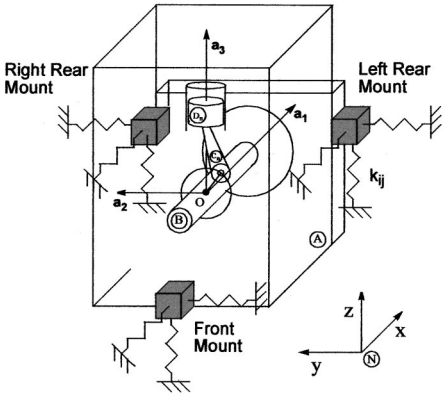

Fig. 2 Schematic showing the seven-degree-of-freedom fully coupled rigid-engine dynamics and vibration model and its coordinates. A single-cylinder (cylinder number *n*) is shown. Engine block deflections are described using three translations and three rotations. The rotational angle of the crankshaft is the final degree-of-freedom. The dark blocks denote engine mounts (resilient supports). Each resilient support is represented by three orthogonally placed linear springs and viscous dampers.

block-rotations around x, y, and z, respectively; and θ the crankshaft rotation angle at cylinder number one ($\theta=0$ when piston number one is at a top dead center). The FCM equations are

$$
[M_c]\begin{Bmatrix} \ddot{x} \\ \ddot{y} \\ \ddot{z} \\ \ddot{q}_1 \\ \ddot{q}_2 \\ \ddot{q}_3 \\ \ddot{\theta} \end{Bmatrix}
= -\begin{bmatrix} C_{tt} & C_{tr} \\ C_{rt} & C_{rr} \\ \hline 0 & 0 \end{bmatrix}\begin{Bmatrix} \dot{x} \\ \dot{y} \\ \dot{z} \\ \dot{q}_1 \\ \dot{q}_2 \\ \dot{q}_3 \end{Bmatrix} - \begin{bmatrix} K_{tt} & K_{tr} \\ K_{rt} & K_{rr} \\ \hline 0 & 0 \end{bmatrix}\begin{Bmatrix} x \\ y \\ z \\ q_1 \\ q_2 \\ q_3 \end{Bmatrix}
$$

$$
-\begin{Bmatrix} 0 \\ P_y \\ P_z \\ P_1 \\ P_2 \\ P_3 \\ \hline P_4 \end{Bmatrix}\dot{\theta}^2 - \begin{Bmatrix} S_x \\ S_y \\ S_z \\ S_1 \\ S_2 \\ S_3 \\ \hline 0 \end{Bmatrix}\dot{\theta} - \begin{Bmatrix} 0 \\ 0 \\ 0 \\ T_{\text{load}} \\ 0 \\ 0 \\ \hline T_{\text{load}} + \sum_n (A_{2_n} F_{c_n}) \end{Bmatrix}
$$

$$
+\begin{Bmatrix} 0 \\ 0 \\ 0 \\ 0 \\ [K'_{rt}]([K_{tt}])^{-1}\begin{Bmatrix} 0 \\ 0 \\ mg \end{Bmatrix} \\ \hline 0 \end{Bmatrix} - \begin{Bmatrix} 0 \\ 0 \\ m \\ (M_2 - M_3 q_1) \\ -(M_1 + M_3 q_2) \\ (M_1 q_1 + M_2 q_2) \\ (N_z + N_y q_1) \end{Bmatrix} g \tag{1}
$$

where the top six equations in this matrix representation govern the engine block motion, and the seventh equation governs the piston-rod-crankshaft mechanism. Here the mass distribution of the engine system changes with crankshaft angle, so the mass matrix $[M_c]$ is a function of θ and is given by

$$[M_c]=\left[\begin{array}{cccccc|c} m & 0 & 0 & 0 & M_3 & -M_2 & 0 \\ 0 & m & 0 & -M_3 & 0 & M_1 & N_y \\ 0 & 0 & m & M_2 & -M_1 & 0 & N_z \\ 0 & -M_3 & M_2 & I_{11} & I_{12} & I_{13} & N_1 \\ M_3 & 0 & -M_1 & I_{12} & I_{22} & I_{23} & N_2 \\ -M_2 & M_1 & 0 & I_{13} & I_{23} & I_{33} & N_3 \\ \hline 0 & N_y & N_z & N_1 & N_2 & N_3 & N_4 \end{array}\right] \tag{2}$$

where m is the mass of the complete engine system; M_1/m, M_2/m, and M_3/m define the instantaneous θ-dependent location of the engine system center of mass with respect to the reference point; and I_{11}, I_{22}, I_{33}, I_{12}, I_{13}, and I_{23} are the instantaneous θ-dependent moments of inertia of the engine system. The remaining variables in (1) and (2) are as follows: n is the cylinder number; F_{c_n} is the combustion force in cylinder number n (a function of θ); A_{2_n} is a factor that converts this combustion force into a rotational moment about the crankshaft; T_{load} is the effective load torque on the flywheel (can be a function of θ); N_y and N_z are the gravitational mass moment arms of the piston-rod-crankshaft mechanism; and the coefficients N_i and P_i ($i=1$, 2, 3, or 4) are the inertial dynamic coupling coefficients between crankshaft rotation and engine block deflections. The six S-terms are all functions of engine block vibratory rotational velocities, and they describe the gyroscopic and Coriolis coupling between the internal piston-rod-crankshaft model and the engine block deflection model.

The resilience of the engine mounts enters (1) through restoring forces and moments applied to the engine block. Each resilient mount is represented by three orthogonally placed linear springs and viscous dampers. The FCM is formulated to handle any number, location, and orientation of engine mounts having both stiffnesses ($[K]$) and damping ($[C]$) through 6×6 matrices built from four 3×3 submatrices for: (i) translation-translation interactions ($[K_{tt}]$ and $[C_{tt}]$), (ii) translation-rotation interactions ($[K_{tr}]$ and $[C_{tr}]$), (iii) rotation-translation interactions ($[K_{rt}]$ and $[C_{rt}]$), and (iv) rotation-rotation interaction ($[K_{rr}]$ and $[C_{rr}]$). The formulation of these submatrices is drawn from Himelblau and Rubin [15], Smollen [16], and Fox [17]. Linear stiffness and damping assumptions are used in this study for simplicity and because subsequent experimental comparisons completed in the companion paper ([12]) provided only linearized mount characteristics. The equation of motion for θ does not have explicit engine-mount coupling terms. However, mount damping does cause parasitic losses via coupling within the other six equations of motion.

This formulation of the FCM allows engines of any size to be simulated with essentially any set of inertia parameters without having to assume that any cylinder, piston, or rod, etc., is identical with any other. This feature of the model makes it applicable for conduct and component tolerance-vibration tradeoff studies.

And finally, the FCM shown above does not linearize the engine block static displacements caused by gravitational loading, and this leads to the second to the last term on the right side of (1).

2.2 Comparison of Fully Coupled Model (FCM) and One-Way Coupled Model (OWCM). First of all, the solution technique differs for the OWCM and the FCM. For the OWCM, the θ-equation is solved first (with all coupling terms to the block motions zeroed), then the remaining block-vibration equations are solved with the solution of the θ-equation used as a constraint input. By comparison the seven FCM equations are all solved simultaneously.

In addition, the OWCM equations are a subset of (1). The OWCM changes to the mass matrix $[M_c]$, defined by (2), involve: (i) taking the 6×6 upper left part of $[M_c]$ as a constant (i.e., evaluating it once for all time at a reference crank angle), (ii) zeroing out the last row of $[M_c]$ except for the final entry, and evaluating its last column based on the solution of the θ-equation. These OWCM changes to the mass matrix $[M_c]$ reflect the current practice for modeling rigid engine dynamics. For the OWCM, all the terms of the S-vector and the $N_y q_1 g$ in the final term (1) are also neglected. Perhaps the most troubling OWCM modification is the necessary changes to $[M_c]$ which renders it nonsymmetric.

2.3 Model Implementation. The equations for the FCM and the OWCM were coded into MATLAB® and integrated in time past the point where the initial transients had subsided to compare predicted steady-state engine vibrations from both models. Initial transient decay is produced by engine mount damping. The initial conditions were those for a stationary computational engine resting on its mounts with the crankshaft rotating at a steady speed. Comparisons are made on engine mount force output as well as engine crankshaft rotational speed. Comparisons of transient engine behavior are possible but were not pursued for this investigation.

For both models, the instantaneous crankshaft dynamics are determined from the inputs of in-cylinder combustion pressures and effective load torque. As for any real engine, if large (small) input pressure(s) and a small (large) load torque are specified, the numerical engine will accelerate (decelerate) and spin faster (slower). Thus, steady-state operating points are only possible when the input pressure and load torque are balanced. In these studies, load torque was adjusted as necessary to achieve steady-state conditions.

Friction in the piston-rod-crankshaft mechanism was assumed constant and lumped into the effective load torque applied to the engine's flywheel. Development and use of a better friction model is possible but was not pursued for this investigation.

3 Internal Consistency Studies

To validate the internal consistency of the FCM and to identify potential limitations of the OWCM, a few simple tests were conducted. These involved comparing results from identical simulations using different reference points O, adding and removing gravity from the models, and determining the energy budget for freely spinning (no combustion and no load) engines to check how well the two models conserve energy. The results of the first two consistency checks validated the FCM formulation but were not otherwise noteworthy.

The final internal consistency check yielded more interesting results. Although both one and six-cylinder engines were simulated in these freely spinning engine studies, qualitatively similar results were found, so only the single cylinder results are presented below. Mechanical and geometrical parameters of the simulated engine(s) are generally representative of commercial heavy-duty Diesel truck engines. Details are provided in Hoffman [9].

FCM and OWCM-predicted results for crankshaft rotational speed for a freely spinning single-cylinder engine with an initial speed of 1208 rpm are shown on Fig. 3 for a time period of six seconds. The simulation illustrated in Fig. 3 provides an exaggerated case to clearly delineate differences between the OWCM and the FCM. The small regular fluctuations seen on each trace are the speed fluctuations associated with the single-cylinder configuration. The average OWCM-predicted speed stays constant while the FCM-predicted speed decreases. For both models the predicted energy dissipation rate caused by vibration damping in the

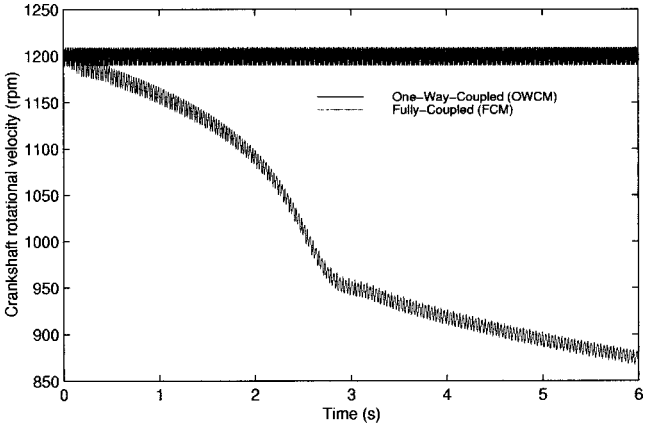

Fig. 3 One-way coupled model (OWCM) and fully coupled model (FCM) results for a freely spinning ($T_{load}=0$ and $F_{cn}=0$) single-cylinder engine showing the instantaneous engine crankshaft rotational speed versus time. The FCM exhibits parasitic energy losses to engine mount dissipation and slows down when compared to the OWCM.

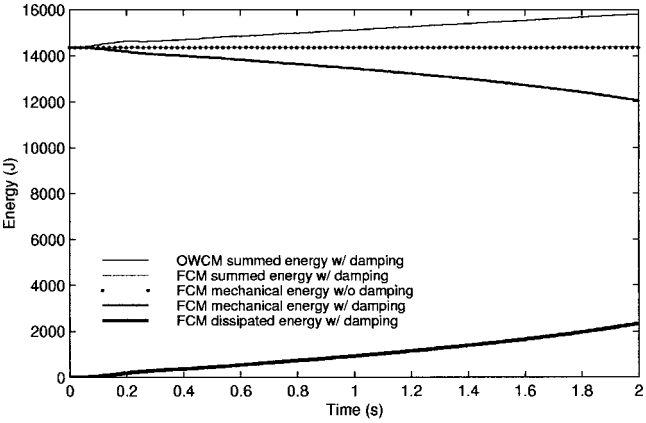

Fig. 4 One-way coupled model (OWCM) and fully coupled model (FCM) freely spinning engine energy balance for a single-cylinder engine with and without engine mount damping. The top line shows the damped OWCM summed energy increasing with time. The dotted line shows the *undamped* FCM mechanical energy constant with time. The thinnest line overlying the dotted line shows the damped FCM summed energy constant with time. The next line down shows the damped FCM mechanical energy decreasing with time, and the thickest solid line shows the damped FCM dissipated energy increasing with time. The damped FCM summed energy is simply the sum of the mechanical energy and the dissipated energy.

engine mounts is nonzero, yet only the FCM trace shows the engine slowing down via parasitic energy transfer from the moving internal engine components to the dissipative engine mounts. The variable rate of engine speed decline in the FCM predictions is due to the presence of a natural mode of the resiliently mounted engine that is excited as engine speed nears 1000 rpm. If mount damping is removed from the simulations, average FCM-predicted engine speed is constant.

To further illustrate model differences, OWCM and FCM energy budgets are provided on Fig. 4 for a freely spinning one-cylinder engine. Here, the principle of conservation of energy implies that the *summed energy*=(engine block and internal-component kinetic energy)+(engine block and internal-component potential energy)+(energy dissipated in the mounts) should be constant through out any simulation. Figure 4 shows the summed energy of the OWCM increasing with time from 14.4 kJ to 15.8 kJ in two seconds, an unphysical result caused by the incomplete dynamics in the OWCM. However, the summed energy from the freely spinning FCM engine is constant (to within numerical error), with and without mount damping. In addition, Fig. 4 shows how the decay of mechanical (kinetic plus potential) energy is balanced by the increase in dissipated energy. These results show that the FCM conserves energy while the OWCM does not.

A similar freely spinning engine study was conducted with the FCM and the OWCM for an in-line six-cylinder engine. The results are qualitatively similar to those shown on Figs. 3 and 4, but are less dramatic. Parasitic energy losses to the engine mounts are much smaller for the well-balanced engine and the OWCM violates energy conservation by merely 1 J out of 39 kJ in two seconds. Therefore, even though the OWCM does not conserve energy, this problem is much less apparent for a well-balanced engine.

4 Running Engine Comparisons and Predictions

This section presents the results from three parameter studies covering dynamic mount forces, variations in cylinder-to-cylinder combustion pressures, and internal component parameter variations. Where possible, results for both the OWCM and FCM will be presented and contrasted for both single and six-cylinder engines.

A sample comparison of FCM and OWCM-predicted mount forces is shown on Fig. 5 for a single-cylinder engine with a constant average crankshaft speed of 1200 rpm but no combustion forces. To counteract parasitic engine-mount losses, a negative load torque has been applied to the FCM engine to prevent it from slowing down. Each column of the three-by-three array of frames on Fig. 5 presents a force component in the same direction. Each row on Fig. 5 corresponds to an engine mount. The coordinate directions and mount locations are shown on Fig. 2. The darker curves on Fig. 5 are from the OWCM while the lighter curves are from the FCM. The horizontal axis on each frame is the number of crankshaft rotations since the beginning of a simulation. The corresponding vertical axes are mount forces in N.

Figure 5 shows the FCM predicts dynamic behavior the OWCM cannot. For example, the FCM mount forces are higher in nearly all cases, and its phasing of the first-order oscillations is different in most cases compared to the OWCM. Moreover, the differences in fluctuating force magnitudes can be a factor of two or more. This mismatch level was also found in other similar studies done at different speeds for the same single-cylinder engine. The engine system in this prediction is inertially asymmetric with respect to the plane of the crank-slider mechanism, therefore nonzero cross-products of inertia in the mass matrix couple all three vibration directions. Here, the x and z-direction engine block and mount motions are large enough to interact with each other.

Repeating these comparison studies for an in-line six-cylinder engine produces qualitatively similar, but much smaller, discrepancies between the OWCM and the FCM than the single-cylinder engine studies. The differences in predicted mount force amplitudes all lie in the single-digit percentage range for the six-cylinder engine.

The vibratory response of a running in-line six-cylinder engine to realistic cylinder-to-cylinder combustion-pressure variations was also studied. First, the FCM and OWCM were run with an identical measured cylinder-pressure time-trace driving all cylinders. These calculations were then repeated with the single time-trace being replaced by a series of six measured cylinder-pressures time-traces having a six percent to seven percent variation in peak pressure. Minor adjustments to the load torque were necessary to match average engine speeds between the various calculations.

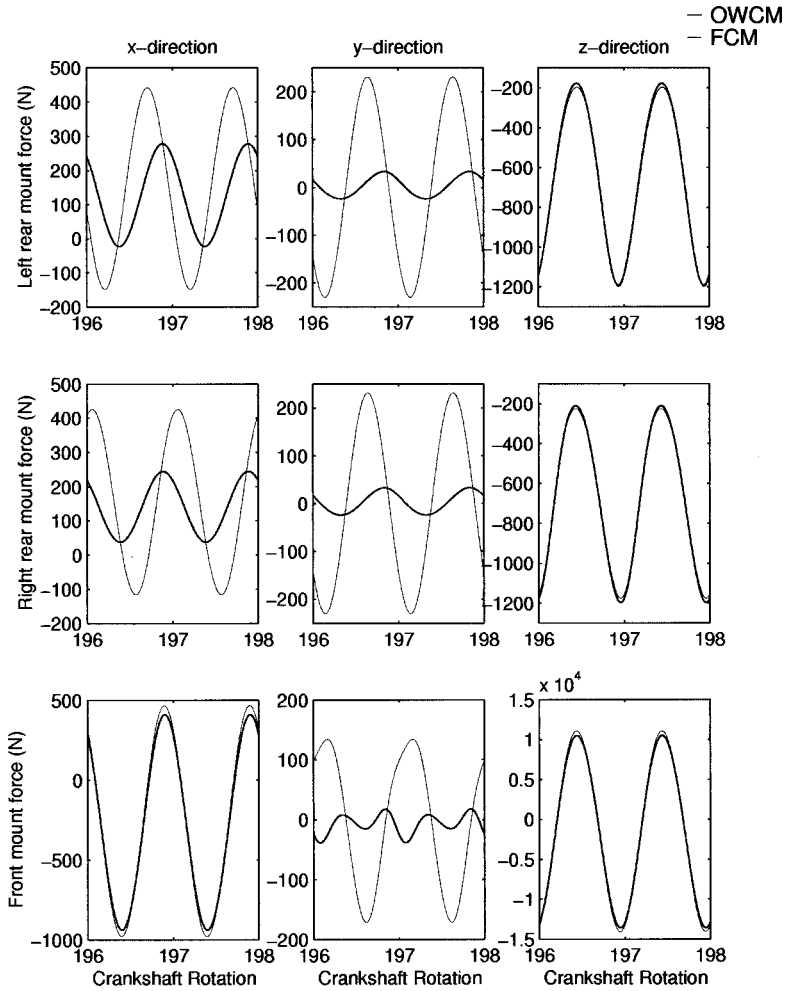

Fig. 5 Freely spinning single-cylinder engine mount forces versus crankshaft rotation at an average crankshaft rotational speed of 1200 rpm. The thin solid line is the fully coupled model (FCM) prediction, and the darker solid line is the one-way coupled model (OWCM) prediction. The differences between the model predictions are not only in first and second-order magnitudes but also in phasing.

A comparison of the frequency-domain output from these FCM calculations is shown on Fig. 6 for the six-cylinder engine running at 2100 rpm. The arrangement of the nine frames on Fig. 6 is the same as that on Fig. 5 except here the horizontal axes are frequency, and vibration force magnitudes are only plotted at integer multiples of a half-engine order (=17.5 Hz). The main differences shown on Fig. 6 occur at the first half-order frequency (17.5 Hz) on all mounts in all directions, and at frequencies below 100 Hz on all mounts in the vertical direction. When comparing such calculations from the two different models, the differences are modest with the FCM generally predicting as much as five percent higher engine-mount force magnitudes than the OWCM.

Up to this point, all simulations for the six-cylinder engine presumed all internal engine components to be identical. Yet, the formulation of both the FCM and OWCM allow essentially arbitrary component variation within the same engine. As a simple example of the influence of internal component variability, Fig. 7 presents results from the six-cylinder FCM engine operating at 1200 rpm when the first piston's weight is increased by two percent. The organization of Fig. 7 is identical to that of Fig. 6. Figure 7 shows that adding piston mass has a strong impact on the front mount *z*-direction force magnitude. This outcome is expected because the heavy piston is at the front of the engine and its increased mass tends to excite vertical oscillations at the front of the engine. Interestingly, second-order force magnitudes on the front mount in the *z*-direction are also slightly effected by this increase in piston mass. This jump in second-order magnitude is expected because the second-order excitation component of the extra piston mass is not balanced by the contributions of the moving internal components of the other cylinders as it was when all pistons are identical ([18]).

In the course of these investigations, other (possibly interesting) observations were made. For example, adding combustion forces to either model of the six-cylinder engine produces an impressive reduction in the third-order engine mount forces at 2100 rpm compared to a freely spinning engine rotating at the same speed. This result verifies the well-known fact that the addition of cylinder pressures to the running engine tends to reduce the inertial loading of the pistons and connecting rods applied to the cranks and engine block. And, relatively small static and dynamic crankshaft imbalances produce first order vibration response that can easily overwhelm the first-order contribution of cylinder-to-cylinder combustion-pressure variations. However, vibration excitation from imbalance was entirely confined to first order alone; static and dynamic imbalances do not appear to cause multiple frequency excitation, unlike cylinder-to-cylinder variations.

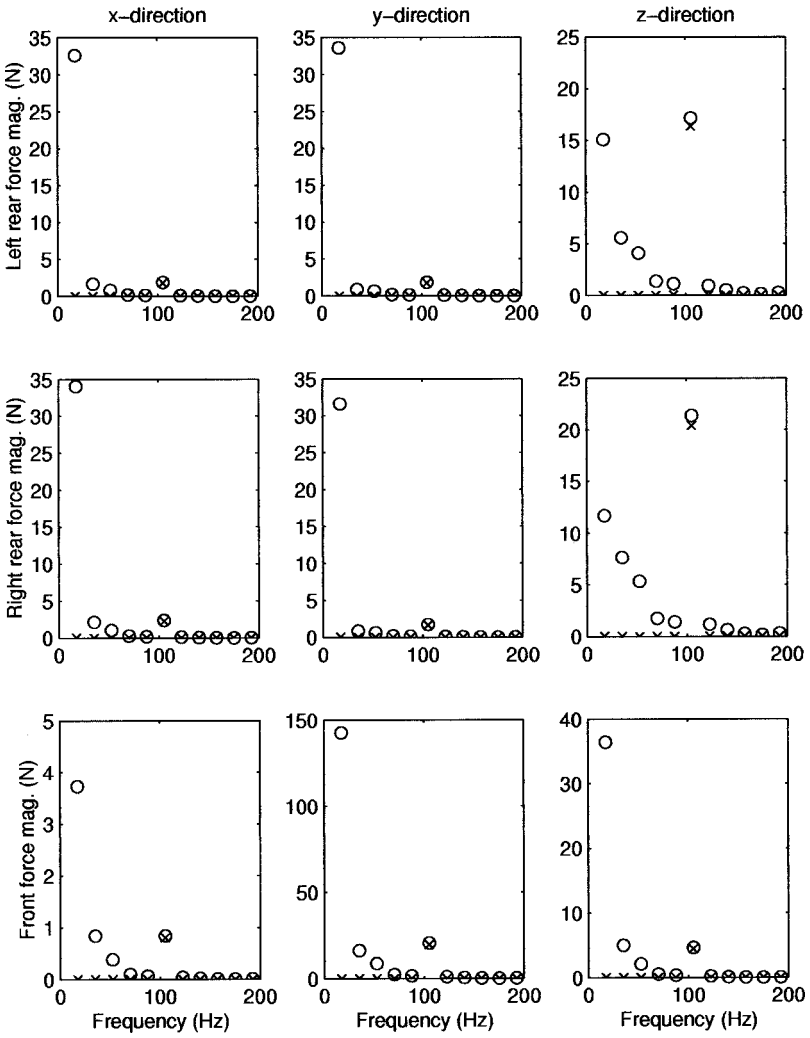

Fig. 6 Running six-cylinder engine mount force magnitudes versus frequency from the fully coupled model (FCM). The engine is running at an average crankshaft rotational speed of 2100 rpm. The circles (○) represent results with measured cylinder-to-cylinder variations and the crosses (×) are without such variations. Here, half-order frequencies starting at 17.5 Hz are excited by cylinder-to-cylinder variations along with the third-order pulses of the combustion pressure. Force magnitudes are only shown at half and whole-order frequencies.

5 Summary and Conclusions

A new and unique model for predicting rigid-body dynamics and vibration in the frequency range from zero to up through the first several engine orders has been developed for internal combustion engines supported on resilient mounts. The model simulates seven degrees-of-freedom and incorporates full rigid-body coupling between the vibrating engine block and its moving internal components. The new model is formulated about a point fixed in the engine and properly handles gravitational forces. The new model has been compared to an equivalent model that follows a common—but more approximate approach—in engine-vibration modeling, and differences have been noted. The main limitation of the new model is its reliance on rigid-body dynamics ([11]). Comparisons of the new model to experimental measurements are provided in a companion paper ([12]).

The results presented here support two conclusions. First of all, the new fully coupled model (FCM) is an improvement over one-way-coupled models (OWCMs). Although the predicted differences may be small for well-balanced engines, a computational mechanics model that properly conserves energy should always be preferred over one that does not. This is especially true here because the execution times for the FCM and the OWCM are comparable. The FCM captures static, dynamic, and vibratory engine behavior that the OWCM cannot, and these differences may be important for simulations of poorly balanced engines, or when the coupling terms missing from a OWCM are significant. These coupling terms are largest at high crankshaft speeds when the engine block is also undergoing large pitch or yaw vibratory rotations, and are likely to be important for small (i.e., lightweight) high-speed engines. And second, the FCM has the ability to simulate a wide variety of engines and predict their vibration sensitivity to a broad range of parametric changes. Only cylinder-to-cylinder combustion-pressure variations, and piston-inertia mismatch were covered here. Other parametric studies involving engine block geometry, size, and inertia; cylinder number and orientation; engine mount properties and locations; combustion timing; misfire; piston, connecting rod or flywheel inertias, etc., are all possible. In fact, the FCM might even be used to address some long-standing engine-vibrations problems, such as those of inline four cylinder engines, by clever insertion of internal component mismatches

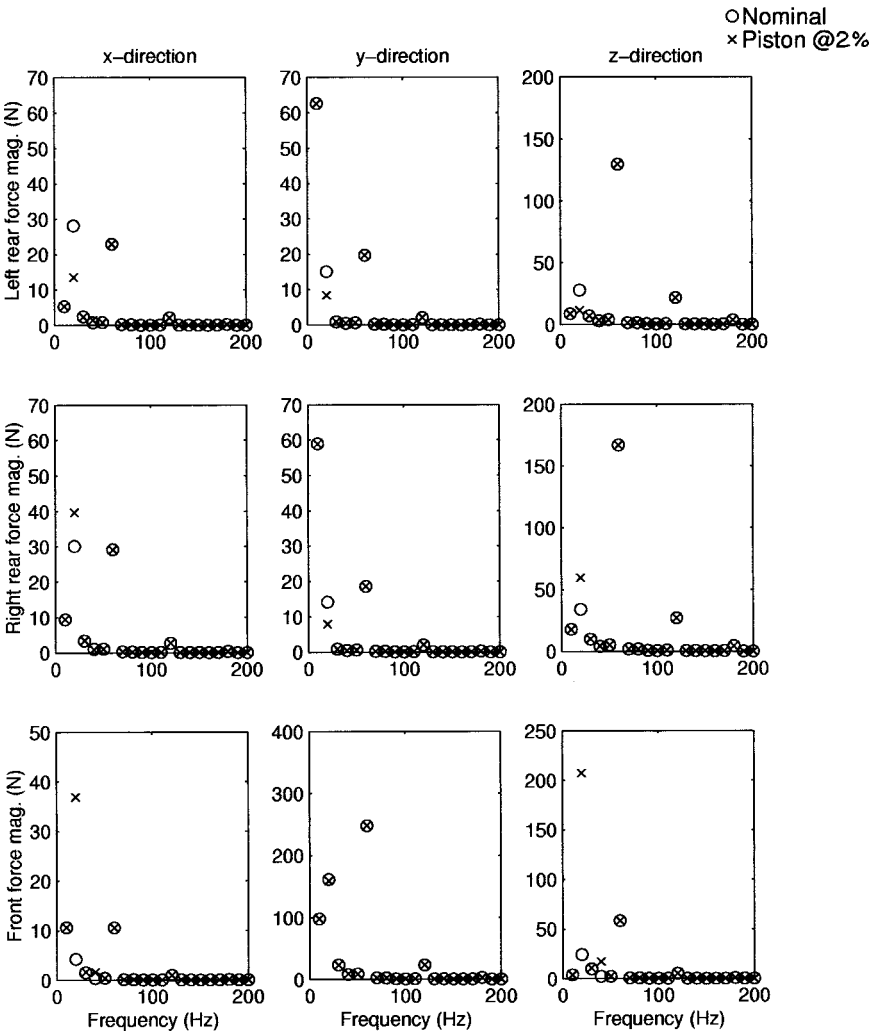

Fig. 7 Engine mount forces versus frequency for the fully coupled model (FCM) six-cylinder fired-engine running at an average crankshaft rotational speed of 1200 rpm and using measured cylinder-to-cylinder variations without (○) and with (×) a two percent increase in the mass of piston No. 1. Piston mismatch has a dominant effect on the vertical response (*z*-direction) on the front mount at first order (20 Hz) with a smaller effect at second order (40 Hz). Force magnitudes are only shown at half and whole-order frequencies.

and rotating imbalances. Furthermore, this model is an important first step in addressing engine block/crankshaft interactions, which has come to the forefront of engine vibration modeling. This model does not yet take into account the remaining rigid-body and torsional degrees-of-freedom of crankshaft motion relative to the engine block; however, extending this model to include these interactions could provide important insight into this growing area of research.

Acknowledgments

The in-cylinder pressure measurements were provided to the authors by Samuel Homsy and Scott Fiveland who were conducting a concurrent thermodynamic performance study of the test engine. This research project was supported by Cummins Engine Company, Inc. and the U.S. Army Tank Automotive Research, Development and Engineering Center (TARDEC) through the Automotive Research Center (Contract No. DAAE07-94-C-R094) at the University of Michigan.

References

[1] Norling, R. L., 1978, ''Continuous Time Simulation of Forces and Motion Within an Automotive Engine,'' SAE paper No. 780665.
[2] Butsuen, T., Okuma, M., and Nagamatsu, A., 1986, ''Application of Direct System Identification Method for Engine Rigid Body Mount System,'' SAE Paper No. 860551.
[3] Okuma, M., Ohara, T., and Nagamatsu, A., 1989, ''Application of a New Experimental Identification Method to Engine Rigid Body Mount System,'' SAE Paper No. 891139.
[4] Pol, P. S., 1989, ''Dynamic Loads in Engine Test Benches,'' *1989 ASME 12th Biennial Conference on Mechanical Vibration and Noise*, Montreal, Quebec, Canada, DE-Vol. 18-4 ASME, New York, pp. 155–159.
[5] Shiao, Y.-J., Pan, C.-H., and Moskwa, J. J., 1994, ''Advanced Dynamic Spark Ignition Engine Modeling for Diagnostics and Control,'' Int. J. Veh. Des., **15**, pp. 578–596.
[6] Snyman, J. A., Heyns, P. S., and Vermeulen, P. J., 1995, ''Vibration Isolation of a Mounted Engine Through Optimization,'' Mech. Mach. Theory, **30**, pp. 109–118.
[7] Suh, C.-H., and Smith, C. G., 1997, ''Dynamic Simulation of Engine-Mount Systems,'' SAE paper No. 971940.
[8] Hoffman, D. M. W., and Dowling, D. R., 1999, ''Modeling Fully Coupled Rigid Engine Dynamics and Vibrations,'' SAE Paper No. 1999-01-1749, *Proceedings, 1999 SAE Noise and Vibrations Conference*, Vol. 2, Traverse City, MI, Society of Automotive Engineers, Warrendale, PA, pp. 747–755.

[9] Hoffman, D. M. W., 1999, ''In-Line Internal Combustion Engine Dynamics and Vibration,'' Ph.D. thesis, University of Michigan, Ann Arbor, MI.
[10] Winton (Hoffman), D. M., and Dowling, D. R., 1997, ''Modal Content of Heavy-Duty Diesel Engine Block Vibration,'' SAE Trans., **106**, Section 6, Part 2, pp. 2802–2811.
[11] Hoffman, D. M. W., and Dowling, D. R., 1999, ''Limitations of Rigid Body Descriptions for Heavy-Duty Diesel Engine Vibration,'' ASME J. Eng. Gas Turbines Power, **121**, pp. 197–204.
[12] Hoffman, D. M. W., and Dowling, D. R., 2001, ''Fully Coupled Rigid Engine Dynamics and Vibrations—Part II: Model Experiment Comparisons,'' ASME J. Eng. Gas Turbines Power, **123**, pp. 685–692.
[13] Kane, T. R., and Levinson, D. A., 1985, *Dynamics: Theory and Applications*, McGraw-Hill, New York.
[14] Greenwood, D. T., 1988, *Principles of Dynamics*, 2nd ed., Prentice-Hall.
[15] Himelblau, H., and Rubin, S., 1961, ''Vibration of Resiliently Supported Rigid Body,'' *Shock and Vibration Handbook*, 2nd ed., C. Crede and C. Harris, eds., McGraw-Hill, New York, Chapter 3.
[16] Smollen, L. E., 1966, ''Generalized Matrix Method for the Design and Analysis of Vibration-Isolation Systems,'' J. Acoust. Soc. Am., **40**, pp. 195–204.
[17] Fox, G. L., 1977, ''Matrix Methods for the Analysis of Elastically Supported Isolation Systems,'' Shock Vib. Bull., **46**, Part 5, pp. 135–145.
[18] Den Hartog, J. P., 1985, *Mechanical Vibrations*, 4th ed., Dover Publications, New York.

Fully Coupled Rigid Internal Combustion Engine Dynamics and Vibration—Part II: Model-Experiment Comparisons

D. M. W. Hoffman[1]

D. R. Dowling

Department of Mechanical Engineering,
The University of Michigan,
Ann Arbor, MI 48109-2121

In internal combustion engine vibration modeling, it is typically assumed that the vibratory state of the engine does not influence the loads transmitted to the engine block from its moving internal components. This one-way-coupling assumption leads to energy conservation problems and does not account for Coriolis and gyroscopic interactions between the engine block and its rotating and reciprocating internal components. A new seven-degree-of-freedom engine vibration model has been developed that does not utilize this assumption and properly conserves energy. This paper presents time and frequency-domain comparisons of this model to experimental measurements made on an inline six-cylinder heavy-duty Diesel engine running at full load at peak-torque (1200 rpm) and rated (2100 rpm) speeds. The model successfully predicts the overall features of the engine's vibratory output with model-experiment correlation coefficients as high as 70 percent for vibration frequencies up through third engine order. The results are robust to variations in the model parameters. Predictions are less successful at the detail level and at higher frequencies because of uncertainties in the actual imperfections of the test engine, and because of the influence of unmodeled engine components.
[DOI: 10.1115/1.1370400]

1 Introduction

Fluctuating mechanical loads from piston-driven internal combustion (IC) engines are frequently the main source of low frequency vibration in transportation systems. Here, low frequencies are understood to lie in the range of the first few rotational orders of the running engine (up to eighth or tenth order). Even though standard isolation schemes provide excellent vibration isolation at higher frequencies, market forces still push for the reduction or elimination of low-frequency vibration in modern vehicles.

The amount of low-frequency vibration transmitted from an IC engine to a vehicle's structure is determined by the vibratory output of the engine, the location and resilience of the vibration-isolating engine mounts, and the characteristics of the vehicle's structure. Although large computationally expensive full-vehicle vibration models are possible, preliminary design work requires simple computationally efficient tools. Thus, simplified low degree-of-freedom models are required. More precisely, robust and accurate design and simulation models are needed to predict the vibratory output of mounted IC engines to minimize possible durability and customer-perceived quality problems associated with excessive vibration. Such models should execute quickly and require only relatively simple inputs so that optimization of engine parameters, engine mount locations, and isolator properties are possible.

Most engine vibration models rely on the assumption that the coupling forces between the engine's moving internal components and block are independent of the engine's vibratory motion ([1–5]). Thus the engine vibration problem is solved in two steps. First the moving internal components are simulated in a hypothetical engine that is rigid and stationary to predict coupling forces. Then, these coupling forces are applied to the resiliently supported engine block to determine its vibratory motion. This approach is approximate because it only allows for one-way coupling between the moving internal components and the block and does not account for Coriolis or gyroscopic coupling.

This paper presents low-frequency vibration comparisons between an actual running engine and the fully coupled seven degree-of-freedom engine dynamics and vibrations model described in a companion paper ([6]), hereafter referred to as Part I) and in Hoffman [7]. This fully coupled model (FCM) is based on rigid-body dynamics and does not rely on the one-way coupling assumption. The FCM properly includes all mechanical inter-actions between the rotating, reciprocating, and vibrating motions of the engine's crankshaft, flywheel, connecting rods, pistons, and block. Previous experimental work has shown that the rigid-body assumption is acceptable for low-frequency engine block vibrations ([8]).

The experimental engine for this study, an inline six-cylinder heavy-duty Diesel engine, was mounted on three-component load cells and run at peak-torque and rated-speed (power) operating points. Measurements from the load cells are compared to FCM simulations in both the time and frequency domains. Modal analysis and parameter optimization are used to determine the various inertial, geometric, and resilience parameters of the test engine and its mounts. These parameters and cycle-averaged combustion pressure measurements from the test engine are the inputs for the FCM. Model-experiment comparisons are made for steady-state engine operations, i.e., after the start-up transients in the test engine and model engine have subsided.

As might be expected, static and dynamic imbalance of the various rotating engine components (crankshaft and flywheel) and mismatch between the primarily reciprocating ones (pistons and connecting rods) can lead to significant vibratory forcing of the engine block at the low engine orders. For a variety of reasons, the resulting engine vibrations are hard to predict in detail. Here, the precise imbalance and mismatch configuration of the test engine was unknown and essentially unobtainable. In addition, the FCM as currently formulated does not include every moving engine

[1]nee Winton. Currently at Ford Motor Company.

Contributed by the Internal Combustion Engine Division of THE AMERICAN SOCIETY OF MECHANICAL ENGINEERS for publication in the ASME JOURNAL OF ENGINEERING FOR GAS TURBINES AND POWER. Manuscript received by the ICE Division July 2000; final revision received by the ASME Headquarters Jan. 2001. Editor: D. N. Assanis.

component. In particular, the front-end gear train, overhead camshaft, and fuel delivery system were not included. Zhao and Reinhart [9] have shown that the gear train and the fuel delivery system are the dominant cause of engine noise at frequencies above a few hundred Hertz. Hence, the hope here is that the dynamics and vibration contributions of these components are small enough to neglect compared to the contributions from the modeled components. Thus, the final model-experiment comparisons presented in this paper are between a model engine having an incomplete set of moving internal components and plausible but hypothetical rotational imbalances and component mismatches, and the test engine having a complete set of moving internal components but unknown imbalances and mismatches.

The remainder of this paper is divided into four sections. The next one covers the experimental setup and the measurement techniques. Section 3 describes how the quiescent engine modal analysis was used to set parameters in the FCM engine vibration model. Section 4 presents comparisons between the model output and experimental engine for vibration loads transmitted to the engine mounting structure. The final section summarizes this effort and provides a few conclusions.

2 Experimental Measurements

The experimental setup has been described in Winton and Dowling [10] and Hoffman and Dowling [8], so the following summary is brief. The test engine was a four-stroke inline six-cylinder heavy-duty Diesel engine with a nominal (wet) weight of 13,000 N, displacement of 12.7 liters, rated power of 350 kW at 2100 rpm, and peak torque of 2100 N-m at 1200 rpm. The engine was loaded by an electric dynamometer and was operated at rated-speed and peak-torque speed for this study. Torque measurements were made with a calibrated strain-gauge load cell and are accurate to ± 2 percent. Engine speed was monitored by magnetically counting teeth on a 60-tooth gear attached to the engine's crankshaft. The engine was supported on three instrumented mounts incorporating elastomeric isolation elements and three-component strain-gauge load cells. The rear mounts each employed one isolator (Lord Corporation CB 2204-2) and one three-component 22,240 N (5,000 lbf) vertical capacity load cell (AMTI MC5-3-5000). The front mount employed two isolators (Lord Corp. SSB33-1000-4) and a three-component 44,480 N (10,000 lbf) vertical capacity load cell (AMTI MC5-4-1000). The use of isolators with this test engine (unlike the hard-mounting common in industrial engine tests) was intended to ensure that the results would be applicable to vehicle design. The nine load-cell outputs (three per mount) were amplified with AMTI signal conditioners, low pass filtered below 1.05 kHz, and 16-bit digitized at 2.1 kHz for 5 seconds using Tektronix data acquisition hardware, LABVIEW™ software (from National Instruments), and a PC-type computer.

Experimental data was acquired in three steps. First, the warmed-up but quiescent engine was subjected to standard impact hammer modal analysis with output force measurements replacing the usual accelerometer or proximity probe measurements. The measured-force time-series data were Fourier analyzed and then curve-fit using commercial software (the STAR system from Spectral Dynamics, Inc.) to determine the modal frequencies, modal dampings, and modal force signatures for the six lowest-frequency modes. The six lowest modal frequencies were found to lie between 5.6 and 26.3 Hz and were assumed to describe the quiescent rigid-body modes of the mounted engine. As described in the next section, these measurements were used to optimize inertial, geometrical, and mount resilience parameters for use in the FCM.

For the second step, data was collected while the test engine was run at two extreme operating points, full load at peak torque speed (1200 rpm, 2061 N-m) and full load at rated speed (2100 rpm, 1654 N-m). These operating points were chosen since they generally represent the extreme vibration cases for this engine and thereby provide a stringent test of the rigid-body-based FCM. Thus, the results presented for the success of the model in Section IV are conservative. Because of experiment-specific limitations associated with the engine's mounting system, vibration frequencies above 200 Hz are not reported because of contamination vibration of the engine's mounting structure.

The final step of the data acquisition involved measurement of the in-cylinder combustion pressures while the engine was running. Here, a special engine cylinder head modified to accept at least one pressure sensor in each cylinder was used to make simultaneous in-cylinder pressure measurements in all six cylinders while the engine was running at steady-state at the two test conditions. The temporal resolution of these measurements was 1/4 of a crank angle degree and data was collected for 86 engine cycles. The final temporal pressure profiles used in the FCM were cycle-averaged measurements.

Unfortunately, the cylinder pressure measurements and the vibratory force measurements both required the full resources of the available data acquisition system so the two types of measurements could not be obtained simultaneously. Because of this limitation, the in-cylinder pressure measurements were made after the vibration measurements and minor (two percent to four percent) adjustments were made to the cycle-averaged pressure measurements to account for the day-to-day variations in engine performance. A time-based trigger was used in vibration data acquisition instead of a crankshaft angle-based trigger for simplicity.

3 Quiescent-Engine Model-Experiment Matching

Some of the parameters needed from the fully instrumented ready-to-run test engine for use in the FCM were either unknown or known with only limited certainty. Such parameters included the components of the engine's moment of inertia, the three-dimensional location of the engine's center of mass, and the engine-mount isolator stiffnesses and dampings. To refine the values of these parameters, modal-analysis measurements were combined with the multi-objective goal attainment capability found in MATLAB®. The procedure was as follows. A set of original estimates for these parameters was produced by the simple calculations, simple measurements, reference to manufacturer's data sheets, or educated guesses. An objective function was formulated that included predicted and experimentally determined modal frequencies, modal dampings, and selected components of the modal force signatures for the six lowest-frequency modes of the quiescent test engine. Limits were then set on the parametric space available for the optimization, and the MATLAB® optimizer was put to work to match the measured modal parameters by adjusting the estimated parameter values to minimize the objective function. Weight factors within the objective function were chosen so that greater emphasis was put on matching modal frequencies compared to modal dampings. The modal analysis optimization was completed for one reference position of the piston-rod-crankshaft system (piston no. 1 at top dead center). Because of the symmetry of the inline six-cylinder configuration and the approximate nature of the optimization, it was not necessary to adjust the experimental engine to the same configuration for the experimental modal analysis.

In principle this modal matching approach is simple but in order to allow the optimizer to attain a solution in a reasonable amount of time, the objective function had to be simplified. This was accomplished in three ways. First, the optimizer was allowed to seek a solution for the engine's inertial parameters without considering damping. This meant that the experimentally measured modal-analysis force signatures had to be projected on to the real axis, e.g., the relative phase of the various modal force signature components was accounted for by positive or negative signs alone. Fortunately, this approximation is acceptable because the measured modal dampings are small (typically less than seven percent of critical damping), and the phases of the components of the modal force signatures are typically close to either 0 deg or 180 deg. Second, only the largest modal signature components for

Table 1 Nonoptimized and optimized moment of inertial (*I*) and center of mass (*a*) parameters for the engine with respect to a reference point that lies at the intersection of the crankshaft axis and the centerline of the cylinder closest to the front of the engine

Engine block parameter	Original numerical value	Optimized numerical value
I_{xx}	214 kg-m^2	256 kg-m^2
I_{yy}	484 kg-m^2	671 kg-m^2
I_{zz}	329 kg-m^2	521 kg-m^2
I_{xy}	0 kg-m^2	42.3 kg-m^2
I_{xz}	0 kg-m^2	-60.4 kg-m^2
I_{yz}	0 kg-m^2	56.7 kg-m^2
a_x	42.2 cm	44.3 cm
a_y	2.0 cm	-8.8 mm
a_z	27.5 cm	28.3 cm

each modal force signature were used in the optimization. And third, the matching of modal dampings was conducted after the engine's inertial parameters were set. The precise implementation details and parametric optimization ranges are provided in Hoffmann [7]. The results of this optimization procedure are given in Tables 1 and 2 that list the original nonoptimized and final optimized values for the engine-inertial and mount-isolator parameters. These individual mount-isolator properties were then implemented into the model using the symmetrical matrix development presented in Part I.

The match obtained with the experimental engine is acceptable or even good. Tables 3 and 4 show a comparison of results for the optimized and experimental modal frequencies and dampings. Here the root-mean-square (RMS) fractional error is given by

$$\text{rms fractional error in } Y = \left[\frac{\Sigma_{i=1}^{6} (Y_{i,\text{exp}} - Y_{i,\text{opt}})^2}{\Sigma_{i=1}^{6} (Y_{i,\text{exp}})^2} \right]^{1/2} \quad (1)$$

where Y is the parameter of interest (frequency, damping, etc.), the subscript ''i'' refers to the mode number, the subscript ''exp'' refers to an experimental measurement, and the subscript ''opt'' refers to an optimized value. A comparison of the measured and optimized nine-component modal force signatures for the six lowest-frequency modes is omitted for brevity; however, the rms errors, when defined similarly to (1), between the measured and optimized modal signatures varied between 0.16 and 0.30. Although larger than the errors on the modal frequencies or dampings, these modal force signature errors are acceptable because they lie near the repeatability accuracy of the experimental modal analysis.

Table 3 Computed and measured quiescent-engine modal frequencies

Mode	Optimized modal frequency (Hz)	Experimental modal frequency (Hz)
1	5.85	5.68
2	9.48	9.76
3	12.47	12.84
4	13.38	13.53
5	21.59	20.98
6	26.01	26.25
	0.021 RMS Error	

Table 4 Computed and measured quiescent-engine modal dampings

Mode	Optimized modal damping (Hz)	Experimental modal damping (Hz)
1	0.3106	0.37644
2	0.4729	0.53009
3	0.7921	0.67417
4	0.4910	0.59505
5	0.6258	0.72919
6	0.7569	0.91734
	0.16 RMS Error	

Table 2 Nonoptimized and optimized engine mount stiffnesses (*k*) and dampings (*c*)

	Stiffness	Original value	Optimized value	Damping	Original value	Optimized value
Left rear	k_x	$1.88 \times 10^6 \frac{N}{m}$	$2.08 \times 10^6 \frac{N}{m}$	c_x	$2990 \frac{N \cdot s}{m}$	$842 \frac{N \cdot s}{m}$
	k_y	same as above	same as above	c_y	same as above	same as above
	k_z	$9.42 \times 10^5 \frac{N}{m}$	$1.86 \times 10^6 \frac{N}{m}$	c_z	$2110 \frac{N \cdot s}{m}$	$6878 \frac{N \cdot s}{m}$
Right rear	k_x	$1.88 \times 10^6 \frac{N}{m}$	$1.96 \times 10^6 \frac{N}{m}$	c_x	same as original left rear c_x	same as optimized left rear c_x
	k_y	same as above	same as above	c_y	same as original left rear c_x	same as optimized left rear c_x
	k_z	$9.42 \times 10^5 \frac{N}{m}$	$2.13 \times 10^6 \frac{N}{m}$	c_z	same as original left rear c_z	same as optimized left rear c_z
Front	k_x	$1.16 \times 10^6 \frac{N}{m}$	$3.22 \times 10^6 \frac{N}{m}$	c_x	$2340 \frac{N \cdot s}{m}$	$0 \frac{N \cdot s}{m}$
	k_y	same as above	same as above	c_y	same as above	same as above
	k_z	$8.48 \times 10^6 \frac{N}{m}$	$12.1 \times 10^6 \frac{N}{m}$	c_z	$6340 \frac{N \cdot s}{m}$	$3652 \frac{N \cdot s}{m}$

Overall, even though the search space for the optimizer was quite large, all the parameters were viable for the test engine. The final optimized parameters are not necessarily unique; however, as this study shows, uniqueness is not essential due to the model's robustness to variations in modal parameters. Thus, the vibration characteristics of the model and experimental quiescent engines were matched.

4 Running Engine Comparisons

This section presents a comparison of the FCM output with experimental measurements. The OWCM presented in Part I [6] is not included here because, as found in Part I, the OWCM and the FCM produce similar results for the well-balanced, inline six-cylinder engine (± 5 percent or smaller differences). There are really two challenges in predicting the vibratory behavior of the experimental engine. First, the geometrical and inertial parameters of the engine, and the geometry, stiffness, and damping of the engine's mounting system must be identified. This was accomplished through the procedure described in Section 3. The second challenge is to determine: (i) the actual variations in the test engine's internal components, (ii) the static and dynamic imbalance of the assembled crankshaft-flywheel system within the test engine, and (iii) the dynamic and vibratory effects of the unmodeled engine components. As described in Part I, small inertial mismatches between components and any static or dynamic imbalances can dramatically change the vibration response of the running engine. Unfortunately, the resources did not exist to disassemble the test engine and identify the various imperfections at a component level so the unique mismatches and imbalances of the test engine were unknown. In addition, the FCM does not include every moving component. Thus, the comparisons provided here are drawn between a model engine with a hypothetical set of imperfections and an incomplete set of moving internal components, and the test engine with an actual set of imperfections and a complete set of moving internal components.

The process for finding appropriate hypothetical component mismatches and imbalances began with a baseline model prediction for an engine lacking any imperfections. The baseline-model vibration amplitudes were up to an order of magnitude below the measured vibration levels. A short slate of engine component parameters were then varied by trial and error within the FCM to enhance the predicted vibration levels and better match the model to the experiment. (Use of optimization routines for this task exceeded the capacity of the available computational resources.) The component parameters varied were the size and location of two crankshaft imbalance masses and the six piston masses. Although a much larger number of components and component parameters exist in the six-cylinder piston-rod-crankshaft mechanism, the parameters selected for trial and error adjustments provided more than enough parameter space in which to attempt the experiment-model matching. Table 5 lists the final adjustments made to the baseline component parameter values. It must be noted here that the selections shown in Table 5 are the results of an incomplete search of the available parameter space and that many other parameter combinations might yield similar (or even superior) results. Although the piston-weight mismatches and imbalance levels may seem too large on an individual basis, they effectively represent the overall inertial mismatch and imbalance level of all the engine's components. Hence, although they are almost surely fictitious, these selected imperfections are not necessarily unreasonable.

The comparisons made here are for the three-component vibration forces transmitted through the elastomeric isolation elements to the engine's supporting structure at the engine's three mounts. The model is driven with the measured (and adjusted) average pressure time-histories for each cylinder. The parameter modifications listed in Table 5 were used to bring the vibration level of the model engine close to the vibration level of the test engine. Both the optimized and nonoptimized engine and mount parameters (see Tables 1 and 2) were used in the model. Two additional adjustments were made to match the FCM and the experiment. First, the load torque used in the model was five to six percent larger than the measurements to account for engine friction. This adjustment causes the model engine to rotate at the same speed as the test engine. Second, because the engine mount forces were measured without an absolute crank angle reference, the model output is shifted in time with respect to the experimental measurements to provide the best matchup between the two types of results.

Figures 1 and 2 show the spectral force magnitudes of the measured and predicted engine mount forces for optimized engine and mount parameters. Figure 1 shows the full load at peak torque speed results, and Fig. 2 shows the full load at rated speed results. Both figures display nine panels in a three-by-three array. Each row of panels comes from the same engine mount. Each column of panels provides force spectra from the same Cartesian direction (x, y, or z). Here the x-direction points from the front to the rear of the engine, the y-direction points out the right side of the engine when the engine is viewed from behind, and the z-direction points vertically upward (opposite gravity). The $\times$'s in each figure denote the predicted spectral amplitude at half and whole engine orders. The solid lines are the experimental spectra.

Although the comparisons shown on Figs. 1 and 2 are far from perfect, the overall trends are captured well. The largest vibration

Table 5 Parameter modifications used in the fully coupled model (FCM) to match the experiment. The piston mass number represent the percentage change in each piston. The numbers for the crankshaft imbalances are: the point mass sizes, their radial distance from the crankshaft axis of rotation, their *x*-locaiton along the crankshaft axis from the reference point (intersection the axis of cylinder No. one with the crankshaft axis), and the angular displacement when piston no. one is at top dead center.

Piston Masses	Crankshaft Imbalance
#1 –> +2.5%	Point Mass No. 1.
#2 –> +2.5%	mass = 1 kg, radius = 5.0 mm, axial distance = -0.282 m, angle = +120°
#3 –> no change	
#4 –> no change	Point Mass No. 2.
#5 –> -2.5%	mass = 1 kg, radius = 6.5 mm, axial distance = 1.006 m, angle = 0°
#6 –> -2.5%	

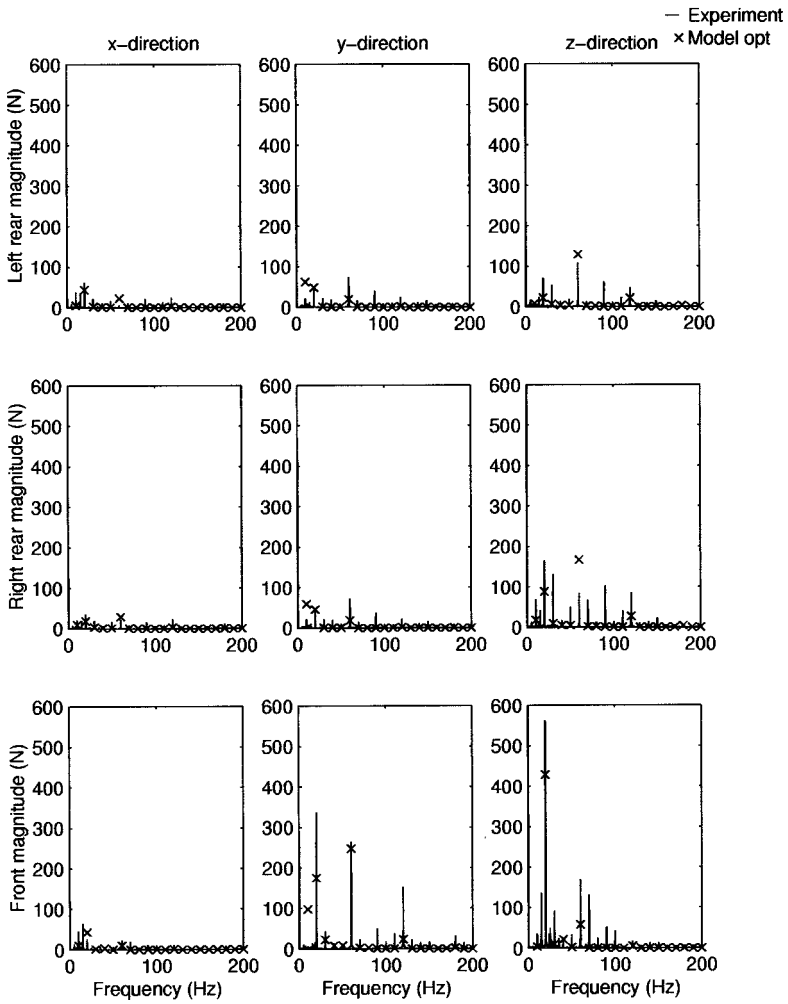

Fig. 1 Measured and simulated engine mount force magnitudes versus frequency for an in-line six-cylinder heavy-duty Diesel engine running at a speed of 1200 rpm with a load torque of 2061 N-m. The simulated engine used the optimized parameters given in Tables 1 and 2 and component imperfections listed in Table 5. The solid line denotes the experimental data. The ×'s denote the simulation results at half and whole engine orders.

forces are predicted to occur in the vertical direction on all mounts and in the *y*-direction (side-to-side) on the front mount. Comparatively smaller vibration forces are expected in the *x*-direction (front-to-back) on all mounts and in the *y*-direction on the rear mounts. The experimental results on Figs. 1 and 2 both follow these trends. All plot vertical axes were constrained to be the same to facilitate component/mount force comparisons. In addition, the FCM only predicts engine vibration at the half, first, second, third, and sixth engine orders while the engine actually vibrates at a greater range of frequencies. First order is the most important engine vibration frequency at both speeds and the match between the model and experiment is reasonable. An appropriate extension of (1) produces an rms fractional error (averaged across mounts and directions) for the model of 0.33 and 0.35 at first order for the peak-torque speed and rated speed results, respectively. At third order, the rms fractional error is larger 0.45 and 0.72 for the peak-torque speed and rated speed results, respectively. These larger third-order differences can be attributed to the high-amplitude cyclic torques exerted on the crankshaft and the engine block by the camshaft-driven fuel-injection system which fires three times per engine rotation, but was not included in the FCM.

There are also important differences between the results from the model and the experiment. The FCM does not adequately predict any of the experimentally measured higher half-order vibration frequencies (e.g., engine orders 3/2, 5/2, 7/2, 9/2, etc.). The engine's response at these frequencies may be nonrigid and therefore beyond the model's capability. This contention is supported by the findings of Nakada [11] and Reinhart [12] who attribute higher half-order vibrations to flexible engine motions.

The comparisons provided on Figs. 1 and 2 can also be cast into the time domain where the temporal phasing of the predicted engine vibration response at the various engine orders is readily apparent. Such comparisons are provided on Figs. 3 and 4, which slow the predicted and measured force-time histories covering two crankshaft rotations at peak-torque and rated speeds, respectively. Here, both the experimental and computational results have been low-pass filtered to include frequencies at third engine order and below. As for Figs. 1 and 2, the three-by-three array of panels in Figs. 3 and 4 are arrayed so that rows correspond to the same engine mount and columns correspond to the same Cartesian direction. The dark solid lines are the experimental measurements. The light solid lines are the FCM results with optimized parameters. The dashed lines are the FCM results with nonoptimized parameters. Again, the overall predictions are good with large

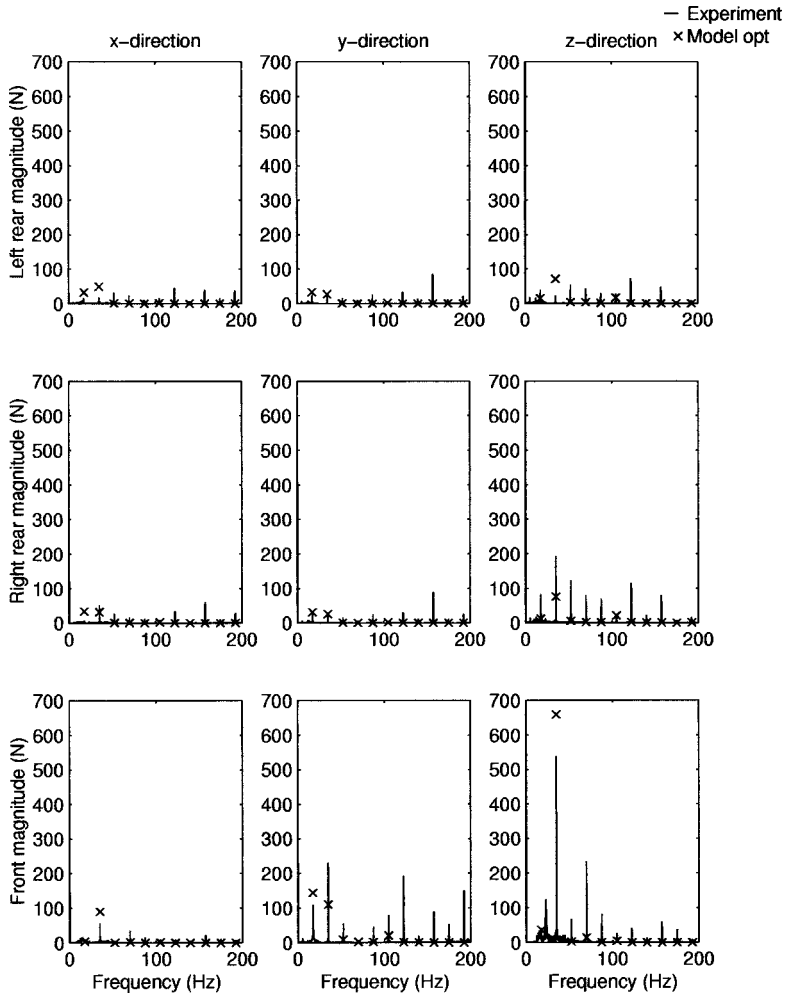

Fig. 2 Same as Fig. 1 except the engine is running at a speed of 2100 rpm with a load torque of 1640 N-m

(small) simulated vibration forces occurring where large (small) forces were measured. The most apparent mismatch between the model and the experiment (more easily seen in Fig. 4) can be traced to the amplitude and phasing of the third-order oscillations. Again, this discrepancy is most likely due to unmodeled third-order cyclic torques that are applied to the crankshaft and engine block by the engine's gear train and overhead camshaft in order to drive the engine's unit fuel injectors.

The results shown on Figs. 1–4 can be summarized by the overall model-experiment correlation coefficient, C:

$$C=\frac{\Sigma_{i=1}^{3}\Sigma_{j=1}^{3}(1/\tau)\int_0^\tau F_{m,ij}(t)F_{p,ij}(t)dt}{[\Sigma_{i=1}^{3}\Sigma_{j=1}^{3}(1/\tau)\int_0^\tau F_{m,ij}^2 dt]^{1/2}[\Sigma_{i=1}^{3}\Sigma_{j=1}^{3}(1/\tau)\int_0^\tau F_{p,ij}^2 dt]^{1/2}}, \tag{2}$$

where i is the direction number, j is the mount number, $F_{m,ij}$ is the measured engine mount force in direction i on mount j, and $F_{p,ij}$ is the FCM predicted mount force in direction i on mount j, and τ corresponds to seven complete engine cycles. Table 6 provides values of C for both operating points, for optimized and nonoptimized engine parameters, and for bandwidths up to 200 Hz and up through third engine order. The purpose of this correlation effort was to evaluate the overall performance of the model with a particular emphasis on matching the dominant mount forces. A detailed comparison of the individual mount and direction correlation coefficients is deferred until a more complete engine model (that includes the camshaft and front-end gear train, for example) is readied. As expected, the correlation coefficients for the more restrictive bandwidths (third engine order and below) are higher because the FCM does not predict as much high-frequency vibration as the test engine produces. However, all the values in Table 6 are above +0.50, which indicates that model and the experiment are in general agreement. Interestingly, the optimized parameters do not produce superior correlation values under both operating conditions. This suggests that the modeling approach embodied by the FCM is robust enough to predict engine mount forces with better than 0.50 correlation even when some important engine block geometrical and inertial parameters are approximations of the actual engine parameters. Hence detailed parameter identification is possibly unnecessary for use of the FCM, a valuable trait in preliminary design.

5 Summary and Conclusions

The key contribution here is the presentation of a comparison of the computational results from a seven degree-of-freedom fully coupled model of engine dynamics and vibration to experimental results obtained from three-component force measurements made at the three main mounts of a running inline six-cylinder heavy-duty Diesel engine. Estimated or poorly known engine parameters were determined through an optimization procedure for the vibration modes of the computational and experimental quiescent engines. Comparisons of the predicted and measured mount forces are presented in both the time and frequency domains with guarded success.

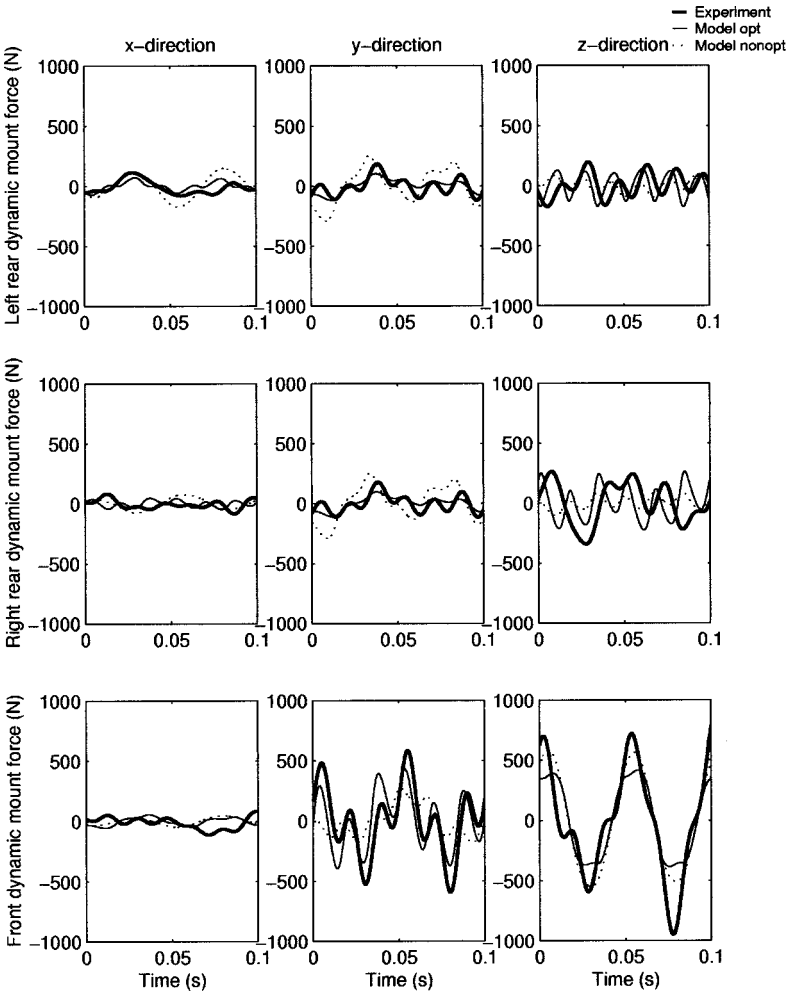

Fig. 3 Measured and simulated engine mount forces versus time for an inline six-cylinder heavy-duty Diesel engine running at a speed of 1200 rpm with a load torque of 2061 N-m. The heavy solid line is the experimental data. The light solid line is the simulated engine with the optimized parameters given in Tables 1 and 2. The dotted line is the simulated engine with the nonoptimized parameters given in Tables 1 and 2. Both simulations use the component imperfections listed in Table 5. All three data sets are low-pass filtered to include only vibration frequencies up to third engine order and the time duration shown corresponds to two engine rotations (720 crankangle degrees).

The results presented here support three conclusions. First, the new engine model described in our companion paper (Part I) is able to provide adequate, but imperfect, predictions of engine vibrations in the frequency range where rigid-body motions of the engine block and its internal components dominate. Vibration force levels were simulated correctly for the various mounts in the various directions. Current model-experiment correlation coefficients are as high as 0.70 and do not fall below 0.50. These correlation values are actually better than they first appear; a model-experiment correlation coefficient of 1.0 is impossible for a rigid-body model because of nonrigid engine components (oil, coolant) and flexible engine motions. In fact, only 85 to 90 percent of the test engine's vibratory motion can be accounted for by rigid-body modes under the test conditions considered here ([8]). Thus, the correlation coefficients found here suggest that the fully coupled model compares favorably to experimental force measurements within the limits imposed by rigid-body modeling. Moreover, the vibration contribution of engine components and systems that were not modeled may explain much of the remaining model-experiment differences.

Second, precise knowledge of an engine's inertial and geometrical parameters, and its mount isolator stiffnesses and dampings is not necessary to obtain acceptable predictions from the fully coupled model. This is a major advantage for preliminary design work when many parameter values may only be known approximately or may be based on historical or benchmark information.

And finally, moving internal-component mismatches and static and rotating imbalances are the most important source of vibration for engines whose configurations are naturally well balanced. In the present study, the computationally perfect inline six-cylinder engine produces vibration levels that are at least an order of magnitude below the measured vibration levels for a nominally identical test engine. Thus, use of a model like the FCM by engine designers could lead to better tolerancing for the inertial and geometrical parameters of moving internal engine components. For example, precise matching of piston masses may not be necessary if the connecting rods cannot be matched to a similarly stringent tolerance.

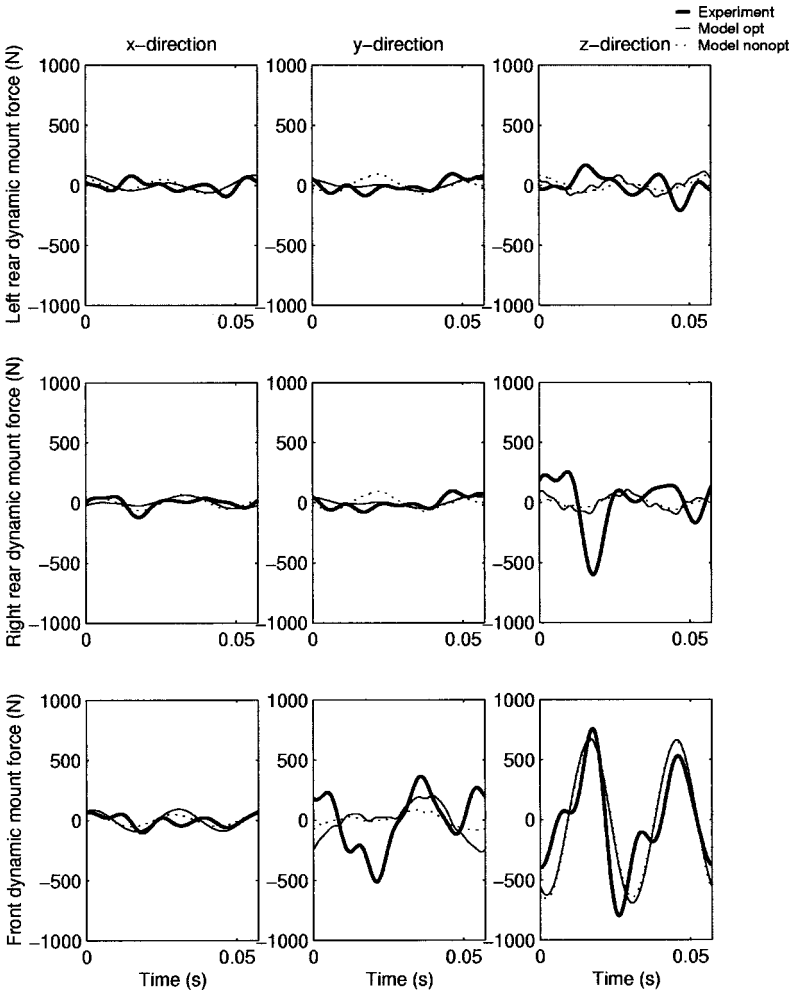

Fig. 4 Same as Fig. 3 except the engine is running at a speed of 2100 rpm with a load torque of 1640 N-m

Table 6 Overall model-experiment correlation coefficients for mount force time-histories low-pass filtered at 200 Hz and third engine order for an inline six-cylinder heavy-duty Diesel engine running at a full load at speeds of 1200 and 2100 rpm using optimized and nonoptimized parameters

		Corr. Coeff.	
Speed	Parameters	≤ 200 Hz	≤ 3rd order
1200 rpm	optimized	0.65	0.70
	non-optimized	0.58	0.63
2100 rpm	optimized	0.52	0.58
	non-optimized	0.57	0.65

Acknowledgments

The in-cylinder pressure measurements were provided to the authors by Samuel Homsy and Scott Fiveland who were conducting a concurrent thermodynamic performance study of the test engine. This research project was supported by Cummins Engine Company, Inc. and the U.S. Army Tank Automotive Research, Development and Engineering Center (TARDEC) through the Automotive Research Center (Contract No. DAAE07-94-C-R094) at the University of Michigan.

References

[1] Norling, R. L., 1978, ''Continuous Time Simulation of Forces and Motion Within an Automotive Engine,'' SAE paper No. 780665.
[2] Shiao, Y.-J., Pan, C.-H., and Moskwa, J. J., 1994, ''Advanced Dynamic Spark Ignition Engine Modeling for Diagnostics and Control,'' Int. J. Veh. Des., **15**, pp. 578–596.
[3] Snyman, J. A., Heyns, P. S., and Vermeulen, P. J., 1995, ''Vibration Isolation of a Mounted Engine Through Optimization,'' Mech. Mach. Theory, **30**, pp. 109–118.
[4] Suh, C.-H., and Smith, C. G., 1997, ''Dynamic Simulation of Engine-Mount Systems,'' SAE paper No. 971940.
[5] Hoffman, D. M. W., and Dowling, D. R., 1999, ''Modeling Fully Coupled Rigid Engine Dynamics and Vibrations,'' SAE Paper No. 1999-01-1749, *Proceedings, 1999 SAE Noise and Vibrations Conference*, Vol. 2, Traverse City, MI, Society of Automotive Engineers, Warrendale, PA, pp. 747–755.
[6] Hoffman, D. M. W., and Dowling, D. R., 2001, ''Fully Coupled Rigid Engine Dynamics and Vibrations—Part I: Model Description,'' ASME J. Eng. Gas Turbines Power, **123**, pp. 677–684.
[7] Hoffman, D. M. W., 1999, ''In-Line Internal Combustion Engine Dynamics and Vibration,'' Ph.D. thesis, University of Michigan, Ann Arbor, MI.
[8] Hoffman, D. M. W., and Dowling, D. R., 1999, ''Limitations of Rigid Body Descriptions for Heavy-Duty Diesel Engine Vibration,'' ASME J. Eng. Gas Turbines Power, **121**, pp. 197–204.
[9] Zhao, H., and Reinhart, T., 1999, ''The Influence of Diesel Engine Architecture on Noise Levels,'' SAE Paper No. 1999-01-1747, *Proceedings, 1999 SAE Noise and Vibrations Conference*, Vol. 2, Traverse City, MI, Society of Automotive Engineers, Warrendale, PA, pp. 729–735.
[10] Winton (Hoffman), D. M., and Dowling, D. R., 1997, ''Modal Content of Heavy-Duty Diesel Engine Block Vibration,'' SAE Trans., **106**, Section 6, Part 2, pp. 2802–2811 (SAE Paper No. 971948).
[11] Nakada, T., and Tonosaki, H., 1994, ''Study of the Excitation Mechanism of Half-Order Vibrations in an In-Line 4-Cylinder Internal Combustion Engine,'' Trans. Jpn. Soc. Mech. Eng., Ser. C, **60**, No. 577, pp. 2977–2983.
[12] Reinhart, T. E., 1997, private communication, Cummins Engine Company, Inc., Columbus, IN.

High-Pressure Steam-Driven Jet Pump—Part I: Mathematical Modeling

N. Beithou
Graduate Student

H. S. Aybar[1]
Associate Professor,
e-mail: hikmet.aybar@emu.edu.tr
Assoc. Mem. ASME

Department of Mechanical Engineering,
Eastern Mediterranean University,
G. Magosa, Mersin 10, Turkey

There are several proposed advanced reactor systems, which consider the utilization of a steam-driven jet pump (SDJP) as an emergency core cooling system. The steam-driven jet pump is a device without moving parts, in which steam is used as an energy source to pump cold water from a pressure much lower than the steam pressure to a pressure higher than the steam pressure. In this study, the mathematical modeling of the SDJP has been done. An experimental analysis of the high-pressure SDJP has been reported by Cattadori et al. The results of the mathematical modeling of the SDJP have been compared with Cattadori's experimental results. The comparisons show that the experimental and calculated pressure distributions are in good qualitative agreement. A parametric analysis of the SDJP is ongoing. [DOI: 10.1115/1.1365934]

1 Introduction

The steam-driven jet pump (SDJP) or injector has been used as a feedwater supply device in ships and locomotives since World War II, and as a steam-driven jet air ejector to remove noncondensable gases from the condenser in modern steam power plants, and to create vacuum in chemical process industries. The jet ejector is used in the ejector refrigeration cycle as well. This engineering device consisting of a set of converging-diverging nozzles (subsonic and supersonic) is named differently depending on what it is used for. In the past years, several passive core injection system which utilize a steam driven jet pump for emergency core cooling of advanced nuclear reactor designs have been proposed ([1–6]). The steam-driven jet pump (injector, or ejector) is a device without moving parts and requires no external energy supply. Because of these passive features of the SDJP it is very attractive in next-generation nuclear power plants, and because of minimum maintenance requirements it is also attractive in chemical processing and power industries.

In the SDJP, steam is used as an energy source to pump cold water from a pressure much lower than the steam pressure to a pressure higher than the steam pressure. Commercially available SDJPs (for instance, for the food, paper industries and fossil-fuel fired power plants) are operated at low pressure (e.g., less than 2MPa). Since mostly companies work on this device and they keep studies confidential, there is not much available information about jet pumps or ejectors in the literature. The works reported in the available literature mentioned above are related to either experimental study or concepts of passive core injection system with steam-driven jet pump. Recently, Narabayashi et al. [4] and Cattadori et al. [6] have developed a multistage high-pressure steam-driven jet pump to use as a feed water pump in advanced nuclear power plants, and reported that the SDJP could work at high pressure (over 7 MPa), as results of their experimental studies show. This paper presents the mathematical modeling of SDJP and the results of the model are compared with Cattadori's experimental results. A parametric study will be the next study to be reported soon.

[1]To whom correspondence should be addressed.

Contributed by the Nuclear Division of THE AMERICAN SOCIETY OF MECHANICAL ENGINEERS for publication in the ASME JOURNAL OF ENGINEERING FOR GAS TURBINES AND POWER. Manuscript received by the Nuclear Division, July 1999; final revision received by the ASME Headquarters Jan. 2000. Editor: H. D. Nelson.

2 Principle of Steam-Driven Jet Pump

The SDJP can be considered as equivalent to a turbine-driven pump ([4]). All thermodynamic processes in the SDJP rely on direct contact transport phenomena between water and steam. Figure 1 shows the steam-driven jet pump principle and the expected pressure distribution from the steam nozzle inlet to diffuser exit. The SDJP utilizes a steam nozzle to create a supersonic steam jet. After the steam nozzle, the supersonic steam blows into cold water in the mixing nozzle. When the steam condenses, the latent heat is converted to supersonic jet kinetic energy which accelerates the water in the mixing nozzle into the diffuser throat, and the water is sucked from the water nozzle by the near vacuum pressure as well. Because of the high pressure in the diffuser, water will be discharged.

The steam-driven jet pump (see Fig. 1) consists of the following sections:

- Steam Nozzle: It is consisting of subsonic nozzle and supersonic nozzle sections, and producing a nearly isentropic expansion and partially converting steam enthalpy into kinetic energy. It has a typical converging-diverging shape.
- Water Nozzle: It is actually a gap between inlet of mixing nozzle and outlet of steam nozzle. Water enters to mixing nozzle through water nozzle. Water nozzle produces a moderate acceleration and distributes the liquid all around the steam that exits from the steam nozzle.
- Mixing Nozzle: It is the section where water and steam come into contact. Steam exiting from the steam nozzle enters to the mixing nozzle, and water enters through the water nozzle. Steam transfers heat to water (because of the temperature difference), mass (because of the related condensation) and momentum (because of the velocity difference). The end state is complete condensation, and the out-flowing is subcooled liquid at relatively high pressure. The mixing nozzle is actually a supersonic diffuser. The mixing section has two overflow lines.
- Overflow Lines: The first overflow line (OF1) is to discharge initial excess water from mixing nozzle at the start up of the jet pump. The first overflow line will be always closed after start up. The OF1 is not shown in Fig. 1. The second overflow line (OF2), near the end of mixing nozzle, is to remove excess water from the mixing nozzle before entering the diffuser. The OF2 valve is set to control water spillage.
- Diffuser: It is the section where the liquid kinetic energy at the mixing section outlet is partially recovered producing a further pressure increase, since it is a subsonic diffuser.

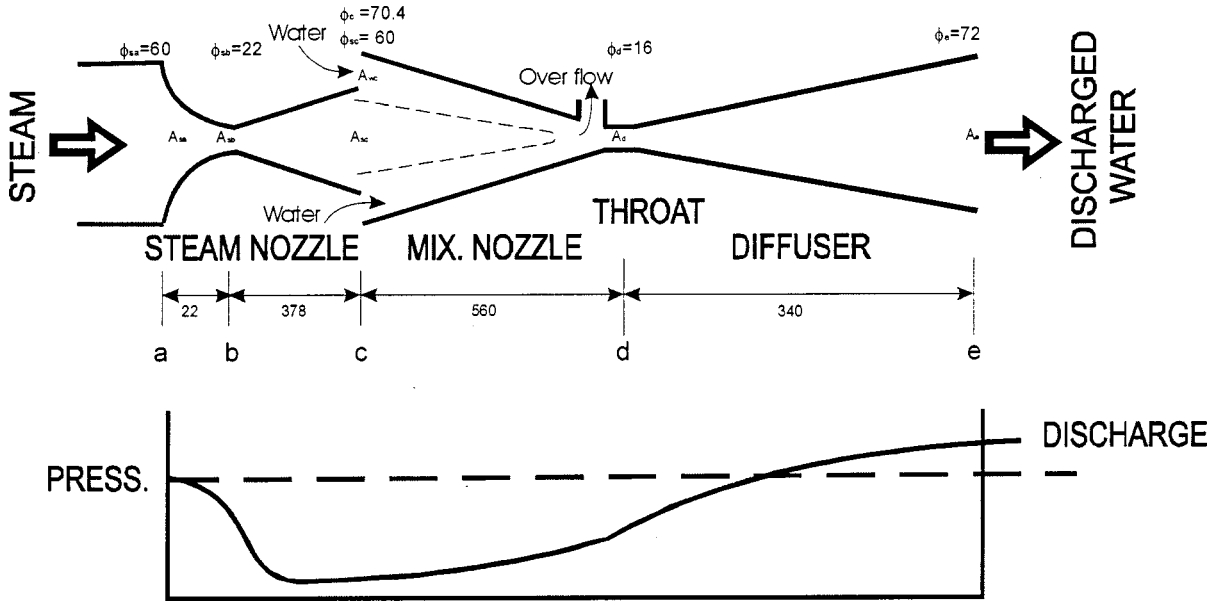

Fig. 1 Steam-driven jet pump analysis model (all dimensions are in mm)

3 Mathematical Modeling

As mentioned above, the steam-driven jet pump consists of four sections: steam nozzle, water nozzle, mixing nozzle, and diffuser, plus an overflow line (OF2), which is not represented in the present mathematical model. It is assumed that the system is a horizontal, frictionless, adiabatic system. The one-dimensional control volume method is used to develop the mathematical model for the SDJP.

3.1 Steam Nozzle. For the steam nozzle, the goal is to evaluate the pressure (P), density (ρ), velocity (V), and internal energy (u) all along the converging-diverging nozzle (i.e., the subsonic-supersonic nozzle). The governing equations (i.e., mass, momentum, and energy equations) can be written as follows for a control volume:

Conservation of mass:

$$\rho VA - \left[\rho VA + \frac{\partial}{\partial x}(\rho VA)dx\right] = \frac{\partial}{\partial t}(\rho A dx) \tag{1}$$

Since the area (A) is not a function of time, Eq. (1) can be rewritten as follows:

$$A\frac{\partial \rho}{\partial t} + \frac{\partial}{\partial x}(\rho VA) = 0. \tag{2}$$

Conservation of momentum:

$$\rho V^2 A - \left[\rho V^2 A + \frac{\partial}{\partial x}(\rho V^2 A)dx\right] + \frac{\partial}{\partial t}(\rho VA)dx = -A\frac{\partial P}{\partial x}dx. \tag{3}$$

The momentum equation can be simplified as follows:

$$\frac{\partial}{\partial x}(\rho V^2 A) + A\frac{\partial}{\partial t}(\rho V) + A\frac{\partial P}{\partial x} = 0. \tag{4}$$

Using the continuity equation (Eq. (2)) the momentum equation can be rewritten as

$$\rho\frac{\partial V}{\partial t} + \rho V\frac{\partial V}{\partial x} + \frac{\partial P}{\partial x} = 0. \tag{5}$$

Conservation of energy:

$$\rho VA\left(h + \frac{V^2}{2}\right) - \left\{\rho VA\left(h + \frac{V^2}{2}\right) + \frac{\partial}{\partial x}\left[\rho VA\left(h + \frac{V^2}{2}\right)\right]dx\right\} = \frac{\partial}{\partial t}\left[\rho A\left(u + \frac{V^2}{2}\right)\right]dx \tag{6}$$

or

$$A\frac{\partial}{\partial t}\left[\rho\left(u + \frac{V^2}{2}\right)\right] + \frac{\partial}{\partial x}\left[\rho VA\left(h + \frac{V^2}{2}\right)\right] = 0 \tag{7}$$

where u is specific internal energy, and h is specific enthalpy. After taking derivatives of the first end second terms, the equation can be rewritten as

$$A\rho\frac{\partial}{\partial t}\left(u + \frac{V^2}{2}\right) + \left(u + \frac{V^2}{2}\right)A\frac{\partial \rho}{\partial t} + \rho VA\frac{\partial}{\partial x}\left(h + \frac{V^2}{2}\right) + \left(h + \frac{V^2}{2}\right)\frac{\partial}{\partial x}(\rho VA) = 0. \tag{8}$$

Using the continuity and the momentum equations (i.e., Eqs. (2) and (5)), the energy equation will be

$$A\rho\frac{\partial u}{\partial t} + \rho VA\frac{\partial h}{\partial x} + (h-u)\frac{\partial}{\partial x}(\rho VA) - VA\frac{\partial P}{\partial x} = 0. \tag{9}$$

The derivative of the enthalpy can be calculated using

$$h = u + \frac{P}{\rho} \tag{10}$$

as follows:

$$\frac{\partial h}{\partial x} = \frac{\partial u}{\partial x} + \frac{1}{\rho}\frac{\partial P}{\partial x} - \frac{P}{\rho^2}\frac{\partial \rho}{\partial x}. \tag{11}$$

Substituting Eq. (11) into the energy equation gives

$$A\rho\frac{\partial u}{\partial t} + \rho VA\frac{\partial u}{\partial x} - \frac{PVA}{\rho}\frac{\partial \rho}{\partial x} + (h-u)\frac{\partial}{\partial x}(\rho VA) = 0. \tag{12}$$

Finally, for the steady-state subsonic or supersonic flow, the governing equations become

$$\frac{d}{dx}(\rho VA)=0 \tag{13}$$

$$V\frac{dV}{dx}+\frac{1}{\rho}\frac{dP}{dx}=0 \tag{14}$$

$$\frac{du}{dx}+\frac{P}{\rho}\left[\frac{1}{V}\frac{dV}{dx}+\frac{1}{A}\frac{dA}{dx}\right]=0. \tag{15}$$

In addition to the governing equations, the state equation $\rho=\rho(P,u)$ is used.

3.2 Water Nozzle (Water Inlet Gap). With knowledge of the steam exit pressure from the steam nozzle and the supply water pressure and temperature, the water nozzle velocity can be determined by applying the Bernoulli equation between the tank and the exit of the water nozzle:

$$\frac{V_T^2}{2}+\frac{P_T}{\rho_T}=\frac{V_{wc}^2}{2}+\frac{P_c}{\rho_{wc}} \tag{16}$$

where the subscript ''T'' denotes the water properties in the water supply tank, and the subscript ''wc'' corresponds to the water properties at the section of ''c'' (see Fig. 1). The water tank is elevated and/or pressurized water tank that is connected to the water inlet of SDJP (see [7]). Thus, P_T is actually expressed in terms of the hydrostatic head of the tank. In Eq. (16), it is assumed that the water nozzle is a frictionless nozzle. Assuming that V_T in the water tank is nearly zero, then the water velocity from the water nozzle can be calculated from the Eq. (16) as

$$V_{wc}=\left[2\left(\frac{P_T}{\rho_T}-\frac{P_c}{\rho_{wc}}\right)\right]^{1/2} \tag{17}$$

where P_c is the pressure at the section ''c,'' and ρ_{wc} is the liquid density at the pressure P_c. To find the water mass flow rate, the continuity equation can be used:

$$\dot{m}_w=\rho_{wc}V_{wc}A_{wc}. \tag{18}$$

3.3 Mixing Nozzle. Vapor exiting from the steam nozzle enters the mixing nozzle with high kinetic energy and relatively low pressure, and vapor mixes with the subcooled liquid creating a lower pressure which sucks the liquid from the water tank. The subcooled water continues to condense the vapor under two-phase flow until complete condensation, after which the flow becomes single-phase flow for the rest of the mixing nozzle. Thus, the mixing nozzle has been modeled by dividing it into two sections: two-phase flow mixing section, and single-phase flow section. The mixing section has been modeled as a nozzle that contains a vapor cone. This cone describes the vapor plume (see Fig. 1). The governing equations for two-phase flow have been taken from the RELAP5/MOD3.2 Code manual ([8]) and modified for this problem.

The mass conservation equation for vapor is

$$\frac{1}{A}\frac{\partial}{\partial x}(\alpha_g\rho_g V_g A)=\Gamma_g \tag{19}$$

and for liquid, it is

$$\frac{1}{A}\frac{\partial}{\partial x}(\alpha_f\rho_f V_f A)=-\Gamma_g \tag{20}$$

where α, ρ, V, A, and Γ_g are void fraction, density, velocity, flow area, and condensation rate, respectively. The condensation rate term can be calculated as follows:

$$\Gamma_g=-\frac{h_s A_s(T_g-T_f)}{h_{fg}} \tag{21}$$

where h_s is the direct contact condensation heat transfer coefficient at surface, and A_s is the contact heat transfer surface area per unit volume between vapor and liquid. Chun [9] suggested the following heat transfer coefficient correlation for direct contact condensation of a steam jet in subcooled water

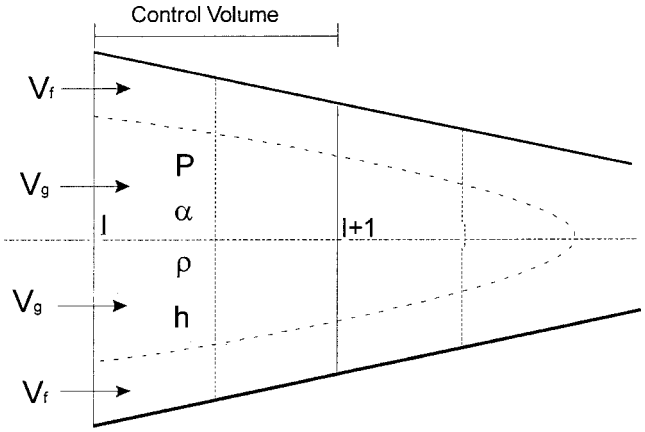

Fig. 2 Nodalization scheme for the mixing nozzle

$$h_s=1.3583c_pG_m\mathrm{Ja}^{0.0405}\left(\frac{G_i}{G_m}\right)^{0.3714} \tag{22}$$

where G_i is the mass flux of the steam at the mixing nozzle inlet, G_m is the mean value of steam mass flux for steam cone (see Fig. 2), and Ja (Jacob Number) is given as follows:

$$\mathrm{Ja}=\frac{c_p(T_g-T_f)}{h_{fg}}. \tag{23}$$

This empirical correlation has been developed in terms of water temperature, and steam mass flux for horizontal steam nozzle. In the test runs of the experiment, the range of water temperature is between 10–80°C, and the range of steam mass flux is given as $G>200\ \mathrm{kg/m^2\text{-}sec}$. The values of the water temperature and the steam mass flux in the simulation are within the ranges of Chun's experiment. Chun [9] has mentioned that the conical and ellipsoidal plume shapes are observed at low water temperature. Thus, the steam plume shape is taken as a cone in the simulation. The empirical correlation given in Eq. (22) gives an average heat transfer coefficient (h_s) for direct-contact condensation for high steam mass flux. In the simulation, the heat transfer coefficient is computed locally starting from the first control volume (see Fig. 2). Since the axial length (Δx) of control volume is small, the mean value can be taken $G_m\approx G_i$ as initial guess. Then, the heat transfer coefficient can be calculated. To calculate the condensation rate from Eq. (21), the lateral surface area (A_s) of the frustum of the cone has to be calculated for the first control volume. Again, the inlet and outlet diameters of this frustum of the cone can be assumed that approximately equals, i.e., $\phi_1\approx\phi_2$. Then, the lateral surface area (A_s) and the condensation rate can be estimated.

For the momentum conservation equations, body forces, wall friction, and the force due to the virtual mass are assumed to be negligible. The pressure change in the condensation region is negligible as well. Then, the momentum conservation equations can be written for vapor

$$\frac{1}{2}\alpha_g\rho_g\frac{\partial V_g^2}{\partial x}=\Gamma_g(V_{in}-V_g)-\alpha_g\rho_g F_{in,g}(V_g-V_f) \tag{24}$$

and for liquid

$$\frac{1}{2}\alpha_f\rho_f\frac{\partial V_f^2}{\partial x}=-\Gamma_g(V_{in}-V_f)-\alpha_f\rho_f F_{in,f}(V_f-V_g). \tag{25}$$

The force terms on the right sides of Eqs. (24) and (25) are, respectively, the momentum transfer due to interface mass transfer, and the interface frictional drag. The coefficients $F_{in,f}$ and

$F_{in,g}$ are phasic interfacial friction coefficients, and parts of the interfacial friction force for liquid and vapor, respectively. These parameters can be written as a function of the global interfacial friction coefficient that depends on densities, void fractions, velocities, and interfacial force. The interfacial velocity V_{in} is function of the phasic velocities (i.e., V_f and V_g). The evaluation of these parameters is explained in detail in RELAP5/MOD3.2 Code Manual ([8]). The void fractions (i.e., α_f and α_g) are calculated using the condensation rate and steam cone geometry (see Fig. 2).

For energy conservation, the insulated surface condition has been applied so that there is no heat transfer to or from the mixing nozzle. Thus, the energy conservation equation for vapor is

$$\frac{1}{A}\frac{\partial}{\partial x}\left(\alpha_g\rho_g V_g A\left(h_g+\frac{V_g^2}{2}\right)\right)=\Gamma_g h_g \tag{26}$$

and for liquid, it is

$$\frac{1}{A}\frac{\partial}{\partial x}\left(\alpha_f\rho_f V_f A\left(h_f+\frac{V_f^2}{2}\right)\right)=-\Gamma_g h_g\,. \tag{27}$$

After complete condensation occurs, the last part of the mixing nozzle will be single-phase liquid. Then, the steady-state governing equations (mass, momentum, and energy equations) for this region become

$$\frac{d}{dx}(\rho_f V_f A)=0 \tag{28}$$

$$\frac{1}{2}\rho_f\frac{dV_f^2}{dx}=-\frac{dP}{dx} \tag{29}$$

$$\frac{d}{dx}\left(\rho_f V_f A\left(h_f+\frac{V_f^2}{2}\right)\right)=0. \tag{30}$$

In addition to the conservation equations, the state equation

$$P=P(h,\rho) \tag{31}$$

is used.

3.4 Diffuser. The diffuser is a subsonic diverging nozzle. The flow area changes and the properties from the mixing nozzle at the diffuser inlet (i.e., the section ''*d*'') are known. To find the pressure, velocity, and temperature profiles along the diffuser, the mass, momentum, and energy equations given in Eqs. (13), (14), and (15) are used.

4 Numerical Solution

In the numerical solution, an iterative finite difference procedure with under-relaxation is used to approximate the derivatives in the governing equations that are expressed in terms of the mesh points in all sections of the SDJP. In the following sections of the paper, the numerical schemes applied to the sections of the SDJP are given.

Steam Nozzle. As it is mentioned before, the steam nozzle has two sections: subsonic flow section, and supersonic flow section. The nozzle shape is such that the flow area variation with distance (i.e., $A(x)$) along the subsonic flow section of the nozzle (converging nozzle) is given by a quadratic function, and the supersonic flow section of nozzle (diverging nozzle) is given by a linear function (see Fig. 1). Two different numerical schemes are applied to the steam nozzle: one for subsonic flow section, and one for supersonic flow section. The mass conservation equation (i.e., Eq. (13)) can be written as

$$\rho_i V_i A_i=\rho_1 V_1 A_1 \tag{32}$$

where the index of 1 corresponds to the inlets of both sections (i.e., section ''*a*'' for subsonic section and section ''*b*'' for supersonic section in Fig. 1) of the steam nozzle.

In the subsonic flow section of steam nozzle, the iterative finite difference procedure involves the following steps:

1 The inlet conditions, i.e., P_1, V_1, ρ_1, u_1, A_1, at the section ''*a*'' in Fig. 1, and the cross-sectional area at each nodal point are specified.

2 The effects of the density changes are negligible, so assuming $\rho_i=\rho_1$ gives the initialization of density at every grid point.

3 The velocity at the each grid point for the first iteration is approximated by

$$V_i=\frac{\rho_1 V_1 A_1}{\rho_i A_i}. \tag{33}$$

4 The pressure at the grid points are then found applying the following equation sequentially

$$P_i=P_{i-1}-\rho_i V_i(V_i-V_{i-1}) \tag{34}$$

from Eq. (14).

5 Using the energy equation, the internal energy is estimated for each grid point

$$u_i=u_{i-1}-\frac{P_i}{\rho_i}\left[\frac{V_i-V_{i-1}}{V_i}+\frac{A_i-A_{i-1}}{A_i}\right] \tag{35}$$

from Eq. (15).

6 Then, the density is estimated using the state equation $\rho_i=\rho(P_i,u_i)$, as a function of pressure and specific internal energy.

7 The density obtained from the state equation is substituted into the following equation, then the density is calculated for the next iteration

$$\rho_i^{n+1}=\rho_i^n+r[\rho_i-\rho_i^n] \tag{36}$$

where the index (n) shows the number of iteration, and r is the underrelaxation factor.

8 The Steps 3–7 will be repeated until a converged solution is obtained. The convergence criterion is given in Eq. (41).

In the supersonic flow section of steam nozzle, the following procedure is applied:

1 The inlet conditions, i.e., P_1, V_1, ρ_1, u_1, A_1, at the section ''*b*'' in Fig. 1, are the exit conditions of the subsonic section of the nozzle. In another word, they are the sonic conditions at the throat. The cross-sectional area at each nodal point is specified as well.

2 In the supersonic flow section of steam nozzle, the velocity changes are relatively small compared to the density changes. Thus, it is assumed that $V_i=V_1$ as a first guess. This allows first estimations to the densities at all the grid points to be found using continuity equation (Eq. (32)) as $\rho_i=(\rho_1 A_1)/A_i$. The initial pressure distribution is estimated in the supersonic nozzle using polytropic equation as following:

$$P_i=P_1\left(\frac{\rho_i}{\rho_1}\right)^{\gamma} \tag{37}$$

where γ is the ratio of specific heats. As a result of these, the initial velocity, density, and pressure distributions are estimated or guessed.

3 The internal energy is calculated using the energy equation given in Eq. (35).

4 Then, the pressure is estimated as a function of internal energy and density using the state equation $P_i=P(u_i,\rho_i)$.

5 Next, the velocities at the mesh points are calculated as follows:

$$V_i=V_{i-1}-\left[\frac{(P_i-P_{i-1})}{\rho_i V_i}\right] \tag{38}$$

from Eq. (34).

6 Updated values of densities are then found using continuity equation which gives

$$\rho_i = \frac{\rho_1 V_1 A_1}{V_i A_i} \tag{39}$$

and the underrelaxation procedure is actually again used so this equation is written in the following way:

$$\rho_i^{n+1} = \rho_i^n + r\left[\frac{\rho_1 V_1 A_1}{V_i A_i} - \rho_i^n\right]. \tag{40}$$

7 The Steps 3–6 will be repeated until the following convergence criterion is satisfied:

$$\left|\frac{\rho_i^{n+1} - \rho_i^n}{\rho_i^n}\right| \leqslant 1.0\text{E-}6. \tag{41}$$

The number of grid points (i.e., the value of Δx), the underrelaxation factor (r), and the value of the convergence criterion in the Eq. (41) are defined as a result of several test runs. The number of grid points is 300 in the subsonic flow and supersonic flow sections of the steam nozzle. The value of the underrelaxation factor is chosen as 0.2, and the value of the convergence criterion is given in Eq. (41) for the steam nozzle. The number of grid points between 300–250 are found to be adequate. The number of iterations is found to be 69 and 28 for the value of underrelaxation factor of 0.2 and 0.4, respectively. The relative difference between the exit pressure of the steam nozzle for those values of the underrelaxation factor is 1.15 percent. The numerical scheme does not converge for the value of the under-relaxation factor of >0.7. The number of iterations is found to be 69 and 47 for the value of convergence criterion of 1.0E-6 and 1.0E-4, respectively, with underrelaxation factor of 0.2. The relative difference between the exit pressure of the steam nozzle for those values of the convergence criterion is less than 1.0 percent. There is no convergence for the convergence criterion of 0.01.

Mixing Nozzle. For the mixing nozzle, the inlet and exit sections are the section ''*c*'' and ''*d*,'' respectively (see Fig. 1). The steam pressure gives the pressure at the section $c(P_c)$, and steam velocity, V_g, steam density, ρ_g, and steam enthalpy, h_g, are obtained from the steam nozzle calculation. These are used to calculate the steam mass flow rate ($\dot{m}_g$). For given water tank conditions, P and T and thus h, Eqs. (17) and (18) are used to determine the water velocity (V_{wc}) and the mass flow rate ($\dot{m}_w$).

In the two-phase region ρ_f, ρ_g, V_f, V_g, h_f, h_g and P are the unknown variables, thus seven equations are needed to solve for these seven unknowns. The nodalization scheme for the mixing nozzle is shown in Fig. 2. Since the density change is small with respect to velocity change, the densities are initialized with the known inlet conditions ($\rho_{f,i} = \rho_{f,1}$ and $\rho_{g,i} = \rho_{g,1}$) first. Then, the velocities are calculated from the momentum equations for the junction,

$$V_{g,i+1} = \left[\frac{(0.5\alpha_{g,i}\rho_{g,i})V_{g,i}^2 + \Gamma_{g,i}(V_{in,i} - V_{g,i})\Delta x - \alpha_{g,i}\rho_{g,i}\Delta x F_{in,g}(V_{g,i} - V_{f,i})}{(0.5\alpha_{g,i}\rho_{g,i})}\right]^{1/2} \tag{42}$$

from Eq. (24)

$$V_{f,i+1} = \left[\frac{(0.5\alpha_{f,i}\rho_{f,i})V_{f,i}^2 - \Gamma_{f,i}(V_{in,i} - V_{f,i})\Delta x - \alpha_{f,i}\rho_{f,i}\Delta x F_{in,f}(V_{f,i} - V_{g,i})}{(0.5\alpha_{f,i}\rho_{f,i})}\right]^{1/2} \tag{43}$$

from Eq. (25).

The densities are calculated from the mass conservation equations as follows:

$$\rho_{g,i+1} = \frac{(\alpha_{g,i}\rho_{g,i}V_{g,i}A_i + \Gamma_{g,i}A_i\Delta x)}{\alpha_{g,i+1}V_{g,i+1}A_{i+1}} \tag{44}$$

from Eq. (19)

$$\rho_{f,i+1} = \frac{(\alpha_{f,i}\rho_{f,i}V_{f,i}A_i - \Gamma_{g,i}A_i\Delta x)}{\alpha_{f,i+1}V_{f,i+1}A_{i+1}} \tag{45}$$

from Eq. (20), and the energy equations give the enthalpies of each cell as follows:

$$h_{g,i+1} = \frac{\left(\alpha_{g,i}\rho_{g,i}V_{g,i}A_i\left(h_{g,i} + \frac{V_{g,i}^2}{2}\right) - \alpha_{g,i+1}V_{g,i+1}A_{i+1}\rho_{g,i+1}\frac{V_{g,i+1}^2}{2} + \Gamma_{g,i}h_{g,i}A_i\Delta x\right)}{\alpha_{g,i+1}V_{g,i+1}A_{i+1}\rho_{g,i+1}} \tag{46}$$

from Eq. (26)

$$h_{f,i+1} = \frac{\left(\alpha_{f,i}\rho_{f,i}V_{f,i}A_i\left(h_{f,i} + \frac{V_{f,i}^2}{2}\right) - \alpha_{f,i+1}V_{f,i+1}A_{i+1}\rho_{f,i+1}\frac{V_{f,i+1}^2}{2} - \Gamma_{g,i}h_{g,i}A_i\Delta x\right)}{\alpha_{f,i+1}V_{f,i+1}A_{i+1}\rho_{f,i+1}} \tag{47}$$

from Eq. (27).

Then the densities are updated using Eq. (36). The pressure is found using the state equation (Eq. (31)) for each node. The iteration continues until the convergence criterion given by Eq. (41) is satisfied. The boundary between the two-phase and single-phase regions (i.e., the end point of the two-phase region) is determined by looking for $\alpha_g = 0$.

In the single-phase liquid region, the velocities are estimated first as $V_{f,i} = V_{f,1}$. Then, from the mass conservation equation, the densities are calculated using the initial guess of the velocities as follows:

$$\rho_{f,i+1} = \frac{(\rho_{f,i}V_{f,i}A_i)}{V_{f,i+1}A_{i+1}} \tag{48}$$

from Eq. (28).

Using the initial guess of the velocities and the calculated densities, the enthalpies are calculated from the energy equation as follows:

$$h_{f,i+1}=\frac{\left(\rho_{f,i}V_{f,i}A_i\left(h_{f,i}+\frac{V_{f,i}^2}{2}\right)-V_{f,i+1}A_{i+1}\rho_{f,i+1}\frac{V_{f,i+1}^2}{2}\right)}{V_{f,i+1}A_{i+1}\rho_{f,i+1}} \tag{49}$$

from Eq. (30).

The state equation $P_i=P(\rho_i,h_i)$ gives the pressure at each cell. The momentum equation is solved for the velocities

$$V_{f,i+1}=\left(V_{f,i}^2+\frac{2(P_i-P_{i+1})}{\rho_{f,i}}\right)^{1/2} \tag{50}$$

from Eq. (29).

The velocities are updated for the next iteration

$$V_i^{n+1}=V_i^n+r[V_i^{n-1}-V_i^n]. \tag{51}$$

The iteration continues until the following convergence criterion is satisfied.

$$\left|\frac{V_i^{n+1}-V_i^n}{V_i^n}\right|\leq 1.0\text{E-}4. \tag{52}$$

In the mixing nozzle, the number of grid points (i.e., the value of Δx), the underrelaxation factor (r), and the value of the convergence criterion in the Eq. (52) are again defined as a result of several test runs. The number of grid points is 560 (i.e., $\Delta x=1$ mm). The value of the underrelaxation factor is chosen as 0.2, and the value of the convergence criterion is 1.0E-4 as given in Eq. (52).

Diffuser. The shape of the diffuser (i.e., $A(x)$) is given a linear function. The exit conditions of the mixing nozzle are the inlet conditions of the diffuser, namely the density, the temperature of liquid. The inlet velocity is function of the inlet mass flow rate. As it is explained in the Section 2, there is an overflow line (OF2) near the throat. Some amount of mass is extracted from the OF2, and the inlet mass flow rate for diffuser will be total mass flow rate in the mixing nozzle minus the mass flow rate from OF2. Then, the inlet velocity is defined from the inlet mass flow rate of the diffuser.

To determine the pressure, velocity, density, and temperature distributions in the diffuser, the numerical procedure given for the subsonic section of the steam nozzle has been applied (see the Section 3). In the diffuser, the number of grid points is 300. The relaxation factor is taken as 0.8 with the converge criterion of 10E-6. The number of iteration with those values is 8.

5 Results and Conclusion

To validate the results of the SDJP mathematical modeling, the results of Cattadori [6] and co-worker's experiment have been used. Cattadori and his co-workers [6] have designed a SDJP for the high-pressure core injection system of advanced light water reactors, and they have presented the experimental results of this test SDJP in their paper. The SDJP dimensions given in Fig. 1 are taken from Cattadori's paper. There are four independent or known parameters: supply steam pressure, supply steam enthalpy (steam may be saturated or superheated), supply water pressure, and supply water temperature (water is always subcooled). On the other hand, there are several dependent or calculated (measured in the experiment) parameters that are: supply water flow rate, water-steam flow rate ratio, discharge water pressure and temperature, and discharge water mass flow rate. The overflow mass flow rate can also be considered an independent parameter.

Table 1 shows the range of the independent parameters used and dependent parameters measured in the Cattadori's experiment. To compare the pressure distribution with the experimental pressure distribution available in the Cattadori's paper, the maximum steam pressure (8.7 MPa) and the other independent parameters (given in the Table 1) have been taken, and the pressure distribution in all sections of the SDJP has been obtained. Figure 3 shows the experimental and calculated pressure distributions in the SDJP for comparison. As it is seen in this figure, the experimental and calculated pressure distributions are generally in good qualitative agreement. There are some discrepancies between experimental and calculated results for the pressure distribution of the steam nozzle. In the Cattadori's paper, the steam nozzle inlet, throat, and exit diameters are given only. There is no information about the shape of steam nozzle, namely about $A(x)$. Then, it is assumed that the shape of steam nozzle can be represented by quadratic function in subsonic section, and by linear function in supersonic section. This may effect the simulation results at the inner grid points. However, if the exit pressure of the steam nozzle is considered, the experimental and computed pressure values are close. Since the steam nozzle exit and velocity are only the data passed to the mixing section calculation, the effects of this difference on the other sections of the SDJP may be negligible. In the diffuser, there are some differences between experimental and

Table 1 The independent and the dependent parameters in the experiment and simulation

	CATTADORI'S EXPERIMENT	SIMULATION
Independent Parameters		
Steam Pressure (MPa)	2.5 - 8.7	8.7
Steam Superheat (°C)	5 - 30	0.0 (T_{sat})
Supply Water Pressure (kPa)	200 - 260	260
Supply Water Temperature (°C)	15 - 37	15
Dependent Parameters		
Supply Water Flow Rate (kg/s)	14 - 21	13.99
Water-Steam Flow Rate Ratio	3 - 14	2.9
Discharge Water Pressure (MPa)	2.8 - 9.8	9.54
Discharge Water Temperature (°C)	61.5 - 193.9	192.47
Overflow Flow Rate (kg/s)	7.2 – 17.6	4.6

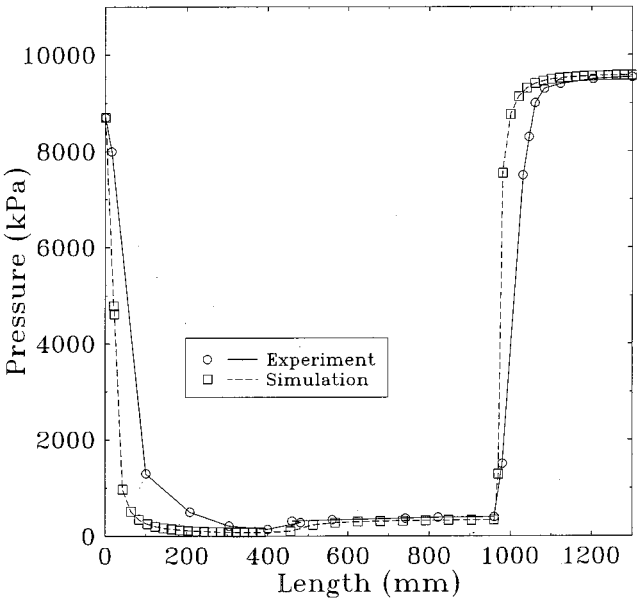

Fig. 3 Pressure distribution in the steam-driven jet pump

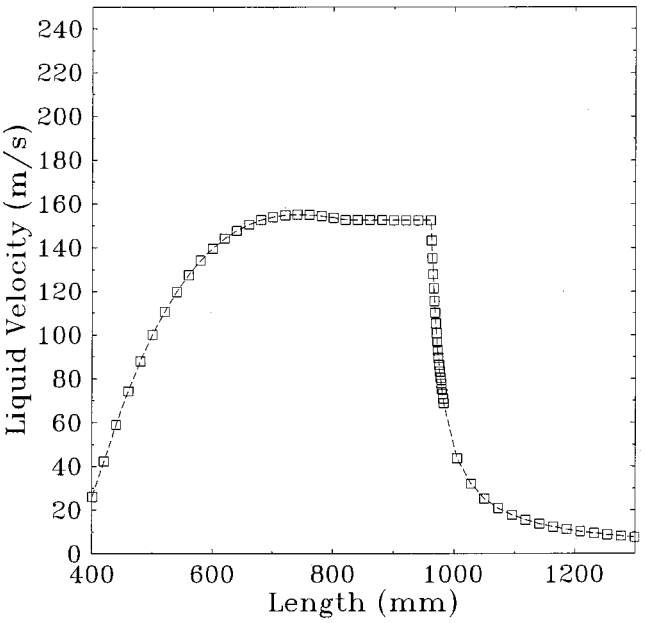

Fig. 4 Computed velocity distribution of water in the mixing nozzle and diffuser

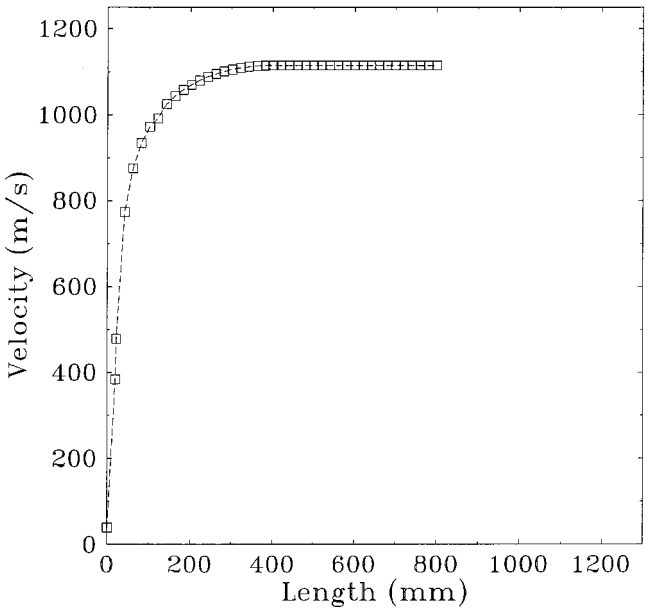

Fig. 5 Computed velocity distribution of steam in the steam nozzle and mixing nozzle

calculated pressure distribution as well. However, the experimental and calculated discharge pressures are close each other. The discharge pressure in the experiment is 9.8 MPa and in the simulation for the same steam inlet pressure of 8.7 MPa is 9.54 Mpa (see Table 1). The relative difference is about two percent. As it is seen in Table 1, the other calculated parameters are within the range of the experimental parameters. However, the adjusted overflow mass flow rate in the simulation is not within the range of the experimental overflow rate. As it is mentioned before, the overflow mass flow rate is adjusted to obtain the exit pressure ten percent higher than steam inlet pressure. This difference between experimental and calculated overflow mass flow rate is because of the steam inlet temperature. The steam used in the experiment is superheated steam. The range of the steam superheat is given as 5–30°C. Since there is no information about exact value of steam temperature for this pressure distribution in the Cattadori's paper, the saturated steam temperature is assumed for the simulation of this case. The lower temperature steam requires the lower water flow rate for condensation. Thus, the overflow mass flow rate will be lower than the experimental overflow rate as seen in Table 1.

In Fig. 4, the computed velocity distribution of water in the mixing nozzle and diffuser is given. As we expected, the water velocity increases in the mixing nozzle because of momentum transfer from the high velocity vapor cone. At the end of the mixing nozzle there is only liquid, and the velocity of the water is about 150 m/s. While the water velocity decreases in the diffuser, the pressure increases. The steam velocity in the steam nozzle (subsonic and supersonic nozzles) increases. Figure 5 shows the distribution of the computed steam velocity in the steam and mixing nozzle. At the exit of the steam nozzle (400 mm), the velocity of 1100 m/s was obtained. Then the steam velocity remains constant in the mixing nozzle. The computed temperature distribution in the SDJP is given in Fig. 6. In the steam nozzle, the temperature of steam decreases. Whereas in the mixing nozzle, the water temperature increases and the steam temperature remains unchanged because of condensation. At about the distance of 800 mm, the condensation is completed and the water temperature starts to increase a little because of contraction. At the beginning of the diffuser, the temperature of the water increases slightly and remains unchanged again.

The steam-driven jet pump is a kind of pump that has no moving parts and requires no external energy supply. In this study, the mathematical modeling of the steam-driven jet pump has been developed to analyze it. In general, it is assumed that the system is a horizontal, frictionless, adiabatic system, and a one-dimensional steady-state control volume method was used in mathematical model. In the numerical solution, an iterative finite difference procedure with underrelaxation is used to approximate the governing equations for each section of the SDJP. To verify the model for the simulation, the simulation results have been compared with the Cattadori's experimental results. In the numerical procedure, the number of grid points in the subsonic and supersonic sections is 300 (i.e., 600 grid points in steam nozzle). The value of the underrelaxation factor, and the convergence criterion are is 0.2

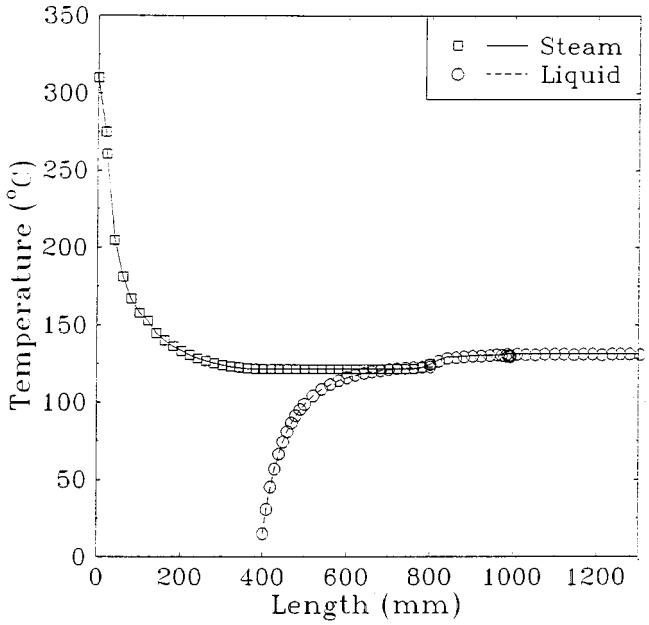

Fig. 6 Computed temperature distribution in the steam-driven jet pump

and 1.0E-6, respectively. The number of iteration is 69. In the mixing nozzle, the number of grid points is 560 (i.e., $\Delta x = 1$ mm). The value of the underrelaxation factor is 0.2, and the value of the convergence criterion is 1.0E-4. In the diffuser, the number of grid points and the relaxation factor are 300 and 0.8, respectively. With the converge criterion of 10E-6, the number of iteration is 8. The number of grid points, the value of the underrelaxation factor, and the value of the convergence criterion are defined after several test runs of computer program. The computer program for the simulation is written in FORTRAN. Several subroutines have been developed to obtain the water and steam properties using Helmholtz functions ([10]). The computer program has been run on a Pentium II-166 MHz personal computer, and the computation time is in the order of minutes. As a last word, the model represents a simplified mathematical treatment of a fairly complex fluid flow, heat transfer, and thermodynamic process.

The next step of this work is a parametric study that is ongoing. According to the experimental studies of Narabayashi [4] and Cattadori [6] the startup procedure of the SDJP is very important. To investigate the startup of the SDJP, a time-dependent mathematical modeling of the SDJP is needed.

Nomenclature

Capital letters

A = area (m^2)
G = mass flux (kg/m^2 s)
P = pressure (Pa)
T = temperature (K)
V = velocity (m/s)

Lowercase letters

c_p = specific heat at constant pressure (J/kg °C)
h = enthalpy (J/kg)
h_s = direct contact heat transfer coefficient at surface (W/m^2K)
$\dot{m}$ = mass flow rate (kg/s)
r = relaxation factor
u = internal energy (J/kg)
t = time (s)
x = distance (m)

Greek letters

Γ = condensation rate (kg/s)
α = void fraction
γ = ratio of specific heats
ϕ = diameter (mm) (in Fig. 1)
ρ = density (kg/m^3)

Subscripts/superscripts

c = section c in Fig. 1
f = liquid (water)
g = vapor (steam)
fg = latent heat
i = volume index, inlet (in Eq. (22))
in = interface
m = mean value (in Eq. (22))
n = iteration index
T = water tank
s = surface
w = water

References

[1] Howard, R. W. 1984, ''Steam Driven Water Injection,'' United States Patent 4.440.719.
[2] Suurman, S., 1986, ''Steam-Driven Injectors act as Emergency Reactor Feedwater Supply,'' Power, **3**, p. 95.
[3] Christensen, R. N., Aldemir, T., and Jayanti, S., 1987, ''An Inherently Safe BWR with A Steam Driven ECCS: Steam Injector,'' Energ. Nucl. (Rome), **2**, pp. 30–37.
[4] Narabayashi T., Miyano, H., Nei, H., Ozaki, O., Mizumachi, W., and Shioiri A., 1992, ''Feasibility Study on Steam Injector Driven Jet Pump for Next-Generation Reactor,'' Int. Conference on Advance Nuclear Power Plant, pp. 36.2.1–36.2.7.
[5] Soplenkov, K. I., 1994, ''Passive Heat Removal System With Injector-Condenser,'' IAEA Advisory Group Meeting on Technical Feasibility and Reliability of Passive Safety System, Juelich, Germany.
[6] Cattadori, G., Galbiati, L., Mazzocchi, L., Vanini, P., 1995, ''A single-Stage High Pressure Steam Injector for Next-Generation Reactors: Test Result and Analysis,'' Int. J. Multiphase Flow, **21**, pp. 591–606.
[7] Aybar, H. S., and Beithou, N., 1999, ''Passive Core Injection System With Steam Driven Jet Pump for Next Generation Nuclear Reactors,'' Ann. Nucl. Energy, **26**, pp. 769–781.
[8] RELAP5 Code Development Team, 1995, *RELAP5/MOD3.2 Code Manual Volume 1: Code Structure, Systems Models and Solution Methods*, NUREG/CR-5535, INEL-95/0174, Idaho National Engineering Laboratory, Idaho Falls, ID.
[9] Chun, M. H., and Kim, Y. S., 1996, ''Direct Condensation of Steam Jets in Subcooled Water,'' ANS Trans., **75**, pp. 385–387.
[10] Moran, M. J., and Shapiro, H. N., 1998, ''Fundamentals of Engineering Thermodynamics,'' 3rd Ed., John Wiley and Sons, West Sussex, UK.

High-Pressure Steam-Driven Jet Pump—Part II: Parametric Analysis

N. Beithou
Graduate Student

H. S. Aybar[1]
Associate Professor
e-mail: hikmet.aybar@emu.edu.tr

Assoc. Mem. ASME
Department of Mechanical Engineering,
Eastern Mediterranean University,
G. Magosa, Mersin 10, Turkey

The steam-driven jet pump (SDJP) is a device without moving parts, in which steam is used as an energy source to pump cold water from a pressure much lower than the steam pressure to a pressure higher than the steam pressure. In the previous part of this study, the mathematical modeling of the SDJP has been done, and reported. The results of the mathematical modeling of the SDJP have been compared with Cattadori's experimental results. The comparisons show that the experimental and calculated pressure distributions are in good qualitative agreement. For the same steam inlet pressure of 8.7 MPa, the discharge pressures in the experiment and in the simulation are 9.8 MPa and 9.54 MPa, respectively. The relative difference is two percent. It can be said that the computed discharge pressure is in good agreement with the experimental result. In the current study, a parametric analysis of the SDJP has been done in terms of four independent parameters: steam inlet pressure and temperature, supply water pressure, and temperature. The output parameters are: discharge pressure, temperature, and mass flow rate. As a result of this parametric study, the operation characteristics of the SDJP have been obtained. [DOI: 10.1115/1.1365935]

1 Introduction

The steam-driven jet pump (SDJP) is an engineering device that consists of a set of converging-diverging nozzles (subsonic and supersonic). It has no moving parts and requires no external energy supply. Because of these passive features of the SDJP, it is very attractive in the design of next generation nuclear power plants. In the past years, several passive safety systems which utilize steam-driven jet pumps (SDJP) as an emergency core cooling system have been proposed for advanced nuclear reactor designs ([1–5]). Recently, Narabayashi et al. [4] and Cattadori et al. [5] have developed a high-pressure steam-driven jet pump to use as a feed water pump in advanced nuclear power plants, and reported that the SDJP could work at high pressures over 7 MPa. In the first part of this study, the mathematical modeling of the SDJP has been done and reported ([6]). A one-dimensional, steady-state model is used in the mathematical modeling. It is assumed that the system is a horizontal, frictionless, adiabatic system. The SDJP has mainly three sections: the steam nozzle, mixing nozzle, and diffuser. The flow in the steam nozzle and diffuser is single-phase steam and liquid, respectively. The flow is two-phase flow in the first part of the mixing nozzle. The governing equations (*mass*, *momentum*, and *energy*) have been written for each section of the SDJP. An iterative finite difference with underrelaxation procedure has been used to solve these equations numerically. In general, the model represents a simplified mathematical treatment of a fairly complex fluid flow, heat transfer, and thermodynamic process.

In this part of the study, the operation characteristics of the SDJP have been investigated using the simulator developed before. There are four independent parameters that are steam pressure, and temperature, and supply water pressure and temperature. The output parameters are discharge water pressure, temperature, and mass flow rate. The effects of the independent parameters on the output parameters have been investigated and are presented in this paper.

2 Design and Operation Principles

Figure 1 shows a schematic view of the steam driven jet pump. All thermodynamics processes in the SDJP rely on direct contact transport phenomena between liquid water and steam. The steam-driven jet pump consists of three longitudinal regions:

- Steam nozzle, consisting of subsonic nozzle and supersonic nozzle sections. It is used to obtain a supersonic steam jet and create low pressure at the inlet section of the mixing nozzle.
- Mixing nozzle, where liquid water and steam come into contact. It has a converging shape. Steam transfers heat to water (because of the temperature difference), mass (because of the related condensation) and momentum (because of the velocity difference).
- Diffuser, where the kinetic energy of the liquid water coming from the mixing nozzle is producing a further pressure increase.

The gap between the steam nozzle exit and the mixing nozzle inlet is called the water nozzle, that is the water inlet section. The water nozzle produces a moderate acceleration and distributing the liquid water all around the steam nozzle exit. The design parameters of the SDJP considered in this study have been taken from the test SDJP that was used in the experiment by Cattadori et al. [5]. Table 1 shows the main design parameters of this test SDJP.

The low-pressure supersonic steam is obtained at the exit of the steam nozzle, and it blows into the cold water in the mixing nozzle. This low-pressure supersonic steam at the exit section of the steam nozzle (i.e., Section c in Fig. 1) creates low-pressure at the inlet of mixing nozzle. The pressure difference between low-pressure at the mixing nozzle inlet and higher pressure in the water supply tank sucks water from a water tank through the water nozzle (Section c in Fig. 1) which distributes the water all around the steam nozzle and gives the water a moderate velocity. As a result of the steam condensation, the supersonic steam kinetic energy is transferred to the water. This accelerates the liquid water coming from the water nozzle in the mixing nozzle into the diffuser throat. Before the throat, the steam is fully condensed, and the water velocity is increased. At the throat, a subsonic flow with a relatively high pressure is obtained. In the diffuser, the

[1]To whom correspondence should be addressed.

Contributed by the Nuclear Division of THE AMERICAN SOCIETY OF MECHANICAL ENGINEERS for publication in the ASME JOURNAL OF ENGINEERING FOR GAS TURBINES AND POWER. Manuscript received by the Nuclear Division, July 1999; final revision received by the ASME Headquarters Jan. 2000. Editor: H. D. Nelson.

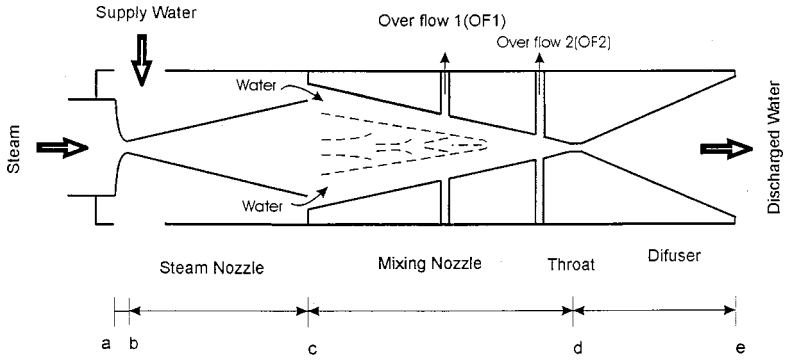

Fig. 1 Schematic view of the steam-driven jet pump

kinetic energy of the water is converted partially to pressure, and then a higher pressure than the steam inlet pressure can be obtained at the exit of diffuser.

As it is seen in Fig. 1, two overflow exit lines are located in the mixing nozzle. The first one is the startup overflow line (OF1). That is, it removes the excess water in the mixing nozzle during the startup of the SDJP only. After the startup, the OF1 line will be always closed. The second overflow line (OF2) is used for the fine control of the discharge mass flow rate and pressure, and it discharges the excess water from the last part of the mixing nozzle during the SDJP operation. The OF2 mass flow rate setting is another parameter that has to be optimized for the operation of the SDJP, especially for the high-pressure operation.

Figure 2 schematically shows the processes of the SDJP on a Mollier diagram. As the steam expands in the steam nozzle (i.e., process a-c), its pressure and temperature drop, and it is expected that the steam starts to condense. However, due to the high velocity, the residence time of the steam in the nozzle is small, and there may not be sufficient time for necessary heat transfer and formation of liquid droplets. As a result of this, the condensation of the steam is delayed for a little while (supersaturated steam state). In the mixing nozzle, since the pressure increases only a little ([4,5]), the process is shown as a constant pressure process (process c-d). The process d-e is the compression process in the diffuser.

Table 1 Main design parameters of the test steam-driven jet pump ([5])

Steam nozzle inlet diameter	60 mm
Steam nozzle throat diameter	22 mm
Steam nozzle outlet diameter	60 mm
Steam nozzle length (total)	400 mm
Water nozzle width	5.2 mm
Mixing nozzle inlet diameter	70.4 mm
Mixing nozzle outlet diameter (throat)	16 mm
Mixing nozzle length	560 mm
Diffuser outlet diameter	72 mm
Diffuser length	340 mm
Total length	1300 mm

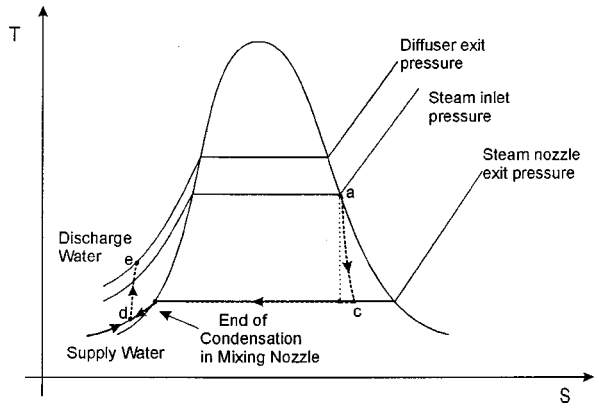

Fig. 2 Mollier diagram representation of the steam-driven jet pump processes

3 Parametric Analysis

The steady-state operation characteristics of the SDJP have been investigated in terms of the four independent parameters which are:

- steam supply pressure,
- steam temperature or superheat,
- supply water pressure (i.e. water tank pressure), and
- supply water temperature.

The main dependent parameters are:

- discharge pressure,
- discharge water temperature, and
- discharge water mass flow rate.

The OF2 mass flow rate setting is another important parameter, and it should be added to these four independent parameters. The range of the independent parameters used in the experiment has been utilized in the parametric analysis. The axial pressure distribution in the SDJP has been computed and compared with experimental data in the previous part of this study ([6]).

Figure 3 shows the discharge pressure variation versus the steam inlet pressure with an optimum OF2 line mass flow rate setting, and comparison with the available experimental data. In the experimental study of Cattadori, they aim to obtain the ten percent higher discharge pressure than the steam inlet pressure. Then, the OF2 mass flow rate was controlled to obtain the ten percent higher discharge pressures in the experiment runs. They have called this OF2 mass flow rate setting as the optimum OF2 setting. In the simulation, the same procedure has been done. The OF2 mass flow rate is adjusted to get the ten percent higher discharge pressure than given steam inlet pressure as in the experiment. As it is seen, the experimental and simulation data look like in good agreement, but the comparisons of the experimental and calculated mass flow rates of the OF2 line give more information to validate to calculation. Since only the range of the experimental mass flow rate (7.2–17.6 kg/s) of the OF2 line is available, it can

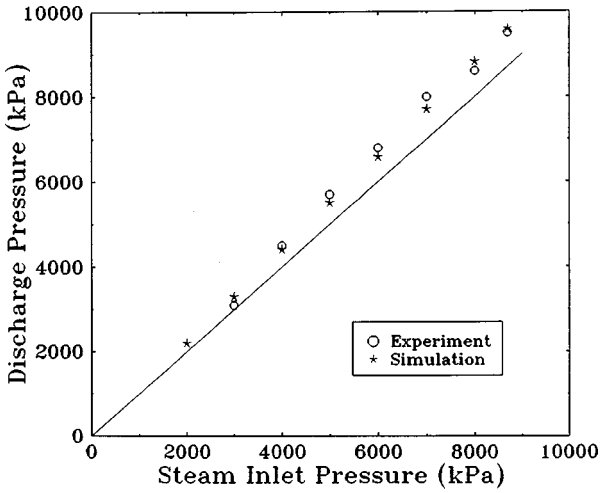

Fig. 3 Discharge pressure versus steam inlet pressure (Steam $T = T_{sat}$, Tank $P = 260$ kPa, Tank $T = 15°C$)

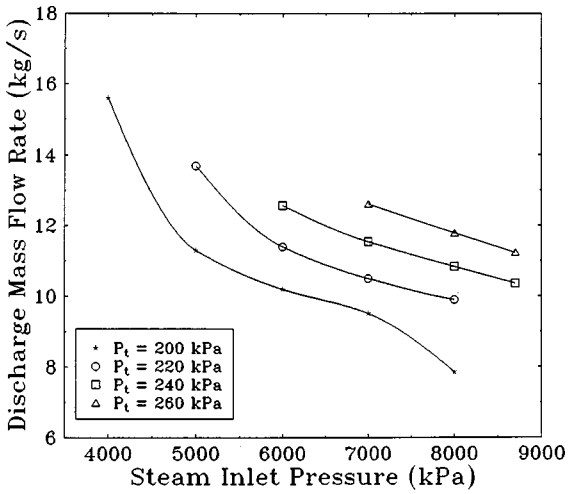

Fig. 5 The discharge mass flow rate versus the steam inlet pressure at the different supply water tank pressure (Tank $T = 15°C$, Steam $T = T_{sat}$)

be checked if the calculated overflow mass flow rate within the experimental range. In the cases of the simulation, the range of the overflow mass flow rate is 1.0–6.5 kg/s (see Fig. 7). Since the steam temperature is taken as saturated steam temperature in the simulation cases, the overflow mass flow rates are obtained lower than experimental range as it is expected.

The variation of the discharge water temperature and discharge water mass flow rate as a function of steam inlet pressure and supply water tank pressure at constant supply water temperature of 15°C are given in Fig. 4 and Fig. 5, respectively. The steam inlet temperature is the corresponding saturation temperature of the steam inlet pressure. When the supply water tank pressure increases, a lower discharge temperature and a higher discharge water mass flow rate are achieved. When the supply water tank pressure increases, the minimum operation steam inlet pressure of the SDJP increases, as well. The steam nozzle outlet pressure decreases if the steam inlet pressure decreases. Then, the pressure difference between water tank and steam nozzle exit will be higher. As a result of this, the supply water mass flow rate increases. The steam cannot accelerate this excess amount of water. Thus, the SDJP cannot be operated at the low steam pressures with a high water tank pressure without controlling the supply water mass flow rate. For example, the lowest steam inlet pressure for operation is 7000 kPa for the tank pressure of 260 kPa. This is the lower bound of the operation range. For the supply tank pressure of 200 and 220 kPa (see Fig. 4), the SDJP cannot work at more than 8000 kPa, because the steam nozzle exit pressure will not be less than the water tank pressure to suck water. It is needed to mention that the back pressure is such that no shocks will occur within or outside the steam nozzle. This phenomenon sets up the upper bound of the operation range. As it seen in Fig. 5, the discharge mass flow rate decreases when the steam inlet pressure increases with a constant water tank pressure. This is due to the pressure gradient between the steam nozzle exit and water tank. In the case of high steam inlet pressure, the steam nozzle exit pressure will be high but less than the water tank pressure. This means the pressure gradient between steam nozzle exit pressure and water tank pressure decreases. Then the amount of water entering to the mixing section decreases. The water flow rate as a function of steam inlet pressure is given in Fig. 6. Of course, the supply water flow rate effects the discharge mass flow rate. As it is seen in Figs. 5 and 6, the supply water flow rate and the discharge flow rate have the same trend. As the supply water pressure increases, the supply water tank and mixing nozzle pressure difference increases, which increases the supply water mass flow rate, and leads to lower discharge temperature.

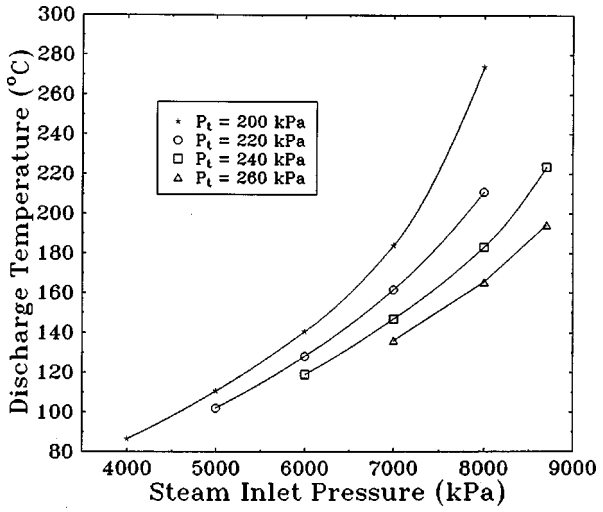

Fig. 4 The discharge temperature versus the steam inlet pressure at the different supply water tank pressure (Tank $T = 15°C$, Steam $T = T_{sat}$)

Figure 7 shows the optimum overflow mass flow rate (i.e., from OF2) for the same operational conditions of Figs. 4, 5, and 6, for various supply water tank pressures. In the operation of the SDJP, some amount of water should be extracted from the OF2 line to obtain desired discharge pressure. As it is mentioned before, the desired discharge pressure is defined as ten percent higher than the steam inlet pressure in the Cattadori's experiment. However, the overflow mass flow rate effects the discharge mass flow rate. Thus, the overflow mass flow rate should be minimum to get high discharge mass flow rate, but it should be at such value that to obtain desired discharge pressure. A valve in the experiment controls the overflow mass flow rate, and the overflow mass flow rate is function of pressure difference between the mixing section pressure at the location of the OF2 line and back pressure of the valve, and opening level of the valve (i.e., valve flow area). In the simulation, the overflow mass flow rate is defined via trial and error. As it is seen in Fig. 7, the overflow mass flow rate decreases while the steam inlet pressure increases for a constant water tank pressure.

The performance of the SDJP can be defined as the ratio of desired output to required input like efficiency of heat engine, or

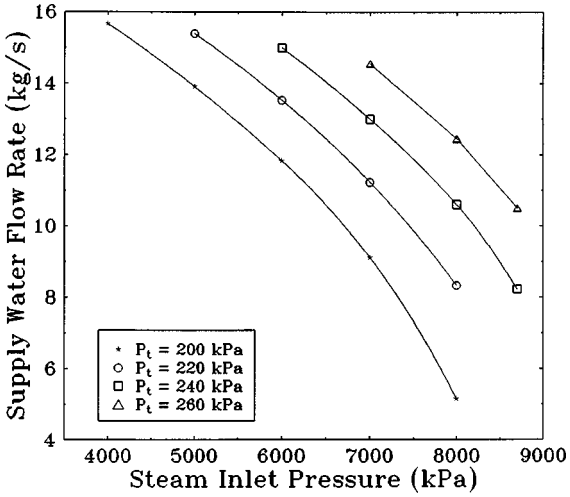

Fig. 6 The supply water mass flow rate versus the steam inlet pressure at the different supply water tank pressure (Tank T = 15°C, Steam $T = T_{sat}$)

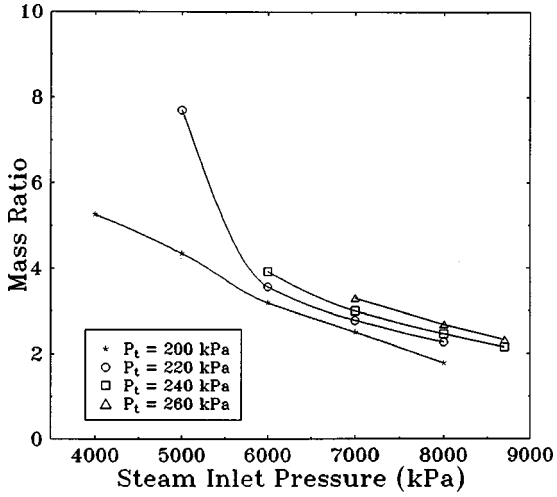

Fig. 8 The mass ratio versus the steam inlet pressure at the different supply water tank pressure (Tank T = 15°C, Steam $T = T_{sat}$)

coefficient of performance of refrigeration or heat pump cycles ([7]). The mass ratio defined as the ratio of the supply water to the steam mass flow rate can be one parameter to show the performance of the SDJP if the desired output is the amount of water to be sucked. It represents the quantity of steam required to suck a given quantity of water. Figure 8 shows the variation of the mass ratio versus inlet steam pressure for various supply water tank pressures. As it is seen in this figure, increasing the supply water pressure increases the mass ratio, and the mass ratio is much sensitive to the supply water pressure at low steam inlet pressures because of the higher pressure differences obtained at the lower inlet steam pressures.

If the desired output is the discharge mass flow rate instead of water mass flow rate to be sucked with a desired discharge pressure, the overflow mass flow rate must be accounted. In that case, the performance parameter is defined as the ratio of discharge mass flow rate (desired output) to steam flow rate (required input). Cattadori et al. has defined as steam rate that is reciprocal of above definition as follows:

$$\text{steamrate} = \frac{\dot{m}_{\text{steam}}}{\dot{m}_{\text{water}} - \dot{m}_{\text{OF2}}}$$

It represents the quantity of steam required to discharge a given quantity of water provided that a desired pressure rise is obtained. In Fig. 9, the steam rate is shown as a function of steam inlet pressures at different values of supply water tank pressure. The OF2 line mass flow rates are minimum values for the desired pressure rise. It can be seen that the amount of steam required is quite low, and it increases with the steam inlet pressure but decreases with the supply water tank pressure.

As mentioned above, the supply water temperature is one of the independent parameters. The effect of the supply water temperature has been investigated as well. Figure 10 shows the variation of the steam rate as a function of steam inlet pressure at different supply water temperatures. The supply water tank pressure is 200 kPa and steam inlet temperature equal to saturation temperature. It is clear that at low steam inlet pressure, an increasing of the supply water temperature does not effect the steam rate because of the high mass flow rate of supply water. At high steam inlet pressures, the supply water mass flow rate decreases and thus the

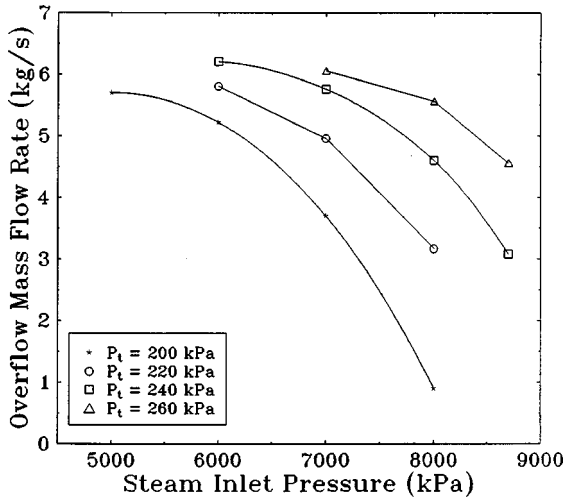

Fig. 7 The overflow mass flow rate versus the steam inlet pressure at the different supply water tank pressure (Tank T = 15°C, Steam $T = T_{sat}$)

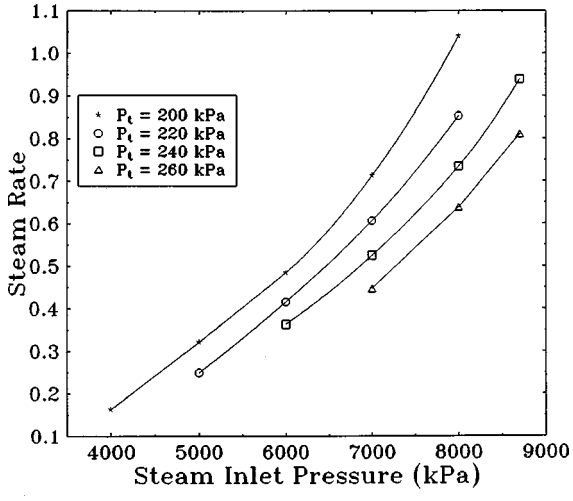

Fig. 9 The steam rate versus the steam inlet pressure at the different supply water tank pressure (Tank T = 15°C, Steam $T = T_{sat}$)

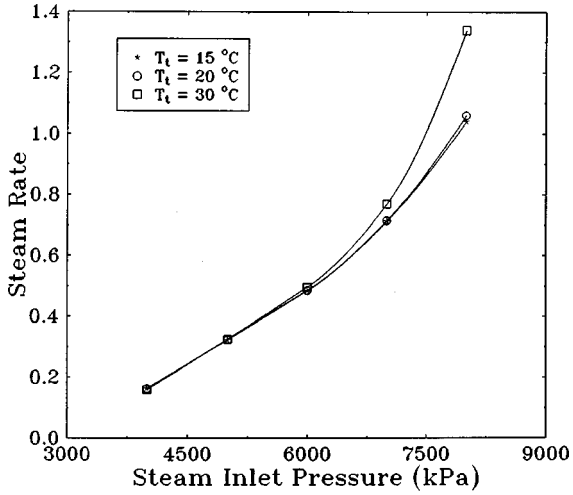

Fig. 10 The steam rate versus the steam inlet pressure at the different supply water tank temperature (Tank $P=200$ kPa, Steam $T=T_{sat}$)

increment in the supply water temperature comes to be important. In general, Fig. 10 shows that increasing the supply water temperature increases the steam consumption, which is the same conclusion achieved by experiment ([5]). By analyzing the other dependent parameters (discharge mass flow rate and temperature) it is found that the effect of increasing the supply water temperature is not much. It increases the discharge temperature and decreases the discharge water mass flow rate, a little. So keeping low supply water temperature is much valuable to be sure of the full condensation of steam.

Figure 11 shows the variation of the discharged temperature and mass flow rate versus the steam inlet temperature for a steam inlet pressure of 8 MPa and supply water tank pressure and temperature of 260 kPa and 15°C, respectively. It shows that increasing the steam inlet temperature decreases the discharge temperature and increases the discharge water mass flow rate. When the steam temperature increases (i.e., superheated steam condition), SDJP needs more water to condense this superheated steam. Then, SDJP is allowed to suck water as much as it can. As a result of this, the discharge mass flow rate increases, and the discharge temperature decreases because of more water less steam.

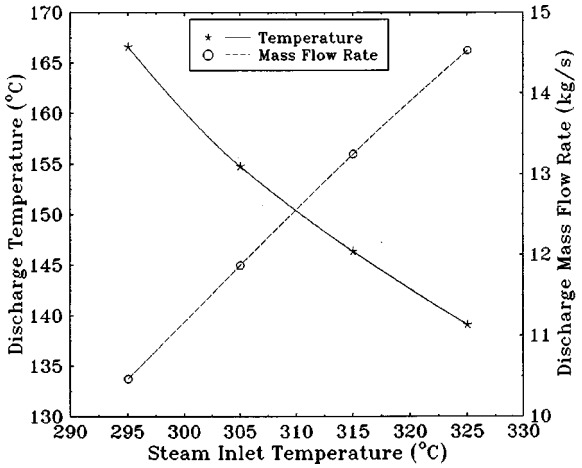

Fig. 11 The discharge temperature and mass flow rate versus the steam inlet temperature (Steam $P=8$ MPa, Tank $P=260$ kPa, Steam $T=15$°C)

4 Conclusions

The mathematical modeling of the steam-driven jet pump has been done before and reported in the previous part of this study ([6]). To validate the results of the SDJP mathematical modeling, the results of Cattadori [5] and co-worker's experiment have been used. In this part of study, the parametric analysis of the SDJP has been done in terms of four independent parameters. As mentioned above, the dependent parameters are the discharge pressure, temperature and mass flow rate. As a result of parametric analysis, the operation characteristics of the SDJP have been obtained. We can summarize the results as following:

- the supply water mass flow rate and the discharge mass flow rate decrease with increasing steam inlet pressure and
- there is an optimum overflow mass flow rate (OF2 line) for the operation of the SDJP for the different steam inlet pressures

Increasing the supply water tank pressure leads to

- decreasing discharge temperature,
- giving higher supply water mass flow rate,
- increasing the water consumption,
- a lower steam rate and higher mass ratio,
- increasing the supply water tank temperature (<30°C) which does not effect much the dependent parameters, and
- increasing the steam inlet temperature that increases the discharge water mass flow rate and decreases the discharged water temperature.

As a conclusion, it is much valuable to operate the SDJP under high steam inlet temperature, high supply water pressure and low water temperature.

From the parametric analysis, it has been noted that there is a fixed operation range for a given SDJP dimension. The SDJP cannot be operated with very high steam inlet pressure and very low supply water pressures. The steam nozzle exit pressure should always be less than water pressure to suck water. In case of very low water pressure, the steam nozzle exit pressure will be equal or higher than the supply water tank pressure even if for very low steam inlet pressure. Thus, the pressure differences between the mixing nozzle and water tank will be either zero or negative in terms of desired flow direction. That is, the SDJP cannot suck water. Another problem is shocks in the inlet of the mixing nozzle. According to Cattadori, it is not desired but shocks may happen there. In that case, the pressure increases in the inlet of mixing nozzle, and this affects the suction of water. The other limit of the SDJP is where the supply water pressure is high and the steam inlet pressure is low. In that case, the pressure difference between the mixing nozzle and water tank will be high. For a constant water nozzle area, a high water mass flow rate will be obtained, and then too much water fills the mixing nozzle. After that, the startup overflow line (OF1) may be required to open again. Higher or lower SDJP operational conditions can be achieved by changing the SDJP dimensions. To determine the optimal dimensions for different SDJP ranges, a dimensional parametric analysis needs to be done which is the subject of a future work.

References

[1] Howard, R. W., 1984, ''Steam Driven Water Injection,'' United States Patent 4.440.719.
[2] Suurman, S., 1986, ''Steam-Driven Injectors Act as Emergency Reactor Feedwater Supply'' Power, **3**, p. 95.
[3] Christensen, R. N., Aldemir, T., and Jayanti, S., 1987, ''An Inherently Safe BWR with A Steam Driven ECCS: Steam Injector'' Energ. Nucl. (Rome), **2**, pp. 30–37.
[4] Narabayashi, T., Miyano, H., Nei, H., Ozaki, O., Mizumachi, W., and Shioiri,

A. 1992, ''Feasibility Study on Steam Injector Driven Jet Pump for Next-Generation Reactor,'' Int. Conference on Advance Nuclear Power Plant, pp. 36.2.1–36.2.7.
[5] Cattadori, G., Galbiati, L., Mazzocchi, L., and Vanini, P., 1995, ''A Single-Stage High Pressure Steam Injector for Next-Generation Reactors: Test Result and Analysis,'' Int. J. Multiphase Flow, **21**, pp. 591–606.
[6] Beithou, N., and Aybar, H. S., 2001, ''High Pressure Steam Driven Jet Pump: Mathematical Modeling,'' ASME J. Eng. Gas Turbines Power, **123**, pp. 693–700.
[7] Cengel, Y. A., and Boles, M. A., (1994), *Thermodynamics: An Engineering Approach*, 2nd Ed., MacGraw-Hill, New York.

Rapid and Accurate Calculation of Water and Steam Properties Using the Tabular Taylor Series Expansion Method

K. Miyagawa
4-12-11-628 Nishiogu,
Arakawa-ku,
Tokyo 116-0011, Japan

P. G. Hill
Department of Mechanical Engineering,
University of British Columbia,
Vancouver V6T 1Z4, Canada

In applications where both speed and accuracy of computation of thermodynamic properties are important and particularly where the independent variables are not those used in Helmholtz equations, direct use of such equations can be excessively time-consuming. This paper introduces the enthalpy-pressure version of the tabular Taylor series (TTSE) method, which has the accuracy and computing speed required for application in power industries. The IAPWS formulation for scientific use, IAPWS-95, was used as the basic Helmholtz equation. The speed and accuracy of the TTSE have been compared with the IAPWS formulation for industrial use, IAPWS-IF97, which has been developed to achieve high-speed calculation with good representation of IAPWS-95 values. Test results show that the TTSE accurately represents the basic equation and that the computation speed is higher than that of IF97. [DOI: 10.1115/1.1367340]

Introduction

The advantage of the tabular Taylor series (TTSE) method is that it enables rapid calculation of thermodynamic properties without any necessary sacrifice of accuracy. The calculations are fast because of the small number of numerical operations required in using a table of stored properties and their derivatives. The stored primitives and derivatives are precisely determined from the basic Helmholtz equation so that the accuracy of the TTSE method depends only on grid spacing of the storage tables.

The objective of this paper is to introduce a new version of TTSE using enthalpy h and pressure p as the independent variables and based on a Helmholtz function whose independent variables are temperature T and density ρ. Previously the method has been demonstrated with pressure and temperature as independent variables for turbine stage-by-stage calculations ([1]). It has also been used with the internal energy and density coordinates appropriate to the Denton three-dimensional time-marching method for the turbine flow field ([2]). In these applications the TTSE method achieves both high speed and high accuracy with modest size of computer memory.

For some applications pressure and temperature are not the best pair of independent variables, especially if temperature is merely an intermediate variable. The TTSE p-T version may require more computational steps than the h-p version. Also the p-T version requires separate grids to cover liquid, vapor, and critical regions. Special grid spacing near the critical point and the saturation line is needed to maintain accuracy. However, with h-p as the independent variable pair, a single grid can cover all regions of water and steam of practical interest.

In this paper the thermodynamic property data sources and range of application of the h-p TTSE method will be defined, as well as the procedure for implementing it in the design of a single grid of states covering liquid, vapor, and critical regions. The results of random access accuracy tests are presented for volume, temperature, entropy, specific heats, speed of sound, and isentropic exponent, all as functions of enthalpy and pressure. Also described are the results of computing speed tests done (in comparison with the IAPWS-IF97 formulation for industrial use) in the contexts of boiler heat surface calculation and turbine expansion calculation.

Thermodynamic Property Source and Range

The basic source of the thermodynamic data used in formulating this version of the TTSE method is the wide-ranging Helmholtz equation included in the IAPWS formulation designated for scientific use ([3,4]). The formulation consists of the main equation, called IAPWS-95, and the supplemental equation, called the GAS equation, for the metastable vapor region.

Figure 1 shows, on the enthalpy-pressure plane, the range of states included: 0 to 4000 kJ/kg in enthalpy and triple point pressure to 100 MPa. The IAPWS-95 formulation covers both single-phase and metastable regions, but it is replaced by the GAS equation in the lower pressure part of the metastable vapor region. The GAS equation connects to IAPWS-95 at the saturation line with little discrepancy. The GAS equation is valid up to 55 kg/m^3 in density, but in this application it is used below 7.4531 MPa.

Shown in Fig. 1 are the experimental data of Evstefeev al. [5] in the metastable liquid region. These data lie between the liquid saturation line as defined by IAPWS-95 and an arbitrary boundary

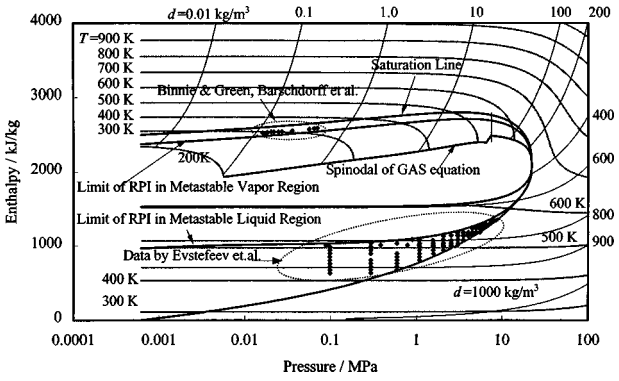

Fig. 1 Enthalpy-pressure chart showing the region of practical interest (RPI)

Contributed by the Power Division of THE AMERICAN SOCIETY OF MECHANICAL ENGINEERS for publication in the ASME JOURNAL OF ENGINEERING FOR GAS TURBINES AND POWER. Manuscript received by the Power Division July, 2000; final revision received by the ASME Headquarters Feb. 2001. Editor: H. D. Nelson.

that we denote as the upper limit of practical interest in the metastable liquid region. It is well below the liquid spinodal of IAPWS-95.

Figure 1 shows data available in the metastable vapor region from nozzle expansions ([6,7]). For these cases the limiting metastable pressures were determined and found to be not strongly dependent on expansion rate. The enthalpy and temperature values were calculated from the assumption of isentropic expansion. In general the data lie somewhat above, but close to, the line denoting five percent equilibrium moisture in these enthalpy and pressure coordinates. This line is accepted as the lowest possible location of the Wilson point and we denote it as the lower limit of practical interest in the metastable vapor region. As Fig. 1 shows, it is well above the vapor spinodal of the basic equations.

In this paper the region of practical interest (RPI) is defined to include the entire range of single-phase states shown in Fig. 1 as well as the metastable states below the upper metastable liquid limit and above the lower metastable vapor limit.

The Tabular Taylor Series Expansion (TTSE) Method

For TTSE calculations of functions of two variables, $z(x,y)$, a grid is chosen composed of rectangular cells on the *x-y* plane. The nodes at which the information on thermodynamic property *z* and its derivatives are stored is located at a point (x_j, y_i), usually the center, of the cell. The Taylor series expansion may be expressed as

$$z = z_{i,j} + (x-x_j)\left(\frac{\partial z}{\partial x}\right)_{i,j} + \frac{1}{2}(x-x_j)^2\left(\frac{\partial^2 z}{\partial x^2}\right)_{i,j} + (y-y_i)\left(\frac{\partial z}{\partial y}\right)_{i,j} + \frac{1}{2}(y-y_i)^2\left(\frac{\partial^2 z}{\partial y^2}\right)_{i,j} + (x-x_j)(y-y_i)\left(\frac{\partial^2 z}{\partial x \partial y}\right)_{i,j} \quad (1)$$

in which the subscripts *i* and *j* represent the locations of cells in the *x-y* plane. It has been found that truncating the Taylor Series expansion to six terms provides high accuracy of property calculation with only modest memory capacity required for storage of the primitive and derivative quantities associated with each node location. The speed of the method is associated with only six coefficients for each property evaluation.

The variables *x* and *y* can be chosen so that they are the arguments of the functions most frequently computed. With enthalpy and pressure as independent coordinates we can use Eq. (1) to calculate $T(p,h)$, $v(p,h)$, and $s(p,h)$ if the appropriate primitive and derivative values are tabulated for cell locations *i* and *j*. Table 1 shows how the appropriate first derivatives of these functions may be obtained directly from the Helmholtz function, which has density and temperature as independent coordinates. The second and cross derivatives appearing in Eq. (1) could also have been obtained in closed form from the Helmholtz equation but it has been much easier to obtain them by a highly precise numerical differentiation.

Table 1 Derivatives of *T*, *v*, and *s*

$$\left(\frac{\partial T}{\partial h}\right)_p = \frac{1}{c_p} \qquad \left(\frac{\partial T}{\partial p}\right)_h = \frac{1}{A}\left(\frac{\partial h}{\partial \rho}\right)_T$$

$$\left(\frac{\partial v}{\partial h}\right)_p = \frac{-1}{A\rho^2}\left(\frac{\partial p}{\partial T}\right)_\rho \qquad \left(\frac{\partial v}{\partial p}\right)_h = \frac{1}{A\rho^2}\left(\frac{\partial h}{\partial T}\right)_\rho$$

$$\left(\frac{\partial s}{\partial h}\right)_p = \frac{1}{T} \qquad \left(\frac{\partial s}{\partial p}\right)_h = \frac{-v}{T}$$

where:

$$A = \left(\frac{\partial p}{\partial T}\right)_\rho \left(\frac{\partial h}{\partial \rho}\right)_T - \left(\frac{\partial p}{\partial \rho}\right)_T \left(\frac{\partial h}{\partial T}\right)_\rho$$

Table 2 Properties derived from the derivatives of basic TTSE functions

$$c_p = 1/\left(\frac{\partial T}{\partial h}\right)_p \qquad w = \sqrt{\frac{v^2}{A}\left(\frac{\partial s}{\partial h}\right)_p}$$

$$c_v = \frac{-AT}{B} \qquad \kappa = \frac{v}{A}\left(\frac{\partial s}{\partial h}\right)_p$$

where:

$$A = \left(\frac{\partial v}{\partial h}\right)_p \left(\frac{\partial s}{\partial p}\right)_h - \left(\frac{\partial v}{\partial p}\right)_h \left(\frac{\partial s}{\partial h}\right)_p$$

$$B = \left(\frac{\partial T}{\partial h}\right)_p \left(\frac{\partial v}{\partial p}\right)_h - \left(\frac{\partial T}{\partial p}\right)_h \left(\frac{\partial v}{\partial h}\right)_p$$

Since derivative quantities such as isobaric specific heat c_p, isochoric specific heat c_v, speed of sound *w*, and isentropic exponent κ are often of importance, it is useful to note that

$$\left(\frac{\partial z}{\partial x}\right)_{x,y} = \left(\frac{\partial z}{\partial x}\right)_{i,j} + (x-x_j)\left(\frac{\partial^2 z}{\partial x^2}\right)_{i,j} + (y-y_i)\left(\frac{\partial^2 z}{\partial x \partial y}\right)_{i,j} . \quad (2)$$

Table 2 shows how specific heats, isentropic exponent and speed of sound can be evaluated using only the derivatives already stored for evaluation of *T*, *v*, and *s*.

Since Eq. (1) is quadratic, the inverse functions, in which *p-T*, *p-s*, and *h-s* are independent variables, can be solved directly. An important feature is that these inverse functions are fully consistent with the forward functions $z(p,h)$.

Grid and Cell Structure

Figure 2 shows the outline of the grid that covers the range of states shown in Fig. 1. The grid lines are shown at every five sections and indexed with an integer *i* in the direction of enthalpy and with another integer *j* in the direction of pressure. Each cell is identified using the indices of the grid lines intersecting at its lower left-hand end corner. Figure 3 shows the detail of the grid around the critical point. The origin of the grid is located at the critical point, where the pressure is 22.064 MPa and the enthalpy is 2084.2563 kJ/kg. The indices $i=104$ and $j=174$ are assigned to the critical point. The spacing of the grid lines in the direction of enthalpy is uniformly 20 kJ/kg. The grid scale in the direction of pressure is a geometric series with the ratio of 1.06215. The minimum and maximum of the indices are 0 and 200 for both *i* and *j*. Thus the grid ranges from 4.26 to 4004.26 kJ/kg and 0.000612 to 105.81 MPa.

The primitives of the temperature *T*, specific volume *v*, entropy *s*, and its derivatives are evaluated at a node point in each cell. As a general rule, the node point is located at the center of the cell, so long as the Helmholtz equation is valid there. At the column $j=173$, and when the center is out of the valid region, the node point is set on the saturation line. In addition at cells where *j*

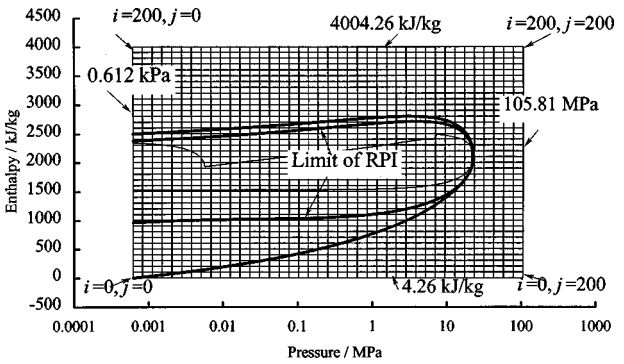

Fig. 2 Outline of 200×200 grid on enthalpy-pressure plane

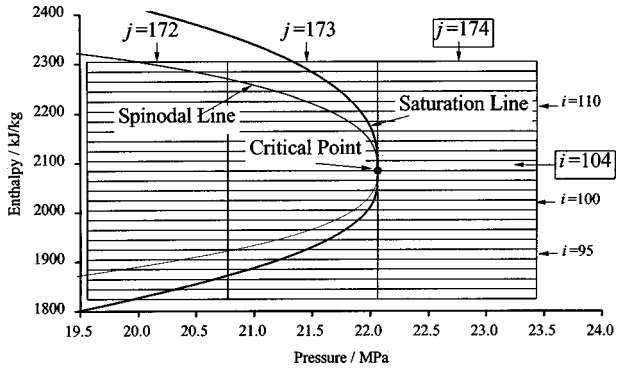

Fig. 3 Grid plan around the critical point

$=172$ and which include the liquid saturation line and their centers are in metastable region, the node point is set on the saturation line. The exceptions are required because if the center is in an invalid region or too far from RPI, evaluation of the primitives and derivatives at the center is invalid.

Then the evaluated values are converted so that the coordinates of the node point x_j and y_i in Eq. (1) and Eq. (2) are shifted to the lowest enthalpy and pressure of the cell. The converted values are used as TTSE coefficients after being stored in single precision and in binary form. Three $6\times200\times200$ arrays include all coefficients needed for the calculation of the properties T, v, and s. The size of the binary file is about 960 kb for each property.

A special rule is required for the cells whose centers are located in the metastable vapor region of the GAS equation and at enthalpies just below the saturation line. If the cell includes the saturation line, the TTSE coefficients are evaluated using IAPWS-95 to preserve accuracy.

For the saturation function $T_{\rm sat}(p)$, a truncated Taylor expansion is applied. With a single dependent variable only three coefficients are required for the primitive and first and second derivatives of temperature with respect to pressure; these have been determined from a subroutine of IAPWS-95. The same pressure scale as for $z(p,h)$ has been used.

Cell Finding Strategy

The time to find the indices of the cell in which the values of the input variables *h-p*, *p-T*, *p-s*, or *h-s* are located is not much smaller than the time for evaluation of the TTSE function itself. Thus an effective search logic is needed. Finding index *i*, for enthalpy, is rather simple since the enthalpy spacing of the grid is uniform. The following FORTRAN statement is sufficiently fast for this purpose.

$$i=\mathrm{MAX}(0,\mathrm{MIN}(199,\mathrm{INT}((h-h0)*rh))$$

Here ''$h0$'' is 4.256263 (kJ/kg) and ''rh'' is 0.05, the inverse of grid spacing 20.0 kJ/kg.

For the pressure index *j* one might use a similar algorithm for the logarithm of the pressure value, but this would take more time than the main calculation of the TTSE. If the function is called with random pressure values, an expanded IF-THEN tree based on the bisection algorithm is the most effective. It takes just eight IF-decisions and these are fast. In practical applications, however, successive pressure values may not differ much from previous ones. In this case, a ''hunt'' algorithm is faster than the IF-THEN tree. In the present work, a special ''hunt'' algorithm has been used. The program first tests the pressure range indicated by the value of *j* found in the last call. If the test fails, it tests the adjacent upper or lower ranges. If the pressure value is within the range of plus or minus two grid spaces, this logic finds the index *j* faster than an IF-THEN tree. Since the spacing of the pressure is about six percent, the range of pressures tested in this way is plus or minus 12 to 18 percent, a range wide enough for many practical applications. If the ''hunt'' fails, *j* is defined by the bisection method. This is much slower than an IF-THEN tree but it does not damage the average computing speed in typical practical applications.

For cell finding with *p-T*, *p-s*, or *h-s*, the ''hunt'' logic is similar except that it is necessary to include the TTSE calculation of $T(p,h)$ or $s(p,h)$. If the ''hunt'' fails, the secant method is used, since the relation between the indices and T or s is not far from linear and the secant method is much faster than bisection.

Accuracy Tests

The deviation of TTSE property values from the basic equation is always zero at node points. The deviation evaluated at any point in the cell increases almost proportionally to the cube of the distance from the point to the node. The maximum deviation appears at one of the corners of the cell. The deviations at opposite corners are almost equal in absolute values and have different sign. Since the same holds for the surrounding cells, there is discontinuity at cell boundaries of about double the maximum deviation. This could cause a problem if, in a given practical application, the TTSE values were being used in numerical differentiation; the problem is, however, avoidable by using proper spacing in the numerical differentiation [1].

As seen in Eq. (1), the TTSE method assumes that the surface is parabolic overlaid with linear twist. The deviations will be particularly large at strong curvatures, such as near a spinodal line. However, as shown by Fig. 1, this region is well outside the RPI.

In 1997 IAPWS adopted the ''IAPWS Industrial Formulation 1997 for the Thermodynamic Properties of Water and Steam (IF97)'' ([8,9]). The IF97 is a good reference for comparison with the TTSE *h-p* version, since both are based on the same basic

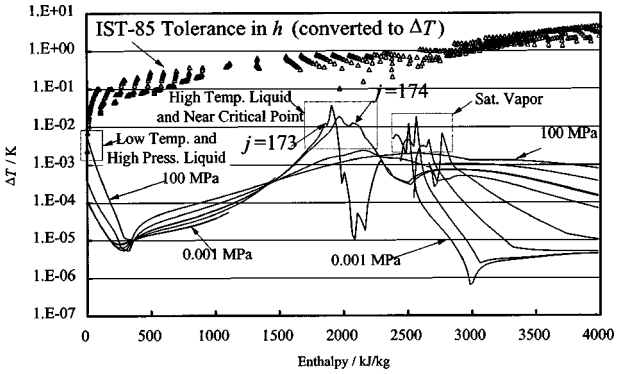

Fig. 4 Deviation from the basic equation in *T*, with IST-85 tolerances

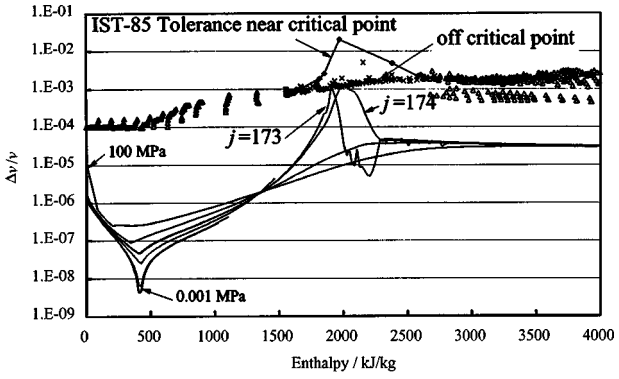

Fig. 5 Deviation from the basic equation in *v*, with IST-85 tolerances

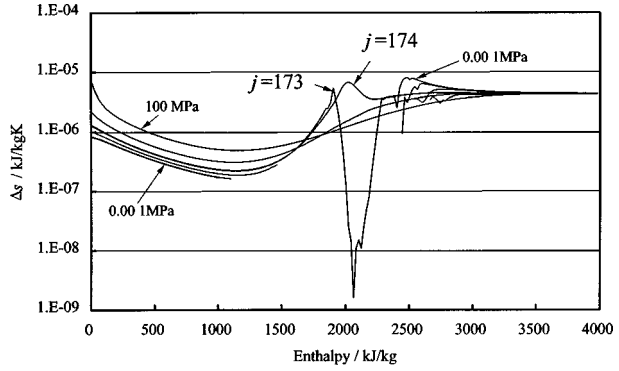

Fig. 6 Deviation from the basic equation in *s*

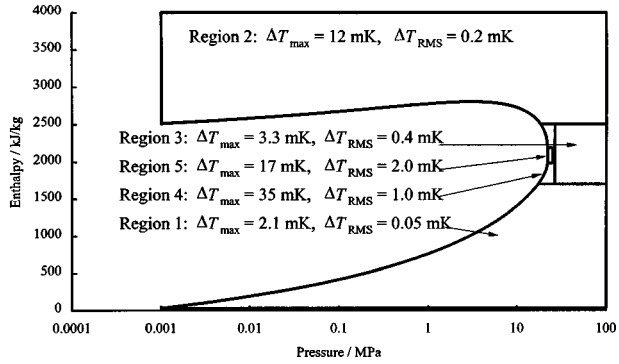

Fig. 7 Test regions for random access test, with the results for deviations in *T*

formulation. The accuracy requirement for IF97 was to reproduce IAPWS-95 v and h values within the tolerances shown in ''International Skeleton Tables (IST-85)'' ([10]). The deviations in T are not specified in IST-85, but equivalent temperature tolerances can be calculated from the tolerances in h by using the values of c_p at the pressures and temperatures of the grid points of the skeleton table where the tolerances are specified.

Accuracy of Functions $T(p,h)$, $v(p,h)$, and $s(p,h)$. The maximum deviations were tested for all cells. Figures 4, 5, and 6 show the results of the tests in RPI at selected values of column index j. Figures 4 and 5 also include the plots of IST-85 tolerances at all grid points in the range of this version. Some lines are labeled with approximate pressure values. The lines labeled ''$j=174$'' and ''$j=173$'' show the deviation at the column $j=174$ and $j=173$, which are just below and just above the critical point. Because the deviations in this test were so low they were evaluated with double precision (even though as noted earlier the TTSE coefficients are stored in single precision).

In Fig. 4, there are three zones where the deviation of $T(p,h)$ exceeds 2 mK. The maximum deviation, 37.2 mK, appears at $j=173$ and slightly below the critical point.

Random Access Test of Functions $T(p,h)$, $v(p,h)$, and $s(p,h)$. Tests of deviation at random p-h inputs in single-phase states were separately performed for the five regions defined as follows and shown in Fig. 7. The tests were performed with single-precision calculations.

Region 1: $p=0.001$ to 100 MPa, $h=30$ to 1700 kJ/kg
Region 2: $p=0.001$ to 100 MPa, $h=2500$ to 4000 kJ/kg
Region 3: $p=26.465$ to 100 MPa, $h=1700$ to 2500 kJ/kg
Region 4: $p=19$ to 26.465 MPa, $h=1700$ to 2500 kJ/kg, except Region 5
Region 5: $p=20.766$ to 24.908 MPa, $h=1984.2563$ to 2184.2563 kJ/kg
Note: Region 5 includes 30 cells ($j=173$ to 175, $i=99$ to 108) near the critical point.

Deviations from the basic equation were calculated using random inputs with uniform distribution in $\log(p)$ and h. The number of test points is 300,000 for each region. The deviation results for $T(p,h)$ are shown for each region in Fig. 7. The maximum and root-mean-square of deviations are listed in Table 3.

From the results of accuracy tests and random access tests, it is concluded that the TTSE represents IAPWS-95 values much better than the specification for IF97.

Random Access Test of Functions $c_p(p,h)$, $c_v(p,h)$, $w(p,h)$, and $\kappa(p,h)$. Table 4 shows the results of 300,000 random access tests for the properties related to the second derivatives, i.e., $c_p(p,h)$, $c_v(p,h)$, $w(p,h)$, and $\kappa(p,h)$. In Regions 1, 2, and 3, the deviations are less than 1.5 percent and thus acceptable in practical applications. In Regions 4 and 5, the maximum deviations are not small. If higher accuracy is required for these quantities, a locally finer grid could be used. Since the residual error of the Eq. (2) is proportional to the square of the distance from the node point, halving the spacing of the p-h grid would

Table 3 Deviation of TTSE from IAPWS-95 (300,000 random access test)

	ΔT / mK		Δv / relative		Δs / J/kgK	
	Max.	RMS	Max.	RMS	Max.	RMS
Region 1	2.1	0.05	2.8×10^{-5}	3.4×10^{-7}	0.0037	0.0003
Region 2	12	0.2	4.1×10^{-5}	1.1×10^{-5}	0.0087	0.0018
Region 3	3.3	0.4	7.0×10^{-5}	2.8×10^{-6}	0.0040	0.0005
Region 4	35	1.0	1.1×10^{-3}	3.3×10^{-5}	0.0048	0.0007
Region 5	17	2.0	1.2×10^{-3}	1.5×10^{-4}	0.0068	0.0011

Table 4 Deviation of TTSE from IAPWS-95 (c_p, c_v, w, and κ)

	Δc_p / relative		Δc_v / relative		Δw / relative		$\Delta\kappa$ / relative	
	Max.	RMS	Max.	RMS	Max.	RMS	Max.	RMS
Region 1	4.0×10^{-3}	5.9×10^{-5}	3.2×10^{-3}	5.6×10^{-5}	6.6×10^{-3}	1.5×10^{-4}	1.3×10^{-2}	2.9×10^{-4}
Region 2	6.6×10^{-3}	1.3×10^{-4}	8.0×10^{-3}	2.6×10^{-4}	2.6×10^{-3}	6.9×10^{-4}	5.3×10^{-3}	1.4×10^{-3}
Region 3	1.2×10^{-2}	4.3×10^{-4}	5.4×10^{-3}	5.6×10^{-4}	7.3×10^{-3}	9.0×10^{-4}	1.5×10^{-2}	1.8×10^{-3}
Region 4	9.6×10^{-2}	4.6×10^{-3}	1.1×10^{-1}	4.4×10^{-3}	1.1×10^{-1}	4.2×10^{-3}	2.4×10^{-1}	8.6×10^{-3}
Region 5	$8.3\times10^{+4}$	$4.1\times10^{+3}$	4.7×10^{-1}	2.4×10^{-2}	3.7×10^{-1}	1.4×10^{-2}	8.7×10^{-1}	3.0×10^{-2}

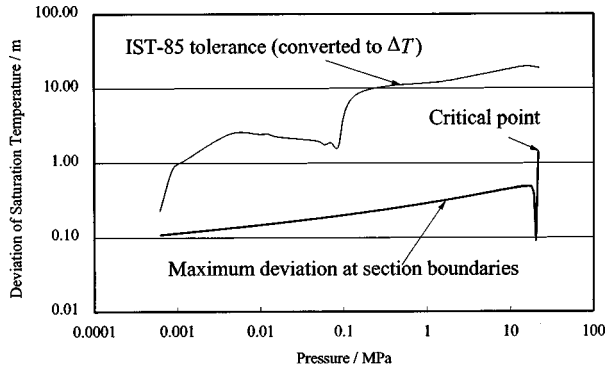

Fig. 8 Deviation from the basic equation in T_{sat} with IST-85 tolerances

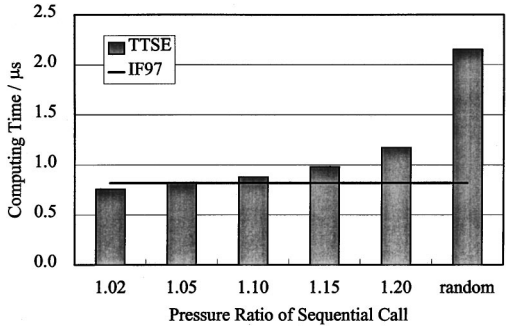

Fig. 10 Computing time for $h(p,T)$

reduce the deviation by a factor of 4. The resulting increase in memory size would not be significant because only 240 cells are included in the affected region.

The specification for IF97 specified that c_p and w should represent the values from IAPWS-95 to within plus and minus 1 percent except for the range very near the critical point where larger deviations were allowed. The accuracy of TTSE meets this specification.

Accuracy of Function for Saturation Temperature $T_{sat}(p)$. Figure 8 shows the absolute values of maximum deviation at section boundaries and, for comparison, the IST-85 tolerance is also seen. The conformity to the basic equation is excellent.

Computing Speed

Reference Code and Test Platform. The computing speeds of TTSE functions were compared with IF97. The FORTRAN codes in ''ASME Steam Properties for Industrial Use Based on IAPWS-IF97, Professional Version'' ([11]) were used as the reference for the speed test. The basic routines of the ASME codes are based on the codes developed by IAPWS Task Group for New Industrial Formulation. The routines have been optimized to achieve highest speed. ASME developed several additional routines, which also have been well optimized in speed. ASME IF97 is therefore a good reference against which to compare the speed of TTSE. The specification of the test platform is as follows:

Compiler: Microsoft FORTRAN Power Station Version 4.0
Computer: PC/AT with Pentium II/450MHz
Operation system: Windows 95
Kind of executable file: Console program in DOS window

Computing Time of Functions $T(p,h)$ and $h(p,T)$. The computing time of the TTSE function $T(p,h)$ was compared with that of the ASME IF97 basic routine $T(p,h)$ for the superheated steam region. This latter routine also calculates $T(p,h)$ without iteration. As the codes of the TTSE functions were optimized for sequential call in pressure, the computing time is dependent on the sequence of pressure values. To see its effect, tests were performed using a sequential pressure series with pressure ratios 1.02, 1.05, 1.10, 1.15, and 1.20. Random access was also tested. The test results are shown in Fig. 9. The TTSE calculates faster than IF97 when called with pressure values within a distance of 15 percent from previous call. Even in case of random access, the time is not very much longer than with IF97.

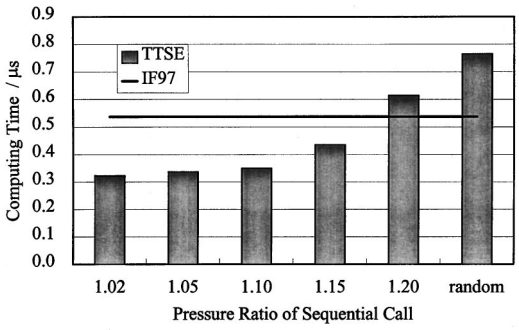

Fig. 9 Computing time for $T(p,h)$

The computing time of $h(p,T)$ was compared with that of the ASME IF97 basic routine $h(p,T)$ for the superheated steam region, which also calculates without iteration. The inverse TTSE function $h(p,T)$ includes a square root process, which takes longer than the calculation of the polynomial of Eq. (1). The test results are shown in Fig. 10. The speed is lower than the forward function but not very much slower than the corresponding IF97 routine.

Simulation of Boiler Heat Surface Calculation. Thermodynamic property evaluation in boiler heat surface design programs is associated with repetition of the following steps:

enthalpy input from a heat transfer routine
pressure input from a pressure drop routine
incremental enthalpy addition at each element of heating surface
evaluation of T and v using new value of h and p
feedback of T and v to heat transfer routine and pressure drop routine

Thus, the functions required in the thermodynamic property routine are just $T(p,h)$ and $v(p,h)$, which are the fastest TTSE functions. As the pressure remains within a small region in the whole boiler calculation, the ''hunt'' logic is very effective. The corresponding IF97 calculation is not simple because the state path crosses the boundaries of the IF97 regions. The calculation starts from Region 1, crosses Region 3, and ends in Region 2. At every call a region test is required to find the appropriate function. The function in Region 3 is a Helmholtz equation. No shortcut function $z(p,h)$ provided in this region and a time-consuming two-dimensional iterative process is required. The following pertain to the model calculation.

Number of heating surface blocks: 50
Enthalpy increment at each block: 48 kJ/kg
Temperature at the inlet of the boiler: 520 K
Pressure at the inlet of the boiler: 28 MPa
Pressure loss in each block: 0.06 MPa
Note: About 40 percent of the calculation points are located in the Region 3 of IF97.

The computing time for 51 calculation points was 0.025 ms for TTSE and 10.1 ms for ASME IF97 code. Here the TTSE method is 400 times faster than IF97.

Simulation of Turbine Expansion Calculation. The computing time for a turbine expansion calculation was performed with the following model:

number of stages: 50
inlet temperature: 870 K
inlet pressure: 25 MPa
pressure ratio in each stage: 0.968
exhaust pressure: approx. 4.92 MPa
internal efficiency η: 0.9

The calculation steps in a stage are as follows in IF97. As all calculation points are in IF97 Region 2, no region test is required.

$T_1 = T(p_1, h_1)$ starting temperature
$s_1 = s(p_1, T_1)$ starting entropy
$T_{ad} = T(p_2, s_1)$ temperature at end of adiabatic expansion
$h_{ad} = h(p_2, T_{ad})$ adiabatic end point enthalpy
$h_2 = h_1 - \eta(h_1 - h_{ad})$ end point enthalpy

With the TTSE method, two computing steps are saved by using p and h as the independent variables.

$s_1 = s(p_1, h_1)$ starting entropy
$h_{ad} = h(p_2, s_1)$ adiabatic end point enthalpy
$h_2 = h_1 - \eta(h_1 - h_{ad})$ end point enthalpy

The computing time was 0.052 ms for TTSE and 0.223 ms for ASME IF97 code. Here the TTSE method is 4.3 times faster than IF97.

Conclusions

1 A new version of the tabular Taylor series expansion (TTSE) method has been developed for fast and accurate calculation of the thermodynamic properties of water and steam, based on IAPWS-95 and (for the metastable vapor states) the GAS equation.

2 With pressure and enthalpy as independent variables a single table requiring under 3 Mb of memory contains all of the coefficients necessary for computation of volumes, temperatures, entropy, specific heats, isentropic exponent, and speed of sound within the region of practical interest (RPI) defined in Fig. 1. As well as single-phase vapor and liquid states the RPI includes the metastable liquid and vapor metastable states defined in Fig. 1.

3 The accuracy of the method has been demonstrated by 300,000 random access tests in which seven properties were calculated and compared with IAPWS-95 (or the GAS equation as appropriate). The pressure-enthalpy version of the TTSE represents IAPWS-95 much better than the accuracy specification of IF97 or at least (for specific heats, isentropic exponent, and speed of sound) satisfies the IF97 specification.

4 The speed of calculation has been compared with that of ASME IF97. For the IF97 function $T(p,h)$ developed for the superheated region the corresponding TTSE calculation is faster or not much slower than the special purpose IF97 routine. In a boiler surface heat transfer application the TTSE method has been shown to be 400 times faster than the IF97. In a turbine stage-by-stage application the TTSE method has been shown to be 4.3 times faster than IF97.

References

[1] Miyagawa, K., and Hill, P. G., 1997, ''A Tabular Taylor Series Expansion Method for Fast Calculation of Steam Properties,'' ASME J. Eng. Gas Turbines Power, **119**, pp. 485–491.
[2] Hill, P. G., Miyagawa, K., and Denton, J. D., 2001, ''Fast and Accurate Inclusion of Steam Properties in Two- and Three-Dimensional CFD Calculations,'' J. Mech. Eng. Sci., accepted for publication.
[3] International Association for the Properties of Water and Steam, 2001, ''IAPWS Formulation 1995 for the Thermodynamic Properties of Ordinary Water Substance for General and Scientific Use,''IAPWS Release.
[4] Wagner, W., and Pruß, A., 2001, ''The IAPWS Formulation 1995 for the Thermodynamic Properties of Ordinary Water Substance for General and Scientific Use,'' J. Phys. Chem. Ref. Data, **30**.
[5] Sato, H., Watanabe, K., Levelt Sengers, J. M. H., Gallagher, J. S., Hill, P. G., Straub, J., and Wagner, W., 1991, ''Sixteen Thousand Evaluated Experimental Thermodynamic Property Data for Water and Steam,'' J. Phys. Chem. Ref. Data, **20**, pp. 1023–1044.
[6] Binnie, A. M., and Green, J. R., 1943, ''An Electrical Detector of Condensation in High Velocity Steam,'' Proc. R. Soc. London, Ser. A, **181**, p. 134.
[7] Barschdorff, D., Haussmann, G., and Ludwig A., 1976, ''Flow and Drop Size Investigations of Wet Steam at Sub- and Supersonic Velocities with the Theory of Homogeneous Condensation,'' Polska Akademia Nauk. Prace Instituta Maszyn Przeplywowych (Translations of the *Institute of Fluid-Flow Machinery*), No. 70–72, 241–256.
[8] International Association for the Properties of Water and Steam, 1997, ''IAPWS Industrial Formulation 1997 for the Thermodynamic Properties of Water and Steam,'' IAPWS release.
[9] Wagner, W., Cooper, J. R., Dittmann, A., Kijima, J., Kretzschmar, H.-J., Kruse, A., Mareš, R., Oguchi, K., Sato, H., Stöcker, I., Šifner, O., Tanishita, I., Trübenbach, J., and Willkommen, Th., 1997, ''The IAPWS Industrial Formulation 1997 for the Thermodynamic Properties of Water and Steam,'' ASME J. Eng. Gas Turbines Power, **122**, pp. 150–182.
[10] International Association for the Properties of Water and Steam, 1985, ''Skeleton Tables 1985 for the Thermodynamic Properties of Ordinary Water Substance,'' IAPWS Release.
[11] ASME, 1999, *ASME Steam Properties for Industrial Use Based on IAPWS-IF97 Professional Version*, ASME Press, New York.